frontiers | Research Topics

Use of cancer imaging in assessing glioma patients

Edited by
Tone Frost Bathen

Published in
Frontiers in Oncology

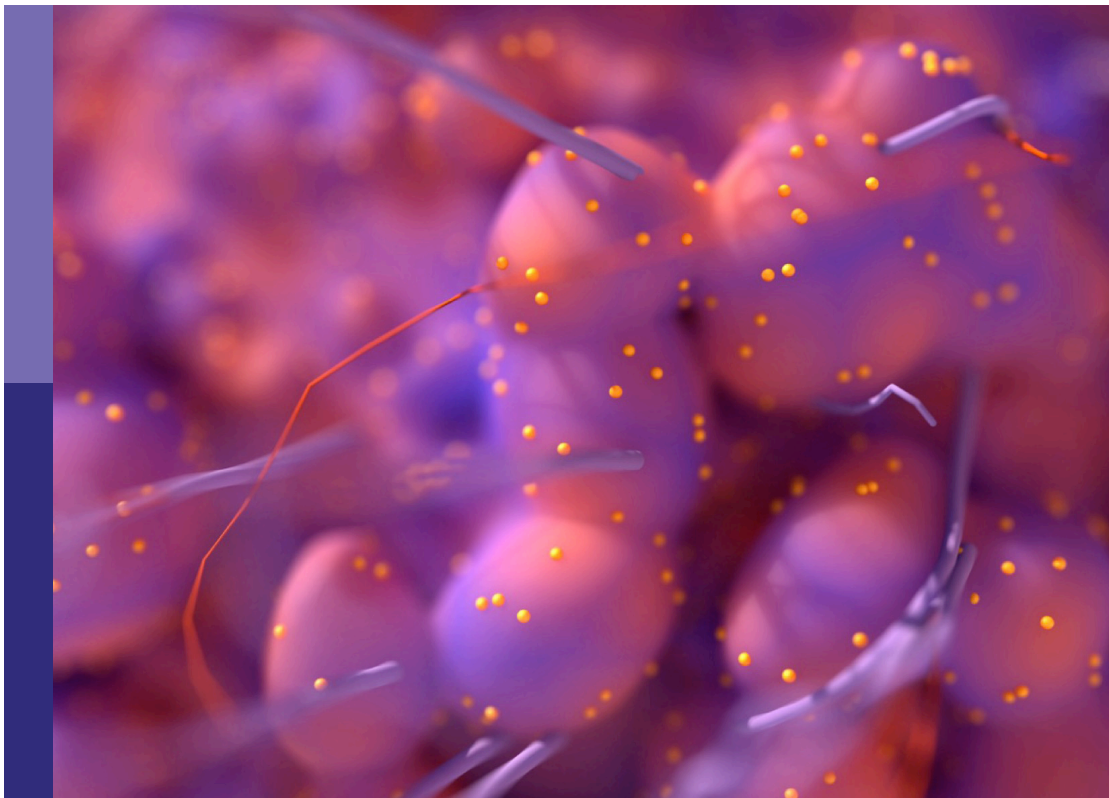

ISSN 1664-8714
ISBN 978-2-8325-2555-5
DOI 10.3389/978-2-8325-2555-5

About Frontiers

Frontiers is more than just an open access publisher of scholarly articles: it is a pioneering approach to the world of academia, radically improving the way scholarly research is managed. The grand vision of Frontiers is a world where all people have an equal opportunity to seek, share and generate knowledge. Frontiers provides immediate and permanent online open access to all its publications, but this alone is not enough to realize our grand goals.

Frontiers journal series

The Frontiers journal series is a multi-tier and interdisciplinary set of open-access, online journals, promising a paradigm shift from the current review, selection and dissemination processes in academic publishing. All Frontiers journals are driven by researchers for researchers; therefore, they constitute a service to the scholarly community. At the same time, the *Frontiers journal series* operates on a revolutionary invention, the tiered publishing system, initially addressing specific communities of scholars, and gradually climbing up to broader public understanding, thus serving the interests of the lay society, too.

Dedication to quality

Each Frontiers article is a landmark of the highest quality, thanks to genuinely collaborative interactions between authors and review editors, who include some of the world's best academicians. Research must be certified by peers before entering a stream of knowledge that may eventually reach the public - and shape society; therefore, Frontiers only applies the most rigorous and unbiased reviews. Frontiers revolutionizes research publishing by freely delivering the most outstanding research, evaluated with no bias from both the academic and social point of view. By applying the most advanced information technologies, Frontiers is catapulting scholarly publishing into a new generation.

What are Frontiers Research Topics?

Frontiers Research Topics are very popular trademarks of the *Frontiers journals series*: they are collections of at least ten articles, all centered on a particular subject. With their unique mix of varied contributions from Original Research to Review Articles, Frontiers Research Topics unify the most influential researchers, the latest key findings and historical advances in a hot research area.

Find out more on how to host your own Frontiers Research Topic or contribute to one as an author by contacting the Frontiers editorial office: frontiersin.org/about/contact

Use of cancer imaging in assessing glioma patients

Topic editor
Tone Frost Bathen — Norwegian University of Science and Technology, Norway

Citation
Bathen, T. F., ed. (2023). *Use of cancer imaging in assessing glioma patients*. Lausanne: Frontiers Media SA. doi: 10.3389/978-2-8325-2555-5

Table of contents

05 Assessment of Overall Survival in Glioma Patients as Predicted by Metabolomic Criteria
María L. Gandía-González, Sebastián Cerdán, Laura Barrios, Pilar López-Larrubia, Pablo G. Feijoó, Alexis Palpan Jr., José M. Roda and Juan Solivera

16 A Critical Appraisal of the Quality of Glioma Imaging Guidelines Using the AGREE II Tool: A EuroAIM Initiative
Valeria Romeo, Arnaldo Stanzione, Lorenzo Ugga, Renato Cuocolo, Sirio Cocozza, Evangelia Ioannidou, Arturo Brunetti and Sotirios Bisdas

24 Diffusion Tensor Imaging Reveals Microstructural Heterogeneity of Normal-Appearing White Matter and Related Cognitive Dysfunction in Glioma Patients
Kerstin Jütten, Verena Mainz, Siegfried Gauggel, Harshal Jayeshkumar Patel, Ferdinand Binkofski, Martin Wiesmann, Hans Clusmann and Chuh-Hyoun Na

35 A Non-invasive Radiomic Method Using ^{18}F-FDG PET Predicts Isocitrate Dehydrogenase Genotype and Prognosis in Patients With Glioma
Longfei Li, Wei Mu, Yaning Wang, Zhenyu Liu, Zehua Liu, Yu Wang, Wenbin Ma, Ziren Kong, Shuo Wang, Xuezhi Zhou, Wei Wei, Xin Cheng, Yusong Lin and Jie Tian

46 Histogram Analysis of Diffusion Weighted Imaging in Low-Grade Gliomas: *in vivo* Characterization of Tumor Architecture and Corresponding Neuropathology
Georg Alexander Gihr, Diana Horvath-Rizea, Elena Hekeler, Oliver Ganslandt, Hans Henkes, Karl-Titus Hoffmann, Cordula Scherlach and Stefan Schob

55 Predicting the Type of Tumor-Related Epilepsy in Patients With Low-Grade Gliomas: A Radiomics Study
Yinyan Wang, Wei Wei, Zhenyu Liu, Yuchao Liang, Xing Liu, Yiming Li, Zhenchao Tang, Tao Jiang and Jie Tian

63 Radiomics Features Predict CIC Mutation Status in Lower Grade Glioma
Luyuan Zhang, Felipe Giuste, Juan C. Vizcarra, Xuejun Li and David Gutman

79 Radiomics Analysis of Postoperative Epilepsy Seizures in Low-Grade Gliomas Using Preoperative MR Images
Kai Sun, Zhenyu Liu, Yiming Li, Lei Wang, Zhenchao Tang, Shuo Wang, Xuezhi Zhou, Lizhi Shao, Caixia Sun, Xing Liu, Tao Jiang, Yinyan Wang and Jie Tian

87 AUCseg: An Automatically Unsupervised Clustering Toolbox for 3D-Segmentation of High-Grade Gliomas in Multi-Parametric MR Images
Botao Zhao, Yan Ren, Ziqi Yu, Jinhua Yu, Tingying Peng and Xiao-Yong Zhang

95 Multiparametric MRI Radiomics for the Early Prediction of Response to Chemoradiotherapy in Patients With Postoperative Residual Gliomas: An Initial Study
Zhaotao Zhang, Keng He, Zhenhua Wang, Youming Zhang, Di Wu, Lei Zeng, Junjie Zeng, Yinquan Ye, Taifu Gu and Xinlan Xiao

105 Imaging Biomarkers of Glioblastoma Treatment Response: A Systematic Review and Meta-Analysis of Recent Machine Learning Studies
Thomas C. Booth, Mariusz Grzeda, Alysha Chelliah, Andrei Roman, Ayisha Al Busaidi, Carmen Dragos, Haris Shuaib, Aysha Luis, Ayesha Mirchandani, Burcu Alparslan, Nina Mansoor, Jose Lavrador, Francesco Vergani, Keyoumars Ashkan, Marc Modat and Sebastien Ourselin

122 The Role of 3D-pCASL MRI in the Differential Diagnosis of Glioblastoma and Brain Metastases
Kristina Solozhentseva, Artem Batalov, Natalia Zakharova, Sergey Goryaynov, Eduard Pogosbekyan and Igor Pronin

132 Preoperative and Noninvasive Prediction of Gliomas Histopathological Grades and IDH Molecular Types Using Multiple MRI Characteristics
Ningfang Du, Xiaotao Zhou, Renling Mao, Weiquan Shu, Li Xiao, Yao Ye, Xinxin Xu, Yilang Shen, Guangwu Lin, Xuhao Fang and Shihong Li

144 Contrast-enhanced ultrasonography for differential diagnosis of adnexal masses
Weihui Shentu, Yin Zhang, Jiaojiao Gu, Fa Wang, Wei Zhao, Chunmei Liu, Zimei Lin, Yao Wang, Chen Liu, Yunyu Chen, Qiyun Fan and Hongying Wang

153 The combination of radiomics features and VASARI standard to predict glioma grade
Wei You, Yitao Mao, Xiao Jiao, Dongcui Wang, Jianling Liu, Peng Lei and Weihua Liao

frontiers in Oncology

ORIGINAL RESEARCH
published: 10 May 2019
doi: 10.3389/fonc.2019.00328

Assessment of Overall Survival in Glioma Patients as Predicted by Metabolomic Criteria

María L. Gandía-González[1], Sebastián Cerdán[2], Laura Barrios[3], Pilar López-Larrubia[2], Pablo G. Feijoó[1], Alexis Palpan Jr.[1], José M. Roda[1] and Juan Solivera[4]*

[1] Department of Neurosurgery, Hospital Universitario La Paz, Madrid, Spain, [2] Institute of Biomedical Research "Alberto Sols" CSIC/UAM, Madrid, Spain, [3] Department of Statistics CSIC, Madrid, Spain, [4] Department of Neurosurgery, University Hospital Reina Sofía, Córdoba, Spain

Objective: We assess the efficacy of the metabolomic profile from glioma biopsies in providing estimates of postsurgical Overall Survival in glioma patients.

Methods: Tumor biopsies from 46 patients bearing gliomas, obtained neurosurgically in the period 1992–1998, were analyzed by high resolution ^{1}H magnetic resonance spectroscopy (HR- ^{1}H MRS), following retrospectively individual postsurgical Overall Survival up to 720 weeks.

Results: The Overall Survival profile could be resolved in three groups; Short (shorter than 52 weeks, $n = 19$), Intermediate (between 53 and 364 weeks, $n = 19$) or Long (longer than 365 weeks, $n = 8$), respectively. Classical histopathological analysis assigned WHO grades II–IV to every biopsy but notably, some patients with low grade glioma depicted unexpectedly Short Overall Survival, while some patients with high grade glioma, presented unpredictably Long Overall Survival. To explore the reasons underlying these different responses, we analyzed HR-^{1}H MRS spectra from acid extracts of the same biopsies, to characterize the metabolite patterns associated to OS predictions. Poor prognosis was found in biopsies with higher contents of alanine, acetate, glutamate, total choline, phosphorylcholine, and glycine, while more favorable prognosis was achieved in biopsies with larger contents of total creatine, glycerol-phosphorylcholine, and myo-inositol. We then implemented a multivariate analysis to identify hierarchically the influence of metabolomic biomarkers on OS predictions, using a Classification Regression Tree (CRT) approach. The CRT based in metabolomic biomarkers grew up to three branches and split into eight nodes, predicting correctly the outcome of 94.7% of the patients in the Short Overall Survival group, 78.9% of the patients in the Intermediate Overall Survival group, and 75% of the patients in the Long Overall Survival group, respectively.

Conclusion: Present results indicate that metabolic profiling by HR-^{1}H MRS improves the Overall Survival predictions derived exclusively from classical histopathological gradings, thus favoring more precise therapeutic decisions.

Keywords: classification decision tree, glioma, metabolomic profile, high resolution proton magnetic resonance spectroscopy, overall survival

OPEN ACCESS

Edited by:
Bo Gao,
Affiliated Hospital of Guizhou Medical University, China

Reviewed by:
Bihong T. Chen,
City of Hope National Medical Center, United States
Ru Jia Wang,
Tangshan Gongren Hospital, China

****Correspondence:***
María L. Gandía-González
marisagg4@hotmail.com

Specialty section:
This article was submitted to Cancer Imaging and Image-directed Interventions, a section of the journal Frontiers in Oncology

Received: *13 February 2019*
Accepted: *11 April 2019*
Published: *10 May 2019*

Citation:
Gandía-González ML, Cerdán S, Barrios L, López-Larrubia P, Feijoó PG, Palpan A Jr, Roda JM and Solivera J (2019) Assessment of Overall Survival in Glioma Patients as Predicted by Metabolomic Criteria. Front. Oncol. 9:328. doi: 10.3389/fonc.2019.00328

INTRODUCTION

Gliomas are the most frequent primary brain tumors, currently managed through surgical resection, radiotherapy, and chemotherapy (1) approaches, but leading inevitably to large disability and mortality outcomes. The selection of the recommended therapeutic intervention in each case relies in estimates overall survival (OS) based commonly in histopathological and genetic criteria. However, current assessments of OS entail considerable uncertainties, limiting concomitantly more precise, effective, and personalized therapies. On these grounds, exploring additional criteria to improve OS predictions acquires vital relevance to improve treatment outcomes in glioma patients.

Histopathological and immunohistochemical criteria have classically provided the basis for the initial WHO classification of gliomas in grades I-IV (2, 3) determining, in general terms, the OS estimate and the recommended therapeutic intervention. More recently, the 2016 WHO classification of central nervous system tumors added an important collection of molecular signatures, restructuring the original histopathological classification of gliomas to include subgroups with specific genetic profiles (4). Although these refinements considerably improved the precision in the treatment prescribed, as well as our knowledge of glioma physiopathology and classification, the limited reproducibility of histopathological evaluations lead, not unfrequently, to imprecise histopathological classification and unreliable OS predictions at the individual level (5–7).

Magnetic Resonance Imaging approaches have been currently used to assess OS of gliomas. Briefly, radiomic parameters including surface area (8), shape features (9), tumor, and necrosis volumes, necrosis-tumor ratio (10) have been used to evaluate OS. However, these studies became many times limited to short OS periods as they evaluated only glioblastoma multiforme cases.

The metabolomic profiles of gliomas are able to provide an additional source of information to improve OS predictions, evaluating the down-stream metabolic alterations of aberrant cellularity and gene expression (11). Magnetic Resonance Spectroscopy (MRS) has been shown to be well-endowed to provide the metabolic profile of gliomas both *in vivo* and *in vitro* (12, 13). Briefly, *in vivo* ^{1}H MRS revealed non-invasively, important hallmarks of cancer, including alterations in pH homeostasis (14), energy related (15), and phospholipid metabolites (16, 17), an ensemble of valuable metabolic fingerprints to classify high grade (HGG) or low grade gliomas (LGG) (16, 18). Moreover, the metabolic profiles determined by ^{1}H MRS *in vivo* reached considerable clinical prognostic relevance (19–22). Alternatively, complementary *in vitro* HR-^{1}H MRS approaches have proved to be able to resolve a larger number of metabolites than *in vivo* ^{1}H MRS, thus increasing the size of the metabolome investigated, the number of potential alterations detected, and their influence on the tumoral phenotype, at the expense of the more invasive *in vitro* methodology (23, 24). However, the predictive role of the metabolomic profiles obtained by HR-^{1}H MRS in providing OS estimates, received considerably less attention.

On these grounds, we aimed here to provide a pilot study evaluating OS estimates derived from metabolomic biomarkers as detected by HR-^{1}H MRS, using a retrospective database of human glioma biopsies.

Abbreviations: Ac, Acetate; Ala, Alanine; Asp, aspartic acid; Cr, creatine; CCM, classification confusion matrix; CRT, Classification Regression Tree; d, doublet multiplicity; dd, doublet of doublets multiplicity; fCho, free choline; GABA, gamma-aminobutyric acid; GLM, General Lineal Model; Gln, glutamine; Glu, glutamate; Gly, glycine; GPC, glycerophosphocholine; GroPEtn, glycerophosphoethanolamine; HGG, high grade glioma ^{1}H MRS, proton magnetic resonance spectroscopy; Lac, lactate; LGG, low grade glioma; Lip, lipid; m, multiplet; MRS, magnetic resonance spectroscopy; MI, myo-inositol; NAA, N-acetyl-aspartic acid; OS, overall survival; PC, phosphorylcholine; PCr, phosphocreatine; PDE, phosphodiester; PE, phosphoethanolamine; PtdCho, phosphatidylcholine; PtdEtn, phosphatidylethanolamine; PtdIns, phosphatidylinositol; s, singlet multiplicity SEM, Standard error of mean; t, triplet; Tau, taurine; tCho, total choline; tCr, total creatine; Val, valine; w, weeks.

MATERIALS AND METHODS

Glioma Patients and Tumor Biopsies

This study was approved by the Ethics Committee of Clinical Research from the University Hospital La Paz (http://www.madrid.org/cs/Satellite?language=es&pagename=HospitalLaPaz/Page/HPAZ_home) and carried out following their recommendations. All subjects gave written informed consent in accordance with the Declaration of Helsinki. We retrospectively reviewed the database of the Neurosurgery Department of the University Hospital La Paz, selecting 66 consecutive patients with glioma (grades I-IV) who underwent neurosurgery during the period 1992–1998 (**Figure 1**). Briefly, solid parts of glioma tumors were extracted from the brain without the use of bipolar coagulation and divided into two adjacent and similar portions, one of them used for HR-^{1}H MRS analysis and the other for histopathological diagnosis, following available WHO criteria (25). Tumor characteristics were evaluated by two independent radiologists and classified according to size, localization, and eloquence (26). Patients lost in follow up ($n = 10$) and those undergoing surgery for recurrence ($n = 7$) were excluded from further analysis. Grade I gliomas ($n = 3$) were also excluded because of their well-known physiopathological differences with the other glioma grades (27, 28). We then recovered the individual demographic, clinical, histopathological and *in vitro* spectroscopic ^{1}H NMR features and gathered the OS information on postsurgical outcomes of these patients, including relevant clinical symptoms, adjuvant therapies, and OS time. No missing data for the variables of interest were found in these patients.

Histopathological Criteria

Histopathological grading of the biopsies was provided by the Anatomopathology Department of the Hospital, following standard WHO criteria (25), and archived until used in this study.

HR-^{1}H MRS

The ^{1}H MRS biopsy was immediately frozen in liquid nitrogen (−169°C) in the operating room of the Hospital and stored at −82°C until transferred in a liquid nitrogen container to the Institute of Biomedical Research CSIC/UAM for further

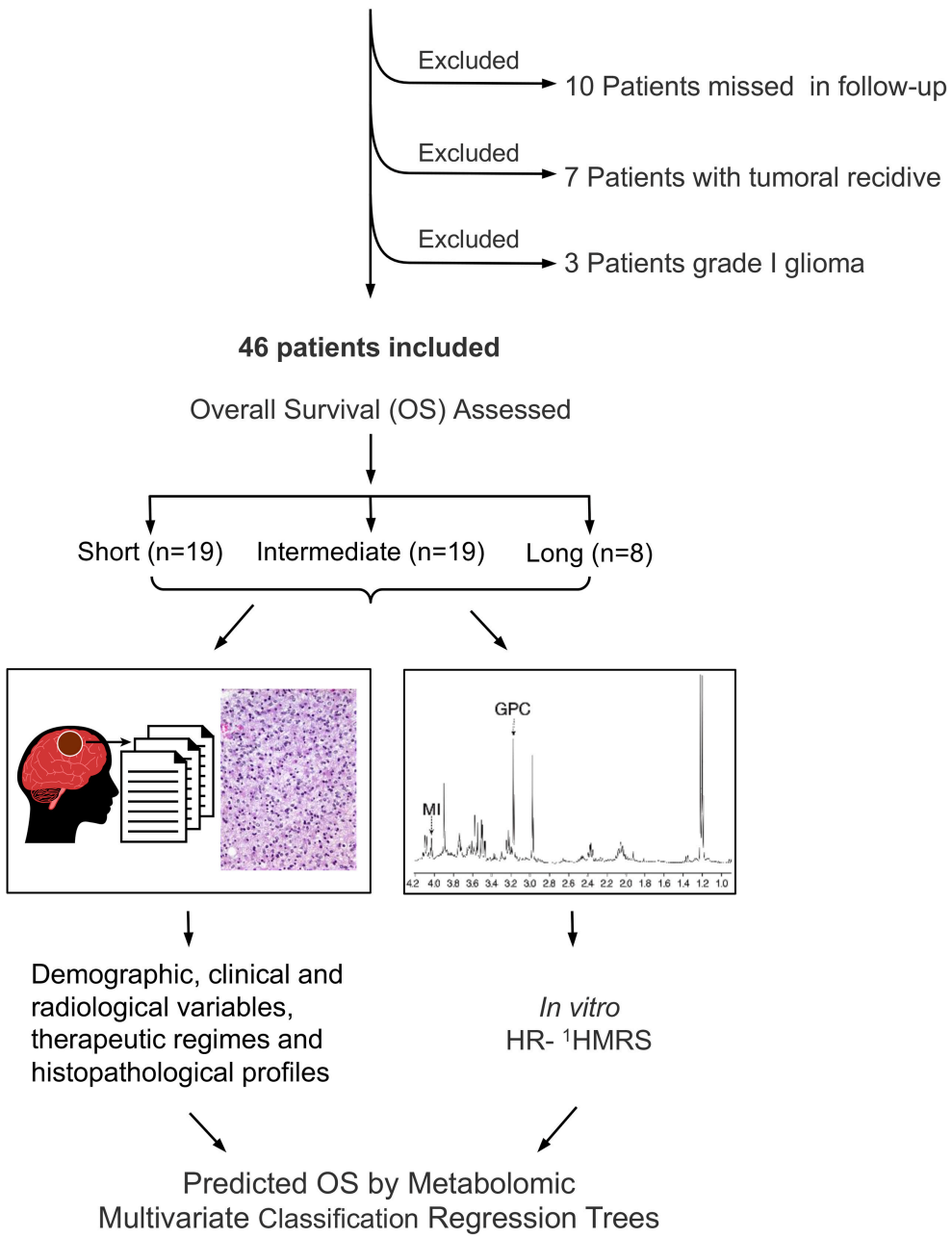

FIGURE 1 | Overview of glioma patient selection and implemented approach.

processing and NMR analysis. Briefly, biopsies were reduced to powder in a previously chilled (methanol/dry ice) mortar, extracted with 6% perchloric acid, neutralized with KOD, lyophilized and resuspended in D_2O (99.9% D) for ^{1}H MRS analysis (12). HR-^{1}H MRS spectra of biopsy extracts were acquired at 8.4 Tesla (360.13 MHz, pH 7.2, 22°C) in a Bruker AM-360 spectrometer equipped with a commercial ^{1}H selective probe using 5-mm tubes and 0.5 ml of tissue extract. Acquisition conditions were: 90° pulses, 16.9 s total cycle time and 16,384 data points acquired in the time domain during of 1.901 s. The intensity of the residual water resonance was further reduced using a 5 s presaturating pulse centered on the water frequency. Prior to Fourier transformation, the free induction decays were zero-filled up to 128 K and multiplied by an exponential

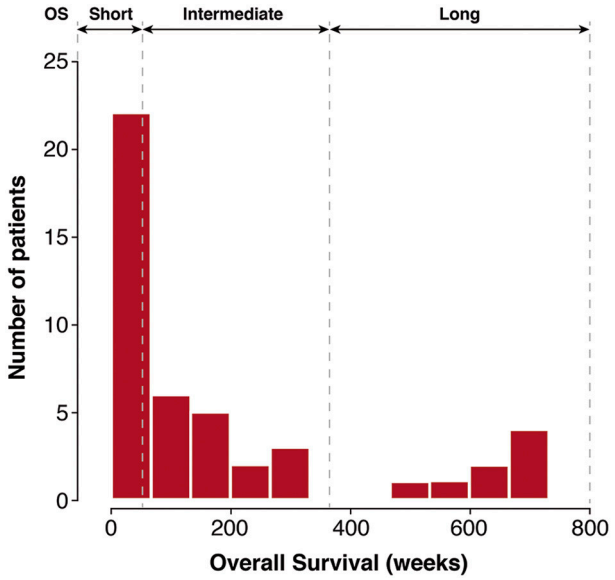

FIGURE 2 | Histogram of OS in glioma patients after surgical resection at the Neurosurgery Department, University Hospital La Paz, in the period 1995–1998. Patient groups depicting Short-OS (1–52 w), Intermediate-OS (53–364 w) and Long-OS (>364 w) are separated by the dotted lines.

function resulting in 0.5 Hz artificial line broadening in the transformed spectrum. Further spectral processing, including phase and baseline corrections were performed by the same operator. Chemical shifts were referred to the methyl signal of TSP (2,2′-3,3′ tetradeutero trimethyl-sylil propionate sodium salt) at 0 ppm as an internal reference.

The following metabolites (resonances used in quantification, number of protons originating the resonance, multiplicity) could be consistently identified in the high resolution proton spectrum (29): Valine (1.09 ppm, 3H, d), Lactate (1.35 ppm, 3H, d), Alanine (1.45 ppm, 3H, d), Acetate (1.93 ppm, 3H, s), N-acetyl-aspartic acid (2.01 ppm, 3H, s), Gamma-amino butyric acid (2.31 ppm, 2H, t), Glutamate (2.43 ppm,2H, m), Glutamine (2.45 ppm, 2H, m), Aspartic acid (2.80 ppm, 2H, dd), Creatine (3.05 ppm, 3H, s) and Phosphocreatine (3.055 ppm, 3H, s), free Choline (3.20 ppm, 9H, s), Phosphorylcholine (3.22ppm, 9H, s), Glycerophophorylcholine (3.25 ppm, 9H, s), Taurine (3.45 ppm, 2H, t), Glycine (3.55 ppm, 2H, s), and Myo-inositol 4.07 ppm, 1H, dd). For every one of these metabolites, lorentzian curves were fitted to the most conveniently resolved proton resonances, and the resulting integral divided by the total number of protons of the corresponding metabolite (6). These values were further standardized by the sum of all the measured metabolites in the HR-^{1}H NMR spectra and expressed as a molar percentage

TABLE 1 | Clinical features and overall survival of glioma patients.

Feature		Overall survival			Total patients *n* (% column)	Chi-square (montecarlo sig.)
		Short *n* (% row)	Intermediate *n* (% row)	Long *n* (% row)		
Age	<25 y	0 (0.0%)	5 (62.5%)	3(37.5%)	8 (17.4%)	0.01
	25–54 y	5 (31.3%)	7 (43.8%)	4(25%)	16 (34.8%)	
	>54 y	14 (63.6%)	7 (31.8%)	1 (4.5%)	22 (47.8%)	
Sex	Female	8 (34.8%)	11(47.8%)	4 (17.4%)	23 (50%)	0.74
	Men	11(47.8%)	8 (34.8%)	4 (17.4%)	23 (50%)	
Comorbility[a]	Yes	10 (34.5%)	13 (44.8%)	6 (20.7%)	29 (63%)	0.56
	No	9 (52.9%)	6 (35.3%)	2 (11.8%)	17 (37%)	
Localization[b]	A	2 (15.4%)	7 (53.8%)	4 (30.8%)	13 (30.2%)	0.04
	B	5 (41.7%)	6 (50%)	1 (8.3%)	12 (27.9%)	
	C	12 (66.7%)	3 (16.7%)	3 (16.7%)	18 (41.9%)	
Tumor volume[b]	Small	13 (39.4%)	15 (45.5%)	5 (15.2%)	33 (73.3%)	0.49
	Big	6 (50%)	3 (25%)	3 (25%)	12 (26.7%)	
Eloquency[b]	Yes	16 (53.3%)	10 (33.3%)	4 (13.3%)	30 (69.8%)	0.19
	No	3 (23.1%)	6 (46.2%)	4(30.8 %)	13 (30.2%)	
Resection	Partial/Complete	10 (52.6%)	5 (26.3%)	4 (21.1%)	19 (41.3%)	0.27
	Biopsy	9 (33.3%)	14 (51.9%)	4 (14.8%)	27 (58.7%)	
Radiotherapy	Yes	19 (54.3%)	12 (34.3%)	4 (11.4%)	35 (76.1%)	0.003
	No	0 (0%)	7 (63.6%)	4 (36.4%)	11 (23.9%)	
Chemotherapy	Yes	0 (0%)	1 (33.3%)	2 (66.7%)	3 (6.5%)	0.07
	No	19(44.2%)	18 (41.9%)	6 (14%)	43 (93.5%)	
Histopathology grade[c]	II	0 (0%)	6 (54.5%)	5 (45.5%)	11 (23.9%)	<0.001
	III	3 (18.8%)	10 (62.5%)	3 (18.8%)	16 (34.8%)	
	IV	16(84.2%)	3 (15.8%)	0 (0%)	19 (41.3%)	

[a]*Arterial hypertension, diabetes mellitus and/or pulmonary, renal, cardiac, oncologic or any severe disease,* [b]*Classification of tumors according to (26).* [c]*Histopathologic grade according to (3).*

(18, 30). Assignments were performed with the aid of chemical shift values reported in the literature (29, 31) and confirmed when necessary by the addition of authentic standards.

Statistical Methods

Statistical analyses were performed using the IBM SPSS Statistics 24 package as implemented on an Intel-PC platform, operating under Windows 10 environment. Univariate statistical approaches provided means and standard errors for the molar fractions of every metabolite. To investigate statistical dependences between clinical features and groups of OS, we used asymptotic chi-square with Monte Carlo exact probability tests, and to test the differences of means within each metabolic variable through the OS groups, we used the ANOVA test and Student *t*-tests. Finally, to explore the hierarchical contribution of individual HR-^{1}H MRS biomarkers to the three groups of OS, we implemented a multivariate Classification Regression Tree (CRT) (32), classifying automatically the database using hierarchical nodes and branches, selecting step-wise the optimal discriminant biomarker for each split from the collection of available HR-^{1}H MRS variables. The dependent variable was OS, using Chi-squared Automatic Interaction Detection (CHAID) as a growing method to provide automatically the optimal splits in every branch. Finally, we used these results to generate a Classification-Confusion Matrix (CCM), summarizing the correct and incorrect classifications provided by the metabolomics CRT, yielding the global percentage of correct classifications. Statistical significance in the ANOVA and multivariate analysis was defined as $p = 0.05$, considering confidence intervals higher than 95%.

RESULTS

Glioma Database

We investigated 46 patients (23 males, 23 females) with a median age of 49 years, presenting the following glioma grade distribution; Grade II (11 cases), Grade III (16 cases), and Grade IV (19 cases). The database of glioma patients (**Figure 2**) showed two clearly separated groups by OS, either depicting a Long Overall Survival (Long-OS) that survive more than 364 weeks (w), or less. The latter group, including patients with a wide range of survival (1–364 w), was further divided in two groups using the median of survival as a cut-point, resulting in Short Overall Survival (Short-OS) patients (1–52 w), or Intermediate Overall Survival (Intermediate-OS) patients (53–364 w), respectively.

Demographic, clinical, and radiological variables, therapeutic regimes and histopathological profiles of these groups are summarized in **Table 1**. A Chi-square Monte Carlo test was performed to compare the differences in independent clinical variables among the three survival categories. Radiotherapy, histopathologic grade, age, and localization showed statistically significant influence on OS.

HR-^{1}H MRS

An illustrative example of underdetermined histopathological OS prediction is provided in **Figure 3**, showing representative HR-^{1}H MRS spectra from extracts of glioma biopsies obtained from two young male patients, assigned the same histopathological Grade II, but resulting in very different OS. Despite both patients underwent complete surgical resection without adjuvant radio- or chemotherapy, the patient represented in **Figure 3A**, survived <3 years (149 w), while the patient represented by **Figure 3B** survived more than 11 years (605 w).

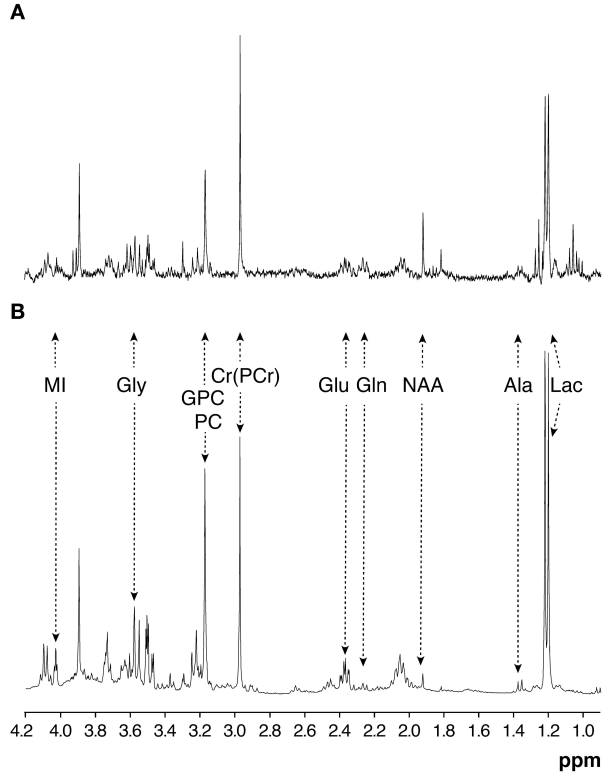

FIGURE 3 | Representative HR-^{1}H MRS (360.13 MHz, 22°C, pH 7.2) from extracts of two glioma grade II biopsies with very different OS outcomes. **(A)** 149 w. **(B)** 600 w. MI, myo-inositol; Gly, glycine; GPC, glycerolphosphorylcholine; PC, phosphorylcholine; Cr, creatine; PCr, phosphocreatine; Glu, glutamate; Gln, glutamie; NAA, N-acetyl-aspartic acid; Ala, alanine; Lac, lactate.

Interestingly, HR-^{1}H MRS spectra of these biopsies disclosed remarkable differences, particularly the relative increases in myo-inositol (MI) and glycerol-phosphorylcholine (GPC) in **Figure 3B**. These findings suggested that HR-^{1}H MRS analysis of biopsy extracts could contribute additional OS criteria to those normally obtained from general histopathological classification, thus prompting further HR-^{1}H MRS analyses of the database.

Univariate Statistics

OS was well-reflected in the metabolic profiles obtained, with evident relationships between OS and specific metabolite changes (**Figure 4**). **Table 2** provides a more detailed analysis of the relationship between OS and specific metabolite molar fractions,

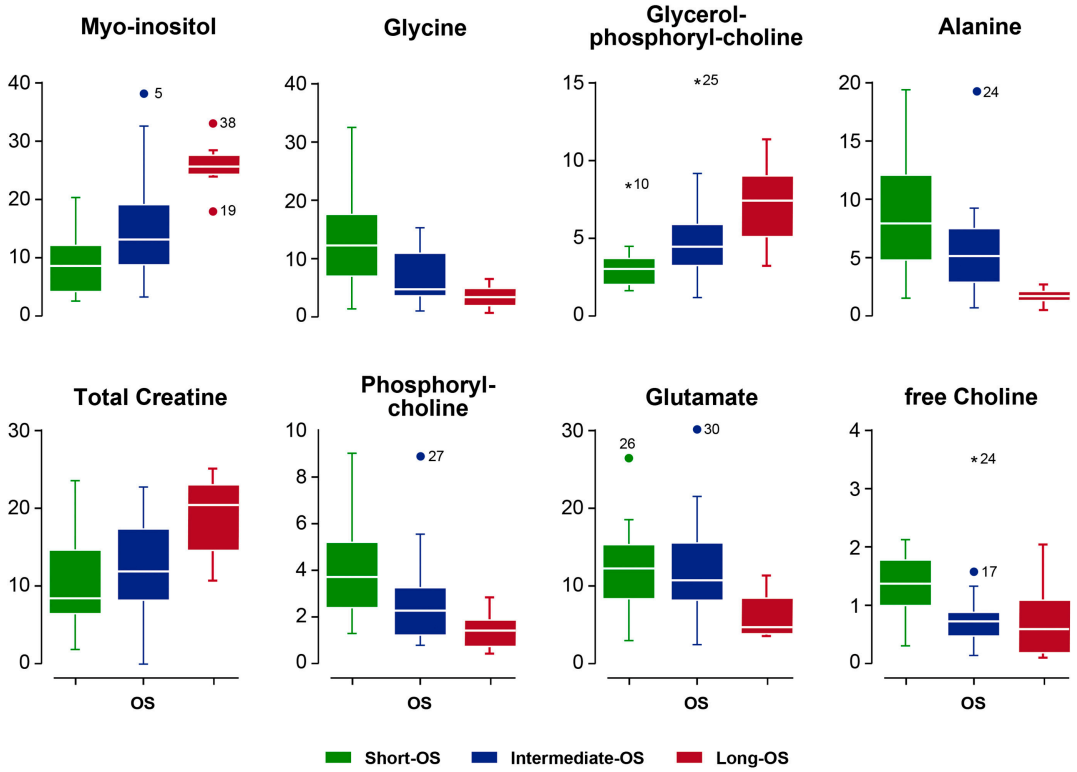

FIGURE 4 | Box-plots of metabolite molar ratios in extracts from glioma biopsies with Short-OS (green), Intermediate-OS (blue) and Long-OS (red). In each box, the central mark (white line) indicates the median, and the bottom and top edges refer to the 25-th and 75-th percentiles, respectively. The upper and lower limits of the box extend to the most extreme data points not considered outliers.

TABLE 2 | General linear model analysis of OS in glioma patients as revealed by the metabolic profile determined by HR-^{1}H MRS.

Metabolite	Short (n = 19)	Intermediate (n = 19)	Long (n = 8)	Total	F^{b}	p
	OVERALL SURVIVAL[a]					
MI	**9.03 ± 1.26**	**14.75 ± 2.14**	**25.72 ± 1.51**	**14.30 ± 1.36**	**15.10**	**<0.001**
Ala	**8.47 ± 1.12**	**5.67 ± 0.95**	**1.67 ± 0.24**	**6.13 ± 0.70**	**13.65**	**<0.001**
GPC	**3.17 ± 0.34**	**5.17 ± 0.72**	**7.18 ± 0.97**	**4.70 ± 0.42**	**9.44**	**<0.001**
Gly	**13.38 ± 1.89**	**6.95 ± 1.03**	**3.61 ± 0.68**	**9.03 ± 1.05**	**9.37**	**<0.001**
PC	**4.17 ± 0.48**	**2.84 ± 0.48**	**1.43 ± 0.28**	**3.14 ± 0.32**	**8.36**	**0.001**
tCr	**13.36 ± 1.10**	**15.03 ± 1.19**	**20.84 ± 1.63**	**15.35 ± 0.81**	**6.53**	**0.003**
Ac	**4.49 ± 0.97**	**3.09 ± 0.81**	**0.94 ± 0.17**	**3.30 ± 0.55**	**5.72**	**0.006**
fCho	**1.33 ± 0.13**	**0.86 ± 0.17**	**0.73 ± 0.24**	**1.03 ± 0.10**	**4.65**	**0.01**
Glu	**12.20 ± 1.27**	**12.09 ± 1.56**	**6.04 ± 1.16**	**11.08 ± 0.91**	**3.62**	**0.03**
Gln	15.47 ± 1.19	18.76 ± 1.38	18.51 ± 1.30	17.36 ± 0.81	2.02	0.14
Val	2.34 ± 0.47	1.60± 0.43	1.45 ± 0.23	1.88 ± 0.27	0.896	0.42
Asp	0.77 ± 0.14	0.70 ± 0.14	0.50 ± 0.12	0.69 ± 0.09	0.584	0.56
NAA	3.35 ± 0.94	4.57 ± 0.95	4.55 ± 0.94	4.06 ± 0.57	0.544	0.58
GABA	1.25 ± 0.31	0.92 ± 0.15	1.17 ± 0.33	1.10 ± 0.15	0.483	0.62
Tau	5.69 ± 0.79	6.17 ± 0.71	4.95 ± 0.63	5.76 ± 0.45	0.416	0.66
tCho	8.67 ± 0.57	8.88 ± 0.76	9.33 ± 1.02	8.87 ± 0.42	0.145	0.86

[a]*Results are given as mean ± standard error of mean.* [b]*A Box Cox transform was performed on the data before running ANOVA analysis. Ac, Acetate; Ala, Alanine; Asp, aspartic acid; fCho, free choline; GABA, gamma-aminobutyric acid; Gln, glutamine; Glu, glutamate; Gly, glycine; GPC, glycerophosphocholine; MI, myo-inositol; NAA, N-acetyl-aspartic acid; PC, phosphorylcholine; Tau, taurine; tCr, total creatine; Val, valine. Bold characters indicate $p < 0.05$.*

TABLE 3 | General linear model analysis of the HR- ^{1}H NMR metabolic profiles associated to different glioma histopathological grades.

	IV	III	II	Total	F	p
	n = 11	*n* = 16	*n* = 19			
HISTOPATHOLOGICAL GRADE[a]						
MI	**8.41 ± 1.09[b]**	**13.94 ± 1.95**	**24.99 ± 2.3**	**14.3 ± 1.36**	**21.71[c]**	**<0.000**
PC	**4.36 ± 0.56**	**2.90 ± 0.36**	**1.40 ± 0.25**	**3.14 ± 0.32**	**11.74**	**<0.000**
GPC	**3.01 ± 0.19**	**5.32 ± 0.84**	**6.70 ± 0.87**	**4.70 ± 0.42**	**9.16**	**<0.000**
Ala	**8.36 ± 1.15**	**5.77 ± 1.09**	**2.82 ± 0.69**	**6.13 ± 0.7**	**8.85**	**0.001**
Gly	**12.74 ± 1.9**	**7.98 ± 1.42**	**4.14 ± 0.53**	**9.03 ± 1.05**	**6.54**	**0.003**
tCr	**13.54 ± 1.17**	**14.35 ± 1.31**	**19.94 ± 1.28**	**15.35 ± 0.81**	**6.30**	**0.004**
Glu	**13.85 ± 1.55**	**10.89 ± 1.32**	**6.59 ± 0.95**	**11.08 ± 0.91**	**5.90**	**0.005**
Succ	**1.36 ± 0.49**	**1.11 ± 0.2**	**0.58 ± 0.08**	**1.09 ± 0.22**	**3.99**	**0.03**
Gln	**14.95 ± 1.14**	**19.05 ± 1.31**	**19.05 ± 1.67**	**17.36 ± 0.81**	**3.47**	**0.04**
fCho	1.23 ± 0.13	1.05 ± 0.21	0.67 ± 0.16	1.03 ± 0.1	3.10	0.05
Val	2.32 ± 0.48	1.97 ± 0.49	0.98 ± 0.11	1.88 ± 0.27	2.51	0.09
Asp	0.88 ± 0.16	0.63 ± 0.12	0.47 ± 0.12	0.69 ± 0.09	1.93	0.16
Ac	3.75 ± 0.96	3.68 ± 0.98	1.95 ± 0.67	3.30 ± 0.55	1.49	0.24
Tau	6.09 ± 0.85	6.05 ± 0.74	4.77 ± 0.46	5.76 ± 0.45	0.42	0.66
tCho	8.60 ± 0.57	9.27 ± 0.86	8.76 ± 0.83	8.87 ± 0.42	0.24	0.79
GABA	1.03 ± 0.19	1.25 ± 0.36	1.02 ± 0.23	1.10 ± 0.15	0.23	0.80
NAA	4.14 ± 1.17	4.06 ± 0.86	3.94 ± 0.49	4.06 ± 0.57	0.01	0.99

[a]According to Louis et al. (3) [b]Results are given as mean ± standard error of mean. [c]A Box Cox transform was performed on the data before running ANOVA analysis. Bold characters indicate p < 0.05.

highlighting the discriminant power in OS of each metabolite (*F*-value) and its statistical significance (*p*-value) as derived from ANOVA tests.

Briefly, OS increased with increasing levels of MI, GPC, and total Creatine (tCr), and decreased with increasing levels of alanine (Ala), free choline (fCho), glutamate (Glu), phosphorylcholine (PC), and glycine (Gly). The remaining metabolites detected by HR-^{1}H NMR, including acetate (Ac), glutamine (Gln), valine (Val), aspartate (Asp), N-acetyl-aspartic acid (NAA), Gamma-amino butyric (GABA), taurine (Tau), and total choline (tCho) were not found to influence significantly OS. The most powerful discriminators of OS were (Metabolite/ F value/ *p*-value) in decreasing order; MI/15.1/0.000, Ala/13.6/0.000, GPC/9.5/0.001, Gly/9.4/0.000, tCr/6.5/0.003, Ac/5.7/0.006, fCho/4.6/0.015, Glu/3.6/0.035.

We also investigated the relationship between histopathological grade and the molar fractions of metabolites detectable in extracts glioma biopsies using ANOVA tests (**Table 3**). Notably, the priority of metabolites providing optimal glioma grade discrimination, was different from the one yielding optimal OS discriminative power (**Table 2**). The following molar ratios of metabolites were found to provide optimal discriminant power between histopathological grades (metabolite/*F*-value/*p*-value); MI/21.7/0.000, PC/11.7/0.000, GPC/9.2/0.000, Ala/8.8/0.001, Gly/6.5/0.003, tCr/6.3/0.004, Glu 5.9/0.005 and Gln/3.5/0.040.

Together, these results show that relevant metabolites contribute with different strengths either to histopathological grading or to OS predictions.

Classification Regression Trees (CRT)

To investigate the hierarchical contribution of these metabolites to the OS observed, we implemented a multivariate CRT (**Figure 5**) (32). Starting with the complete patient database (Node 0), high MI levels (Branch 1) provided the most powerful biomarker to predict Long-OS survival within the three OS groups. MI levels ≤23.35 were found in 37 biopsies (Node 1). Of these, only one patient survived more than 7 years (Long-OS), while the rest of the patients depicted either Intermediate- (17 patients) or Short-OS (19 patients). In contrast, MI levels >23.35 were detected in nine biopsies (Node 2), of which seven (77.8%) depicted Long-OS, two showed Intermediate-OS, and none had a Short-OS, suggesting that high MI levels dismiss a Short-OS prediction.

Patients with MI levels ≤23.35 could be further split in two groups using GPC (Brach 2). Sixty-nine percent of the patients with GPC levels ≤4.36 (Node 3) were classified as Short-OS, while 91% of the patients with GPC > 4.36 (Node 4) were classified as Intermediate-OS. GPC provided thus a convenient biomarker to distinguish between Short- and Intermediate-OS estimates.

The metabolomic CRT grew beyond Branch 2, improving the classification using either Gly or Ala splits (Branch 3). All patients of Node 3 with Gly levels higher 13.87 (Node 6), depicted Short-OS, suggesting that high Gly levels are predictive of a negative outcome. Patients from Node 4, could be further stratified by their Ala levels. Those having Ala levels lower than 8.48 (Node 7) indicated Intermediate-OS (100%). Summarizing, the metabolomic CRT indicated dominant roles of MI, GPC, Ala, and Gly OS prediction of glioma patients.

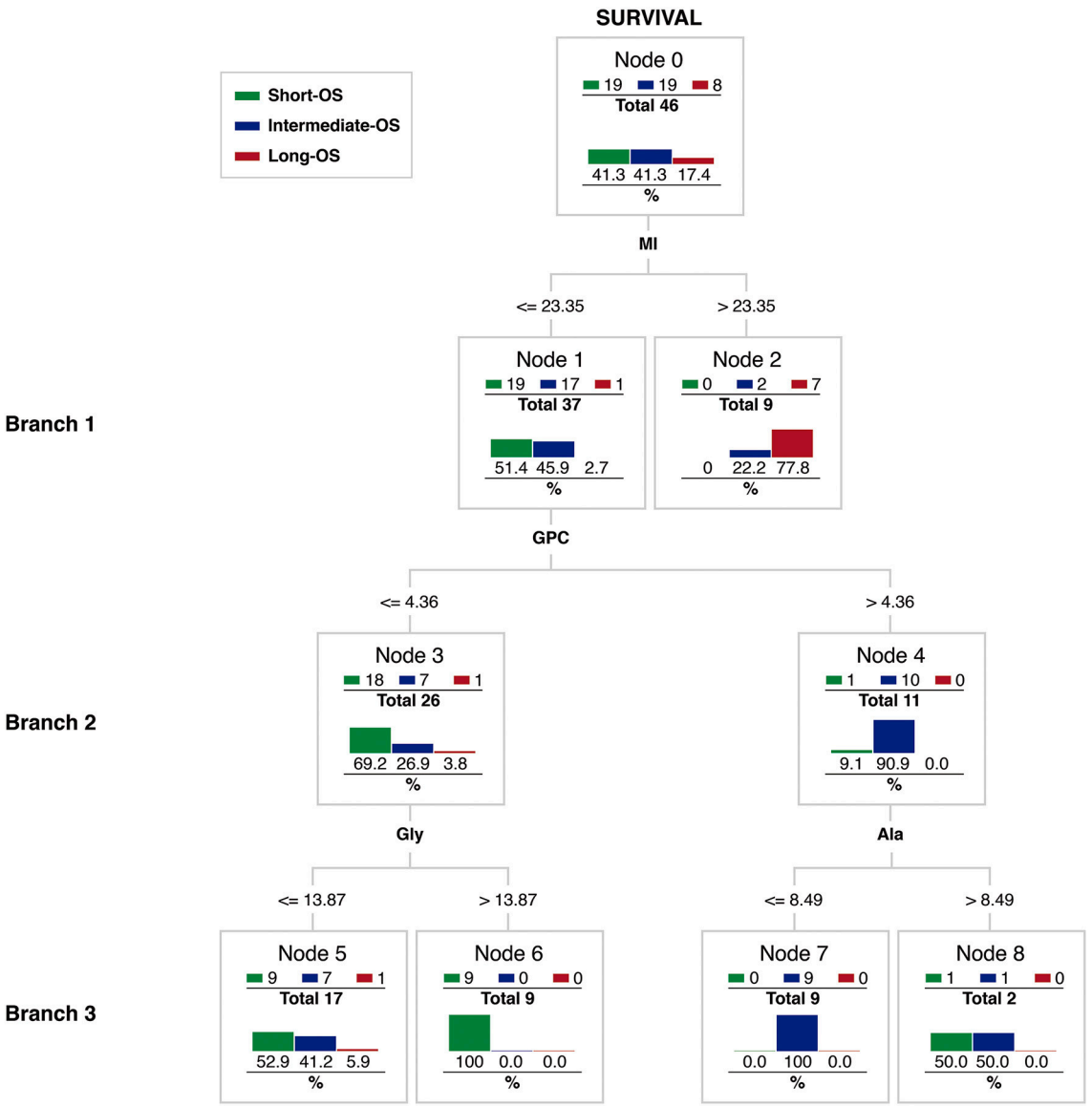

FIGURE 5 | Classification Regression Tree (CRT) of glioma OS based in metabolomic biomarkers detectable by HR-^{1}H MRS.

Finally, we compared the number of correct predictions derived from the metabolomic CRT with those observed clinically, in the Classification-Confusion Matrix of **Table 4**. Out of 19 patients in the Short-OS group, the metabolomic approach classified correctly 18 patients. In the Intermediate-OS group, the metabolomic approach classified correctly 15 of 19 patients. Finally, out of the 8 patients identified with Long-OS, the metabolomic approach correctly classified 6 patients.

In summary, the metabolomic classification reached defined OS predictions in all three groups, separating well the longer OS groups (Intermediate-OS and Long-OS). This entails considerable relevance, since the prediction of Long-OS in glioma patients remains currently a vital challenge for neurosurgeons, with important implications in the definition of the recommended therapeutic strategy.

DISCUSSION

Previous OS Studies

The present study complements and extends earlier OS predictors based on the WHO classification (2–4) or *in vivo* MRI/MRS studies (19–21, 33–40), contributing a novel array of metabolomic biomarkers organized hierarchically by a multivariate CRT. Earlier studies implementing *in vivo* MRS/MRI approaches investigated mainly glioblastoma patients (**Table 5**), associating Short-OS to increases in PC (4) and tCho/NAA (20, 36–40, 42), and longer OS to higher contents

TABLE 4 | Classification confusion matrix of correct/incorrect classifications of overall survival in patients bearing gliomas using metabolomic criteria.

Observed overall survival ($n = 46$)	Predicted overall survival			Percent correct classifications
	Short	Intermediate	Long	
Short ($n = 19$)	**18**[a]	1	0	**94.7**
Intermediate ($n = 19$)	4	**15**	0	**78.9**
Long ($n = 8$)	1	1	**6**	**75.0**
All patients ($n = 46$)				**84.7**

[a]*Numbers in bold indicate number and percentages of correct classifications. Growing Methods: CRT, dependent variable OS.*

TABLE 5 | Overview of literature correlating OS and MRS biomarkers.

Authors & year	Patients	Glioma grade	Follow-up period[a,b]
Li et al. (39)	72	HGG[c]	17.2 m[a]
Reijneveld et al. (40)	14	LGG[d]	30 m (9–40)[b]
Hattingen et al. (41)	45	LGG	37 m (52.1–260.5)
Chang et al. (38)	143	LGG & HGG	n.s.
Yamasaki et al. (33)		HGG	26.1 m (6.5–83.8)
Steffen-Smith et al. (37)	39	HGG	7.1 m (1.6–61.6)
Quon et al. (36)	26	HGG	22.9 m (5–37)
Hattingen et al. (35)	32	HGG (recidives)	8.1 m
Tolia et al. (21)	12	HGG	n.s.
Steidl et al. (34)	37	HGG (recidives)	n.s.
Roldán et al. (20)	28	HGG	3–98 m
Present serie	46	LGG & HGG	14.9 m (0.24–170.4)

[a]*Median of the duration of the study in months,* [b]*Parenthesis includes the range of the study in months (m),* [c]*HGG: High grade glioma,* [d]*LGG: Low grade glioma, n.s.: not specified.*

in GPC (35). Additionally, Cho/Cr ratio has been proposed as a biomarker of cellular proliferation and prognosis (22). More recently, a correlation between 2-hydroxiglutarate and the IDH1 mutation (43), suggested that *in vivo* detection of 2-hydroxiglutarate could become a useful prognostic biomarker. However, routinely and regular detection *in vivo* of 2-hydroxyglutarate still remains an important technological challenge in most imaging centers, limiting wider applications. In summary, the present study contributes a larger cohort of patients examined by routinely available *in vitro* MRS, followed during a longer period of time, including also a collection of both Low Grade Gliomas (LGG) and High Grade Gliomas (HGG). Notably, some of the metabolomic biomarkers found valuable here in OS prediction, like MI or GPC (**Table 2**), are difficult to resolve, or not even detectable *in vivo*. Consequently, our results suggest that postsurgical HR-^{1}H NMR analysis of extracted tumor biopsies may provide a useful complement to available *in vivo* MRS explorations when addressing OS predictions.

Metabolomic CRT

We implemented a CRT methodology to find, hierarchically, the best classification of OS estimates, using metabolomic criteria. These results complement the earlier decision tree of Li et al. (39), who considered age, MRI features (T_2, T_1, Volume Contrast Enhancement) and *in vivo* spectroscopic biomarkers (Lip+Lac, Cho/Cr, and Cr/NAA), as the main determinants predicting glioblastoma OS.

Our metabolomic CRT grew up to three branches. In the first branch, MI became the most robust biomarker of survival, with larger MI contents revealing longer survivals. Increased MI levels have been reported in inflammatory diseases as Alzheimer (41), renal failure (44), diabetes mellitus (44), and traumatic brain injury (45, 46), suggesting a universal role of this osmolite in pathophysiolological volume regulation. However, MI levels were reported previously to increase (47–49) or decrease (44) with increasing glioma grade *in vivo*. Present results reveal that higher MI levels are associated to longer OS, and lower tumoral grades (**Table 3**). Since MI occurs primarily in normal astrocytes (44), we hypothesize that the MI resonances detected in the tumor biopsies reveal the healthy astrocyte content within the tumor mass. Larger relative MI contents reveal indirectly relatively larger normal astrocyte populations and smaller tumoral cell burdens, supporting consequently longer OS (41, 50, 51).

The second hierarchical branch classifying the lower MI content group, is GPC, with higher GPC levels predicting longer OS. We, and others, have previously reported that relatively higher contributions of GPC and PC are associated to low and high grade gliomas, respectively (16, 52). Interestingly, GPC and PC levels are thought to reflect the balance between phospholipid degradation and phospholipid synthesis, respectively, with increased GPC levels revealing relatively a negative balance between synthesis and degradation, lower tumoral proliferation, and more prolonged survivals.

Gly and Ala provided the third branch of OS discrimination for patient groups with low or high levels of GPC, respectively. High Gly and Ala levels revealed poor prognosis, associated to shorter OS. Indeed, Ala and Gly levels previously reported as hypoxia and redox stress biomarkers (53), revealing tumoral progression to hypoxia, redox stress, and fatal energy failure. They can now be associated to shorter OS predictions.

Limitations

The time span of biopsy collection in this study preceded some of the advances in the characterization of glioma genetics and their influence in malignancy and OS. This circumstance, and the long survival period investigated, precluded the use of genetic biomarkers validated later in the coverage of the present retrospective study. Thus, the correlations between metabolomic and genomic biomarkers of OS in glioma deserve further investigation. Finally, the number of patients involved in the present pilot study is admittedly small but sufficiently robust to support the use of metabolomic biomarkers detected by *in vitro* HR-^{1}HMRS in OS predictions of postsurgical survival from glioma patients. A multicenter study to extend the number of patients and hospitals involved, is currently being implemented.

CONCLUSION

We used a multivariate CRT to assess postsurgical OS predictions based in the ^{1}H HR-MRS analysis of the metabolomic profile from neurosurgical biopsies of glioma patients. Present results show that the metabolic profiles of glioma biopsies constitute accurate and independent biomarkers of OS in glioma patients.

DATA AVAILABILITY

All datasets generated for this study are included in the manuscript.

ETHICS STATEMENT

This study was carried out in accordance with the recommendations of the Ethics Committee of the Hospital La Paz with the approval number PI-2097 with written informed consent from all subjects. All subjects gave written informed consent in accordance with the Declaration of Helsinki.

AUTHOR CONTRIBUTIONS

MG-G collected and integrated retrospective patient data, investigated survival patterns, and wrote the first draft. SC analyzed HR-^{1}H NMR spectra. LB provided the univariate and multivariate statistical analyses. PL-L acquired HR-^{1}H NMR spectra. PF and AP validated demographic, radiological, and histopathological assessments. JR performed many of the neurosurgical procedures providing integrated clinical information, and JS conceived the study and wrote the final draft with all authors commenting.

FUNDING

This work was supported in part by grants PI2017/00361 from Instituto de Investigación Carlos III to JR, grant B2017/BMD-3688 from the Community of Madrid to JR and SC, and grant PI-0143-2016 from the Regional Ministry of Health of the Regional Government of Andalucía to JS.

ACKNOWLEDGMENTS

Authors are grateful to Mr. Javier Pérez CSIC for the professional drafting of the illustrations, to Mrs. Maria José Guillén CSIC for skillful processing of the biopsies and to Mrs. Teresa Navarro CSIC for granting access to the HR-^{1}HMRS facility of the Institute of Biomedical Research Alberto Sols.

REFERENCES

1. Bush NA, Chang SM, Berger MS. Current and future strategies for treatment of glioma. *Neurosurg Rev*. (2017) 40:1–14. doi: 10.1007/s10143-016-0709-8
2. Biernat W. 2000 World Health Organization classification of tumors of the nervous system. *Pol J Pathol*. (2000) 51:107–114.
3. Louis DN, Ohgaki H, Wiestler OD, Cavenee WK, Burger PC, Jouvet A, et al. The 2007 WHO classification of tumours of the central nervous system. *Acta Neuropathol*. (2007) 114:97–109. doi: 10.1007/s00401-007-0243-4
4. Louis DN, Perry A, Reifenberger G, von Deimling A, Figarella-Branger D, Cavenee WK, et al. The 2016 World Health Organization classification of tumors of the central nervous system: a summary. *Acta Neuropathol*. (2016) 131:803–20. doi: 10.1007/s00401-016-1545-1
5. Mittler MA, Walters BC, Stopa EG. Observer reliability in histological grading of astrocytoma stereotactic biopsies. *J Neurosurg*. (1996) 85:1091–4. doi: 10.3171/jns.1996.85.6.1091
6. Prayson RA, Agamanolis DP, Cohen ML, Estes ML, Kleinschmidt-DeMasters BK, Abdul-Karim F, et al. Interobserver reproducibility among neuropathologists and surgical pathologists in fibrillary astrocytoma grading. *J Neurol Sci*. (2000) 175:33–9. doi: 10.1016/S0022-510X(00)00274-4
7. Castillo MS, Davis FG, Surawicz T, Bruner JM, Bigner S, Coons S, et al. Consistency of primary brain tumor diagnoses and codes in cancer surveillance systems. *Neuroepidemiology*. (2004) 23:85–93. doi: 10.1159/000073980
8. Cui Y, Tha KK, Terasaka S, Yamaguchi S, Wang J, Kudo K, et al. Prognostic imaging biomarkers in glioblastoma: development and independent validation on the basis of multiregion and quantitative analysis of MR images. *Radiology*. (2016) 278:546–53. doi: 10.1148/radiol.2015150358
9. Sanghani P, Ang BT, King NKK, Ren H. Overall survival prediction in glioblastoma multiforme patients from volumetric, shape and texture features using machine learning. *Surg Oncol*. (2018) 27:709–14. doi: 10.1016/j.suronc.2018.09.002
10. Henker C, Kriesen T, Glass Ä, Schneider B, Piek J. Volumetric quantification of glioblastoma: experiences with different measurement techniques and impact on survival. *J Neurooncol*. (2017) 135:391–402. doi: 10.1007/s11060-017-2587-5
11. Cuperlovic-Culf M, Ferguson D, Culf A, Morin P, Touaibia M. 1H NMR metabolomics analysis of glioblastoma subtypes: correlation between metabolomics and gene expression characteristics. *J Biol Chem*. (2012) 287:20164–75. doi: 10.1074/jbc.M111.337196
12. Roda JM, Pascual JM, Carceller F, González-Llanos F, Pérez-Higueras A, Solivera J, et al. Nonhistological diagnosis of human cerebral tumors by 1H magnetic resonance spectroscopy and amino acid analysis. *Clin Cancer Res*. (2000) 6:3983–93.
13. Opstad KS, Wright AJ, Bell BA, Griffiths JR, Howe FA. Correlations between *in vivo* (1)H MRS and *ex vivo* (1)H HRMAS metabolite measurements in adult human gliomas. *J Magn Reson Imaging*. (2010) 31:289–97. doi: 10.1002/jmri.22039
14. García-Martín ML, Hérigault G, Rémy C, Farion R, Ballesteros P, Coles JA, et al. Mapping extracellular pH in rat brain gliomas *in vivo* by 1H magnetic resonance spectroscopic imaging: comparison with maps of metabolites. *Cancer Res*. (2001) 61:6524–31.
15. Vander Heiden MG, Cantley LC, Thompson CB. Understanding the Warburg effect: the metabolic requirements of cell proliferation. *Science*. (2009) 324:1029–33. doi: 10.1126/science.1160809
16. Righi V, Roda JM, Paz J, Mucci A, Tugnoli V, Rodriguez-Tarduchy G, et al. 1H HR-MAS and genomic analysis of human tumor biopsies discriminate between high and low grade astrocytomas. *NMR Biomed*. (2009) 22:629–37. doi: 10.1002/nbm.1377
17. Glunde K, Bhujwalla ZM, Ronen SM. Choline metabolism in malignant transformation. *Nat Rev Cancer*. (2011) 11:835–48. doi: 10.1038/nrc3162
18. Solivera J, Cerdán S, Pascual JM, Barrios L, Roda JM. Assessment of 31P-NMR analysis of phospholipid profiles for potential differential diagnosis of human cerebral tumors. *NMR Biomed*. (2009) 22:663–74. doi: 10.1002/nbm.1387
19. Hattingen E, Raab P, Franz K, Lanfermann H, Setzer M, Gerlach R, et al. Prognostic value of choline and creatine in WHO grade II gliomas. *Neuroradiology*. (2008) 50:759–67. doi: 10.1007/s00234-008-0409-3
20. Roldan-Valadez E, Rios C, Motola-Kuba D, Matus-Santos J, Villa AR, Moreno-Jimenez S. Choline-to-N-acetyl aspartate and lipids-lactate-to-creatine ratios

together with age assemble a significant Cox's proportional-hazards regression model for prediction of survival in high-grade gliomas. *Br J Radiol.* (2016) 89:20150502. doi: 10.1259/bjr.20150502
21. Tolia M, Verganelakis D, Tsoukalas N, Kyrgias G, Papathanasiou M, Mosa E, et al. Prognostic value of MRS metabolites in postoperative irradiated high grade gliomas. *Biomed Res Int*. (2015) 2015:341042. doi: 10.1155/2015/341042
22. Gao W, Wang X, Li F, Shi W, Li H, Zeng Q. Cho/Cr ratio at MR spectroscopy as a biomarker for cellular proliferation activity and prognosis in glioma: correlation with the expression of minichromosome maintenance protein 2. *Acta Radiol*. (2019) 60:106–12. doi: 10.1177/0284185118770899
23. Shao W, Gu J, Huang C, Liu D, Huang H, Huang Z, et al. Malignancy-associated metabolic profiling of human glioma cell lines using 1H NMR spectroscopy. *Mol Cancer*. (2014) 13:197. doi: 10.1186/1476-4598-13-197
24. Guidoni L, Ricci-Vitiani L, Rosi A, Palma A, Grande S, Luciani AM, et al. 1H NMR detects different metabolic profiles in glioblastoma stem-like cells. *NMR Biomed*. (2014) 27:129–45. doi: 10.1002/nbm.3044
25. Kleihues P, Burger PC, Scheithauer BW. The new WHO classification of brain tumours. *Brain Pathol*. (1993) 3:255–68. doi: 10.1111/j.1750-3639.1993.tb00752.x
26. Shinoda J, Sakai N, Murase S, Yano H, Matsuhisa T, Funakoshi T. Selection of eligible patients with supratentorial glioblastoma multiforme for gross total resection. *J Neurooncol*. (2001) 52:161–71. doi: 10.1023/A:1010624504311
27. Matyja E, Grajkowska W, Stępień K, Naganska E. Heterogeneity of histopathological presentation of pilocytic astrocytoma - diagnostic pitfalls. A review. *Folia Neuropathol*. (2016) 54:197–211. doi: 10.5114/fn.2016.62530
28. Collins VP, Jones DT, Giannini C. Pilocytic astrocytoma: pathology, molecular mechanisms and markers. *Acta Neuropathol*. (2015) 129:775–88. doi: 10.1007/s00401-015-1410-7
29. Cerdàn S, Parrilla R, Santoro J, Rico M. 1H NMR detection of cerebral myo-inositol. *FEBS Lett*. (1985) 187:167–72. doi: 10.1016/0014-5793(85)81235-7
30. Klunk WE, Xu CJ, Panchalingam K, McClure RJ, Pettegrew JW. Analysis of magnetic resonance spectra by mole percent: comparison to absolute units. *Neurobiol Aging*. (1994) 15:133–40. doi: 10.1016/0197-4580(94)90153-8
31. Govindaraju V, Young K, Maudsley AA. Proton NMR chemical shifts and coupling constants for brain metabolites. *NMR Biomed*. (2000) 13:129–53. doi: 10.1002/1099-1492(200005)13:3<129::AID-NBM619>3.0.CO;2-V
32. Breiman L. *Classification and Regression Trees*. Belmont, CA: Wadsworth International Group (1984).
33. Yamasaki F, Kurisu K, Kajiwara Y, Watanabe Y, Takayasu T, Akiyama Y, et al. Magnetic resonance spectroscopic detection of lactate is predictive of a poor prognosis in patients with diffuse intrinsic pontine glioma. *Neuro Oncol*. (2011) 13:791–801. doi: 10.1093/neuonc/nor038
34. Steidl E, Pilatus U, Hattingen E, Steinbach JP, Zanella F, Ronellenfitsch MW, et al. Myoinositol as a biomarker in recurrent glioblastoma treated with bevacizumab: A 1H-magnetic resonance spectroscopy study. *PLoS ONE*. (2016) 11:e0168113. doi: 10.1371/journal.pone.0168113
35. Hattingen E, Bähr O, Rieger J, Blasel S, Steinbach J, Pilatus U. Phospholipid metabolites in recurrent glioblastoma: *in vivo* markers detect different tumor phenotypes before and under antiangiogenic therapy. *PLoS ONE*. (2013) 8:e56439. doi: 10.1371/journal.pone.0056439
36. Quon H, Brunet B, Alexander A, Murtha A, Abdulkarim B, Fulton D, et al. Changes in serial magnetic resonance spectroscopy predict outcome in high-grade glioma during and after postoperative radiotherapy. *Anticancer Res*. (2011) 31:3559–65.
37. Steffen-Smith EA, Shih JH, Hipp SJ, Bent R, Warren KE. Proton magnetic resonance spectroscopy predicts survival in children with diffuse intrinsic pontine glioma. *J Neurooncol*. (2011) 105:365–73. doi: 10.1007/s11060-011-0601-x
38. Chang SM, Nelson S, Vandenberg S, Cha S, Prados M, Butowski N, et al. Integration of preoperative anatomic and metabolic physiologic imaging of newly diagnosed glioma. *J Neurooncol*. (2009) 92:401–15. doi: 10.1007/s11060-009-9845-0
39. Li X, Jin H, Lu Y, Oh J, Chang S, Nelson SJ. Identification of MRI and 1H MRSI parameters that may predict survival for patients with malignant gliomas. *NMR Biomed*. (2004) 17:10–20. doi: 10.1002/nbm.858
40. Reijneveld JC, van der Grond J, Ramos LM, Bromberg JE, Taphoorn MJ. Proton MRS imaging in the follow-up of patients with suspected low-grade gliomas. *Neuroradiology*. (2005) 47:887–91. doi: 10.1007/s00234-005-1435-z
41. Hattingen E, Raab P, Franz K, Zanella FE, Lanfermann H, Pilatus U. Myo-inositol: a marker of reactive astrogliosis in glial tumors? *NMR Biomed*. (2008) 21:233–41. doi: 10.1002/nbm.1186
42. Jaskólski DJ, Fortuniak J, Majos A, Gajewicz W, Papierz W, Liberski PP, et al. Magnetic resonance spectroscopy in intracranial tumours of glial origin. *Neurol Neurochir Pol*. (2013) 47:438–49. doi: 10.5114/ninp.2013.32999
43. Leather T, Jenkinson MD, Das K, Poptani H. Magnetic resonance spectroscopy for detection of 2-hydroxyglutarate as a biomarker for IDH mutation in gliomas. *Metabolites*. (2017) 7:E29. doi: 10.3390/metabo7020029
44. Castillo M, Smith JK, Kwock L. Correlation of myo-inositol levels and grading of cerebral astrocytomas. *AJNR Am J Neuroradiol*. (2000) 21:1645–9.
45. Pascual JM, Solivera J, Prieto R, Barrios L, López-Larrubia P, Cerdán S, et al. Time course of early metabolic changes following diffuse traumatic brain injury in rats as detected by (1)H NMR spectroscopy. *J Neurotrauma*. (2007) 24:944–59. doi: 10.1089/neu.2006.0190
46. Croall I, Smith FE, Blamire AM. Magnetic resonance spectroscopy for traumatic brain injury. *Top Magn Reson Imaging*. (2015) 24:267–74. doi: 10.1097/RMR.0000000000000063
47. Kim JH, Chang KH, Na DG, Song IC, Kwon BJ, Han MH, et al. 3T 1H-MR spectroscopy in grading of cerebral gliomas: comparison of short and intermediate echo time sequences. *AJNR Am J Neuroradiol*. (2006) 27:1412–8.
48. Natsumeda M, Igarashi H, Nomura T, Ogura R, Tsukamoto Y, Kobayashi T, et al. Accumulation of 2-hydroxyglutarate in gliomas correlates with survival: a study by 3.0-tesla magnetic resonance spectroscopy. *Acta Neuropathol Commun*. (2014) 2:158. doi: 10.1186/s40478-014-0158-y
49. Fan G, Sun B, Wu Z, Guo Q, Guo Y. *In vivo* single-voxel proton MR spectroscopy in the differentiation of high-grade gliomas and solitary metastases. *Clin Radiol*. (2004) 59:77–85. doi: 10.1016/j.crad.2003.08.006
50. Galanaud D, Nicoli F, Chinot O, Confort-Gouny S, Figarella-Branger D, Roche P, et al. Noninvasive diagnostic assessment of brain tumors using combined *in vivo* MR imaging and spectroscopy. *Magn Reson Med*. (2006) 55:1236–45. doi: 10.1002/mrm.20886
51. Opstad KS, Ladroue C, Bell BA, Griffiths JR, Howe FA. Linear discriminant analysis of brain tumour (1)H MR spectra: a comparison of classification using whole spectra versus metabolite quantification. *NMR Biomed*. (2007) 20:763–70. doi: 10.1002/nbm.1147
52. Sabatier J, Gilard V, Malet-Martino M, Ranjeva JP, Terral C, Breil S, et al. Characterization of choline compounds with *in vitro* 1H magnetic resonance spectroscopy for the discrimination of primary brain tumors. *Invest Radiol*. (1999) 34:230–5. doi: 10.1097/00004424-199903000-00013
53. Tsun ZY, Possemato R. Amino acid management in cancer. *Semin Cell Dev Biol*. (2015) 43:22–32. doi: 10.1016/j.semcdb.2015.08.002

Conflict of Interest Statement: The authors declare that the research was conducted in the absence of any commercial or financial relationships that could be construed as a potential conflict of interest.

frontiers in Oncology

ORIGINAL RESEARCH
published: 07 June 2019
doi: 10.3389/fonc.2019.00472

A Critical Appraisal of the Quality of Glioma Imaging Guidelines Using the AGREE II Tool: A EuroAIM Initiative

*Valeria Romeo[1], Arnaldo Stanzione[1], Lorenzo Ugga[1], Renato Cuocolo[1], Sirio Cocozza[1], Evangelia Ioannidou[2,3], Arturo Brunetti[1] and Sotirios Bisdas[3,4]**

[1] Department of Advanced Biomedical Sciences, University of Naples "Federico II", Naples, Italy, [2] Medical School, University of Ioannina, Ioannina, Greece, [3] Department of Neuroradiology, The National Hospital for Neurology and Neurosurgery, University College London NHS Foundation Trust, London, United Kingdom, [4] Department of Brain Repair and Rehabilitation, Institute of Neurology, University College London, London, United Kingdom

OPEN ACCESS

Edited by:
Bo Gao,
Affiliated Hospital of Guizhou Medical University, China

Reviewed by:
Seyedmehdi Payabvash,
Yale University, United States
Shanshan Jiang,
The Johns Hopkins Hospital, Johns Hopkins Medicine, United States

***Correspondence:**
Sotirios Bisdas
s.bisdas@ucl.ac.uk

Specialty section:
This article was submitted to Cancer Imaging and Image-directed Interventions, a section of the journal Frontiers in Oncology

Received: 14 March 2019
Accepted: 16 May 2019
Published: 07 June 2019

Citation:
Romeo V, Stanzione A, Ugga L, Cuocolo R, Cocozza S, Ioannidou E, Brunetti A and Bisdas S (2019) A Critical Appraisal of the Quality of Glioma Imaging Guidelines Using the AGREE II Tool: A EuroAIM Initiative. Front. Oncol. 9:472. doi: 10.3389/fonc.2019.00472

Background: Following the EuroAIM initiative to assess the quality of medical imaging guidelines by using the Appraisal of Guidelines for Research and Evaluation (AGREE) II instrument, we aimed to evaluate the quality of the current imaging guidelines in patients with gliomas.

Methods: A literature search was conducted to identify eligible imaging guidelines considered in the management of adult patients with gliomas. The selected guidelines were evaluated using the AGREE II instrument by four independent appraisers. The agreement among the four appraisers was estimated using the intraclass correlation coefficient (ICC) analysis.

Results: Seven guidelines were selected for the appraisal. Six out of the seven guidelines showed an average level of quality with only one showing a low quality. The highest scores were found in Domain 1 "Scope and purpose" (mean score = 81.2%) and Domain 4 "Clarity of presentation" (mean score = 77.6%). The remaining domains showed a low level of quality and, in particular, Domain 5 "Applicability" was the most critical with a mean score of 41.7%, mainly related to a minor attention to barriers and facilitators as well as costs and resources implications of applying the guidelines. The ICC analysis showed a very good agreement among the four appraisers with ICC values ranging from 0.907 to 0.993.

Conclusions: The available guidelines on glioma imaging emerged as of average quality according to the AGREE II tool analysis. Based on these results, further efforts should be made in order to involve different professional bodies and stakeholders and increase patient and public involvement in any future guideline drafting as well as to improve the applicability of these guidelines into the clinical practice.

Keywords: AGREE II, glioma, imaging, guidelines, evidence-based medicine

INTRODUCTION

Malignant primary brain tumors still represent one of the most difficult cancers to treat with a rather low 5 year overall survival (1). Among these, glioma constitutes the largest subgroup with high grade-glioma, specifically glioblastoma, accounting for almost 50% of cases (2). Diagnostic imaging, particularly magnetic resonance imaging (MRI), plays a fundamental role in diagnosis, staging and follow-up of glioma patients (3, 4). Considering the very poor prognosis of such patients and the lack of an effective treatment, especially for recurrent disease, the patient management is very demanding whereas major endeavors are constantly made to develop more effective drug treatments (5, 6) and sensitive methods for early tumor detection, in particular recurrent disease as it appears crucial for prolonging survival. In this perspective, imaging and especially MRI make a substantial contribution to the assessment of response to treatment using conventional and advanced techniques that probe the tumor biology (7). The possibility to leverage the efforts by conducting multicenter studies in different research and clinical domains (e.g., treatment trials, identification of diagnostic, and prognostic imaging biomarkers) necessitates a standardization of the imaging protocols, especially in terms of clinical indications and acquisition techniques. To achieve a reasonable level of standardization, diagnostic imaging guidelines covering clinical indications, acquisition protocols, and technical details have been previously realized. However, the reliability of clinical practice guidelines has been questioned and the proposed recommendation statements should be rather judged based on the methodological rigor followed in their drafting process. In order to assess the quality of guidelines, several useful tools have been proposed (8). In particular, the updated Appraisal of Guidelines for Research & Evaluation version 2.0 (AGREE II) (9, 10), first established in 1998, is the most comprehensively validated and has been widely adopted for the quality assessment of clinical practice guidelines (11). A recent initiative to assess meticulously the quality of the current imaging guidelines has been promoted by the European Network for the Assessment of Imaging in Medicine (EuroAIM), founded by the European Institute for Biomedical Imaging Research (EIBIR) (12). First evaluations conducted in this matter revealed that the quality of imaging guideline is heterogeneous, ranging from low to high levels (13–16). In the context of the EuroAIM initiative, we aimed to evaluate the quality of the existing guidelines on the role of imaging in glioma patients.

MATERIALS AND METHODS

Literature Search

Between October and November 2018, an exhaustive literature search was conducted on PubMed using MeSH and non-MeSH terms with and without customizing the search for "Consensus Development Conference," "Guideline," "Clinical Practice Guideline," and "Government Document." The following terms and their expansions were entered: "glioma," "neoplasms," "brain tumors," "guideline," "practice guideline," "recommendations, health planning," "official positions," "diagnostic imaging," "imaging." Similarly, EMBASE, Scopus, Wiley Online Library and Google, including gray literature sources, were also searched. The search was focused on the most up-to-date version of the identified guidelines. Inclusion criteria were: (1) guidelines focused on the role of imaging in the management of primary brain tumors and specifically gliomas; (2) guidelines dealing with the adult population; and (3) papers with available English full text. Exclusion criteria were the following: (1) guidelines not developed under the auspices of recognized professional institutions, associations, and/or working groups; (2) clinical practice guidelines in which imaging was included in a wider, rather abstract context (e.g., guidelines dealing with cancer clinical management and treatment); (3) guidelines not dealing with the major imaging techniques employed for the assessment of gliomas, particularly MRI.

Guideline Evaluation

Selected papers were evaluated by four independent radiologists (VR, AS, LU, RC) with 6 to 9 years of clinical expertise and research in a university hospital setting. The appraisers used the AGREE II instrument (http://www.agreetrust.org/), made of six quality domains, each "…capturing a unique dimension of guideline quality," and including a total of 23 key items (9). Specifically: domain 1 "Scope and Purpose" includes items from 1 to 3; domain 2 "Stakeholder Involvement" comprises items from 4 to 6; domain 3 "Rigor of Development" provides items from 7 to 14; domain 4 "Clarity of presentation" contains items from 15 to 17; domain 5 "Applicability" covers items from 18 to 21; and domain 6 "Editorial Independence" includes items from 21 to 22. Domains and items are summarized in **Table 1**. Each item is rated on a 7-point scale, ranging from "strongly disagree" (score = 1), to "strongly agree" (score = 7). Finally, an Overall Assessment section is provided to summarize in a comprehensive way the quality of the guideline. Each appraiser was asked to assign a score to each item and to the Overall Assessment section as well as to indicate whether he/she would recommend the use of the guideline in clinical practice. Whereas they had previous exposure to the AGREE II tool (15), the appraisers also carried out the freely available online training tool consisting of an overview tutorial and a practice exercise (17).

Quality Assessment

Following the AGREE II manual instructions, domain scores were "…calculated by summing up all the scores of the individual items in a domain and by scaling the total as a percentage of the maximum possible score for that domain" (17). Guideline overall quality was considered "high" when 5 or more domains scored more than 60%, "average" when 3 or 4 domains scored more than 60%, and "low" when no more than two domains scored more than 60%, as previously performed (13–16). Mean scores ± standard deviations of each guideline were then calculated. Domain overall quality was assessed by calculating the mean scores of each domain being considered as good (≥80%), acceptable (60–79.9%), low (40–59.9%), or very low (<40%).

TABLE 1 | AGREE II domains and items (9).

DOMAIN 1. SCOPE AND PURPOSE
Item 1: the overall objective(s) of the guideline is (are) specifically described
Item 2: the health question(s) covered by the guideline is (are) specifically described
Item 3: the population (patients, public, etc.) to whom the guideline is meant to apply is specifically described
DOMAIN 2. STAKEHOLDER INVOLVEMENT
Item 4: the guideline development group includes individuals from all the relevant professional groups
Item 5: the views and preferences of the target population (patients, public, etc.) have been sought
Item 6: the target users of the guideline are clearly defined
DOMAIN 3. RIGOR OF DEVELOPMENT
Item 7: systematic methods were used to search for evidence
Item 8: the criteria for selecting the evidence are clearly described
Item 9: the strengths and limitations of the body of evidence are clearly described
Item 10: the methods for formulating the recommendations are clearly described
Item 11: the health benefits, side effects, and risks have been considered in formulating the recommendations
Item 12: there is an explicit link between the recommendations and the supporting evidence
Item 13: the guideline has been externally reviewed by experts prior to its publication
Item 14: a procedure for updating the guideline is provided
DOMAIN 4. CLARITY OF PRESENTATION
Item 15: the recommendations are specific and unambiguous
Item 16: the different options for management of the condition or health issue are clearly presented
Item 17: key recommendations are easily identifiable
Domain 5. APPLICABILITY
Item 18: the guideline describes facilitators and barriers to its application
Item 19: the guideline provides advice and/or tools on how the recommendations can be put into practice
Item 20: the potential resource implications of applying the recommendations have been considered
Item 21: the guideline presents monitoring and/or auditing criteria
Domain 6. EDITORIAL INDEPENDENCE
Item 22: the views of the funding body have not influenced the content of the guideline
Item 23: competing interests of guideline development group members have been recorded and addressed

Statistical Analysis

The level of agreement among the four appraisers was assessed using the intraclass correlation coefficient (ICC) analysis and rated as: poor (ICC $\leq$ 0.20); fair (ICC from 0.21 to 0.40); moderate (ICC from 0.41 to 0.60); good (ICC from 0.61 to 0.80); and very good (ICC $\geq$ 0.81) (13–16). Scores collection and calculation as well as the statistical analysis were performed by an independent reviewer (SC) with 9 years of experience in scientific research and biostatistics.

RESULTS

Literature Search and Guidelines Selection

The literature search returned 162 records. The majority of the retrieved papers was excluded after the evaluation of title and abstract, with 29 remaining articles extensively reviewed in full-text and 7 guidelines finally eligible for the appraisal process (18–24). A flow-chart of the guideline selection process is illustrated in **Figure 1**. Details of the selected recommendation papers are reported in **Table 2**.

Statistical Analysis

The ICC analysis showed a very good agreement among the four appraisers with values ranging from 0.907 to 0.993; the ICC scores with their 95% confidence intervals are reported in **Table 3**.

Guideline Scores

According to the AGREE II tool, six out of seven guidelines showed an "average" quality with one guideline demonstrating "low" quality. The highest domain scores were found in Domain 1 "Scope and purpose" (mean score = 81.2%) indicating good quality, followed by Domain 4 "Clarity of presentation" (mean score = 77.6%) suggesting an acceptable quality. The remaining domains showed a low level of quality and in particular Domain 5 "Applicability" was the most critical with a mean score of 41.7%. Similarly, Domain 2 "Stakeholder involvement," Domain 3 "Rigor of development" and Domain 6 "Editorial independence" were considered of low quality achieving mean scores of 52, 55.1, and 58.9%, respectively.

The highest variability in domain scores was observed in Domain 3 "Rigor of development" and Domain 6 "Editorial independence" with a SD of 21.8 and 22.7%, respectively, while the lowest variability was found in Domain 4 "Clarity of presentation" with SD of 9.5%. In the remaining domains, the variability ranged from 12 to 14.4%. All domains and guidelines scores are shown in **Table 4** and **Figure 2**. Detailed scores of each guideline are reported in the **Supplementary Materials**.

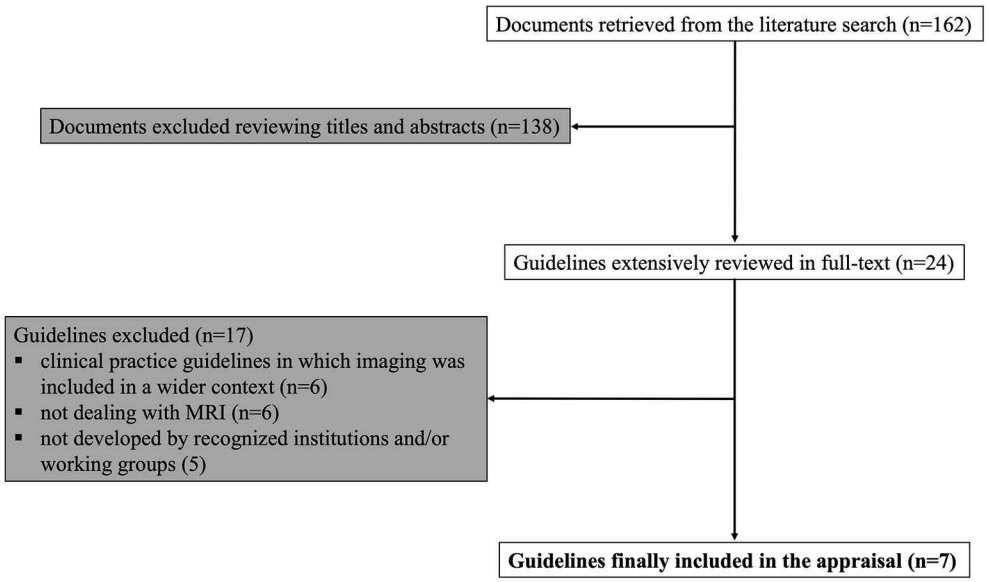

FIGURE 1 | Guideline selection process.

DISCUSSION

Overall, the current imaging guidelines for the management of glioma patients showed an intermediate level of quality according to the AGREE II analytical approach. In detail, six out of the seven guidelines showed an average level of quality with only one revealing low quality.

Domain Scores

Domain 1 "Scope and purpose" and Domain 4 "Clarity of presentation" presented with the highest scores as they are primarily taken into account by guideline developers when defining the objectives and convey the recommendations. Domain 4 was the only one performing higher than 60% in all investigated guidelines. The remaining domains were judged with lower mean scores, ranging from 41.7% (Domain 5) to 58.9% (Domain 6). In particular, Domain 2 "Stakeholder involvement" performed poorly (mean score = 52%) as not all relevant professional groups (e.g., medical and/or radiation oncologist) were involved in the guideline drafting. In almost all cases, authors consisted of radiologists along with neurosurgeons. Moreover, the views and preferences of the target patient group were not considered e.g., in terms of experiences and expectations. Although this issue may appear unwonted and not customary for medical/radiological guidelines, the AGREE II tool provides suggestions about how to facilitate patient and public involvement (e.g., by prior conferring with patients to understand main issues, using interviews or literature review on their preferences or by stakeholder's external review on the draft). Of note, target users have been scarcely specified; this is an issue that could be easily addressed by clearly indicating which professionals are meant to use the guideline.

Domain 3 "Rigor of development" assesses the methodology by which the guideline is elaborated and unfortunately obtained a low mean score (55.1%), ranging from 20.3 to 73.4% with a SD of 21.8%. The high variability discerned is due to the opacity in the methodology employed for evidence search and evaluation, enabled usually through the performance of systematic literature reviews. Only Thust et al. specifically discussed the possible methodological limitations (24). Furthermore, methods for formulating the recommendations were not always clearly named and structured techniques (e.g., the Delphi method) to reach a final consensus were not used. The most critical results were presented in Domain 5 "Applicability," in which none of the guidelines achieved a score higher than 60%. It should be noted that issues addressed in this Domain are conventionally difficult to be considered given that resources and costs are heterogeneous among different countries and national healthcare systems. This domain also contains very specific criteria, such as the inclusion of dedicated sections to provide solutions to barrier analysis, tools to capitalize on guideline facilitators or methods by which the cost information was sought. Finally, Domain 6 "Editorial independence," even if showing a low-quality mean score (58.9%), did not emerge as critical as occurred in previous AGREE-II evaluations (13, 14). In almost all papers, conflict of interests and funding disclosures have been stated, as the majority of guidelines is published on peer-reviewed journals, which oblige for such statements. However, in none guideline the declaration "the views of the funding body have not influenced the content of the guideline" was included.

Considerations

General remarks can be made in light of the present appraisal, especially regarding the overall average scores of

TABLE 2 | Details of the selected guidelines.

Title	Year	Author/Organization	Source	Topic
Recommendations for cross-sectional imaging in cancer management, Second edition-Tumors of the brain (18)	2014	Byrne et al. Royal College of Radiologists	www.rcr.ac.uk	Imaging recommendations for the management of brain tumors
Consensus recommendations for a standardized Brain Tumor Imaging Protocol in clinical trials (19)	2015	Ellingson et al. US Food and Drug Administration, National Cancer Institute	Neuro-Oncology	Recommendations for a standardized MRI protocol for the assessment of glioblastoma
MR Imaging of Neoplastic Central Nervous System Lesions: Review and Recommendations for Current Practice (20)	2012	Essig et al. Meeting expert at the "Improving Patient Management by optimizing MR Imaging of Neoplastic CNS Lesions" meeting, Zurich, 2010	American Journal of Neuroradiology	Imaging recommendations for the assessment of CNS lesions
The role of imaging in the management of adults with diffuse low-grade glioma—A systematic review and evidence-based clinical practice guideline (21)	2015	Fouke et al. Supported by the AANS/CNS Joint Guidelines Committee	Journal of Neuro-Oncology	Imaging recommendations for the assessment of diffuse low-grade glioma
Neuroradiological assessment of newly diagnosed glioblastoma (22)	2008	Mukundan et al. Supported by the AANS/CNS Joint Guidelines Committee	Journal of Neuro-Oncology	Imaging recommendations for the assessment of glioblastoma
The role of imaging in the management of progressive glioblastoma- A systematic review and evidence-based clinical practice guideline (23)	2014	Ryken et al. Supported by the AANS/CNS Joint Guidelines Committee	Journal of Neuro-Oncology	Imaging recommendations for the assessment of progressive glioblastoma
Glioma imaging in Europe: A survey of 220 centres and recommendations for best clinical practice (24)	2018	Thust et al. Endorsed by the European Society of Neuroradiology and the European Organization for Research and Treatment of Cancer	European Radiology	Clinical practice recommendations for glioma conventional and advanced MRI protocol

the evaluated guidelines, with none of them fulfilling high quality. While in certain guidelines the recommendations were well-underpinned by a rigorous systematic review of literature, the recommendations were disadvantaged by lacking contributions from international expert panels, other disciplines-of-interest and considerations for the routine application of the recommended procedures. On the other hand, European guidelines did not immerse in detail for the evidence search and synthesis methodology. It is worth mentioning that 4 out of 7 guidelines though close to reach a final "high" score, having each 4 domains scoring higher than 60%, they overall scored moderately as Domain 2 "Stakeholder involvement" and Domain 5 "Applicability" performed poorly. Thus, emphasizing to these domains will improve dramatically the future guidelines quality. The results of the current guidelines appraisal are better than those of a previous AGREE II evaluation of clinical practice and management guidelines in glioma patients (25). In the previous evaluation, tangible concerns were voiced for Domain 2 "Stakeholder involvement," Domain 3 "Rigor of development," Domain 5 "Applicability," and Domain 6 "Editorial independence." A further AGREE II evaluation of the clinical practice guidelines for rehabilitation on brain tumor patients also showed moderate quality results (26). Furthermore, an improvement in terms of guidelines quality over time seems to emerge from our analysis. Based on the aforementioned results, the quality of future imaging guidelines in gliomas could be further improved by summarizing the key evidence elements derived from literature review and expert consultation and to report them close to the final recommendations. Data related to any guideline external review and update process should also be provided.

TABLE 3 | Results of the Intraclass correlation coefficient analysis.

References	ICC	95% CI
Byrne et al. (18)	0.907	0.663–0.986
Ellingson et al. (19)	0.977	0.920–0.986
Essig et al. (20)	0.982	0.937–0.997
Fouke et al. (21)	0.992	0.970–0.999
Mukundan et al. (22)	0.992	0.972–0.999
Ryken et al. (23)	0.991	0.969–0.999
Thust et al. (24)	0.993	0.973–0.999

ICC, intraclass correlation coefficient; CI, confidence interval.

Limitations

The heterogeneity of the selected guidelines, dealing either with the definition of a standardized MRI protocol or with clinical indications of other than MRI techniques, pose an inherent limitation in our evaluation. We attempted to mitigate this risk by a universal and robust appraising tool as the AGREE II domains; we acknowledge, however, that the AGREE II instrument does not directly assess the quality of the guideline content (8). Furthermore, it is sensible that guidelines aiming to assess the role of imaging in the management of glioma patients might

TABLE 4 | Results of the AGREE II-based guidelines evaluation.

Guideline	Domain 1	Domain 2	Domain 3	Domain 4	Domain 5	Domain 6	Mean score	Guideline Overall Quality
Byrne et al.	59.7	25.0	20.3	65.3*	32.3	37.5	40.0	Low
Ellingson et al.	81.9*	72.2*	44.8	69.4*	50.0	56.3	62.4	Average
Essig et al.	75.0*	61.1*	34.9	84.7*	59.4	35.4	58.4	Average
Fouke et al.	97.2*	54.2	75.5*	88.9*	38.5	85.4*	73.3	Average
Mukundan et al.	80.6*	47.2	72.4*	70.8*	31.3	37.5	56.6	Average
Ryken et al.	91.7*	52.8	73.4*	76.4*	27.1	81.3*	67.1	Average
Thust et al.	81.9*	51.4	64.1*	87.5*	53.1	79.2*	69.5	Average
Mean Score	81.2	52.0	55.1	77.6	41.7	58.9		
SD	12.0	14.4	21.8	9.5	12.5	22.7		
Domain Overall Quality	Good	Low	Low	Acceptable	Low	Low		

*Scores are expressed as percentages; SD, standard deviation; *Domain scoring >60%. Guideline Overall quality was defined "high" when 5 or more domains scored >60%, "average" when 3 or 4 domains scored >60%, "low" when ≤2 domains scored >60%. Domain Overall quality was defined good when ≥80%; acceptable when = 60–79%; low when = 40–59%; very low when <40%.*

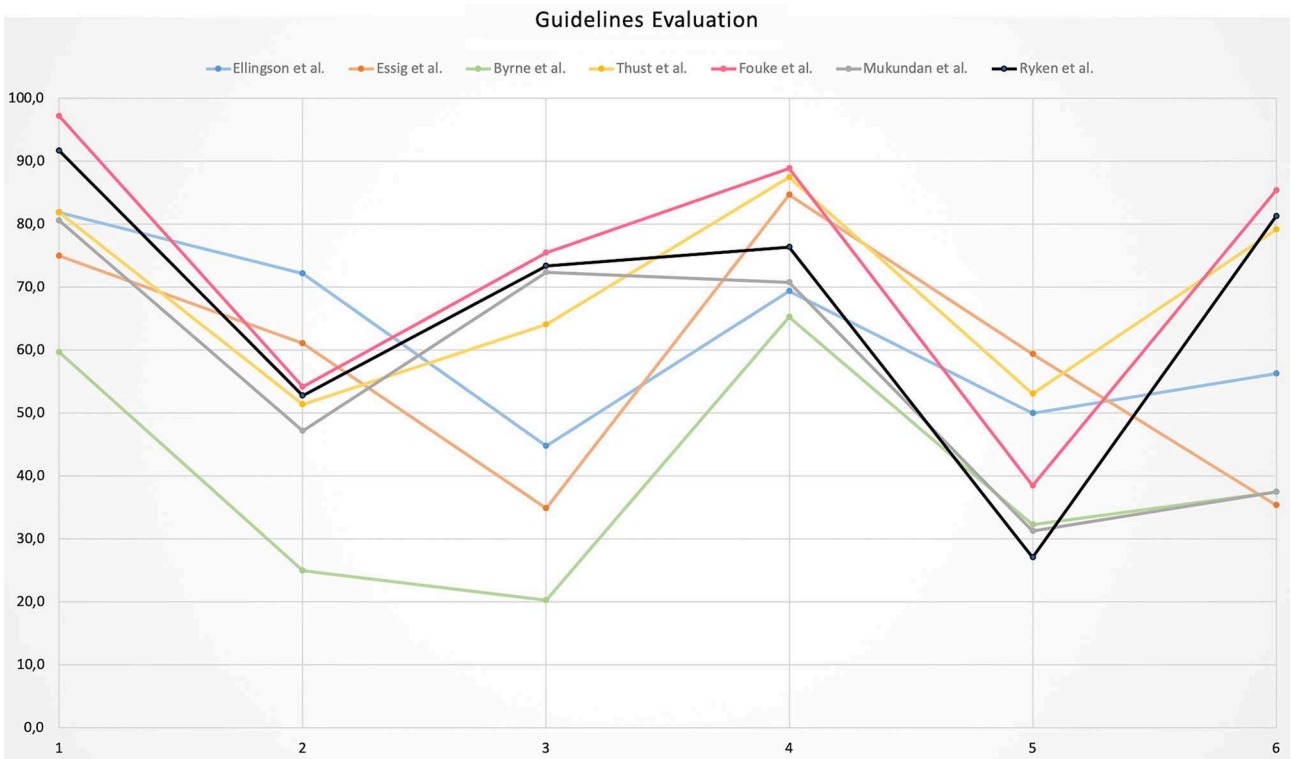

FIGURE 2 | Line chart illustrating the overall domain scores of each guideline.

differ in terms of tumor sub-types (i.e., low- vs. high-grade], overall setting or even be published as appendices in wider clinical guidelines. This makes difficult a broad-based acceptance, an obvious finding in the paper of Thust et al. (24), who probed the adherence of European centers to the "mainstay" glioma MRI protocol proposed by Ellingson et al. (19). A further limitation in our study might be the exclusion of guidelines in non-English language. Finally, while initial evidence suggests to weight the domain scores for the overall quality assessment (27), we decided not to embrace this approach. Nevertheless, the possibility to prioritize one domain over the other could be considered in future AGREE II appraisals.

CONCLUSIONS

The existing guidelines on the role of imaging in glioma patients showed an overall intermediate level of quality according to the AGREE II tool evaluation. The fairly high number

of available guidelines highlights the profound interest of the oncological and radiological communities to significantly improve the management in terms of clinical indications, protocol appropriateness, and acquisition techniques. In this perspective, issues and suggestions transpired from this appraisal could be taken into account to improve the quality of imaging guidelines in neuro-oncology.

CONTRIBUTION TO THE FIELD STATEMENT

The quality of imaging guidelines in terms of methodological rigor has been recently questioned and found to be heterogeneous, thus potentially affecting the reliability of guidelines themselves. The use of imaging guidelines is crucial for the assessment of glioma patients, especially in the context of multicenter studies and clinical trials for new drugs development and the assessment of response to treatment. We therefore joined a recent initiative of the European Network for the Assessment of Imaging in Medicine (EuroAIM) and assessed the quality of imaging guidelines focused on glioma using the Appraisal of Guidelines for Research & Evaluation version 2.0 (AGREE II) tool. According to our results, existing guidelines on glioma imaging emerged as of average quality. We also provided suggestions to further increase the quality of future guidelines on glioma imaging on the basis of the raised criticisms.

AUTHOR CONTRIBUTIONS

VR, SC, and EI performed the literature search. VR, AS, LU, and RC evaluated the guidelines. SC provided the statistical analysis. The manuscript was drafted by VR, AS, LU, RC, SC, and AB. Data curation was carried out by VR and SC. Critical revision was made by AB and SB. SB was responsible for project administration, study conception and design. All authors revised and approved the manuscript.

ACKNOWLEDGMENTS

This work was promoted by European Network for Assessment of Imaging in Medicine (EuroAIM), research platform of the European Institute for Biomedical Research (EIBIR, http://www.eibir.org/scientific-activities/joint-initiatives/euroaim/). SB receives support from the NIHR Biomedical Research Centre at University College London Hospitals NHS Foundation Trust and University College London.

SUPPLEMENTARY MATERIAL

The Supplementary Material for this article can be found online at: https://www.frontiersin.org/articles/10.3389/fonc.2019.00472/full#supplementary-material

REFERENCES

1. Lamborn KR. Prognostic factors for survival of patients with glioblastoma: recursive partitioning analysis. *Neuro Oncol*. (2004) 6:227–35. doi: 10.1215/S1152851703000620
2. Ostrom QT, Bauchet L, Davis FG, Deltour I, Fisher JL, Langer CE, et al. The epidemiology of glioma in adults: a state of the science review. *Neuro Oncol*. (2014) 16:896–913. doi: 10.1093/neuonc/nou087
3. Upadhyay N, Waldman AD. Conventional MRI evaluation of gliomas. *Br J Radiol*. (2011) 84:S107–11. doi: 10.1259/bjr/65711810
4. Kao HW, Chiang SW, Chung HW, Tsai FY, Chen CY. Advanced MR imaging of gliomas: an update. *Biomed Res Int*. (2013) 2013:970586. doi: 10.1155/2013/970586
5. Shergalis A, Bankhead A, Luesakul U, Muangsin N, Neamati N. Current challenges and opportunities in treating glioblastoma. *Pharmacol Rev*. (2018) 70:412–45. doi: 10.1124/pr.117.014944
6. O'Duibhir E, Carragher NO, Pollard SM. Accelerating glioblastoma drug discovery: convergence of patient-derived models, genome editing and phenotypic screening. *Mol Cell Neurosci*. (2017) 80:198–207. doi: 10.1016/j.mcn.2016.11.001
7. Dhermain FG, Hau P, Lanfermann H, Jacobs AH, van den Bent MJ. Advanced MRI and PET imaging for assessment of treatment response in patients with gliomas. *Lancet Neurol*. (2010) 9:906–20. doi: 10.1016/S1474-4422(10)70181-2
8. Eikermann M, Holzmann N, Siering U, Rüther A. Tools for assessing the content of guidelines are needed to enable their effective use - a systematic comparison. *BMC Res Notes*. (2014) 7:853. doi: 10.1186/1756-0500-7-853
9. Brouwers MEA. *Appraisal of Guidelines for Research & Evaluation II AGREE*. Agree Next Steps Consortium (2009).
10. Brouwers MC, Kho ME, Browman GP, Burgers JS, Cluzeau F, Feder G, et al. AGREE II: advancing guideline development, reporting and evaluation in health care. *J Clin Epidemiol*. (2010) 63:1308–11. doi: 10.1016/j.jclinepi.2010.07.001
11. Siering U, Eikermann M, Hausner E, Hoffmann-Eßer W, Neugebauer EA. Appraisal tools for clinical practice guidelines: a systematic review. *PLoS ONE*. (2013) 8:e82915. doi: 10.1371/journal.pone.0082915
12. Sardanelli F, Bashir H, Berzaczy D, Cannella G, Espeland A, Flor N, et al. The role of imaging specialists as authors of systematic reviews on diagnostic and interventional imaging and its impact on scientific quality: report from the EuroAIM Evidence-based Radiology Working Group. *Radiology*. (2014) 272:533–40. doi: 10.1148/radiol.14131730
13. Messina C, Bignotti B, Tagliafico A, Orlandi D, Corazza A, Sardanelli F, et al. A critical appraisal of the quality of adult musculoskeletal ultrasound guidelines using the AGREE II tool: an EuroAIM initiative. *Insights Imaging*. (2017) 8:491–7. doi: 10.1007/s13244-017-0563-4
14. Messina C, Bignotti B, Bazzocchi A, Phan CM, Tagliafico A, Guglielmi G, et al. A critical appraisal of the quality of adult dual-energy X-ray absorptiometry guidelines in osteoporosis using the AGREE II tool: an EuroAIM initiative. *Insights Imaging*. (2017) 8:311–17. doi: 10.1007/s13244-017-0553-6
15. Romeo V, Stanzione A, Cocozza S, Ugga L, Cuocolo R, Brunetti A, et al. A critical appraisal of the quality of head and neck cancer imaging guidelines using the AGREE II tool: a EuroAIM initiative. *Cancer Med*. (2018) 8:209–15. doi: 10.1002/cam4.1933
16. Doniselli FM, Zanardo M, Manfrè L, Papini GDE, Rovira A, Sardanelli F, et al. A critical appraisal of the quality of low back pain practice guidelines using the AGREE II tool and comparison with previous evaluations: a EuroAIM initiative. *Eur Spine J*. (2018) 27:2781–90. doi: 10.1007/s00586-018-5763-1
17. AGREE Next Steps Consortium. *The AGREE II Instrument* (2017).
18. Byrne J, Dwivedi R, Minks D. Tumors of the brain. In: Nicholson T editor. *Recommendations for Cross-Sectional Imaging in Cancer Management*, Second edition. London: The Royal College of Radiologists (2014).
19. Ellingson BM, Bendszus M, Boxerman J, Barboriak D, Erickson BJ, Smits M, et al. Consensus recommendations for a standardized Brain Tumor Imaging Protocol in clinical trials. *Neuro Oncol*. (2015) 17:1188–98. doi: 10.1093/neuonc/nov095

20. Essig M, Anzalone N, Combs SE, Dörfler A, Lee SK, Picozzi P, et al. MR imaging of neoplastic central nervous system lesions: review and recommendations for current practice. *Am J Neuroradiol*. (2012) 33:803–17. doi: 10.3174/ajnr.A2640
21. Fouke SJ, Benzinger T, Gibson D, Ryken TC, Kalkanis SN, Olson JJ. The role of imaging in the management of adults with diffuse low grade glioma: a systematic review and evidence-based clinical practice guideline. *J Neurooncol*. (2015) 125:457–79. doi: 10.1007/s11060-015-1908-9
22. Mukundan S, Holder C, Olson JJ. Neuroradiological assessment of newly diagnosed glioblastoma. *J Neurooncol*. (2008) 89:259–69. doi: 10.1007/s11060-008-9616-3
23. Ryken TC, Aygun N, Morris J, Schweizer M, Nair R, Spracklen C, et al. The role of imaging in the management of progressive glioblastoma: a systematic review and evidence-based clinical practice guideline. *J Neurooncol*. (2014) 118:435–60. doi: 10.1007/s11060-013-1330-0
24. Thust SC, Heiland S, Falini A, Jäger HR, Waldman AD, Sundgren PC, et al. Glioma imaging in Europe: a survey of 220 centres and recommendations for best clinical practice. *Eur Radiol*. (2018) 28:3306–17. doi: 10.1007/s00330-018-5314-5
25. Tian H, Gou Y, Pan Y, Li Q, Wei D, Wang Z, et al. Quality appraisal of clinical practice guidelines on glioma. *Neurosurg Rev*. (2015) 38:39–47. doi: 10.1007/s10143-014-0569-z
26. Kim W, Novotna K, Amatya B, Khan F. Clinical practice guidelines for the management of brain tumours: a rehabilitation perspective. *J Rehabil Med*. (2018) 51:89–96. doi: 10.2340/16501977-2509
27. Hoffmann-Eßer W, Siering U, Neugebauer EAM, Brockhaus AC, McGauran N, Eikermann M. Guideline appraisal with AGREE II: online survey of the potential influence of AGREE II items on overall assessment of guideline quality and recommendation for use. *BMC Health Serv Res*. (2018) 18:143. doi: 10.1186/s12913-018-2954-8

Conflict of Interest Statement: The authors declare that the research was conducted in the absence of any commercial or financial relationships that could be construed as a potential conflict of interest.

frontiers in Oncology

ORIGINAL RESEARCH
published: 26 June 2019
doi: 10.3389/fonc.2019.00536

Diffusion Tensor Imaging Reveals Microstructural Heterogeneity of Normal-Appearing White Matter and Related Cognitive Dysfunction in Glioma Patients

Kerstin Jütten[1,2], Verena Mainz[2], Siegfried Gauggel[2], Harshal Jayeshkumar Patel[3,4], Ferdinand Binkofski[3,4,5], Martin Wiesmann[6], Hans Clusmann[1] and Chuh-Hyoun Na[1]*

[1] Department of Neurosurgery, RWTH Aachen University, Aachen, Germany, [2] Faculty of Medicine, Institute of Medical Psychology and Medical Sociology, RWTH Aachen University, Aachen, Germany, [3] Division of Clinical Cognitive Sciences, RWTH Aachen University, Aachen, Germany, [4] Research Center Jülich GmbH, Institute of Neuroscience and Medicine (INM-4), Jülich, Germany, [5] Jülich Aachen Research Alliance, Translational Brain Medicine, Aachen, Germany, [6] Department of Diagnostic and Interventional Neuroradiology, RWTH Aachen University, Aachen, Germany

OPEN ACCESS

Edited by:
Sebastian Cerdan, Spanish National Research Council (CSIC), Spain

Reviewed by:
Michael Albert Thomas, University of California, Los Angeles, United States
Zhongxiang Ding, Hangzhou First People's Hospital, China
Pilar López-Larrubia, Spanish National Research Council (CSIC), Spain

***Correspondence:**
Kerstin Jütten
kjuetten@ukaachen.de

Specialty section:
This article was submitted to Cancer Imaging and Image-directed Interventions, a section of the journal Frontiers in Oncology

Received: *20 March 2019*
Accepted: *03 June 2019*
Published: *26 June 2019*

Citation:
Jütten K, Mainz V, Gauggel S, Patel HJ, Binkofski F, Wiesmann M, Clusmann H and Na C-H (2019) Diffusion Tensor Imaging Reveals Microstructural Heterogeneity of Normal-Appearing White Matter and Related Cognitive Dysfunction in Glioma Patients. Front. Oncol. 9:536. doi: 10.3389/fonc.2019.00536

Immunohistochemical data based on isocitrate–dehydrogenase (IDH) mutation status have redefined glioma as a whole-brain disease, while occult tumor cell invasion along white matter fibers is inapparent in conventional magnetic resonance imaging (MRI). The functional and prognostic impact of focal glioma may however relate to the extent of white matter involvement. We used diffusion tensor imaging (DTI) to investigate microstructural characteristics of whole-brain normal-appearing white matter (NAWM) in relation to cognitive functions as potential surrogates for occult white matter involvement in glioma. Twenty patients (12 IDH-mutated) and 20 individually matched controls were preoperatively examined using DTI combined with a standardized neuropsychological examination. Tumor lesions including perifocal edema were masked, and fractional anisotropy (FA) as well as mean, radial, and axial diffusivity (MD, RD, and AD, respectively) of the remaining whole-brain NAWM were determined by using Tract-Based Spatial Statistics and histogram analyses. The relationship between extratumoral white matter integrity and cognitive performance was examined using partial correlation analyses controlling for age, education, and lesion volumes. In patients, mean FA and AD were decreased as compared to controls, which agrees with the notion of microstructural impairment of NAWM in glioma patients. Patients performed worse in all cognitive domains tested, and higher anisotropy and lower MD and RD values of NAWM were associated with better cognitive performance. In additional analyses, IDH-mutated and IDH-wildtype patients were compared. Patients with IDH-mutation showed higher FA, but lower MD, AD, and RD values as compared to IDH-wildtype patients, suggesting a better preserved microstructural integrity of NAWM, which may relate to a less infiltrative nature of IDH-mutated gliomas. Diffusion-based phenotyping and monitoring microstructural integrity of extratumoral whole-brain NAWM may aid in estimating occult white matter involvement and should be considered as a complementary biomarker in glioma.

Keywords: glioma, diffusion tensor imaging, normal-appearing white matter, microstructural integrity, neuropsychology, IDH mutation

INTRODUCTION

While the extent of tumor resection is regarded as an important therapy-dependent prognostic factor, the infiltrative nature of diffuse glioma remains a diagnostic and therapeutic problem and an obstacle to curative treatment. Infiltrative glioma growth preventing the definition of clear tumor borders has been described early on based on histological findings (1). With identification of the isocitrate–dehydrogenase (IDH) mutation in codon 132 of IDH1 (or infrequently in codon 172 of IDH2) as being the most common molecular genetic alteration in grade II and grade III gliomas, immunohistochemical data using antibodies specific to IDH1 R132H mutant protein have revealed a more widespread tumor cell distribution than expected. Occult tumor cell invasion has thereby been delineated even in areas remote to the primary tumor site, which had macro- and microscopically appeared unaffected (2). These findings have redefined cerebral glioma as a systemic rather than focal brain disease, which is supported by cellular observations of diffusively invading tumor cells expanding to extensive intracerebral networks (3).

In view of these findings, standard treatment and disease monitoring strategies focusing only on the focal tumor and its borders seem to be insufficient. With immunohistochemical analyses being limited to post-mortem IDH-mutant glioma, and conventional magnetic resonance imaging (MRI) incapable of delineating diffuse tumor cell migration, the extent of occult tumor cell burden has not been determined *in vivo*, although it might offer prognostically valuable information. As diffuse infiltrative glioma growth has histologically been characterized to occur typically along white matter (WM) tracts (4), diffusion tensor imaging (DTI) appears of particular interest. It provides indirect information about the microstructural WM architecture and its integrity *in vivo*, based on water diffusion properties in the intra- and extracellular space (5). This notion is based on a simplified model, in which water diffusion within a given voxel can be described as diffusion tensor or ellipsoid. The shape of the ellipsoid is characterized by three eigenvalues (λ1–3), providing measures of the three primary axes of the ellipsoid. Diffusivity along the principal axis (λ1) is called axial diffusivity (AD), and diffusivity along the two minor axes (λ2 and 3) is called radial diffusivity (RD) (6, 7). While AD has been related to axonal integrity, RD has been assumed to provide information about the degree of myelination (8, 9). These eigenvalues can be used to calculate scalar DTI summary measures such as fractional anisotropy (FA), reflecting the orientation preference of water diffusion within a given voxel (5, 10), and mean diffusivity (MD), reflecting the mean amount of water diffusion irrespective of its direction (11). While higher FA and AD in WM have been linked to preserved fiber integrity, increases in MD and RD have been related to structural disintegration (12).

Studies on glioma-induced WM changes in regions remote to the primary tumor site are only sparse, but suggest DTI to allow tracing glioma cell infiltration into brain regions distant to the primary tumor site, which is inapparent in conventional imaging (13–16). Previous studies in this regard were based on region-of-interest (ROI) analyses, in which DTI metrics were determined locally at assumed tumor projections along predefined WM structures such as the corticospinal tract or in peritumoral areas, with restriction to observer-dependent predefined regions. Based on peritumoral anisotropy and diffusivity measures (17), the more favorable prognosis in IDH-mutated glioma (18, 19) has been related to a less invasive behavior as compared to IDH-wildtype gliomas. A ROI-independent diffusion-based microstructural characterization of whole-brain normal-appearing white matter (NAWM) under consideration of IDH-mutation status and in relation to cognitive functions has, to the best of our knowledge, not yet been attempted.

While glioma patients with "non-eloquent" tumor locations do not exhibit apparent deficits in basic sensory-motor functions, cognitive impairment has been described across different tumor locations in most of the patients already at the time of diagnosis (20, 21), which has been linked to early WM involvement (22). While patients with lower-grade gliomas initially may present with impressive tumor volumes but only minor cognitive dysfunctions, patients with high-grade tumors at comparable anatomical sites can be more severely impaired (21, 23). This might be based on different dynamics of tumor-induced cortical deafferentation or reorganization processes, depending on the local tumor growth rate. Alternatively, this could also be related to varying degrees of occult systemic tumor cell burden, with immunohistochemically proven diffuse tumor cell migration into brain regions remote to the primary tumor site (2).

This study aimed to preoperatively investigate microstructural and functional characteristics of whole brain NAWM as potential measures of occult systemic WM involvement in glioma. In order to restrict analyses to NAWM, contrast-enhancing and non-contrast-enhancing tumor lesions including any perifocal T2- or T1-weighted signal alterations such as perifocal edema were captured in tumor lesion masks and excluded from analyses. We hypothesized that global microstructural WM integrity and related cognitive functions would be compromised in glioma. Moreover, WM integrity was assumed to be more preserved in IDH-mutated than in IDH-wildtype glioma, which would agree with the notion of a more favorable prognosis and less infiltrative nature of IDH-mutated glioma.

MATERIALS AND METHODS

Subjects

Twenty patients (mean age: 44.8 years, $SD = 15.5$, 13 males, 12 IDH-mutated) and 20 matched healthy controls (mean age: 45.3 years, $SD = 15.9$, 13 males) were prospectively enrolled in the study at a single university hospital center. All subjects underwent anatomical MRI, DTI, and standardized neuropsychological testing. Patients were examined preoperatively and histopathological diagnoses were determined (based on tumor specimens obtained by biopsy or tumor resection) according to the revised WHO tumor classification of 2016 (24), integrating imaging, histological, and molecular genetic criteria. IDH-mutation status was determined by immunohistochemical analysis with identification of the IDH1

R132H mutation or, when results were negative or unequivocal, by additional DNA analysis using next-generation sequencing. IDH-mutation status was defined by presence of mutations of IDH1 on exon 4, codon 132 or of IDH2 on exon 4, codon 172.

All participants gave written informed consent prior to study enrollment. This study was approved (EK 294/15) by the local ethics committee, and conducted in accordance with the standards of Good Clinical Practice and the Declaration of Helsinki. Only patients >18 and <80 years of age with unilateral supratentorial tumor and a Karnofsky index of >70 were included. All patients except one were naive to tumor-specific treatment prior to enrollment in the study. One patient with presumed low-grade glioma (according to neuroradiological criteria) consented in participation in the study, but finally refrained from surgery, so that histopathological confirmation could not be obtained in this subject. For detailed information on patients' demographics and tumor characteristics (see **Table 1**).

Neuropsychological Assessment

All participants underwent a cognitive assessment using a standardized neuropsychological examination. Duration of testing was about 60 min and included the following tests: The Verbal Learning and Memory Test (25) (VLMT) is designed as a list-learning paradigm and included eight trials: five trials (Trials 1–5) of repeated presentation and immediate recall of a list of 15 words (Trial A), followed by the presentation and recall of a second "interference" list of 15 words (Trial B), another trial assessing immediate post-interference recall of list A (Trial 6), and an additional recall trial after a 20-min delay (Trial 7). A final recognition trial (Trial 8) included those words from Lists A and B, and 20 phonologically or semantically similar words to Lists A and B. Participants needed to identify and recognize the words that were part of List A. This study focused on VLMT scores including total learning (the sum of scores for Trials 1–5, VLMT_rec), consolidation performance as number of words forgotten over time (Trial 5 score – Trial 7 score, VLMT_con), and recognition (Trial 8 score, VLMT_recog).

The Attention Network Test (ANT), a modified Posner task (26), is a selective reaction time task that is used to examine three attentional systems, including tonic and phasic alertness, spatial, and executive attention. The participants' task is to react as quickly as possible to directional stimuli (arrows) that are imbedded in special cues or distractors intending to stimulate the various attention components. Specifically, an arrow, which can point to the right or left, appears in the middle of the screen below or above a fixation cross, and participants should indicate that arrow's direction by button press. By varying cues and distracters, responses address either the alertness or spatial (orientation) or executive (conflict) condition. The ANT consists of four blocks and 288 trials, including one practice block (24 trials) as well as three test blocks (96 trials each), which takes participants about 20 min to finish. Specifically, this study focused on overall alertness by investigating mean reaction times (RTs) in seconds (RT of correct trials, ANT_RTcor) as well as the number of errors in the according subtrials of the test (number of errors, ANT_err).

As a test for executive functions, the Trail-Making Test (27) (TMT) was carried out in which participants first have to connect numbers in ascending order (TMT-A). In the second part, numbers and letters are connected alternating in ascending order (TMT-B). RTs in seconds are recorded separately for each part of the test and the difference between the two is regarded to reflect task-switching (difference in RT between TMT-A and TMT-B, TMT_RTexe).

MRI Data Acquisition

All participants underwent MRI examination on a 3-Tesla Siemens Prisma MRI scanner equipped with a standard 32-channel head coil. The scanning protocol included a 3D T1-weighted as well as a 3D inversion recovery scan for tumor volume segmentation, as well as diffusion-weighted imaging (DWI) to investigate WM integrity. Pulse sequences were as follows: First, a sagittal 3D T1 magnetization-prepared rapid acquisition gradient echo (MPRAGE) sequence was acquired [repetition time (TR) = 2,300 ms, echo time (TE) = 2.01 ms, 176 slices with a slice thickness of 1 mm, flip angle = 9°, field of view (FoV) = 256 mm, voxel size = 1 mm isotropic, and 256 × 256 matrix]. In addition, DWI data were acquired using an echo planar imaging (EPI) sequence (64 diffusion directions with *b*-value = 1,000 s/mm^2, one b0 image, TR = 6,300 ms; TE = 81 ms; 55 axial slices with 2.4 mm slice thickness, FoV = 216 mm, voxel resolution = 2.4 mm isotropic) and a fluid attenuation inversion recovery (FLAIR) sequence was applied (TR = 4,800 ms, TE = 304.0 ms, number of slices = 160 with 1 mm slice thickness, FoV m s250 mm, and 1 mm isotropic voxel resolution). For tumor identification purposes, a contrast-enhanced, T1-weighted turbo inversion recovery magnitude (TIRM) dark-fluid sequence was acquired (TR = 2,200 ms, TE = 32 ms, slice thickness = 3 mm, flip angle = 150°, FOV = 230 mm, voxel size = 0.9 × 0.9 × 3.0 mm^3, matrix = 256 × 256) as well as a T2-weighted TIRM dark-fluid scan (TR = 9,000 ms, TE = 79 ms, slice thickness = 3 mm, flip angle = 150°, FOV = 230 mm, voxel size = 0.9 × 0.9 × 3 mm^3, matrix = 256 × 256).

MRI Data Processing

Tumor Masking

In a first step, tumor lesions were segmented semi-automatically on the basis of each patient's anatomical 3D T1-weighted and 3D-FLAIR weighted images using ITK-SNAP software (28). In a second step, tumor lesion masks were manually corrected and lesion volumes (Tvol in cm^3) were computed. Any apparent tumor lesions including contrast-enhancing and non-contrast-enhancing tumor, as well as any perifocal T2 hyper- or T1 hypointensities including perifocal edema, were included in the lesion masks and excluded from analysis, thereby restricting the analyses to the remaining whole-brain NAWM. In addition, lesion masks were binarized for later use in the normalization procedure of image preprocessing.

DTI Preprocessing

The first part of DTI data preprocessing was performed using the FDT diffusion toolbox as implemented in FSL (29) and included distortion and motion correction (eddy current

TABLE 1 | Clinical description of included patients.

Patients	IDH-mutation	Diagnosis	Grade	Location	Side	Volume (in cm^3)	AE	Steroids	Age (years)	Education* (years)
1	y	Astrocytoma	II	Temporal	r	30	y	n	30–35	13
2	y	Astrocytoma	II	Frontal	l	51	y	n	20–25	16
3	y	Astrocytoma	II	Parietal	l	64	y	n	55–60	18
4	y	Astrocytoma	II	Frontal	l	158	y	n	26–30	13
5	y	Oligodendro-glioma	II	Frontal	r	2	n	n	36–40	13
6	y	Oligodendro-glioma	II	Frontal	l	22	n	n	26–30	13
7	y	Anaplastic astrocytoma	III	Frontal	l	21	y	y	50–55	13
8	y	Anaplastic astrocytoma	III	Parietal	l	119	y	n	20–25	13
9	y	Anaplastic astrocytoma	III	Frontal	r	155	n	n	30–35	15
10	y	Anaplastic astrocytoma	III	Frontal, insular	r	175	y	y	30–35	13
11	y	Anaplastic oligodendro-glioma	III	Frontal	l	39	y	n	50–55	15
12	y	Anaplastic oligodendro-glioma	III	Frontal	r	96	n	n	30–35	18
13	n	Dysembryo-plastic neuroepithelial tumor	I	Hippocampal	l	24	y	n	40–45	15
14	n	Anaplastic astrocytoma	III	Temporo-parieto-occipital	l	144	n	n	66–70	12
15	n	Glioblastoma multiforme	IV	Fronto-temporal, insular	l	204	y	y	60–65	15
16	n	Glioblastoma multiforme	IV	Temporal, insular	l	111	y	n	56–60	10
17	n	Glioblastoma multiforme	IV	Fronto-temporal, insular	l	145	n	y	66–70	9
18	n	Glioblastoma multiforme	IV	Frontal	r	182	n	y	50–55	12
19	n	Glioblastoma multiforme[a]	IV	Parietal, thalamic	l	65	y	y	50–55	13
20	–	Presumed low-grade glioma[b]	–	Occipital	r	1	n	n	60–65	12

IDH, isocitrate–dehydrogenase; y, yes; n, no; l, left; r, right; AE, anti-epileptics; m, male; f, female.

[a] *Recurrent glioblastoma 5 months after first tumor resection and adjuvant radiochemotherapy.*

[b] *Patient refrained from surgery so that no histopathological confirmation could be obtained.*

**Years of education were computed by the sum of years spent for school career and further training/study.*

correction) as well as skull stripping (BET brain extraction tool). Diffusion tensors were estimated using DTIFIT, and individual FA, MD, RD, and AD images were created for every subject. Further preprocessing was carried out using SPM12 (30, 31) as implemented in Matlab 9.3. First, subjects' T1-weighted anatomical images were segmented using the segmentation approach, which allows the inclusion of the individual tumor masks for patients as masking image, saving deformation field matrices for standard space as well as subject space (inverse) transformation. After this, diffusion images were co-registered to the corresponding T1-weighted anatomical images. For control subjects, diffusion images were then normalized to their matched patients' diffusion space by means of inverse transformation using the unified segmentation approach (32). Finally, the individual binary tumor mask was applied to patients' FA, MD, RD, and AD images in order to mask out tumor tissue for further analyses. For controls, the tumor mask of the corresponding patient match was applied accordingly, thereby controlling for known WM heterogeneities depending on anatomical site, gender, and age.

DTI Metrics

For between-group comparisons of patients and controls, an approach analogous to TBSS as implemented in FSL was applied. For this purpose, individual diffusion space FA images were skeletonized and thresholded at an FA value of 0.2. The FA-derived skeleton was then applied to MD, RD, and AD diffusion images and masked with patients' WM masks. In order to obtain a most complex characterization of diffusion properties of NAWM, two categories of diffusion values were calculated, resulting in eight dependent diffusivity parameters: First, the mean (M) of each diffusivity parameter across all voxels within the skeleton was computed, producing four mean parameters (in units and mm^2/s) for each subject (FA_M, MD_M, RD_M, and AD_M). In a second step, these voxel-based diffusivity parameters were further computed using histogram analyses according to Baykara and colleagues' approach (33): Accordingly, the peak width of the skeletonized diffusion parameters was determined by computing the difference between the 95th and 5th percentile of each of the skeletonized FA, MD, RD, and AD values (PS in mm^2/s), resulting in four additional diffusion parameters for each subject (FA_{PS}, MD_{PS}, RD_{PS}, and AD_{PS}). For a better comparability to the FA parameters, all mean and PS values of MD, RD, and AD were multiplied with a factor of 1,000. An overview of DTI preprocessing steps and DTI metrics computation is given in **Figure 1**.

Statistics

All statistical analyses were performed with SPSS 24. Based on our hypotheses, group differences in FA, MD, RD, and

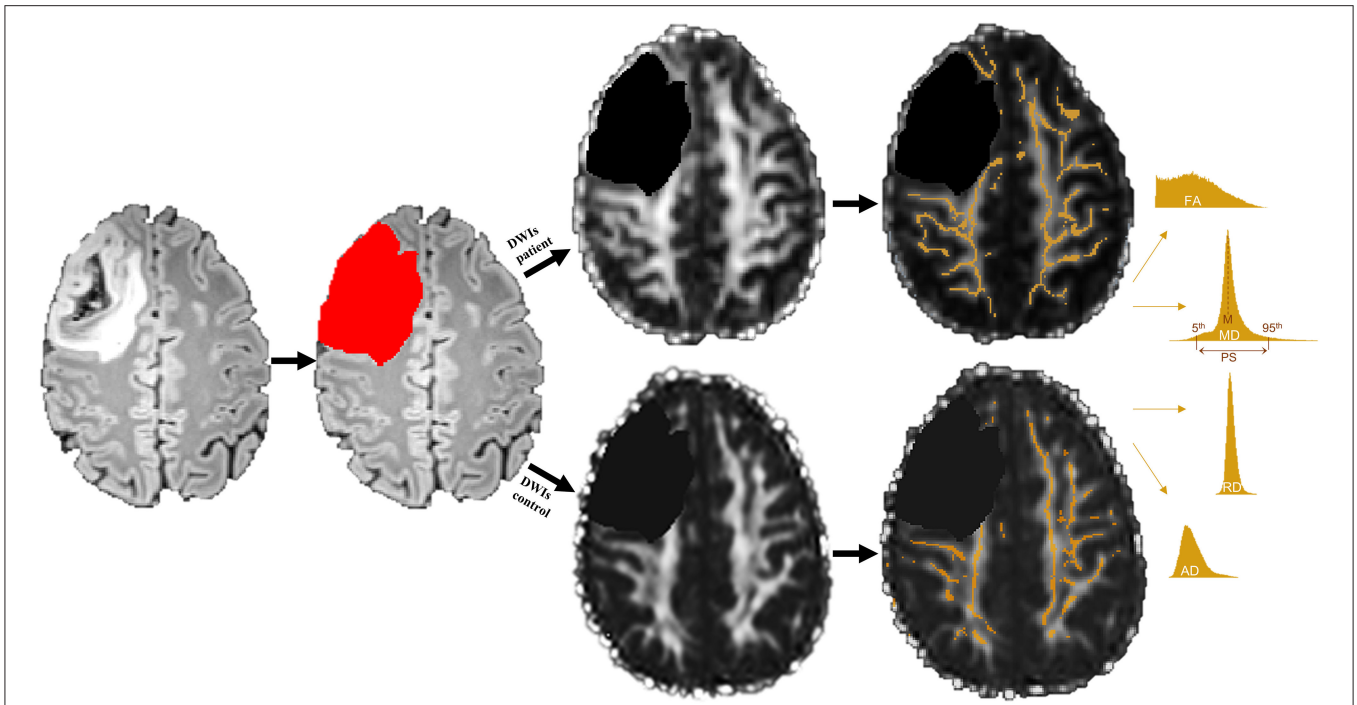

FIGURE 1 | Example of a grade III tumor segmentation based on a fluid attenuation inversion recovery (FLAIR) image. Segmented tumor tissue (red) was excluded in both patients' diffusion weighted images (DWIs) as well as their matched controls' DWIs (black) prior to white matter (WM) skeleton extraction. Only those WM voxels revealing a fractional anisotropy (FA) value of 0.2 or higher were used to create a WM skeleton mask (orange), which was then applied to mean, radial, and axial diffusivity (MD, RD, and AD) maps. Mean (M) and peak width difference between the 95th and 5th percentile (PS) of each skeletonized diffusion parameter were computed by means of histogram analyses.

AD parameters (FA_M, MD_M, M_{RD}, M_{AD}, FA_{PS}, MD_{PS}, RD_{PS}, and AD_{PS}) and cognitive performance (VLMT_rec, VLMT_con, VLMT_recog, ANT_RTcor, ANT_err, and TMT_RTexe) between patients and controls as well as between IDH-mutated (IDHmut) and wildtype patients (IDHwt) were analyzed using independent-samples t test, tested one-sided with a significance level of $p < 0.05$. In addition, standardized effect sizes (ES) with the respective confidence intervals (CIs, Hedges bias corrected) were computed.

The relationship between WM integrity (FA_M, MD_M, RD_M, AD_M, FA_{PS}, MD_{PS}, RD_{PS}, and AD_{PS}) and cognitive performance (VLMT_rec, VLMT_con, VLMT_recog, ANT_RTcor, ANT_err, and TMT_RTexe) was analyzed using Pearson's partial correlation analyses separately for patients and controls, tested one-tailed with a significance level of $p < 0.05$ and controlled for effects of age, education, and tumor volume. Furthermore, intercorrelations between respective diffusivity parameters (FA_M-FA_{PS}, MD_M-MD_{PS}, RD_M-RD_{PS}, and AD_M-AD_{PS}) were computed using partial correlations corrected for age, education and tumor volume.

RESULTS

Diffusion Parameters and Cognitive Performance

NAWM of patients and controls differed in anisotropy, with significantly lower FA and AD values in patients compared to controls (FA_M: $M_{PAT} = 0.42$ and $M_{CG} = 0.43$ units, $t = 1.85$, $p = 0.04$, ES = −=49, CI = [−1.12–0.14]; AD_M: $M_{PAT} = 1.17$ and $M_{CG} = 1.18$ mm²/s, $t = 2.01$, $p = 0.03$, ES = −=49, CI = [−1.12–0.14]). Significant group differences in cognitive performance were found for verbal learning and task switching (VLMT_rec: $M_{PAT} = 47$ and $M_{CG} = 57$ words, $t = 2.65$, $p = 0.01$, ES = −=91, CI = [−1.64 to −0.18]; TMT_RTexe: $M_{PAT} = 43$ and $M_{CG} = 23$ s, $t = -2.54$, $p = 0.01$, ES = 0.98, CI = [0.19–1.76]) (see **Figure 2**). For detailed results on diffusivity and behavioral measures (see **Table 2**).

Correlations Between Diffusivity Parameters and Cognitive Performance

Intercorrelations between M and PS diffusion parameters revealed significant associations for FA and MD (CG: FA_M-FA_{PS}: $r_{partial} = 0.77$, $p < 0.001$, and MD_M-MD_{PS}: $r_{partial} = 0.51$, $p = 0.02$; PAT: FA_M-FA_{PS}: $r_{partial} = 0.80$, $p = 0.003$ and MD_M-MD_{PS}: $r_{partial} = 0.78$, $p = 0.004$).

In the patient group, significant correlations were found between diffusion parameters and verbal learning, attention, and task switching. Higher FA values were associated with better performances in verbal learning (FA_M-VLMT_rec: $r_{partial} = 0.59$, $p = 0.04$), attention (FA_M-ANT_RTcor: $r_{partial} = -0.60$, $p = 0.03$; FA_{PS}-ANT_RTcor: $r_{partial} = -0.71$, $p = 0.01$), and task switching (FA_M-TMT_RTexe: $r_{partial} = -0.63$, $p = 0.03$). In contrast, higher MD and RD correlated significantly with worse attentional

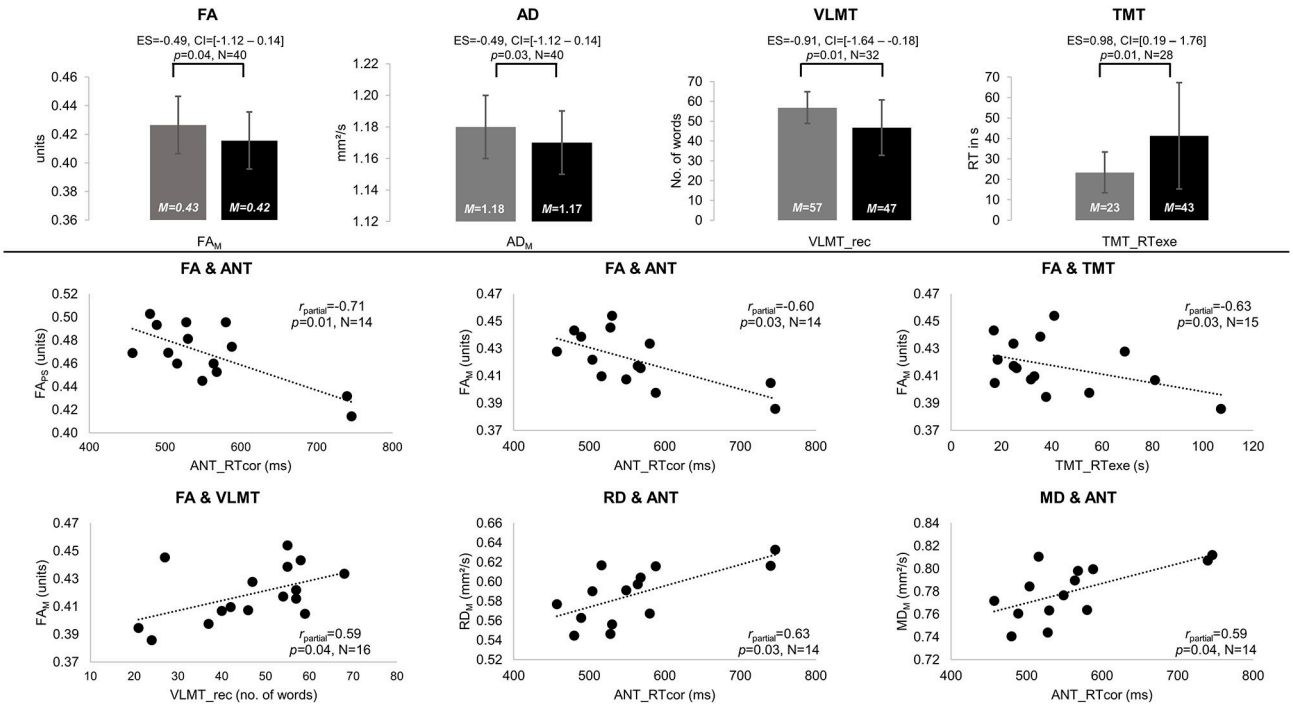

FIGURE 2 | Significant results of between-group and partial correlation analyses. Significant differences in fractional anisotropy (FA) and axial diffusivity (AD) as well as performance on the Verbal Learning and Memory Test (VLMT, VLMT_rec = number of words recalled) and the Trail-Making Test (TMT, TMT_RTexe = reaction times on differences between TMT parts A and B) are displayed in gray for the control group (CG) and black for patients (PAT) in the upper panel. All significant partial correlations ($r_{partial}$) between mean (M) and peak width of skeletonized (PS) FA, mean, radial, and axial diffusivity (MD, RD, and AD), and behavioral performance are visualized for patients in the lower panel. Significances for each analysis (N = number of subjects included) were computed at $p < 0.05$, including standardized effect sizes (ES) and confidence intervals (CI).

performance (MD_M-ANT_RTcor: $r_{partial} = 0.59$, $p = 0.04$; RD_M-ANT_RTcor: $r_{partial} = 0.63$, $p = 0.03$) (see **Figure 2**). In controls, higher MD values correlated significantly with worse attentional performance (MD_{PS}-ANT_err: $r_{partial} = 0.53$, $p = 0.02$).

IDH-Mutation Status

Patients differed in diffusion parameters depending on IDH-mutation status, revealing higher FA (FA_M: $M_{IDHmut} = 0.43$ and $M_{IDHwt} = 0.40$ units, $t = -3.45$, $p = 0.002$, ES $= -1.43$, CI $= [-2.47$ to $-0.04]$) as well as lower MD, RD, and AD values for IDH-mutated than for IDH-wildtype gliomas (MD_M: $M_{IDHmut} = 0.78$ and $M_{IDHwt} = 0.81$ mm²/s, $t = 3.28$, $p = 0.002$, ES $= 1.43$, CI $= [0.40–2.47]$; MD_{PS}: $M_{IDHmut} = 0.29$ and $M_{IDHwt} = 0.36$ mm²/s, $t = 2.54$, $p = 0.01$, ES $= 1.24$, CI $= [0.23–2.26]$; RD_M: $M_{IDHmut} = 0.58$ and $M_{IDHwt} = 0.62$ mm²/s, $t = 3.55$, $p = 0.001$, ES $= 1.27$, CI $= [0.26–2.29]$; RD_{PS}: $M_{IDHmut} = 0.41$ and $M_{IDHwt} = 0.45$ mm²/s, $t = 2.60$, $p = 0.01$, ES $= 1.33$, CI $= [0.31–2.36]$; AD_M: $M_{IDHmut} = 1.16$ and $M_{IDHwt} = 1.18$ mm²/s, $t = 2.02$, $p = 0.03$, ES $= 0.96$, CI $= [-0.03–1.94]$) (see **Figure 3**). Furthermore, cognitive performance differed significantly between IDH-mutated and IDH-wildtype patients with regard to verbal recall and verbal recognition (VLMT_rec: $M_{IDHmut} = 51$ and $M_{IDHwt} = 35$ words, $t = -2.35$, $p = 0.02$, ES $= -1.29$, CI $= [-2.52$ to $-0.05]$; VLMT_recog: $M_{IDHmut} = 13$ and $M_{IDHwt} = 11$ words, $t = -2.24$, $p = 0.02$, ES $= -1.23$, CI $= [-2.48–0.01]$).

DISCUSSION

DTI revealed functionally relevant microstructural alterations of NAWM in glioma patients, which agrees with the notion of glioma as a systemic rather than a focal brain disease. Microstructural heterogeneity of NAWM was related to the prognostically relevant IDH-mutation status.

DTI of NAWM

DTI was used to investigate glioma as systemic brain disease by voxel-wise comparison of extralesional WM of patients and individually matched healthy controls. Prior lesion masking excluded any macroanatomically apparent tumor lesions including perifocal T2- or T1-weighted signal alterations such as caused by edema or perifocal tumor infiltration, which are known to be associated with altered diffusion properties (34, 35).

Agreeing with our hypothesis, diffusion properties of NAWM differed between patients and controls, showing decreases of FA and AD in patients. Furthermore, IDH-mutated gliomas were associated with higher FA, but lower MD, RD, and AD values of NAWM than IDH-wildtype gliomas. These results agree with the notion of a compromised microarchitecture of

TABLE 2 | Results of group statistics on differences between patients and controls.

DV	CG ($N = 20$)		PAT ($N = 20$)						IDHmut ($N = 12$)		IDHwt ($N = 7$)					
	M	*SD*	*M*	*SD*	*t*	*p**	ES	CI	*M*	*SD*	*M*	*SD*	*t*	*p**	ES	CI
FA_M	0.43	0.02	0.42	0.02	1.85	**0.04**	**−0.49**	**[−1.12–0.14]**	0.43	0.02	0.40	0.02	−3.45	**0.002**	**−1.43**	**[−2.47–0.04]**
FA_{PS}	0.48	0.02	0.46	0.02	1.74	0.05	−0.98	[−1.64 to −0.32]	0.47	0.02	0.45	0.02	−1.81	0.05	−0.96	[−1.94–0.03]
MD_M	0.79	0.02	0.79	0.03	0.05	0.48	0.00	[−0.62–0.62]	0.78	0.02	0.81	0.02	3.28	**0.002**	**1.43**	**[0.40–2.47]**
MD_{PS}	0.29	0.05	0.32	0.06	−1.39	0.09	0.53	[−0.10–1.16]	0.29	0.05	0.36	0.06	2.54	**0.01**	**1.24**	**[0.23–2.26]**
RD_M	0.59	0.03	0.60	0.03	−0.69	0.25	0.33	[−0.33–0.95]	0.58	0.03	0.62	0.03	3.55	**0.001**	**1.27**	**[0.26–2.29]**
RD_{PS}	0.41	0.03	0.42	0.04	−0.95	0.17	0.28	[−0.35–0.90]	0.41	0.02	0.45	0.04	2.60	**0.01**	**1.33**	**[0.31–2.36]**
AD_M	1.18	0.02	1.17	0.02	2.01	**0.03**	**−0.49**	**[−1.12–0.14]**	1.16	0.02	1.18	0.02	2.02	**0.03**	**0.96**	**[−0.03–1.94]**
AD_{PS}	0.75	0.04	0.74	0.05	0.67	0.25	−0.22	[−0.84–0.41]	0.72	0.04	0.75	0.06	1.25	0.11	0.60	[−0.35–1.55]
VLMT_rec	57	8	47	14	2.65	**0.01**	**−0.91**	**[−1.64–0.18]**	51	11	35	16	−2.35	**0.02**	**−1.29**	**[−2.52–0.05]**
VLMT_con	1	2	2	2	−1.32	0.10	0.50	[−0.22–1.23]	2	1	3	5	0.41	0.35	0.35	[−0.82–1.51]
VLMT_recog	14	1	12	2	1.61	0.06	−1.04	[−1.80 to −0.28]	13	2	11	2	−2.24	**0.02**	**−1.23**	**[−2.48–0.01]**
ANT_RTcor (ms)	505	64	560	87	−1.28	0.11	0.70	[−0.06–1.46]	546	75	613	123	1.21	0.13	0.73	[−0.57–2.04]
ANT_F	4	3	3	4	0.68	0.25	−0.27	[−1.01–0.48]	3	4	2	1	−0.45	0.33	−0.27	[−1.55–1.01]
TMT_RTexe (s)	23	10	43	26	−2.54	**0.01**	**0.98**	**[0.19–1.76]**	32	15	55	38	1.65	0.06	0.91	[−0.30–2.12]

*DV, dependent variable; CG, control group; PAT, patient group; IDH, isocitrate–dehydrogenase; IDHmut, IDH-mutated glioma; IDHwt, IDH-wildtype glioma; N, number of included subjects; M, mean; SD, standard deviation; t, value of test statistic; p, significance; ES, effect size; CI, confidence interval; FA, fractional anisotropy; MD, mean diffusivity; RD, radial diffusivity; AD, axial diffusivity; PS, peak width difference of skeletonized diffusivity; VLMT, Verbal Learning and Memory Test; ANT, Attention Network Test; TMT, Trail-Making Test; VLMT_rec, recall; VLMT_con, consolidation; VLMT_recog, recognition; ANT_RTcor, reaction time of correct trials; ANT_F, number of errors; TMT_RTexe, difference in reaction time between TMT-A and TMT-B. *Significant results ($p < 0.05$, one-tailed), ES, and CI are printed in bold.*

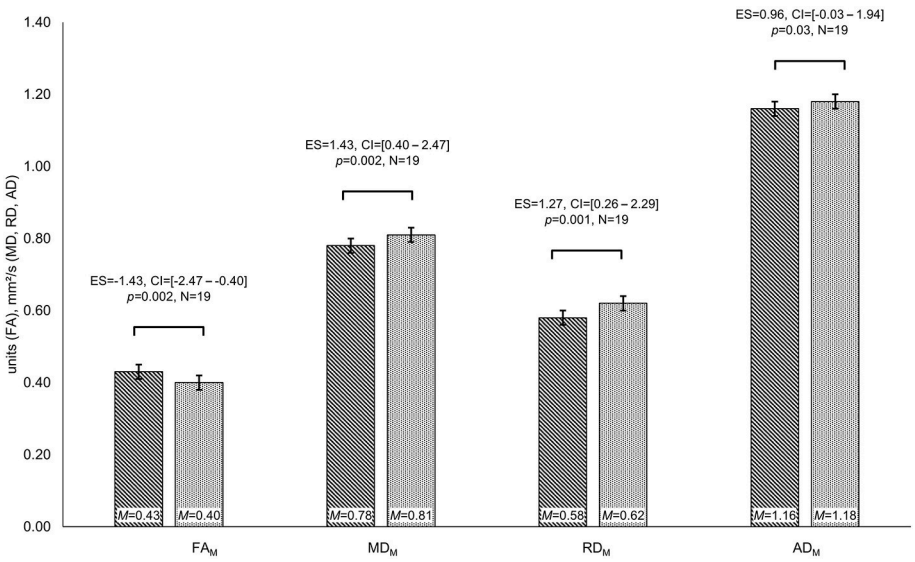

FIGURE 3 | Group differences in diffusivity parameters depending on IDH-mutation status. Significant differences in fractional anisotropy (FA), mean diffusivity (MD), and radial diffusivity (RD) are displayed for patients with isocitrate–dehydrogenase (IDH)-mutation status (lined bar) and IDH-wildtype patients (dotted bar). Significances for each analysis (N = number of patients) were computed at $p < 0.05$, including standardized effect sizes (ES) and confidence intervals (CI).

NAWM in gliomas, with decreases in FA and increases in isotropic diffusion values having been linked to WM degradation (33) and tumor cell infiltration (2, 36). Our results agree with previous findings on decreases of FA and increases of the apparent diffusion coefficient (ADC) at presumed tumor infiltration trajectories along the corticospinal tract in children with diffuse intrinsic pontine glioma (DIPG): Wagner et al. examined patients with DIPG and patients with low-grade brainstem glioma in comparison to controls. They found lower AD and increases in RD at assumed tumor projections remote to the primary lesion site. Decreases of AD were related to axonal damage by disruption of microstructural fiber tract architecture, accompanied by increases of isotropic tissue, which was assumed to reflect diffuse tumor infiltration with increased cellular density

in the extracellular matrix (15). Another study applying serial measurements of diffusion properties in children with pontine glioma showed longitudinal changes of diffusion parameters; they suggested those changes to reflect different disease stages, with a transient increase of FA and decrease of ADC relating to transient treatment response, while a subsequent decrease of FA and increase of ADC were regarded to reflect tumor progression (37). Accordingly, Kallenberg et al. described increases in ADC and decreases in FA values in tumor projection areas onto the corpus callosum in glioma patients as an indicator of an occult transcallosal tumor progression (14).

Price and colleagues previously correlated histopathological specimens obtained by image-guided biopsies with DTI metrics. Tumor infiltration was related to increases in the isotropic component, while tumor was associated with reduced anisotropy relative to the contralesional hemisphere. Authors furthermore showed that tumor infiltration occurred in normal-appearing regions on T2-weighted images in 40% of cases (36). Another study described biopsies taken from normal-appearing brain areas with identification of tumor infiltration in half of these specimens (38). Based on those findings, in which histologically proven tumor cell infiltration in NAWM was linked to decreases in anisotropy and increases in diffusivity (MD and RD) values, the diffusion changes found in our study appear to be compatible with previous observations of occult tumor cell infiltration into NAWM, although histopathological evidence cannot be provided here. Although FA is regarded as highly sensitive for microstructural alterations, the scalar measure seems unspecific as to its precise histoanatomical correlate, unless complementary information is available. Interpretation of differences in diffusion values therefore has to be regarded with caution, as values can be ambiguous as they are modulated by multiple factors (39). Moreover, interpretation of diffusion data with regard to tumor pathology is further complicated, as diffusion measures can relate to different pathologies and might offer different possible attributions (39). Related to tumor pathology, diffusion changes might be caused by vasogenic edema, by tumor-infiltration-induced changes of the extracellular milieu with increases in cellular density, or by local tumor effected fiber disruption and secondary Wallerian degeneration. Even neuroplasticity accompanying chronically progressive tumor lesions could be assumed, while aging-related WM changes have to be considered in addition, as well as region-specific dynamics and longitudinal changes during the disease course. Moreover, different tumor-induced processes may even occur in parallel.

However, irrespective of the precise histoanatomical nature of the here observed altered diffusion properties of NAWM, present results indicate that glioma may impact on systemic microstructural WM properties, which cannot be delineated in conventional imaging. Furthermore, cognitive dysfunction was shown not only to depend on local tumor effects but also to be associated with occult WM involvement, which could be regarded as structural correlate of a more widely distributed cognitive network disintegration. It therefore appears promising to monitor and further investigate microstructural characteristics of NAWM in glioma, as it could provide a better understanding of the correlation between the macroscopically apparent tumor lesion and its clinical manifestation and might offer additional non-invasive biomarker *in vivo*. Whole-brain WM characteristics in glioma patients should be further explored with regard to histopathological and molecular genetic specifications, as they might reflect local tumor characteristics which may precede locally apparent disease dynamics.

Cognitive Performance and Its Association With WM Integrity

In accordance with previous research, treatment-naive patients in our study presented with cognitive impairment in all cognitive domains tested. Most distinctive deficits were found in verbal memory and executive functions, which have been described to manifest early in the disease course, and often prior to other tumor-related symptoms (21, 22). Although it has to be assumed that tumor site had an impact on the type of cognitive domain affected, further subanalysis of different tumor locations and behavioral performance was not attempted, not only in view of the small sample sizes but also because this study did not aim at a clinicotopographical correlation with tumor site. Instead, we intended to investigate the potential impact of a focal tumor lesion on systemic microstructural WM integrity and its relation to cognitive dysfunction. Systemic WM disintegrity contributing to cognitive decline is known from normal aging (40), WM diseases, or neurodegenerative disorders (33, 41). In view of spatiotemporally widely distributed cognitive network representations (42), we thus aimed to investigate cognitive deficits as functional surrogates of tumor-induced systemic network alterations based on occult WM involvement.

Agreeing with this notion, decreases in FA and increases in MD and RD as potential signs of WM disintegrity were associated with worse cognitive performance in our study. Previous studies suggested cognitive performance in glioma patients to be regarded as a prognostically relevant factor, with better performances on verbal memory and executive tests correlating with longer survival rates and less aggressive tumor growth in high-grade gliomas (43, 44). Moreover, the post-treatment cognitive status has been suggested as a clinical predictor of tumor recurrence, even in the absences of structural evidence in conventional imaging (45). While subtle cognitive impairment is often neglected in clinical routine, standardized neuropsychological assessment combined with information about microstructural NAWM characteristics may improve treatment monitoring by increasing the clinical sensitivity to disease dynamics.

IDH-Mutation Status

With IDH-mutation having emerged as a major prognostic disease marker (18, 19, 46), the more favorable prognosis in IDH-mutated gliomas has been attributed to slower local tumor growth rates (46), to anatomical predelection sites that are more accessible to extensive tumor resection (47, 48), or to a less infiltrative nature of diffuse tumor cell migration (17). In our sample, IDH-wildtype patients showed lower FA, but higher MD, RD, and AD values of NAWM as compared to IDH-mutated glioma, which may indicate a less preserved microstructural integrity of NAWM than in IDH-mutated patients: With glioma

cells invading the intercellular space along WM fibers (4), initial fiber displacement is ensued by axonal damage and disruption of the blood–brain barrier and leads to vasogenic edema. While increases in isotropic diffusion values have previously been linked to tumor cell infiltration with increased cellular density in the extracellular matrix and later on with vasogenic edema, decreases in anisotropy components have been related to increased fiber density or axonal damage and fiber disruption (14, 15, 37, 38). Higher MD, RD, and AD but lower FA values in our IDH-wildtype glioma patients thus might reflect an increased cellular density in the extracellular matrix due to tumor cell invasion with fiber compression and ensuing axonal damage. Decreased AD values in IDH-mutated glioma might relate to the slower and presumably less invasive growth behavior, more prone to remote axonal degeneration due to secondary Wallerian degeneration. Microstructural disintegrity and occult tumor cell invasion cannot be proven based on the present data. However, our results agree with findings by Price and colleagues (17), who found differences in peritumoral isotropic and anisotropic diffusion properties related to IDH-mutation status, suggesting IDH-mutated glioblastomas to have a less invasive phenotype than IDH-wildtype glioblastomas (17). With the IDH1 R132 (Arginine 132) mutation leading to an accumulation of 2 hydroxyglutarate, magnetic resonance spectroscopy (MRS) allows the measurement of this oncometabolite *in vivo* (49, 50), which has been applied for non-invasively predicting IDH-mutation status in glioma patients (51) and for investigating remote glioma cell infiltration *in vivo* (52–54). Recent studies even used MRS to identify tumor-specific metabolic profiles and investigated metabolic–transcriptional alterations under consideration of genetic profiles (55–57). A multimodal approach combining MRS and a diffusion-based characterization of NAWM microarchitecture may allow future studies to further specify histopathological correlates of NAWM diffusion properties *in vivo*.

Microstructural alterations of NAWM were accompanied by worse verbal memory performance in IDH wildtype as compared to IDH-mutated patients, which supports previous observations of higher cognitive dysfunction related to tumor grade (21, 23) and is in line with increasing evidence of the prognostic predominance of molecular rather than histopathological tumor characteristics (18, 46).

Limitations

It cannot be excluded that pharmacological effects caused by corticosteroids or anticonvulsants may have influenced behavioral performance and diffusion values in the patient group. NAWM integrity was however associated with cognitive performance even in subjects without medication. Furthermore, a recent study examined patients with gliomas and found increased neurocognitive dysfunction associated with grade IV as compared to grade II or III tumors, which was found to be independent of steroids and anti-epileptic medication (23). In addition, dexamethasone has been reported to affect diffusion only within tumor, but not in normal brain, and steroid-related reductions of MD have been observed in peritumoral tissue in high-grade gliomas, whereas FA values have remained unchanged despite corticosteroid treatment (58). It may thus be assumed that decreases in MD under steroid treatment are more likely related to reductions in vasogenic edema, whereas anisotropy values appear to be less sensitive to steroid effects and to reflect structural fiber integrity independent thereof.

A further limitation is the small sample size and tumor heterogeneity in our cohort, which has impeded further analyses of the potential impact of different tumor characteristics such as tumor grade or histoanatomical specifications on structural and functional properties of NAWM. Nevertheless, a particular strength of the present study is the matching of patients with healthy subjects controlling for age, gender, lesion volumes, and educational level. A further appeal of the method used is the potential clinical perspective, as the ROI-independent approach reduces interobserver variability and allows integration of patients with different tumor locations and sizes. Even among the small number of subjects examined in this study, differences in behavioral performance as well as in diffusion properties of NAWM were observed. While the strength of the effect sizes further reinforce the informative value of the present results, larger patient studies are needed to validate and further extend the present findings.

CONCLUSIONS

DTI revealed microstructural alterations of NAWM in glioma patients in association with cognitive dysfunction, adding to local tumor effects. Microstructural heterogeneity of NAWM was furthermore associated with IDH-mutation status, which might reflect a more preserved microstructural integrity of NAWM and less occult systemic tumor burden in IDH-mutated as compared to IDH-wildtype glioma. Diffusion-based phenotyping microstructural properties of NAWM may aid in estimating occult WM involvement and in disease monitoring and should be considered as a complementary biomarker in glioma.

DATA AVAILABILITY

The datasets for this manuscript are not publicly available because the raw MRI data contain non-anonymized, subject-specific personal information. Converted and anonymized data can be provided upon request. Requests to access the datasets should be directed to Kerstin Jütten, kjuetten@ukaachen.de.

ETHICS STATEMENT

The study was carried out in accordance with the standards of Good Clinical Practice with written informed consent from all subjects. All subjects gave written informed consent in accordance with the Declaration of Helsinki. The protocol was approved by the local ethics Committee of the Medical Faculty of the University of the RWTH Aachen (EK 294/15).

AUTHOR CONTRIBUTIONS

CH-N, VM, HC, and SG contributed to the conception and design of the study. Data collection and evaluation were carried out by KJ and VM (neuropsychological assessment) as well as by MW, KJ, CH-N, HP, and FB (MRI data). Statistical analyses and visualization were performed by KJ. The manuscript was written by CH-N, KJ, and VM. All authors critically reviewed and approved the manuscript.

FUNDING

This research project was supported by a grant from the START Programme (AZ141/16) of the Faculty of Medicine, RWTH Aachen University.

REFERENCES

1. Bailey P, Cushing H. *A Classification of the Tumors of the Glioma Group on a Histogenetic Basis: With a Correlated Study of Prognosis*. Philadelphia, PA: Lippincott (1926).
2. Sahm F, Capper D, Jeibmann A, Habel A, Paulus W, Troost D, et al. Addressing diffuse glioma as a systemic brain disease with single-cell analysis. *Arch Neurol*. (2012) 69:523–6. doi: 10.1001/archneurol.2011.2910
3. Osswald M, Jung E, Sahm F, Solecki G, Venkataramani V, Blaes J, et al. Brain tumour cells interconnect to a functional and resistant network. *Nature*. (2015) 528:93–8. doi: 10.1038/nature16071
4. Scherer HJ. A critical review: the pathology of cerebral gliomas. *J Neurol Psychiatry*. (1940) 3:147–77. doi: 10.1136/jnnp.3.2.147
5. Le Bihan-Levaufre B, Francoual J, Labrune P, Chalas J, Capel L, Lindenbaum A. Refinement and role of the diagnosis of Gilbert disease with molecular biology. *Ann Biol Clin*. (2001) 59:61–6.
6. Mori S, Zhang J. Principles of diffusion tensor imaging and its applications to basic neuroscience research. *Neuron*. (2006) 51:527–39. doi: 10.1016/j.neuron.2006.08.012
7. Madden DJ, Bennett IJ, Burzynska A, Potter GG, Chen N-K, Song AW. Diffusion tensor imaging of cerebral white matter integrity in cognitive aging. *BBA Mol Basis Dis*. (2012) 1822:386–400. doi: 10.1016/j.bbadis.2011.08.003
8. Song SK, Sun SW, Ju WK, Lin SJ, Cross AH, Neufeld AH. Diffusion tensor imaging detects and differentiates axon and myelin degeneration in mouse optic nerve after retinal ischemia. *Neuroimage*. (2003) 20:1714–22. doi: 10.1016/j.neuroimage.2003.07.005
9. Song SK, Yoshino J, Le TQ, Lin SJ, Sun SW, Cross AH, et al. Demyelination increases radial diffusivity in corpus callosum of mouse brain. *Neuroimage*. (2005) 26:132–40. doi: 10.1016/j.neuroimage.2005.01.028
10. Le Bihan-Levaufre B, Francoual J, Chalas J, Trioche P, Capel L, Lindenbaum A, et al. Genetic incidence of Gilbert's syndrome in France. *Gastroenterol Clin Biol*. (2001) 25:557–8.
11. Assaf Y, Pasternak O. Diffusion tensor imaging (DTI)-based white matter mapping in brain research: a review. *J Mol Neurosci*. (2008) 34:51–61. doi: 10.1007/s12031-007-0029-0
12. Winklewski PJ, Sabisz A, Naumczyk P, Jodzio K, Szurowska E, Szarmach A. Understanding the physiopathology behind axial and radial diffusivity changes—What do we know? *Front Neurol*. (2018) 9:92. doi: 10.3389/fneur.2018.00092
13. Price SJ, Burnet NG, Donovan T, Green HA, Pena A, Antoun NM, et al. Diffusion tensor imaging of brain tumours at 3T: a potential tool for assessing white matter tract invasion? *Clin Radiol*. (2003) 58:455–62. doi: 10.1016/S0009-9260(03)00115-6
14. Kallenberg K, Goldmann T, Menke J, Strik H, Bock HC, Stockhammer F, et al. Glioma infiltration of the corpus callosum: early signs detected by DTI. *J Neuro-Oncol*. (2013) 112:217–22. doi: 10.1007/s11060-013-1049-y
15. Wagner MW, Bell WR, Kern J, Bosemani T, Mhlanga J, Carson KA, et al. Diffusion tensor imaging suggests extrapontine extension of pediatric diffuse intrinsic pontine gliomas. *Eur J Radiol*. (2016) 85:700–6. doi: 10.1016/j.ejrad.2016.02.004
16. Won YI, Chung CK, Kim CH, Park CK, Koo BB, Lee JM, et al. White matter change revealed by diffusion tensor imaging in gliomas. *Brain Tumor Res Treat*. (2016) 4:100–6. doi: 10.14791/btrt.2016.4.2.100
17. Price SJ, Allinson K, Liu H, Boonzaier NR, Yan JL, Lupson VC, et al. Less invasive phenotype found in isocitrate dehydrogenase-mutated glioblastomas than in isocitrate dehydrogenase wild-type glioblastomas: a diffusion-tensor imaging study. *Radiology*. (2017) 283:215–21. doi: 10.1148/radiol.2016152679
18. Eckel-Passow JE, Lachance DH, Molinaro AM, Walsh KM, Decker PA, Sicotte H, et al. Glioma groups based on 1p/19q, IDH, and TERT promoter mutations in tumors. *N Engl J Med*. (2015) 372:2499–508. doi: 10.1056/NEJMoa1407279
19. Khan I, Waqas M, Shamim MS. Prognostic significance of IDH 1 mutation in patients with glioblastoma multiforme. *J Pak Med Assoc*. (2017) 67:816–7. doi: 10.1186/1748-717x-6-115
20. Miotto EC, Silva Junior A, Silva CC, Cabrera HN, Benute GRG, Lucia MCS, et al. Cognitive impairments in patients with low grade gliomas and high grade gliomas. *Arq Neuropsiquiatr*. (2011) 69:596–601. doi: 10.1590/S0004-282X2011000500005
21. Van Kessel E, Baumfalk AE, Van Zandvoort MJE, Robe PA, Snijders TJ. Tumor-related neurocognitive dysfunction in patients with diffuse glioma: a systematic review of neurocognitive functioning prior to anti-tumor treatment. *J Neuro-Oncol*. (2017) 134:9–18. doi: 10.1007/s11060-017-2503-z
22. Habets EJ, Kloet A, Walchenbach R, Vecht CJ, Klein M, Taphoorn MJ. Tumour and surgery effects on cognitive functioning in high-grade glioma patients. *Acta Neurochir*. (2014) 156:1451–9. doi: 10.1007/s00701-014-2115-8
23. Noll KR, Sullaway C, Ziu M, Weinberg JS, Wefel JS. Relationships between tumor grade and neurocognitive functioning in patients with glioma of the left temporal lobe prior to surgical resection. *Neuro Oncol*. (2015) 17:580–7. doi: 10.1093/neuonc/nou233
24. Louis DN, Perry A, Reifenberger G, Von Deimling A, Figarella-Branger D, Cavenee WK, et al. The 2016 World Health Organization classification of tumors of the central nervous system: a summary. *Acta Neuropathol*. (2016) 131:803–20. doi: 10.1007/s00401-016-1545-1
25. Helmstaedter C, Lendt M, Lux S. *Verbaler Lern- und Merkfähigkeitstest: VLMT; Manual*. Göttingen: beltz-Test (2001).
26. Fan J, Mccandliss BD, Sommer T, Raz A, Posner MI. Testing the efficiency and independence of attentional networks. *J Cogn Neurosci*. (2002) 14:340–7. doi: 10.1162/089892902317361886
27. Reitan RM, Wolfson D. The Trail Making Test as an initial screening procedure for neuropsychological impairment in older children. *Arch Clin Neuropsychol*. (2004) 19:281–8. doi: 10.1016/S0887-6177(03)00042-8
28. Yushkevich PA, Piven J, Hazlett HC, Smith RG, Ho S, Gee JC, et al. User-guided 3D active contour segmentation of anatomical structures: significantly improved efficiency and reliability. *NeuroImage*. (2006) 31:1116–28. doi: 10.1016/j.neuroimage.2006.01.015
29. Jenkinson M, Beckmann CF, Behrens TEJ, Woolrich MW, Smith SM. FSL. *NeuroImage*. (2012) 62:782–90. doi: 10.1016/j.neuroimage.2011.09.015
30. Penny W, Friston K, Ashburner J, Kiebel S, Nichols T. *Statistical Parametric Mapping: The Analysis of Functional Brain Images*. London: Academic Press (2006).
31. Friston KJ, Ashburner J, Kiebel SJ, Nichols TE, Penny WD. *Statistical Parametric Mapping: The Analysis of Functional Brain Images*. London: Academic Press (2007).
32. Ashburner J, Friston KJ. Unified segmentation. *NeuroImage*. (2005) 26:839–51. doi: 10.1016/j.neuroimage.2005.02.018
33. Baykara E, Gesierich B, Adam R, Tuladhar AM, Biesbroek JM, Koek HL, et al. A novel imaging marker for small vessel disease based on skeletonization of white matter tracts and diffusion histograms. *Ann Neurol*. (2016) 80:581–92. doi: 10.1002/ana.24758
34. Lu P, Shi L, Du H, Xie B, Li C, Li S, et al. Reduced white matter integrity in primary open-angle glaucoma: a DTI study using tract-based

spatial statistics. *J Neuroradiol*. (2013) 40:89–93. doi: 10.1016/j.neurad.2012.04.001
35. Fathi Kazerooni A, Nabil M, Zeinali Zadeh M, Firouznia K, Azmoudeh-Ardalan F, Frangi AF, et al. Characterization of active and infiltrative tumorous subregions from normal tissue in brain gliomas using multiparametric MRI. *J Magn Reson Imaging*. (2018) 48:938–50. doi: 10.1002/jmri.25963
36. Price SJ, Jena R, Burnet NG, Hutchinson PJ, Dean AF, Pena A, et al. Improved delineation of glioma margins and regions of infiltration with the use of diffusion tensor imaging: an image-guided biopsy study. *AJNR Am J Neuroradiol*. (2006) 27:1969–74.
37. Prabhu SP, Ng S, Vajapeyam S, Kieran MW, Pollack IF, Geyer R, et al. DTI assessment of the brainstem white matter tracts in pediatric BSG before and after therapy: a report from the Pediatric Brain Tumor Consortium. *Childs Nerv Syst*. (2011) 27:11–8. doi: 10.1007/s00381-010-1323-7
38. Kelly PJ, Daumas-Duport C, Kispert DB, Kall BA, Scheithauer BW, Illig JJ. Imaging-based stereotaxic serial biopsies in untreated intracranial glial neoplasms. *J Neurosurg*. (1987) 66:865–74. doi: 10.3171/jns.1987.66.6.0865
39. Jones DK, Knosche TR, Turner R. White matter integrity, fiber count, and other fallacies: the do's and don'ts of diffusion MRI. *Neuroimage*. (2013) 73:239–54. doi: 10.1016/j.neuroimage.2012.06.081
40. Kuznetsova KA, Maniega SM, Ritchie SJ, Cox SR, Storkey AJ, Starr JM, et al. Brain white matter structure and information processing speed in healthy older age. *Brain Struct Funct*. (2016) 221:3223–35. doi: 10.1007/s00429-015-1097-5
41. Giulietti G, Torso M, Serra L, Spano B, Marra C, Caltagirone C, et al. Whole brain white matter histogram analysis of diffusion tensor imaging data detects microstructural damage in mild cognitive impairment and Alzheimer's disease patients. *J Magn Reson Imaging*. (2018) 48:767–79. doi: 10.1002/jmri.25947
42. Bullmore E, Sporns O. Complex brain networks: graph theoretical analysis of structural and functional systems. *Nat Rev Neurosci*. (2009) 10:186–98. doi: 10.1038/nrn2575
43. Meyers CA, Hess KR, Yung WK, Levin VA. Cognitive function as a predictor of survival in patients with recurrent malignant glioma. *J Clin Oncol*. (2000) 18:646–50. doi: 10.1200/JCO.2000.18.3.646
44. Klein M, Postma TJ, Taphoorn MJ, Aaronson NK, Vandertop WP, Muller M, et al. The prognostic value of cognitive functioning in the survival of patients with high-grade glioma. *Neurology*. (2003) 61:1796–8. doi: 10.1212/01.WNL.0000098892.33018.4C
45. Armstrong CL, Goldstein B, Shera D, Ledakis GE, Tallent EM. The predictive value of longitudinal neuropsychologic assessment in the early detection of brain tumor recurrence. *Cancer*. (2003) 97:649–56. doi: 10.1002/cncr.11099
46. Carrillo JA, Lai A, Nghiemphu PL, Kim HJ, Phillips HS, Kharbanda S, et al. Relationship between tumor enhancement, edema, IDH1 mutational status, MGMT promoter methylation, and survival in glioblastoma. *AJNR Am J Neuroradiol*. (2012) 33:1349–55. doi: 10.3174/ajnr.A2950
47. Beiko J, Suki D, Hess KR, Fox BD, Cheung V, Cabral M, et al. IDH1 mutant malignant astrocytomas are more amenable to surgical resection and have a survival benefit associated with maximal surgical resection. *Neuro Oncol*. (2014) 16:81–91. doi: 10.1093/neuonc/not159
48. Sonoda Y, Shibahara I, Kawaguchi T, Saito R, Kanamori M, Watanabe M, et al. Association between molecular alterations and tumor location and MRI characteristics in anaplastic gliomas. *Brain Tumor Pathol*. (2015) 32:99–104. doi: 10.1007/s10014-014-0211-3
49. Andronesi OC, Kim GS, Gerstner E, Batchelor T, Tzika AA, Fantin VR, et al. Detection of 2-hydroxyglutarate in IDH-mutated glioma patients by *in vivo* spectral-editing and 2D correlation magnetic resonance spectroscopy. *Sci Transl Med*. (2012) 4:116ra114. doi: 10.1126/scitranslmed.3002693
50. Choi C, Ganji SK, Deberardinis RJ, Hatanpaa KJ, Rakheja D, Kovacs Z, et al. 2-Hydroxyglutarate detection by magnetic resonance spectroscopy in IDH-mutated patients with gliomas. *Nat Med*. (2012) 18:624–9. doi: 10.1038/nm.2682
51. Picca A, Di Stefano AL, Sanson M. Current and future tools for determination and monitoring of isocitrate dehydrogenase status in gliomas. *Curr Opin Neurol*. (2018) 31:727–32. doi: 10.1097/WCO.0000000000000617
52. Inglese M, Brown S, Johnson G, Law M, Knopp E, Gonen O. Whole-brain N-acetylaspartate spectroscopy and diffusion tensor imaging in patients with newly diagnosed gliomas: a preliminary study. *AJNR Am J Neuroradiol*. (2006) 27:2137–40.
53. Kallenberg K, Bock HC, Helms G, Jung K, Wrede A, Buhk JH, et al. Untreated glioblastoma multiforme: increased myo-inositol and glutamine levels in the contralateral cerebral hemisphere at proton MR spectroscopy. *Radiology*. (2009) 253:805–12. doi: 10.1148/radiol.2533071654
54. Busch M, Liebenrodt K, Gottfried S, Weiland E, Vollmann W, Mateiescu S, et al. Influence of brain tumors on the MR spectra of healthy brain tissue. *Magn Reson Med*. (2011) 65:18–27. doi: 10.1002/mrm.22612
55. Heiland DH, Mader I, Schlosser P, Pfeifer D, Carro MS, Lange T, et al. Integrative network-based analysis of magnetic resonance spectroscopy and genome wide expression in glioblastoma multiforme. *Sci Rep*. (2016) 6:29052. doi: 10.1038/srep29052
56. Heiland DH, Worner J, Gerrit Haaker J, Delev D, Pompe N, Mercas B, et al. The integrative metabolomic–transcriptomic landscape of glioblastome multiforme. *Oncotarget*. (2017) 8:49178–90. doi: 10.18632/oncotarget.16544
57. Diamandis E, Gabriel CPS, Wurtemberger U, Guggenberger K, Urbach H, Staszewski O, et al. MR-spectroscopic imaging of glial tumors in the spotlight of the 2016 WHO classification. *J Neuro Oncol*. (2018) 139:431–40. doi: 10.1007/s11060-018-2881-x
58. Sinha S, Bastin ME, Wardlaw JM, Armitage PA, Whittle IR. Effects of dexamethasone on peritumoural oedematous brain: a DT-MRI study. *J Neurol Neurosurg Psychiatry*. (2004) 75:1632–5. doi: 10.1136/jnnp.2003.028647

Conflict of Interest Statement: The authors declare that the research was conducted in the absence of any commercial or financial relationships that could be construed as a potential conflict of interest.

frontiers in Oncology

ORIGINAL RESEARCH
published: 14 November 2019
doi: 10.3389/fonc.2019.01183

A Non-invasive Radiomic Method Using ^{18}F-FDG PET Predicts Isocitrate Dehydrogenase Genotype and Prognosis in Patients With Glioma

Longfei Li[1,2†], Wei Mu[2†], Yaning Wang[3†], Zhenyu Liu[2], Zehua Liu[1,2], Yu Wang[3], Wenbin Ma[3], Ziren Kong[3], Shuo Wang[2], Xuezhi Zhou[2,4], Wei Wei[2,4,5], Xin Cheng[6], Yusong Lin[1,7*] and Jie Tian[2,4,8,9*]*

[1] Collaborative Innovation Center for Internet Healthcare, Zhengzhou University, Zhengzhou, China, [2] CAS Key Laboratory of Molecular Imaging, Institute of Automation, Chinese Academy of Sciences, Beijing, China, [3] Department of Neurosurgery, Peking Union Medical College Hospital, Chinese Academy of Medical Sciences and Peking Union Medical College, Beijing, China, [4] Engineering Research Center of Molecular and Neuro Imaging of Ministry of Education, School of Life Science and Technology, Xidian University, Xi'an, China, [5] School of Electronics and Information, Xi'an Polytechnic University, Xi'an, China, [6] Department of Nuclear Medicine, Peking Union Medical College Hospital, Chinese Academy of Medical Sciences and Peking Union Medical College, Beijing, China, [7] School of Software, Zhengzhou University, Zhengzhou, China, [8] School of Artificial Intelligence, University of Chinese Academy of Sciences, Beijing, China, [9] Beijing Advanced Innovation Center for Big Data-Based Precision Medicine, Beihang University, Beijing, China

OPEN ACCESS

Edited by:
Sebastian Cerdan,
Spanish National Research Council (CSIC), Spain

Reviewed by:
Xiaohua Zhu,
Huazhong University of Science and Technology, China
Zheng Wang,
Capital Medical University, China

***Correspondence:**
Xin Cheng
pumch_chengxin@126.com
Yusong Lin
yslin@ha.edu.cn
Jie Tian
jie.tian@ia.ac.cn

[†] These authors have contributed equally to this work

Specialty section:
This article was submitted to Cancer Imaging and Image-directed Interventions, a section of the journal Frontiers in Oncology

Received: 25 June 2019
Accepted: 21 October 2019
Published: 14 November 2019

Citation:
Li L, Mu W, Wang Y, Liu Z, Liu Z, Wang Y, Ma W, Kong Z, Wang S, Zhou X, Wei W, Cheng X, Lin Y and Tian J (2019) A Non-invasive Radiomic Method Using ^{18}F-FDG PET Predicts Isocitrate Dehydrogenase Genotype and Prognosis in Patients With Glioma. Front. Oncol. 9:1183. doi: 10.3389/fonc.2019.01183

Purpose: We aimed to analyze ^{18}F-fluorodeoxyglucose positron emission tomography (^{18}F-FDG PET) images via the radiomic method to develop a model and validate the potential value of features reflecting glioma metabolism for predicting isocitrate dehydrogenase (IDH) genotype and prognosis.

Methods: PET images of 127 patients were retrospectively analyzed. A series of quantitative features reflecting the metabolic heterogeneity of the tumors were extracted, and a radiomic signature was generated using the support vector machine method. A combined model that included clinical characteristics and the radiomic signature was then constructed by multivariate logistic regression to predict the IDH genotype status, and the model was evaluated and verified by receiver operating characteristic (ROC) curves and calibration curves. Finally, Kaplan-Meier curves and log-rank tests were used to analyze overall survival (OS) according to the predicted result.

Results: The generated radiomic signature was significantly associated with IDH genotype ($p < 0.05$) and could achieve large areas under the ROC curve of 0.911 and 0.900 on the training and validation cohorts, respectively, with the incorporation of age and type of tumor metabolism. The good agreement of the calibration curves in the validation cohort further validated the efficacy of the constructed model. Moreover, the predicted results showed a significant difference in OS between high- and low-risk groups ($p < 0.001$).

Conclusions: Our results indicate that the ^{18}F-FDG metabolism-related features could effectively predict the IDH genotype of gliomas and stratify the OS of patients with different prognoses.

Keywords: ^{18}F-FDG PET, radiomics, glioma, isocitrate dehydrogenase, non-invasive prediction

INTRODUCTION

Glioma is a common type of primary malignant central nervous system tumor and causes significant morbidity and mortality (1), with an incidence of 4–5 per 100,000 individuals. The prognosis of patients is grim; <50% of patients with low-grade glioma have no recurrence 10 years after diagnosis (2), and the 5-year survival rate of patients with high-grade glioma is just 5% (3). Isocitrate dehydrogenase (IDH) is emphasized as a key biomarker for glioma prediction and prognosis in the 2016 update of the WHO diagnostic criteria (4), and the overall survival (OS) of patients with IDH mutants is significantly better than the OS of those with wild-type IDH (5). The IDH biomarker is also critical for accurate glioma classification (4), planning of the scope of surgical resection (6), and guiding of the chemotherapy regimen (7, 8). Thus, accurate IDH genotype prediction may have a positive impact on the individualized treatment plan of patients with glioma.

The status of IDH mutation is currently mainly detected through immunohistochemistry, PCR product sequencing, and other technologies, using surgical or biopsy tumor samples. However, there is still an unmet clinical need for easily accessible biomarkers that can be used to acquire the underlying tumor genotype and achieve patient survival stratification accurately. Several exploratory studies have tried to use detection and analysis techniques that use circulating tumor cells, circulating tumor DNA, and serum/cerebrospinal fluid biomarkers to identify IDH mutants. Nevertheless, these studies are still at a relatively early stage (9, 10). At the same time, other studies have attempted to predict the status of IDH genotypes in patients with glioma through magnetic resonance (MR) or positron emission tomography (PET) imaging parameters, including the apparent diffusion coefficient and relative cerebral-blood-volume for MR and the tumor-to-brain ratio and time-to-peak for PET (11, 12). However, the above studies of IDH genotype identification based on image parameters lacked the necessary validation data to verify the performance of the proposed methods.

An emerging radiomic method based on the combination of artificial intelligence and medical imaging has attracted wide attention due its potential value for accurate diagnosis and prognosis assessment (13). The radiomic method aims to perform non-invasive tumor analysis by extracting a suite of quantitative features from medical images (14–16). These features include a variety of gene expression types that provide a more comprehensive description of tumor characteristics, enabling researchers to obtain an effective signature to inform objective clinical decisions (17–19). Some studies have been carried out based on MR images and radiomic methods and have demonstrated the potential value of radiomic features in predicting the gene status of gliomas (20–22). It is well-known that PET imaging is functional molecular imaging that uses tracers to visualize biological processes such as uptake of glucose, consumption of amino acid analogs, cell proliferation, etc. Specifically, ^{18}F-fluorodeoxyglucose positron emission tomography (^{18}F-FDG PET) reflects the uptake of glucose in tumor areas and determines the spatial distribution of radioactive PET imaging agents quantitatively *in vivo*, using elevated metabolism at the molecular level to map tumorigenic activity (23). This imaging method provides additional insight beyond MR imaging (MRI) into the biology of gliomas, which facilitates the analysis of the tumor from the perspective of glucose metabolism. In glioma research, ^{18}F-FDG PET is widely applied, for example for tumor grading (24), determination of tumor extent (25), surgical planning (26), differentiation of tumor progression and necrosis (27), and prognosis prediction (28). However, to the best of our knowledge, few studies have used ^{18}F-FDG PET images and the radiomic method to predict IDH genotype.

Therefore, in this study, we performed a comprehensive analysis and developed a combined model based on ^{18}F-FDG PET radiomic signatures and the preoperative clinical characteristics of patients for non-invasive prediction of glioma IDH genotype status. We hypothesized that this radiomic analysis may identify differences in ^{18}F-FDG metabolism between tumors with different IDH genotypes and thereby help to assess patient IDH genotype and prognosis.

MATERIALS AND METHODS

Patients

For this retrospective study, we used database records of patients who were diagnosed with primary glioma between 2010 and 2017 at the Peking Union Medical College Hospital, Beijing, China. A total of 127 consecutive cases were included in this study according to the inclusion and exclusion criteria presented in **Supplementary Methods 1** and **Supplementary Figure 1**. The design and protocol of the study were conducted in accordance with the Declaration of Helsinki and were approved by the Ethics Committee of Peking Union Medical College Hospital, with all requirements for informed patient consent waived. These patients were randomly divided into two groups, two-thirds ($N = 84$) in the training cohort and one-third ($N = 43$) in the validation cohort.

IDH Mutant Detection

IDH1 and IDH2 mutations were detected postoperatively in patient tumor tissue using direct sequencing, as described by Horbinski et al. (29). DNA was isolated from formalin-fixed, paraffin-embedded tumor tissue using the Simplex OUP® FFPE DNA extraction kit (TIB, China), and the quantity was assessed by spectrophotometry using a NanoDrop 2000 (Thermo Fisher, US). Polymerase chain reaction (PCR) was accomplished with IDH1 primer (IDH1-F) 5′-TGATGAGAAGAGGGTTGAG-3′, (IDH1-R) 5′-TTACTTGATCCCCATAAGCC-3′, and IDH2 primer (IDH2-F) 5′-GACCCCCGTCTGGCTGTG-3′, (IDH2-R) 5′-CAAGAGGATGGCTAGGCGAG-3′ using the DRR007 kit (Takara, Japan) and a Verity 96-Well Thermal Cycler (Thermo Fisher, US) to amplify the fragment that contains two mutation hotspots. PCR products were treated with Exonuclease I and Antarctic Phosphatase (New England Biolabs, UK) and sequenced using a Genetic Analyzers 3500 (Thermo Fisher, US).

^{18}F-FDG PET Data Acquisition and Tumor Segmentation

^{18}F-FDG was produced *in situ* using an RDS-111 Cyclotron (CTI, US). After a fast of at least 4 h, patient blood glucose level was tested and confirmed as not exceeding the normal limit (6.4 mM). A dose of 5.55 MBq (0.15 mCi) ^{18}F-FDG per kg of body weight was injected intravenously under standardized conditions in a quiet, dark room with the patient's eyes closed. An ^{18}F-FDG PET/CT scan was performed 40–60 min after the ^{18}F-FDG injection using a Biograph 64 TruePoint TrueV PET system (Siemens Medical Solutions, Germany). The reconstruction of PET imaging used a 336 × 336 pixel matrix, corresponding to a voxel size of 1 × 1 mm with a 3 mm slice thickness.

The three-dimensional region of interest (ROI) of every tumor was manually segmented within each slice using ITK-SNAP software (http://www.itksnap.org) by two neurosurgeons with >10 years' experience in neuro-oncology and neuro-PET, respectively, who were blinded to the final pathological result. The result of each segmentation was reviewed by a senior nuclear medicine physician with over 20 years' experience in this field. If the divergence between segmentations by the two neurosurgeons was <5%, the final ROI was determined as the overlapping region of the two ROIs, and if the divergence was more than 5%, the senior nuclear medicine physician made the final decision.

Radiomic Feature Extraction and Feature Selection

The radiomic analysis workflow of our study is illustrated in **Figure 1**. Calculations for all radiomics features were implemented from a standard uptake value (SUV) image using the open-source PyRadiomics package (https://github.com/Radiomics/pyradiomics) in Python (30). The PET image normalization method is detailed in **Supplementary Method 2**. Ninety-nine quantitative radiomics features were calculated from the ROI within each original SUV image, comprising 13 shape and size features, 18 first-order statistical features, and 68 texture features (22 gray-level co-occurrence matrix, 14 gray-level dependence matrix, 16-gray level run length matrix, and 16 gray-level size zone matrix features) (31). By applying eight different decomposition level wavelet filters, 688 first-order statistical and texture radiomics features were obtained. A total of 774 first-order statistical and texture features were calculated after applying the "logarithm, square, exponential, gradient, squareroot, lbp" filter. Filter descriptions and mathematical definitions for the computed radiomics features are described at (http://pyradiomics.readthedocs.io/en/latest/features.html). After applying different filters, the same number of features was extracted, including 18 first-order statistical features and 68 texture features (22 gray-level co-occurrence matrix, 14 gray-level dependence matrix, 16 gray-level run length matrix, and 16 gray-level size zone matrix features).

In order to facilitate the construction of the radiomic signature and control the feature coefficients, all radiomic feature values were normalized to between 0 and 1 according to the maximum and minimum value for the subsequent analysis. The method of feature selection with the elastic net is considered as an extension of the least absolute shrinkage and selection operator, which is appropriate in situations where the number of predictors exceeds the number of cases. With the elastic net method, which is considered an extension of the least absolute shrinkage and selection operator (32, 33) and is appropriate in situations where the number of predictors exceeds the number of cases (34). In this study, the key IDH-associated radiomics features were selected first, and then the final feature set was determined according to the greatest area under curve (AUC) value of 10-fold cross-validation. The *p*-value, based on univariate analysis, was used to assess the potential impact of clinical characteristics (**Supplementary Table 1**) on IDH genotype prediction.

Model Construction and Validation

With these selected key radiomic features, a support vector machine model with a radial basis function kernel was then used to construct a radiomic signature for IDH genotype prediction in the training cohort with 10-fold cross-validation. Details of the model are provided in **Supplementary Method 3**. Training cohort data and the radiomic signature generated together with selected clinical features were used to establish a multiple logistic regression model for predicting the patient's IDH genotype.

The accuracy of the IDH status predictions using the above methods was assessed using the receiver operating characteristic (ROC) curve and the AUC values in the training cohort and a completely independent validation cohort. The most valuable IDH genotype prediction model was determined by comparing the predicted performance indicator values and the ROC curves (Delong's test) of the three models in the training cohort and the validation cohort and was evaluated based on the calibration curve and Hosmer-Lemeshow test (35). Decision curve analysis was used to manifest the clinical usefulness of the model by quantifying the net benefit at different threshold probabilities (36).

Survival Analysis

Furthermore, the patients in the training and validation cohorts were divided into high- and low-risk groups according to the predicted result of the optimal model developed. The Kaplan-Meier curve was used to stratify the survival trend between patients in the two risk groups. The log-rank test was then used to verify whether there were statistical differences in survival between the two groups.

Statistical Analysis

The differences between features were assessed using Pearson's Chi-Square tests or Fisher's exact tests for categorical variables and Student's *t*-tests or Mann-Whitney *U*-tests for continuous variables, as appropriate. The above statistical analyses were performed with SPSS Statistics software, version 18.0 (Chicago, IL, USA) or R software, version 3.4.1 (www.R-project.org). The two-tailed threshold of $p < 0.05$ was considered statistically significant.

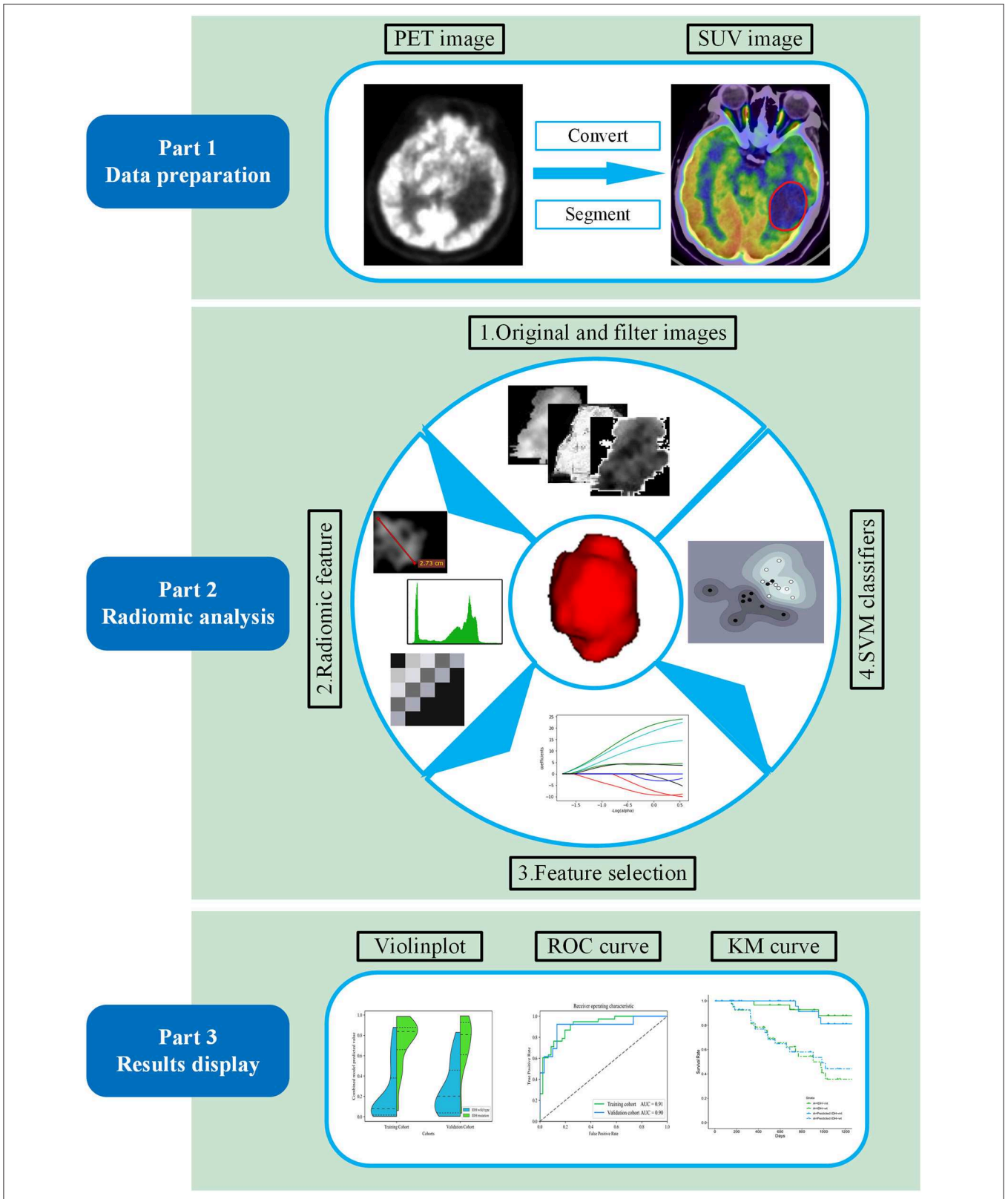

FIGURE 1 | Workflow of the proposed radiomic analysis for non-invasively predicting isocitrate dehydrogenase (IDH) genotype and prognosis in glioma patients.

TABLE 1 | Clinical characteristics of patients in the training cohort and validation cohort.

Characteristics	Training cohort ($n = 84$)		Validation cohort ($n = 43$)		p
	IDH-mt ($n = 38$)	IDH-wt ($n = 46$)	IDH-mt ($n = 13$)	IDH-wt ($n = 30$)	
Age (years)	43.84 ± 11.11	51.30 ± 15.33	41.85 ± 9.60	50.10 ± 20.43	0.92
Sex					0.26
Male	21	25	7	21	
Female	17	21	6	9	
Weight (kg)	67.99 ± 11.78	66.44 ± 14.72	69.00 ± 12.18	67.83 ± 13.38	0.67
Metabolism					0.42
Cystic	31	24	10	15	
Solid	7	22	3	15	
SUV_{max}	10.32 ± 5.54	10.24 ± 5.12	10.09 ± 5.53	9.03 ± 4.02	0.33
SUV_{mean}	4.48 ± 2.38	4.54 ± 1.86	3.80 ± 1.99	3.89 ± 1.89	0.09

IDH, isocitrate dehydrogenase; IDH-mt, IDH mutant; IDH-wt, IDH wild-type; SUV, standard uptake value.
Chi-Square or Fisher's exact tests, as appropriate, were used to compare the differences in categorical variables, while independent sample t-tests or Mann-Whitney U-tests were used to compare the differences in continuous variables.
Age, Weight, SUV_{max}, and SUV_{mean} are represented as (mean ± standard deviation).

RESULTS

Clinical Characteristics

All patients underwent surgery to remove tumors, and their IDH genotype status was assessed. Of the 84 patients in the training cohort, 38 were identified as having an IDH mutant and 46 as having the IDH wild-type gene. Of the 43 patients in the independent validation cohort, 13 had an IDH mutant and 30 had the IDH wild-type gene. The baseline characteristics of the training and validation cohorts are shown in **Table 1** and showed no significant differences between the two groups ($p = 0.09$–0.92), which justified their applicability as training and validation cohorts. The baseline information of patients with different IDH phenotypes is shown in **Supplementary Table 2**.

Radiomic Feature Extraction and Feature Selection

In total, 1,561 radiomic features were computed in our study. After applying the elastic net method, 11 key radiomic features were selected from the training cohort for generating the radiomic signature (**Figure 2**), all of which showed significant differences (independent t-test $p < 0.05$) between IDH mutant and IDH wild-type cases (feature details are shown in **Figure 2**). These key radiomic features included 1 shape, 7 texture, and 3 first-order statistical features. The results of the univariate analysis of clinical characteristics revealed age and the type of tumor metabolism as significant predictors ($p < 0.05$), as presented in detail in **Supplementary Table 1**.

Model Construction and Validation

IDH genotype prediction using the above radiomic signature achieved a noteworthy result, producing AUCs of 0.904 [95% confidence interval (CI), 0.886–0.923] and 0.890 (95% CI, 0.861–0.919) in the training and validation cohorts, respectively. The predictive potential of the selected clinical characteristics was assessed by establishing and evaluating the clinical model, obtaining AUCs of 0.705 (95% CI, 0.673–0.738) and 0.664 (95% CI, 0.634–0.695) in the training and validation cohorts, respectively. A multivariable combined model was developed through the combination of age, type of tumor metabolism, and radiomic signature, which was visualized through a nomogram (**Supplementary Figure 2**). Detailed information such as the feature coefficients and predicted probability calculation method of the combined model are indicated in **Supplementary Table 3**. The combined model achieved the best result, with AUCs of 0.911 (95% CI, 0.895–0.931) for the training cohort and 0.900 (95% CI, 0.877–0.923) for the validation cohort. **Figure 3** shows the ROC curves and the probability distribution of the predicted IDH mutants in the training and validation cohorts for the three models. More details on the predictive indicators obtained by these models are given in **Table 2**. The predictive performance of the combined model in the training and validation cohorts is also depicted by the barplots in **Figure 4**. Subgroup analysis shows that our model can also show good predictive performance with different glioma grades. The AUC was 0.88 and 0.93 in lower-grade tumors (WHO II and WHO III) and glioblastoma (WHO IV), respectively. Details are shown in **Supplementary Figure 3**.

Based on the results shown in **Table 2** and **Supplementary Table 4**, the radiomic signature and the combined model showed significantly better discrimination performance ($p < 0.05$) than the clinical model alone according to the AUCs in the training and validation cohorts. Here, our results also confirm that the combined model, with more incorporated information, had the highest AUC value and showed more obvious differences in the predicted probability distribution trends of patients with different genotypes in the two cohorts. The combined model calibration curve displayed good agreement between prediction and observation in the training and validation cohorts, and the Hosmer-Lemeshow test did not show a significant difference ($p > 0.05$), demonstrating a good fit in both cohorts (**Figure 5**). As shown in **Supplementary Figure 4**, decision curves were used

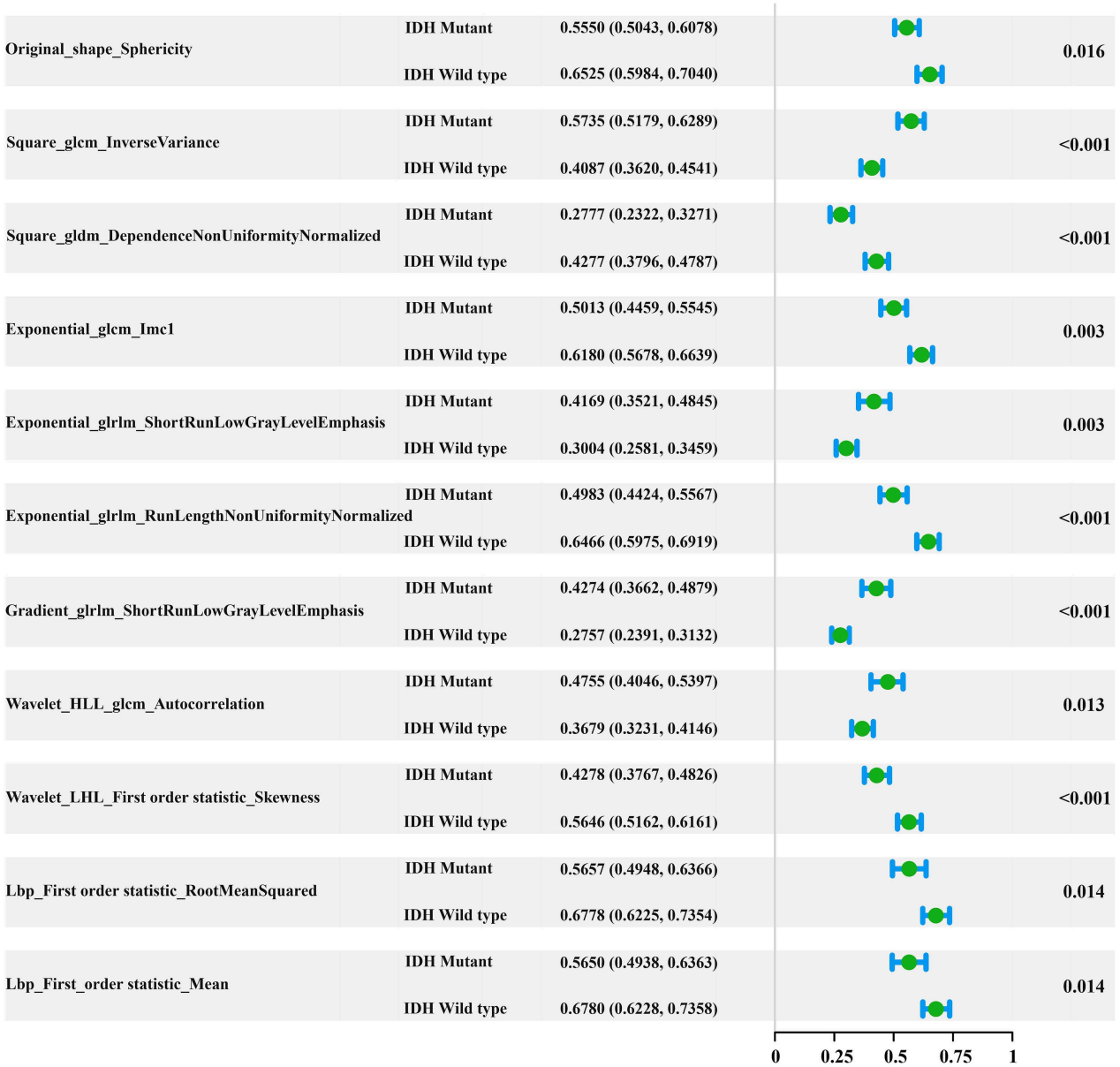

FIGURE 2 | Forest plot of the 11 selected radiomic features. All features yielded significant differences in IDH mutant and IDH wild-type patients (independent *t*-test, $p < 0.05$).

to demonstrate the benefits of the combined model. We found that if the threshold probability of clinical decision was >0% or >8% in training or validation cohorts, then patients would benefit more from the combined model than if genotype was not predicted.

Survival Analysis

Our results suggest that the combined model not only has great potential for predicting IDH genotypes but can also help to stratify the OS of patients through Kaplan-Meier analysis (**Figure 6**). The predicted value of the combined model divided patients into high-risk (predicted probability <0.5) and low-risk (predicted probability ≥0.5) groups. Meanwhile, our results indicated significant statistical differences in the OS of patients, using a log-rank test between the two groups in the training and validation cohorts ($p < 0.05$).

DISCUSSION

In this study, we obtained 11 metabolism-related radiomic features that could reflect significant differences in different

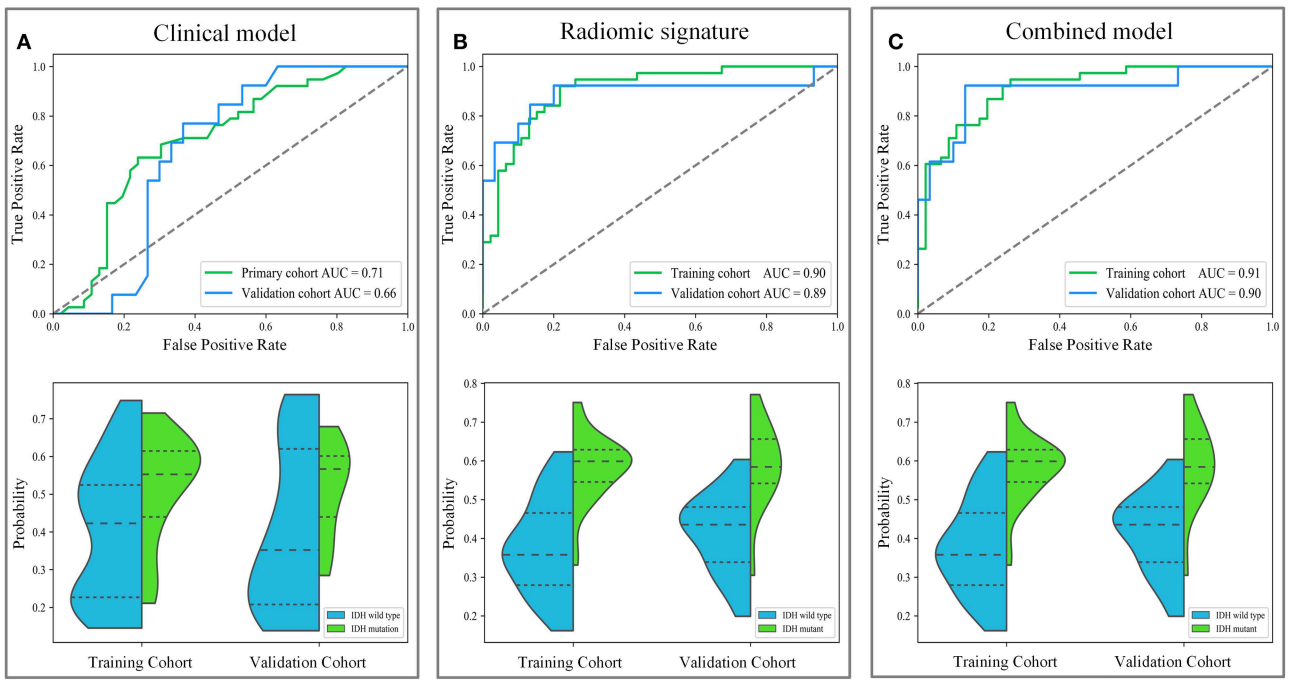

FIGURE 3 | The diagnostic performance of these different models in predicting IDH genotype. The first row depicts the receiver operating characteristic (ROC) curves of the three models. The second row depicts the distribution of the IDH mutant probabilities predicted by the three models, where the horizontal dash lines are the quartiles. Subgraph **(A–C)** show the performance of clinical model, radiomic signature and combined model to predict IDH genotype, respectively.

TABLE 2 | Diagnostic performance of the radiomic signature, clinical model, and combined model.

Method	Cohort	AUC (95% CI)	ACC (95% CI)	SEN (95% CI)	SPE (95% CI)
Radiomic signature	Training cohort	0.904 (0.886, 0.923)	82.1% (79.8, 84.5)	86.8.1% (83.6, 90.0)	78.3% (74.9, 81.5)
	Validation cohort	0.890 (0.871, 0.924)	81.4% (79.6, 83.9)	92.3% (89.4, 95.3)	80.0% (77.2, 82.9)
Clinical model	Training cohort	0.705 (0.673, 0.738)	66.7% (63.8, 69.5)	71.1% (66.8, 75.3)	63.0% (59.2, 67.0)
	Validation cohort	0.664 (0.631, 0.695)	65.1% (62.1, 68.0)	61.5% (56.1, 67.2)	66.7% (63.0, 70.1)
Combined model	Training cohort	0.911 (0.895, 0.931)	79.8% (77.2, 82.3)	78.9% (75.2, 82.7)	80.4% (77.0, 83.9)
	Validation cohort	0.900 (0.877, 0.923)	83.7% (81.5, 86.0)	92.3% (89.3, 95.3)	80.0% (77.1, 82.9)

95% CI, 95% confidence interval; AUC, area under the curve; ACC, accuracy; SEN, sensitivity; SPE, specificity.

IDH genotypes of gliomas. Specifically, we developed a combined model that links the above metabolic features and clinical information to predict the IDH genotype of a glioma effectively. Moreover, our results also demonstrate that there is a significant correlation between the probabilities predicted with the combined model and patient prognosis.

Our study extended previous radiomic studies on predicting IDH genotypes in patients with glioma, which predominantly linked quantitative features based on MR images to predict glioma patient IDH genotype. Yu et al. (20) showed that a radiomic study based on 110 T2-FLAIR MR images was potentially useful for non-invasive prediction of IDH genotype in grade II gliomas. Zhang et al. (21) used a combination of radiomic features based on multiparameter MRI and clinical features to predict IDH genotype in 120 high-grade gliomas. Lu et al. (22) used 214 MR images from The Cancer Image Archive and 70 collected preoperative MR images to predict the IDH mutant in low-grade gliomas. However, these studies do not fully reflect the advantages of non-invasive prediction because they all used knowledge of pathological tumor grade to select patients. The difference is that our study extracts quantitative features based on PET images that reflect tumor FDG metabolic information. Moreover, the combined model is a promising method for predicting a patient's IDH genotype and does not require prior selection of the patients based on pathological grade. **Figure 7** illustrates a comparison of two representative patient cases with similar image and clinical representation; the combined model effectively distinguished between the individual with an IDH mutant and the IDH wild-type patient.

PET imaging is widely used in clinical tumor therapy and can non-invasively provide information related to tumor

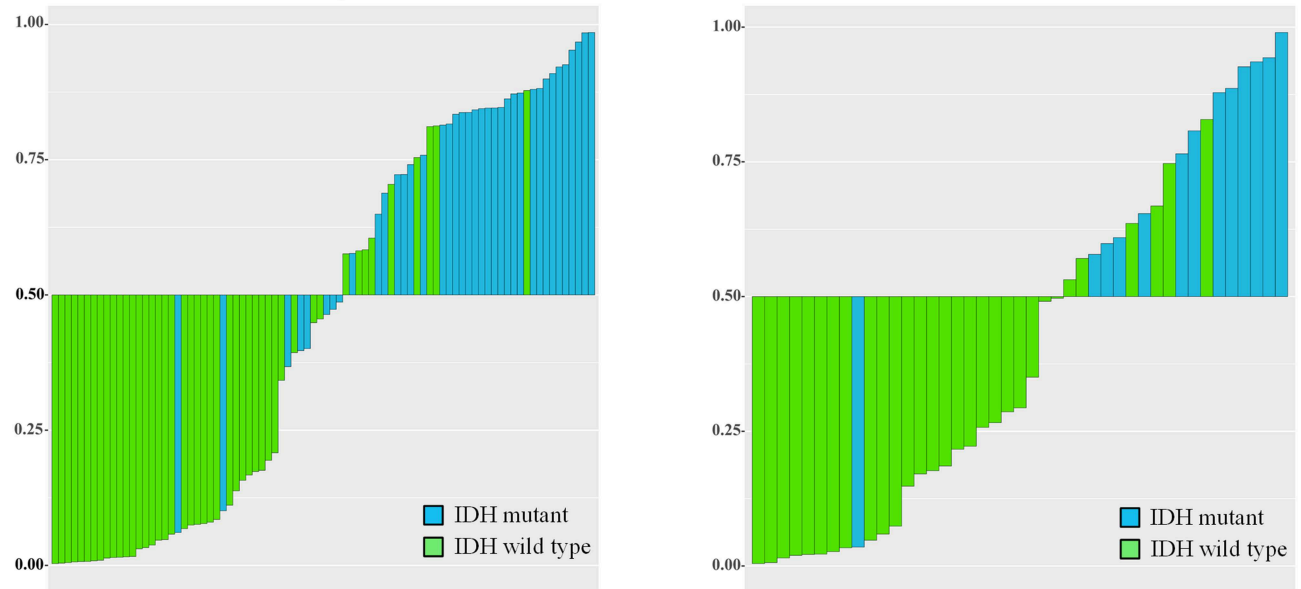

FIGURE 4 | Barplots depicting the predictive performance of the combined model. A blue bar with a predicted probability value > cutoff (0.5) indicates that the model successfully identifies the IDH mutant patients; a blue bar with a predicted value < cutoff indicates that the signature fails to identify the IDH mutant patients. For the green bars, the opposite applies.

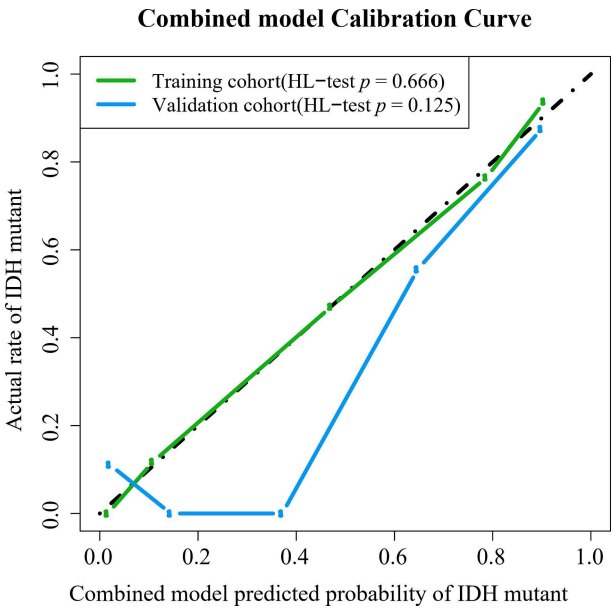

FIGURE 5 | Calibration curves of the combined model in the training and validation cohorts.

metabolism, predicting the progression and recurrence of glioma more effectively than MRI (37). ^{18}F-FDG PET imaging can show alterations in the tumor microenvironment glucose metabolism, also known as the oncological Warburg effect (38). The differences in metabolic microenvironments between the two genotypes of glioma were reflected by the radiomic signature that combined 11 prominent high-dimensional radiomic features. The results show that the combined model has extraordinary predictive potential and can combine more information to enhance and perfect the predictive ability for IDH genotype; thus, as an indicator parameter, it may provide important predictive power for future IDH prediction. Until now, radiomic studies using ^{18}F-FDG PET images for IDH genotype classification of gliomas have not been well-described in the literature. Our study clarifies the association between the radiomic features of ^{18}F-FDG metabolism and IDH genotypes and has achieved noteworthy predictive and prognostic performance.

Our findings were in line with previous radiomic studies showing that features of PET images are potentially useful for solving clinical problems (39, 40). For example, the radiomic feature sphericity is a measure of how spherical tumors are and, here, shows the metabolic shape of the tumor. A recent radiomic study demonstrated that the sphericity feature based on ^{18}F-FDG PET is associated with low therapeutic benefit and survival in colorectal cancer (40). Results from our study suggest that there are also significant differences in the shape feature based on ^{18}F-FDG PET images in gliomas with different IDH genotypes ($p = 0.016$, Student's t-test). The sphericity of IDH-mutant glioma is lower than that of the IDH wild-type. These conclusions indicate that radiomic features based on ^{18}F-FDG PET images play an important role, have robust applicability in solid tumor analysis, and may serve as valuable indicators to assist clinicians in making decisions.

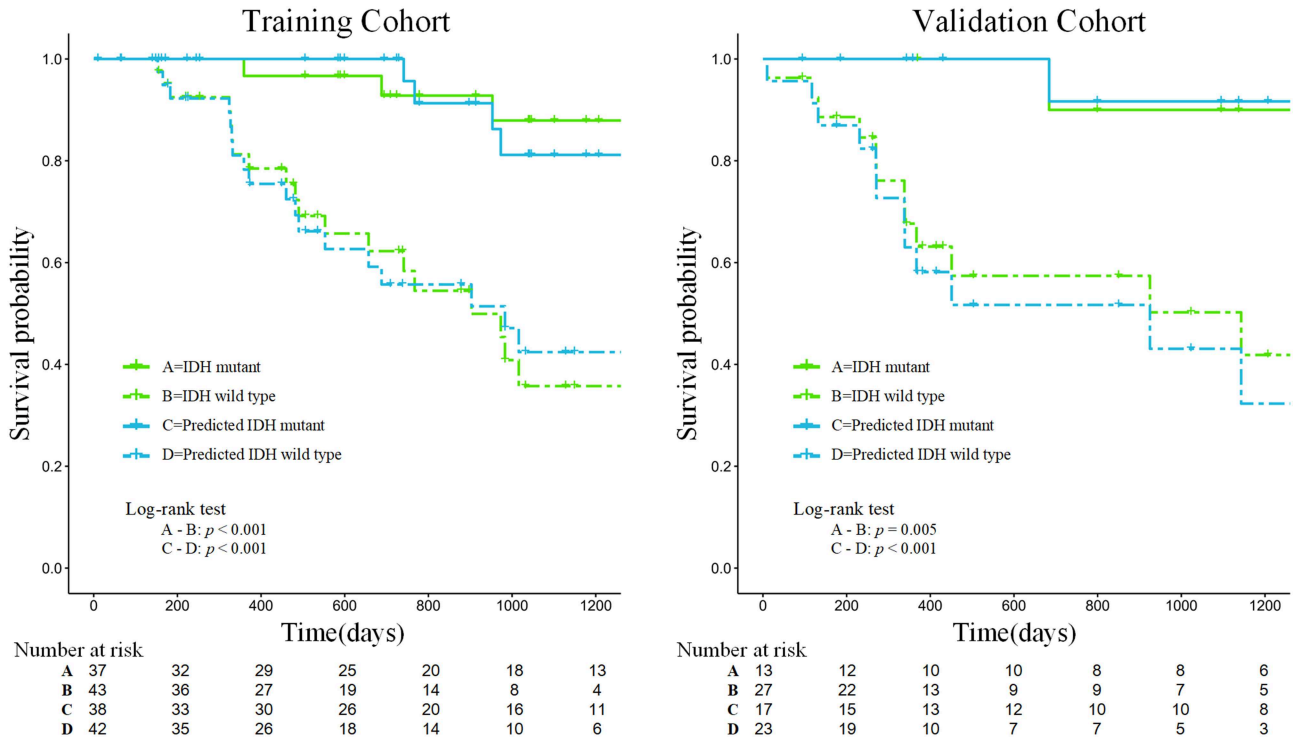

FIGURE 6 | Kaplan-Meier analysis of overall survival according to the actual IDH status and the IDH status predicted by the combined model in the training and validation cohorts.

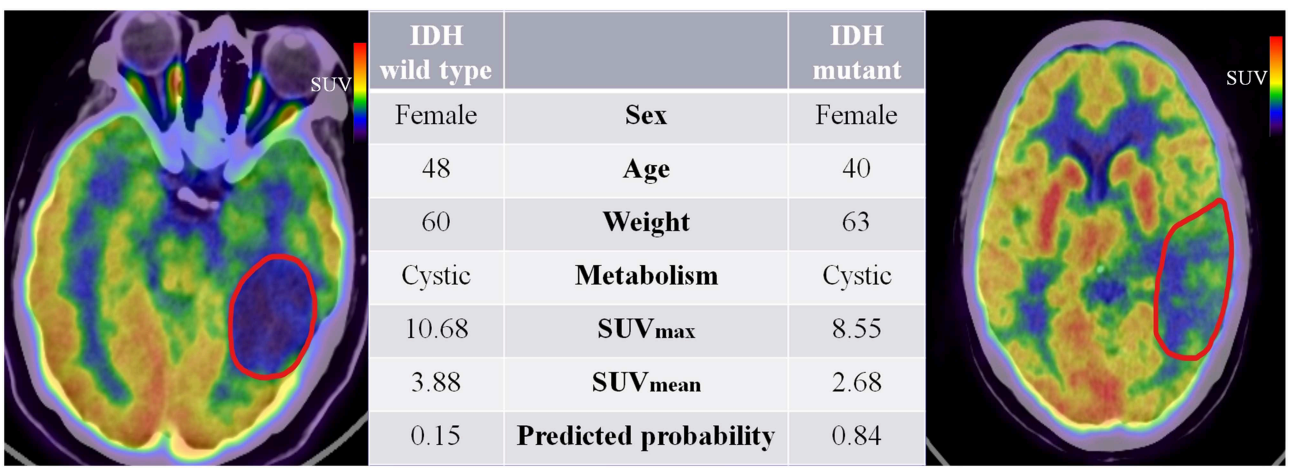

IDH wild type		IDH mutant
Female	**Sex**	Female
48	**Age**	40
60	**Weight**	63
Cystic	**Metabolism**	Cystic
10.68	**SUV_{max}**	8.55
3.88	**SUV_{mean}**	2.68
0.15	**Predicted probability**	0.84

FIGURE 7 | ^{18}F-fluorodeoxyglucose positron emission tomography images of two patients with IDH mutant and IDH wild-type status. The red boundaries in the images were manually delineated as the region of interest. All the clinical characteristics and predicted probabilities of the combined model are presented in the center table.

Furthermore, the prognostic value of ^{18}F-FDG PET textural features before treatment has been confirmed in several types of extracranial tumors (41, 42). It is well-known that patients with gliomas of different IDH genotypes differ in their survival times. According to follow-up information on patients, our study found that the survival curves predicted by the combined model achieved similar performance to the survival curves of patients with actual IDH genotypes, which could be used to effectively stratify the prognosis of patients (see **Figure 6**). Therefore, the predicted outcome of the combined model we developed was proved to be an independent risk factor for prognosis, providing a new method for predicting the

prognosis of patients with glioma and showing promise as a prognostic biomarker.

Nevertheless, our study has several limitations. We used retrospective data and did not combine our analysis with baseline CT and MRI features. As this was a single-center study, larger data sets from multiple centers should be interrogated to assess the potential clinical utility of our model further. Moreover, large datasets based on multi-modal imaging may be used for refining the model to improve its predictive performance. Furthermore, although our PET-based imaging method had good predictive performance, the clinical implications of these radiomic features are currently difficult to interpret.

In summary, our results confirm that the radiomic analysis of PET images reflecting glucose metabolism in gliomas could reveal metabolic differences among gliomas with different IDH genotypes, which provides the possibility of non-invasive identification of IDH genotypes in patients. Moreover, we found a strong association between the predicted probabilities and the OS of patients, which further proved the prognostic value of the combined model.

DATA AVAILABILITY STATEMENT

The datasets of this study will not be made publicly available because they are not yet complete.

ETHICS STATEMENT

The studies involving human participants were reviewed and approved by Peking Union Medical College Hospital. Written informed consent from the participants' legal guardian/next of kin was not required to participate in this study in accordance with the national legislation and the institutional requirements. Written informed consent was not obtained from the minor(s)' legal guardian/next of kin for the publication of any potentially identifiable images or data included in this article.

AUTHOR CONTRIBUTIONS

JT, YL, and XC: conception and design. YaW, YuW, WMa, ZK, and XC: collection and assembly of data. JT, YL, WMu, ZhL, LL, ZeL, XZ, SW, and WW: data analysis and interpretation. LL, JT, WMu, YaW, YL, and XC: manuscript writing.

FUNDING

This paper was supported by the National Natural Science Foundation of China (Grant Nos. 81772009, 81922040, 81772012, and 81227901), the National Key Research and Development Plan of China (Grant Nos. 2017YFA0205200, 2016YFA0100900, and 2016YFA0100902), the Scientific and Technological Research Project of Henan Province (Grant No. 182102310162), the Beijing Natural Science Foundation (Grant No. 7182109), the Chinese Academy of Sciences (Grant No. GJJSTD20170004 and QYZDJ-SSW-JSC005), the Chinese Academy of Medical Sciences Innovation Fund for Medical Sciences (Grant numbers 2016-I2M-2-001 and 2018-I2M-3-001), the Fundamental Research Funds for the Central Universities (Grant No. 3332018029), and the Youth Innovation Promotion Association CAS (Grant No. 2019136).

SUPPLEMENTARY MATERIAL

The Supplementary Material for this article can be found online at: https://www.frontiersin.org/articles/10.3389/fonc.2019.01183/full#supplementary-material

REFERENCES

1. Ostrom QT, Bauchet L, Davis FG, Deltour I, Fisher JL, Langer CE, et al. The epidemiology of glioma in adults: a "state of the science" review. *Neuro-oncology*. (2014) 16:896–913. doi: 10.1093/neuonc/nou087
2. Schomas DA, Laack NNI, Rao RD, Meyer FB, Shaw EG, O'Neill BP, et al. Intracranial low-grade gliomas in adults: 30-year experience with long-term follow-up at Mayo Clinic. *Neuro Oncol.* (2009) 11:437–45. doi: 10.1215/15228517-2008-102
3. Ostrom QT, Gittleman H, Truitt G, Boscia A, Kruchko C, Barnholtz-Sloan JS. CBTRUS statistical report: primary brain and other central nervous system tumors diagnosed in the United States in 2011-2015. *Neuro Oncol.* (2018) 20(suppl_4):iv1–86. doi: 10.1093/neuonc/noy131
4. Louis DN, Perry A, Reifenberger G, Von Deimling A, Figarella-Branger D, Cavenee WK, et al. The 2016 World Health Organization classification of tumors of the central nervous system: a summary. *Acta Neuropathol.* (2016) 131:803–20. doi: 10.1007/s00401-016-1545-1
5. Hartmann C, Hentschel B, Wick W, Capper D, Felsberg J, Simon M, et al. Patients with IDH1 wild type anaplastic astrocytomas exhibit worse prognosis than IDH1-mutated glioblastomas, and IDH1 mutation status accounts for the unfavorable prognostic effect of higher age: implications for classification of gliomas. *Acta Neuropathol.* (2010) 120:707–18. doi: 10.1007/s00401-010-0781-z
6. Beiko J, Suki D, Hess KR, Fox BD, Cheung V, Cabral M, et al. IDH1 mutant malignant astrocytomas are more amenable to surgical resection and have a survival benefit associated with maximal surgical resection. *Neuro Oncol.* (2013) 16:81–91. doi: 10.1093/neuonc/not159
7. Jiang T, Mao Y, Ma W, Mao Q, You Y, Yang X, et al. CGCG clinical practice guidelines for the management of adult diffuse gliomas. *Cancer Lett.* (2016) 375:263–73. doi: 10.1016/j.canlet.2016.01.024
8. Bady P, Kurscheid S, Delorenzi M, Gorlia T, van den Bent MJ, Hoang-Xuan K, et al. The DNA methylome of DDR genes and benefit from RT or TMZ in IDH mutant low-grade glioma treated in EORTC 22033. *Acta Neuropathol.* (2018) 135:601–15. doi: 10.1007/s00401-018-1810-6
9. Kros JM, Mustafa DM, Dekker LJ, Sillevis Smitt PA, Luider TM, Zheng P-P. Circulating glioma biomarkers. *Neuro Oncol.* (2014) 17:343–60. doi: 10.1093/neuonc/nou207
10. Westphal M, Lamszus K. Circulating biomarkers for gliomas. *Nat Rev Neurol.* (2015) 11:556. doi: 10.1038/nrneurol.2015.171
11. Xing Z, Yang X, She D, Lin Y, Zhang Y, Cao D. Noninvasive assessment of IDH mutational status in World Health Organization grade II and III astrocytomas using DWI and DSC-PWI combined with conventional MR imaging. *Am J Neuroradiol.* (2017) 38:1138–44. doi: 10.3174/ajnr.A5171
12. Verger A, Stoffels G, Bauer EK, Lohmann P, Blau T, Fink GR, et al. Static and dynamic 18 F–FET PET for the characterization of gliomas defined by IDH and 1p/19q status. *Eur J Nucl Med Mol Imaging.* (2018) 45:443–51. doi: 10.1007/s00259-017-3846-6

13. Liu ZWS, Dong D, Wei J, Fang C, Zhou X, Sun K, et al. The applications of radiomics in precision diagnosis and treatment of oncology: opportunities and challenges. *Theranostics*. (2019) 9:1303–22. doi: 10.7150/thno.30309
14. Aerts HJ, Velazquez ER, Leijenaar RT, Parmar C, Grossmann P, Carvalho S, et al. Decoding tumour phenotype by noninvasive imaging using a quantitative radiomics approach. *Nat Commun*. (2014) 5:4006. doi: 10.1038/ncomms5006
15. Shen C, Liu Z, Guan M, Song J, Lian Y, Wang S, et al. 2D and 3D CT radiomics features prognostic performance comparison in non-small cell lung cancer. *Transl Oncol*. (2017) 10:886–94. doi: 10.1016/j.tranon.2017.08.007
16. Wang S, Shi J, Ye Z, Dong D, Yu D, Zhou M, et al. Predicting EGFR mutation status in lung adenocarcinoma on CT image using deep learning. *Eur Respir J*. (2019) 53:1800986. doi: 10.1183/13993003.00986-2018
17. Wang S, Liu Z, Rong Y, Zhou B, Bai Y, Wei W, et al. Deep learning provides a new computed tomography-based prognostic biomarker for recurrence prediction in high-grade serous ovarian cancer. *Radiother. Oncol*. (2019)132:171–7. doi: 10.1016/j.radonc.2018.10.019
18. Liu Z, Zhang XY, Shi YJ, Wang L, Zhu HT, Tang ZC, et al. Radiomics analysis for evaluation of pathological complete response to neoadjuvant chemoradiotherapy in locally advanced rectal cancer. *Clin Cancer Res*. (2017) 23:7253–62. doi: 10.1158/1078-0432.CCR-17-1038
19. Shen C, Liu Z, Wang Z, Guo J, Zhang H, Wang Y, et al. Building CT radiomics based nomogram for preoperative esophageal cancer patients lymph node metastasis prediction. *Transl Oncol*. (2018) 11:815–24. doi: 10.1016/j.tranon.2018.04.005
20. Yu J, Shi Z, Lian Y, Li Z, Liu T, Gao Y, et al. Noninvasive IDH1 mutation estimation based on a quantitative radiomics approach for grade II glioma. *Eur Radiol*. (2016) 27:3509–22. doi: 10.1007/s00330-016-4653-3
21. Zhang B, Chang K, Ramkissoon S, Tanguturi S, Bi WL, Reardon DA, et al. Multimodal MRI features predict isocitrate dehydrogenase genotype in high-grade gliomas. *Neuro Oncol*. (2016) 19:109. doi: 10.1093/neuonc/now121
22. Lu CF, Hsu FT, Hsieh KL, Kao YJ, Cheng SJ, Hsu JB, et al. Machine learning-based radiomics for molecular subtyping of gliomas. *Clin Cancer Res Clincanres*. (2018) 24:4429–36. doi: 10.1158/1078-0432.CCR-17-3445
23. Jones T, Price P. Development and experimental medicine applications of PET in oncology: a historical perspective. *Lancet Oncol*. (2012) 13:e116–25. doi: 10.1016/S1470-2045(11)70183-8
24. Yoon JH, Kim JH, Kang WJ, Sohn CH, Choi SH, Yun TJ, et al. Grading of cerebral glioma with multiparametric MR imaging and 18F-FDG-PET: concordance and accuracy. *Eur Radiol*. (2014) 24:380–9. doi: 10.1007/s00330-013-3019-3
25. Takahashi M, Soma T, Mukasa A, Koyama K, Arai T, Momose T. An automated voxel-based method for calculating the reference value for a brain tumour metabolic index using 18 F-FDG-PET and 11 C-methionine PET. *Ann Nucl Med*. (2017) 31:250–9. doi: 10.1007/s12149-017-1153-8
26. Ideguchi M, Nishizaki T, Ikeda N, Okamura T, Tanaka Y, Fujii N, et al. A surgical strategy using a fusion image constructed from 11C-methionine PET, 18F-FDG-PET and MRI for glioma with no or minimum contrast enhancement. *J Neuro Oncol*. 138:1–12. doi: 10.1007/s11060-018-2821-9
27. Dankbaar J, Snijders T, Robe P, Seute T, Eppinga W, Hendrikse J, et al. The use of 18 F-FDG PET to differentiate progressive disease from treatment induced necrosis in high grade glioma. *J Neurooncol*. (2015) 125:167–75. doi: 10.1007/s11060-015-1883-1
28. Santra A, Kumar R, Sharma P, Bal C, Julka PK, Malhotra A. F-18 FDG PET-CT for predicting survival in patients with recurrent glioma: a prospective study. *Neuroradiology*. (2011) 53:1017–24. doi: 10.1007/s00234-011-0898-3
29. Horbinski C, Kofler J, Kelly LM, Murdoch GH, Nikiforova MN. Diagnostic use of IDH1/2 mutation analysis in routine clinical testing of formalin-fixed, paraffin-embedded glioma tissues. *J Neuropathol Exp Neurol*. (2009) 68:1319–25. doi: 10.1097/NEN.0b013e3181c391be
30. Vallières M, Kayrivest E, Perrin LJ, Liem X, Furstoss C, Aerts HJWL, et al. Radiomics strategies for risk assessment of tumour failure in head-and-neck cancer. *Sci Rep*. (2017) 7:10117. doi: 10.1038/s41598-017-10371-5
31. van Griethuysen JJM, Fedorov A, Parmar C, Hosny A, Aucoin N, Narayan V, et al. Computational radiomics system to decode the radiographic phenotype. *Cancer Res*. (2017) 77:e104–7. doi: 10.1158/0008-5472.can-17-0339
32. Guo J, Liu Z, Shen C, Li Z, Yan F, Tian J, et al. MR-based radiomics signature in differentiating ocular adnexal lymphoma from idiopathic orbital inflammation. *Euro Radiol*. 28:3872–81. doi: 10.1007/s00330-018-5381-7
33. Liu Z, Wang Y, Liu X, Du Y, Tang Z, Wang K, et al. Radiomics analysis allows for precise prediction of epilepsy in patients with low-grade gliomas. *Neuroimage Clin*. (2018) 19:271–8. doi: 10.1016/j.nicl.2018.04.024
34. Sanchezpinto LN, Venable LR, Fahrenbach J, Churpek MM. Comparison of variable selection methods for clinical predictive modeling. *Int J Med Informatics*. (2018) 116:10–7. doi: 10.1016/j.ijmedinf.2018.05.006
35. Kramer AA, Zimmerman JE. Assessing the calibration of mortality benchmarks in critical care: The Hosmer-Lemeshow test revisited. *Crit Care Med*. (2007) 35:2052–6. doi: 10.1097/01.CCM.0000275267.64078.B0
36. Vickers A, Elkin E. Decision curve analysis: a novel method for evaluating prediction models. Medical Decision Making. *Int J Soc Med Dec. Making*. (2006) 26:565. doi: 10.1177/0272989X06295361
37. Galldiks N, Stoffels G, Filss C, Rapp M, Blau T, Tscherpel C, et al. The use of dynamic O-(2-18F-fluoroethyl)-l-tyrosine PET in the diagnosis of patients with progressive and recurrent glioma. *Neuro Oncol*. (2015) 17:1293–300. doi: 10.1093/neuonc/nov088
38. Maher EA, Marin-Valencia I, Bachoo RM, Mashimo T, Raisanen J, Hatanpaa KJ, et al. Metabolism of [U-13 C]glucose in human brain tumors *in vivo*. *NMR Biomed*. (2012) 25:1234–44. doi: 10.1002/nbm.2794
39. Lohmann P, Lerche C, Bauer EK, Steger J, Stoffels G, Blau T, et al. Predicting IDH genotype in gliomas using FET PET radiomics. *Sci Rep*. (2018) 8:13328. doi: 10.1038/s41598-018-31806-7
40. van Helden E, Vacher Y, van Wieringen W, van Velden F, Verheul H, Hoekstra O, et al. Radiomics analysis of pre-treatment [18 F] FDG PET/CT for patients with metastatic colorectal cancer undergoing palliative systemic treatment. *Eur J Nucl Med Mol Imaging*. (2018) 45:2307–17. doi: 10.1007/s00259-018-4100-6
41. Cook GJR, Connie Y, Muhammad S, Vicky G, Sugama C, Arunabha R, et al. Are pretreatment 18F-FDG PET tumor textural features in non-small cell lung cancer associated with response and survival after chemoradiotherapy? *J Nucl Med*. (2013) 54:19–26. doi: 10.2967/jnumed.112.107375
42. Nai-Ming C, Yu-Hua Dean F, Joseph Tung-Chieh C, Chung-Guei H, Din-Li T, Shu-Hang N, et al. Textural features of pretreatment 18F-FDG PET/CT images: prognostic significance in patients with advanced T-stage oropharyngeal squamous cell carcinoma. *J Nucl Med*. (2013) 54:1703–9. doi: 10.2967/jnumed.112.119289

Conflict of Interest: The authors declare that the research was conducted in the absence of any commercial or financial relationships that could be construed as a potential conflict of interest.

frontiers in Oncology

ORIGINAL RESEARCH
published: 25 February 2020
doi: 10.3389/fonc.2020.00206

Histogram Analysis of Diffusion Weighted Imaging in Low-Grade Gliomas: *in vivo* Characterization of Tumor Architecture and Corresponding Neuropathology

Georg Alexander Gihr[1], Diana Horvath-Rizea[1], Elena Hekeler[2], Oliver Ganslandt[3], Hans Henkes[1], Karl-Titus Hoffmann[4], Cordula Scherlach[4] and Stefan Schob[4]*

[1] Katharinenhospital Stuttgart, Clinic for Neuroradiology, Stuttgart, Germany, [2] Department for Pathology, Katharinenhospital Stuttgart, Stuttgart, Germany, [3] Katharinenhospital Stuttgart, Clinic for Neurosurgery, Stuttgart, Germany, [4] Department for Neuroradiology, University Hospital Leipzig, Leipzig, Germany

Background: Low-grade gliomas (LGG) in adults are usually slow growing and frequently asymptomatic brain tumors, originating from glial cells of the central nervous system (CNS). Although regarded formally as "benign" neoplasms, they harbor the potential of malignant transformation associated with high morbidity and mortality. Their complex and unpredictable tumor biology requires a reliable and conclusive presurgical magnetic resonance imaging (MRI). A promising and emerging MRI approach in this context is histogram based apparent diffusion coefficient (ADC) profiling, which recently proofed to be capable of providing prognostic relevant information in different tumor entities. Therefore, our study investigated whether histogram profiling of ADC distinguishes grade I from grade II glioma, reflects the proliferation index Ki-67, as well as the IDH (isocitrate dehydrogenase) mutation and MGMT (methylguanine-DNA methyl-transferase) promotor methylation status.

Material and Methods: Pre-treatment ADC volumes of 26 LGG patients were used for histogram-profiling. WHO-grade, Ki-67 expression, IDH mutation, and MGMT promotor methylation status were evaluated. Comparative and correlative statistics investigating the association between histogram-profiling and neuropathology were performed.

Results: Almost the entire ADC profile (p25, p75, p90, mean, median) was significantly lower in grade II vs. grade I gliomas. Entropy, as second order histogram parameter of ADC volumes, was significantly higher in grade II gliomas compared with grade I gliomas. Mean, maximum value (ADCmax) and the percentiles p10, p75, and p90 of ADC histogram were significantly correlated with Ki-67 expression. Furthermore, minimum ADC value (ADCmin) was significantly associated with MGMT promotor methylation status as well as ADC entropy with IDH-1 mutation status.

Conclusions: ADC histogram-profiling is a valuable radiomic approach, which helps differentiating tumor grade, estimating growth kinetics and probably prognostic relevant genetic as well as epigenetic alterations in LGG.

Keywords: low-grade glioma, apparent diffusion coefficient, histogram analysis, radiomics, histopathology, imaging biomarker

OPEN ACCESS

Edited by:
Tone Frost Bathen, Norwegian University of Science and Technology, Norway

Reviewed by:
Morteza Esmaeili, Akershus University Hospital, Norway
Weiguo Zhang, Daping Hospital, China

****Correspondence:***
Georg Alexander Gihr
g.gihr@klinikum-stuttgart.de

Specialty section:
This article was submitted to Cancer Imaging and Image-directed Interventions, a section of the journal Frontiers in Oncology

Received: *27 August 2019*
Accepted: *06 February 2020*
Published: *25 February 2020*

Citation:
Gihr GA, Horvath-Rizea D, Hekeler E, Ganslandt O, Henkes H, Hoffmann K-T, Scherlach C and Schob S (2020) Histogram Analysis of Diffusion Weighted Imaging in Low-Grade Gliomas: in vivo Characterization of Tumor Architecture and Corresponding Neuropathology. Front. Oncol. 10:206. doi: 10.3389/fonc.2020.00206

INTRODUCTION

Gliomas are primary central nervous system (CNS) tumors originating from sustaining glial cells of the CNS and account for approximately 30 percent of all symptomatic brain neoplasms in adults (1). Based upon histopathologic characteristics like mitotic activity, necrosis, cytological atypia and anaplasia, gliomas are subdivided by the World Health Organization (WHO) into four grades, ranging from WHO grade I—which represents biologically rather benign lesions—to WHO grade IV (2), which entails the most aggressive entities. Only tumors matching the WHO criteria for grade I- and II are classified low-grade gliomas (LGG). Most frequently encountered manifestations of LGG are pilocytic astrocytomas (WHO grade I) and diffuse astrocytomas (WHO grade II). Pilocytic astrocytoma is the most common primary brain tumor in childhood, rarely occurring in adults, which commonly follows an uneventful course. However, malignant transformation has been reported in a number of patients and observation vs. intervention remains an individually challenging decision (3).

Diffuse astrocytoma accounts for the vast majority of LGG in adults and generally exhibits a more protracted course with significantly greater long-term survival compared to high-grade gliomas (HGG) (4). Therefore, and related to the fact that diffuse astrocytomas often occur in eloquent brain regions, a conservative "wait and see"-approach including periodic controls is usually employed as standard management for most of these patients, aiming to avoid disabling surgical morbidity but to preserve functional independence as long as possible. On the contrary, several studies in recent years indicated better prognosis and overall survival of patients after partial or total resection, which has partially led to a paradigm shift in therapy from "watchful waiting" toward early tumor surgery (5–7).

The major obstacle rendering the decision for the optimal personalized therapy very difficult is related to the unpredictable course of the individual LGG.

Therefore, precise recognition of the individual neoplasm including information on its tumor heterogeneity and probable tumor-biological evolution is pivotal.

Magnetic resonance imaging (MRI), offering the highest detail of anatomical as well as functional information in CNS neoplasms has become the gold standard for diagnosis and follow up imaging (8). Among the variety of functional imaging techniques like spin labeling, spectroscopy, perfusion weighted imaging etc., especially diffusion-weighted imaging (DWI) has gained significant importance for assessment of brain tumors (9).

By mapping the diffusibility of water molecules in biological tissues through apparent diffusion coefficient (ADC) maps (10), DWI allows assessment of the underlying microscopic architecture of the examined tissue (11). In context of glioma imaging, DWI including ADC-mapping were shown to be especially valuable for tumor grading and the differentiation of LGG from HGG (12), for assessment of prognosis (13), for estimation of tumor growth potential (14) and the differentiation of gliomas from other, morphologically indistinguishable lesions (15).

However, most of the DWI studies investigated simple, mostly two-dimensional region-of-interest-based estimations of the ADC, neither accounting for the three-dimensional complexity of the tissue nor considering all parameters of the ADC histogram. As introduced by Just and coworkers (16), histogram analysis can provide more than first order histogram characteristics, which basically represent specific proportions of one investigated value (in our case the ADC). Those second order characteristics—kurtosis, skewness, and entropy—describe more complex aspects of the (ADC-) distribution and its particular shape, which notoriously facilitate the assessment of the microarchitecture of the particular lesion. The entropy of a histogram profile for example, describing the degree of randomness of the respective distribution, has been established as an important biomarker reflecting tumor heterogeneity in numerous studies (17–19). Interestingly, even the entropy of simple T1-post-contrast image histograms is able to reflect tumor characteristics like mitotic activity to a limited extent (20).

Therefore, our study aimed to evaluate whether whole tumor histogram analysis of ADC maps can (I) differentiate WHO grade I and WHO grade II tumors, (II) predict the proliferative potential of those neoplasms and (III) predict the presence of prognostic relevant MGMT (methylguanine-DNA methyl-transferase) promotor methylation and IDH (isocitrate dehydrogenase) mutation status.

PATIENTS, PROCEDURES, AND METHODS

Ethics Approval

The study was approved by the ethics committee of the medical council of Baden-Württemberg (Ethik-Kommission Landesärztekammer Baden-Württemberg, F-2017-047).

Patients Collective

The institutional radiological information system (RIS) was searched for patients with the diagnosis glioma and primary brain tumor. Histopathologic diagnosis, Ki-67 proliferation index, IDH-1 mutation status and MGMT promotor methylation status were obtained by searching the hospital patient database. Forty-two patients were identified between 01/2012 and 02/2017, all of which had at least diagnostic biopsy or even surgical removal of the tumor in our hospital and subsequent neuropathological workup. Only patients who received pretreatment MRI scans with sufficient DWI were included. MRI examinations of patients indicating hemorrhage, significant calcifications or artificial MRI data due to other causes were excluded, since these conditions severely influence quantification, and hence, produce incorrect ADC values. Therefore, only 26 patients (12 females, 14 males; ranging from 5 to 58 years with a mean age of 34.2 years) were included in our retrospective analysis: 7 patients with the diagnosis of pilocytic astrocytoma (WHO grade I), 19 patients with the diagnosis of diffuse astrocytoma (WHO grade II); 15 out of 26 patients with IDH-1 mutation and 8 out of 26 patients with IDH-1 wildtype (of 3 patients no IDH-1 mutation status was available); 9 out of 26 patients patients with MGMT promotor methylation and 6 out of 26 patients with unmethylated MGMT promotor (of 11 patients no MGMT promotor methylation status

was available); of 2 out of 26 patients no Ki-67 proliferation index was available.

MRI Specifics

For all patients MRI of the brain was performed using a 1.5 T device (MAGNETOM Aera and MAGNETOM Symphony Tx/Rx CP head coil, Siemens, Erlangen, Germany). The imaging protocol included the following sequences:

1. Axial T2 weighted (T2w) turbo spin echo (TSE) sequence (TR/TE: 5390/99, flip angle: 150°, slice thickness: 5 mm, acquisition matrix: 512 x 291, field of view: 230 x 187 mm);
2. Axial DWI (readout-segmented, multi-shot EPI sequence; TR/TE: 5500/103, flip angle 90°, slice thickness: 5 mm, acquisition matrix: 152 x 144, field of view: 230 x 230 mm) with b values of 0 and 1,000 s/mm^2. ADC maps were generated automatically by the implemented software package.

All images were available in digital form and analyzed by two experienced radiologists (DHR, SS) without knowledge of the histopathological diagnosis on a PACS workstation (Impax EE R20 XII).

Histogram Profiling of ADC Maps

ADC maps and T2 weighted images were exported from our institutional archive in DICOM format *via* the aforementioned AGFA PACS. Whole lesion histogram profiling was performed by using a custom-made DICOM image analysis tool (programmed by N.G. using Matlab, The Mathworks, Natick, MA): T2 weighted images were loaded into a graphical user interface (GUI) to tag the tumor suspected lesion of each patient in all respective MRI sections. All regions of interest (ROIs) were then automatically co-registered with the corresponding ADC maps and the whole lesion histogram profile was consecutively calculated, providing the following set of parameters: ADCmean, ADCmin, ADCmax, ADCp10, ADCp25, ADCp75, ADCp90, ADCmodus, ADCmedian, ADC standard deviation (SD), Skewness, Kurtosis, and Entropy.

Neuropathology

All tumor specimens were used for neuro-histological confirmation of the diagnosis. The tumor samples, obtained either by stereotactic biopsy, partial or complete resection were formalin-fixed and paraffin-embedded for histopathologic diagnostics, immunohistochemistry and PCR sequencing. The embedded samples were sectioned at 3 µm and stained by hematoxylin and eosin (H&E). Immunhistochemistry was performed with specific antibodies against IDH1-R132H (dilution 1:20, product no. DIA-H09; Dianova, Hamburg, Germany) and Ki67 M7240 (dilution 1: 800; Dako Denmark A/S, Glostrup, Denmark). The histopathological images were digitalized with a Leica microscope, carrying a DFC290 HD digital camera and LAS V4.4 software (Leica Microsystems, Wetzlar, Germany). Sample sections for immunohistochemistry and PCR sequencing were analyzed histologically for presence of viable tumor infiltration and absence of necrotic areas and hemorrhage. In case of IDH1 immunohistochemistry a strong cytoplasmic staining was interpreted as positive result. Tumor proliferation index was estimated by dividing the number of specifically stained (Ki-67 positive) cell nuclei by all nuclei. The area showing the highest number of positive cell nuclei was selected in each case.

To determine the methylation status of the MGMT gene, tumor DNA was isolated from micro-dissected 10 µm sections from the paraffin-embedded tissue blocks using the Maxwell® RSC FFPE Plus DNA Kit AS1720 (Promega, USA) with a Maxwell® RSC Instrument (Promega, USA), followed by conversion of unmethylated cytosine residues to uracil by bisulfite treatment using the EpiTect® Bisulfite Kit (QIAGEN, Germany), each step according to the manufacturer's procedures. Bisulfite-converted DNA was amplified in a PCR reaction and the methylation status was determined by pyrosequencing according to the manufacturer's protocol using the Therascreen MGMT Pyro® Kit (QIAGEN, Germany), testing 4 CpG islands (chromosome 10, Exon 1, range 131265519-131265537, CGACGCCCGCAGGTCCTCG). Methylation percentage of 10% and higher was considered as methylation positive.

Statistical Analysis

Statistical analysis including graphics creation was performed using GraphPad Prism 8 (GraphPad Software, San Diego, CA, USA). In a first step, DWI data and histopathological information were investigated using descriptive statistics. In a second step, data was tested for Gaussian distribution using the Shapiro-Wilk-Test. *T*-test was performed to compare evaluated, normally distributed parameters of DWI histogram profiling between grade I and grade II astrocytoma. Also, normally distributed DWI histogram profiling parameters between IDH mutated and IDH wildtype gliomas as well as between MGMT promotor methylated and unmethylated gliomas were compared using unpaired *T*-test. Mann-Whitney-U Test was performed to compare parameters exhibiting a non-Gaussian distribution between grade I and grade II, between IDH mutation positive and negative as well as between MGMT promotor methylated and unmethylated astrocytomas. Finally, correlation analysis for normally distributed parameters was performed using Pearson Correlation Coefficient. In case of non-Gaussian distribution, Spearman-Rho Rank-Order Correlation was calculated. p-values < 0.05 were taken to indicate statistical significance in all instances. Finally, to assess the accuracy of ADC volume histogram profiling, receiver operating characteristics (ROC) curve analysis was performed and the respective area under the curve (AUC) was calculated as well as Youden's Index for those ADC parameters with the best test accuracy to estimate possible cut-off values.

RESULTS

Figure 1 demonstrates examples of cranial MRI from patients with WHO grade I (upper row) and WHO grade II astrocytoma (lower row) including the corresponding whole tumor ADC histogram, H&E staining and Ki-67 immunohistochemistry.

The results of the descriptive analysis of DWI data of all investigated gliomas are summarized in **Table 1**. Shapiro-Wilk-Test revealed Gaussian distribution for ADCmean, ADCmin,

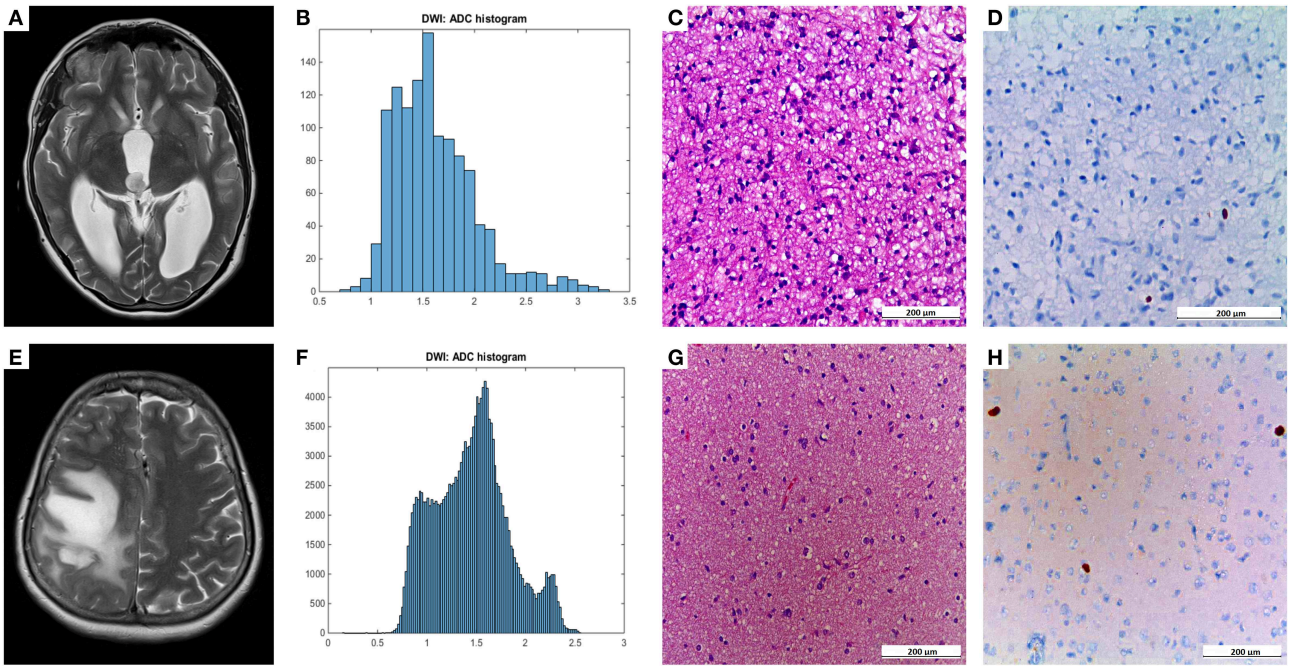

FIGURE 1 | Compares representative MRI sections, the corresponding whole tumor ADC histogram, H&E staining, and Ki-67 immunohistochemistry of a grade I **(A–D)** and a grade II glioma **(E–H)**. The first image of the upper case shows a T2 weighted turbo-spin-echo (TSE) sequence of a grade I glioma, originating from the right thalamus with intraventricular tumor mass in the third ventricle and consecutive hydrocephalus **(A)**. The first image of the lower case displays a T2 weighted TSE sequence of a grade II diffuse astrocytoma located in the right frontal and parietal lobe with distinct mass effect **(E)**. The second images of each row show the ADC histograms (**B,F**; x-axis: ADC values in incremental order, y-axis: number of voxels) followed by H&E staining and Ki-67 immunohistochemistry on the right side **(C–D**, **G–H)**. For the first case (pilocytic astrocytoma), a proliferation index of 1% was calculated. In the second case (diffuse astrocytoma), proliferation index was 5%.

TABLE 1 | DWI histogram profiling parameters of all investigated low-grade gliomas.

Parameters	Mean ± standard deviation	Minimum	Maximum
ADC_{mean}, × 10^{-5} mm^2s^{-1}	148.73 ± 31.41	88.10	230.91
ADC_{min}, × 10^{-5} mm^2s^{-1}	53.75 ± 24.97	0.10	93.20
ADC_{max}, × 10^{-5} mm^2s^{-1}	260.53 ± 57.92	159.30	352.80
P10 ADC, × 10^{-5} mm^2s^{-1}	109.99 ± 15.15	71.60	136.80
P25 ADC, × 10^{-5} mm^2s^{-1}	129.33 ± 26.08	77.40	203.60
P75 ADC, × 10^{-5} mm^2s^{-1}	167.85 ± 41.31	98.10	272.70
P90 ADC, × 10^{-5} mm^2s^{-1}	185.28 ± 46.16	107.20	279.10
Median ADC, × 10^{-5} mm^2s^{-1}	148.91 ± 35.51	86.50	263.30
Mode ADC,	153.24 ± 45.35	84.00	276.90
SD ADC, × 10^{-5} mm^2s^{-1}	30.11 ± 13.57	12.76	64.11
Kurtosis	4.23 ± 2.71	2.00	11.20
Skewness	0.32 ± 0.87	−1.35	2.47
Entropy	5.19 ± 0.69	3.79	6.19

ADCmax, ADCp10, ADCp25, ADCp75, ADCp90, ADCmodus, ADCmedian, ADC SD, Entropy and Ki-67 (all $p < 0.05$). Non-Gaussian distribution was determined for Kurtosis and Skewness.

Statistical significant differences between grade I and grade II astrocytomas were identified for the following set of ADC histogram parameters: ADCmean, ADCmax, ADCp25, ADCp75, ADCp90, ADCmedian, ADC SD, and Entropy (all $p < 0.05$). Mean values of ADC fractions, except the lowest percentile (ADCp10), the minimum values (ADCmin) and the ADC modus, were all significantly lower in the WHO grade II group, whereas Entropy was significantly greater in WHO grade II gliomas compared to grade I gliomas. The standard deviation (SD) of ADC histogram profiles of grade II astrocytomas was significantly lower than in the group of grade I tumors. Differences in Ki-67 expression, representing the actively proliferating tumor fraction, also achieved statistical significance, with increased values in the WHO grade II group. Furthermore, significant differences between MGMT promotor methylated and unmethylated gliomas were identified for ADCmin, being increased in unmethylated gliomas. Comparison of ADC histogram profiles of IDH-1 mutated and IDH-1 wildtype astrocytomas revealed significant differences for Entropy, with higher values in case of muted IDH-1. For reasons of comprehensibility and clarity, results of the comparative statistical analysis are summarized in **Tables 2–4**. **Figures 2A–H** shows significant differences in ADC histogram profile parameters between WHO grade I and II astrocytomas, **Figures 2I,J** illustrates differences of ADC Entropy and ADCmin considering IDH-1 mutation status and MGMT promotor methylation status of the investigated gliomas.

Correlative statistics revealed significant correlations ($p < 0.05$) between Ki-67 and ADCmean, ADCmax, ADCp10,

TABLE 2 | Comparison of DWI histogram profiles and Ki-67 index between grade I and grade II glioma.

Parameters	WHO grade 1		WHO grade 2		*T*-test
	Mean ± SD		Mean ± SD		*p*-values
ADC_{mean}, × 10^{-5} mm^2s^{-1}	171.90	36.80	140.20	26.25	**0.0221**
ADC_{min}, × 10^{-5} mm^2s^{-1}	61.67	32.25	50.84	22.82	0.3463
ADC_{max}, × 10^{-5} mm^2s^{-1}	315.30	34.31	240.40	53.46	**0.0022**
P10 ADC, × 10^{-5} mm^2s^{-1}	116.90	9.53	107.40	16.60	0.1692
P25 ADC, × 10^{-5} mm^2s^{-1}	146.4	31.88	123.10	22.12	**0.0452**
P75 ADC, × 10^{-5} mm^2s^{-1}	197.70	51.56	156.90	33.25	**0.0251**
P90 ADC, × 10^{-5} mm^2s^{-1}	222.50	52.55	171.60	37.69	**0.0112**
Median ADC, × 10^{-5} mm^2s^{-1}	172.00	47.97	140.40	27.76	**0.0460**
Mode ADC, × 10^{-5} mm^2s^{-1}	179.70	67.76	143.50	32.65	0.0753
SD ADC, 10^{-5} mm^2s^{-1}	42.16	14.76	25.67	10.78	**0.0045**
Kurtosis	5.50	3.91	3.76	2.16	0.2542
Skewness	0.70	1.25	0.18	0.70	0.2307
Entropy	4.72	0.67	5.37	0.65	**0.0350**
Ki-67	3.00	1.73	5.41	2.58	**0.0340**

Values displayed in bold indicate findings of statistical significance ($p \leq 0.05$).

TABLE 3 | Comparison of DWI histogram profiles between low-grade gliomas with and without MGMT promotor methylation.

Parameters	MGMT promotor methylation positive		MGMT promotor methylation negative		*p*-values
	Mean ± SD		Mean ± SD		
ADC_{mean}, × 10^{-5} mm^2s^{-1}	142.30	27.35	141.1	25.71	0.9286
ADC_{min}, × 10^{-5} mm^2s^{-1}	41.76	19.13	62.62	24.47	**0.033**
ADC_{max}, × 10^{-5} mm^2s^{-1}	246.40	55.41	226.70	68.03	0.5480
P10 ADC, × 10^{-5} mm^2s^{-1}	108.60	17.04	106.90	15.41	0.8429
P25 ADC, × 10^{-5} mm^2s^{-1}	125.40	23.76	121.20	18.74	0.7201
P75 ADC, × 10^{-5} mm^2s^{-1}	159.80	32.75	157.20	36.64	0.8861
P90 ADC, × 10^{-5} mm^2s^{-1}	173.10	34.43	177.90	46.59	0.8202
Median ADC, × 10^{-5} mm^2s^{-1}	143.50	29.87	139.10	24.84	0.7678
Mode ADC, × 10^{-5} mm^2s^{-1}	145.10	35.54	139.10	22.84	0.7224
SD ADC, × 10^{-5} mm^2s^{-1}	25.34	7.88	28.93	16.00	0.5697
Kurtosis	3.25	0.81	3.50	2.21	0.6889
Skewness	0.02	0.38	0.40	0.95	0.6070
Entropy	5.62	0.49	4.97	0.80	0.0719

Values displayed in bold indicate findings of statistical significance ($p \leq 0.05$).

ADCp75, ADCp90 as well as ADC SD. **Table 5** summarizes the complete results of the correlative analysis. The scatter plot graphically demonstrating the association of ADCmax and Ki-67, the set of parameters with the strongest correlation ($r = -0.5218$, $p = 0.0089$), is shown in **Figure 2K**.

Furthermore, AUC values were calculated for each of the evaluated parameters exhibiting statistically significant differences between grade I and grade II astrocytomas with the following results (CI: confidence interval): ADCmean [AUC = 0.737, (CI: 0.502–0.972), $p = 0.067$], ADCmax [AUC = 0.895, (CI: 0.768–1.000), $p = 0.0024$], ADCp25 [AUC= 0.722, (CI: 0.494–0.949), $p = 0.088$], ADCp75 [AUC = 0.744, (CI: 0.518–0.970), $p = 0.060$], ADCp90 [AUC = 0.797, (CI: 0.576–1.000), $p = 0.022$], ADCmedian [AUC = 0.729, (CI: 0.494–0.965), $p = 0.078$], ADC SD [AUC = 0.805, (CI: 0.613–0.996), $p = 0.019$] and Entropy [AUC = 0.752, (CI: 0.559–0.945), $p = 0.053$]. **Figure 3** displays the corresponding ROC of ADCmax, the parameter with the best accuracy. Finally, Youden's Index for ADCmax was calculated to estimate the most promising cut-off value revealing the following result: ADCmax values of 0.002632 and greater indicate grade I astrocytoma (sensitivity: 0.684, specificity: 1.00).

TABLE 4 | Comparison of DWI histogram profiles between low-grade gliomas with and without IDH-1 mutation.

Parameters	IDH-1 mutation		IDH-1 wildtype		
	Mean ± SD		Mean ± SD		*p*-values
ADC_{mean}, × 10^{-5} mm^2s^{-1}	143.10	22.50	148.30	34.58	0.6678
ADC_{min}, × 10^{-5} mm^2s^{-1}	53.17	25.88	65.08	14.91	0.2465
ADC_{max}, × 10^{-5} mm^2s^{-1}	241.70	53.59	278.20	60.52	0.1514
P10 ADC, × 10^{-5} mm^2s^{-1}	110.40	15.21	108.90	18.47	0.8390
P25 ADC, × 10^{-5} mm^2s^{-1}	126.00	19.93	124.80	24.53	0.8987
P75 ADC, × 10^{-5} mm^2s^{-1}	158.80	27.96	171.90	49.04	0.4201
P90 ADC, × 10^{-5} mm^2s^{-1}	174.70	30.90	191.60	56.67	0.3601
Median ADC, × 10^{-5} mm^2s^{-1}	143.20	24.73	144.30	32.66	0.9325
Mode ADC, × 10^{-5} mm^2s^{-1}	145.50	30.31	153.50	57.96	0.6623
SD ADC, × 10^{-5} mm^2s^{-1}	25.91	9.84	33.38	13.75	0.1457
Kurtosis	3.51	1.42	4.97	3.87	0.9748
Skewness	0.15	0.75	0.77	0.92	0.1688
Entropy	5.5	0.63	4.75	0.69	**0.0144**

Values displayed in bold indicate findings of statistical significance ($p \leq 0.05$).

DISCUSSION

Despite the revision of the WHO classification of CNS tumors in 2016, which integrated a panel of molecular parameters (2), general histology obtained by light microscopy still remains a major pillar in the glioma grading system. As a consequence, presurgical determination of a tumor's microarchitecture including the identification of potential hot spots, resembling areas of above-average increased proliferation, as targets for biopsy or partial resection is pivotal.

In this regard, our study showed significantly lower values in a variety of the ADC histogram items, more specifically ADCmean, ADCmax, ADCp25, ADCp75, and ADCp90 as well as ADCmedian when comparing grade II with grade I LGG. This finding is in line with earlier reports on the connection between ADC and decreased extracellular space related to increased proliferation and subsequently cellularity (21–24), inherently restricting Brownian motion of extracellular water molecules. As a substantial corroboration, our study confirmed significant differences in Ki-67 expression-based proliferation index when comparing WHO grade I and WHO grade II LGG, varifying higher values in grade II gliomas.

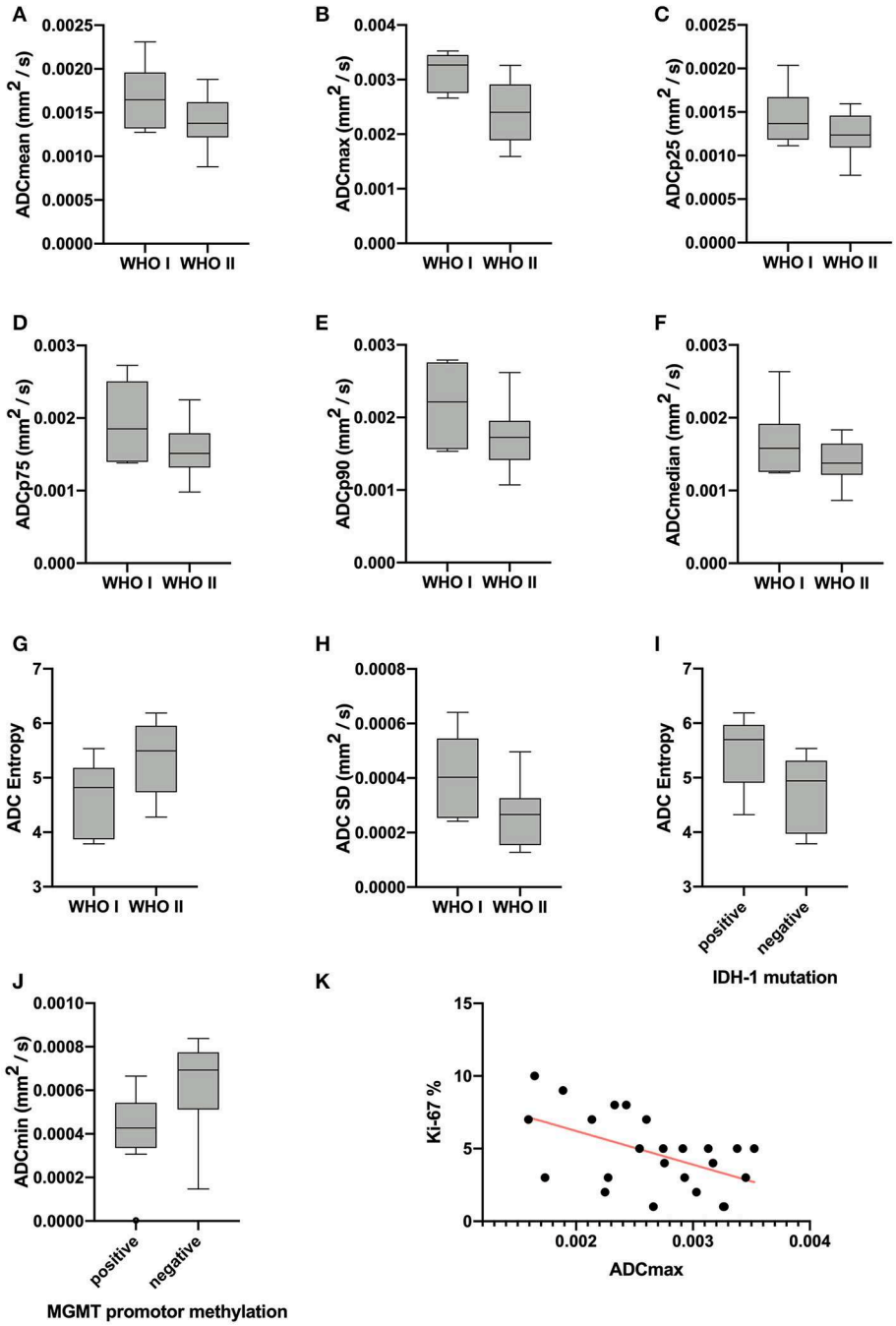

FIGURE 2 | Provides boxplots of statistically significant differences between the diffusion profile of grade I and grade II gliomas **(A–H)** as well as between IDH-1 mutation status **(I)** and MGMT promotor methylation status **(J)** positive and negative tumors. The last image **(K)** shows the significant correlation between ADCmax of the whole tumor ADC histograms and the proliferation index Ki-67, the set of parameters with the strongest correlation ($r = -0.5218$, $p = 0.0089$).

Considering those results, diffusion profiles are valuable tools in addition to anatomic imaging to identify subtle, but biologically distinct tumor compartments in LGG.

Increasing body of evidence suggests the superior value of additionally using the second order histogram dimensions skewness, kurtosis and entropy of the ADC-continuum, for better reflection of tumor heterogeneity and associated tumor-biology (16, 17, 20, 21, 25–32). In this regard, our results show the significant differences of ADC-entropy in grade I vs. grade II LGG, with higher values being associated with higher tumor grade. A comparable relation has been shown in other tumor entities (29). It is indisputable, that higher tumor grades entail

TABLE 5 | Correlations between DWI histogram profile parameters and Ki-67 in all investigated gliomas.

DWI histogram profile parameters	Ki-67
ADC_{mean}, × 10^{-5} mm^2s^{-1}	***r* = −0.4389**
	***p* = 0.0319**
ADC_{min}, × 10^{-5} mm^2s^{-1}	*r* = −0.03701
	p = 0.8637
ADC_{max}, × 10^{-5} mm^2s^{-1}	***r* = −0.5218**
	***p* = 0.0089**
ADCp10, × 10^{-5} mm^2s^{-1}	***r* = −0.4187**
	***p* = 0.0417**
ADCp25, × 10^{-5} mm^2s^{-1}	*r* = −0.3767
	p = 0.0696
ADCp75, × 10^{-5} mm^2s^{-1}	***r* = −0.4328**
	***p* = 0.0347**
ADCp90, × 10^{-5} mm^2s^{-1}	***r* = −0.4512**
	***p* = 0.0269**
ADCMedian, × 10^{-5} mm^2s^{-1}	*r* = −0.3759
	p = 0.0702
ADCModus, × 10^{-5} mm^2s^{-1}	*r* = −0.3179
	p = 0.1011
SD ADC, × 10^{-5} mm^2s^{-1}	***r* = −0.4475**
	***p* = 0.0283**
Kurtosis	*r* = 0.1312
	p = 0.5412
Skewness	*r* = 0.0885
	p = 0.6810
Entropy	*r* = 0.2186
	p = 0.3048

Values displayed in bold indicate findings of statistical significance ($p \leq 0.05$).

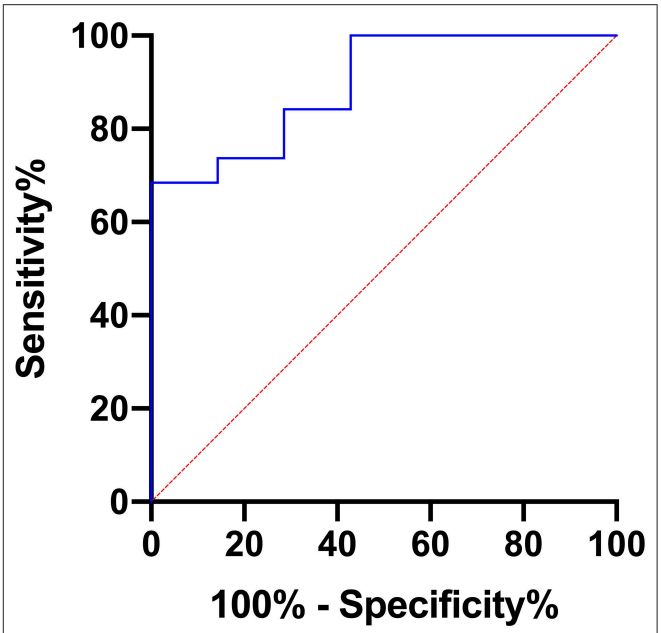

FIGURE 3 | Provides the receiver operating characteristics (ROC) curve of ADCmax, the parameter with the best accuracy in terms of differentiating grade I and grade II gliomas.

increased heterogeneity at the microstructural level, which is accurately reflected by ADC histogram profiles derived from LGG in our analysis.

Low-grade gliomas (LGG) often harbor mutations in one of both genes for IDH. A growing body of evidence indicates that these mutations are at least co-causative for glioma-genesis (33) and therefore represent promising future therapeutic targets. So far, IDH mutation status is a well-established and important prognostic factor in low-grade glioma with better prognosis and survival in case of mutated IDH genes compared to wild-type genes (34–36). The presented ADC histogram analysis elucidates the (so far unreported) potential of ADC entropy to distinguish IDH-mutated and IDH-wild-type LGG. The meaningfulness of this feature cannot be proven by this singular report, but it indicates the potential value of this imaging biomarker and should stimulate further investigations.

A second, equally important molecular property in gliomas bearing great prognostic relevance is the MGMT promotor methylation status. MGMT is a very important DNA repair enzyme. Its expression may be silenced by methylation of its promotor during tumor development, which in turn increases the anti-proliferative effect of alkylating chemotherapeutics. MGMT promotor methylation is associated with an improvement in overall survival (37) in patients suffering from glioblastoma and influences the overall survival of patients with LGG (38). A number of studies investigated the potential of ADC histogram parameters obtained by presurgical MRI for prediction of the MGMT promotor methylation status in glioblastoma, but the results concurrently remain ambiguous (39–43). Also, studies investigating ADC histogram profiling regarding MGMT promotor methylation status in low-grade glioma are completely lacking. Our study shows a significant difference in ADCmin values of LGG with vs. LGG without MGMT promotor methylation. This association is definitely interesting and has the potential to substantiate the importance of histogram profiling for presurgical assessment of individual brain neoplasms, but certainly requires confirmation in a larger cohort.

Finally, significant inverse correlations between Ki-67 expression and ADCmean, ADCmax and the percentiles ADCp10, ADCp75, and ADCp90 were demonstrated. These results are in line with previously published reports on primary CNS lymphomas and meningiomas, proving an inverse correlation between different ADC fractions and Ki-67 expression (25, 29). As discussed above, high Ki-67 expression is a hallmark of increased proliferative activity in neoplastic tissue, naturally resulting in increased cellular density and restricted interstitial diffusion, which is reflected by altered ADC values. In contrast to the first order histogram characteristics, none of the second order characteristics, namely entropy, kurtosis and skewness, showed a significant correlation with Ki-67 expression.

Our study suffers from the following relevant limitations. First of all, it is only a retrospective investigation of a relatively small patient cohort. Furthermore, only data from 1.5-T MRI systems were available, which inevitably leads to lower signal to noise ratios of the MRI data, necessitating acquisition of MRI pictures with smaller pixel matrix and therefore reduced spatial information compared to examinations with a higher field strength. Finally, ADC was calculated by using only 2 b values (0 and 1,000 s/mm^2) and small vessel perfusion could therefore have an impact on ADC values in our patient collective.

CONCLUSION

ADC histogram profiling of LGG provides first and second order characteristics allows to draw inferences about the proliferative activity of the lesion at hand and facilitates differentiation of grade I from grade II neoplasms, which may be important for risk stratification especially in cases of extended tumor infiltration or tumors in eloquent brain areas associated with high perioperative morbidity. Furthermore, our results indicate that ADC histogram profiling enables to draw conclusions about the prognostic relevant IDH mutation status and MGMT promotor methylation status in LGG. As a consequence, inclusion of ADC histogram profiling for presurgical definition of morphologically inapparent, tumor-evolutional significant compartmentation is recommended to increase the accuracy of diagnosis and prognosis and to help the treating physician to identify the most appropriate treatment strategy.

DATA AVAILABILITY STATEMENT

Data of the descriptive analysis, group comparisons, and correlative analysis are provided in the supplement. Additional data on the individual case level can be requested from the corresponding author.

ETHICS STATEMENT

The studies involving human participants were reviewed and approved by ethics committee of the medical council of Baden-Württemberg (Ethik-Kommission Landesärztekammer Baden-Württemberg, F-2017-047). The patients/participants provided their written informed consent to participate in this study.

AUTHOR CONTRIBUTIONS

GG and SS conceived and planned the present study and supervised the project. GG and DH-R were responsible for data acquisition. GG performed statistical analyses and took lead in writing the manuscript. EH was responsible for histopathological workup and figures. HH, K-TH, OG, and CS contributed to the interpretation of the results, provided critical feedback and helped shape the research and manuscript.

REFERENCES

1. Ostrom QT, Gittleman H, Liao P, Vecchione-Koval T, Wolinsky Y, Kruchko C, et al. CBTRUS statistical report: primary brain and other central nervous system tumors diagnosed in the United States in 2010-2014. *Neuro Oncol.* (2017) 19:v1–88. doi: 10.1093/neuonc/nox158
2. Louis DN, Perry A, Reifenberger G, von Deimling A, Figarella-Branger D, Cavenee WK, et al. The 2016 World Health Organization classification of tumors of the central nervous system: a summary. *Acta Neuropathol.* (2016) 131:803–20. doi: 10.1007/s00401-016-1545-1
3. Ishkanian A, Laperriere NJ, Xu W, Millar BA, Payne D, Mason W, et al. Upfront observation versus radiation for adult pilocytic astrocytoma. *Cancer.* (2011) 117:4070–9. doi: 10.1002/cncr.25988
4. Forst DA, Nahed BV, Loeffler JS, Batchelor TT. Low-grade gliomas. *Oncologist.* (2014) 19:403–13. doi: 10.1634/theoncologist.2013-0345
5. Duffau H, Lopes M, Arthuis F, Bitar A, Sichez JP, Van Effenterre R, et al. Contribution of intraoperative electrical stimulations in surgery of low grade gliomas: a comparative study between two series without (1985-96) and with (1996-2003) functional mapping in the same institution. *J Neurol Neurosurg Psychiatry.* (2005) 76:845–51. doi: 10.1136/jnnp.2004.048520
6. Capelle L, Fontaine D, Mandonnet E, Taillandier L, Golmard JL, Bauchet L, et al. Spontaneous and therapeutic prognostic factors in adult hemispheric World Health Organization Grade II gliomas: a series of 1097 cases: clinical article. *J Neurosurg.* (2013) 118:1157–68. doi: 10.3171/2013.1.JNS121
7. Jakola AS, Myrmel KS, Kloster R, Torp SH, Lindal S, Unsgård G, et al. Comparison of a strategy favoring early surgical resection vs a strategy favoring watchful waiting in low-grade gliomas. *JAMA.* (2012) 308:1881–8. doi: 10.1001/jama.2012.12807
8. Soffietti R, Baumert BG, Bello L, von Deimling A, Duffau H, Frénay M, et al. Guidelines on management of low-grade gliomas: report of an EFNS-EANO task force. *Eur J Neurol.* (2010) 17:1124–33. doi: 10.1111/j.1468-1331.2010.03151.x
9. Svolos P, Kousi E, Kapsalaki E, Theodorou K, Fezoulidis I, Kappas C, et al. The role of diffusion and perfusion weighted imaging in the differential diagnosis of cerebral tumors: a review and future perspectives. *Cancer Imaging.* (2014) 14:20. doi: 10.1186/1470-7330-14-20
10. Mori S, Barker PB. Diffusion magnetic resonance imaging: its principle and applications. *Anat Rec.* (1999) 257:102–109. doi: 10.1002/(SICI)1097-0185(19990615)257:3<102::AID-AR7>3.0.CO;2-6
11. Charles-Edwards EM, deSouza NM. Diffusion-weighted magnetic resonance imaging and its application to cancer. *Cancer Imaging.* (2006) 6:135–43. doi: 10.1102/1470-7330.2006.0021
12. Zhang L, Min Z, Tang M, Chen S, Lei X, Zhang X. The utility of diffusion MRI with quantitative ADC measurements for differentiating high-grade from low-grade cerebral gliomas: evidence from a meta-analysis. *J Neurol Sci.* (2017) 373:9–15. doi: 10.1016/j.jns.2016.12.008
13. Cui Y, Ma L, Chen X, Zhang Z, Jiang H, Lin S. Lower apparent diffusion coefficients indicate distinct prognosis in low-grade and high-grade glioma. *J Neurooncol.* (2014) 119:377–85. doi: 10.1007/s11060-014-1490-6
14. Yin Y, Tong D, Liu XY, Yuan TT, Yan YZ, Ma Y, et al. Correlation of apparent diffusion coefficient with Ki-67 in the diagnosis of gliomas. *Zhongguo Yi Xue Ke Xue Yuan Xue Bao.* (2012) 34:503–8. doi: 10.3881/j.issn.1000-503X.2012.05.012
15. Horvath-Rizea D, Surov A, Hoffmann KT, Garnov N, Vörkel C, Kohlhof-Meinecke P, et al. The value of whole lesion ADC histogram profiling to differentiate between morphologically indistinguishable ring enhancing lesions-comparison of glioblastomas and brain abscesses. *Oncotarget.* (2018) 9:18148–59. doi: 10.18632/oncotarget.24454
16. Just N. Improving tumour heterogeneity MRI assessment with histograms. *Br J Cancer.* (2014) 111:2205–13. doi: 10.1038/bjc.2014.512
17. Schob S, Meyer HJ, Pazaitis N, Schramm D, Bremicker K, Exner M, et al. ADC Histogram analysis of cervical cancer aids detecting lymphatic metastases-a preliminary study. *Mol Imaging Biol.* (2017) 19:953–62. doi: 10.1007/s11307-017-1073-y

18. Suo S, Zhang K, Cao M, Suo X, Hua J, Geng X, et al. Characterization of breast masses as benign or malignant at 3.0T MRI with whole-lesion histogram analysis of the apparent diffusion coefficient. *J Magn Reson Imaging.* (2016) 43:894–902. doi: 10.1002/jmri.25043
19. Foroutan P, Kreahling JM, Morse DL, Grove O, Lloyd MC, Reed D, et al. Diffusion MRI and novel texture analysis in osteosarcoma xenotransplants predicts response to anti-checkpoint therapy. *PLoS ONE.* (2013) 8:e82875. doi: 10.1371/journal.pone.0082875
20. Gihr GA, Horvath-Rizea D, Kohlhof-Meinecke P, Ganslandt O, Henkes H, Richter C, et al. Histogram profiling of postcontrast T1-weighted MRI gives valuable insights into tumor biology and enables prediction of growth kinetics and prognosis in meningiomas. *Transl Oncol.* (2018) 11:957–61. doi: 10.1016/j.tranon.2018.05.009
21. Surov A, Meyer HJ, Wienke A. Correlation between apparent diffusion coefficient (ADC) and cellularity is different in several tumors: a meta-analysis. *Oncotarget.* (2017) 8:59492–9. doi: 10.18632/oncotarget.17752
22. Chen L, Liu M, Bao J, Xia Y, Zhang J, Zhang L, et al. The correlation between apparent diffusion coefficient and tumor cellularity in patients: a meta-analysis. *PLoS ONE.* (2013) 8:e79008. doi: 10.1371/journal.pone.0079008
23. Surov A, Caysa H, Wienke A, Spielmann RP, Fiedler E. Correlation between different ADC fractions, cell count, Ki-67, total nucleic areas and average nucleic areas in meningothelial meningiomas. *Anticancer Res.* (2015). 35:6841–6.
24. Surov A, Meyer HJ, Wienke A. Correlation between minimum apparent diffusion coefficient (ADCmin) and tumor cellularity: a meta-analysis. *Anticancer Res.* (2017) 37:3807–10. doi: 10.21873/anticanres.11758
25. Schob S, Meyer J, Gawlitza M, Frydrychowicz C, Müller W, Preuss M, et al. Diffusion-weighted MRI reflects proliferative activity in primary CNS lymphoma. *PLoS ONE.* (2016) 11:e0161386. doi: 10.1371/journal.pone.0161386
26. Woo S, Cho JY, Kim SY, Kim SH. Histogram analysis of apparent diffusion coefficient map of diffusion-weighted MRI in endometrial cancer: a preliminary correlation study with histological grade. *Acta Radiol.* (2014) 55:1270–7. doi: 10.1177/0284185113514967
27. Surov A, Gottschling S, Mawrin C, Prell J, Spielmann RP, Wienke A, et al. Diffusion-weighted imaging in meningioma: prediction of tumor grade and association with histopathological parameters. *Transl Oncol.* (2015) 8:517–23. doi: 10.1016/j.tranon.2015.11.012
28. Schob S, Meyer HJ, Dieckow J, Pervinder B, Pazaitis N, Höhn AK, et al. Histogram analysis of diffusion weighted imaging at 3T is useful for prediction of lymphatic metastatic spread, proliferative activity, and cellularity in thyroid cancer. *Int J Mol Sci.* (2017) 18:821. doi: 10.3390/ijms18040821
29. Gihr GA, Horvath-Rizea D, Garnov N, Kohlhof-Meinecke P, Ganslandt O, Henkes H, et al. Diffusion profiling via a histogram approach distinguishes low-grade from high-grade meningiomas, can reflect the respective proliferative potential and progesterone receptor status. *Mol Imaging Biol.* (2018) 18:v1–9. doi: 10.1055/s-0038-1641416
30. Meyer HJ, Schob S, Münch B, Frydrychowicz C, Garnov N, Quäschling U, et al. Histogram analysis of T1-weighted, T2-weighted, and postcontrast T1-weighted images in primary CNS lymphoma: correlations with histopathological findings—a preliminary study. *Mol Imaging Biol.* (2017) 20:318–23. doi: 10.1007/s11307-017-1115-5
31. Meyer HJ, Leifels L, Hamerla G, Höhn AK, Surov A. Histogram analysis parameters derived from conventional T1- and T2-weighted images can predict different histopathological features including expression of Ki67, EGFR, VEGF, HIF-1α, and p53 and cell count in head and neck squamous cell carcinoma. *Mol Imaging Biol.* (2018) 21:740–6. doi: 10.1007/s11307-018-1283-y
32. Meyer HJ, Hamerla G, Höhn AK, Surov A. Whole lesion histogram analysis derived from morphological MRI sequences might be able to predict EGFR- and Her2-expression in cervical cancer. *Acad Radiol.* (2018) 26:e208–15. doi: 10.1016/j.acra.2018.09.008
33. Cohen AL, HolmenSL, Colman H. IDH1 and IDH2 mutations in gliomas. *Curr Neurol Neurosci Rep.* (2013) 13:345. doi: 10.1007/s11910-013-0345-4
34. Houillier C, Wang X, Kaloshi G, Mokhtari K, Guillevin R, Laffaire J, et al. IDH1 or IDH2 mutations predict longer survival and response to temozolomide in low-grade gliomas. *Neurology.* (2010) 75:1560–6. doi: 10.1212/WNL.0b013e3181f96282
35. Xia L, Wu B, Fu Z, Feng F, Qiao E, Li Q, et al. Prognostic role of IDH mutations in gliomas: a meta-analysis of 55 observational studies. *Oncotarget.* (2015) 6:17354–65. doi: 10.18632/oncotarget.4008
36. Olar A, Wani KM, Alfaro-Munoz KD, Heathcock LE, van Thuijl HF, Gilbert MR, et al. IDH mutation status and role of WHO grade and mitotic index in overall survival in grade II-III diffuse gliomas. *Acta Neuropathol.* (2015) 129:585–96. doi: 10.1007/s00401-015-1398-z
37. Zhao H, Wang S, Song C, Zha Y, Li L. The prognostic value of MGMT promoter status by pyrosequencing assay for glioblastoma patients' survival: a meta-analysis. *World J Surg Oncol.* (2016) 14:261. doi: 10.1186/s12957-016-1012-4
38. Franceschi E, Mura A, De Biase D, Tallini G, Pession A, Foschini MP, et al. The role of clinical and molecular factors in low-grade gliomas: what is their impact on survival? *Future Oncol.* (2018) 14:1559–67. doi: 10.2217/fon-2017-0634
39. Pope WB, Lai A, Mehta R, Kim HJ, Qiao J, Young JR, et al. Apparent diffusion coefficient histogram analysis stratifies progression-free survival in newly diagnosed bevacizumab-treated glioblastoma. *AJNR Am J Neuroradiol.* (2011) 32:882–9. doi: 10.3174/ajnr.A2385
40. Romano A, Calabria LF, Tavanti F, Minniti G, Rossi-Espagnet MC, Coppola V, et al. Apparent diffusion coefficient obtained by magnetic resonance imaging as a prognostic marker in glioblastomas: correlation with MGMT promoter methylation status. *Eur Radiol.* (2013) 23:513–20. doi: 10.1007/s00330-012-2601-4
41. Gupta A, Prager A, Young RJ, Shi W, Omuro AM, Graber JJ. Diffusion-weighted MR imaging and MGMT methylation status in glioblastoma: a reappraisal of the role of preoperative quantitative ADC measurements. *AJNR Am J Neuroradiol.* (2013) 34:E10–1. doi: 10.3174/ajnr.A3467
42. Choi YS, Ahn SS, Kim DW, Chang JH, Kang SG, Kim EH, et al. Incremental prognostic value of ADC histogram analysis over MGMT promoter methylation status in patients with glioblastoma. *Radiology.* (2016) 281:175–84. doi: 10.1148/radiol.2016151913
43. Han Y, Yan LF, Wang XB, Sun YZ, Zhang X, Liu ZC, et al. Structural and advanced imaging in predicting MGMT promoter methylation of primary glioblastoma: a region of interest based analysis. *BMC Cancer.* (2018). 18:215. doi: 10.1186/s12885-018-4114-2

Conflict of Interest: The authors declare that the research was conducted in the absence of any commercial or financial relationships that could be construed as a potential conflict of interest.

frontiers in Oncology

ORIGINAL RESEARCH
published: 13 March 2020
doi: 10.3389/fonc.2020.00235

Predicting the Type of Tumor-Related Epilepsy in Patients With Low-Grade Gliomas: A Radiomics Study

Yinyan Wang[1†], Wei Wei[2,3,4,5†], Zhenyu Liu[2,6†], Yuchao Liang[1], Xing Liu[7], Yiming Li[1,7], Zhenchao Tang[2,4], Tao Jiang[1,7,8,9] and Jie Tian[2,4,5,6*]*

[1] Beijing Tiantan Hospital, Capital Medical University, Beijing, China, [2] CAS Key Laboratory of Molecular Imaging, Institute of Automation, Chinese Academy of Sciences, Beijing, China, [3] School of Electronics and Information, Xi'an Polytechnic University, Xi'an, China, [4] Beijing Advanced Innovation Center for Big Data-Based Precision Medicine, School of Medicine, Beihang University, Beijing, China, [5] Engineering Research Center of Molecular and Neuro Imaging of Ministry of Education, School of Life Science and Technology, Xidian University, Xi'an, China, [6] School of Artificial Intelligence, University of Chinese Academy of Sciences, Beijing, China, [7] Department of Molecular Pathology, Beijing Neurosurgical Institute, Capital Medical University, Beijing, China, [8] Center of Brain Tumor, Beijing Institute for Brain Disorders, Beijing, China, [9] China National Clinical Research Center for Neurological Diseases, Beijing, China

Purpose: The majority of patients with low-grade gliomas (LGGs) experience tumor-related epilepsy during the disease course. Our study aimed to build a radiomic prediction model for LGG-related epilepsy type based on magnetic resonance imaging (MRI) data.

Methods: A total of 205 cases with LGG-related epilepsy were enrolled in the retrospective study and divided into training and validation cohorts (1:1) according to their surgery time. Seven hundred thirty-four radiomic features were extracted from T2-weighted imaging, including six location features. Pearson correlation coefficient, univariate area under curve (AUC) analysis, and least absolute shrinkage and selection operator regression were adopted to select the most relevant features for the epilepsy type to build a radiomic signature. Furthermore, a novel radiomic nomogram was developed for clinical application using the radiomic signature and clinical variables from all patients.

Results: Four MRI-based features were selected from the 734 radiomic features, including one location feature. Good discriminative performances were achieved in both training (AUC = 0.859, 95% CI = 0.787–0.932) and validation cohorts (AUC = 0.839, 95% CI = 0.761–0.917) for the type of epilepsy. The accuracies were 80.4 and 80.6%, respectively. The radiomic nomogram also allowed for a high degree of discrimination. All models presented favorable calibration curves and decision curve analyses.

Conclusion: Our results suggested that the MRI-based radiomic analysis may predict the type of LGG-related epilepsy to enable individualized therapy for patients with LGG-related epilepsy.

Keywords: epilepsy type, low-grade gliomas, machine learning, radiomics, T2-weighted imaging

OPEN ACCESS

Edited by:
Bo Gao,
Affiliated Hospital of Guizhou Medical University, China

Reviewed by:
Seyedmehdi Payabvash,
Yale University, United States
Guolin Ma,
China-Japan Friendship Hospital, China

***Correspondence:**
Yinyan Wang
tiantanyinyan@126.com
Jie Tian
jie.tian@ia.ac.cn

† These authors have contributed equally to this work

Specialty section:
This article was submitted to Cancer Imaging and Image-directed Interventions, a section of the journal Frontiers in Oncology

Received: *20 November 2019*
Accepted: *12 February 2020*
Published: *13 March 2020*

Citation:
Wang Y, Wei W, Liu Z, Liang Y, Liu X, Li Y, Tang Z, Jiang T and Tian J (2020) Predicting the Type of Tumor-Related Epilepsy in Patients With Low-Grade Gliomas: A Radiomics Study. Front. Oncol. 10:235. doi: 10.3389/fonc.2020.00235

INTRODUCTION

World Health Organization (WHO) grade II or low-grade glioma (LGG) (1) accounts for the majority of primary brain tumors in young adults (2, 3). The majority of patients with LGG experiences tumor-related epilepsy (4, 5) that impacts their quality of life and may contribute to long-term disability (6–8). Broadly, the type of epilepsy can be generalized or focal based on its presentation (9) and require different methods of treatment. Generalized epilepsy occurs more frequently, is more severe, and requires a relatively higher dose of antiepileptic therapy with the potential for increased side effects, compared to focal epilepsy. An accurate prediction of epilepsy type that occurs in patients with brain tumors could allow customization of antiepileptic therapy.

Radiomics is a research branch in the field of medical imaging (10). Based on the rapid development of machine learning and image processing techniques, radiomic analyses have been successfully applied in the field of oncology (11–16), including glioma (17). Magnetic resonance imaging (MRI) is a routinely used diagnostic tool for glioma management. A lot of tumor information that is not recognized by human eye remains unmined (12). Radiomics can extract high-dimensional radiomic features from medical images to fully exploit the in-depth information of tumors (18). Based on T2-weighted imaging (T2WI), Liu et al. successfully predicted the occurrence of LGG-associated epilepsy by radiomic analysis (19). However, the prediction of the type of epilepsy remains to be determined.

The current study conducted a radiomic analysis to explore the relationship between quantitative radiomic features and the type of tumor-related epilepsy in patients with LGG. Precise radiomic prediction models for epilepsy type could be established and further validated using the screened features.

METHODS

Patients

In this retrospective study, we consecutively enrolled a total of 205 patients with LGG who underwent surgery at the Beijing Tiantan Hospital from September 2012 to December 2014. The inclusion criteria of all enrolled cases were (a) pathologically confirmed grade II gliomas according to WHO criteria 2016 (20) and (b) presurgical T2-weighted imaging. The exclusion criteria of all enrolled cases were no craniotomy or stereotactic biopsy before MRI scan. The enrolled cases were allocated to either the training or the validation cohort according to the surgery time with a 1:1 ratio, i.e., the first 102 cases enrolled formed the training cohort, and the other 103 cases formed the validation cohort. Data on routine clinical variables were collected, including age, gender, tumor pathology, and epilepsy type. The present study further utilized clinical and MRI data from all enrolled cases. The ethics committee of Beijing Tiantan Hospital approved this study, and the requirement for informed consent was waived. Our study was conducted in accordance with the Declaration of Helsinki. The study design is illustrated in **Figure 1**.

Patients were considered to have experienced tumor-related epilepsy when a history of at least one seizure with the presence of an enduring alteration (i.e., LGG) in the brain (21) was reported. The history and type (generalized and focal) of epilepsy were evaluated by an epileptologist based on the patient's presentation according to the classification and terminology of the International League Against Epilepsy (9, 22). The epilepsy type was determined consistently for all the enrolled patients with a history of epilepsy based on the aforementioned criteria.

Brain MRI and Tumor Segmentation

All MRI examinations were performed using a Magnetom Trio 3.0 T scanner (Siemens, Erlangen, Germany) with a 12-channel receive-only head coil scan acquisition. The T2WI parameters were as follows: repetition time (TR), 5,800 ms; echo time (TE), 110 ms; flip angle, 150°; the field of view (FOV), 240 × 188 mm^2; voxel size, 0.6 × 0.6 × 5.0 mm^3; and matrix, 384 × 300. The MRI data were stored in DICOM format.

Regions of interest (ROIs) of the gliomas were drawn by two neuroradiologists with more than 5 years of clinical experience with ITK-snap (www.itksnap.org). The neuroradiologists were blinded to each other's results. Gliomas were segmented on each MRI slice. We defined ROIs of the LGGs as areas of the MRI images that exhibited abnormal hyperintense signals. The intraclass correlation coefficient (ICC) was used to assess whether the segmentation results of the two doctors were significantly different. No difference was defined as ICC >0.8. In the absence of a difference, each patient would obtain a segmentation result from one of the two neuroradiologists randomly.

Extraction of Quantitative Radiomic Features

A total of 734 radiomic features were extracted based on the research of Liu et al. (19) and Li et al. (23, 24), including 6 location features, 17 first order statistics (FOS) features, 8 shape and size features, 26 gray-level co-occurrence matrix (GLCM) features, 16 gray-level run-length matrix (GLRLM) features, 16 gray-level size zone matrix (GLSZM) features, 5 neighborhood gray-tone difference matrix (NGTDM) features, and 640 wavelet features.

The location features were extracted based on our previous research (19) using (a) polar coordinates parameters (r, θ, and Φ) based on the centroid of the tumor, and (b) City Block distance, (c) Chebyshev distance, and (d) Euclidean distance from the anterior commissure (AC) to the centroid of the tumor. The FOS features reflected the distribution of voxel values within the ROI 3D matrix and the overall information of the tumor. The shape and size features reflected the volume, surface area, and shape of the tumor. GLCM, GLRLM, GLSZM, and NGTDM were collectively referred to as texture features. The GLCM

Abbreviations: AC, anterior commissure; AUC, area under curve; DCA, decision curve analysis; DICOM, Digital Imaging and Communications in Medicine; FOS, first-order statistics; GLCM, gray-level co-occurrence matrix; GLRLM, gray-level run-length matrix; GLSZM, gray-level size zone matrix; IBE, International Bureau for Epilepsy; ICC, intraclass correlation coefficient; ILAE, International League Against Epilepsy; LASSO, least absolute shrinkage and selection operator; LGG, low-grade glioma; LOOCV, leave one out cross-validation; MRI, magnetic resonance imaging; NGTDM, neighborhood gray-tone difference matrix; ROC, receiver operating characteristic; ROI, region of interest; WHO, World Health Organization

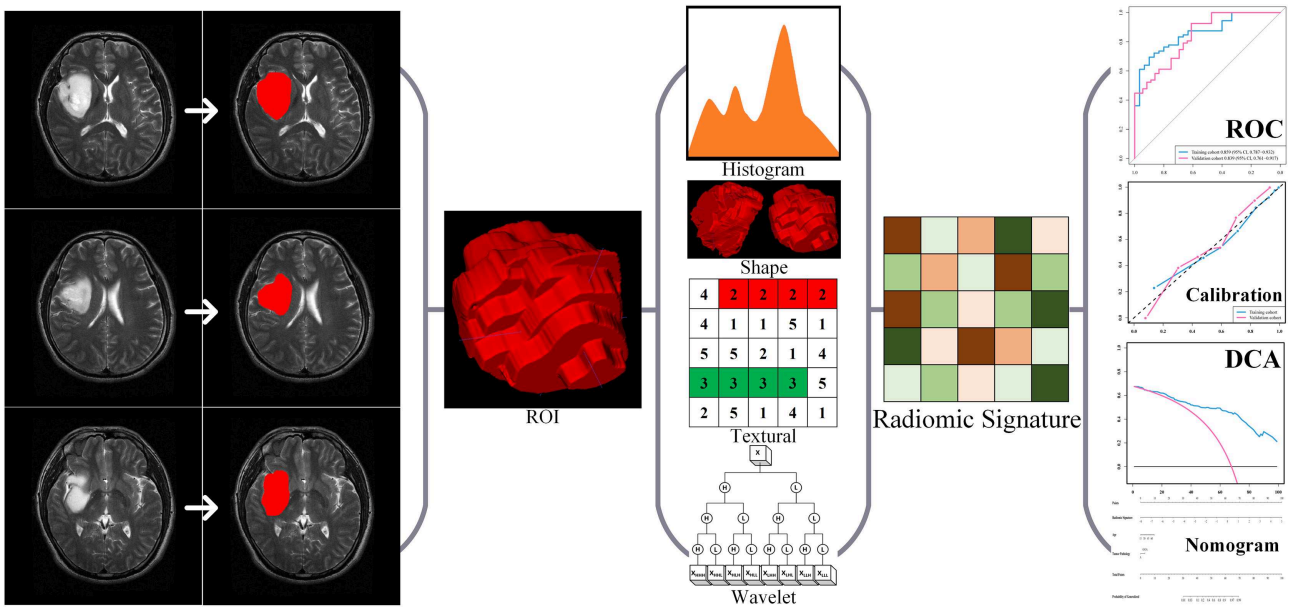

FIGURE 1 | Study design and flowchart. The flowchart of the current study.

reflected the arrangement of voxels. The GLRLM reflected the arrangement of voxels with equal voxel values. The GLSZM reflected the characteristics of the homogeneous region. The NGTDM reflected the difference between each voxel in the ROI and the adjacent voxels. The wavelet features were calculated by FOS, GLCM, GLRLM, GLSZM, and NGTDM features through Coiflet 1 3D wavelet transform. The detailed information and formulas for the detection of the 734 features were published in our previous researches (19, 24).

Feature Selection and Radiomic Signature Building

The 734 radiomic features were normalized before feature selection using the *z*-score method. A univariate analysis was used to screen the radiomic features. The criteria for screening features include (a) *p*-values of Pearson correlation coefficient <0.05 and (b) area under curve (AUC) of the radiomic features >0.6. Least absolute shrinkage and selection operator (LASSO) regression was widely used to compress the coefficients of features and select features to prevent overfitting. Logistic regression was used for data classification to build a reliable prediction model. Thereafter, LASSO and logistic regression were used to calculate the radiomic signature for epilepsy-type prediction using Glmnet package (25). Features dimension reduction and selection, i.e., univariate analyses and LASSO regression, were based on the training cohort. The optimal value of the LASSO's parameter λ was determined by leave-one-out cross-validation (LOOCV) using classification error as criterion during the training phase. We calculated the radiomic signature for the patients after determining the selected features' values using the optimal value of the LASSO's parameter λ. Radiomic signature was the linear weighting of the selected features' coefficients. Radiomic analyses of the study were implemented by MATLAB R2016a (MathWorks, Natick, MA).

Development of an Individualized Prediction Model

Based on cohort of all patients, a multivariable logistic regression analysis was built to predict epilepsy type with clinical information, using the radiomic signature, age, gender, and tumor pathology. Akaike's information criterion was used to select the indicator with the predictive ability for building the multivariable logistic regression model (26, 27). With this radiomics-based model, we also built a novel radiomic nomogram for quantitative prediction of the epilepsy type (28).

Performance Evaluation of the Models

The classification performance of the radiomic signature and radiomic nomogram was assessed by the receiver operating characteristic (ROC) curves and AUCs in each cohort. Calibration curves were plotted to assess the calibration of the radiomic signature and radiomic nomogram (29), accompanied by the Hosmer–Lemeshow test (30). Decision curve analyses (DCAs) determined the clinical usefulness of the radiomic signature and radiomic nomogram by quantifying the net benefits at different threshold probabilities in cohort of all patients (31).

Statistical Analysis

Age and radiomic signature were reported as median and range. The differences between subgroups were assessed by independent samples *t*-test. Gender and histopathology were reported in frequencies and proportions, and differences between subgroups were assessed by Fisher's exact test. The statistical tests were two sided, and $p < 0.05$ were defined as significant. Nomogram

building and models' validation were implemented with R software (version 3.6.1, Vienna, Austria).

RESULTS

Demographic and Clinical Data

The main clinical and pathological characteristics of all 205 patients are listed in **Table 1**. Of the 205 enrolled patients, 139 (67.8%) had generalized and 66 (32.2%) had focal seizures. Those with generalized epilepsy accounted for 72 (70.6%) and 67 (65.0%) patients, while those with focal epilepsy accounted for 30 (29.4%) and 36 (35.0%) patients in the training and validation cohorts, respectively. There were no significant differences between the two epilepsy types based on age, gender, and tumor histopathology in cohort of all patients, training cohort, and validation cohort. However, radiomic signature was significantly different between the two epilepsy types ($p < 0.001$) and hence a potential indicator for diagnosing the types of epilepsy.

Performance of Radiomic Signature

Based on the training cohort, a logistic regression prediction model was constructed by integrating the four key radiomic features selected using the univariate analyses and LASSO regression (**Table 2**). The parameter $\lambda = 0.067$ was used as the optimal value. The radiomic signature for each patient in both cohorts was calculated with the train-based model. The predictive ability of the radiomic signature was interpreted from the ROC curve (**Figure 2A**), where it achieved a performance with classification accuracy = 80.4%, AUC = 0.859 [95% confidence interval (CI), 0.787–0.932] in the training cohort and classification accuracy = 80.6%, AUC = 0.839 (95% CI, 0.761–0.917) in the validation cohort. The radiomic signature demonstrated favorable calibration in the training and validation cohorts (**Figure 2B**). The *p*-values of the Hosmer–Lemeshow test for classification predictive ability of the radiomic signature were 0.12 and 0.10, respectively. The DCA showed that using radiomic signature to predict epilepsy type adds more benefit than either the treat-all-patients scheme or the treat-none scheme (**Figure 2C**).

Performance of Radiomic Nomogram

Radiomic nomogram for epilepsy type prediction was developed based on the radiomic signature, age, and tumor pathology data (**Figure 3**). It showed excellent performance in predicting epilepsy type with AUC = 0.863 (95% CI, 0.810–0.916) in cohort of all patients (**Figure 2D**). The calibration curve and DCA of the radiomic nomogram for the epilepsy type prediction also demonstrated favorable results (**Figures 2E**,**F**). The *p*-value of the Hosmer–Lemeshow test was 0.11.

DISCUSSION

This study develops and presents a quantitative and individualized epilepsy type radiomic prediction model using a series of radiomic T2-weighted imaging features associated with the type of LGG-related epilepsy. The results demonstrate that the MRI-based radiomic model could successfully stratify patients according to their epilepsy type. This easy-to-use

TABLE 2 | Four radiomic features selected by LASSO regression.

Radiomic features	AUC	*p*-values of Pearson	Coefficients of LASSO regression
$Coiflet_{LLL}$ GLSZM zone percentage	0.683	0.003	0.445876806974411
$Coiflet_{LLH}$ NGTDM contrast	0.650	0.029	0.135681539773941
$Coiflet_{LHL}$ GLCM maximum probability	0.685	0.023	0.336605042219162
Location features: Chebyshev distance	0.656	0.032	0.281620532274246

p-values are the result of Pearson correlation coefficient.
AUC, area under curve; LASSO, least absolute shrinkage and selection operator; GLSZM, gray-level size zone matrix; NGTDM, neighborhood gray tone difference matrix; GLCM, gray-level co-occurrence matrix.

TABLE 1 | Clinical characteristic of patients in the training and validation cohorts.

Characteristics	All cohort (*n* = 205)		*p*-value	Training cohort (*n* = 102)		*p*-value	Validation cohort (*n* = 103)		*p*-value
	G (*n* = 139)	F (*n* = 66)		G (*n* = 72)	F (*n* = 30)		G (*n* = 67)	F (*n* = 36)	
Age, median (range)	37 (15–64)	39.5 (15–66)	0.181	36 (15–58)	35.5 (21–59)	0.995	41 (15–64)	44.5 (15–66)	0.118
Gender (%)			0.645			1.000			0.519
Male	85 (61)	43 (65)		44 (61)	18 (60)		41 (61)	25 (69)	
Female	54 (39)	23 (35)		28 (39)	12 (40)		26 (39)	11 (31)	
Tumor histopathology (%)			0.155			0.124			0.504
Oligodendrial glioma	97 (70)	39 (59)		48 (67)	15 (50)		49 (73)	24 (67)	
Astrocytoma	42 (30)	27 (41)		24 (33)	15 (50)		18 (27)	12 (33)	
Radiomic signature, mean ± SD	0.63 ± 1.04	−0.99 ± 1.39	<0.001	0.35 ± 0.83	−0.85 ± 0.85	<0.001	0.92 ± 1.17	−1.10 ± 1.73	<0.001

p-values of age and radiomic signature are the results of independent-samples t-tests; p-values of gender and tumor histopathology are the results of Fisher's exact tests.
G, generalized; F, focal; SD, standard deviation.

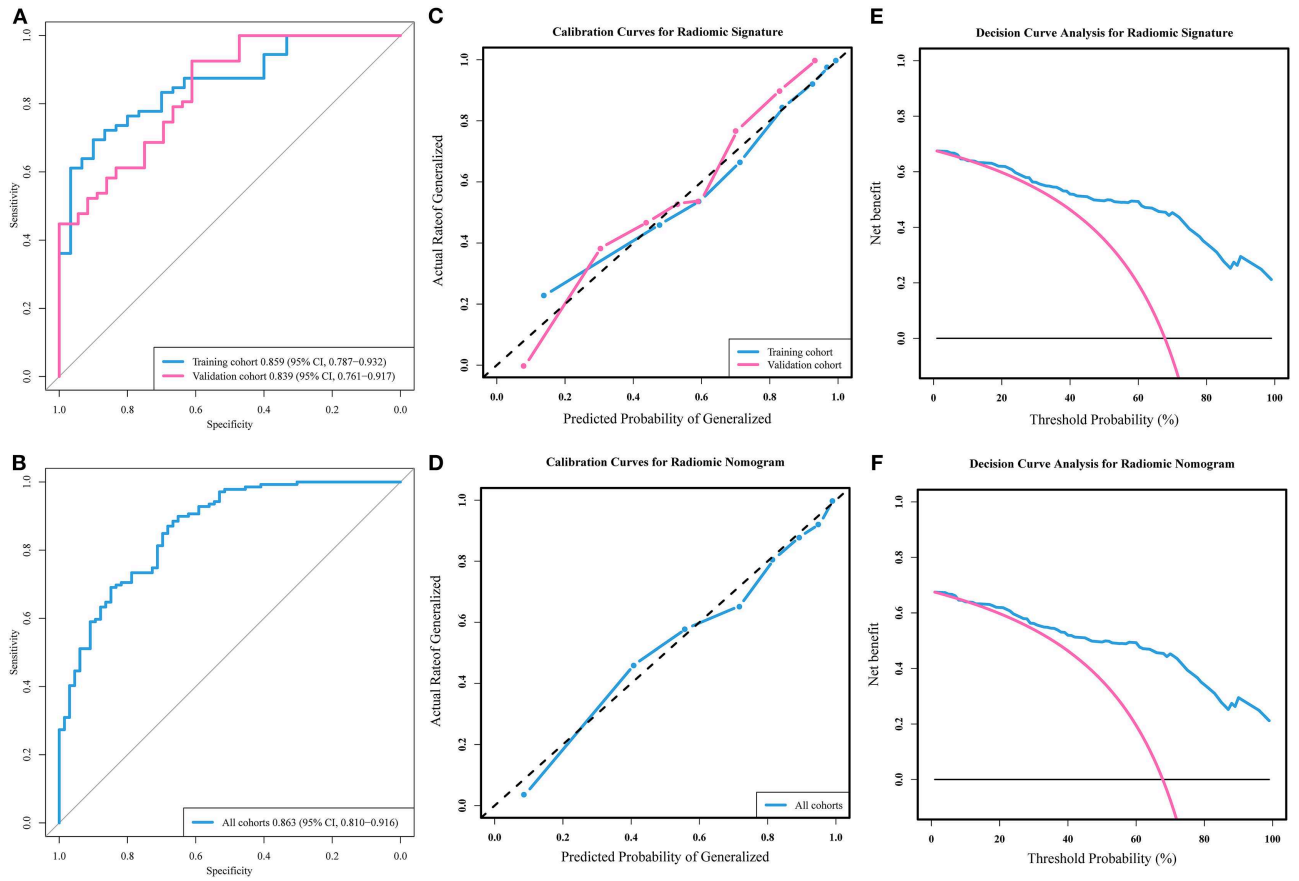

FIGURE 2 | Receiver operating characteristic (ROC) curves, calibration curves, and decision curve analyses of models. **(A)** ROC curves and **(B)** calibration curves of the radiomic signature in training and validation cohorts. **(C)** Decision curve analysis of the radiomic signature. **(D)** ROC curve and **(E)** calibration curve of the radiomic nomogram in all patients' cohort. **(F)** Decision curve analysis of the radiomic nomogram.

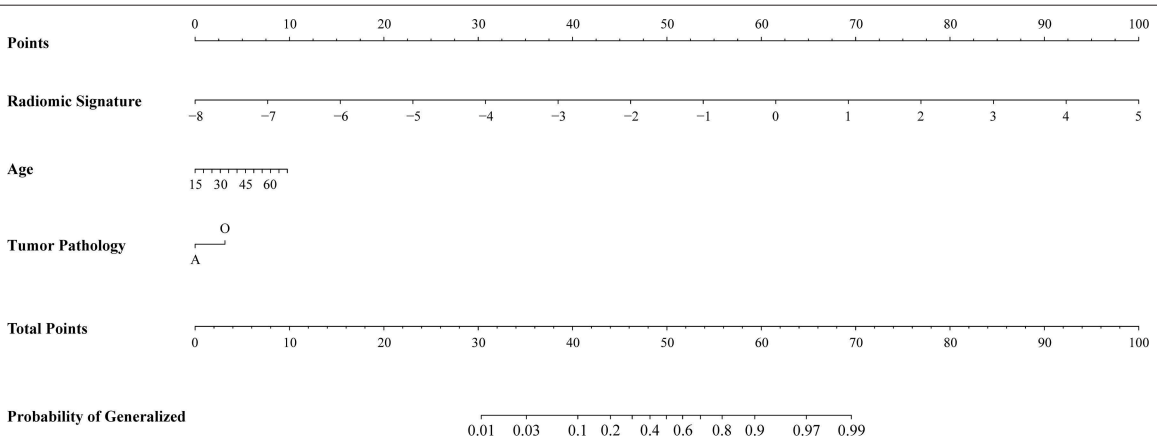

FIGURE 3 | Radiomic nomogram for prediction of epilepsy type. The radiomic-based nomogram was built using radiomics signature, age, and tumor pathology data.

nomogram may be a powerful clinical tool for assisting clinicians with personalized therapeutic decisions.

Treatment based on the type of LGG-related epilepsy allows for a more targeted use of antiepileptic drugs, thus minimizing therapy-related side effects in patients with LGG. However, determining the epilepsy type based on its clinical presentation imposes an apparent lag. Thus, there is a need for a clinical model capable of predicting epilepsy type before treatment initiation. In

this study, a newly developed radiomic signature and radiomic nomogram predict the epilepsy type for each patient in the study. Thus, patients identified as either generalized or focal epilepsy are subjected to appropriate therapies. Therefore, the radiomic signature and radiomic nomogram provided clinicians with a reliable tool for better prediction of LGG-related epilepsy type.

For the better prediction of epilepsy type, a large number of high-throughput radiomic features that were widely used in previous radiomics studies (18) were also extracted in this study, including location features designed for brain tumor studies by Liu et al. (19). Specifically, we extracted many high-dimensional features that are intuitively challenging to be recognized by humans. Radiomic features provide abundant information on the heterogeneity and microenvironments of gliomas (32), including reliable information for its personalized treatment (33). The use of radiomics-based research in the field of oncology has indisputably impacted the survival outcomes (34, 35), lymph node metastasis (36), and treatment responses (37–39).

Furthermore, based on the quantitative MRI features, radiomic analyses have the ability to assess the clinical characteristics and molecular background of gliomas (40, 41). Therefore, this study further suggests the associations of these radiomics-based MRI features with the type of LGG-related epilepsy.

Tumor location is an influential factor associated with LGG-related epilepsy. Several MRI-based studies indicate the association between the involvement of eloquent (42), cortical (45), and insular regions (43) with epilepsy occurrence, along with the probabilistic risk atlas of LGG-related epilepsy (44). However, there is a need to investigate and predict the type of epilepsy. Furthermore, previous studies not only used the location information as categorized data but also ignored the imaging information inside the tumor area. Since various subregions of a brain lobe may differently influence the occurrence of epilepsy type, we used a quantitative description of tumor location for brain tumors. The distances from the AC to the centroid and the polar coordinates based on centroid of the tumor accurately described tumor location. These location features provide more detailed information for the radiomic prediction models in the current study.

LASSO and logistic regression are widely accepted algorithms in the field of machine learning. In this study, the 734 features extracted could cause overfitting when building the radiomic prediction model, which makes the model lose its generalization ability. Therefore, we performed feature dimension reduction and selection to detect the key features most closely related to the type of epilepsy to improve the discriminative power in the present model. The LASSO regression was used to achieve the best performance in predicting the type of LGG-related epilepsy. With features associated with epilepsy type, a prediction model was constructed using logistic regression. As a sensitive and stable machine learning method for dichotomous forecast, logistic regression has been widely used in feature-based classification. In the current study, the application of LASSO and logistic regression raises the predictive capability of the established model and consequently provided relatively high discrimination accuracies and AUCs.

There are some limitations to the present study. First, the diagnoses provided by experienced epileptologists was based on clinical presentations, and patient's epilepsy originations were unconfirmed because the stereotactic electroencephalographic data were incomplete. Second, the divergence of tumor histopathology in causing various types of epilepsy was not quantitatively assessed by the radiomic model in this study. Third, a multicenter, prospective clinical trial is required to address the limitation caused by small samples. Fourth, the interpretability of radiomic features has always been an intractable task in the study of radiomics.

CONCLUSIONS

Radiomic location features and wavelet-based textural features are associated with the type of LGG-related epilepsy. Radiomics-based prediction models allow for non-invasive, preoperative, and low-cost prediction of epilepsy type. The results of this study suggest that radiomics could be a reliable tool for personalized treatment in patients with LGG-related epilepsy.

DATA AVAILABILITY STATEMENT

The datasets generated for this study are available on request to the corresponding author.

ETHICS STATEMENT

The ethics committee of Beijing Tiantan Hospital approved this study, and the requirement for informed consent was waived. Our study was conducted in accordance with the Declaration of Helsinki.

AUTHOR CONTRIBUTIONS

YW, WW, ZL, TJ, and JT conceived of and designed the study. YW, WW, ZL, YLia, XL, YLi, ZT, and TJ collected and assembled all data. YW, WW, and ZL performed data analysis. WW, ZL, and YLia wrote the manuscript. YW revised the manuscript. All authors approved of the final manuscript.

FUNDING

This research was supported by the National Natural Science Foundation of China (81772012, 81922040, 81227901, and 61231004), the National Key R&D Program of China (2017YFA0205200, 2016YFA0100900, and 2016YFA0100902), the Beijing Municipal Natural Science Foundation (7182109), and the Youth Innovation Promotion Association CAS (2019136).

ACKNOWLEDGMENTS

The authors would like to acknowledge the instrumental and technical support of the multimodal biomedical imaging experimental platform at the Chinese Academy of Sciences Institute of Automation.

REFERENCES

1. Scheithauer BW, Fuller GN, VandenBerg SR. The 2007 WHO classification of tumors of the nervous system: controversies in surgical neuropathology. *Brain Pathol*. (2008) 18:307–16. doi: 10.1111/j.1750-3639.2008.00179.x
2. Schiff D. Molecular profiling optimizes the treatment of low-grade glioma. *Neuro Oncol*. (2016) 18:1593–4. doi: 10.1093/neuonc/now262
3. Avila EK, Chamberlain M, Schiff D, Reijneveld JC, Armstrong TS, Ruda R, et al. Seizure control as a new metric in assessing efficacy of tumor treatment in low-grade glioma trials. *Neuro Oncol*. (2017) 19:12–21. doi: 10.1093/neuonc/now190
4. van Breemen MS, Wilms EB, Vecht CJ. Epilepsy in patients with brain tumours: epidemiology, mechanisms, and management. *Lancet Neurol*. (2007) 6:421–30. doi: 10.1016/S1474-4422(07)70103-5
5. Chang EF, Potts MB, Keles GE, Lamborn KR, Chang SM, Barbaro NM, et al. Seizure characteristics and control following resection in 332 patients with low-grade gliomas. *J Neurosurg*. (2008) 108:227–35. doi: 10.3171/JNS/2008/108/2/0227
6. Maschio M, Dinapoli L. Patients with brain tumor-related epilepsy. *J Neurooncol*. (2012) 109:1–6. doi: 10.1007/s11060-012-0867-7
7. Weller M, Stupp R, Wick W. Epilepsy meets cancer: when, why, and what to do about it? *Lancet Oncol*. (2012) 13:e375–82. doi: 10.1016/S1470-2045(12)70266-8
8. Shan X, Fan X, Liu X, Zhao Z, Wang Y, Jiang T. Clinical characteristics associated with postoperative seizure control in adult low-grade gliomas: a systematic review and meta-analysis. *Neuro Oncol*. (2018) 20:324–31. doi: 10.1093/neuonc/nox130
9. Fisher RS, Cross JH, French JA, Higurashi N, Hirsch E, Jansen FE, et al. Operational classification of seizure types by the International League Against Epilepsy: Position Paper of the ILAE Commission for Classification and Terminology. *Epilepsia*. (2017) 58:522–30. doi: 10.1111/epi.13670
10. Lambin P, Rios-Velazquez E, Leijenaar R, Carvalho S, van Stiphout RG, Granton P, et al. Radiomics: extracting more information from medical images using advanced feature analysis. *Eur J Cancer*. (2012) 48:441–6. doi: 10.1016/j.ejca.2011.11.036
11. Lambin P, Leijenaar RTH, Deist TM, Peerlings J, de Jong EEC, van Timmeren J, et al. Radiomics: the bridge between medical imaging and personalized medicine. *Nat Rev Clin Oncol*. (2017) 14:749–62. doi: 10.1038/nrclinonc.2017.141
12. Bi WL, Hosny A, Schabath MB, Giger ML, Birkbak NJ, Mehrtash A, et al. Artificial intelligence in cancer imaging: clinical challenges and applications. *CA Cancer J Clin*. (2019) 69:127–57. doi: 10.3322/caac.21552
13. Lei C, Wei W, Liu Z, Xiong Q, Yang C, Yang M, et al. Mammography-based radiomic analysis for predicting benign BI-RADS category 4 calcifications. *Eur J Radiol*. (2019) 121:108711. doi: 10.1016/j.ejrad.2019.108711
14. Liu ZY, Wang S, Dong D, Wei JW, Fang C, Zhou XZ, et al. The applications of radiomics in precision diagnosis and treatment of oncology: opportunities and challenges. *Theranostics*. (2019) 9:1303–22. doi: 10.7150/thno.30309
15. Wei W, Liu Z, Rong Y, Zhou B, Bai Y, Wei W, et al. A computed tomography-based radiomic prognostic marker of advanced high-grade serous ovarian cancer recurrence: a multicenter study. *Front Oncol*. (2019) 9:255. doi: 10.3389/fonc.2019.00255
16. Wei W, Wang K, Liu Z, Tian K, Wang L, Du J, et al. Radiomic signature: a novel magnetic resonance imaging-based prognostic biomarker in patients with skull base chordoma. *Radiother Oncol*. (2019) 141:239–46. doi: 10.1016/j.radonc.2019.10.002
17. Xi YB, Guo F, Xu ZL, Li C, Wei W, Tian P, et al. Radiomics signature: a potential biomarker for the prediction of MGMT promoter methylation in glioblastoma. *J Magn Reson Imag*. (2018) 47:1380–7. doi: 10.1002/jmri.25860
18. Aerts HJWL, Velazquez ER, Leijenaar RTH, Parmar C, Grossmann P, Carvalho S, et al. Decoding tumour phenotype by noninvasive imaging using a quantitative radiomics approach. *Nat Commun*. (2014) 5:4006. doi: 10.1038/ncomms5006
19. Liu Z, Wang Y, Liu X, Du Y, Tang Z, Wang K, et al. Radiomics analysis allows for precise prediction of epilepsy in patients with low-grade gliomas. *NeuroImage Clin*. (2018) 19:271–8. doi: 10.1016/j.nicl.2018.04.024
20. Louis DN, Perry A, Reifenberger G, von Deimling A, Figarella-Branger D, Cavenee WK, et al. The 2016 World Health Organization classification of tumors of the central nervous system: a summary. *Acta Neuropathol*. (2016) 131:803–20. doi: 10.1007/s00401-016-1545-1
21. Fisher RS, van Emde Boas W, Blume W, Elger C, Genton P, Lee P, et al. Epileptic seizures and epilepsy: definitions proposed by the International League Against Epilepsy (ILAE) and the International Bureau for Epilepsy (IBE). *Epilepsia*. (2005) 46:470–2. doi: 10.1111/j.0013-9580.2005.66104.x
22. (1981). Proposal for revised clinical and electroencephalographic classification of epileptic seizures. From the Commission on Classification and Terminology of the International League Against Epilepsy. *Epilepsia* 22:489–501. doi: 10.1111/j.1528-1157.1981.tb06159.x
23. Li L, Mu W, Wang Y, Liu Z, Liu Z, Wang Y, et al. A non-invasive radiomic method using 18F-FDG PET predicts isocitrate dehydrogenase genotype and prognosis in patients with glioma. *Front Oncol*. (2019) 9:1183. doi: 10.3389/fonc.2019.01183
24. Li L, Wang K, Ma X, Liu Z, Wang S, Du J, et al. Radiomic analysis of multiparametric magnetic resonance imaging for differentiating skull base chordoma and chondrosarcoma. *Eur J Radiol*. (2019) 118:81–7. doi: 10.1016/j.ejrad.2019.07.006
25. Tibshirani R, Bien J, Friedman J, Hastie T, Simon N, Taylor J, et al. Strong rules for discarding predictors in lasso-type problems. *J R Stat Soc Series B Stat Methodol*. (2012) 74:245–66. doi: 10.1111/j.1467-9868.2011.01004.x
26. Sauerbrei W, Boulesteix AL, Binder H. Stability investigations of multivariable regression models derived from low- and high-dimensional data. *J Biopharm Stat*. (2011) 21:1206–31. doi: 10.1080/10543406.2011.629890
27. Collins GS, Reitsma JB, Altman DG, Moons KG. Transparent Reporting of a multivariable prediction model for Individual Prognosis or Diagnosis (TRIPOD): The TRIPOD Statement. *Eur Urol*. (2015) 67:1142–51. doi: 10.1016/j.eururo.2014.11.025
28. Iasonos A, Schrag D, Raj GV, Panageas KS. How to build and interpret a nomogram for cancer prognosis. *J Clin Oncol*. (2008) 26:1364–70. doi: 10.1200/Jco.2007.12.9791
29. Stallard N. Simple tests for the external validation of mortality prediction scores. *Stat Med*. (2009) 28:377–88. doi: 10.1002/sim.3393
30. Kramer AA, Zimmerman JE. Assessing the calibration of mortality benchmarks in critical care: the Hosmer-Lemeshow test revisited. *Crit Care Med*. (2007) 35:2052–6. doi: 10.1097/01.Ccm.0000275267.64078.B0
31. Vickers AJ, Elkin EB. Decision curve analysis: a novel method for evaluating prediction models. *Med Decis Making*. (2006) 26:565–74. doi: 10.1177/0272989X06295361
32. Gillies RJ, Kinahan PE, Hricak H. Radiomics: images are more than pictures, they are data. *Radiology*. (2016) 278:563–77. doi: 10.1148/radiol.2015151169
33. Lambin P, van Stiphout RG, Starmans MH, Rios-Velazquez E, Nalbantov G, Aerts HJ, et al. Predicting outcomes in radiation oncology—multifactorial decision support systems. *Nat Rev Clin Oncol*. (2013) 10:27–40. doi: 10.1038/nrclinonc.2012.196
34. Kim JY, Park JE, Jo Y, Shim WH, Nam SJ, Kim JH, et al. Incorporating diffusion- and perfusion-weighted MRI into a radiomics model improves diagnostic performance for pseudoprogression in glioblastoma patients. *Neuro Oncol*. (2018) 21:404–4. doi: 10.1093/neuonc/noy133
35. Wang S, Liu Z, Rong Y, Zhou B, Bai Y, Wei W, et al. Deep learning provides a new computed tomography-based prognostic biomarker for recurrence prediction in high-grade serous ovarian cancer. *Radiother Oncol*. (2019) 132:171–7. doi: 10.1016/j.radonc.2018.10.019
36. Shen C, Liu Z, Wang Z, Guo J, Zhang H, Wang Y, et al. Building CT radiomics based nomogram for preoperative esophageal cancer patients lymph node metastasis prediction. *Transl Oncol*. (2018) 11:815–24. doi: 10.1016/j.tranon.2018.04.005
37. Grossmann P, Narayan V, Chang K, Rahman R, Abrey L, Reardon DA, et al. Quantitative imaging biomarkers for risk stratification of patients with recurrent glioblastoma treated with bevacizumab. *Neuro Oncol*. (2017) 19:1688–97. doi: 10.1093/neuonc/nox092
38. Liu ZY, Zhang XY, Shi YJ, Wang L, Zhu HT, Tang ZC, et al. Radiomics analysis for evaluation of pathological complete response to neoadjuvant

chemoradiotherapy in locally advanced rectal cancer. *Clin Cancer Res*. (2017) 23:7253–62. doi: 10.1158/1078-0432.CCR-17-1038
39. Liu Z, Li Z, Qu J, Zhang R, Zhou X, Li L, et al. Radiomics of multi-parametric MRI for pretreatment prediction of pathological complete response to neoadjuvant chemotherapy in breast cancer: a multicenter study. *Clin Cancer Res*. (2019). doi: 10.1158/1078-0432.CCR-18-3190
40. Gevaert O, Mitchell LA, Achrol AS, Xu J, Echegaray S, Steinberg GK, et al. Glioblastoma Multiforme: Exploratory Radiogenomic Analysis by Using Quantitative Image Features. *Radiology*. (2015) 276:313. doi: 10.1148/radiol.2015154019
41. Itakura H, Achrol AS, Mitchell LA, Loya JJ, Liu T, Westbroek EM, et al. Magnetic resonance image features identify glioblastoma phenotypic subtypes with distinct molecular pathway activities. *Sci Transl Med*. (2015) 7:303ra138. doi: 10.1126/scitranslmed.aaa7582
42. Pallud J, Audureau E, Blonski M, Sanai N, Bauchet L, Fontaine D, et al. Epileptic seizures in diffuse low-grade gliomas in adults. *Brain*. (2014) 137:449–62. doi: 10.1093/brain/awt345
43. Lee JW, Wen PY, Hurwitz S, Black P, Kesari S, Drappatz J, et al. Morphological characteristics of brain tumors causing seizures. *Arch Neurol*. (2010) 67:336–42. doi: 10.1001/archneurol.2010.2
44. Wang YY, Zhang T, Li SW, Qian TY, Fan X, Peng XX, et al. Mapping p53 mutations in low-grade glioma: a voxel-based neuroimaging analysis. *AJNR Am J Neuroradiol*. (2015) 36:70–6. doi: 10.3174/ajnr.A4065
45. You G, Sha ZY, Yan W, Zhang W, Wang YZ, Li SW, et al. Seizure characteristics and outcomes in 508 Chinese adult patients undergoing primary resection of low-grade gliomas: a clinicopathological study. *Neuro Oncol*. (2012) 14:230–41. doi: 10.1093/neuonc/nor205

Conflict of Interest: The authors declare that the research was conducted in the absence of any commercial or financial relationships that could be construed as a potential conflict of interest.

frontiers in Oncology

ORIGINAL RESEARCH
published: 26 June 2020
doi: 10.3389/fonc.2020.00937

Radiomics Features Predict CIC Mutation Status in Lower Grade Glioma

Luyuan Zhang[1,2], *Felipe Giuste*[3], *Juan C. Vizcarra*[3], *Xuejun Li*[1] *and David Gutman*[4]*

[1] Department of Neurosurgery, Xiangya Hospital, Central South University, Changsha, China, [2] Department of Neurosurgery, First Affiliated Hospital, School of Medicine, Zhejiang University, Hangzhou, China, [3] Department of Biomedical Engineering of the Georgia Institute of Technology, Emory University, Atlanta, GA, United States, [4] Department of Neurology, Emory University, Atlanta, GA, United States

MRI in combination with genomic markers are critical in the management of gliomas. Radiomics and radiogenomics analysis facilitate the quantitative assessment of tumor properties which can be used to model both molecular subtype and predict disease progression. In this work, we report on the Drosophila gene capicua (CIC) mutation biomarker effects alongside radiomics features on the predictive ability of CIC mutation status in lower-grade gliomas (LGG). Genomic data of lower grade glioma (LGG) patients from The Cancer Genome Atlas (TCGA) ($n = 509$) and corresponding MR images from TCIA ($n = 120$) were utilized. Following tumor segmentation, radiomics features were extracted from T1, T2, T2 Flair, and T1 contrast enhanced (CE) images. Lasso feature reduction was used to obtain the most important MR image features and then logistic regression used to predict CIC mutation status. In our study, CIC mutation rarely occurred in Astrocytoma but has a high probability of occurrence in Oligodendroglioma. The presence of CIC mutation was found to be associated with better survival of glioma patients ($p < 1e{-}4$, HR: 0.2445), even with co-occurrence of IDH mutation and 1p/19q co-deletion ($p = 0.0362$, HR: 0.3674). An eleven-feature model achieved glioma prediction accuracy of 94.2% (95% CI, 94.03–94.38%), a six-feature model achieved oligodendroglioma prediction accuracy of 92.3% (95% CI, 91.70–92.92%). MR imaging and its derived image of gliomas with CIC mutation appears more complex and non-uniform but are associated with lower malignancy. Our study identified CIC as a potential prognostic factor in glioma which has close associations with survival. MRI radiomic features could predict CIC mutation, and reflect less malignant manifestations such as milder necrosis and larger tumor volume in MRI and its derived images that could help clinical judgment.

Keywords: glioma, radiomics, MRI, CIC, prediction

OPEN ACCESS

Edited by:
Fu Wang,
Xidian University, China

Reviewed by:
Yuming Jiang,
Stanford University, United States
Guolin Ma,
China-Japan Friendship Hospital, China

***Correspondence:**
David Gutman
dgutman@emory.edu

Specialty section:
This article was submitted to Cancer Imaging and Image-directed Interventions, a section of the journal Frontiers in Oncology

Received: *24 December 2019*
Accepted: *12 May 2020*
Published: *26 June 2020*

Citation:
Zhang L, Giuste F, Vizcarra JC, Li X and Gutman D (2020) Radiomics Features Predict CIC Mutation Status in Lower Grade Glioma. Front. Oncol. 10:937. doi: 10.3389/fonc.2020.00937

INTRODUCTION

Glioma is the most common primary tumor in the adult central nervous system (CNS). High-grade gliomas (grade IV) have poor median survival [~14 months (1)] compared with grade II and III (2). In 2016, the World Health Organization (3) updated its glioma classification scheme to incorporate genomic information including IDH (Isocitrate dehydrogenase) mutation and 1p/19q

codeletion (4). In addition to facilitating the diagnosis of gliomas, genomic information is also used in guiding the extent of surgical tumor resection and therapeutic strategy. In patients with IDH mutation, gross total resection (GTR) has been found to result in longer survival times compared to non-GTR (5, 6). Although confirming the genetic status of glioma is instructive for surgery and post-surgical treatment, it is still subject to methodological limitations. Neurosurgical biopsies during craniotomy are the current standard used to obtain genomic information about glioma. However, a single biopsy is unlikely to represent the full set of mutations present in the cancer due to high tumor genomic and histological heterogeneity (7–9). Therefore, there is a need to develop a method that can reflect the global characteristics of gliomas which is robust to regional variation and provides clinically actionable conclusions.

The homolog of the Drosophila gene capicua (CIC) gene is a member of the high mobility group (HMG)-box superfamily of transcriptional repressors on chromosome 19q. The role of CIC mutations in human disease is still unclear. It has been reported that CIC mutation promotes glioma cell proliferation, differentiation, and aggression and results in a poor outcome (10–12). However, Jiao et al. (13) found that patients with IDH mutations combined with either 1p19q loss, FUBP1 mutations, or CIC mutations will have longer overall survival than patients with IDH mutations combined with ATRX mutation. However, because CIC mutation is closely related to IDH mutation and 1p/19q co-deletion, whether CIC mutation is an independent prognostic factor remains to be clarified. In addition, CIC mutation tends to occur in oligodendroglioma but not in the astrocytoma (14, 15). But associated studies are mainly based on the 2007 WHO classification; whether these findings will remain when employing the latest 2016 WHO classification still needs to be explored.

Because of the heterogeneity of gliomas, genomic and histological data obtained from biopsies can fail at representing the entire glioma heterogeneity. Magnetic resonance imaging (MRI) provides a possibility to break this limitation, since information about the entire glioma can be obtained. VASARI (Visually AcceSAble Rembrandt Images) MRI features (16) and radiomics features (17) are two common methods to extract features from MR images. Radiomics is a process that converts digital medical images into mineable high-dimension data (18). It provides high-dimensional quantitative information and comprehensive information regarding tumor heterogeneity (18) that may fail to be appreciated by the naked eye of radiologists. Radiogenomics is an emerging field that explores the associations between radiomics and genomics (19). IDH mutation and 1p/19q codeletion have been predicted accurately by radiomics features (20–23), but there has been no reports using radiomics features to predict CIC mutation. Another obstacle of radiomics features is that they are difficult to understand and cannot be related to tumor physiological changes (24).

In this study we aim to identify the value of CIC mutations in gliomas by analyzing the relationship between CIC mutations and the clinical characteristics, key molecular markers, and patient survival. Then, by extracting radiomics features from lower-grade glioma MRI, a robust CIC mutation prediction model is established. The relationship between key features and glioma structural changes in MRI is analyzed to explore the possible physiological changes of gliomas behind structural changes.

MATERIALS AND METHODS

Data Sources

A total of 516 lower-grade glioma (LGG) patients' genomic data and clinical data were downloaded from the TCGA data portal [https://portal.gdc.cancer.gov/]. Among these 516 TCGA patients, 199 patients have MR images stored in the Cancer Imaging Archive (TCIA) (25). Additional genomic and clinical metadata of TCGA was obtained through cBioPortal (26, 27). In addition, the genomics dataset of glioblastoma was also obtained from cBioPortal. All TCGA related data were previously anonymized and are publicly available.

Genomics Data

All genomic data were downloaded from the TCGA dataset. Single nucleotide polymorphism (SNP) data was used to identify gene mutations, including CIC and IDH. Missense, frameshift, and nonsense mutations were included in the definition. Copy number variation (CNV) data was used to identify 1p/19q co-deletion status. A segment mean value < -0.2 was considered as deletion in the corresponding region (28). Because TCGA CNV probes didn't cover the whole chromosome, 1p/19q codeletion status was derived using copy number data as shown in (29).

Histological Type

There are two different WHO CNS tumor classifications, namely from 2007 and 2016. The 2007 classification used in the TCGA defines the histological types as Astrocytoma, Oligodendroglioma, and Oligoastrocytoma. The 2016 classification incorporated molecular biomarkers in their classification scheme, mainly IDH mutation and 1p/19q co-deletion. Oligodendroglioma is defined as Glioma with IDH mutation and 1p/19q co-deletion, and Diffuse Astrocytoma is defined as glioma with IDH mutation but without 1p/19q co-deletion or IDH wild-type (3) (**Figure S1**).

Image Pre-processing

Quality control (QC) was done manually by reviewing images on a local instance of the Digital Slide Archive (DSA) (30), which allows the rapid review of DICOM files. MRIcron (31) was then used to convert all images from DICOM format to NIFTI format for subsequent analysis.

Image Masking

The FSL image viewer (FSLeyes 0.10.1) (32) was used to draw regions of interest (ROIs) slice-by-slice. A total of 120 T1-weighted (T1W), T1 contrast-enhanced (T1CE), and T2-weighted (T2W) image ROI masks, and FLAIR image ROI masks were generated. All radiomic features were extracted using the T1W image ROI mask.

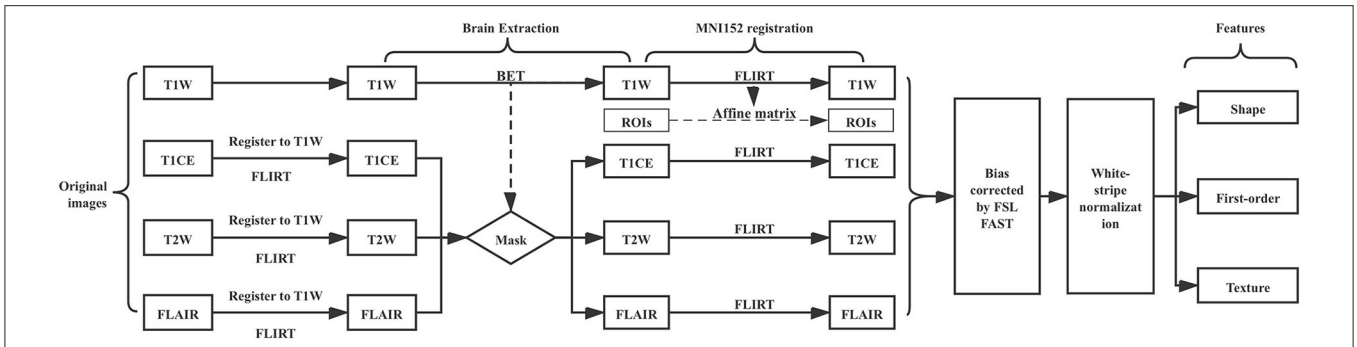

FIGURE 1 | MRI preprocessing pipeline.

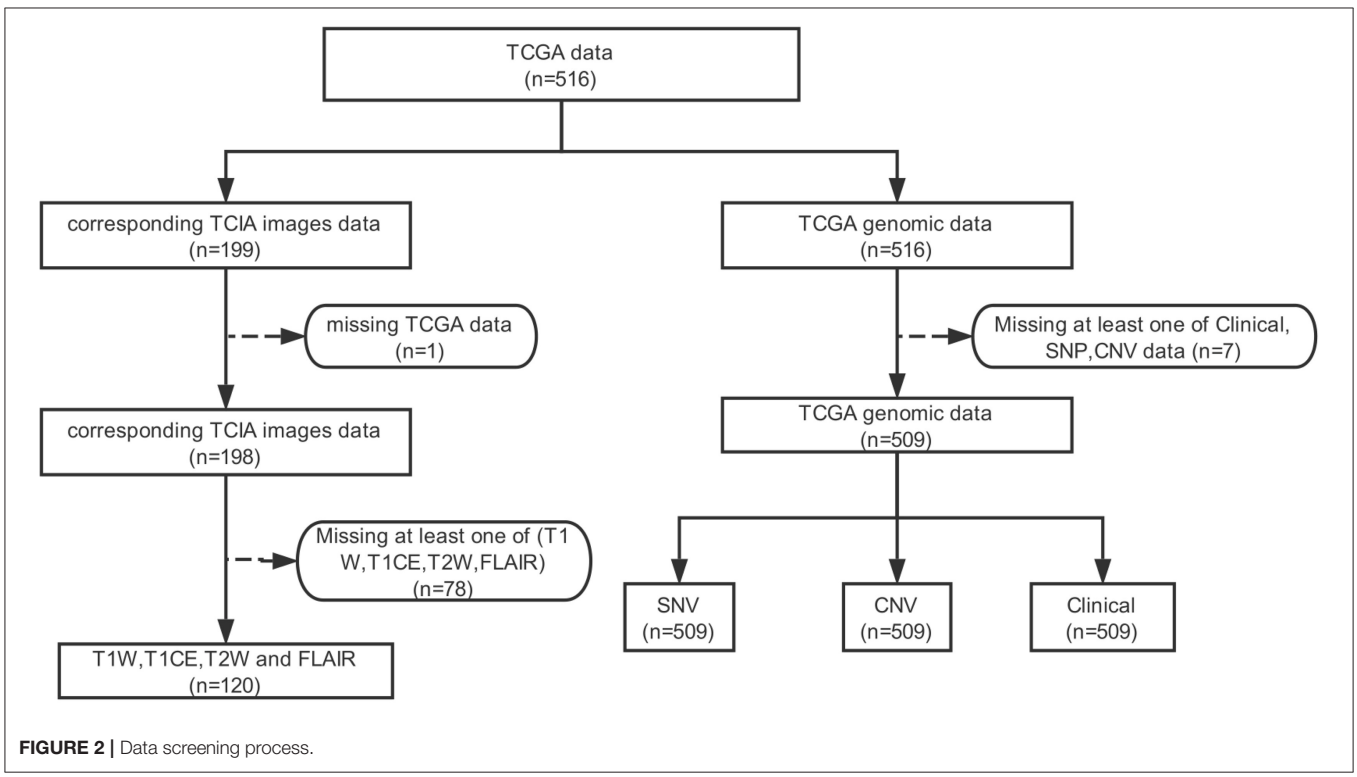

FIGURE 2 | Data screening process.

Image Processing Pipeline

The image processing pipeline is illustrated in (**Figure 1**). First, we used the FSL Brain Extraction Tool (BET) to remove the skull, eyes, and other non-brain tissue within T1W images (33). We found that the quality of lower-grade glioma images from the TCIA is variable, oftentimes resulting in poor brain extraction using BET. To address this limitation, we manually corrected the BET extraction results to be consistent between images. This approach allowed us to obtain good quality brain tissue masks while speeding up the process in comparison to completely manual brain mask delineation. We used the T1W brain region as a mask to get T1CE, T2, and FLAIR images' brain tissue after we registered T1CE, T2W, and FLAIR to T1W images. FSL FLIRT was used for image registration. In order to make all patients' images comparable, we registered all images and masks to the 1 mm MNI152 atlas. Registered images were bias corrected by FSL FAST. White-stripe normalization (34) was conducted to normalize image intensities.

Feature Extraction

Radiomics features were extracted using the Python package PyRadiomics V2.0.0 (35). PyRadiomics can perform various transformations on the original input image prior to extracting features. The transformations we used include: Original, Wavelet, Square, Square Root, Logarithm, Exponential, Gradient, Local Binary Pattern 2D (2D-LBP), and Local Binary Pattern 3D (3D-LBP). After image transformations, 105 radiomics features can be extracted from each transformed image using PyRadiomics, these features are summarized in **Table S1**. In 3D-LBP images, a rotational invariant operator using spherical harmonics was

utilized. Three different radii for the spherical harmonics were used, with radius similar to those used in 2D-LBP images, resulting in three different 3D-LBP images. The information stored in the transformed images of different radii in 3D-LBP is different. In wavelet transformed images, each dimension in the 3D image was divided into high frequency components (H) and low frequency components (L). Combining the H and L of three different dimensions of the 3D image can produce eight different combinations: LLL, LLH, LHL, LHH, HLH, HHL, HLL, HHH.

Feature Selection

LassoCV in the scikit-learn Python package was used for radiomics feature selection (36). It combines cross-validation (CV) and Lasso regression. The advantage of LassoCV is that it does not need to manually set regularization coefficient (λ). It can try the default series of λ through CV iteration, and then automatically select the best model (**Figure S2**). In LassoCV, to avoid selection bias due to the low proportion of CIC mutations, we used stratified sampling. Both 10-fold CV and 5-fold CV are common (37) but limited by the number of CIC mutation samples, the variance of the 10-fold CV will be great (38), so we choose 5-fold CV. "StratifiedKFold" in the scikit-learn Python package was used. Before the CV splitter splits the samples, all samples are shuffled.

Because of 5-fold CV and data shuffle, only 80% of the total samples were used to train the Lasso model, and these samples should be different each time the Lasso model is built (**Figure S2**). In addition, for some highly relevant features, Lasso will randomly select one and exclude the others. This results in the features selected by LassoCV

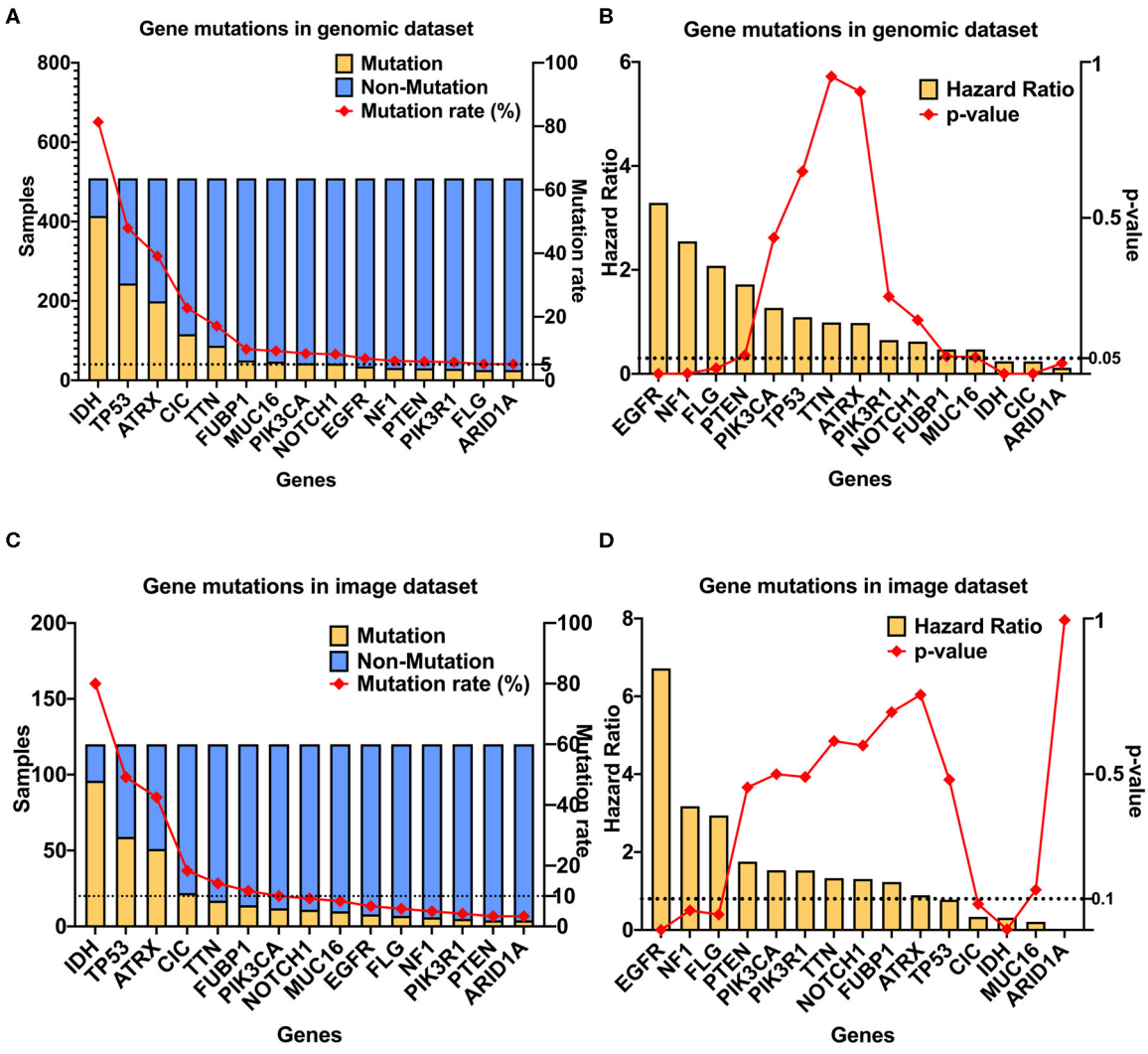

FIGURE 3 | CIC mutation has a high occurrence rate and association with survival in LGG. **(A)** CIC mutation rate in gliomas. GBM, GBM dataset from cBioPortal (TCGA Cell 2103); LGG (509), TCGA LGG dataset; LGG (120), from TCIA. **(B)** Gene mutations in the TCGA dataset ($n = 509$), 15 gene mutation rates are >5%. **(C)** Gene mutations in the TCIA image dataset ($n = 120$), 12 gene mutation rates are >5%. **(D)** Multivariate Cox regression result of gene mutations in the genomic dataset, age was included as covariate. Only seven gene mutations are significant.

TABLE 1 | Associations between CIC mutation presence and clinical characteristics.

Clinical characteristic	Subgroup	CIC mutation	CIC wild-type	*P*-value[a]
Age	<50 years old	68	278	0.01398
	≥50 years old	48	115	
Gender	Female	58	169	0.1828
	Male	58	224	
Grade	G2	67	180	0.02356
	G3	49	213	
KPS[b]	<90	17	75	0.3212
	≥90	48	155	
Cancer status	With tumor	53	216	0.1629
	Tumor free	45	133	
Tumor location	Frontal	81	217	0.003967
	Temporal	19	126	
	Parietal	11	35	
Laterality	Left	55	191	0.6083
	Right	61	190	
Seizures	Yes	73	224	0.3592
	No	37	140	
Headaches	Yes	27	142	0.0119
	No	76	215	
Mental status changes	Yes	21	92	0.2295
	No	82	259	
Visual changes	Yes	9	56	0.06461
	No	94	294	
Sensory changes	Yes	10	62	0.05633
	No	91	286	
Motor movement changes	Yes	29	81	0.304
	No	74	268	
First symptom	Seizures	57	188	0.5352
	Headaches	18	87	
	Mental status changes	8	31	
	Visual changes	3	9	
	Sensory changes	3	15	
	Motor movement changes	12	26	

[a] *Chi-square test p-value.*
[b] *KPS, Karnofsky Performance Score: an assessment tool for functional impairment.*

not being the same every time. But the probability of important features being selected is always large, so we repeated LassoCV 100 times (**Figure S3**). The selected features and its coefficient each time were recorded. The features whose sum of the coefficients unequal to zero are included. Features are sorted according to the number of times selected, and the top $\sqrt[3]{n}$ (n: sample size) (39) features are selected, so, $11(\sqrt[3]{120})$ and $6(\sqrt[3]{35})$ radiomics features were used to predict the CIC mutation in glioma and oligodendroglioma, respectively.

In order to detect the collinearity between the radiomics features, we performed a Pearson product moment correlation coefficient analysis between the radiomics features, then clustered the correlation coefficients between the features, and then used the clustermap to visualize.

Texture-Based CIC Prediction

A logistic regression model, defined by the function below, was created in Python utilizing the SciKit-Learn package:

$$h_\theta(\chi) = \frac{1}{1+e^{-z}}$$

In the model, $h_\theta(\chi)$ is the estimated probability of CIC mutation status. CIC mutation presence is defined as one, and absence is defined as zero. z represents ordinary linear regression:

$$z = \theta_0 + \theta_1\chi_1 + \theta_2\chi_2 + \theta_3\chi_3 ... + \theta_n\chi_n$$

z is the dependent variable. n represents the number of features. $(\chi_1,\chi_2,\chi_3...\chi_n)$ is independent variables. $(\theta_1,\theta_2,\theta_3...\theta_n)$ is features' partial regression coefficient. $\theta_0$is the intercept of the linear model.

Because the CIC mutation in our dataset is unbalanced, the weight of two classes are corrected by: n_samples / [n_classes * n_label (CIC mutant or CIC wild-type)]. All features were z-scored before being placed in the model. Because the unit differences between features are eliminated, the coefficients of each feature in the prediction model represent the importance of the feature in the model.

Statistics

Univariate Cox regression was used to find associations between gene mutation and survival. To analyze the classification, clinical characteristics, and other known molecular markers of gliomas and the relationship between CIC mutations, we used the two-sided Chi-square test. To analyze the prognostic value of CIC mutations as molecular markers, we used Log-rank test, Kaplan-Meier survival analysis, and multivariate COX regression analysis. We used the Log-rank test to analyze the relationship between IDH mutation, 1p/19q co-deletion and CIC mutation and overall survival, and Kaplan-Meier survival analysis curve to visualize. To identify whether the CIC mutation is an independent prognostic factor, multivariate Cox tests were used, including age, gender, grade, histological type, IDH mutation, 1p/19q codeletion, and FUBP1 mutation as covariates. The differences were considered significant if the p-value was < 0.05. The image dataset was stratified random sampling into training and testing sets (80% train, 20% test). Training set was used to train the logistic model and the test set was used to test model performance. Because of the stratified random split of the dataset, there will be differences between the training set and the test set each time, resulting in different trained

logistic regression models and prediction results, so we repeat the above process 1,000 times (**Figure S4**). Then we will obtain 1,000 logistic regression models trained by different training sets and the corresponding prediction results. So we sum coefficients of each feature of these 1,000 models as the importance of features. The mean AUC, prediction accuracy, sensitivity, and specificity of model were calculated for the testing set. Receiver operating characteristic (ROC) curve and Precision-recall (PR) curve analysis was conducted to evaluate the models. The coordinate points of the ROC curve and PR curve of 1,000 prediction models are averaged to obtain the average ROC curve and PR curve. The optimal cutoff value in the ROC curve and PR curve is the coordinate point closest to the upper left corner (0,1.0) and the upper right corner (1.0,1.0), respectively (40).

Image Analysis

In order to evaluate the importance of radiomics features and its correlation with CIC mutations, we used the Mann-Whitney *U*-test to test features in the logistic model. *U*-test was performed on the features value of CIC mutation and wild-type samples. Significance was defined as $p < 0.05$. The radiomics features that are significant in *U*-test and ranked in top 1/3 by importance were used for further analysis. So 3 (11/3) radiomics features from the CIC mutation prediction model in glioma and 2 (6/3) radiomics features from the CIC mutation prediction model in oligodendroglioma will be selected. Images corresponding to the maximum and minimum values of the most significant features were selected. Because some radiomics features were extracted from transformed image, for these features, we show the transformed image but not the original input image. The

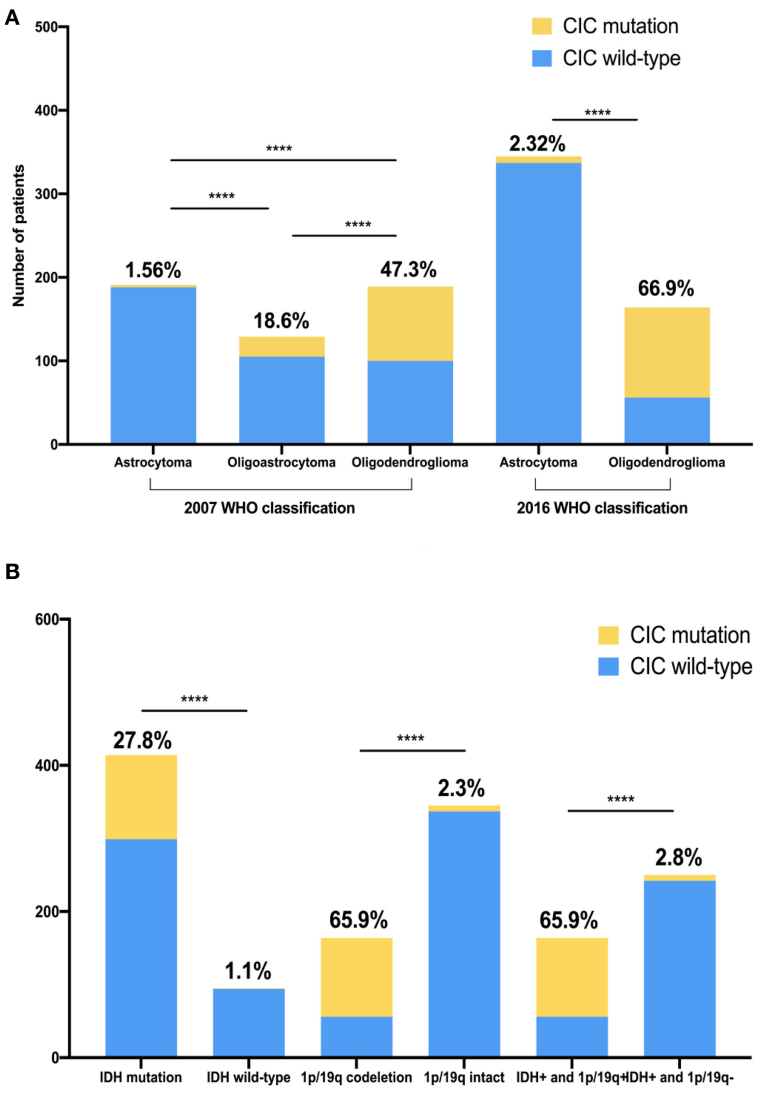

FIGURE 4 | CIC mutation rate is unequal in different glioma classifications and genotypes. **(A)** CIC mutation in two different WHO CNS tumor classifications. **(B)** CIC mutation in different genotype glioma. IDH+, IDH mutation; 1p/19q+, 1p/19q codeletion; 1p/19q-, 1p/19q intact. The value above the bar is the ratio of CIC mutation. Chi-square test, ****$P < 0.0001$.

probability estimates of each sample in the test set results of above mentioned 1,000 logistic regression models are summed, and then the average probability estimates of each sample are obtained. The samples with the largest and smallest average probability estimates are selected. The original T1W, T1CE, T2, and FLAIR images but not transformed images of these two

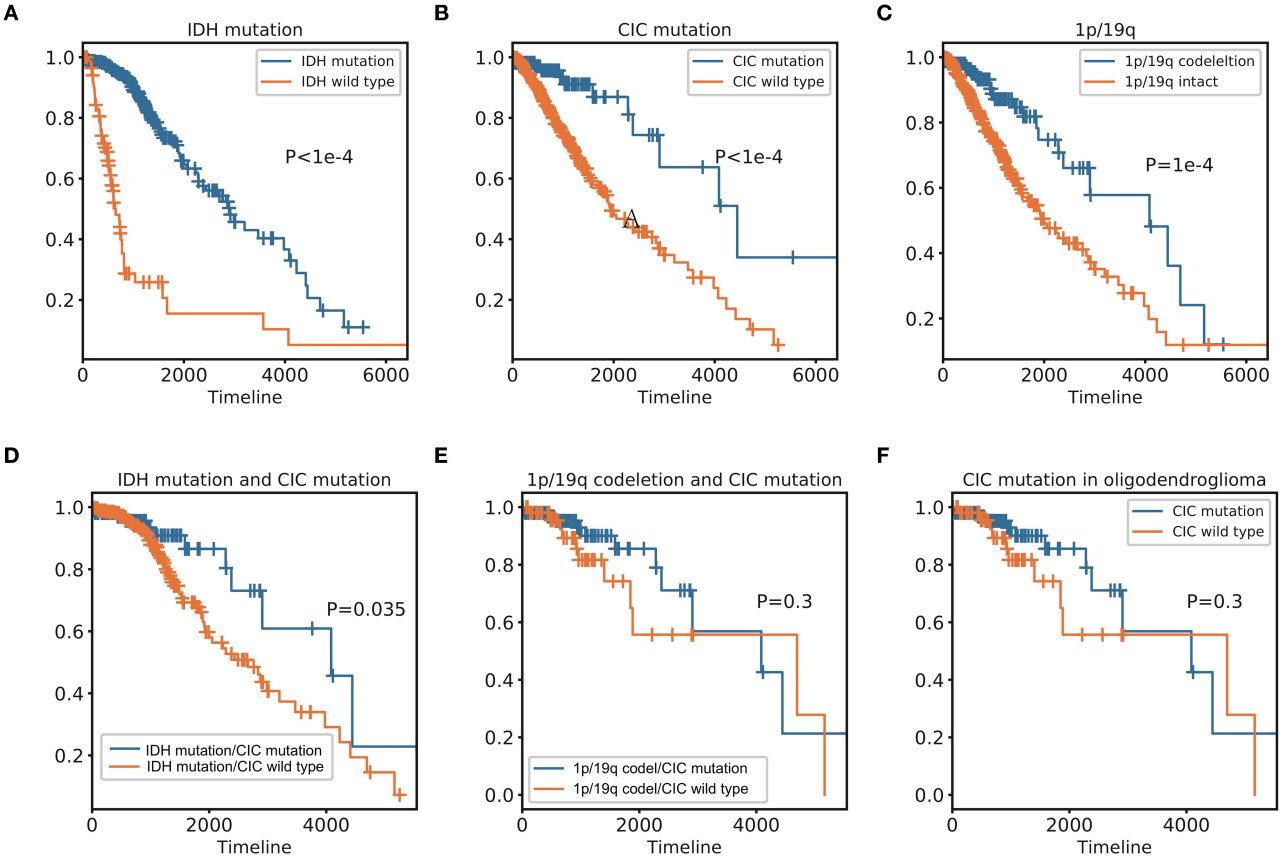

FIGURE 5 | Kaplan Meier curve and Log-Rank test of IDH, 1p/19q, and CIC. **(A)** IDH mutation Kaplan-Meier curve shows that patients with IDH mutation have a significantly better prognosis than IDH wild type. **(B)** CIC mutation Kaplan-Meier curve shows that patients with CIC mutation have significantly longer OS than those whose CIC is wild type. **(C)** Patients with 1p/19q codeletion have significantly longer OS than those without 1p/19q codeletion. **(D)** Patients with IDH and CIC mutation have longer OS than patients have IDH mutation only. **(E)** There is no significant difference in OS between CIC mutation and CIC wild-type of patients with 1p/19q codeletion. **(F)** 2016 classification Oligodendroglioma. In the Log-Rank test, there is no significant survival difference between patients with and without CIC mutation.

TABLE 2 | Survival analysis results.

	Status	OS (median)[a]	Patients	Logrank_p[b]	Cox_p[c]	HR[d]
IDH	Mutant	2,907	414	<1e-4	<1e-4	0.3173
	Wild-type	648	95			
CIC	Mutant	4,445	116	<1e-4	<1e-4	0.2445
	Wild-type	1,933	393			
1p/19q	Codeletion	4,084	164	1e-4	0.3246	0.3322
	Intact	2,000	345			
IDH mutant	1p/19q codeletion	4,084	164	0.1646	0.7011	0.8639
	1p/19q intact	2,660	345			
IDH mutant	CIC mutant	4,084	116	0.035	0.0287	0.4178
	CIC wild-type	2,660	393			

[a] *OS (median), the median overall survival time of the Kaplan Meier curve.*
[b] *Logrank_p, p-value of Log-Rank test.*
[c] *Cox_p, p-value of the Multivariate Cox test, including age, gender, grade, histological type, IDH mutation, 1p/19q codeletion, CIC mutation.*
[d] *HR, hazard ratio from the Multivariate Cox test.*

TABLE 3 | Associations between CIC mutation and OS of patients with Oligodendroglioma.

Classification	Subgroup	OS (median)	Logrank_p[b]	Cox_p[c]	HR[d]
Oligodendroglioma[a]	CIC mutant	4,695	0.2992	0.0362	0.3674
	CIC wild-type				

[a] *Oligodendroglioma, 2016 WHO CNS tumor classification.*
[b] *Logrank_p, p-value of Log-Rank test.*
[c] *Cox_p, p-value of the Multivariate Cox test, including age, gender, grade, histological type, IDH mutation, 1p/19q codeletion, CIC mutation e.*
[d] *HR, hazard ratio from the Multivariate Cox test.*

samples were shown. Because the radiomics feature represents the information of the entire glioma, but the 3D image is not conducive to display, so we choose the one with the largest ROI area in the transverse plane slice to represent the entire glioma.

RESULTS

Data Summary

Of the lower-grade gliomas cases downloaded from TCGA, 509 cases had CNV data, SNP data, and clinical data. This 509 cohort was used as our genomics dataset. One hundred ninety-nine MRI cases were downloaded from TCIA, 78 of which were removed due to the lack of at least one of T1W, T1CE, T2W, and FLAIR MRI, and one sample was removed due to the lack of corresponding genomic data in TCGA. A total of 120 cases remained and was used as the image dataset (**Figure 2**, **Table S2**). The two cohorts used in this work (TCGA LGG cohort and TCIA imaging cohort) did not differ significantly, with the exception of patient age (42.9 vs. 45.9; $p = 0.0356$) (**Table S2**).

Identification of Mutation Frequency in the LGG Cohort

The cBioPortal was used to obtain information on multiple glioblastoma databases. Through the glioblastoma dataset in cBioPortal, we found that the incidence of CIC mutations in glioblastoma is low (0.3%). Our genomic dataset had a higher incidence of CIC mutations (22.8%), similar to the incidence of CIC mutations found in the imaging dataset (18.3%) (**Figure S5**). SNP was downloaded from the TCGA data portal for LGG patients, which identifies 14,014 unique SNPs. Among these, only 15 occurred in > 5% of patients (25 of 509 total patients) (**Figure 3A**). Six of these SNPs were significantly associated with overall patient survival. Among these six, EGFR (HR: 5.04, 95%CI: 3.16–8.02), NF1 (HR: 2.84, 95%CI: 1.64–4.91), and FLG (HR: 2.07, 95% CI: 1.13–3.78) mutation were associated with poor survival. IDH (HR: 0.17, 95% CI: 0.12–0.24), CIC (HR: 0.30, 95% CI: 0.17–0.55), and ARID1A (HR: 0.11, 95% CI: 0.02–0.80) mutation were found to improve survival (**Figure 3B**). We focused on genes that were present in at least 5% or more LGG cases for the genomic dataset. But on the imaging dataset, since the number of samples is smaller, we looked for genes present in at least 10% of the cases. Similarly, we also adjusted the *p*-value of survival regression to 0.1. In the imaging dataset, there are a total of seven gene mutations with an incidence rate >10%, namely IDH, TP53, ATRX, CIC, FUBP1, TTN, and PIK3CA mutation (**Figure 3C**). However, when considering only the samples in the imaging dataset, only IDH mutations ($p = 0.0023$, HR = 0.3166) and CIC mutations ($p = 0.0831$, HR = 0.3387) were significantly associated with survival (**Figure 3D**). Since IDH mutation has been the focus of previous studies (20, 41, 42), with high accuracy prediction results reported, we chose to focus on CIC mutation for our analysis. In conclusion, CIC mutation is the only molecular marker other than IDH mutation that satisfies the sufficiently large incidence, prognostic value, and conditions of radiomics prediction.

Association Between CIC Mutations and Clinical Data

We analyzed the association between CIC mutations and clinical data in the genomics dataset. CIC mutations have close association with age, the probability of patients 50 years or older having CIC mutations is significantly greater than those <50 years old ($p = 0.0140$). The probability of grade 2 patients having CIC mutation is significantly greater than grade 3 patients ($p = 0.0236$). CIC mutation also have close association with the glioma location ($p = 0.003967$), the probability of CIC mutations in the temporal lobe is significantly lower than that in the frontal lobe ($p = 0.0009$) and the temporal lobe ($p = 0.0792$), but there is no significant difference between the frontal lobe and parietal lobe ($p = 0.6411$). CIC mutations are also related to clinical symptoms, the probability of samples without headache having CIC mutations is significantly greater than the probability of samples with headache ($p = 0.0119$), and there is a possible trend that the probability of CIC mutation in samples without visual change is greater than samples with visual changes ($p = 0.0646$), there is also a strong tendency that the probability of CIC mutation in samples without sensory change is greater than samples with sensory change ($p = 0.0563$) (**Table 1**).

The TCGA classification for the glioma cohort is given using the 2007 WHO classification criteria. We reclassified all cases in our cohorts using the 2016 WHO classification criteria. CIC mutation was found in 65.9% of oligodendrogliomas and 2.32% of diffuse astrocytoma. The probability of CIC mutation occurring in oligodendroglioma is significantly greater than that in diffuse astrocytoma ($p < 1e{-}4$) (**Figure 4A**, **Table S3**).

Associations Between CIC Mutation and Genomic Data

We analyzed the association between CIC mutations and genomic data in the genomics dataset. CIC mutations are also closely related to some important molecular markers. IDH wild-type and CIC mutation is mutually exclusive. IDH mutation is found in nearly all patients with CIC mutation (99.1%) but only 1.1% IDH wild-type patients have CIC mutation. Similarly, almost all patients with CIC mutations have 1p/19q co-deletion (93.1%) but the proportion of CIC mutations in 1p/19q intact patients was only 2.32%, the probability of CIC mutations in 1p/19q co-deletion samples was significantly greater than 1p/19q intact samples ($p < 1e{-}4$). 78% of FUBP1 mutation patients

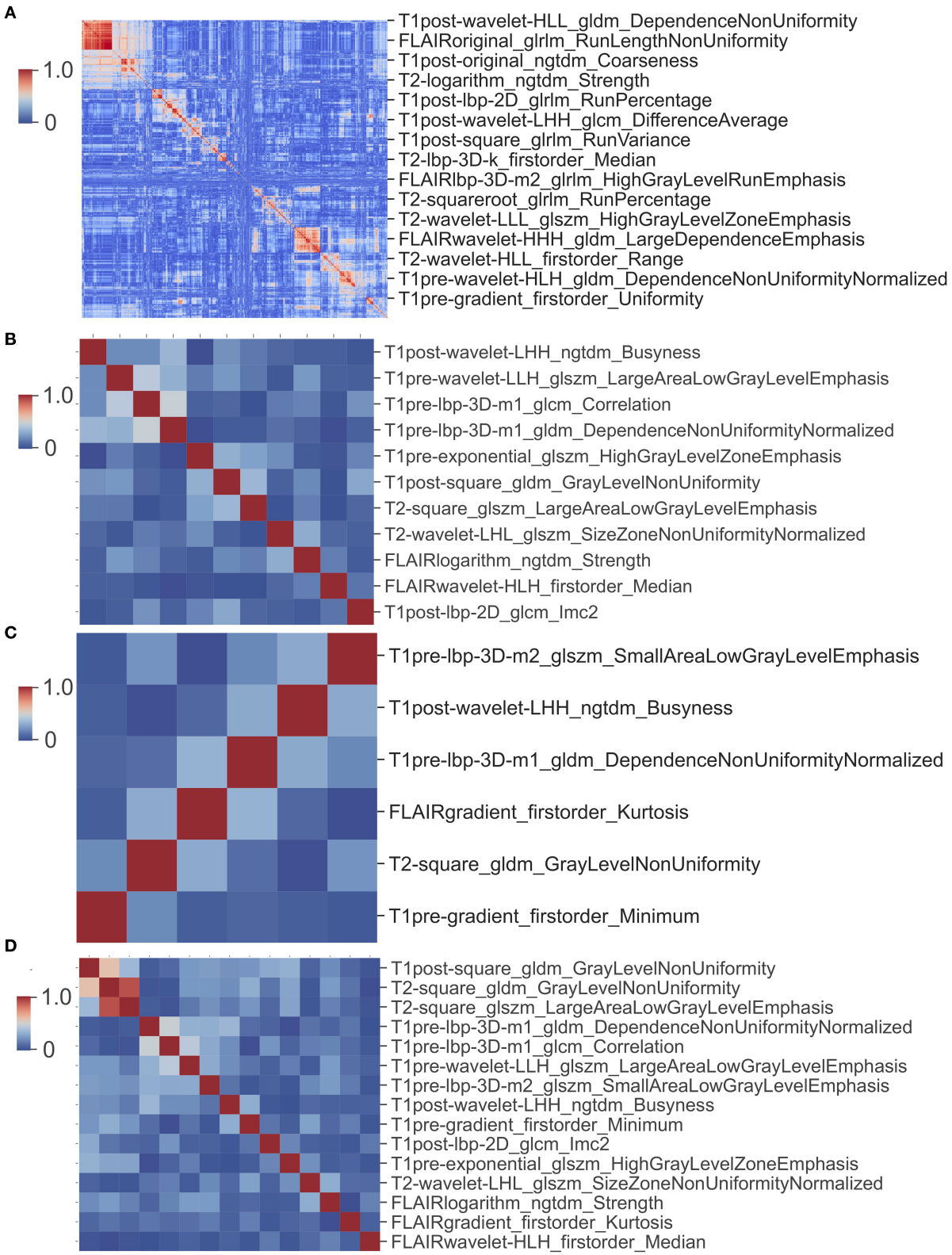

FIGURE 6 | Cluster map of correlation between image features. **(A)** Cluster map of correlation of 6,676 image features. **(B)** Cluster map of correlation of 11 features used in glioma CIC mutation prediction model. **(C)** Cluster map of correlation of six features used in oligodendroglioma CIC mutation prediction model. **(D)** Cluster map of correlation between 15 image features from **(B)** and **(C)**.

TABLE 4 | Eleven features used to predict CIC mutation in gliomas.

No.	Features	Importance[a]	*P*-value[b]
1	T2-wavelet-LHL_glszm_SizeZoneNonUniformityNormalized	2011.95	<10e-4
2	T1post-wavelet-LHH_ngtdm_Busyness	1842.85	0.0047
3	T1post-square_gldm_GrayLevelNonUniformity	1505.67	0.1402
4	FLAIR-wavelet-HLH_firstorder_Median	1046.31	0.0162
5	T2-square_glszm_LargeAreaLowGrayLevelEmphasis	1029.85	0.2475
6	T1pre-lbp-3D-m1_glcm_Correlation	935.72	0.0006
7	FLAIR-logarithm_ngtdm_Strength	758.25	0.5041
8	T1pre-wavelet-LLH_glszm_LargeAreaLowGrayLevelEmphasis	407.44	0.4334
9	T1post-lbp-2D_glcm_Imc2	−374.89	0.0013
10	T1pre-exponential_glszm_HighGrayLevelZoneEmphasis	270.67	0.0313
11	T1pre-lbp-3D-m1_gldm_DependenceNonUniformityNormalized	203.2	0.0009

[a]*Importance, Sum of coefficients of features in 1,000 prediction models.*
[b]*P-value: Mann-Whitney U-test p-value.*

had CIC mutation but the proportion of CIC mutations in FUBP1 wild-type patients was only 16.78%, the probability of CIC mutation in FUBP1 mutant samples is significantly greater than that of FUBP1 wild-type samples ($p < 1e{-}4$). Among the patients with CIC mutation, 93.1% had IDH mutation combined with 1p/19q co-deletion. 68.35% patients with IDH mutation combined with 1p/19q co-deletion had CIC mutation, but 2.28% other patients had CIC mutations. Patients with IDH mutation combined with 1p/19q co-deletion had a significantly higher probability of having CIC mutations than other samples ($p < 1e{-}4$) (**Figure 4B**, **Table S3**).

Associations Between Overall Survival and CIC Mutation

In genomic dataset, IDH mutation patients have longer overall survival (OS) than IDH wild-type patients ($p < 1e{-}4$, Median OS (days): 2,907 vs. 648) (**Figure 5A**), CIC mutation patients have longer OS than CIC wild-type patients ($p < 1e{-}4$, Median OS (days): 4,445 vs. 1,933) (**Figure 5B**), 1p/19q codeletion patients have longer OS than 1p/19q intact patients ($p = 1e{-}4$, Median OS (days): 4,084 vs. 2,000) (**Figure 5C**, **Table 2**). Patients with IDH mutation combined CIC mutation have longer OS than those with IDH mutation only ($p = 0.035$, Median OS (days): 4,084 vs. 2,660) (**Figure 5D**), and there is also no significant difference between 1p/19q co-deletion patients with and without CIC mutation in our study ($p = 0.3$) (**Figure 5E**). Multivariate cox analysis including age, gender, grade, histological type, IDH mutation, 1p/19q codeletion and CIC mutation showed that IDH mutation and CIC mutation are both associated with better prognosis ($p < 1e{-}4$, HR = 0.3173; $p < 1e{-}4$, HR = 0.2445), and 1p/19q codeletion is not an independent prognostic factor ($p = 0.3246$, HR = 0.3322). Patients with IDH mutation combined 1p/19q codeletion don't have significant differences in OS with those with IDH mutation only ($p = 0.1646$, Median OS: 4,084 vs. 2,660) (**Table 2**). In log-rank test, CIC mutation doesn't show a significant association with OS in oligodendroglioma ($p = 0.2992$) (**Figure 5F**), but the multivariate cox analysis shows CIC mutation improves survival ($p = 0.0362$, HR = 0.3674) (**Table 3**).

Image Feature Extraction and CIC Mutation Prediction

A total of 1,669 features were extracted from each image (**Table S1**) and a total of 6,676 imaging features from T1W, T1CE, T2W, and FLAIR for each patient. The cluster map of the correlation of 6,676 features shows that there is collinearity between these features, but the collinearity is not very strong. Features can be clustered into some modules, but the size of modules are relatively small (**Figure 6A**). There is only one large module in the top-left (**Figure 6A**), but none of features in this module were selected to build the model.

For the prediction of CIC mutation in glioma, a total of 11 features were selected via Lasso regularization to build a logistic regression model (**Table 4**). The cluster map of the correlation of 11 features shows that the collinearity between features is weak (**Figure 6B**). The mean accuracy of the 1,000 repetition data split was 94.2% (95% CI, 94.03–94.38%), significantly higher than the no-information rate (81.7%). The mean AUC of the ROC curve was 0.985 (95% CI, 0.9841–0.9857) (**Figure 7**). The optimal cutoff value (0.0606) of the ROC curve exhibited a sensitivity, specificity, and accuracy of 94.83, 93.94, and 94.10%, respectively. The mean AUC of the Precision Recall (PR) curve is 0.923 (95% CI, 0.9183–0.9275). The optimal cutoff value (0.8485) of the PR curve exhibited sensitivity, precision, and accuracy of 84.85, 89.51, and 95.4%, respectively.

For the prediction of CIC mutation in Oligodendroglioma, a total of six features from 35 Oligodendroglioma patients were selected via Lasso regularization to build a logistic regression model (**Table 5**). The cluster map of the correlation of six features shows that the collinearity between features is weak (**Figure 6C**). There are two features that overlap with the 11 features set above. The cluster map of the correlation of 15 features shows that the collinearity between features is weak except T2-square_glszm_LargeAreaLowGrayLevelEmphasis and T2-square_gldm_GrayLevelNonUniformity (**Figure 6D**). The mean accuracy of the 1,000 repetition data split was 92.3% (95% CI, 91.70–92.92%), significantly higher than the no-information rate (62.9%). The mean AUC of the ROC curve is 0.967 (95% CI,

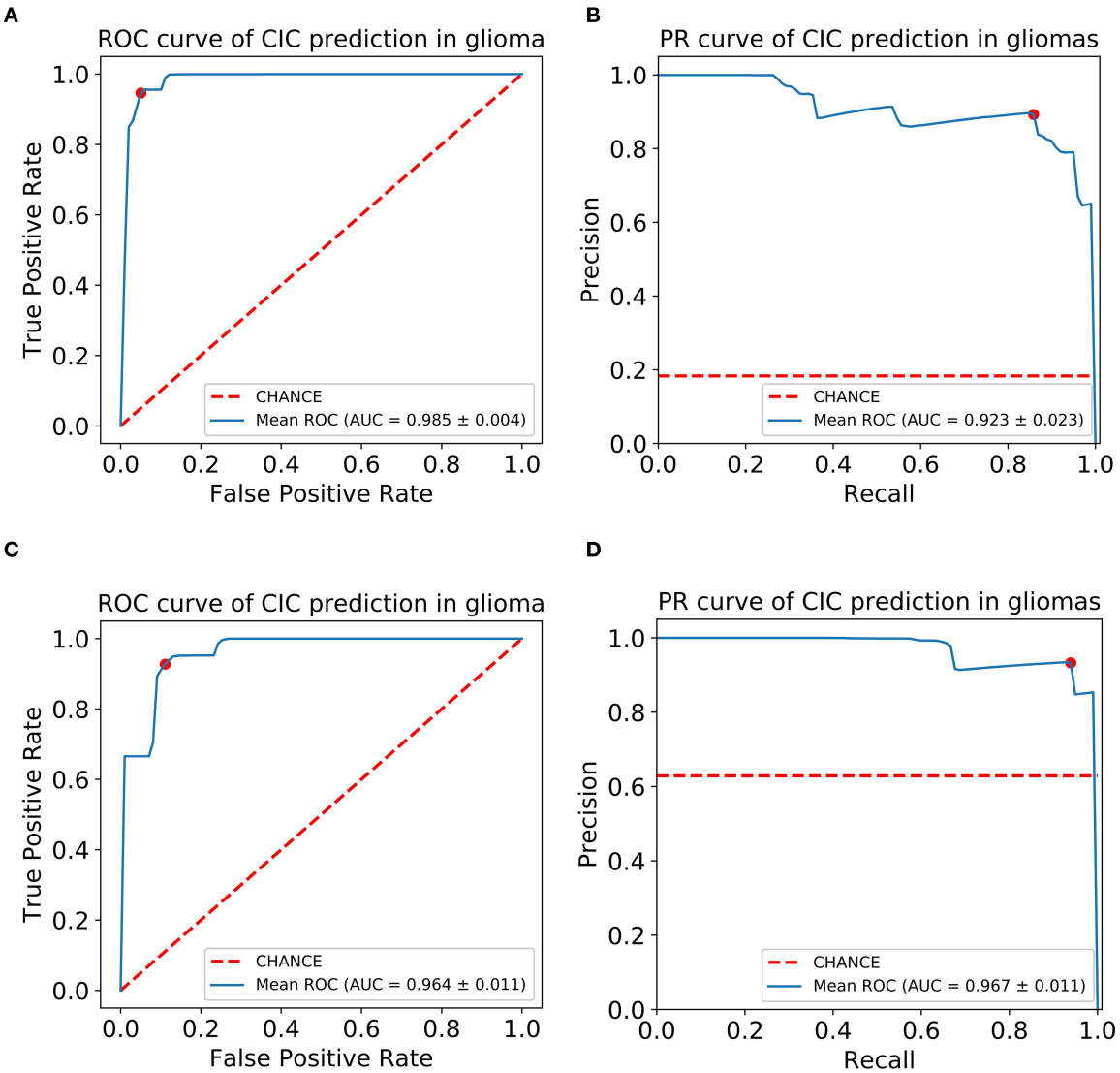

FIGURE 7 | CIC mutation has a potential diagnosis value in glioma. **(A)** Receiver operating characteristic (ROC) curve of glioma CIC mutation prediction model. **(B)** Precision-recall (PR) curve of glioma CIC mutation prediction model. **(C)** Receiver operating characteristic (ROC) curve of oligodendroglioma CIC mutation prediction model. **(D)** Precision-recall (PR) curve of oligodendroglioma CIC mutation prediction model. The optimal cutoff value in ROC curve is the point (red dot) that has the smallest distance to (0,1), or (1,1) in PR curve.

0.9643–0.9687) (**Figure 7**). The optimal cutoff value (0.1010) of the ROC curve exhibited a sensitivity, specificity, and accuracy of 94.26, 89.90, and 92.64%, respectively. The mean AUC of the PR curve is 0.9705 (95% CI, 0.9684–0.9726). The optimal cutoff value (0.9596) of the PR curve exhibited sensitivity, precision, and accuracy of 95.96, 93.51, and 93.27%, respectively.

Image Feature Analysis

Among the 11 features of the logistic regression model of CIC mutation prediction in gliomas, seven features were found significant (Mann-Whitney *U*-test, alpha = 0.05). To help illustrate some of these imaging characteristics, we extracted 2D image slices that maximize or minimize the top 3 selected features (**Figure 8**). T2-wavelet-LHL_glszm_SizeZoneNonUniformityNormalized, T1post-wavelet-LHH_ngtdm_Busyness, and FLAIR-wavelet-HLH_firstorder_Median are the top 3 significant features. Among the six features of the logistic regression model of CIC mutation prediction in Oligodendrogliomas (**Table S4**, **Figure 9**), three features were found to be significant (Mann-Whitney *U*-test, alpha = 0.05). T1post-wavelet-LHH_ngtdm_Busyness and T1pre-lbp-3D-m1_gldm_DependenceNonUniformityNormalized were the top 2 significant features. Images corresponding to the highest and lowest probability of CIC mutation (based on logistic regression) were selected (**Figure 10**).

TABLE 5 | Six features used to predict CIC mutation in oligodendrogliomas.

No.	Features	Importance[a]	*P*-value[b]
1	T1pre-lbp-3D-m2_glszm_SmallAreaLowGrayLevelEmphasis	2022.39	0.2209
2	T1post-wavelet-LHH_ngtdm_Busyness	1527.58	0.0047
3	T2-square_gldm_GrayLevelNonUniformity	1140.3	0.2108
4	T1pre-lbp-3D-m1_gldm_DependenceNonUniformityNormalized	696.76	0.0009
5	T1pre-gradient_firstorder_Minimum	−694.92	0.6766
6	FLAIR-gradient_firstorder_Kurtosis	81.75	0.0096

[a]*Importance, Sum of coefficients of features in 1,000 prediction models.*
[b]*P-value, Mann-Whitney U-test p-value.*

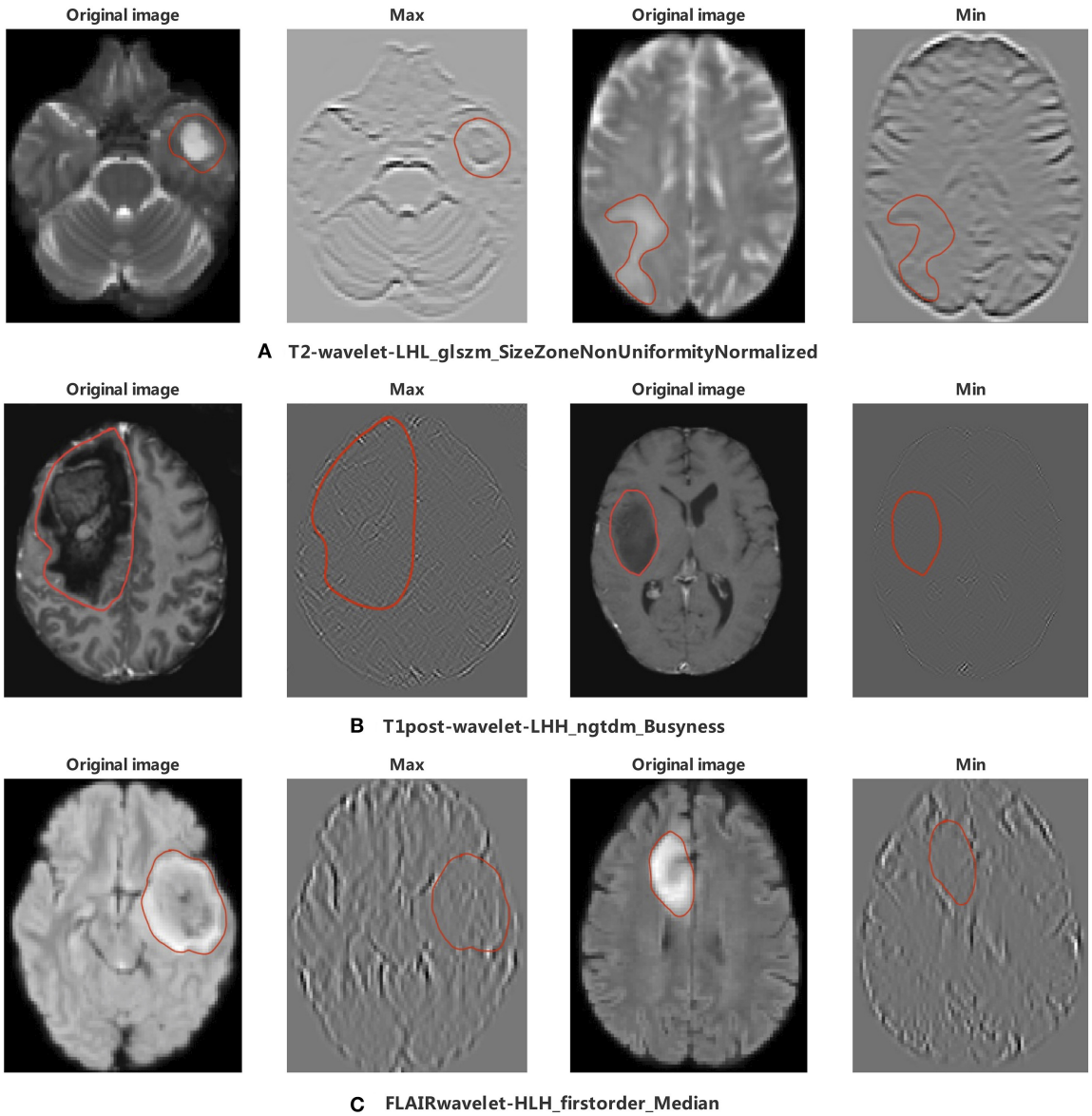

FIGURE 8 | The appearance of the MR image corresponding to the top 3 radiomic features in glioma. The region encircled in red represents the lesion boundary. **(A)** Images corresponding to the maximum and minimum of T2-wavelet-LHL_glszm_SizeZoneNonUniformityNormalized. **(B)** First column images are the Wavelet images corresponding to the maximum and minimum value of T1post-wavelet_LHH_ngtdm_Busyness, second column images are original images of wavelet images. **(C)** Images corresponding to the maximum and minimum value of FLAIR-wavelet-HLH_firstorder_Median.

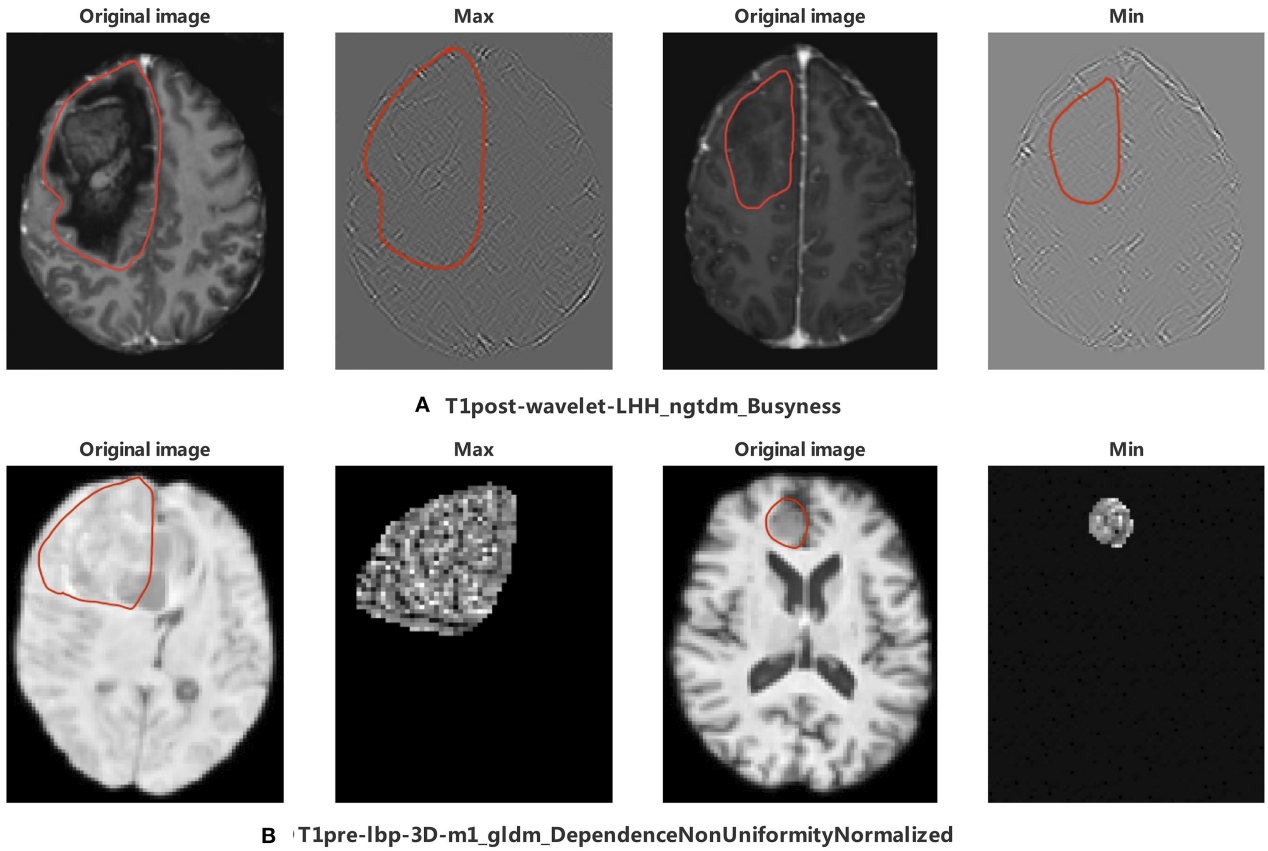

FIGURE 9 | The appearance of the MR image corresponds to top 2 radiomics features in Oligodendroglioma. The region encircled in red represents the legion boundary. **(A)** wavelet images and corresponding original images of the maximum and minimum value of T1post-wavelet_LHH_ngtdm_Busyness. **(B)** LBP images and corresponding original images of the maximum and minimum value of T1pre-lbp-3D-m1_gldm_DependenceNonUniformityNormalized. LBP image only included mask region in PyRadiomics (35).

DISCUSSION

In our study, we utilized TCGA and TCIA to explore the potential to predict genomics based on MR images. We found that CIC mutation has excellent diagnostic value in LGG, and that CIC mutation is mutually exclusive with glioblastoma (**Figure 3**), so we excluded the TCGA GBM cohort from further study. CIC mutation mainly occurs in IDH mutation and 1p/19q co-deletion patients and is mutually exclusive with IDH wild-type or 1p/19q intact patients (**Figure 4**). CIC mutation is also associated with clinical characteristics as described in (**Table 1**). We can speculate IDH mutation, 1p/19q codeletion, and histological type information from CIC mutation status. Grade 2 patients and elder patients are more likely to have CIC mutation. Interestingly, patients without clinical symptoms (headache, visual changes, sensory changes) have higher probability of having CIC mutation. This is probably seen because CIC mutations occur primarily in grade 2 gliomas and oligodendrogliomas. These grades of gliomas have a lower degree of malignancy, slower disease progression, and clinical symptoms occur later and are not obvious, leading to patients being diagnosed at an older age.

In our study, CIC mutation is present in 65.9% of 1p/19q codeletion patients, but rarely in 1p/19q intact patients (2.3%). In order to find out whether the significant correlation between CIC mutations and OS comes from the 1p/19q codeletion, we performed multivariate cox regression analysis. In the result of multivariate cox regression analysis, which included IDH mutation, 1p/19q codeletion, CIC mutation, age, gender, grade, and histological type, CIC mutation is significant ($p < 1e{-}4$), but 1p/19q codeletion is not significant ($p = 0.3246$) (**Table 2**). We also found that CIC mutation in IDH mutation patients is associated with a better prognosis ($p = 0.0287$, HR = 0.4178), but there is no significant difference between 1p/19q codeletion and prognosis ($p = 0.7011$) (**Table 2**). In addition, in oligodendroglioma (IDH mutation and 1p/19q codeletion) patients, CIC mutation is associated with a better prognosis ($p = 0.0362$). It was reported that almost every glioma with a CIC or FUBP1 mutation exhibited an IDH gene mutation (13). Thus, we also analyzed FUBP1 status in our study. There are 50 FUBP1 mutation patients, almost all FUBP1 patients exhibited an IDH mutation, and most FUBP1 mutation patients combined CIC mutation. But not all CIC mutation patients have

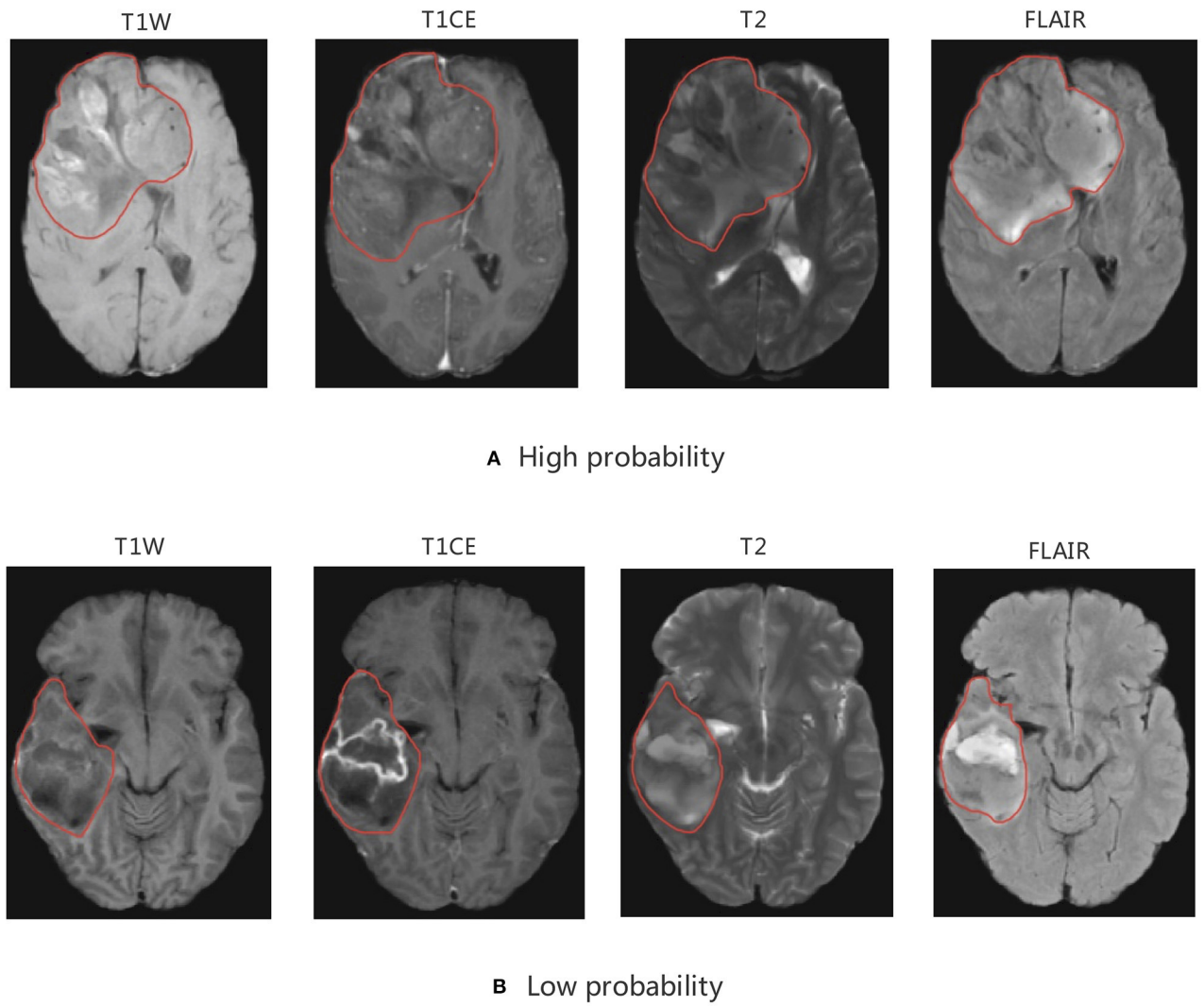

FIGURE 10 | MRI of model-based CIC mutation prediction patients. Image with the **(A)** high probability of being CIC mutation and **(B)** low probability of being CIC mutation. The region inside the red line represents glioma region.

FUBP1 mutation. We did multivariate cox analysis including FUBP1 mutation and found no significant association between FUBP1 mutation and survival ($p = 0.2959$) (**Table S4**). Therefore, CIC mutation was an independent good prognostic factor in our study.

As reported, gliomas with different genotypes have different MRI appearances (43–46). In our study we focused on 11 extracted radiomics features. The top 2 of these 11 radiomic features were T2-wavelet-LHL _glszm_SizeZoneNonUniformityNormalized (SZNN) and T1post-wavelet-LHH_ngtdm_Busyness (Busyness). Both features are extracted from wavelet transform images which reflect fine details of the original images. SZNN measures the variability of size zone volumes throughout the image, with a lower value indicating more homogeneity among zone size volumes in the image (35). Busyness is a measure of the change from a pixel to its neighbor. A high Busyness indicates rapid changes in intensity (35). In other words, both Busyness and SZNN are measures of image heterogeneity and non-uniformity. SZNN minimal value corresponding image is flat but the tumor region appears as obvious protruding ridges and depressed trenches in the maximum value (**Figure 8**).

CIC mutation mainly occurs in Oligodendroglioma but not all. To identify the difference between Oligodendrogliomas with and without CIC mutations, six features were selected after the Lasso process. Top 2 features are T1post-wavelet-LHH_ngtdm_Busyness (Busyness) and T1pre-lbp-3D-m1_gldm_ DependenceNonUniformityNormalized (DNN). DNN measures the similarity of dependence defined as the number of connected voxels within distance δ that are dependent on the center voxel, a lower value indicating more homogeneity among dependencies in the image (35) (**Figure 9**). The DNN

max value corresponding image is extremely complex and heterogeneous but the tumor region appears smaller and simpler in the minimum value. From the images, we find that the appearance of Oligodendrogliomas with or without CIC mutation are similar, not as obvious as the difference between all types of gliomas with or without CIC mutation. Both Oligodendrogliomas with or without CIC mutation are heterogeneous and non-uniform. But according to the meaning of image features, we still speculate that Oligodendroglioma with CIC mutation still appears more heterogeneous and complex.

As discussed above, CIC mutation suggests a better prognosis in patients with IDH mutation and 1p/19q codeletion. Therefore, we concluded that patients with CIC mutation have the best prognosis and longest survival. In our study, most CIC mutation gliomas have a relatively larger tumor region, more obvious mass effect, greater non-uniformity, heterogeneity, and scattered areas of intratumorally necrosis with or without corresponding areas of contrast enhancement. The special appearance may be due to the low malignancy of glioma with CIC mutation. The relatively weak proliferative, invasive and migration ability leads to CIC mutation gliomas growing slowly, resulting in not obvious clinical symptoms and larger tumor volume. This is consistent with published results that show CIC mutation is more likely to occur in patients of older age, grade 2 glioma, and without clinical symptoms. The cause for scattered areas of weak contrast enhancement may be that the tumor is less malignant, resulting in slow tumor growth, less ischemia and hypoxia, and less damage to the blood brain barrier (BBB) which prevents media from leaking through the BBB. On the other hand, gliomas which have a small tumor region but severe necrosis, obvious contrast enhancement, and obvious peritumoral edema (reflects rapid growth) which indicated strong invasion and severe BBB damage have a lower probability of CIC mutation.

Although radiomic features perform well, there are some limitations to our study analysis. First, all data is from public datasets (TCGA and TCIA), which displays large variance in quality of images that may influence predictive analysis. Second, data was imbalanced because of the low incidence of CIC mutation. Third, only structural MRIs were included. Functional and diffusion-weighted MR images are an area of interest that could be included in similar analysis in future work. Lastly, in this study, all images were obtained from one cohort (TCIA). Future work could benefit from using a second independent cohort for testing, which would provide a better measure of model generalizability / reliability.

In conclusion, our results support CIC mutation status as a valuable diagnostic and prognostic biomarker of lower-grade glioma. We showed that CIC mutation could be accurately predicted by MRI radiomic features. MRI of CIC mutation gliomas were found to display visually less malignant manifestations, such as milder necrosis and larger tumor volume. Radiomics plays an important role in the accurate diagnosis and personalized treatment of gliomas. The exploration of its association with medical imaging appearance and its clinical application are worth further efforts.

DATA AVAILABILITY STATEMENT

Publicly available datasets were analyzed in this study. This data can be found here: https://portal.gdc.cancer.gov/, https://www.cancerimagingarchive.net/.

AUTHOR CONTRIBUTIONS

LZ and FG contributed to experimental design, data analysis, and manuscript writing. DG, XL, and JV contributed to experimental design and manuscript writing. All authors contributed to the article and approved the submitted version.

ACKNOWLEDGMENTS

We would like to acknowledge the support of the DG lab at Emory University where the conducted research took place and provided the software and computational hardware used.

SUPPLEMENTARY MATERIAL

The Supplementary Material for this article can be found online at: https://www.frontiersin.org/articles/10.3389/fonc.2020.00937/full#supplementary-material

REFERENCES

1. Delgado-López PD, Corrales-García EM. Survival in glioblastoma: a review on the impact of treatment modalities. *Clin Transl Oncol*. (2016) 18:1062–71. doi: 10.1007/s12094-016-1497-x
2. van Meir EG, Hadjipanayis CG, Norden AD, Shu H-K, Wen PY, Olson JJ. Exciting new advances in neuro-oncology: the avenue to a cure for malignant glioma. *CA Cancer J Clin*. (2010) 60:166–93. doi: 10.3322/caac.20069
3. Louis DN, Perry A, Reifenberger G, von Deimling A, Figarella-Branger D, Cavenee WK, et al. The 2016 world health organization classification of tumors of the central nervous system: a summary. *Acta Neuropathol*. (2016) 131:803–20. doi: 10.1007/s00401-016-1545-1
4. Bush NAO, Butowski N. The effect of molecular diagnostics on the treatment of glioma. *Curr Oncol Rep*. (2017) 19:26. doi: 10.1007/s11912-017-0585-6
5. Kawaguchi T, Sonoda Y, Shibahara I, Saito R, Kanamori M, Kumabe T, et al. Impact of gross total resection in patients with WHO grade III glioma harboring the IDH 1/2 mutation without the 1p/19q co-deletion. *J Neurooncol*. (2016) 129:505–14. doi: 10.1007/s11060-016-2201-2
6. Beiko J, Suki D, Hess KR, Fox BD, Cheung V, Cabral M, et al. IDH1 mutant malignant astrocytomas are more amenable to surgical resection and have a survival benefit associated with maximal surgical resection. *Neuro Oncol*. (2014) 16:81–91. doi: 10.1093/neuonc/not159
7. Sottoriva A, Spiteri I, Piccirillo SGM, Touloumis A, Collins VP, Marioni JC, et al. Intratumor heterogeneity in human glioblastoma reflects cancer evolutionary dynamics. *Proc Natl Acad Sci USA*. (2013) 110:4009–14. doi: 10.1073/pnas.1219747110
8. Kani Y, Cecere TE, Lahmers K, LeRoith T, Zimmerman KL, Isom S, et al. Diagnostic accuracy of stereotactic brain biopsy for intracranial neoplasia in dogs: comparison of biopsy, surgical resection, and necropsy specimens. *J Vet Intern Med*. (2019) 33:1384–91. doi: 10.1111/jvim.15500
9. Reardon DA, Wen PY. Glioma in 2014: unravelling tumour heterogeneity-implications for therapy. *Nat Rev Clin Oncol*. (2015) 12:69–70. doi: 10.1038/nrclinonc.2014.223

10. Chan AK-Y, Pang JC-S, Chung NY-F, Li KK-W, Poon WS, Chan DT-M, et al. Loss of CIC and FUBP1 expressions are potential markers of shorter time to recurrence in oligodendroglial tumors. *Mod Pathol*. (2014) 27:332–42. doi: 10.1038/modpathol.2013.165
11. Gleize V, Alentorn A, Connen de Kérillis L, Labussière M, Nadaradjane AA, Mundwiller E, et al. CIC inactivating mutations identify aggressive subset of 1p19q codeleted gliomas. *Ann Neurol*. (2015) 78:355–74. doi: 10.1002/ana.24443
12. Padul V, Epari S, Moiyadi A, Shetty P, Shirsat NV. ETV/Pea3 family transcription factor-encoding genes are overexpressed in CIC-mutant oligodendrogliomas. *Genes Chromosomes Cancer*. (2015) 54:725–33. doi: 10.1002/gcc.22283
13. Jiao Y, Killela PJ, Reitman ZJ, Rasheed AB, Heaphy CM, de Wilde RF, et al. Frequent ATRX, CIC, FUBP1 and IDH1 mutations refine the classification of malignant gliomas. *Oncotarget*. (2012) 3:709–22. doi: 10.18632/oncotarget.588
14. Yip S, Butterfield YS, Morozova O, Chittaranjan S, Blough MD, An J, et al. Concurrent CIC mutations, IDH mutations, and 1p/19q loss distinguish oligodendrogliomas from other cancers. *J Pathol*. (2012) 226:7–16. doi: 10.1002/path.2995
15. Komotar RJ, Starke RM, Sisti MB, Connolly ES. CIC and FUBP1 mutations in oligodendroglioma. *Neurosurgery*. (2012) 70:N22–3. doi: 10.1227/01.neu.0000414948.56225.36
16. Rios Velazquez E, Meier R, Dunn WD Jr, Alexander B, Wiest R, Bauer S, et al. Fully automatic GBM segmentation in the TCGA-GBM dataset: prognosis and correlation with VASARI features. *Sci Rep*. (2015) 5:16822. doi: 10.1038/srep16822
17. Cho H-H, Park H. Classification of low-grade and high-grade glioma using multi-modal image radiomics features. *Conf Proc IEEE Eng Med Biol Soc*. (2017) 2017:3081–4. doi: 10.1109/EMBC.2017.8037508
18. Gillies RJ, Kinahan PE, Hricak H. Radiomics: images are more than pictures, they are data. *Radiology*. (2016) 278:563–77. doi: 10.1148/radiol.2015151169
19. Bai HX, Lee AM, Yang L, Zhang P, Davatzikos C, Maris JM, et al. Imaging genomics in cancer research: limitations and promises. *Br J Radiol*. (2016) 89:20151030. doi: 10.1259/bjr.20151030
20. Zhou H, Vallières M, Bai HX, Su C, Tang H, Oldridge D, et al. MRI features predict survival and molecular markers in diffuse lower-grade gliomas. *Neuro Oncol*. (2017) 19:862–70. doi: 10.1093/neuonc/now256
21. Shofty B, Artzi M, Ben Bashat D, Liberman G, Haim O, Kashanian A, et al. MRI radiomics analysis of molecular alterations in low-grade gliomas. *Int J Comput Assist Radiol Surg*. (2018) 13:563–71. doi: 10.1007/s11548-017-1691-5
22. Akkus Z, Ali I, Sedlár J, Agrawal JP, Parney IF, Giannini C, et al. Predicting deletion of chromosomal arms 1p/19q in low-grade gliomas from MR images using machine intelligence. *J Digit Imaging*. (2017) 30:469–76. doi: 10.1007/s10278-017-9984-3
23. Rui W, Ren Y, Wang Y, Gao X, Xu X, Yao Z. MR textural analysis on T2 FLAIR images for the prediction of true oligodendroglioma by the 2016 WHO genetic classification. *J Magn Reson Imaging*. (2018) 48:74–83. doi: 10.1002/jmri.25896
24. Grossmann P, Stringfield O, El-Hachem N, Bui MM, Rios Velazquez E, Parmar C, et al. Defining the biological basis of radiomic phenotypes in lung cancer. *Elife*. (2017) 6:e23421. doi: 10.7554/eLife.23421
25. Clark K, Vendt B, Smith K, Freymann J, Kirby J, Koppel P, et al. The cancer imaging archive (TCIA): maintaining and operating a public information repository. *J Digit Imaging*. (2013) 26:1045–57. doi: 10.1007/s10278-013-9622-7
26. Gao J, Aksoy BA, Dogrusoz U, Dresdner G, Gross B, Sumer SO, et al. Integrative analysis of complex cancer genomics and clinical profiles using the cBioPortal. *Sci Signal*. (2013) 6:l1. doi: 10.1126/scisignal.2004088
27. Cerami E, Gao J, Dogrusoz U, Gross BE, Sumer SO, Aksoy BA, et al. The cBio cancer genomics portal: an open platform for exploring multidimensional cancer genomics data. *Cancer Discov*. (2012) 2:401–4. doi: 10.1158/2159-8290.CD-12-0095
28. Laddha SV, Ganesan S, Chan CS, White E. Mutational landscape of the essential autophagy gene BECN1 in human cancers. *Mol Cancer Res*. (2014) 12:485–90. doi: 10.1158/1541-7786.MCR-13-0614
29. Park H, Chun S-M, Shim J, Oh J-H, Cho EJ, Hwang HS, et al. Detection of chromosome structural variation by targeted next-generation sequencing and a deep learning application. *Sci Rep*. (2019) 9:3644. doi: 10.1038/s41598-019-40364-5
30. Gutman DA, Khalilia M, Lee S, Nalisnik M, Mullen Z, Beezley J, et al. The digital slide archive: a software platform for management, integration, and analysis of histology for cancer research. *Cancer Res*. (2017) 77:e75–8. doi: 10.1158/0008-5472.CAN-17-0629
31. Rorden C, Brett M. Stereotaxic display of brain lesions. *Behav Neurol*. (2000) 12:191–200. doi: 10.1155/2000/421719
32. Jenkinson M, Beckmann CF, Behrens TEJ, Woolrich MW, Smith SM. FSL. *Neuroimage*. (2012) 62:782–90. doi: 10.1016/j.neuroimage.2011.09.015
33. Smith SM. Fast robust automated brain extraction. *Hum Brain Mapp*. (2002) 17:143–55. doi: 10.1002/hbm.10062
34. Shinohara RT, Sweeney EM, Goldsmith J, Shiee N, Mateen FJ, Calabresi PA, et al. Statistical normalization techniques for magnetic resonance imaging. *Neuroimage Clin*. (2014) 6:9–19. doi: 10.1016/j.nicl.2014.08.008
35. van Griethuysen JJM, Fedorov A, Parmar C, Hosny A, Aucoin N, Narayan V, et al. Computational radiomics system to decode the radiographic phenotype. *Cancer Res*. (2017) 77:e104–7. doi: 10.1158/0008-5472.CAN-17-0339
36. Tibshirani R. Regression shrinkage and selection via the lasso. *J R Stat Soc Series B Stat Methodol*. (1996) 58:267–88. doi: 10.1111/j.2517-6161.1996.tb02080.x
37. Rodríguez JD, Pérez A, Lozano JA. Sensitivity analysis of kappa-fold cross validation in prediction error estimation. *IEEE Trans Pattern Anal Mach Intell*. (2010) 32:569–75. doi: 10.1109/TPAMI.2009.187
38. Gianola D, Schön C-C. Cross-validation without doing cross-validation in genome-enabled prediction. *G3*. (2016) 6:3107–28. doi: 10.1534/g3.116.033381
39. Hua J, Xiong Z, Lowey J, Suh E, Dougherty ER. Optimal number of features as a function of sample size for various classification rules. *Bioinformatics*. (2005) 21:1509–15. doi: 10.1093/bioinformatics/bti171
40. Song B, Zhang G, Zhu W, Liang Z. ROC operating point selection for classification of imbalanced data with application to computer-aided polyp detection in CT colonography. *Int J Comput Assist Radiol Surg*. (2014) 9:79–89. doi: 10.1007/s11548-013-0913-8
41. Arita H, Kinoshita M, Kawaguchi A, Takahashi M, Narita Y, Terakawa Y, et al. Lesion location implemented magnetic resonance imaging radiomics for predicting IDH and TERT promoter mutations in grade II/III gliomas. *Sci Rep*. (2018) 8:11773. doi: 10.1038/s41598-018-30273-4
42. Li Z-C, Bai H, Sun Q, Zhao Y, Lv Y, Zhou J, et al. Multiregional radiomics profiling from multiparametric MRI: Identifying an imaging predictor of IDH1 mutation status in glioblastoma. *Cancer Med*. (2018) 7:5999–6009. doi: 10.1002/cam4.1863
43. Haase S, Garcia-Fabiani MB, Carney S, Altshuler D, Núñez FJ, Méndez FM, et al. Mutant ATRX: uncovering a new therapeutic target for glioma. *Expert Opin Ther Targets*. (2018) 22:599–613. doi: 10.1080/14728222.2018.1487953
44. Reyes-Botero G, Dehais C, Idbaih A, Martin-Duverneuil N, Lahutte M, Carpentier C, et al. Contrast enhancement in 1p/19q-codeleted anaplastic oligodendrogliomas is associated with 9p loss, genomic instability, and angiogenic gene expression. *Neuro Oncol*. (2014) 16:662–70. doi: 10.1093/neuonc/not235
45. Sonoda Y, Shibahara I, Kawaguchi T, Saito R, Kanamori M, Watanabe M, et al. Association between molecular alterations and tumor location and MRI characteristics in anaplastic gliomas. *Brain Tumor Pathol*. (2015) 32:99–104. doi: 10.1007/s10014-014-0211-3
46. Yamauchi T, Ohno M, Matsushita Y, Takahashi M, Miyakita Y, Kitagawa Y, et al. Radiological characteristics based on isocitrate dehydrogenase mutations and 1p/19q codeletion in grade II and III gliomas. *Brain Tumor Pathol*. (2018) 35:148–58. doi: 10.1007/s10014-018-0321-4

Conflict of Interest: The authors declare that the research was conducted in the absence of any commercial or financial relationships that could be construed as a potential conflict of interest.

frontiers in Oncology

ORIGINAL RESEARCH
published: 08 July 2020
doi: 10.3389/fonc.2020.01096

Radiomics Analysis of Postoperative Epilepsy Seizures in Low-Grade Gliomas Using Preoperative MR Images

Kai Sun[1,2†], Zhenyu Liu[2†], Yiming Li[3†], Lei Wang[3], Zhenchao Tang[2,4], Shuo Wang[2,4], Xuezhi Zhou[1,2], Lizhi Shao[2,5], Caixia Sun[2,6], Xing Liu[3], Tao Jiang[3], Yinyan Wang[3] and Jie Tian[1,2,4,7]**

[1] Engineering Research Center of Molecular and Neuro Imaging of Ministry of Education, School of Life Science and Technology, Xidian University, Xi'an, China, [2] CAS Key Laboratory of Molecular Imaging, Institute of Automation, Beijing, China, [3] Beijing Tiantan Hospital, Capital Medical University, Beijing, China, [4] Beijing Advanced Innovation Center for Big Data-Based Precision Medicine, School of Medicine, Beihang University, Beijing, China, [5] School of Computer Science and Engineering, Southeast University, Nanjing, China, [6] Key Laboratory of Intelligent Medical Image Analysis and Precise Diagnosis of Guizhou Province, School of Computer Science and Technology, Guizhou University, Guiyang, China, [7] University of Chinese Academy of Science, Beijing, China

Purpose: The present study aimed to evaluate the performance of radiomics features in the preoperative prediction of epileptic seizure following surgery in patients with LGG.

Methods: This retrospective study collected 130 patients with LGG. Radiomics features were extracted from the T2-weighted MR images obtained before surgery. Multivariable Cox-regression with two nested leave-one-out cross validation (LOOCV) loops was applied to predict the prognosis, and elastic net was used in each LOOCV loop to select the predictive features. Logistic models were then built with the selected features to predict epileptic seizures at two time points. Student's *t*-tests were then used to compare the logistic model predicted probabilities of developing epilepsy in the epilepsy and non-epilepsy groups. The *t*-test was used to identify features that differentiated patients with early-onset epilepsy from their late-onset counterparts.

Results: Seventeen features were selected with the two nested LOOCV loops. The index of concordance (C-index) of the Cox model was 0.683, and the logistic model predicted probabilities of seizure were significantly different between the epilepsy and non-epilepsy groups at each time point. Moreover, one feature was found to be significantly different between the patients with early- or late-onset epilepsy.

Conclusion: A total of 17 radiomics features were correlated with postoperative epileptic seizures in patients with LGG and one feature was a significant predictor of the time of epilepsy onset.

Keywords: low-grade glioma, epilepsy, radiomics, elastic net, Cox regression

OPEN ACCESS

Edited by:
Yanmei Tie,
Harvard Medical School,
United States

Reviewed by:
Yinsheng Chen,
Sun Yat-sen University Cancer Center (SYSUCC), China
Raymond Yi-Kun Huang,
Brigham and Women's Hospital and Harvard Medical School,
United States

***Correspondence:**
Yinyan Wang
tiantanyinyan@126.com
Jie Tian
jie.tian@ia.ac.cn

[†] These authors have contributed equally to this work

Specialty section:
This article was submitted to Cancer Imaging and Image-directed Interventions, a section of the journal Frontiers in Oncology

Received: *20 January 2020*
Accepted: *02 June 2020*
Published: *08 July 2020*

Citation:
Sun K, Liu Z, Li Y, Wang L, Tang Z, Wang S, Zhou X, Shao L, Sun C, Liu X, Jiang T, Wang Y and Tian J (2020) Radiomics Analysis of Postoperative Epilepsy Seizures in Low-Grade Gliomas Using Preoperative MR Images. Front. Oncol. 10:1096. doi: 10.3389/fonc.2020.01096

INTRODUCTION

Low-grade gliomas (LGGs) are slow-growing, infiltrative tumors frequently associated with seizures. Up to 90% of the patients with LGG may have seizures as the initial presentation leading to tumor diagnosis. Additionally, epilepsy seizure could be used as a clinical predictor for early tumor recurrence with LGGs (1). The persistence of seizures in these patients may be associated with the worsening of their neurological, neuropsychological, and psychological status, reducing their quality of life (2, 3). With a prolonged duration of epilepsy, the symptoms of LGG may spread to the neocortex and subcortical structures, gradually disrupting normal brain networks and causing dysfunction of both the peritumoral area and remote brain tissues (1). The reported recurrence of epilepsy in 20–40% of patients demonstrates that the current conventional treatment strategy used to address glioma-related epilepsy, including antiepileptic drugs (AEDs) and anti-tumor therapies, remain unsatisfactory (4–6). The application of AEDs has been a controversial issue for a long time, there still has no strategy for individualized prophylactic. Thus, the preoperative prediction of epilepsy seizures following surgery could help clinicians evaluate the risk of patients for epilepsy after surgery, further to make decision of individualized treatment strategy, which was significant for clinical treatment.

Several studies identified risk factors for the development of gliomas related epilepsy: tumor location, tumor histology, microenvironment, and genetic mutation (4, 7–9). Some investigations have used medical imaging to study the correlation between LGG and epilepsy (10, 11), and Wang et al. developed a probabilistic risk atlas of gliomas related epilepsy (8). However, few studies evaluated the correlation between these factors and the risk of epilepsy seizure after surgery. In addition, research has neglected temporal concerning the condition—despite the value of such information to enhance the timeliness of interventions.

The development of pattern recognition technology has driven the development of medical imaging data analysis, and advances in data mining and machine learning have rendered it possible to convert medical images into minable data. The concept of "radiomics" first described in 2012 (12, 13), calls a comprehensive analysis of medical images (14). By converting medical images into high-dimensional, mineable, and quantitative imaging features, radiomics could offer large amounts of information inaccessible to the human eye. Recently, radiomics had been widely and successfully applied to inform decision making in the treatment of tumors and neuropsychiatric diseases (15–17), including in gliomas and epilepsy (18, 19). Liu et al. built a radiomics signature using quantitative imaging features to predict LGG-related epilepsy (20). Based on the successful application, we hypothesized that radiomics analysis could provide a chance for preoperative prediction of epilepsy seizures following surgery in LGG patients. Hence, by incorporating the temporal information, the model could provide a timelier and finer prediction for the intervention.

In this study, we retrospectively collected pretreatment neuroimaging data and prognosis outcomes of 130 patients with LGG who underwent surgery. We attempted to explore the relationship between radiomics features and the prognosis of postoperative epilepsy by performing a multivariable analysis.

METHODS

Patients

A total of 130 patients who were surgically treated at Beijing Tiantan Hospital between October 2005 and August 2008 were collected in this retrospective study. The tumor types of all patients were identified according to WHO 2016 classification. The inclusion criteria were set as: all patients underwent standard surgery and were diagnosed with LGGs confirmed by postsurgical histopathology. To ensure that prognoses were accurate for each patient, we assured that at least two years of follow-up records were available for each patient. All patients were postoperatively followed up every 6 months during the first year, and then annually thereafter. The Ethics Committee of the Beijing Tiantan Hospital approved the study, and written informed consent was obtained from all participants.

Brain Imaging and Tumor Masking

The feature extraction in the current study followed the Image Biomarker Standardization Initiative (IBSI) guideline (21). T2-weighted images were obtained on a Magnetom Trio 3.0T scanner (Siemens, Erlangen, Germany) with a 12-channel receive-only head coil. The parameters were set as follows: repetition time = 5,800 ms; echo time = 110 ms; flip angle = 150 degrees; 24 slices; field of view = 240 × 188 mm^2; voxel size = 0.6 × 0.6 × 5.0 mm^3; matrix = 384 × 300. Tumors were semi-automatically segmented along the lesion contour on each patient's T2-weighted images in native space by at least two experienced neuroradiologists using the ITK-SNAP software (v 3.6.0; www.itksnap.org), while two other board-certified experts reviewed the segmentations using imaging features in combination with seizure history, clinical examination, neuroimaging data to solve any discrepancies. The areas with abnormal hyperintense signals on the images were identified as tumor volumes, and the cerebrospinal fluid signals should not be involved in. When the concordance between the tumor masks of one patient identified by the two neuroradiologists was higher than 95%, the tumor masks were combined.

Feature Extraction

The delineated tumor area was used as the region of interest (ROI) to extract radiomics features. The features were calculated with the largest slice of ROI. A total of 4,650 features were extracted. These features could be divided into 4 types: shape-based features, first-order statistical features, textural features and wavelet features. Detailed information and formula are described in the supplemental content. The radiomics feature extraction was performed using in-house software written in MATLAB 2017b (MathWorks, Inc., Natick, MA, USA).

Feature Selection and Model Development

This study aimed to find the discriminative radiomics features capable of predicting epileptic seizures after tumor resection, and further to distinguish early-onset seizures (patients who would

develop epilepsy within 6 months after surgery) from late-onset ones (patients who would develop epilepsy more than 6 months after surgery). In order to take full advantage of the temporal information, this study adopted a proportional hazards model (Cox model) (22). The end point of this study was disease-free survival (DFS), which was defined as the time from the date of surgery until the date of epileptic seizures (event) or until the latest date at which the patient was known to be free of epilepsy (censored).

Since the dimensionality of the radiomics feature space was high, and could easily lead to over-fitting or bias in the multivariable analysis, dimensional reduction was necessary to ensure the reliability of our results. All features were initially normalized as z-scores. After normalization, we performed univariate Cox regression on each feature, retained the significant features ($P < 0.05$). Then elastic net (E-net) Cox regression was used as a multivariable analysis to choose the most important features. The E-net penalty was a weighted sum of the least absolute shrinkage and selection operator (LASSO) penalty and ridge penalty, which retained the advantage of feature selection while at the same time, compared with LASSO, avoiding the interference of feature collinearity. The relative weight of LASSO and ridge penalty was selected to maximize the Cox's log-partial likelihood (23):

$$\sum_{i=1}^{n} \delta_i \left\{ X'_i\beta - log\left[\sum_{j\in R(t_i)} \exp\left(X'_j\beta\right)\right]\right\} - \lambda\left[\alpha \left\|\beta\right\|_1 + 0.5\left(1-\alpha\right)\left\|\beta\right\|_2^2\right]$$

where t_i was the survival time (observed or censored) for the ith patient, $R(t_i)$ was the risk set at time t_i, $X_i = \left(X_{i1}, \cdots, X_{ip}\right)'$ was the regression vector of p-variables for the ith patient, $\beta = \left(\beta_1, \cdots, \beta_p\right)'$ was the column vector of the regression parameters.

Since the sample size of this study was relatively small, we used two nested leave-one-out cross validation (LOOCV) to maximize the utilization of samples and to select the regularization parameters (**Figure 1**) (24, 25). In the outer LOOCV loop, each subject in turn was left out as the validation set, the other 129 being used to train an optimal E-net Cox model using the inner LOOCV loop. Specifically, the inner LOOCV loop was performed to train the optimal E-net Cox model with a pair of best parameters λ and α maximizing the Cox's log-partial likelihood based on the training data (all 130 samples excepting the one reserved for validation). We thus obtained 130 different models, since the training samples used in each model training were not identical. The features retained in more LOOCV loops were more stable, implying that they played more important roles. Therefore, we chose the features which were retained in at least 90% of the loops (117 loops) as the most important ones.

The features thus selected were used to build a Cox model and the Harrell concordance index (C-index) was calculated to evaluate its performance (26). We also built two separate logistic models to predict the status at 6 and 24 months using LOOCV, since the 6-month time point was used to define early-onset and the 24-month time point represented the longest available follow-up time for the whole dataset. We then computed the point-biserial-correlation between the probabilities of epilepsy predicted by the logistic model and the true labels (27), computing the correlation coefficient and the corresponding P-values. Additionally, we divided the patients into epilepsy and non-epilepsy groups based on the true label, and used the Student's t-test to compare the predicted probabilities between the two groups separately at 6 and 24

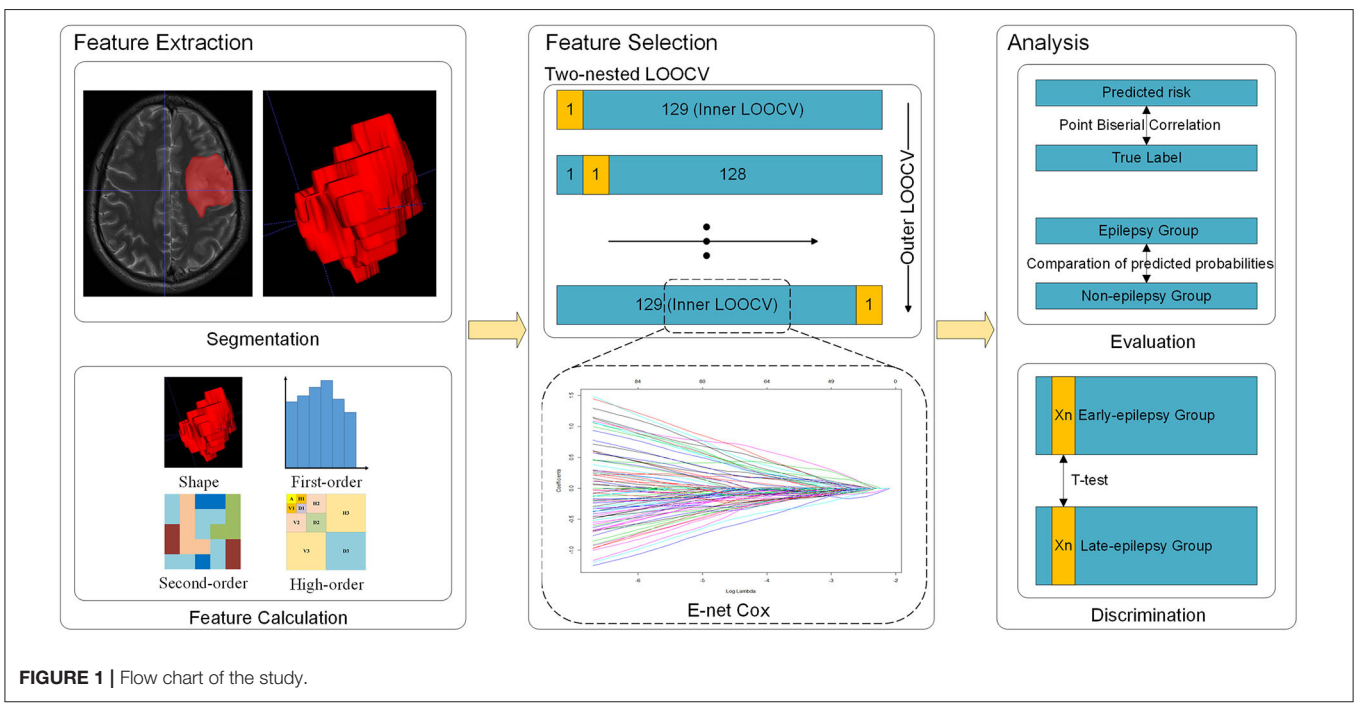

FIGURE 1 | Flow chart of the study.

TABLE 1 | Demographics and clinical characteristics of patients with low-grade gliomas.

	Epilepsy recurrence	Non-epilepsy recurrence	*P*
Age (mean ± deviation)	37.667 ± 9.651	38.101 ± 9.517	0.802
Sex			0.856
Male	30	49	
Female	21	30	
Tumor location			0.365
Frontal lobe	36	60	
Temporal lobe	23	22	
Parietal lobe	4	9	
Insula	8	9	
Preoperative epilepsy			0.342
Yes	39	53	
No	12	26	
Tumor pathology			0.725
Diffuse Astrocytoma			
IDH-mutant with 1p/19q no-deleted	17	31	
IDH-wildtype	10	13	
Oligodendroglioma			
IDH-mutant with 1p/19q co-deleted	16	27	
NOS	8	8	
IDH status			0.875
IDH-mutant	41	64	
IDH-wildtype	10	13	

The status of epilepsy recurrence is determined at 24 months. The location of the tumor is determined by the region of the tumor involved, where some patients have tumors involving multiple regions. Chi-Square test or Student's t-test were used to compare the differences between epilepsy and non-epilepsy groups.

months. Finally, Student's *t*-test was performed on each selected feature to identify differences between the patients with early- or late-onset of epilepsy.

To evaluate the impact of preoperative epilepsy on radiomics features, we performed a subgroup analysis based on preoperative seizures status. Specifically, we used Student's *t*-test to compare the predicted risk of the Cox model between preoperative epilepsy and no-epilepsy groups.

Since the pathological type, tumor location and the tumor volume could be the risk factors that may lead to postoperative epileptic seizure, we further investigated the correlation between the selected radiomics features with clinical factors.

RESULTS

Demographic and Clinical Data

According to the follow-up records, 51 patients were considered to have developed epilepsy by the end of the follow-up, specifically, 41 patients within 6 months after surgery, 10 patients within 6 to 24 months after surgery, and 79 patients were seizure-free through the end of the follow-up period. We collected six main clinical factors, age, sex, tumor location, the status of preoperative epilepsy, the tumor pathology types and the IDH status. There was no significant difference in the clinical factors between the epileptic and non-epileptic groups (**Table 1**). The age range of the patients was from 18 to 68 when they did the surgery.

TABLE 2 | The features selected by the two-nest LOOCV loop.

Name	The number of loops	*P*
gabor3_glszm_SZHGE	117	0.007*
gabor7_glcm_cluster_shade	123	0.247
gabor14_glcm_cluster_tendency	129	0.461
gabor18_glcm_IMC2	122	0.591
gabor18_glszm_LZLGE	120	0.564
gabor29_glszm_SZSE	129	0.406
gabor29_glszm_SZHGE	125	0.375
gabor30_glszm_SZHGE	117	0.692
gabor35_glszm_SZLGE	129	0.510
gabor36_glrlm_LGLRE	119	0.979
gabor36_glrlm45_LGLRE	121	0.958
gabor36_glszm_LGLZE	129	0.402
W5S5_fos_skewness	123	0.486
W5S5_fos_mass	129	0.919
W5W5_fos_mean	128	0.431
W5W5_fos_mass	129	0.853
R5S5_fos_median	129	0.847

*The number of loops indicates how many LOOCV loops have selected the feature. The P-value is calculated by the Student's T-test between the early- and late-onset of epilepsy patients. *Significant difference.*

Feature Selected

The features were selected by E-net cox in each inner LOOCV loop, and the loop in which each feature was retained was recorded. After feature selection, we retained 17 features. The number of LOOCV loops in which each feature were selected is listed in **Table 2**. The features selected by more loops were considered more robust.

Performance

The C-index of the Cox model built with the features selected by the two-nested LOOCV was 0.683, meaning that the selected features were predictive for the risk of epileptic seizures after surgery in LGG patients. When the predicted risk was compared between the two groups (no epilepsy and epilepsy) based on the true labels (**Figure 2**), the *t*-test revealed a significant difference between the two groups ($P < 0.001$).

The point-biserial-correlation between the probabilities predicted by the logistic model and the true labels was computed separately at the two time points of 6 and 24 months after surgery. At 6 months, the R- and *P*-values were 0.235 and 0.007, respectively, indicating that the selected features could predict whether patients would develop epilepsy at 6 months after surgery. Similarly, the R- and *P*-values at 24 months were 0.300 and <0.001, respectively, indicating that the predictive power of the selected features was retained at 24 months after surgery. Moreover, the Student's t-test comparing the probabilities predicted by the logistic model between the epilepsy

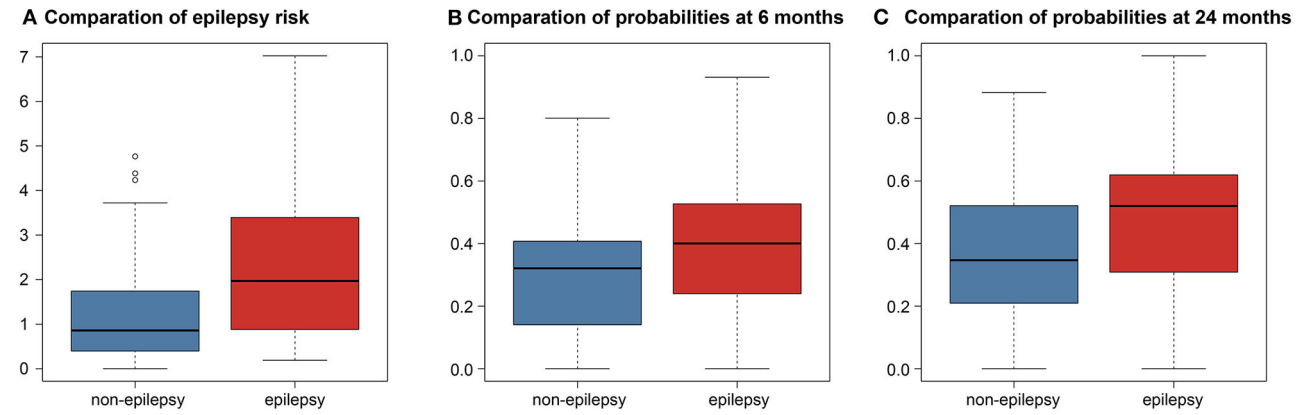

FIGURE 2 | Boxplots comparison differences between predictions in the non-epilepsy and epilepsy groups. **(A)** Comparation of epilepsy risk. Boxplot of the predicted risk values of the Cox model corresponding to both the no epilepsy and epilepsy groups. **(B)** Comparation of probabilities at 6 months. Boxplot of the predicted probabilities of the logistic model at 6 months. **(C)** Comparation of probabilities at 24 months. Boxplot of the predicted probabilities of the logistic model at 24 months.

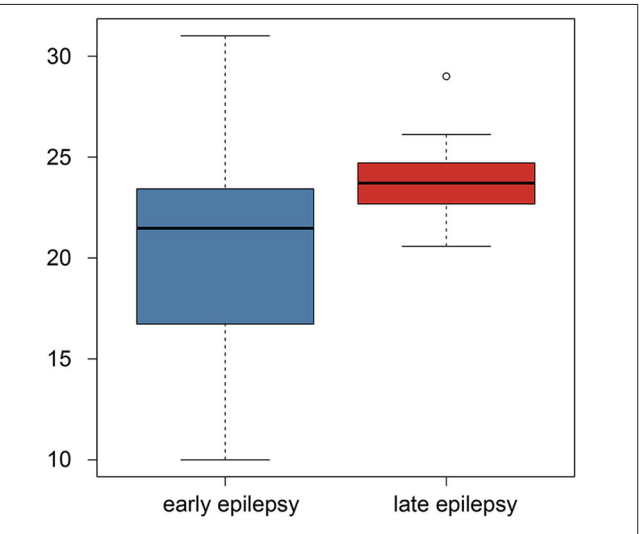

FIGURE 3 | Boxplot of the selected feature comparison between the early-onset and late-onset epilepsy patients.

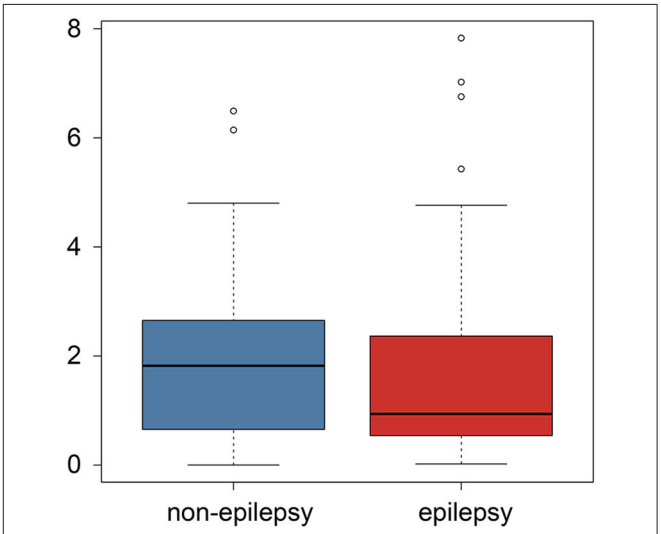

FIGURE 4 | Boxplot of the postoperative epilepsy risk comparison between the preoperative epilepsy and non-epilepsy patients.

and non-epilepsy groups, separately at the two time points, gave *P*-values both smaller than 0.001 indicating that the features could distinguish patients with epilepsy from those without epilepsy independently of the time point (**Figure 2**).

Using Student's *t*-test, we also compared the early- and late-onset epilepsy patients in terms of each selected feature. The *P*-values are listed in **Table 2**. The feature named "gabor3_glszm_SZHGE" was significantly different between the early- and late-onset of epilepsy groups, implying that the early- or late-onset of epilepsy in LGG patients could be predicted based on this feature, as shown in **Figure 3** and **Figure S1**, the values of the early-onset group were lower than the late-onset group, indicating that the lower the value of this feature, the sooner that post-operative seizures would occur.

The subgroup analysis of the preoperative seizures status demonstrated that preoperative epilepsy was not associated with the predictive value of the radiomics analysis ($P = 0.847$), as shown in **Figure 4**.

Analysis of Clinical Correlation Analysis

With regard to the pathological type, the corresponding R-values and *P*-values were listed in the **Table S1**. We found there were no correlation between the selected radiomics features and the pathological type.

To the tumor location, we determined the location of tumors based on the region of the tumors involve, and segmented into frontal lobe, temporal lobe, parietal lobe and Insula. The Students' *T*-tests were used to determine that if there were

any differences in the selected radiomics features when a certain brain region was involved in or not. The results were listed in **Table S2**. We found that the radiomics feature named "gabor3_glszm_SZHGE" was significantly different when the tumor region located in the frontal lobe or not ($P = 0.022$).

To the tumor volume, we used the Pearson's correlation to explore the relationship between the selected radiomics features and the tumor volume. The corresponding R-value and *P*-values were listed in the **Table S3**. We found six radiomics features were still significant after multiple correlation. For the radiomics feature named "gabor3_glszm_SZHGE," which was a significant predictor of early or late epilepsy onset, was also significant after Bonferroni correlation ($P < 0.001$). The result showed that this feature was negatively related to the tumor volume.

DISCUSSION

In the present study, we aimed to evaluate the performance of the radiomics features in the pretreatment prediction of epileptic seizure after surgery in patients with LGG. We used a two-nested LOOCV loop and recorded the frequency of the features to select the most robust and distinguishable features, obtaining in the end 17 radiomics features. The results suggested that the radiomics features could be successfully used for the pretreatment prediction of epileptic seizures following surgery. In addition, we further analyzed the correlation between radiomics features and the time of seizure utilizing the time information, and the results demonstrated that the radiomics features could be used to predict the patients with early- or late-onset epilepsy. The subgroup analysis proved that the radiomics features were not influenced by the status of preoperative epilepsy. The study details according to IBSI was reported in **Table S4**.

Since the introduction of radiomics, it has gained wide application to the treatment of brain tumors: from diagnosis, through treatment evaluation, to prognosis (28–30). This increased application of radiomics is attributable to its use in helping clinicians to extract more high-throughput information from medical images with higher efficacy, thus improving decision making (31). The use of radiomics has been recently extended to neuropsychiatric diseases with success, suggesting that radiomics might be employable in preoperative prediction of epileptic seizures following surgery in LGG patients. The present study extracted 4650 radiomics features which contained much high-throughput information that beyond of human eyes. By combining the high-throughput information and the time information, we utilized a Cox model to evaluate the performance of radiomics features for preoperative prediction of epileptic seizure after surgery, and the results demonstrated that radiomics could successfully be applied to the pretreatment prediction of postoperative epileptic seizures in LGG patients.

Although the radiomics features contained much information, there were also some redundant information. Hence, we used the E-net regularization to choose the features most predictive of epilepsy status following surgery. Considering the small sample size and the randomness of sample, we performed two-nested LOOCV loops. The features chosen by E-net in each loop would not be identical since the samples were not identical, thus we record the number of loops in which each of the selected features presented because they were chosen by more loops would be more robust. The 17 radiomics features were the most predictive and robust features for the pretreatment prediction of epileptic seizure following surgery, which meant these features had universality for clinical application. In addition, our findings suggest that the radiomics feature named "gabor3_glszm_SZHGE" might be the most important indicator for clinical application since it was predictive of whether and when epilepsy occurs following the operation. Additionally, the mean value of the feature was higher when the frontal lobe was involved in (25.7 in the frontal lobe involved group > 20.8 in the frontal lobe no involved group) according to the clinical correlation analysis. It implied that the larger the feature (gabor3_glszm_SZHGE) value, the later the onset time may be combining with **Figure 3**, which means that when tumors involved in the frontal lobe, seizure may occur early after surgery. This finding might be helpful for postoperative epilepsy prevention. The result from **Table S3** showed that this feature was negatively related to the tumor volume. It implied that the smaller the feature (gabor3_glszm_SZHGE) value, the earlier the onset time may be, which means that the larger the tumor volume, the earlier the onset time based on the current analysis.

The administration of AEDs was a major prophylactic strategy used to address postoperative epilepsy. Details concerning the administration of AEDs to glioma patients, including the drug dosage and duration of prescription, depended on clinical risk factors such as preoperative GRE and tumor resection, etc. (6, 32–34). The standard of AEDs was still controversial and too broad for subjects, and lack of an accurate strategy for individuals now. The present study would help to inform research on the development of individualized prophylactic strategies. Moreover, future clinical applications of our research would help clinicians plan strategies to address the potential onset of epilepsy when treating patients with LGG: the dosages of AEDs need to be raised, and the duration prolonged. Furthermore, our methodology would allow oncologists to perform more frequent and timely follow-up observations of the patients with low values of "gabor3_glszm_SZHGE" and administer an appropriate early intervention.

This study has some limitations. First, the epilepsy status of LGG patients was diagnosed based on clinical presentation, and the patients underwent surgery shortly following diagnosis, so that many of them could not undergo electroencephalography necessary to confirm the diagnosis prior to surgery. Second, the sample size of this study is small, it is difficult to divide an independent validation dataset in this study. For this reason, we adopted a two-nested LOOCV loops to maximize the utility of our sample size and improve the credibility of this study. Despite the above limitations, the features selected in this study performed well, as shown by the C-index. We intend to use a deep learning model and a larger sample size in future studies.

CONCLUSIONS

In conclusion, we selected 17 radiomics features that correlated with postoperative epileptic seizure in patients with LGGs, and found one feature to be a significant predictor of early or late epilepsy onset. Our findings indicate that the features we chose are useful in the management of postoperative epilepsy and that radiomics analysis can potentially be applied to the individualization of prophylactic treatment strategies that address postsurgical epileptic.

DATA AVAILABILITY STATEMENT

The datasets presented in this article are not readily available because they belong to Beijing Tiantan Hospital. Requests to access the datasets should be directed to Yinyan Wang (tiantanyinyan@126.com).

ETHICS STATEMENT

The studies involving human participants were reviewed and approved by The Ethics Committee of the Beijing Tiantan Hospital. Written informed consent to participate in this study was provided by the participants' legal guardian/next of kin.

AUTHOR CONTRIBUTIONS

Study conception and design: JT and YW. Acquisition of data: YL, LW, XL, TJ, and YW. Analysis and interpretation of data: KS, ZL, ZT, SW, XZ, LS, and CS. Drafting of manuscript: KS. Critical revision: KS, ZL, YL, YW, and JT. All authors contributed to the article and approved the submitted version.

FUNDING

This study was supported by the National Natural Science Foundation of China under Grant Nos. 81922040, 81930053, 81527805, and 81772012, the Beijing Natural Science Foundation under Grant No. 7182109, the National Key R&D Program of China under Grant Nos. 2017YFA0205200, 2017YFA0700401, and 2016YFA0100902, the Strategic Priority Research Program of Chinese Academy of Sciences under Grants Nos. XDB32030200 and XDB01030200, Chinese Academy of Sciences under Grant Nos. QYZDJ-SSW-JSC005, KFJ-STS-ZDTP-059, and Shou Fa Ji Jin No. SFH 2018-2-1072, and the Youth Innovation Promotion Association CAS (Grant No. 2019136).

ACKNOWLEDGMENTS

The authors would like to acknowledge the instrumental and technical support of multi-modal biomedical imaging experimental platform, Institute of Automation, Chinese Academy of Sciences.

SUPPLEMENTARY MATERIAL

The Supplementary Material for this article can be found online at: https://www.frontiersin.org/articles/10.3389/fonc.2020.01096/full#supplementary-material

Figure S1 | T2-weighted images with tumor masks for two cases with similar tumor location and size. Case 1 corresponds to a patient who developed epilepsy within 6 months of surgery, the radiomics feature named gabor3_glszm_SZHGE equaled 21.8373. Case 2 corresponds to a patient who developed epilepsy within 6–12 months of surgery, the radiomics feature named gabor3_glszm_SZHGE equaled 27.0216. The non-overlaid and ROI-overlaid source images of case 1 were shown in **(A,C)** separately. The non-overlaid and ROI-overlaid source images of case 2 were shown in **(B,D)** separately.

REFERENCES

1. Santos-Pinheiro F, Park M, Liu D, Kwong LN, Cruz S, Levine NB, et al. Seizure burden pre- and postresection of low-grade gliomas as a predictor of tumor progression in low-grade gliomas. *Neurooncol Pract.* (2019) 6:209–17. doi: 10.1093/nop/npy022
2. Shin JY, Kizilbash SH, Robinson SI, Uhm JH, Hammack JE, Lachance DH, et al. Seizures in patients with primary brain tumors: what is their psychosocial impact? *J Neurooncol.* (2016) 128:285–91. doi: 10.1007/s11060-016-2108-y
3. Vaugier L, Lagarde S, McGonigal A, Trebuchon A, Milh M, Lepine A, et al. The role of stereoelectroencephalography (SEEG) in reevaluation of epilepsy surgery failures. *Epilepsy Behav.* (2018) 81:86–93. doi: 10.1016/j.yebeh.2018.02.005
4. van Breemen MS, Wilms EB, Vecht CJ. Epilepsy in patients with brain tumours: epidemiology, mechanisms, and management. *Lancet Neurol.* (2007) 6:421–30. doi: 10.1016/s1474-4422(07)70103-5
5. Kerkhof M, Dielemans JC, van Breemen MS, Zwinkels H, Walchenbach R, Taphoorn MJ, et al. Effect of valproic acid on seizure control and on survival in patients with glioblastoma multiforme. *Neuro Oncol.* (2013) 15:961–7. doi: 10.1093/neuonc/not057
6. Liang S, Fan X, Zhao M, Shan X, Li W, Ding P, et al. Clinical practice guidelines for the diagnosis and treatment of adult diffuse glioma-related epilepsy. *Cancer Med.* (2019) 8:4527–35. doi: 10.1002/cam4.2362
7. You G, Huang L, Yang P, Zhang W, Yan W, Wang Y, et al. Clinical and molecular genetic factors affecting postoperative seizure control of 183 Chinese adult patients with low-grade gliomas. *Eur J Neurol.* (2012) 19:298–306. doi: 10.1111/j.1468-1331.2011.03509.x
8. Wang Y, Qian T, You G, Peng X, Chen C, You Y, et al. Localizing seizure-susceptible brain regions associated with low-grade gliomas using voxel-based lesion-symptom mapping. *Neuro Oncol.* (2015) 17:282–8. doi: 10.1093/neuonc/nou130
9. Zhou XW, Wang X, Yang Y, Luo JW, Dong H, Liu YH, et al. Biomarkers related with seizure risk in glioma patients: a systematic review. *Clin Neurol Neurosurg.* (2016) 151:113–9. doi: 10.1016/j.clineuro.2016.10.001
10. Lee JW, Wen PY, Hurwitz S, Black P, Kesari S, Drappatz J, et al. Morphological characteristics of brain tumors causing seizures. *Arch Neurol.* (2010) 67:336–42. doi: 10.1001/archneurol.2010.2
11. Pallud J, Audureau E, Blonski M, Sanai N, Bauchet L, Fontaine D, et al. Epileptic seizures in diffuse low-grade gliomas in adults. *Brain.* (2014) 137(Pt 2):449–62. doi: 10.1093/brain/awt345
12. Kumar V, Gu Y, Basu S, Berglund A, Eschrich SA, Schabath MB, et al. Radiomics: the process and the challenges. *Magn Reson Imaging.* (2012) 30:1234–48. doi: 10.1016/j.mri.2012.06.010
13. Lambin P, Rios-Velazquez E, Leijenaar R, Carvalho S, van Stiphout RG, Granton P, et al. Radiomics: extracting more information from medical images using advanced feature analysis. *Eur J Cancer.* (2012) 48:441–6. doi: 10.1016/j.ejca.2011.11.036

14. Liu Z, Wang S, Dong D, Wei J, Fang C, Zhou X, et al. The applications of radiomics in precision diagnosis and treatment of oncology: opportunities and challenges. *Theranostics.* (2019) 9:1303–22. doi: 10.7150/thno.30309
15. Tang Z, Liu Z, Li R, Yang X, Cui X, Wang S, et al. Identifying the white matter impairments among ART-naive HIV patients: a multivariate pattern analysis of DTI data. *Eur Radiol.* (2017) 27:4153–62. doi: 10.1007/s00330-017-4820-1
16. Cui LB, Liu L, Wang HN, Wang LX, Guo F, Xi YB, et al. Disease definition for schizophrenia by functional connectivity using radiomics strategy. *Schizophr Bull.* (2018) 44:1053–9. doi: 10.1093/schbul/sby007
17. Wang Y, Sun K, Liu Z, Chen G, Jia Y, Zhong S, et al. Classification of unmedicated bipolar disorder using whole-brain functional activity and connectivity: a radiomics analysis. *Cereb Cortex.* (2019) 30:1117–28. doi: 10.1093/cercor/bhz152
18. Kong Z, Li J, Liu Z, Liu Z, Zhao D, Cheng X, et al. Radiomics signature based on FDG-PET predicts proliferative activity in primary glioma. *Clin Radiol.* (2019) 74:815.e815-23. doi: 10.1016/j.crad.2019.06.019
19. Zhang Y, Yan P, Liang F, Ma C, Liang S, Jiang C. Predictors of epilepsy presentation in unruptured brain arteriovenous malformations: a quantitative evaluation of location and radiomics features on T2-weighted imaging. *World Neurosurg.* (2019) 125:e1008–15. doi: 10.1016/j.wneu.2019.01.229
20. Liu Z, Wang Y, Liu X, Du Y, Tang Z, Wang K, et al. Radiomics analysis allows for precise prediction of epilepsy in patients with low-grade gliomas. *Neuroimage Clin.* (2018) 19:271–8. doi: 10.1016/j.nicl.2018.04.024
21. Zwanenburg A, Vallieres M. The image biomarker standardization initiative: standardized quantitative radiomics for high-throughput image-based phenotyping. *Radiology*. (2020) 295:328–38. doi: 10.1148/radiol.2020191145
22. Cox DR. Regression models and life-tables. *J R Stat Soc.* (1972) 34:187–220.
23. Iuliano A, Occhipinti A, Angelini C, De Feis I, Lio P. Cancer markers selection using network-based cox regression: a methodological and computational practice. *Front Physiol.* (2016) 7:208. doi: 10.3389/fphys.2016.00208
24. Khundrakpam BS, Tohka J, Evans AC. Prediction of brain maturity based on cortical thickness at different spatial resolutions. *Neuroimage.* (2015) 111:350–9. doi: 10.1016/j.neuroimage.2015.02.046
25. Tian L, Ma L, Wang L. Alterations of functional connectivities from early to middle adulthood: clues from multivariate pattern analysis of resting-state fMRI data. *Neuroimage.* (2016) 129:389–400. doi: 10.1016/j.neuroimage.2016.01.039
26. Harrell FE Jr. *Regression Modeling Strategies: with Applications to Linear Models, Logistic and Ordinal Regression, and Survival Analysis*. Springer (2015).
27. De Caceres M, Legendre P. Associations between species and groups of sites: indices and statistical inference. *Ecology.* (2009) 90:3566–74. doi: 10.1890/08-1823.1
28. Bai Y, Lin YS, Tian J, Shi DP, Cheng JL, Haacke EM, et al. Grading of gliomas by using monoexponential, biexponential, and stretched exponential diffusion-weighted MR imaging and diffusion kurtosis MR imaging. *Radiology.* (2016) 278:496–504. doi: 10.1148/radiol.2015142173
29. Kickingereder P, Burth S, Wick A, Gotz M, Eidel O, Schlemmer HP, et al. Radiomic profiling of glioblastoma: identifying an imaging predictor of patient survival with improved performance over established clinical and radiologic risk models. *Radiology.* (2016) 280:880–9. doi: 10.1148/radiol.2016160845
30. Perez-Beteta J, Molina-Garcia D, Ortiz-Alhambra JA, Fernandez-Romero A, Luque B, Arregui E, et al. Tumor surface regularity at MR imaging predicts survival and response to surgery in patients with glioblastoma. *Radiology.* (2018) 288:218–25. doi: 10.1148/radiol.2018171051
31. Lambin P, Leijenaar RTH, Deist TM, Peerlings J, de Jong EEC, van Timmeren J, et al. Radiomics: the bridge between medical imaging and personalized medicine. *Nat Rev Clin Oncol.* (2017) 14:749–62. doi: 10.1038/nrclinonc.2017.141
32. Wu AS, Trinh VT, Suki D, Graham S, Forman A, Weinberg JS, et al. A prospective randomized trial of perioperative seizure prophylaxis in patients with intraparenchymal brain tumors. *J Neurosurg.* (2013) 118:873–83. doi: 10.3171/2012.12.jns111970
33. Dewan MC, White-Dzuro GA, Brinson PR, Zuckerman SL, Morone PJ, Thompson RC, et al. The influence of perioperative seizure prophylaxis on seizure rate and hospital quality metrics following glioma resection. *Neurosurgery.* (2017) 80:563–70. doi: 10.1093/neuros/nyw106
34. Kerkhof M, Koekkoek JAF, Vos MJ, van den Bent MJ, Taal W, Postma TJ, et al. Withdrawal of antiepileptic drugs in patients with low grade and anaplastic glioma after long-term seizure freedom: a prospective observational study. *J Neurooncol.* (2019) 142:463–70. doi: 10.1007/s11060-019-03117-y

Conflict of Interest: The authors declare that the research was conducted in the absence of any commercial or financial relationships that could be construed as a potential conflict of interest.

frontiers in Oncology

ORIGINAL RESEARCH
published: 14 June 2021
doi: 10.3389/fonc.2021.679952

AUCseg: An Automatically Unsupervised Clustering Toolbox for 3D-Segmentation of High-Grade Gliomas in Multi-Parametric MR Images

*Botao Zhao[1,2], Yan Ren[3], Ziqi Yu[1,2], Jinhua Yu[4], Tingying Peng[5] and Xiao-Yong Zhang[1,2,6]**

[1] Institute of Science and Technology for Brain-inspired Intelligence, Fudan University, Shanghai, China, [2] Key Laboratory of Computational Neuroscience and Brain-Inspired Intelligence (Fudan University), Ministry of Education, Shanghai, China, [3] Department of Radiology, Huashan Hospital, Fudan University, Shanghai, China, [4] School of Information Science and Technology, Fudan University, Shanghai, China, [5] Helmholtz AI, Helmholtz zentrum Muenchen, Munich, Germany, [6] Ministry of Education (MOE) Frontiers Center for Brain Science, Fudan University, Shanghai, China

OPEN ACCESS

Edited by:
Bo Gao,
Affiliated Hospital of Guizhou Medical University, China

Reviewed by:
Laura Bell,
Barrow Neurological Institute (BNI), United States
Kajari Bhattacharya,
Tata Memorial Hospital, India

***Correspondence:**
Xiao-Yong Zhang
xiaoyong_zhang@fudan.edu.cn
orcid.org/0000-0001-8965-1077

Specialty section:
This article was submitted to Cancer Imaging and Image-directed Interventions, a section of the journal Frontiers in Oncology

Received: *12 March 2021*
Accepted: *25 May 2021*
Published: *14 June 2021*

Citation:
Zhao B, Ren Y, Yu Z, Yu J, Peng T and Zhang X-Y (2021) AUCseg: An Automatically Unsupervised Clustering Toolbox for 3D-Segmentation of High-Grade Gliomas in Multi-Parametric MR Images. Front. Oncol. 11:679952. doi: 10.3389/fonc.2021.679952

The segmentation of high-grade gliomas (HGG) using magnetic resonance imaging (MRI) data is clinically meaningful in neurosurgical practice, but a challenging task. Currently, most segmentation methods are supervised learning with labeled training sets. Although these methods work well in most cases, they typically require time-consuming manual labeling and pre-trained models. In this work, we propose an automatically unsupervised segmentation toolbox based on the clustering algorithm and morphological processing, named AUCseg. With our toolbox, the whole tumor was first extracted by clustering on T2-FLAIR images. Then, based on the mask acquired with whole tumor segmentation, the enhancing tumor was segmented on the post-contrast T1-weighted images (T1-CE) using clustering methods. Finally, the necrotic regions were segmented by morphological processing or clustering on T2-weighted images. Compared with K-means, Mini-batch K-means, and Fuzzy C Means (FCM), the Gaussian Mixture Model (GMM) clustering performs the best in our toolbox. We did a multi-sided evaluation of our toolbox in the BraTS2018 dataset and demonstrated that the whole tumor, tumor core, and enhancing tumor can be automatically segmented using default hyper-parameters with Dice score 0.8209, 0.7087, and 0.7254, respectively. The computing time of our toolbox for each case is around 22 seconds, which is at least 3 times faster than other state-of-the-art unsupervised methods. In addition, our toolbox has an option to perform semi-automatic segmentation *via* manually setup hyper-parameters, which could improve the segmentation performance. Our toolbox, AUCseg, is publicly available on Github. (https://github.com/Haifengtao/AUCseg).

Keywords: glioma, unsupervised segmentation, MRI, toolbox, clustering

INTRODUCTION

High-grade gliomas (HGG) are the most common type of central nervous cancer among adults. It has the characteristics of rapid growth, blurred margins, irregular shapes, and invading into the surrounding tissue (1). Currently, HGG segmentation in magnetic resonance imaging (MRI) plays an important role in clinical treatment (2). Manually labeling gliomas in MRI images by doctors has been regarded as the gold standard of tumor segmentation. But it is a tedious and time-consuming job. Several studies have reported that the variabilities of manual tumor segmentation are over 20% (2–4). In the past two decades, computer-aided methods for the segmentation of HGG have been used to save time for clinicians and address the problem of manual variabilities. Despite the emergence of many excellent algorithms in recent years, the segmentation of HGG is still a challenging job (5).

Deep learning-based methods have achieved high Dice similarity in HGG segmentation. The U-net (6) based network architectures were widely used in this task and performed well. Myronenko et al. (7) proposed a 3D U-net with autoencoder regularization, which ranked the top-1 in BraTS2018. Later, Jiang et al. (8) using the two-stage cascaded U-net won the first prize in BraTS2019. Recently, T Henry et al. (9) took first place in BraTS2020 by a deep supervised 3D U-net. Although these supervised methods perform well for HGG segmentation, they require a large amount of labeled data. However, labeling tumors manually not only requires medical expertise, but also is a time-consuming task.

By contrast, clustering is an unsupervised method, which does not require labeling data for training. Vijay J et al. proposed an HGG segmentation method based on K-means clustering, which can quickly segment the whole tumor from 2D images (10). But simply clustering could cause inaccurate results because of the image noise. To solve this, Tripathy et al. (11) improved the fuzzy c-means with spatial context information and intuitionistic set, also named SIFCM. However, this method is time-consuming. Cai et al. proposed the FGFCM algorithm, which reduced the computing time by only considering the partial value instead of the whole image size (12). However, the above advanced clustering methods have not been applied to HGG segmentation because of the lack of a suitable pipeline.

In addition to clustering-based methods, other unsupervised segmentation methods have been investigated for HGG segmentation. Guo et al. (13) reported a semi-automatic method for the segmentation of HGG based on active contour, which was evaluated on 20 cases (a small portion of BraTS2013 training data) and could segment the whole tumor (WT), the tumor core (TC), necrotic (NC) and enhancing tumor (ET). However, this method requires a region of interest (ROI) provided by the user. Juan-Albarracín et al. (14) further proposed an automatic strategy for the HGG segmentation based on Gaussian Hidden Markov Random Field (GHMRF) on the 21 cases from BraTS2013. However, this method is slow and takes 140 ± 32 minutes for the whole segmentation pipeline. N. Sauwen et al. (15) proposed a method based on hierarchical non-negative matrix factorization (HNMF) and gained acceptable segmentation performance on two independent cross-site datasets (21 cases and 14 cases, respectively).

Although the above unsupervised methods achieved acceptable performance, they used a small dataset with limited sample size so that the conclusions may result in bias. To provide clinicians with more robust and reliable assistance, a much larger dataset should be used to have a more thorough evaluation. Moreover, a ready-to-use toolbox is a big advance for its clinical translation. To address these issues, we aim to propose an automatically unsupervised tumor segmentation strategy based on clustering and morphological methods, and to evaluate our method on BraTS2018, a much larger dataset that includes over 200 cases (2–4). Furthermore, we release our segmentation pipeline as a toolbox to provide clinicians with assistance.

METHODS

Pipeline

The pipeline is shown in **Figure 1**. There are three steps for preprocessing: 1) skull-stripping; 2) co-registration on different MRI modalities; 3) Normalization (0~1).

For segmentation, the core concept of this pipeline is based on the pathological and radiological characteristics of HGG. In the T2-FLAIR images, the HGG edema region shows higher signal intensity than other regions due to high water content. In post-contrast T1-weighted images (T1-CE) images, enhancing area shows a significantly higher signal intensity, which means the damage to the blood-brain barrier. Based on the above two features, the edema and enhancing area of the tumor can be first segmented from T2-FLAIR images and T1-CE images by clustering and selecting the subclass with the highest intensity. According to the characteristics of tumor growth, edema is generally located on the boundary of the tumor, while the necrotic (NC) area is generally within the tumor. Therefore, we can fill the connected domain inside the edema region by analyzing the connected components and regard the edema region as the part of the whole tumor (WT) region. After that, the WT was used as the ROI on T1-CE images and segment the enhancing tumor (ET) on it using clustering. The tumor core (TC) is composed of NC and ET.

Additionally, because NC often occurs in the interior of the rapidly growing area of the tumor (the enhancing area), the necrotic area can be segmented using the connected component analysis. However, due to image quality and clustering accuracy, the segmented enhancing regions may not constitute a closed connected domain. When there is little or no enhancing regions, our pipeline still performs well for the segmentation of WT and TC. Note that for these cases the NC cannot be segmented directly due to lacking a completely connected domain. To solve the problem, we propose an alternative solution that segments the tumor core by clustering intensities in the T2 images instead of T2-FLAIR images (**Supplementary Figure S1**). Therefore, the NC region can be segmented by subtracting ET from TC. With above concept, the WT, the TC, the ET, and the NC can be successfully segmented in most cases.

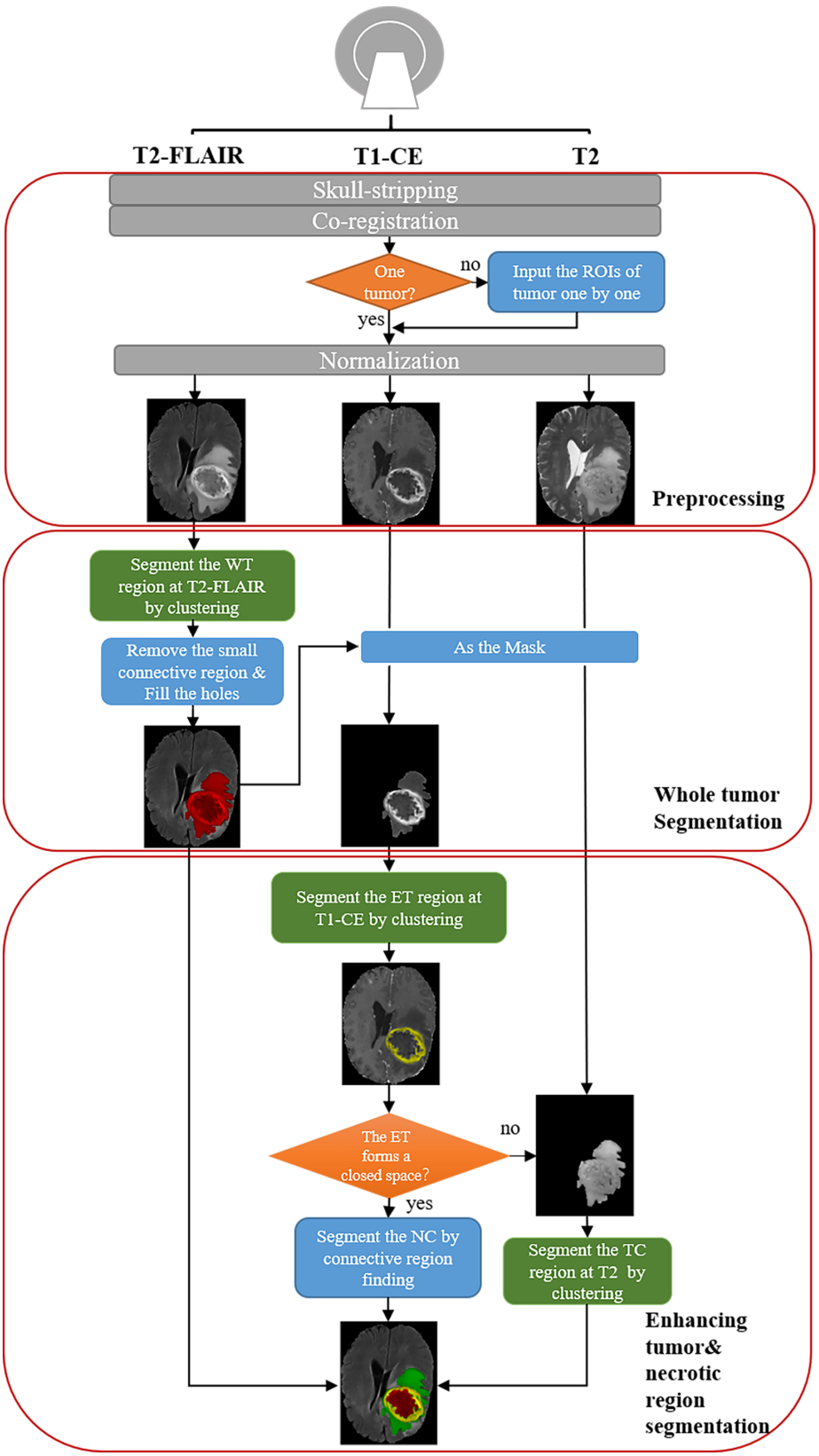

FIGURE 1 | Schematic diagram of our automatic unsupervised pipeline. The orange and green boxes indicate a hyper-parameter there.

Moreover, we also provide an option to segment two or more tumors (**Supplementary Figure S2**). When there is more than one tumor, the hyper-parameter 'ROI' (**Table 1**) is provided for tumor segmentation. Then tumors can be segmented using our pipeline one by one.

Based on the proposed pipeline, our method has the five hyper-parameters as shown in **Table 1**.

Clustering Algorithms

K-Means and Mini-Batch K-Means

K-Means clustering is an unsupervised unstructured iterative partitioning method based on distance. K-means builds a distance model:

$$J = \Sigma_{j=1}^{k}\Sigma_{i=1}^{n}||x_i - c_j||^2 \quad (1)$$

In (1), k represents the number of classes; N is the number of elements to be clustered; $||x_i\text{-}c_j||^2$ is the distance between points x_i and c_j, usually using Euclidean distance. The process of clustering is to find the parameter that minimizes J. Mini-batch K-means (16) is an optimization for K-means clustering. The main idea of this method is that mini-batches have lower stochastic noise than classic stochastic gradient descent, but do not suffer the large computational cost.

Fuzzy C Means (FCM)

FCM introduces the concept of membership degree in fuzzy mathematics based on k-means clustering. After introducing a membership degree, the distance model becomes as follows:

$$\{u_{ij}\} = arg \ \ min \ \Sigma_{j=1}^{c}\Sigma_{i=1}^{n}u_{ij}^{m}||x_i - c_j||^2, \quad (2)$$
$$\text{s.t. } \Sigma_{j=1}^{c}u_{ij} = 1(i = 1, 2, 3, \ldots, n)$$

FCM algorithm is used for clustering, which is to solve the minimum value of equation (2). The u_{ij}^{m} is the membership of element i for class j. It is a conditional extremum problem. The local extremum can be obtained by using the Lagrange multiplier method to incorporate the constraint conditions into the model.

Gaussian Mixture Model (GMM)

GMM uses a probability model to express the clustering prototype. Multidimensional Gaussian distribution is hypothesized for each class. The Gaussian mixture distribution is as:

$$p(x) = \frac{1}{(2\pi)^{\frac{n}{2}}|\Sigma|^{\frac{1}{2}}}e^{-\frac{1}{2}(x-\mu)^{T}\Sigma^{-1}(x-\mu)} \quad (3)$$

$$p_M(x) = \Sigma_{j=1}^{c}\alpha_j \cdot p(x|\mu_j, \Sigma_j) \ , \quad \Sigma_j^c\alpha_j \ = \ 1 \quad (4)$$

Where formula (3) is the multi-dimensional Gaussian distribution, Σ is the covariance matrix, μ is the mean vector. Formula (4) represents the Gaussian mixture distribution. Where α_j represents the mixture coefficient and the probability of the Jth Gaussian distribution. The maximum likelihood method is used to solve the parameters of equation (5):

$$\{\alpha_j, \mu_j, \Sigma_j\} = arg \ \ max_{\alpha,\mu, \ \Sigma}\ln(\Pi_i^n p_M(x_i)) \quad (5)$$

Since equation (5) contains hidden variables, the Expectation-Maximization (EM) algorithm is generally used to optimize parameters. After the Gaussian distribution is known, we divide the elements according to the posterior probability corresponding to the prototype, that is:

$$\lambda_i = \arg \ \max_{j\in\{1,2,\ldots,k\}}\frac{\alpha_j \cdot p(x_i|\mu_j, \Sigma_j)}{\Sigma_{l=1}^{k}\alpha_l \cdot p(x_i|\mu_l, \Sigma_l)} \quad (6)$$

TABLE 1 | Hyper-parameters in our pipeline.

Hyper-params	Default	Describe
n_cluster1	5	Number of clustering for WT segmentation.
n_cluster2	3	Number of clustering for ET segmentation.
ROI	None	If you provide a ROI, the raw image will be cropped by it. If more than one tumor present, it is required to provide ROIs of each tumor for the segmentation.
nc_seg_mode	cc	We provide two modes to segment the necrotic region, 'cc' and 't2'. If the ET region could not wrap up the NC area, it would be better to choose mode 't2'. When you choose 't2', the T2 image must be provided.
n_cluster3	3	Number of clustering for TC segmentation. If the "cc" is chosen as the 'nc_seg_mode', n_cluster3 will not be used.

Morphological Methods

The morphological methods were used for dilation and connected components analysis. The connected component analysis is to find the aggregation region of the same voxel. There are three levels of connectivity for 3D images. The analysis of connected components adopts the accelerated algorithm proposed by Wu et al. (17), which greatly reduces the computing time. Dilation refers to local maximum substitution, which is to calculate the maximum value of pixels in the region covered by the core to replace centrosomes, as shown in equation (7).

$$dst_{dilate}(x, y) = \max_{(x',y')\in kernel} src(x', y') \quad (7)$$

Evaluation

Multi-parametric MRI images of 210 HGG patients from BraTS2018 (2–4) training sets were used to evaluate the pipeline. Our method was implemented with Python3.6, and the main external packages included Numpy, Scikit-learn, Scikit-image, and so on. The experiments were run at the workstation DELL FC430 with CentOS 7.5.1804, Intel (R) Xeon(R) E5-2640 v4 2.4GHz and the memory 256GB. To search for the most suitable clustering method, the main hyper-parameters of the model were set as the default value shown in **Table 1**. K-means++ method or K-means is adopted in the clustering to initialize the clustering center. Dice coefficients, false-positive volume fractions, and false-negative volume fractions were calculated to evaluate the segmentation results. We also adjusted the hyper-parameters to evaluate the performance of our pipeline and analyzed the hyper-parameters distribution. Because the hyper-parameter 'roi' is subjective, we mainly adjusted the remaining four hyper-parameters.

RESULTS

Comparison of Clustering Algorithms

Using the same default hyper-parameters, we compared tumor segmentation results with different clustering methods. It can be found that K-means is faster than other methods (**Table 2**).

The DICE coefficients of segmentation with different clustering methods are shown in **Table 3**. The dice coefficient lower than 0.5 is considered as failed detection. The highest mean values of DICE coefficients and success rates are shown in bold. It can be seen that GMM has the best performance in our pipeline.

Table 4 shows the DICE, false positive, and false negative of segmentation results with GMM clustering in this pipeline. The whole tumor segmentation under this parameter has a problem of over-segmentation, while the segmentation of the tumor core and enhancing region has a problem of under-segmentation. One possible reason for the problem is that we use the same default parameters for different cases.

As shown in **Figure 2**, the WT, the TC, and the ET area can be isolated using our method. TC is composed of NC and ET areas.

Adjusting Hyper-Parameters

Table 5 shows the segmentation result after adjusting the hyper-parameters, including 'n_cluster1', 'n_cluster2', 'nc_seg_mode', and 'n_cluster3'. Compared with the results before adjusting shown in **Table 4**, there is a great improvement in Dice and Success Case rate.

For the whole 210 cases, the distribution of adjusted hyper-parameters 'n_cluster1', 'n_cluster2', and 'n_cluster3' was plotted in **Figure 3A** using the kernel density estimation method. The distribution of 'nc_seg_mode' was shown in **Figure 3B**. We could find that the suitable 'n_cluster1' is mainly in the range of 3~10, and both 'n_cluster2' and 'n_cluster3' were mainly in the range of 3~5. As for the 'nc_seg_mode', 'cc' and 't2' were equally likely to be chosen. So, there are mainly 96 (8*3*4) choices, because the 'n_cluster3' would not be used if 'cc' was chosen. In practice, we do not have to try every possible option and adjust the parameters in the order of 'n_cluster1', 'n_cluster2', 'nc_seg_mode', and 'n_cluster3'. For clustering, the large number of subclasses always means big FN. We can use this to speed up the tuning of parameters.

TABLE 2 | Computing time per patient (second).

	K-means	Mini-batch K-means	GMM	FCM
Time	**10.28 ± 1.95**	14.49 ± 3.64	19.12 ± 4.27	181.20 ± 51.87

The value in bold means the best performance.

TABLE 4 | Results of the GMM based HGG segmentation pipeline.

	WT	TC	ET
DICE	0.8209 ± 0.1051	0.7087 ± 0.1210	0.7254 ± 0.1080
FPVN	0.2600 ± 0.3049	0.1228 ± 0.1714	0.2030 ± 0.3042
FNVN	0.1325 ± 0.1438	0.3732 ± 0.1648	0.3163 ± 0.162

Comparison With Other Unsupervised Methods

As shown in **Table 6**, we compare our methods with several state-of-the-art unsupervised methods. With our method, the WT, TC, and ET can be automatically segmented using default hyper-parameters with Dice score 0.8209, 0.7087, and 0.7254, respectively, which are similar to the published methods. Note that we tested our methods in 210 cases from BraTS2018, which is almost 10 times larger than the datasets other methods used. Another highlight is that the average computing time of our toolbox for each case using the default hyper-parameters is 19 seconds. If adjusted hyper-parameters are used, the average computing time for the segmentation of each case is 22 seconds, which is still comparable to the default setting. As shown in **Table 7**, both settings are at least 3 times faster than other unsupervised methods.

DISCUSSION

We propose an automatically unsupervised clustering method for 3D-segmentation of HGG on multi-parametric MR images. Compared with previous unsupervised methods, our method achieved a stable performance in BraTS2018 dataset including 210 subjects, which is much larger than the previous studies. On the other hand, our method takes less computing time (**Table 7**). Therefore, it may have a broad application, such as clinical translation, preprocessing for supervised learning, etc.

Comparison of Unsupervised Learning Methods

Among the methods of unsupervised learning, the method-based Markov random field and gaussian hybrid model (GHMRF)

TABLE 3 | Dice index of different clustering methods for WT, TC, and ET.

		WT	TC	ET
K-means	Mean ± Std	0.8248 ± 0.1092	0.6975 ± 0.1162	**0.7266 ± 0.0975**
	Success Case	155/210	104/210	135/210
Mini-batch K-means	Mean ± Std	0.8147 ± 0.1093	0.6833 ± 0.1249	0.7168 ± 0.1019
	Success Case	151/210	99/210	127/210
GMM	Mean ± Std	0.8209 ± 0.1051	**0.7087 ± 0.1210**	0.7254 ± 0.1080
	Success Case	**161/210**	**120/210**	**149/210**
FCM	Mean ± Std	**0.8293 ± 0.1045**	0.6874 ± 0.1158	0.7218 ± 0.0988
	Success Case	147/210	100/210	126/210

The value in bold means the best performance.

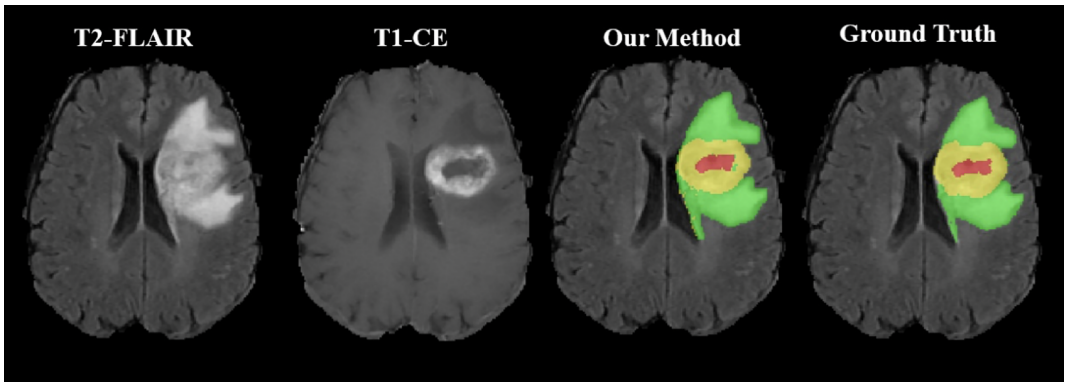

FIGURE 2 | Representative segmentation results using our toolbox. The green area represents the tumor edema area; the yellow area represents the ET area; the red area represents the NC area.

TABLE 5 | Comparison of segmentation results with manually adjusted hyper-parameters.

	WT	TC	ET
DICE	0.8420 ± 0.0982	0.7531 ± 0.1093	0.7496 ± 0.1005
FPVN	0.1836 ± 0.2091	0.1287 ± 0.1476	0.1436 ± 0.1884
FNVN	0.1438 ± 0.1180	0.3123 ± 0.1425	0.3095 ± 0.1458
Success Case	198/210	171/210	180/210

ranked first among the same kind of unsupervised methods in BraTS2013 challenge (14). Supervised methods based on deep learning have been used in the BraTS challenge since 2013. The two-stage Cas-Cascade U-Net method proposed by Jiang et al. won the championship in BraTS2019 (8). In addition, N. Sauwen et al. (15) introduced more types of MRI data for HGG segmentation, including magnetic resonance spectroscopic imaging (MRSI) et al. They proposed a method based on hierarchical non-negative matrix factorization (HNMF), and tested it on two independent cross-site datasets, which reached a higher place among unsupervised HGG segmentation methods.

Compared with the above methods, our method performs well among unsupervised methods although the performance of our method is not as good as supervised method (**Table 6**). According to BraTS2018 Leaderboard (https://www.cbica.upenn.edu/BraTS18/lboardValidation.html), the Dice for ET, WT, and TC are in range of 0.517~0.825, 0.618~0.913, and 0.537~0.872. Note that the performance of our method is in the similar range with most of deep leaning-based methods for the segmentation of brain tumors. Although some state-of-the-art deep leaning-based models have achieved higher performance than our method, their interpretability remains unclear. By contrast, the clustering model we used is interpretable and maybe easier for the clinical translation, which is another advantage of our method.

Limitations

Although adjusting hyper-parameters can improve the segmentation performance with default hyper-parameters, our method does not perform well for a few cases. We have summarized potential causes for suboptimal segmentation

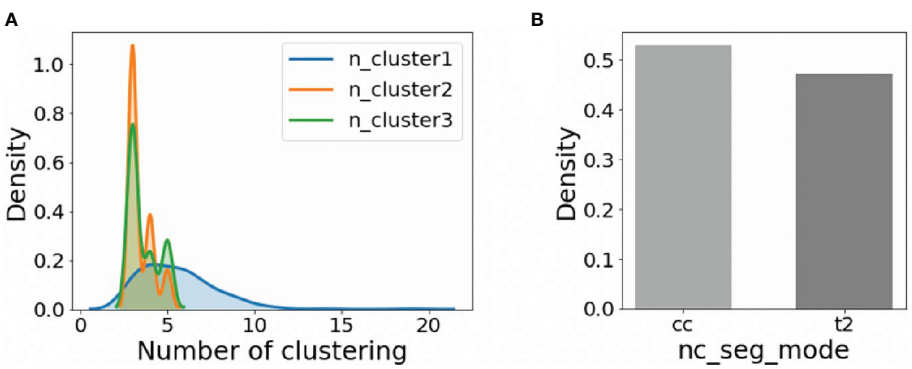

FIGURE 3 | The distribution of hyper-parameters on BraTS2018 HGG training data (n=210). **(A)** The distribution of 'n_cluster1', 'n_cluster2', and 'n_cluster3'. **(B)** The distribution of 'nc_seg_mode'.

TABLE 6 | Performance comparison of several unsupervised methods.

Author	Method	Testing data	Cases	WT	TC	ET
Guo et al. (13)	Active contour	BraTS2013	20	0.82	0.82	0.71
Juan-Albarracín et al. (14)	GHMRF	BraTS2013	21	0.72	0.62	0.59
N. Sauwen et al. (15)	HNMF	UZ Gent	21	0.81	0.74	0.68
		UZ Leuven	14	0.85	0.84	0.73
Our method (Default hyperparameters)	GMM	BraTS2018	210	0.82	0.71	0.73
Our method (Adjusted hyperparameters)	GMM	BraTS2018	210	0.84	0.75	0.75

TABLE 7 | Comparison of computing time (seconds).

Methods	Juan-Albarracín et al. (14)	Guo et al. (13)	N. Sauwen et al. (15)	Our method (Default hyperparameters)	Our method (Adjusted hyperparameters)
Average Time	7620	60	208	19	22

performance with low segmentation DICE scores, which can be roughly grouped into four categories (**Supplementary Figure S3**): a) uncompleted skull stripping; b) abnormal white matter hyperintensities caused by pathological change, such as demyelination; c) low contrast difference between tumor and normal tissue, and d) blurred images caused by head motion or other reasons.

CONCLUSION

We proposed a novel 3D-unsupervised method and implemented a toolbox based on that to automatically segment the whole HGG, tumor core, and enhancing tumor in MR images with Dice score 0.8209, 0.7087, and 0.7254, respectively using default hyper-parameters. Our toolbox has the option to do semi-automatic segmentation *via* manually adjusting hyper-parameters, which could further improve segmentation performance. The combination of GMM with our method performs better than K-means, Mini-Batch K-means, and Fuzzy C Means (FCM). Besides, the computing speed of our method is faster than other unsupervised pipelines. We release our toolbox to provide clinicians with assistance.

DATA AVAILABILITY STATEMENT

The original contributions presented in the study are included in the article/**Supplementary Material**. Further inquiries can be directed to the corresponding author.

AUTHOR CONTRIBUTIONS

BZ: conceived this study, analyzed the data, and drafted the initial manuscript. YR: discussed and finalized the manuscript. ZY: analyzed the data, discussed and finalized the manuscript. JY: discussed and finalized the manuscript. TP: discussed and finalized the manuscript. X-YZ: conceived this study, interpreted the results, and wrote the manuscript. All authors contributed to the article and approved the submitted version.

FUNDING

This study was supported in part by grants from the Shanghai Science and Technology Committee (20ZR1407800), the National Natural Science Foundation of China (81873893), Shanghai Municipal Science and Technology Major Project (No.2018SHZDZX01), ZJ Lab, and Shanghai Center for Brain Science and Brain-Inspired Technology, Fudan University original project (IDH2306024/007), and Shanghai Science and Technology Commission (18411967300).

SUPPLEMENTARY MATERIAL

The Supplementary Material for this article can be found online at: https://www.frontiersin.org/articles/10.3389/fonc.2021.679952/full#supplementary-material

REFERENCES

1. Price S, Jena R, Burnet N, Hutchinson P, Dean A, Pena A, et al. Improved Delineation of Glioma Margins and Regions of Infiltration With the Use of Diffusion Tensor Imaging: An Image-Guided Biopsy Study. *Am J Neuroradiol* (2006) 27(9):1969–74. doi: 10.1016/s0513-5117(08)79144-0
2. Menze BH, Jakab A, Bauer S, Kalpathy-Cramer J, Farahani K, Kirby J, et al. The Multimodal Brain Tumor Image Segmentation Benchmark (BRATS). *IEEE Trans Med Imaging* (2014) 34(10):1993–2024. doi: 10.1109/TMI.2014.2377694
3. Bakas S, Akbari H, Sotiras A, Bilello M, Rozycki M, Kirby JS, et al. Advancing the Cancer Genome Atlas Glioma MRI Collections With Expert Segmentation Labels and Radiomic Features. *Sci Data* (2017) 4(1):1–13. doi: 10.1038/sdata.2017.117
4. Bakas S, Reyes M, Jakab A, Bauer S, Rempfler M, Crimi A, et al. Identifying the Best Machine Learning Algorithms for Brain Tumor Segmentation, Progression Assessment, and Overall Survival Prediction in the BRATS Challenge. *The International Multimodal Brain Tumor Segmentation (BraTS) Challenge* (2018). Available at: https://arxiv.org/abs/1811.02629.

5. Wadhwa A, Bhardwaj A, Verma VS. A Review on Brain Tumor Segmentation of MRI Images. *Magnetic Resonance Imaging* (2019) 61:247–59. doi: 10.1016/j.mri.2019.05.043
6. Ronneberger O, Fischer P, Brox T, eds. U-Net: Convolutional Networks for Biomedical Image Segmentation. In: *International Conference on Medical Image Computing and Computer-Assisted Intervention*. Cham: Springer (2015). pp. 234–41.
7. Myronenko A ed. 3d MRI Brain Tumor Segmentation Using Autoencoder Regularization. In: *International MICCAI Brainlesion Workshop*. Cham: Springer (2018). pp. 311–20.
8. Jiang Z, Ding C, Liu M, Tao D, eds. Two-Stage Cascaded U-Net: 1st Place Solution to Brats Challenge 2019 Segmentation Task. In: *International MICCAI Brainlesion Workshop*. Cham: Springer (2019). pp. 231–41.
9. Henry T, Carre A, Lerousseau M, Estienne T, Robert C, Paragios N, et al. Top 10 BraTS 2020 Challenge Solution: Brain Tumor Segmentation With Self-Ensembled, Deeply-Supervised 3D-Unet Like Neural Networks. *BraTS 2020 Proceedings* (2020). doi: 10.1007/978-3-030-72084-1_30
10. Vijay J, Subhashini J, eds. An Efficient Brain Tumor Detection Methodology Using K-Means Clustering Algoriftnn. In: *2013 International Conference on Communication and Signal Processing*. IEEE (2013). pp. 653–7.
11. Tripathy B, Basu A, Govel S, eds. Image Segmentation Using Spatial Intuitionistic Fuzzy C Means Clustering. In: *2014 IEEE International Conference on Computational Intelligence and Computing Research*. IEEE (2014). pp. 1–5.
12. Cai W, Chen S, Zhang D. Fast and Robust Fuzzy C-Means Clustering Algorithms Incorporating Local Information for Image Segmentation. *Pattern Recog* (2007) 40(3):825–38. doi: 10.1016/j.patcog.2006.07.011
13. Guo X, Schwartz L, Zhao B. Semi-Automatic Segmentation of Multimodal Brain Tumor Using Active Contours. *Multimodal Brain Tumor Segmentation* (2013) 27:27–30.
14. Juan-Albarracín J, Fuster-Garcia E, Manjon JV, Robles M, Aparici F, Martí-Bonmatí L, et al. Automated Glioblastoma Segmentation Based on a Multiparametric Structured Unsupervised Classification. *PloS One* (2015) 10 (5):e0125143. doi: 10.1371/journal.pone.0125143
15. Sauwen N, Acou M, Van Cauter S, Sima D, Veraart J, Maes F, et al. Comparison of Unsupervised Classification Methods for Brain Tumor Segmentation Using Multi-Parametric MRI. *NeuroImage: Clin* (2016) 12:753–64. doi: 10.1016/j.nicl.2016.09.021
16. Sculley D. Web-Scale K-Means Clustering. In: *Proceedings of the 19th International Conference on World Wide Web* (2010). pp. 1177–8. doi: 10.1145/1772690.1772862
17. Wu K, Otoo E, Shoshani A. Optimizing Connected Component Labeling Algorithms. In: *Medical Imaging 2005: Image Processing*. International Society for Optics and Photonics (2005). Vol. 5747, pp. 1965-76.v. doi: 10.1117/12.596105

Conflict of Interest: The authors declare that the research was conducted in the absence of any commercial or financial relationships that could be construed as a potential conflict of interest.

frontiers in Oncology

ORIGINAL RESEARCH
published: 18 November 2021
doi: 10.3389/fonc.2021.779202

Multiparametric MRI Radiomics for the Early Prediction of Response to Chemoradiotherapy in Patients With Postoperative Residual Gliomas: An Initial Study

Zhaotao Zhang[1†], Keng He[1†], Zhenhua Wang[1], Youming Zhang[2], Di Wu[3], Lei Zeng[4], Junjie Zeng[5], Yinquan Ye[1], Taifu Gu[1] and Xinlan Xiao[1]*

[1] Department of Radiology, The Second Affiliated Hospital of Nanchang University, Nanchang, China, [2] Department of Radiology, Hsiang-ya Hospital, Changsha, China, [3] Department of Radiology, The First Affiliated Hospital of Gannan Medical College, Ganzhou, China, [4] Department of Oncology, The Second Affiliated Hospital of Nanchang University, Nanchang, China, [5] Department of Radiology, The Fifth Affiliated Hospital of Jinan University, Heyuan, China

OPEN ACCESS

Edited by:
Fu Wang,
Xi'an Jiaotong University, China

Reviewed by:
Jun Liu,
Central South University, China
Lizhi Liu,
Sun Yat-sen University Cancer Center (SYSUCC), China

***Correspondence:**
Xinlan Xiao
jx_xiaoxinlan@sina.com

[†]These authors have contributed equally to this work

Specialty section:
This article was submitted to Cancer Imaging and Image-directed Interventions, a section of the journal Frontiers in Oncology

Received: 18 September 2021
Accepted: 29 October 2021
Published: 18 November 2021

Citation:
Zhang Z, He K, Wang Z, Zhang Y, Wu D, Zeng L, Zeng J, Ye Y, Gu T and Xiao X (2021) Multiparametric MRI Radiomics for the Early Prediction of Response to Chemoradiotherapy in Patients With Postoperative Residual Gliomas: An Initial Study. Front. Oncol. 11:779202. doi: 10.3389/fonc.2021.779202

Purpose: To evaluate whether multiparametric magnetic resonance imaging (MRI)-based logistic regression models can facilitate the early prediction of chemoradiotherapy response in patients with residual brain gliomas after surgery.

Patients and Methods: A total of 84 patients with residual gliomas after surgery from January 2015 to September 2020 who were treated with chemoradiotherapy were retrospectively enrolled and classified as treatment-sensitive or treatment-insensitive. These patients were divided into a training group (from institution 1, 57 patients) and a validation group (from institutions 2 and 3, 27 patients). All preoperative and postoperative MR images were obtained, including T1-weighted (T1-w), T2-weighted (T2-w), and contrast-enhanced T1-weighted (CET1-w) images. A total of 851 radiomics features were extracted from every imaging series. Feature selection was performed with univariate analysis or in combination with multivariate analysis. Then, four multivariable logistic regression models derived from T1-w, T2-w, CET1-w and Joint series (T1+T2+CET1-w) were constructed to predict the response of postoperative residual gliomas to chemoradiotherapy (sensitive or insensitive). These models were validated in the validation group. Calibration curves, receiver operating characteristic (ROC) curves, and decision curve analysis (DCA) were applied to compare the predictive performances of these models.

Results: Four models were created and showed the following areas under the ROC curves (AUCs) in the training and validation groups: Model-Joint series (AUC, 0.923 and 0.852), Model-T1 (AUC, 0.835 and 0.809), Model-T2 (AUC, 0.784 and 0.605), and Model-CET1 (AUC, 0.805 and 0.537). These results indicated that the Model-Joint series had the best performance in the validation group, followed by Model-T1, Model-T2 and finally Model-CET1. The calibration curves indicated good agreement between the Model-Joint

series predictions and actual probabilities. Additionally, the DCA curves demonstrated that the Model-Joint series was clinically useful.

Conclusion: Multiparametric MRI-based radiomics models can potentially predict tumor response after chemoradiotherapy in patients with postoperative residual gliomas, which may aid clinical decision making, especially to help patients initially predicted to be treatment-insensitive avoid the toxicity of chemoradiotherapy.

Keywords: radiomics, magnetic resonance imaging, residual gliomas, chemoradiotherapy, early prediction

INTRODUCTION

Glioma is the most common tumor of the brain and is associated with high rates of disability and death, which is part because the tumor lesion is difficult to completely remove surgically due to its invasive growth characteristics. Presently, according to the international guidelines for the treatment of neurological tumors, concurrent postoperative chemoradiotherapy is recommended for some grade 2, grade 3 and grade 4 glioma patients to treat residual tumor lesions. Radiotherapy and chemotherapy have a definite therapeutic effect on gliomas, but there are also some negative effects, such as hair loss, vomiting, decreased immunity and high cost. Clinical practices have shown that not all gliomas are sensitive to chemoradiation due to the heterogeneity of tumor tissues. Therefore, some patients not only are unable to benefit from the treatment but also unnecessarily suffer from the effects of chemoradiation. Therefore, identifying treatment-insensitive patients has become a critical area of research.

Previously, most studies predicting the response of tumors to radiotherapy and chemotherapy have been based on conventional computed tomography/magnetic resonance imaging (CT/MRI), functional MRI or positron emission tomography (PET), but the predictive performances have not been satisfactory. One of the important reasons is because the deep information within images cannot be comprehended with the naked eye. However, radiomics, an emerging method, can acquire the detailed characteristics from medical imaging data of the entire lesion in a high-throughput manner with computer technology (1–3). These extracted data can then be deeply mined and analyzed, correlated with the clinical or biological information of the disease, and finally used to construct prediction models.

Some studies evaluating tumor response with radiomics have been reported, but the research has mainly focused on colorectal cancer, nasopharyngeal cancer, breast cancer and lung cancer (4–7), showing improved predictive performance with radiomics. However, to the best of our knowledge, few studies predicting the curative effect of chemoradiotherapy for residual gliomas with a radiomics approach have been reported, but this area is very important for choosing treatment for glioma patients.

Thus, the purpose of this study was to extract high-throughput radiomics features from conventional multiparametric MR images, screen for features highly correlated with chemoradiation sensitivity, and establish logistic regression models based on the selected features to predict the treatment sensitivity of gliomas. Ultimately, the model was expected to accurately identify treatment-insensitive patients and thus aid clinicians in optimizing treatment regimens for such patients.

MATERIALS AND METHODS

Patients

This is a retrospective study approved by our institution's review board, and the requirement for informed consent was waived. In total, the images and pathological data of 231 consecutive patients were collected from three institutions from January 2015 to September 2020 (institution 1: The Second Affiliated Hospital of Nanchang University; institution 2: The First Affiliated Hospital of Gannan Medical College; and institution 3: Hsiang-ya Hospital). In total, 84 glioma patients with residual gliomas after surgery who were treated with concurrent chemotherapy and radiotherapy were enrolled in this study (institution 1, 57 patients; institution 2, 8 patients; and institution 3, 19 patients). The inclusion criteria were as follows: 1) tumors located above the cerebellar tentorium; 2) pathologically confirmed grade II-IV gliomas; 3) a definite residual tumor confirmed by conventional and advanced MRIs acquired within 72 hours after surgery, as well as clear surgical records of a residual lesion; 4) treatment with concurrent radiotherapy and chemotherapy after surgery within 3 weeks; and 5) available and complete preoperative and postoperative images, pathological data and clinical data. The exclusion criteria were as follows: 1) unclear presence of a residual tumor after surgery; 2) atypical postoperative treatment; and 3) missing or incomplete imaging or pathological data. All patients from institution 1 (57 patients), with a treatment-sensitive-to-treatment-insensitive ratio of 16:41, were defined as the training cohort. Patients from institution 2 and institution 3 (a total of 27 patients), with a treatment-sensitive-to-treatment-insensitive ratio of 9:18, were defined as the validation cohort.

Image Acquisition

Preoperatively and postoperatively, conventional MR scans and contrast enhancement scans were acquired for the 84 glioma patients using different devices with similar scanning protocols. In institution 1, 57 patients underwent head MRI using a 1.5-T (Signa HDxt;GE Medical System, Inc, Waukesha, WI, USA) or

3.0-T device (Discovery 750; GE Healthcare, Milwaukee, WI, USA) with an 8-channel head coil. In institution 2, 8 patients underwent head MRI using 3.0-T device (Discovery 750; GE Healthcare, Milwaukee, WI, USA). In institution 3, 19 patients underwent head MRI using a 1.5-T (Avanto Magnetom; Siemens, Erlangen, Germany) or 3.0-T device (Discovery 750; GE Healthcare, Milwaukee, WI, USA). Preoperative MR images were taken within 2 weeks before the operation. Postoperative images were taken within 72 hours after surgery and 3 months after recurrent concurrent chemotherapy and radiotherapy. All of the scanning protocols and imaging parameters were similar among the different MR machines. Axial T1-weighted (T1-w), T2-weighted (T2-w) and axial contrast-enhanced T1-weighted (CET1-w) images in Digital Communications in Medicine (DICOM) format were selected for further analysis. Pathology results and clinical data were obtained from the Electronic Hospital Information System (EHIS).

Image Normalization

To eliminate the heterogeneity among the MR scan parameters and devices, all images were resampled to 1*1*1 mm^3 voxels, and their intensity range was normalized to 0 to 255 using the open-source 3D-Slicer 4.10.2 platform (https://www.softpedia.com/get/Science-CAD/3D- Slicer. shtml).

Treatment and Response Evaluation

All 84 glioma patients from the three institutions began chemoradiotherapy within 3 weeks after surgery. Regarding, radiation range and dose, the gross tumor volume (GTV) included areas of abnormal enhancement and the lumen shown by postoperative MR CET1-w images and areas with abnormal signal on T2-w/FLAIR images. The clinical target volume (CTV) was defined as the GTV plus a margin of 1–2 cm. The radiotherapy dose was 60 Gy/30 fractions, avoiding any organs at risk. The chemotherapy regimen was implemented simultaneously and composed of temozolomide (75 mg/m^2). The Response Assessment in Neuro Oncology (RANO) criteria (8) was currently widely used around the world to evaluate the effect of therapy on brain tumors and was also applied in this study to evaluate the treatment sensitivity of residual gliomas. The details of the RANO criteria were shown in the **Supplementary Material** (1). Partial remission and complete remission were defined by the presence of treatment-sensitive tumors that disappeared or decreased by ≥ 50% on CET1-w images. Stable disease and progressive disease were defined by the presence of treatment-insensitive tumors that increased or decreased by -25% ~ +25% on CET1-w images, lesions that increased by ≥ 25% and any new lesions. The therapeutic sensitivity of a tumor was defined by a combination of imaging findings and some clinical indexes. The approximate evaluation formula for tumor volume change was as follows: Tumor volume ≈ (Maximum long diameter) * (Vertical Maximum short diameter) * (Sum of all layer spacing and layer thickness). The first follow-up MRI was conducted within 72 hours postoperatively and applied as the baseline data.

ROI Segmentation and Feature Extraction

Regions of interest (ROIs) were segmented on preoperative images (T1-w, T2-w, and CET1-w images) using the 3D-Slicer 4.10.2 platform, which was also used for feature extraction. All ROI boundaries in each tumor were delineated on every slice of the T1-w, T2-w and CET1-w images. Twenty random patients' MR images were chosen and manually segmented by a radiologist with 10 years of experience in diagnosing central nervous system diseases (reader 1), and this process was repeated after 3 weeks to evaluate intraobserver reproducibility. The same segmentation procedure was conducted by another radiologist (reader 2) with 15 years of clinical experience to evaluate interobserver reproducibility.

Four types of radiomics features, shape, first-order, textural, and filter-based features (wavelet features), were extracted from the ROIs through the 3D-Slicer 4.10.2 platform. Additionally, four groups of features were extracted from the T1-w, T2-w, CET1-w and Joint series images.

Semantic features of the lesions, such as enhancement grade, cystic grade and edema grade were extracted from the conventional images. The enhancement, cystic and edema features were all graded into three levels, and the details were shown in **Table 1**.

Feature Selection, Radiomics Model Development, Model Performance Evaluation

The feature data from T1-w, T2-w, CET1-w and Joint series (T1-w+T2-w+CET1-w) were loaded into the GE IPMs platform. The synthetic minority oversampling technique (SMOTE) algorithm was used to balance the training datasets, and Z-score standardization was used for data normalization. After SMOTE, the training cohort contained 82 samples, with a treatment-sensitive -to -treatment-insensitive ratio of 41:41. To establish the radiomics signature, we used univariate analysis and multivariate analysis, including the Student's t test, Rank sum test, Variance analysis, Correlation_analysis, Univariate _Logistic analysis and multivariate logistic analysis, to select feature sets from the normalized data. The detailed extraction process was showed in the **Supplementary Materials** (2–5).

R-4.0.3 (https://www.r-project.org/) and the R studio platform (https://rstudio.com/products/rstudio/download/#download) were used to develop the radiomics models. Features selected from the T1-w, T2-w, CET1-w, and Joint series were analyzed with multiple logistic regression to construct the radiomics models. Model validation was conducted in the validation cohort. Calibration plots and receiver operating characteristic (ROC) curves were generated to evaluate model performance. Decision curve analysis (DCA) was performed to evaluate the clinical utility of the models.

Statistical Analysis

Statistical analysis was performed with IBM SPSS Statistics 25 and R software (version 4.0.3). Student's t test, Chi-square tests and Fisher's exact tests were used to compare the clinical characteristics, image and pathology data of the training and

TABLE 1 | Clinical characteristics of the patients and semantic image features in the training and validation cohorts.

Characteristic	All patients	Training cohort	Validation cohort	P-value	Training and Validation cohort		P-value
	(n = 84)	(n = 57)	(n = 27)		Sensitive (n = 25)	Insensitive (n = 59)	
Age (years)	48.452 (12.619)	49.491 (11.386)	46.259 (14.891)	0.276	47.360 (12.312)	48.915 (12.823)	0.609
Gender:				0.840			0.535
male	48 (57.1%)	33 (57.9%)	15 (55.6%)		13 (52.0%)	35 (59.3%)	
female	36 (42.9%)	24 (42.1%)	12 (44.4%)		12 (48.0%)	24 (40.7%)	
Pathological grade:				0.262			0.330
grade 2	16 (19.0%)	12 (21.1%)	4 (14.8%)		7 (28.0%)	9 (15.3%)	
grade 3	19 (22.6%)	10 (17.5%)	9 (33.3%)		4 (16.0%)	15 (25.4%)	
grade 4	49 (58.3%)	35 (61.4%)	14 (51.9%)		14 (56.0%)	35 (59.3%)	
Enhancement grade:				0.605			0.474
grade 1	11 (13.1%)	8 (14.0%)	3 (11.1%)		5 (20.0%)	6 (10.2%)	
grade 2	40 (47.6%)	25 (43.9%)	15 (55.6%)		11 (44.0%)	29 (49.2%)	
grade 3	33 (39.3%)	24 (42.1%)	9 (33.3%)		9 (36.0%)	24 (40.7%)	
Cystic grade:				0.936			0.747
grade 1	20 (23.8%)	14 (24.6%)	6 (22.2%)		6 (24.0%)	14 (23.7%)	
grade 2	29 (34.5%)	20 (35.1%)	9 (33.3%)		10 (40.0%)	19 (32.2%)	
grade 3	35 (41.7%)	23 (40.4%)	12 (44.4%)		9 (36.0%)	26 (44.1%)	
Edema grade:				0.246			0.765
grade 1	10 (11.9%)	8 (14.0%)	2 (7.4%)		2 (8.0%)	8 (13.6%)	
grade 2	33 (39.3%)	19 (33.3%)	14 (51.9%)		10 (40.0%)	23 (39.0%)	
grade 3	41 (48.8%)	30 (52.6%)	11 (40.7%)		13 (52.0%)	28 (47.5%)	
Sensitive:				0.622			
yes	25 (29.8%)	16 (28.1%)	9 (33.3%)				
no	59 (70.2%)	41 (71.9%)	18 (66.7%)				

Continuous variables were presented as the mean (SD). Categorical variables were presented as absolute numbers (n) and proportions (%). Student's t-test, $\chi 2$ test and Fisher's exact test were used for comparisons of continuous variables and categorical variables, respectively.
Enhancement grade, according to visual enhancement:
grade 1 (mild enhancement); grade 2 (moderate enhancement); grade 3 (severe enhancement).
Cystic grade, according to the ratio of cystic volume to total lesion volume:
grade 1 (none); grade 2 (<50%); grade 3 (>50%).
Edema grade, according to the distance between the edge of the area of edema and lesion:
grade 1 (none); grade 2 (<2 cm); and grade 3 (>2 cm).

validation cohorts. The Delong test was used to compare differences in the ROC curves among various models. The intraclass correlation coefficient (ICC) was applied to assess the stability of each extracted radiomics feature. ICCs were calculated through the 'irr' package. Multivariate binary logistic regression was performed with the 'glmnet' package. The 'pROC', 'rms' and 'rmda' packages were used to obtain ROC curves, calibration curves and DCA curves, respectively. A two-tailed P-value < 0.05 was considered statistically significant.

RESULTS

Patient Characteristics

No significant differences in patient characteristics were observed between the training and validation cohorts (age, sex, sensitivity to treatment, pathological grade, enhancement grade, cystic grade, and edema grade, **Table 1**, all P > 0.05), indicating that it was reasonable to use external data from institutions 2 and 3 for validation.

Intraobserver and Interobserver Reproducibility of the Radiomics Features

A total of 2553 (851×3) radiomics features were extracted from the ROIs of the T1-w, T2-w and CET1-w images, respectively, including 18 first-order features,14 shape features, and 75 texture features [gray level dependence matrix (GLDM, 14), gray-level co-occurrence matrix (GLCM, 24), gray-level run length matrix (GLRLM, 16), gray-level size zone matrix (GLSZM, 16) and neighborhood gray-tone difference matrix (NGTDM, 5)], and 744 wavelet features [(18 + 14+24+16+16+5)*8]. Features with intraobserver and interobserver ICCs <0.75 were discarded. Therefore, 467 features from the T1-w images, 380 features from the T2-w images, and 490 features from the CET1-w images were obtained.

Radiomics Signature and Model Construction

After univariate analysis with or without multivariate analysis, several features highly correlated with sensitivity to chemoradiation were identified (6 features from the T1-w images, 7 features from the T2-w images, 6 features from the CET1-w images, and 5 features from the Joint series images). The detailed screening procedures were showed in the **Supplementary Materials** (2–5). The data acquisition and analysis workflow was showed in **Figure 1**. These final features were introduced to build four radiomics models through multivariate binary logistic regression:

Model(T1-w)=-0.1262+(0.9157*wavelet-LLL_glcm_Idmn)-(0.1732*wavelet-LHL_glcm_Imc2)

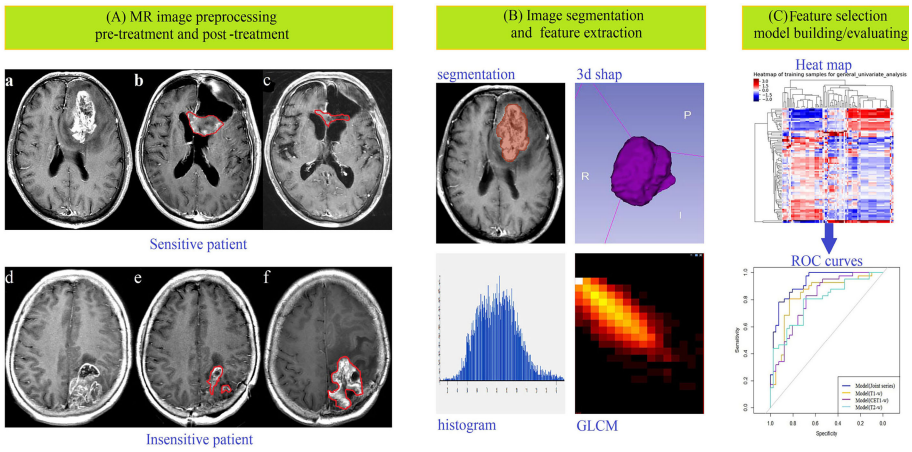

FIGURE 1 | Data acquisition and analysis workflow. All patients were divided into treatment-sensitive and treatment-insensitive groups. **(A)** Pictures a and d showed the original images before treatment, b and e showed the postoperative images acquired within 24–72 hours, and c and f showed the postoperative images acquired after approximately 3 months of follow-up. **(B)** ROIs were defined, and feature extraction, including for first-order, shape-, high-order texture-, and filter-based features, was performed. **(C)** Feature selection, model building and model evaluation were used to predict the response of glioma patients to chemoradiation by multiple logistic regression analysis.

+(0.8470*original_firstorder_Skewness)-(0.3914*wavelet-HLL_glcm_DifferenceAverage)

+(0.5724*wavelet-LHH_firstorder_Median)+(0.4312*wavelet-LHH_glcm_SumEntropy)

Model(T2-w)=0.0267-(0.2443*wavelet-LHL_gldm_LargeDependenceEmphasis)-(0.6148*original_glrlm_LongRunHighGrayLevelEmphasis)+(0.6830*wavelet-HHL_glcm_SumEntropy)

-(0.0707*original_glcm_Idn)+(0.7691*wavelet-HHL_glcm_Contrast)+(0.1583*wavelet-LHH

_firstorder_Maximum) -(0.1271*wavelet-LLL_glcm_Imc1)

Model(CET1-w)=-0.0983+(0.1927*wavelet-LHL_glrlm_RunVariance)-(0.9772*wavelet-LHH_glcm_Idmn)+(0.3411*wavelet-HLH_glszm_HighGrayLevelZoneEmphasis)-(0.8397*wavelet

-LHH_firstorder_Kurtosis)+(0.5278*wavelet-HLH_glszm_SmallAreaHighGrayLevelEmphasis)

-(0.5460*wavelet-HHL_firstorder_Kurtosis)

Model(Joint series)=-0.7185-(2.0591*T1_wavelet-LLL_glszm_GrayLevelNon

UniformityNormalized)-(1.9826*CET1_wavelet-LHH_glcm_Idmn)-(2.5979*CET1_wavelet

-LHH_firstorder_Kurtosis)+(1.2404*T1_wavelet-LLH_firstorder_Kurtosis)-(1.2912*CET1

_wavelet-LLH_firstorder_Median)

Model Performance Evaluation

The ROC curves (**Figure 2**) showed the Model-Joint series and Model-T1 had better performances, with areas under the ROC curves (AUCs) of 0.923 and 0.835 in the training cohort and 0.852 and 0.809 in the validation cohort, whereas Model-CET1 and Model-T2 had poor performances with low AUCs in the validation cohorts. Model-T1 had the best sensitivity, specificity and accuracy compared to the other models. The detailed performance results of the different models were listed in **Table 2**. The Delong tests did not find significant differences between the ROC curves of the Model-Joint series and Model-T1 (p values of 0.113 and 0.738 in the training and validation sets, respectively). However, the differences between the Model-Joint series and Model-CET1-w and between the Model-Joint series and Model-T2 were significant in the training sets, with p values of 0.014 and 0.012, respectively. Nonsignificant unreliability U test (P=0.982 and 0.052) and Hosmer-Lemeshow test results (P=0.7303 and 0.9084) showed good calibration in the training cohort and validation cohort regarding Model-Joint series. The calibration curves were showed in **Figure 3**. The DCA curves indicated that the Model-Joint series had the most clinical utility, as showed in **Figure 4**.

DISCUSSION

In our study, four MRI-based radiomics logistic regression models were established, derived from T1-w, T2-w, CET1-w and Joint series. Model-Joint series and Model-T1 yielded better predictivity in determining whether glioma patients were sensitive to chemoradiation. Hence, MRI-based radiomics models may help clinicians identify treatment-sensitive and treatment-insensitive patients to tailor treatment to each individual.

Radiotherapy and chemotherapy are important adjuvant treatments for patients with residual tumors postoperatively.

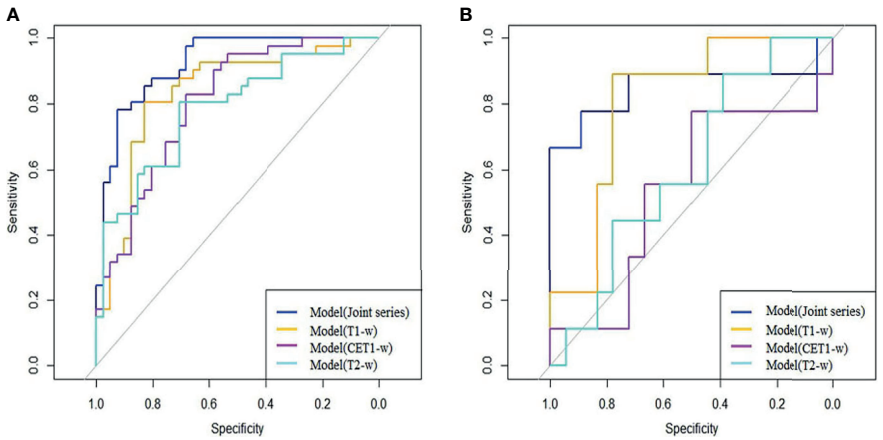

FIGURE 2 | **(A, B)** showed the ROC curves of the four prediction models in the training and validation cohorts: the blue curve represented the Model(Joint series), the orange curve represented Model(T1-w), the purple curve represented Model(CET1-w), and the turquoise curve represented model(T2-w).

Multiparameter MRI, a noninvasive and repeatable examination method, has been widely used to evaluate the efficacy of chemoradiotherapy for tumors. However, there are few studies predicting the curative effect of chemoradiotherapy for residual gliomas before treatment, which is crucial for choosing the right therapeutic schedule. We know that not all glioma patients are susceptible to chemoradiotherapy. Therefore, if we can detect poor responders early, many unnecessary injuries and side effects can be avoided. Additionally, alternative treatments can be chosen earlier, such as targeted therapy (9–12), immunotherapy (13–16), interstitial brachytherapy (17, 18), or even sonodynamic therapy based on ultrasound stimulation and a sonosensitizer (19). In our study, we used radiomics models to predict the sensitivity of residual gliomas to chemoradiotherapy and compared the histopathological grade and conventional MR semantic features between treatment-sensitive and treatment-insensitive patients. The results showed no significant difference in the histopathological grade of gliomas between the treatment-sensitive and treatment-insensitive groups. This may be because the histological grade was determined by the degree of differentiation of a small specimen, which cannot represent the whole tumor, whereas radiomics features provide the tumor's overall biological information (20, 21). The pretreatment conventional MR semantic features of the tumor lesions, including enhancement, cystic and edema grades, also showed no difference between the two groups. Therefore, conventional MR semantic features may not predict the sensitivity of the tumor to chemoradiation.

Radiomics, an emerging and noninvasive research method, is used to extract high-throughput imaging features that cannot be recognized by the human eye and to evaluate and quantify biological information such as tumor heterogeneity, tumor cell growth and the surrounding microenvironment (22, 23). According to previous studies on locally advanced rectal cancer, radiomics features, including skewness, entropy and several GLCM parameters, extracted from MRI have can be highly significant predictors for the response to neoadjuvant chemoradiotherapy (24–27). In our present work, four groups of radiomics features were selected to establish predictive models, including first-order features, shape-based features, textural features, and wavelet features. The wavelet features were extracted by a three-dimensional discrete wavelet transform using high-frequency and low-frequency filters, which can accurately obtain the detailed features of the images. In the four models (**Table 3**), the wavelet_firstorder_Kurtosis feature appeared four times, indicating that kurtosis was closely

TABLE 2 | The performances of the four logistic regression models in predicting sensitivity to treatment in the training and validation cohorts.

Modality	Features screening	Remainedfeatures	Cohorts	AUC (95%CI)	Sen	Spe	Acc
Model-Joint series	univariate analysis+ multivariate analysis	5	training	0.923 (0.866-0.979)	0.829	0.829	0.829
			validation	0.852 (0.644-1.000)	0.778	0.722	0.741
Model-T1	univariate analysis	6	training	0.835 (0.743-0.927)	0.805	0.756	0.780
			validation	0.809 (0.638-0.979)	0.889	0.778	0.815
Model-CET1	univariate analysis	6	training	0.805 (0.712-0.899)	0.780	0.683	0.732
			validation	0.537 (0.284-0.790)	0.778	0.389	0.519
Model-T2	univariate analysis	7	training	0.784 (0.685-0.883)	0.732	0.707	0.720
			validation	0.605 (0.381-0.829)	0.444	0.556	0.519

AUC, area under the curve; Sen, sensitivity; Spe, specificity; Acc, accuracy.
Univariate analysis included 'General_Univariate_analysis' (Student's t test or Rank sum test), 'Variance', 'Correlation_xx' and 'Univariate _Logistic'analysis.
The multivariate analysis used in this study was 'MultiVariate_Logistic' analysis.

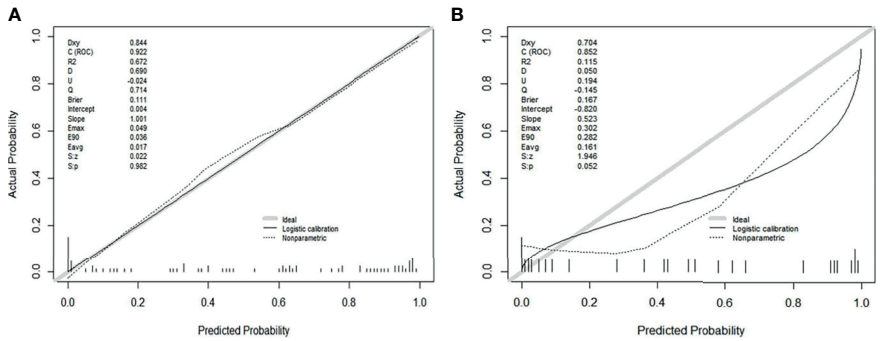

FIGURE 3 | **(A, B)** showed the calibration curves of the Model(Joint series) in the training cohort and validation cohort. The y-axis represented the actual probability of treatment-sensitive patients. The x-axis represented the predicted probability of treatment-insensitive patients. The diagonal gray line represented a perfect prediction by an ideal model. The black solid line represented the prediction performance of the Model(Joint series), and the closer the black line was to the gray line, the better the prediction performance of the model.

associated with chemoradiotherapy in gliomas; this feature described the overall distribution curve of voxel intensity in the ROI with a flat or sharp peak. However, this result was different from that of Dinapoli N et al. (26), who conducted a study based on an intensity histogram signature to predict the probability of achieving a pathologic complete response using a Laplacian of Gaussian (LoG) filter. We inferred that there may be two reasons for the different results: one was the different types of tumors studied, and the other was the different feature extraction methods. The wavelet_glcm_Idmn feature was the second most repeated feature in all models. GLCM described the joint gray-level distribution of any two pixels in the ROI with some spatial positioning information, and the gray-level distribution can be mined with repetitive regularity. Idmn measured the local variations in the image texture and reflected the homogeneity of the texture. The more uniform the local image was, the stronger the texture regularity, and the larger the Idmn value. The Wavelet_firstorder_Median, wavelet_glcm_Imc and wavelet_glcm _SumEntropy features were repeated twice in the models. Median represented the median gray level intensity within the ROI, which was likely related to chemotherapeutic efficacy according the Ng SH' study (28). Imc assessed the correlation of the probability distributions, quantifying the complexity of the texture. SumEntropy was the sum of the neighborhood intensity value differences. In the Model-Joint series, the Idmn and median values from the CET1-w scans were both inversely proportional to the sensitivity of glioma to chemoradiation. This meaned that the more heterogeneous the image texture, the smaller the median gray value, and the more sensitive the tumors were to treatment. In our four models, no shape-based features appeared, suggesting that tumor morphology was not closely related to sensitivity to treatment. Additionally, it was noteworthy that no feature was selected from the T2-w images to construct the Model-Joint series. We found most of the features selected from T1-w, T2-w and CET1-w images were texture features, which reflected the internal distribution law of image pixels. Usually, T2-w was significantly

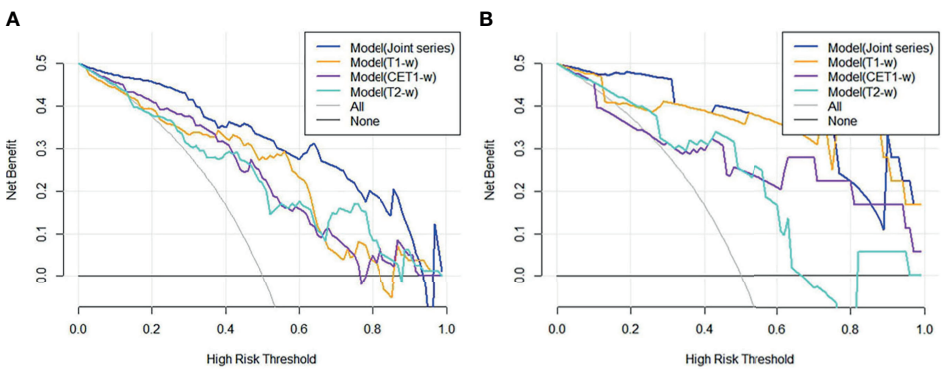

FIGURE 4 | **(A, B)** showed the DCA results for four models in the training cohort and validation cohort. The blue curve was for the Model(Joint series), the orange curve was for Model(T1-w), the purple curve was for Model(CET1-w), and the turquoise curve was for Model(T2-w). The x- and y-axes indicated the high-risk threshold and net benefit, respectively. The gray curve represented the assumption that all patients were sensitive to treatment; the black line represented the assumption that all patients were insensitive to treatment.

TABLE 3 | Four groups of radiomics features extracted from MR images were showed.

Model(T1-w)	wavelet-LLL _glcm_Idmn	wavelet-LHL _glcm_Imc2	Original _firstorder_Skewness	wavelet-HLL glcm_DifferenceAverage	wavelet-LHH _firstorder_Median	wavelet-LHH _glcm_SumEntropy
Model(T2-w)	wavelet-LHL_gldm _LargeDependenceEmphasis	Original_glrlm _LongRunHighGrayLevelEmphasis	wavelet-HHL _glcm_SumEntropy	Original _glcm_Idn	wavelet-HHL _glcm_Contrast	wavelet-LHH _firstorder_Maximum
Model(CET1-w)	wavelet-LHL _Glrlm_RunVariance	wavelet-LHH _glcm_Idmn	wavelet-HLH_glszm _HighGrayLevelZoneEmphasis	wavelet-LHH firstorder_Kurtosis	wavelet-HLH_glszm _SmallAreaHighGrayLevelEmphasis	wavelet-HHL firstorder_Kurtosis
Model(Joint series)	T1_wavelet-LLL_glszm _GrayLevelNonUniformity Normalized	CET1_wavelet-LHH _glcm_Idmn	CET1_wavelet-LHH firstorder_Kurtosis	T1_wavelet-LLH firstorder_Kurtosis	CET1_wavelet-LLH firstorder_Median	wavelet-LLL _glcm_Imc1

Features of the same class appeared in the same color to distinguish them from other features.

superior to T1-w in depicting lesions, but it may focus more on differences in signal strength. However, in analyzing the deep texture structure of the image, T1-w seemed to perform better than T2-w based on machine vision. In future studies, we will focus on this problem and further verify it.

Among all four models, the Model-Joint series had the best prediction performance for the sensitivity of residual gliomas to treatment, followed by Model-T1, but the Delong test showed that the difference in AUC was not significant between these two models. The reason for this may be because the sample size was not large enough. However, the Delong tests for the comparisons between the Model-Joint series and Model-CET1(p=0.014) and between the Model-Joint series and Model-T2(p=0.012) in the training cohort showed significant differences. In addition, more samples and more complex deep learning algorithms need to be used to further improve the sensitivity, specificity and accuracy of the Model-Joint series in the validation cohort. Nonetheless, one strength of this study was that MRI was used to noninvasively predict both radiotherapy and chemotherapy outcomes for gliomas before treatment beginning, which was worthy of further study in the future.

There are several limitations to this work. First, although the RANO criteria are the current standard for evaluating clinical therapeutic effects in tumors, there are still a few cases that are difficult to classify. Therefore, we asked a chief physician with 30 years of experience to confirm the results. Second, it is more reasonable to enlarge sample in future to compare differences in clinical, pathological, and semantic features between treatment-sensitive and treatment-insensitive patients. In addition, many previous studies have shown that genotype, such as IDH mutation, 1p19q codeletion and MGMT promoter methylation status, has a great correlation with therapeutic effect and tumor prognosis (29, 30). Due to the absence of genetic tests in some patients, genetic phenotype was not included as a predictor of treatment response in this study. However, in the future, it is necessary to conduct prospective studies that integrate additional genetic information into the predictive models.

In conclusion, we explored the potential role of radiomics-based models derived from preoperative multiparametric MRI in predicting the response to concurrent radiotherapy and chemotherapy in residual glioma patients. These models may help clinicians personalize patient treatment and help treatment-insensitive patients avoid unnecessary injuries and side effects from chemoradiotherapy.

DATA AVAILABILITY STATEMENT

The original contributions presented in the study are included in the article/**Supplementary Material**. Further inquiries can be directed to the corresponding author.

ETHICS STATEMENT

The studies involving human participants were reviewed and approved by The Second Affiliated Hospital of Nanchang

University Medical Research Ethics Committee. Written informed consent for participation was not required for this study in accordance with the national legislation and the institutional requirements.

AUTHOR CONTRIBUTIONS

ZZ and KH carried out the research and drafted the original manuscript. ZZ, YZ, and DW collected the data. ZZ, ZW, and JZ analyzed the data and built the prediction models. LZ and YY evaluated the efficacy of tumor treatment. TG and XX revised the manuscript. All authors contributed to the article and approved the submitted version.

FUNDING

This study was supported by the National Natural Science Foundation of China (NO. 82060557), the Key Research & Development Program of Jiangxi Province, China (NO. 20171ACG70002), Natural Science Foundation of Hunan province, China (NO. 2018JJ2271), as well as Science and technology planning project of Jiangxi Provincial Health and Family Planning Commission (No. 20195247).

SUPPLEMENTARY MATERIAL

The Supplementary Material for this article can be found online at: https://www.frontiersin.org/articles/10.3389/fonc.2021.779202/full#supplementary-material

REFERENCES

1. Kocher M, Ruge MI, Galldiks N, Lohmann P. Applications of Radiomics and Machine Learning for Radiotherapy of Malignant Brain Tumors. *Strahlenther Onkol* (2020) 196(10):856–67. doi: 10.1007/s00066-020-01626-8
2. Zhang B, Tian J, Dong D, Gu D, Dong Y, Zhang L, et al. Radiomics Features of Multiparametric MRI as Novel Prognostic Factors in Advanced Nasopharyngeal Carcinoma. *Clin Cancer Res* (2017) 23(15):4259–69. doi: 10.1158/1078-0432.CCR-16-2910
3. Xi YB, Guo F, Xu ZL, Li C, Wei W, Tian P, et al. Radiomics Signature: A Potential Biomarker for the Prediction of MGMT Promoter Methylation in Glioblastoma. *J Magn Reson Imaging* (2018) 47(5):1380–7. doi: 10.1002/jmri.25860
4. Giannini V, Mazzetti S, Bertotto I, Chiarenza C, Cauda S, Delmastro E, et al. Predicting Locally Advanced Rectal Cancer Response to Neoadjuvant Therapy With (18)F-FDG PET and MRI Radiomics Features. *Eur J Nucl Med Mol Imaging* (2019) 46(4):878–88. doi: 10.1007/s00259-018-4250-6
5. Lo Gullo R, Eskreis-Winkler S, Morris EA, Pinker K. Machine Learning With Multiparametric Magnetic Resonance Imaging of the Breast for Early Prediction of Response to Neoadjuvant Chemotherapy. *Breast* (2020) 49:115–22. doi: 10.1016/j.breast.2019.11.009
6. Zhang L, Dong D, Li H, Tian J, Ouyang F, Mo X, et al. Development and Validation of a Magnetic Resonance Imaging-Based Model for the Prediction of Distant Metastasis Before Initial Treatment of Nasopharyngeal Carcinoma: A Retrospective Cohort Study. *EBioMedicine* (2019) 40:327–35. doi: 10.1016/j.ebiom.2019.01.013
7. Avanzo M, Stancanello J, Pirrone G, Sartor G. Radiomics and Deep Learning in Lung Cancer. *Strahlenther Onkol* (2020) 196(10):879–87. doi: 10.1007/s00066-020-01625-9
8. Chukwueke UN, Wen PY. Use of the Response Assessment in Neuro-Oncology (RANO) Criteria in Clinical Trials and Clinical Practice. *CNS Oncol* (2019) 8(1):Cns28. doi: 10.2217/cns-2018-0007
9. Cheng F, Guo D. MET in Glioma: Signaling Pathways and Targeted Therapies. *J Exp Clin Cancer Res* (2019) 38(1):270. doi: 10.1186/s13046-019-1269-x
10. Ameratunga M, Pavlakis N, Wheeler H, Grant R, Simes J, Khasraw M. Anti-Angiogenic Therapy for High-Grade Glioma. *Cochrane Database Syst Rev* (2018) 11(11):CD008218. doi: 10.1002/14651858.CD008218.pub4
11. Meng X, Zhao Y, Han B, Zha C, Zhang Y, Li Z, et al. Dual Functionalized Brain-Targeting Nanoinhibitors Restrain Temozolomide-Resistant Glioma *via* Attenuating EGFR and MET Signaling Pathways. *Nat Commun* (2020) 11(1):594. doi: 10.1038/s41467-019-14036-x
12. Yun T, Koo Y, Kim S, Lee W, Kim H, Chang D, et al. Characteristics of 18F-FDG and 18F-FDOPA PET in an 8-Year-Old Neutered Male Yorkshire Terrier Dog With Glioma: Long-Term Chemotherapy Using Hydroxyurea Plus Imatinib With Prednisolone and Immunoreactivity for PDGFR-β and LAT1. *Vet Q* (2021) 41(1):163–71. doi: 10.1080/01652176.2021.1906466
13. Liu C, Zhang Z, Ping Y, Qin G, Zhang K, Maimela NR, et al. Comprehensive Analysis of PD-1 Gene Expression, Immune Characteristics and Prognostic Significance in 1396 Glioma Patients. *Cancer Manag Res* (2020) 12:4399–410. doi: 10.2147/CMAR.S238174
14. Kline C, Liu SJ, Duriseti S, Banerjee A, Nicolaides T, Raber S, et al. Reirradiation and PD-1 Inhibition With Nivolumab for the Treatment of Recurrent Diffuse Intrinsic Pontine Glioma: A Single-Institution Experience. *J Neurooncol* (2018) 140(3):629–38. doi: 10.1007/s11060-018-2991-5
15. Liu F, Huang J, Liu X, Cheng Q, Luo C, Liu Z. CTLA-4 Correlates With Immune and Clinical Characteristics of Glioma. *Cancer Cell Int* (2020) 20:7. doi: 10.1186/s12935-019-1085-6
16. Zhang C, Zhang Z, Li F, Shen Z, Qiao Y, Li L, et al. Large-Scale Analysis Reveals the Specific Clinical and Immune Features of B7-H3 in Glioma. *Oncoimmunology* (2018) 7(11):e1461304. doi: 10.1080/2162402X.2018.1461304
17. Watson J, Romagna A, Ballhausen H, Niyazi M, Lietke S, Siller S, et al. Long-Term Outcome of Stereotactic Brachytherapy With Temporary Iodine-125 Seeds in Patients With WHO Grade II Gliomas. *Radiat Oncol* (2020) 15(1):275. doi: 10.1186/s13014-020-01719-9
18. Chatzikonstantinou G, Zamboglou N, Archavlis E, Strouthos I, Zoga E, Milickovic N, et al. CT-Guided Interstitial HDR-Brachytherapy for Recurrent Glioblastoma Multiforme: A 20-Year Single-Institute Experience. *Strahlenther Onkol* (2018) 194(12):1171–9. doi: 10.1007/s00066-018-1358-3
19. Qu F, Wang P, Zhang K, Shi Y, Li Y, Li C, et al. Manipulation of Mitophagy by "All-In-One" Nanosensitizer Augments Sonodynamic Glioma Therapy. *Autophagy* (2020) 16(8):1413–35. doi: 10.1080/15548627.2019.1687210
20. Gillies RJ, Kinahan PE, Hricak H. Radiomics: Images Are More Than Pictures, They Are Data. *Radiology* (2016) 278(2):563–77. doi: 10.1148/radiol.2015151169
21. Zanfardino M, Franzese M, Pane K, Cavaliere C, Monti S, Esposito G, et al. Bringing Radiomics Into a Multi-Omics Framework for a Comprehensive Genotype-Phenotype Characterization of Oncological Diseases. *J Trans Med* (2019) 17(1):337. doi: 10.1186/s12967-019-2073-2
22. Eloyan A, Yue MS, Khachatryan D. Tumor Heterogeneity Estimation for Radiomics in Cancer. *Stat Med* (2020) 39(30):4704–23. doi: 10.1002/sim.8749
23. Yoon HJ, Kang J, Park H, Sohn I, Lee SH, Lee HY. Deciphering the Tumor Microenvironment Through Radiomics in Non-Small Cell Lung Cancer: Correlation With Immune Profiles. *PloS One* (2020) 15(4):e0231227. doi: 10.1371/journal.pone.0231227
24. Chen H, Shi L, Nguyen KNB, Monjazeb AM, Matsukuma KE, Loehfelm TW, et al. MRI Radiomics for Prediction of Tumor Response and Downstaging in Rectal Cancer Patients After Preoperative Chemoradiation. *Adv Radiat Oncol* (2020) 5(6):1286–95. doi: 10.1016/j.adro.2020.04.016
25. Nie K, Shi L, Chen Q, Hu X, Jabbour SK, Yue N, et al. Rectal Cancer: Assessment of Neoadjuvant Chemoradiation Outcome Based on Radiomics of Multiparametric MRI. *Clin Cancer Res* (2016) 22(21):5256–64. doi: 10.1158/1078-0432.CCR-15-2997
26. Dinapoli N, Barbaro B, Gatta R, Chiloiro G, Casà C, Masciocchi C, et al. Magnetic Resonance, Vendor-Independent, Intensity Histogram Analysis

Predicting Pathologic Complete Response After Radiochemotherapy of Rectal Cancer. *Int J Radiat oncol biol Phys* (2018) 102(4):765–74. doi: 10.1016/j.ijrobp.2018.04.065

27. Cusumano D, Dinapoli N, Boldrini L, Chiloiro G, Gatta R, Masciocchi C, et al. Fractal-Based Radiomic Approach to Predict Complete Pathological Response After Chemo-Radiotherapy in Rectal Cancer. *La Radiologia Med* (2018) 123 (4):286–95. doi: 10.1007/s11547-017-0838-3
28. Ng SH, Liao CT, Lin CY, Chan SC, Lin YC, Yen TC, et al. Dynamic Contrast-Enhanced MRI, Diffusion-Weighted MRI and (18)F-FDG PET/CT for the Prediction of Survival in Oropharyngeal or Hypopharyngeal Squamous Cell Carcinoma Treated With Chemoradiation. *Eur Radiol* (2016) 26(11):4162–72. doi: 10.1007/s00330-016-4276-8
29. Shboul ZA, Chen J, Iftekharuddin KM. Prediction of Molecular Mutations in Diffuse Low-Grade Gliomas Using MR Imaging Features. *Sci Rep* (2020) 10 (1):3711. doi: 10.1038/s41598-020-60550-0
30. Kim M, Jung SY, Park JE, Jo Y, Park SY, Nam SJ, et al. Diffusion- and Perfusion-Weighted MRI Radiomics Model May Predict Isocitrate Dehydrogenase (IDH) Mutation and Tumor Aggressiveness in Diffuse Lower Grade Glioma. *Eur Radiol* (2020) 30(4):2142–51. doi: 10.1007/s00330-019-06548-3

Conflict of Interest: The authors declare that the research was conducted in the absence of any commercial or financial relationships that could be construed as a potential conflict of interest.

The reviewer JL declared a shared parent affiliation with one of the authors, YZ, to the handling editor at time of review.

Publisher's Note: All claims expressed in this article are solely those of the authors and do not necessarily represent those of their affiliated organizations, or those of the publisher, the editors and the reviewers. Any product that may be evaluated in this article, or claim that may be made by its manufacturer, is not guaranteed or endorsed by the publisher.

SYSTEMATIC REVIEW
published: 31 January 2022
doi: 10.3389/fonc.2022.799662

Imaging Biomarkers of Glioblastoma Treatment Response: A Systematic Review and Meta-Analysis of Recent Machine Learning Studies

Thomas C. Booth[1,2], Mariusz Grzeda[1], Alysha Chelliah[1], Andrei Roman[3,4], Ayisha Al Busaidi[2], Carmen Dragos[5], Haris Shuaib[6,7], Aysha Luis[2], Ayesha Mirchandani[8], Burcu Alparslan[2,9], Nina Mansoor[2], Jose Lavrador[10], Francesco Vergani[10], Keyoumars Ashkan[10], Marc Modat[1] and Sebastien Ourselin[1]*

[1] School of Biomedical Engineering & Imaging Sciences, King's College London, St. Thomas' Hospital, London, United Kingdom, [2] Department of Neuroradiology, King's College Hospital National Health Service Foundation Trust, London, United Kingdom, [3] Department of Radiology, Guy's & St. Thomas' National Health Service Foundation Trust, London, United Kingdom, [4] Department of Radiology, The Oncology Institute "Prof. Dr. Ion Chiricuță" Cluj-Napoca, Cluj-Napoca, Romania, [5] Department of Radiology, Buckinghamshire Healthcare National Health Service Trust, Amersham, United Kingdom, [6] Department of Medical Physics, Guy's & St. Thomas' National Health Service Foundation Trust, London, United Kingdom, [7] Institute of Psychiatry, Psychology & Neuroscience, King's College London, London, United Kingdom, [8] Department of Radiology, Cambridge University Hospitals National Health Service Foundation Trust, Cambridge, United Kingdom, [9] Department of Radiology, Kocaeli University, İzmit, Turkey, [10] Department of Neurosurgery, King's College Hospital National Health Service Foundation Trust, London, United Kingdom

OPEN ACCESS

Edited by:
Tone Frost Bathen,
Norwegian University of Science and Technology, Norway

Reviewed by:
Endre Grøvik,
Møre and Romsdal Hospital Trust, Norway
Weiwei Zong,
Henry Ford Health System, United States

***Correspondence:**
Thomas C. Booth
tombooth@doctors.org.uk

Specialty section:
This article was submitted to Cancer Imaging and Image-directed Interventions, a section of the journal Frontiers in Oncology

Received: 21 October 2021
Accepted: 03 January 2022
Published: 31 January 2022

Citation:
Booth TC, Grzeda M, Chelliah A, Roman A, Al Busaidi A, Dragos C, Shuaib H, Luis A, Mirchandani A, Alparslan B, Mansoor N, Lavrador J, Vergani F, Ashkan K, Modat M and Ourselin S (2022) Imaging Biomarkers of Glioblastoma Treatment Response: A Systematic Review and Meta-Analysis of Recent Machine Learning Studies. Front. Oncol. 12:799662. doi: 10.3389/fonc.2022.799662

Objective: Monitoring biomarkers using machine learning (ML) may determine glioblastoma treatment response. We systematically reviewed quality and performance accuracy of recently published studies.

Methods: Following Preferred Reporting Items for Systematic Reviews and Meta-Analysis: Diagnostic Test Accuracy, we extracted articles from MEDLINE, EMBASE and Cochrane Register between 09/2018–01/2021. Included study participants were adults with glioblastoma having undergone standard treatment (maximal resection, radiotherapy with concomitant and adjuvant temozolomide), and follow-up imaging to determine treatment response status (specifically, distinguishing progression/recurrence from progression/recurrence mimics, the target condition). Using Quality Assessment of Diagnostic Accuracy Studies Two/Checklist for Artificial Intelligence in Medical Imaging, we assessed bias risk and applicability concerns. We determined test set performance accuracy (sensitivity, specificity, precision, F1-score, balanced accuracy). We used a bivariate random-effect model to determine pooled sensitivity, specificity, area-under the receiver operator characteristic curve (ROC-AUC). Pooled measures of balanced accuracy, positive/negative likelihood ratios (PLR/NLR) and diagnostic odds ratio (DOR) were calculated. PROSPERO registered (CRD42021261965).

Results: Eighteen studies were included (1335/384 patients for training/testing respectively). Small patient numbers, high bias risk, applicability concerns (particularly confounding in reference standard and patient selection) and low level of evidence, allow limited conclusions from studies. Ten studies (10/18, 56%) included in meta-analysis gave 0.769 (0.649-0.858) sensitivity [pooled (95% CI)]; 0.648 (0.749-0.532) specificity; 0.706

(0.623-0.779) balanced accuracy; 2.220 (1.560-3.140) PLR; 0.366 (0.213-0.572) NLR; 6.670 (2.800-13.500) DOR; 0.765 ROC-AUC.

Conclusion: ML models using MRI features to distinguish between progression and mimics appear to demonstrate good diagnostic performance. However, study quality and design require improvement.

Keywords: glioblastoma, machine learning, monitoring biomarkers, meta-analysis, artificial intelligence, treatment response, deep learning, glioma

1 INTRODUCTION

Glioblastoma is the most common primary malignant brain tumor with a median 14.6 month overall survival (1). This is in spite of a standard care regimen comprising maximal debulking surgery, followed by radiotherapy with concomitant temozolomide, followed by adjuvant temozolomide. Monitoring biomarkers (2) identify longitudinal change in the growth of tumor or give evidence of response to treatment, with magnetic resonance imaging (MRI) proving particularly useful in this regard. This is due both to the non-invasive nature of MRI, and its ability to capture the entire tumor volume and adjacent tissues, leading to its recommended incorporation into treatment response evaluation guidelines in trials (3, 4). Yet challenges occur when false-positive progressive disease (pseudoprogression) is encountered, which may take place during the 6 month period following the completion of radiotherapy and is manifest as an increase in contrast enhancement on T_1-weighted MRI images, which reflects the non-specific disruption of the blood-brain barrier (**Figure 1**) (5, 6).

Non-specific increased contrast enhancement occurs in approximately 50% of patients undergoing the standard care regimen. There is an approximately equal chance that the tumor may represent pseudoprogression or true progression because pseudoprogression occurs in approximately 10-30% of all patients (7, 8). For more than a decade, researchers have attempted to distinguish pseudoprogression from true progression at the time of increased contrast enhancement because of the substantial potential clinical impact. If there is true progression the treating clinical team typically will initiate a prompt modification in treatment strategy with termination of ineffectual treatment or initiation of second-line surgery or therapies (9). If there is pseudoprogression the treating clinical team typically will continue with the standard care regimen. However, the decision making can only be made retrospectively with current treatment response evaluation guidelines (4). A monitoring biomarker (2) that reliably distinguishes pseudoprogression from true progression at the time of increased contrast enhancement would fully inform the difficult decision contemporaneously.

Under the standard care regimen, pseudoprogression occurs as an early-delayed treatment effect as opposed to radiation necrosis which is a late-delayed radiation effect (10). Radiation necrosis also manifests as non-specific increased contrast enhancement, however, pseudoprogression appears within 6 months of radiotherapy completion whereas radiation necrosis occurs beyond 6 months. Radiation necrosis occurs with an incidence an order of magnitude less than that of pseudoprogression (11). Another difference between the two entities is that much evidence suggests that pseudoprogression is significantly correlated with O^6-methylguanine DNA methyltransferase (MGMT) promoter methylation. As with pseudoprogression, there is a need to distinguish radiation necrosis from true progression at the time of increased contrast enhancement because, again, there is substantial potential clinical impact. In particular, if there is true progression the treating clinical team typically would initiate second-line surgery or therapies. However, the decision making can only be made retrospectively with current treatment response evaluation guidelines (3). Therefore, a monitoring biomarker (2) that reliably distinguishes radiation necrosis from true progression at the time of increased contrast enhancement would fully inform the treating clinical team's decision contemporaneously.

Developing monitoring biomarkers to determine treatment response has been the subject of many studies, with many incorporating machine learning (ML). A review of such neuro-oncology studies up to September 2018 showed that the evidence is relatively low level, given that it has usually been obtained in single centers retrospectively and often without hold-out test sets (11, 12). The review findings suggested that those studies taking advantage of enhanced computational processing power to build neuro-oncology monitoring biomarker models, for example deep learning techniques using convolutional neural networks (CNNs), have yet to show benefit compared to ML techniques using explicit feature engineering and less computationally expensive classifiers, for example using support vector machines or even multivariate logistic regressions. Furthermore, studies show that using ML to make neuro-oncology monitoring biomarker models does not appear to be superior to applying traditional statistical methods when analytical validation and diagnostic performance is considered (the fundamental difference between ML and statistics is that statistics determines population inferences from a sample, whereas ML extracts generalizable predictive patterns). Nonetheless, the rapidly evolving discipline of applying radiomic studies to neuro-oncology imaging reflects a recent exponential increase in published studies applying ML to neuroimaging (13), and specifically to neuro-oncology imaging (14). It also mirrors the notable observation that in 2018, arXiv (a repository where computer science papers are self-archived before publication in a peer-reviewed journal) surpassed 100 new ML pre-prints per day (15). Given these developments, there is a need to appraise the

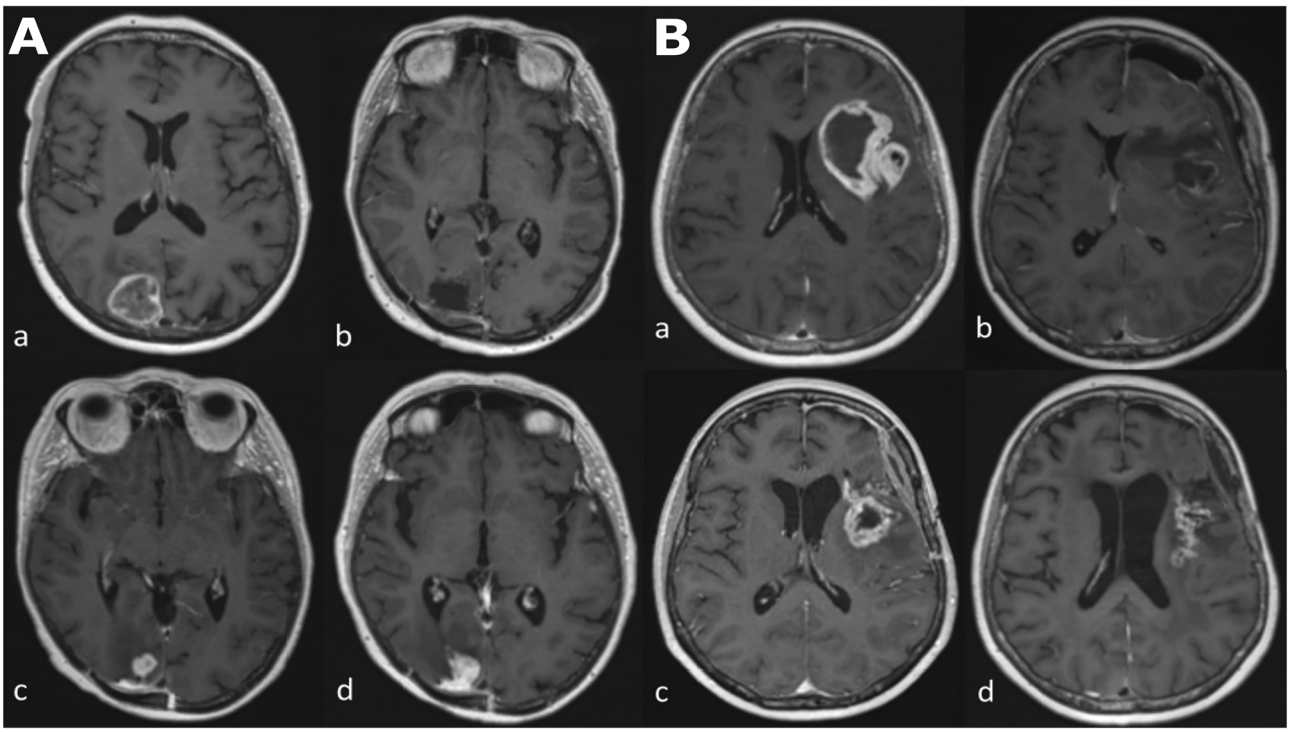

FIGURE 1 | Longitudinal series of MRI images in two patients **(A, B)** with glioblastoma, IDH-wildtype. All images are axial T_1-weighted after contrast administration. Images **(Aa–Ad)** demonstrate tumor progression. **(Aa)** Pre-operative MRI of a glioblastoma in the occipital lobe. **(Ab)** Post-operative MRI five days after resection; there is no contrast enhancement therefore no identifiable residual tumor. **(Ac)** The patient underwent a standard care regimen of radiotherapy and temozolomide. A new enhancing lesion at the inferior margin of the post-operative cavity was identified on MRI at three months after radiotherapy completion. **(Ad)** The enhancing lesion continued to increase in size three months later and was confirmed to represent tumor recurrence after repeat surgery. Images **(Ba–Bd)** demonstrate pseudoprogression. **(Ba)** Pre-operative MRI of a glioblastoma in the insula lobe. **(Bb)** Post-operative MRI at 24 hours after surgery; post-operative blood products are present but there is no contrast enhancement therefore no identifiable residual tumor. **(Bc)** The patient underwent a standard care regimen of radiotherapy and temozolomide. A new rim-enhancing lesion was present on MRI at five months after radiotherapy completion. **(Bd)** Follow-up MRI at monthly intervals showed a gradual reduction in the size of the rim-enhancing lesion without any change in the standard care regimen of radiotherapy and temozolomide or corticosteroid use. The image shown here is the MRI four months later.

evidence of ML applied to monitoring biomarkers determining treatment response since September 2018.

The aim of the study is to systematically review and perform a meta-analysis of diagnostic accuracy of ML-based treatment response monitoring biomarkers for glioblastoma patients using recently published peer-reviewed studies. The study builds on previous work to incorporate the rapidly growing body of knowledge in this field (11, 16), providing promising avenues for further research.

2 MATERIALS AND METHODS

This systematic review and meta-analysis are registered with PROSPERO (CRD42021261965). The review was organized in line with the Preferred Reporting Items for Systematic Reviews and Meta-Analysis: Diagnostic Test Accuracy (PRISMA-DTA) (17) incorporating Cochrane review methodology relating to "developing criteria for including studies" (18), "searching for studies" (19), and "assessing methodological quality" (20).

Pseudoresponse (bevacizumab-related response mimic), an important concern in the United States where it is licensed, was not the focus of the systematic review and meta-analysis.

2.1 Search Strategy and Selection Criteria

Recommendations were followed to perform a sensitive search (with low precision), including the incorporation of subject headings with exploded terms, and without any language restrictions (19). Search terms were applied to MEDLINE, EMBASE and the Cochrane Register to capture original research articles published from September 2018 to January 2021 (**Supplementary Table S1**). Pre-prints and non-peer reviewed material were excluded.

2.1.1 Inclusion Criteria

Study participants included were adult glioblastoma patients treated with a standard care regimen (maximal debulking surgery, followed by radiotherapy with concomitant temozolomide, followed by adjuvant temozolomide) who underwent follow-up imaging to determine treatment response

status (explicitly, differentiating true progression/recurrence from mimics of progression/recurrence (defined below), and designated as the target condition of the systematic review).

2.1.2 Exclusion Criteria

Studies were excluded if they focused on pediatrics, pseudoresponse, or had no ML algorithm employed in the extraction or selection of features, or in classification/regression.

2.1.3 Index Test and Reference Standard

The ML model determined the treatment response outcome, and was designated as the index test of the systematic review. Either clinicoradiological follow up or histopathology at re-operation or a combination of both, were designated as the reference standard of the systematic review. The bibliography of each included article was checked manually for other relevant studies.

A neuroradiologist, T.C.B., and a data scientist, A.C., with 16 and 2 years, respectively, of experience in neuroimaging applied to neuro-oncology, independently performed the literature search and selection.

2.2 Data Extracted and Risk of Bias Assessment

For every study, risk of bias as well as concerns regarding applicability, were assessed by applying QUADAS 2 methodology (21) alongside proformas incorporating items from the Checklist for Artificial Intelligence in Medical Imaging (CLAIM) (22). Data was extracted from published studies to determine: whether the datasets analyzed contained any tumors other than glioblastomas, especially anaplastic astrocytomas and anaplastic oligodendrogliomas; the index test ML algorithm and any cross validation processes; training and hold-out test set information; what reference standard(s) were employed; non-imaging features and MRI sequence(s) included in the analysis.

The appropriateness of reference standard follow-up imaging protocols was reviewed. The handling of confounding factors such as second-line medication therapy, temozolomide cessation, and steroid use were assessed. It was also determined whether the treatment response (target condition) used in the published study was appropriate. Under the standard care regimen, contrast-enhancing lesions enlarging due to pseudoprogression typically occur within 0-6 months after radiotherapy, whereas contrast-enhancing lesions enlarging due to radiation necrosis typically occur beyond this 6 month window, according to the evidence. When "post-treatment related effects" (PTRE) is employed as a term for treatment response outcome, the phenomena of pseudoprogression and radiation necrosis are both included (23, 24). These three terms therefore capture detail regarding the time period when the mimics of progression/recurrence occur. Deviations in the use of the three terms defined here were noted. Data on the length of follow-up imaging after contrast-enhancing lesions enlarged were additionally extracted and evaluated. Clinicoradiological strategies considered optimal in designating outcomes as PTRE or true progression/recurrence included the following: assigning an MRI scan as baseline after radiotherapy (25); excluding outcomes based on T_2-w lesion enlargement (25); permitting a period of 6-month follow up from the first time when contrast-enhancing lesions enlarged; during this 6-month period having two subsequent follow-up scans as opposed to a single short interval "confirmatory" follow-up scan. Two follow-up scans mitigate against some scenarios where the contrast-enhancing lesions due to PTRE continue to enlarge over a short interval, and this continued enlargement is seen at a short interval scan confounding assessment by falsely "confirming" true progression (26, 27). This might be termed an "upslope effect".

A neuroradiologist (US attending, UK consultant), T.C.B., and a data scientist, A.C., with 16 and 2 years, respectively, of experience in neuroimaging applied to neuro-oncology, independently performed the data extraction and quality assessment. Discrepancies between the two reviewers were considered at a research meeting chaired by a third neuroradiologist (US attending, UK consultant), A.A-B. (8 years experience of neuroimaging applied to neuro-oncology), until a consensus was reached.

2.3 Data Synthesis and Statistical Analysis

2.3.1 Performance Accuracy for Individual Studies

Based on the published study data, 2 x 2 contingency tables were made for hold-out test sets from which the principal diagnostic accuracy measures of sensitivity (recall) and specificity were calculated. The area under the receiver operating characteristic curve (ROC-AUC) values and confidence intervals were extracted in studies where these were published. Additional secondary outcome measures of balanced accuracy, precision (positive predictive value) and F1-score were also determined from the contingency tables. In those studies where there was a discrepancy in the principal diagnostic accuracy measures and the accessible published study raw data, this was highlighted. If both internal and external hold-out test sets were published in a study, the principal diagnostic accuracy measures for the external test set alone were calculated. In studies without hold-out test sets, "no test set" was recorded (22) and the training set principal diagnostic accuracy measures from the training set were summarized. The unit of evaluation was per-patient. All test set data included glioblastoma.

2.3.2 Meta-Analysis

The principal diagnostic accuracy measures of sensitivity (recall) and specificity were subject to meta-analysis. We determined two pooled primary measures of accuracy: the true positive rate (sensitivity/recall) and the false negative rate (1-specificity). A bivariate random-effect model (28), which allows for two important circumstances (29–31) (**Supplementary Statistical Information**), was chosen to determine the two pooled primary measures of accuracy. Briefly, the circumstances are first, that the values of the selected principal diagnostic accuracy measures are usually highly related to one another through the cut-off value. With an increase of sensitivity, specificity is likely to decrease and, as a consequence, these two measures are usually negatively correlated. Second, a relatively high level of heterogeneity is commonly observed among the results of diagnostic studies. This is verified in various ways ranging from visual assessment through chi-square based tests to random-intercept models decomposing total variance of results into between- and within- study levels. The bivariate random-effect model not only allows for the simultaneous analysis

of diagnostic measures but also addresses their heterogeneity (28). Bivariate joint modelling of the primary measures of accuracy assumes that the logits of these quantities follow a bivariate normal distribution and allows for a non-zero correlation. Based on this assumption, a linear random-effect model is applied to the data and estimates of mean true positive rate (sensitivity) and false positive rate (1-specificity), along with their variances and correlation between them, can be obtained. The pooled estimates of true positive rate and false positive rate are initially estimated on the logit scale (**Supplementary Statistical Information**). To be interpretable they require transformation back to the original probability scale (ranging within 0-1 limits).

The parameters of this model also allowed us to plot the summary ROC (SROC) curve and determine the summary ROC-AUC. Using a resampling approach (32), the model estimates were also used to derive the pooled measures of balanced accuracy as well as the positive and negative likelihood ratios and the diagnostic odds ratio.

The meta-analysis was conducted by a statistician, M.G., with 15 years of relevant experience. All the statistical analyses were performed in R (v 3.6.1). The R package mada (v 0.5.10) (33) was used for the bivariate model. Since some of the 2 x 2 contingency table input cell values (true positive, false positive, false negative, true negative) derived from the individual studies contained zeros, a continuity correction (0.5) was applied.

2.4 Prognostic Biomarkers Predicting Future Treatment Response

Most studies of prognostic imaging biomarkers in glioblastoma predict the outcome measure of overall survival using baseline images. Nonetheless, we found a small group of studies using ML models that predicted the outcome measure of future treatment response using baseline images. The studies were examined using identical methodology to that applied to monitoring biomarkers.

3 RESULTS

3.1 Characteristics and Bias Assessment of Studies Included

In all, 2362 citations fulfilled the search criteria of which the full text of 57 potentially eligible articles were reviewed (**Figure 2**). Twenty-one studies from September 2018 to January 2021 (including the publication of "online first" articles prior to September 2018) were included, 19 of which were retrospective. The total number of patients in the training sets were 1335 and in the test set 384. The characteristics of the 18 monitoring biomarker studies are presented in **Table 1** and the characteristics of the 3 studies that applied the ML models to serve as prognostic biomarkers to predict future treatment response using baseline images (or genomic alterations) are presented in **Table 2**.

3.1.1 Treatment Response Target Conditions

The treatment response target conditions varied between studies (**Table 1**). Around a quarter of studies (5/18, 28%) designated only 0-12 weeks after radiotherapy as the time period when pseudoprogression appears – as opposed to the entire 6-month time period when pseudoprogression might occur. A third of studies (6/18, 33%) assigned PTRE as the target condition. No study assigned radiation necrosis alone as the target condition. Five studies in the systematic review (5/18, 28%) included grade 3 gliomas. Only two of these five studies employed test sets; the test set in one study did not contain any grade 3 gliomas and the number in the test set in the other study was unclear although the number was small (14% grade 3 in combined training and test datasets). Therefore, as a minimum, all but one test set in the systematic review and meta-analysis contained only glioblastoma, the previous equivalent of glioma grade 4 according to c-IMPACT classification ("glioblastomas, IDH-wildtype" or "astrocytoma, IDH-mutant, grade 4") (55).

3.1.2 Reference Standards: Clinicoradiological Follow-Up and Histopathology Obtained at Re-Operation

The majority of studies (13/18, 67%) employed a combination of clinicoradiological follow up and histopathology at re-operation, to distinguish true progression from a mimic. A few individual studies employed one reference standard for one decision (true progression) and another reference standard for the alternative decision (mimic); this and other idiosyncratic rules led to a high risk of bias in terms of the reference standard used, as well as how patients were selected, in several studies.

3.1.3 Selected Features

Most studies only analyzed imaging features alone (15/18, 83%) whereas the remainder incorporated additional non-imaging features. A third of studies (6/18, 33%) used deep learning methodology to derive features (specifically, convolutional neural networks).

3.1.4 Test Sets

A third of studies did not have hold-out test sets (6/18, 33%) and instead the performance accuracy was determined using training data through cross-validation (**Table 1**). Therefore, there was a high risk of bias for the index test used in these six studies. A third of studies had external hold-out test sets (6/18, 33%). The ranges of mean diagnostic accuracy measures in these six studies were: recall (sensitivity) = 0.61-1.00; specificity = 0.47-0.90; precision (positive predictive value) = 0.58-0.88; balanced accuracy = 0.54-0.83; F1 score = 0.59-0.94; ROC-AUC = 0.65-0.85.

3.1.5 Bias Assessment and Concerns Regarding Applicability Summary

The risk of bias evaluation for each study was summarized (**Supplementary Figure S1**). All or most studies were assigned to the highest class for risk of bias in terms of the reference standard (18/18, 100%) and patient selection (15/18, 83%) QUADAS 2 categories respectively. A third or nearly a half of studies were either in the highest class for risk of bias or the risk was unclear in terms of flow and timing (6/18, 33%) and the index test (8/28, 44%) QUADAS 2 categories respectively. The results from the "concerns regarding applicability" evaluation largely mirrored the results of the risk of bias evaluation.

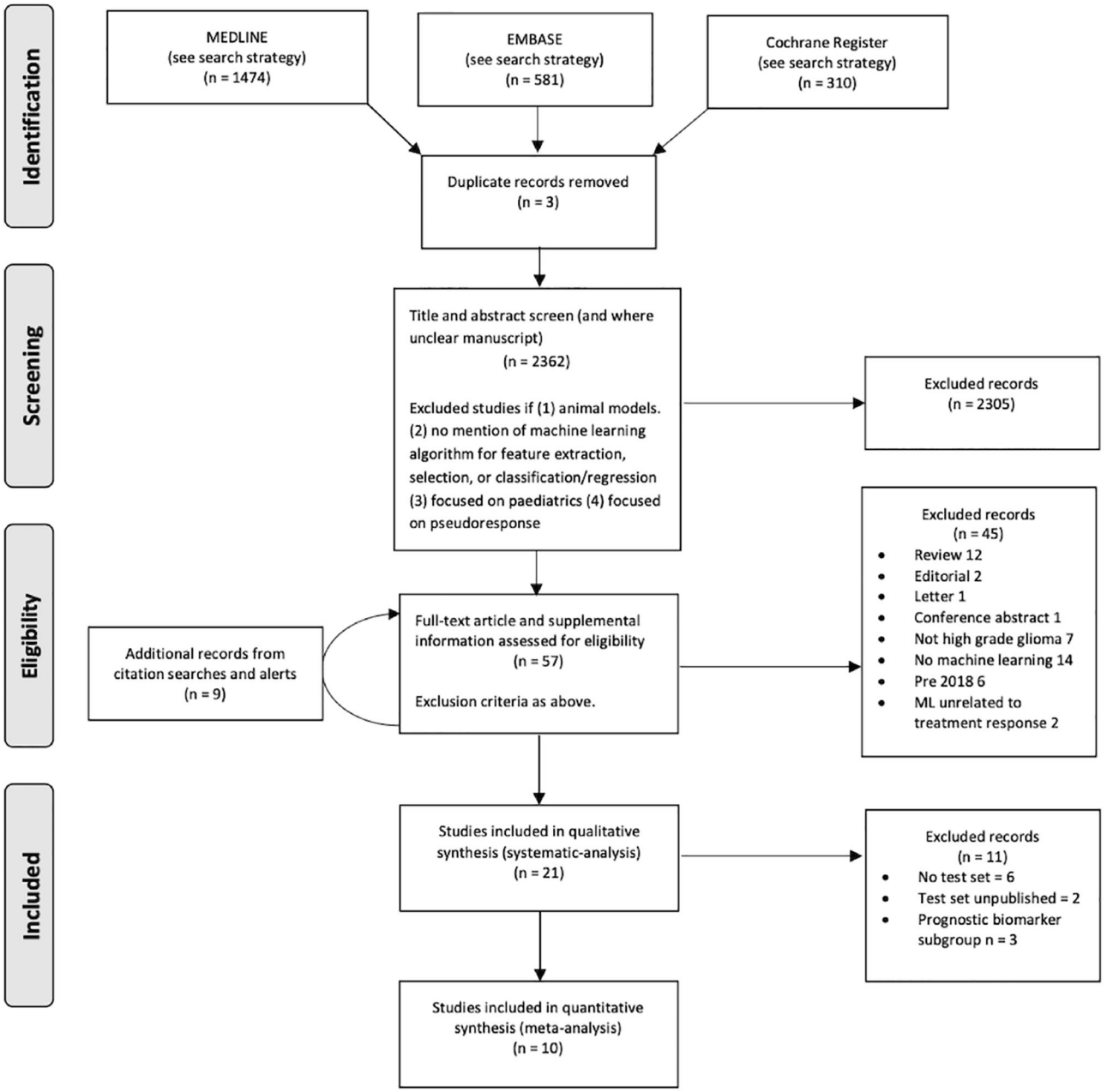

FIGURE 2 | Flow diagram of search strategy.

3.1.6 Prognostic Biomarkers Predicting Future Treatment Response (Subgroup)

There were two studies which were prospective, both of which had a small sample size (n = 10); the third study in this subgroup was retrospective. One study applied genomic alterations alone as features to predict future MRI treatment response. All studies (3/3, 100%) were in the highest class for risk of bias in terms of the reference standard, patient selection and index test QUADAS 2 categories (**Supplementary Figure S2**). In terms of "concerns regarding applicability" evaluation, the results mirrored the risk of bias evaluation exactly. Diagnostic accuracy measures could not be calculated because of study design. Design constraints included units of assessment in one study being per-lesion whilst another was per-voxel. One study also incorporated a prognostic metric of 1-year progression free survival for the predicted treatment

TABLE 1 | Studies using machine learning in the development of glioblastoma monitoring biomarkers.

Author	Target condition	Reference standard	Dataset(s)	Available demographic information	Methodology	Features selected	Test set performance
[a]Kim J.Y. et al. (34)	Early true progression or Early pseudoprogression	Mixture of histopathology and imaging follow up	Training = 61 Testing = 34 T_1 C, FLAIR, DWI, DSC	Training = age mean ± SD (range) 58 ± 11 (34–83) male 38 (62%) Testing = age mean ± SD 62 ± 12 male 25 (74%) Data from Korea	Retrospective 2 centers: 1 train & 1 external test set. LASSO feature selection with 10-fold CV Linear generalized model	First-order, volume/shape, Second-order (texture), wavelet. ADC & CBV parameters included.	Recall 0.71 Specificity 0.90 Precision 0.83 BA 0.81 F1 0.77 AUC 0.85 (CI 0.71 – 0.99)
Kim J.Y. et al. (35)	Early true progression or Early pseudoprogression	Mixture of histopathology and imaging follow up	Training = 59 Testing = 24 T_1 C, FLAIR, DTI, DSC	Training = age mean ± SD 61 ± 11 male 37 (63%) Testing = age mean ± SD 59 ± 12 male 9 (38%) Data from Korea	Retrospective 1 center LASSO feature selection with 10-fold CV Linear generalized model	First-order, Second-order (texture), wavelet. FA & CBV parameters included.	Recall 0.80 Specificity 0.63 Precision 0.36 BA 0.72 F1 0.50 AUC 0.67 (0.40 – 0.94)
Bacchi S. et al. (36)	True progression or PTRE (HGG)	Histopathology for progression and imaging follow up for pseudoprogression	Training = 44 Testing = 11 T_1 C, FLAIR, DWI	Combined = age mean ± SD 56 ± 10 male 26 (47%) Data from Australia	Retrospective 1 center 3D CNN & 5-fold CV	CNN. FLAIR & DWI parameters	Recall 1.00 Specificity 0.60 Precision 0.75 BA 0.80 F1 0.86 AUC 0.80
Elshafeey N. et al. (37)	True progression or [b]PTRE	Histopathology	Training = 98 Testing = 7 DSC, DCE	Training = age mean ± SD 50 ± 13 male 14 (58%) No testing demographic information Data from USA	Retrospective 3 centers mRMR feature selection. 1 test. 1) decision tree algorithm C5.0 2) SVM including LOO and 10-fold CV	K_{trans} & CBV parameters	Insufficient published data to determine diagnostic performance (CV training results available recall 0.91; specificity 0.88)
Verma G. et al. (38)	True progression or Pseudoprogression	Mixture of histopathology and imaging follow up	Training = 27 3D-EPSI	Training = age mean ± SD 64 ± 10 male 14 (52%) Data from USA	Retrospective 1 center Multivariate logistic regression LOOCV	Cho/NAA & Cho/Cr	No test set (CV training results available recall 0.94; specificity 0.87)
Ismail M. et al. (39)	True progression or Pseudoprogression	Mixture of histopathology and imaging follow up	Training = 59 Testing = 46 T_1 C, T_2/FLAIR	Training = age mean(range) 61 (26–74) male 39 (66%) Testing = age mean (range) 56 (25–76) male 30 (65%) Data from USA	Retrospective 2 centers: 1 train & 1 external test set. SVM & 4-fold CV	Global & curvature shape	Recall 1.00 Specificity 0.67 Precision 0.88 BA 0.83 F1 0.94
[a]Bani-Sadr A. et al. (40)	True progression or Pseudoprogression	Mixture of histopathology and imaging follow up	Training = 52 Testing = 24 T_1 C, FLAIR MGMT promoter status	Combined = age mean ± SD 58 ± 11 male 45 (59%) Data from France	Retrospective 1 center Random Forest.	Second-order features +/- MGMT promoter status	Recall 0.94 (0.71 - 1.00) Specificity 0.38 (0.09 - 0.76) Precision 0.36 BA 0.66 F1 0.84 AUC 0.77 & non-MRI: Recall 0.80 (0.56 - 0.94) Specificity 0.75 (0.19 - 0.99)

(Continued)

TABLE 1 | Continued

Author	Target condition	Reference standard	Dataset(s)	Available demographic information	Methodology	Features selected	Test set performance
							Precision 0.86 BA 0.74 F1 0.83 AUC 0.85
Gao X.Y. et al. (41)	True progression or PTRE (HGG)	Mixture of histopathology and imaging follow up	Training = 34 Testing = 15 (per lesion) T_1 C, FLAIR	Combined = age mean ± SD 51 ± 11 male 14 (36%) (per patient) Data from China	Retrospective 2 centers SVM & 5-fold CV	T_1 C, FLAIR subtraction map parameters	Recall 1.00 Specificity 0.90 Precision 0.83 BA 0.95 F1 0.91 AUC 0.94 (0.78 – 1.00)
Jang B-S. et al. (42)	True progression or Pseudoprogression	Mixture of histopathology and imaging follow up	Training = 59 Testing = 19 T_1 C & clinical features & IDH/ MGMT promoter status	Training = age median (range) 56 (22–77) male 41 (70%) Testing = age mean ± SD 53 (28–75) male 10 (53%) Data from Korea	Retrospective 2 centers 1 train & 1 external test set. CNN LSTM & 10-fold CV (compared to Random Forest)	CNN T_1 C parameters +/- Age; Gender; MGMT status; IDH mutation; radiotherapy dose and fractions; follow-up interval	Recall 0.64 Specificity 0.50 Precision 0.64 BA 0.57 F1 0.63 AUC 0.69 & non-MRI: Recall 0.72 Specificity 0.75 Precision 0.80 BA 0.74 F1 0.76 AUC 0.83
Li M. et al. (43)	True progression or [b]PTRE	Imaging follow up	Training = 84 DTI	No demographic information Data from USA	Retrospective. 1 center DC-AL GAN CNN with SVM including 5 and 10 and 20-fold CV (compared to DCGAN, VGG, ResNet, and DenseNet)	CNN. DTI	No test set (CV training results only available: Recall 0.98 Specificity 0.88 AUC 0.95)
Akbari H. et al. (44)	True progression or Pseudoprogression	Histopathology	Training = 40 Testing = 23 Testing = 20 T_1 C, T_2/FLAIR, DTI, DSC, DCE	Combined internal = age mean (range) 57 (33–82) male 38 (60%) No external demographic information Data from USA	Retrospective 2 centers. 1 train & test. 1 external test set. imagenet_vgg_f CNN SVM & LOOCV	First-order, second-order (texture). CBV, PH, TR, T_1 C, T_2/FLAIR parameters included.	Recall 0.70 Specificity 0.80 Precision 0.78 BA 0.75 F1 0.74 AUC 0.80
Li X. et al. (45)	Early True progression or early pseudoprogression (HGG)	Mixture of histopathology and imaging follow up	Training = 362 T_1 C, T_2, multi-voxel & single-voxel 1H-MRS, ASL	Training = age mean (range) 50 (19–70) male 218 (60%) Data from China	Retrospective Gabor dictionary and sparse representation classifier (SRC)	Sparse representations	No test set (CV training results only available: Recall 0.97 Specificity 0.83)
Manning P et al. (46)	True progression or pseudoprogression	Mixture of histopathology and imaging follow up	Training = 32 DSC, ASL	Training = age mean ± SD 56 ± 13 male 22 (69%) Data from USA	Retrospective 1 center Linear discriminant analysis & LOOCV	CBF and CBV parameters included.	No test set (CV training results only available: Recall 0.92 Specificity 0.86 AUC 0.95)
Park J.E. et al., 2020 (47)	Early True progression or early pseudoprogression	Mixture of histopathology and imaging follow up	Training = 53 Testing = 33 T_1 C	Training = age mean ± SD 56 ± 11 male 31 (59%) Testing = age mean ± SD	Retrospective 2 centers. 1 train & test. 1 external test set.	First-order, volume/shape, Second-order (texture), wavelet	Recall 0.61 Specificity 0.47 Precision 0.58 BA 0.54

(Continued)

TABLE 1 | Continued

Author	Target condition	Reference standard	Dataset(s)	Available demographic information	Methodology	Features selected	Test set performance
				62 ± 12 male 25 (76%) Data from Korea	Random Forest feature selection with 10-fold CV (Automated segmentation)	parameters included.	F1 0.59 AUC 0.65 (0.46 – 0.84)
Lee J. et al. (48)	True progression or [b]PTRE (HGG)	Histopathology	Training = 43 T_1, T_1 C, T_2, FLAIR, (subtractions: T_1 C - T_1, T_2- FLAIR) ADC parameters.	Training =age mean ± SD (range) 52 ± 13 (16–74) male 24 (56%) Data from USA	Retrospective 1 center CNN-LSTM. 3-fold CV	CNN-LSTM parameters.	No test set (CV training results only available: AUC 0.81 (0.72 - 0.88))
Kebir S. et al. (49)	True progression or [b]PTRE	Imaging follow up	Training = 30 Testing = 14 O-(2[^{18}F]-fluoroethyl)-L-tyrosine (FET)	Combined = age mean ± SD (range) 57 ± 11 (34-79) male 34 (77%) Data from Germany	Retrospective 1 center Linear discriminant analysis. 3-fold CV	TBR_{mean} TBR_{max} TTP_{min} parameters.	Recall 1.00 Specificity 0.80 Precision 0.90 BA 0.92 F1 0.95 AUC 0.93 (0.78 - 1.00)
Cluceru J. et al. (50)	Early True progression or early pseudoprogression (HGG)	Histopathology	Training = 139 DSC, MRSI, DWI, DTI	Training = age median (range) 52 (21–84) Male 83 (60%) Data from USA Ethnicity: White 112 (80%) American Indian 1 (1%) Asian 6 (4%(Pacific Islander 2 (1%) Other 18 (13%)	Retrospective 1 center Multivariate logistic regression. 5-fold CV	Cho, Cho/Cr, Cho/NAA & CBV parameters.	No test set (CV training results only available: Recall 0.65 (0.33 - 0.96); Specificity 0.62 (0.21 - 1.00) AUC 0.69 (0.51 - 0.87))
Jang B.S. et al. (51)	True progression or [b]PTRE	Mixture of histopathology and imaging follow up (including PET)	(i) (trained model = 78) testing = 104 (ii) all training = 182 T_1 C & clinical, molecular, timings, radiotherapy data	Testing = age median (range) 55 (25-76) male 59 (67%) Data from Korea	Retrospective (i) 6 centers 1 external test set. CNN LSTM (ii) 7 centers 1 training set CNN LSTM & 10-fold CV	CNN T_1 C parameters and Age; Gender; MGMT status; IDH mutation; radiotherapy dose and fractions; follow-up interval	(i) Insufficient published data to determine diagnostic performance (ii) No test set (CV training results available AUPRC 0.87)

[a]*Within publication some data appears mathematically discrepant.*

[b]*Within publication discrepant or unclear information (e.g. interval after radiotherapy).*

Unless otherwise stated, glioblastoma alone was analyzed.

PTRE, post-treatment related effects; HGG, high-grade glioma.

MRI sequences: T_1 C, postcontrast T_1-weighted; T_2, T_2-weighted; FLAIR, fluid-attenuated inversion recovery; DSC, dynamic susceptibility-weighted; DCE, dynamic contrast-enhanced; DWI, diffusion-weighted imaging; DTI, diffusor tensor imaging; ASL, arterial spin labelling; MRI parameters: ADC, apparent diffusion coefficient; FA, fractional anisotropy; TR, trace (DTI); CBV, cerebral blood volume; PH, peak height; K_{trans}, volume transfer constant.

Magnetic resonance spectroscopy: 1H-MRS, 1H-magnetic resonance spectroscopy; 3D-EPSI, 3D echo planar spectroscopic imaging.

1H-MRS parameters: Cr, creatine; Cho, choline; NAA, N-acetyl aspartate.

Nuclear medicine: TBR, tumor-to-brain ratio; TTP, time-to-peak.

Molecular markers: MGMT, O6-methylguanine-DNA methyltransferase; IDH, isocitrate dehydrogenase.

Machine learning methodology: CV, cross validation; LOOCV, leave-one-out cross validation; SVM, support vector machine; CNN, convolutional neural network; LASSO, least absolute shrinkage and selection operator; LSTM, long short-term memory; mRMR, minimum redundancy and maximum relevance; VGG, Visual Geometry Group (algorithm); DCGAN, deep convolutional generative adversarial network; DC-AL GAN, DCGAN with AlexNet.

Statistical measures: CI, confidence intervals; BA, balanced accuracy; AUC, area under the receiver operator characteristic curve; AUPRC, area under the precision-recall curve.

TABLE 2 | Studies applying machine learning models to baseline MRI images (or genomic signatures) to operate as glioblastoma prognostic biomarkers to predict future treatment response.

Author	Target condition	Reference standard	Dataset(s)	Available demographic information	Methodology	Features selected	Test set performance
Wang S. et al. (52)	True progression or pseudoprogression (immunotherapy for EGFRvIII mutation) Baseline prediction	Histopathology	model testing set = 10 DTI, DSC and 3D-EPSI	Testing = age mean (range) 55 (45-77) ± 8 male 4 (40%) Data from USA	Prospective. 1 center. Multivariate logistic regression.	CL, CBV, FA parameters	Insufficient data to determine per patient diagnostic performance (per lesion results only available: Recall = 0.86 Specificity = 0.60)
Yang K. et al. (53)	True progression or not (stable disease, partial & complete response & pseudoprogression) Baseline prediction	Imaging follow up	Training = 49 Genomic alterations	Training = age median (range) 57 (22-82) male 30 (61%) Data from Korea	Retrospective. 1 center. Analysis including Gene Set Enrichment Analysis (GSEA).	Genomic alterations including CDKN2A and EGFR mutations	No test set (Insufficient data to determine per patient diagnostic performance. From training dataset: 1-year PFS for responder 45%; non-responder 0%)
Lundemann M. et al. (54)	Early recurrence or not (voxel-wise) Baseline prediction	Mixture of histopathology and imaging follow up	Training = 10 18F-FET PET/CT; 18F-FDG PET/MRI; T_1 C; T_2/FLAIR; DTI; DCE	Training = age mean (range) 54 (40-71) male 7 (78%) Data from Denmark	Prospective. 1 center. Multivariate logistic regression LOOCV.	FET; FDG; MD, FA; F, Vb, Ve, Ki, and MTT parameters.	No test set (Insufficient data to determine per patient diagnostic performance. From training dataset: Voxel-wise recurrence probability AUC 0.77)

EGFR, epidermal growth factor receptor; EGFRvIII, epidermal growth factor receptor variant III; CDKN2A, cyclin-dependent kinase Inhibitor 2A.

MRI sequences: T_1 C, post-contrast T_1-weighted; T_2, T_2-weighted; FLAIR, fluid-attenuated inversion recovery; DSC, dynamic susceptibility-weighted; DCE, dynamic contrast-enhanced; DTI, diffusor tensor imaging.

Other imaging techniques: 3D-EPSI, 3D echo planar spectroscopic imaging; PET/CT, positron emission tomography and computed tomography; PET/MRI, positron emission tomography and magnetic resonance imaging; 18F-FDG, [18F]-fluorodeoxyglucose; 18F-FET, [18F]-fluoroethyl-L-tyrosine.

MRI parameters: FA, fractional anisotropy; MD, mean diffusivity; CL, linear anisotropy; CBV, cerebral blood volume; MTT, mean transit time; F, blood flow; Ve, extra-vascular extra-cellular blood volume; Vb, vascular blood volume; Ki, vascular permeability.

Statistical and machine learning methodology: LOOCV, leave-one-out cross validation; AUC, area under the receiver operator characteristic curve; PFS, progression free survival.

response target condition. Overall, the studies are best considered as proof of concept. Overall, there was insufficient data to perform a subgroup meta-analysis.

3.2 Results of Meta-Analysis

Eleven studies appeared eligible for inclusion in a meta-analysis of monitoring biomarker studies as there was information regarding internal or external hold-out test set data. However, one test was ineligible (n < 10; 3 cells in the 2 x 2 contingency table n = 0). Ten (10/18, 56%) remaining studies were subject to further analyses. Forest plots of sensitivity and specificity (**Figure 3**) graphically showed a high level of heterogeneity. Also, chi-square tests were applied separately to both primary measures. The p values resulting from these tests were 0.017 and 0.110 for sensitivities and specificities, respectively thus indicating the significant heterogeneity. This supported the choice of the bivariate random-effect model. The pooled true positive rate (sensitivity) = 0.769 (0.649 - 0.858) and the pooled false positive rate (1-specificity) = 0.352 (0.251 - 0.468).

A scatter plot of false positive rates (1-specificity) and true positive rates (sensitivity) shown in **Figure 4** demonstrates individual ROC point estimates and a summary ROC (SROC) curve giving summary ROC-AUC = 0.765.

The derived pooled measures of balanced accuracy = 0.706 (0.623-0.779); positive likelihood ratio = 2.220 (1.560-3.140); negative likelihood ratio = 0.366 (0.213- 0.572); diagnostic odds ratio = 6.670 (2.800-13.500).

4 DISCUSSION

4.1 Summary of Findings

To date, available evidence is relatively low level (12) for determining the diagnostic accuracy of ML-based glioblastoma treatment response monitoring biomarkers in adults. The available evidence is subject to a number of limitations because recent studies are at a high risk of bias and there are concerns about its applicability, especially when determining the status of response to treatment using the reference standards of follow-up imaging or pathology at re-operation. There are similar and associated concerns regarding the selection of study patients. A third of the studies did not include any type of hold-out test set. Most of the studies employed classic ML approaches based on radiomic features. A third of studies employed deep learning methodologies.

4.2 Limitations

4.2.1 Studies Assessed

Limitations encompassed three main areas. First, the reference standards used in all studies resulted in a high risk of bias and concerns about applicability. With the exception of the prognostic biomarker subgroup of studies, all the studies were retrospective, which increased the risk of confounding. Confounding factors, in relation to imaging follow-up and pathology at re-operation reference standards, were second-line drug therapy and cessation of temozolomide, all of which were rarely considered. Likewise, the

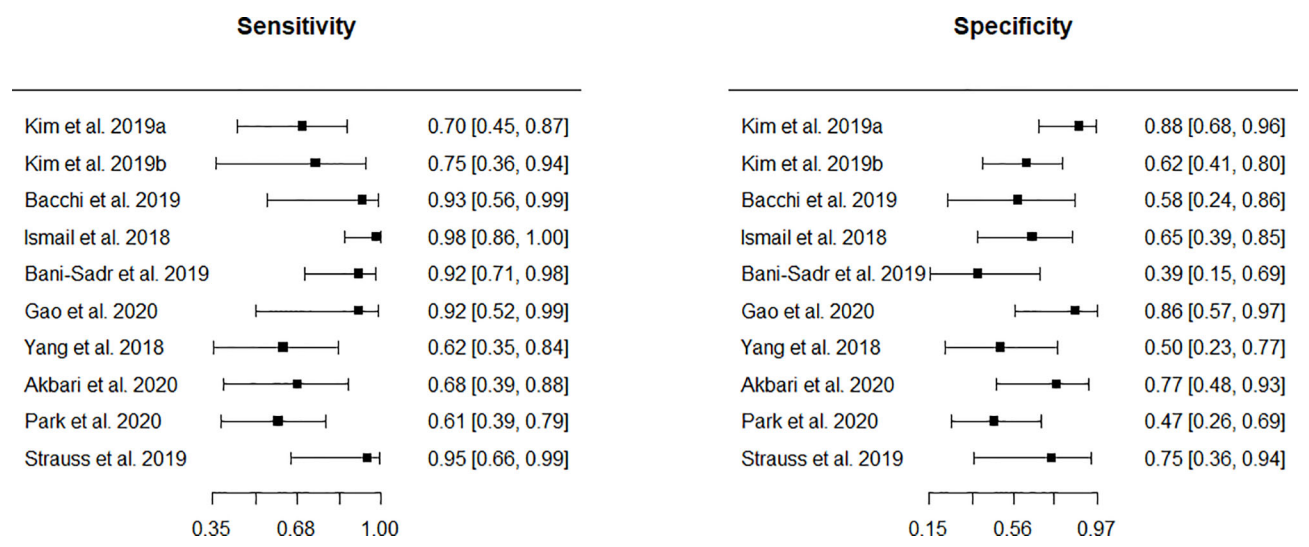

FIGURE 3 | Forest plots showing sensitivity and specificity.

use of corticosteroids was rarely considered despite being a confounding factor in relation to the imaging follow-up reference standard. If unaccounted for, an increase in corticosteroid dose may cause false negative treatment response. Some authors provided a statement within their methodology that they followed RANO guidelines (4) which if followed meticulously would surmount some of these clinicoradiological limitations, such as the use of corticosteroids which is integrated with the imaging assessment. One limitation in using the RANO guidelines, however, is that in some scenarios the contrast-enhancing lesions due to PTRE continue to enlarge over a short interval, confounding assessment by falsely confirming true progression if continued enlargement is seen at a second short interval scan; RANO guidelines do not account for this upslope effect (26, 27).

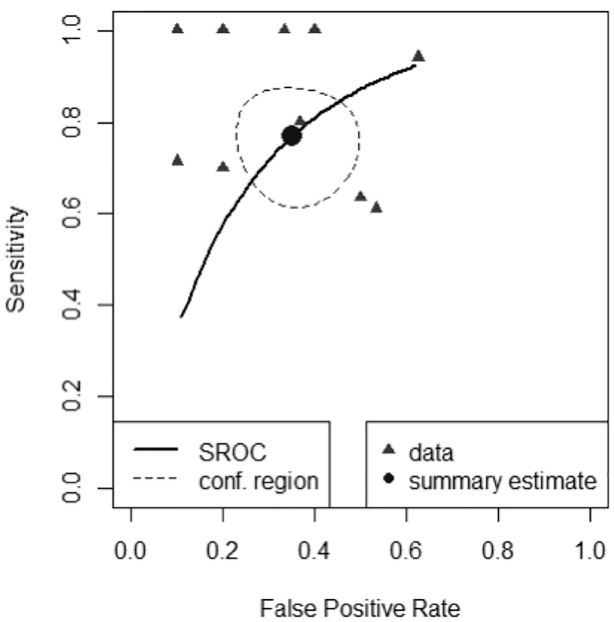

FIGURE 4 | Summary Receiver Operator Characteristic Curve (SROC) of diagnostic performance accuracy. The summary point estimate and surrounding 95% confidence region is shown.

Second, patient selection was problematic and is associated with confounding. For example, patients receiving second-line drug therapy should have been excluded as response assessment may be altered. It is also noteworthy that astrocytoma, IDH-mutant, grade 4 are biologically and prognostically distinct from glioblastomas, IDH-wildtype (55). Variable proportions in individual studies introduces between-study heterogeneity and therefore this is a source of potential confounding when comparing or pooling data. Nonetheless, it is acknowledged that for grade 4 tumors, IDH-mutants have a prevalence an order of magnitude less than IDH-wildtype, likely limiting the impact of such confounding.

Third, hold-out test sets should be used for diagnostic accuracy assessment in ML studies (22) as it is a simple demonstration as to whether the trained model overfits data; nonetheless more than a third of studies did not use either an internal or external hold-out test set. Nonetheless, six studies did use external hold-out tests which might be considered optimal practice for determining generalizability.

4.2.2 Review Process

Imaging reference standards, especially RANO trial guidelines (4) and later iterations (25), are rarely applied correctly and are themselves confounded (56). Because tumors have a variety of shapes, may have an outline that is difficult to delineate, and may be located only within the cavity rim, it can be challenging to perform seemingly simple size measurements (11). For example, large, cyst-

like glioblastomas may be "non-measurable" unless a solid nodular component of the rim fulfils the "measurable" criteria.

As well as the scenario described above highlighting the upslope effect of PTRE (26, 27), another limitation of RANO is a failure to acknowledge that pseudoprogression appears over a 6-month period rather than a 3-month period (although it is accepted that even a 6 month cut-off is arbitrary) (26). Follow-up imaging of adequate duration is therefore required in study design. This leads to a further limitation of this or other systematic reviews – it is extremely difficult to design studies with enough nuance to be at low risk of bias in regards to the reference standard.

Another limitation of this systematic review is that pathology at re-operation, where used as a reference standard, is typically not an entirely reliable reference standard for two reasons (57). First, there is the potential for biopsy sampling bias because the entire enhancing tissue may represent an admixture of PTRE and tumor (58). Second, there is a lack of pathological standardization causing a variety of inter-observer diagnostic interpretations given the background of extensive post-therapy related changes (59). Nonetheless, in the absence of more reliable available reference standards at re-operation, it was pragmatically included as an acceptable reference standard. Additionally, according to many authors, it is closer to being a more accurate reference standard compared to follow-up imaging.

Publication bias may also have affected the range of diagnostic accuracy of the monitoring biomarkers included in this systematic review and meta-analysis. Related to this, the exclusion of pre-prints and non-peer reviewed material may exacerbate publication bias. In particular, given that some in the data science community may not submit their work in peer-reviewed journals as peer review is relatively slow compared to the speed at which data science develops, it is plausible that publication bias relates to the make-up of the researcher team. For example, more clinically-orientated teams may be more inclined to publish in a peer reviewed journal compared to more data science-orientated teams.

4.3 Explanation of the Results in the Context of Other Published Evidence

After treatment, "monitoring biomarkers" are measured serially to detect change in the extent of tumor infiltration or to provide evidence of response to treatment (2). In nearly all glioblastomas the integrity of the blood brain barrier is disrupted and MRI is used to take advantage of this. Following intravenous administration of gadolinium-based contrast agents, the hydrophilic contrast molecules diffuse from the vessel lumen and accumulate in the extravascular extracellular space, manifesting on T_1-weighted sequences as contrast-enhancing hyperintense regions (60). Subsequently, MRI has been incorporated into recommendations for determining response to treatment in trials (4). In these recommendations, treatment response assessment is based on simple linear metrics of contrast-enhancing tumor, specifically, the product of maximal perpendicular cross-sectional dimensions in "measurable" lesions defined as > 10 mm in all perpendicular dimensions. The recommendations are based on expert opinion informed by observational studies and derived from the biologically plausible assumption that an increase in the size of a tumor identifies disease progression, potentially resulting in a lead time improvement for therapeutic intervention before the tumor becomes clinically apparent (61). The rationale is that there may be advantages in altering management early on before the onset of irreversible disability or the tumor extent precludes intervention. Justification for enhancement as a proxy for tumor has been inferred from data showing that the size of the enhancing region and extent of resection of the enhancing region are "prognostic biomarkers" (2) at both initial presentation and confirmed recurrence (62–64).

The trial assessment recommendations, incorporated in a less stringent form during routine clinical assessment (65), allow for an early change in treatment strategy (9). However, there are important challenges using conventional structural MRI protocols.

First, treatment response assessment typically is made in a retrospective manner as confirmatory imaging is required to demonstrate a sustained increase or a sustained decrease in enhancing volume. This leads to a delay in diagnosis.

Second, contrast enhancement is biologically non-specific, which can result in false negative, false positive, and indeterminate outcomes, especially in regards to the post-treatment related pseudophenomena observed in glioblastoma patients (61). Pseudoprogression is an early post-treatment related effect characteristically appearing within 6 months of glioblastoma patients completing radiotherapy and concomitant temozolomide, whereas pseudoresponse (not examined in this systematic review) appears after patients have been treated with anti-angiogenic agents such as bevacizumab. False-negative treatment response and false-positive progression appear as a decrease or an increase in the volume of MRI contrast enhancement, respectively. Delayed post-treatment related effects caused by radiation necrosis similarly appear as an increase in volume of MRI contrast enhancement, again potentially causing false-positive progression. A different scenario where contrast enhancement is biologically non-specific includes post-operative peritumoral parenchymal enhancement after operative "tissue handling"; or after operative infarction.

Conventional structural MRI protocols are therefore limited and contemporaneous, accurate and reliable monitoring biomarkers are required for glioblastoma treatment response assessment. Three potential solutions are highlighted here:

First, an emerging alternative approach is to harness the potential value of circulating biomarkers (including circulating tumor cells, exosomes, and microRNAs) to monitor disease progression in glioma patients (66). However, as with any potential monitoring blood or cerebral spinal fluid biomarker, potential use requires further evaluation and validation in large scale prospective studies before implementation into standard clinical practice can be envisaged.

Second, another promising approach is to use advanced imaging techniques (67). The last three decades have seen considerable technical developments in MRI (for example, those related to perfusion, permeability and diffusion), 1H-MR spectroscopic imaging, and positron emission tomography (for example using radiolabelled amino acids). A meta-analysis of 28 perfusion and

permeability imaging studies showed that the pooled sensitivities and specificities of each study's best performing parameter were 90% and 88% (95% confidence interval (CI), 0.85 - 0.94; 0.83 - 0.92) and 89% and 85% (95% CI, 0.78 - 0.96; 0.77 - 0.91) for dynamic susceptibility-weighted (DSC) and dynamic contrast-enhanced (DCE) MRI, respectively (68). Clinical translation is far from ubiquitous (65) reflecting that further investigation and consensus standardization is required before implementing any particular widespread quantitative strategy (68). Indeed, advanced imaging is not yet recommended for determining treatment response in trials (4), and there is a lack of evidence that using advanced MRI techniques leads to a reduction in morbidity or mortality (61). However, compared to ML where accuracy-driven performance metrics have resulted in increasingly opaque models, particularly when using structural images, the underlying biological processes relating to advanced imaging appear to be well understood whilst also demonstrating high performance accuracy.

A third approach is to use ML, whether applied to conventional structural MRI, advanced imaging techniques or a combination of both imaging and non-imaging features. Indeed, an advantage of machine learning applied to MRI is that wide data can be handled relatively easily (11) which might allow the wide spectrum of signatures from multiparametric advanced MRI to be captured together to improve performance accuracy. However, a disadvantage when compared to a single modality approach is that combinations of outputs from individual modalities that are without frameworks for technical and clinical use, might compound inter-center variability and reduce generalizability considerably. The advantages and disadvantages of using ML-based monitoring biomarkers for glioblastoma treatment response assessment have been described recently (summarised in **Table 3**) (61). However, a number of factors demonstrate that only limited conclusions on performance can be drawn from recent studies in our systematic review. These include the high risk of bias and concerns about applicability in study designs, the small number of patients analysed in ML studies, and the low level of evidence of the monitoring biomarker studies given their retrospective nature.

Nonetheless, overall there appears to be good diagnostic performance of ML models using MRI features to differentiate between progressive disease and mimics. For now, if ML models are to be used they may be best confined to the centers where the data was obtained from, badged as research tools and undergo further improvement.

Concordant with a previous review of studies published up to Sept 2018 (11), the diagnostic performance of ML using implicit features did not appear to be superior to ML using explicit features. However, the small number of studies precluded meaningful quantitative comparison.

4.4 Implications for Clinical Practice and Future Research

The results demonstrate that glioblastoma treatment response monitoring biomarkers using ML are promising but are still at the early development stage and are not yet ready to be integrated into clinical practice. All studies would benefit from the improvements in methodology described above. Methodological profiles or standards might be developed through consortiums such as the European Cooperation in Science and Technology (COST) Glioma MR Imaging 2.0 (GliMR) (67) initiative or the ReSPOND Consortium (76). Determining an accurate reference standard for treatment response is challenging and performing prospective studies capturing contemporaneous detailed information on steroids and second line treatments is likely to mitigate the effects of confounding. Additionally, multiple image-localized biopsies at recurrence may lessen sampling bias due to PTRE and tumor admixture.

In future studies, it would be beneficial to perform analytical validation using external hold-out tests as epitomized by several studies in the current review. Using larger datasets which include a

TABLE 3 | Advantages and disadvantages of using ML-based monitoring biomarkers for glioblastoma treatment response assessment (61).

Advantages	Disadvantages
Using ML requires less formal statistical training given the huge developments in software (69), and the programming expertise for researchers has now been transformatively reduced, enabled by standardized implementations of open source software (70, 71).	The clinical context may not be represented with a decreased ability to perform holistic evaluations of patients, with loss of valuable and irreducible aspects of the human experience such as psychological, relational, social, and organizational issues (72).
Wide data can be handled relatively easily (11) and ML can be applied to conventional structural MRI, advanced imaging techniques or a combination of both imaging and non-imaging features.	Linking the empirical data to a categorical analysis can neglect an intrinsic ambiguity in the observed phenomena (72), which might adversely affect the intended performance (69).
ML models have the ability to determine implicitly any complex nonlinear relationship between independent and dependent variables (69), and have the ability to determine all possible interactions between predictor variables (73).	Overreliance on the capabilities of automation can lead to the related phenomenon of radiologist deskilling (74).
	Algorithms may be unreliable due to several technical constraints: domain adaptation is currently limited, and more solutions are required to help algorithms extrapolate well to new centers. Ultimately models may require calibration or retraining.
	Robustness to unintended data, such as artifacts, is also a technical constraint that needs to be overcome. Finally, the presence of more than one pathology (e.g., stroke or abscess associated with a tumor following treatment) can also confound algorithms as these cases are scarce and often unlabeled.
	Accuracy-driven performance metrics have led to a trend towards increasingly opaque models (73), although recent developments in interpretability and explainability may help to mitigate this to some extent (75).

wider range of tumors and mimics as well as parameters from different sequences, manufacturers and coils, and thereby reduce overfitting, would also improve future studies. Multidisciplinary efforts and multicenter collaborations are therefore necessary (61). However, datasets will always be relatively small in neuro-oncological imaging even if distributed machine learning approaches such as federated learning, where the model comes to the data rather than the data comes to the model, overcome data sharing regulatory bottlenecks (61). Therefore, strategies to improve ML performance using small datasets, some of which are at the research stage, should be exploited further. Strategies include data augmentation (generate more varied image examples, within a single classification task) and the related process of meta-augmentation (generate more varied tasks, for a single example) (77) as well as transfer learning and the overlapping process of one- or few-shot learning (78). Transfer learning aims to learn representations from one domain (does not need to consist of brain tumors) and transfer the learned features to a closely related target domain (glioblastoma). Few-shot learning allows classifiers to be built from very small labelled training sets. Another research direction could be reducing the demand for image labelling. This field is known as self-supervised learning (79). Finally, an entirely different approach to counter the challenges of small datasets is to use synthetic data, for example using generative adversarial networks (80).

Predictions can also be made more informative through the modelling of prediction uncertainty including the generation of algorithms that would "know when they don't know" what to predict (11).

Further downstream challenges for clinical adoption will be the completion of clinical validation (2) as well as the deployment of the clinical decision support (CDS) software to clinical settings. Clinical validation consists of evaluating the CDS software containing the locked machine learning model in a clinical trial thereby producing high level evidence (12). The CDS software deployment brings both technical and non-technical challenges. In terms of technical challenges, the CDS software must be easily integrated into the radiologist's workflow (electronic health record system and picture archiving and communication system) and preferably deliver a fully automated process that analyzes images in real time and provides a quantitative and probabilistic report. Currently there has been little translation of CDS software into radiological departments however there are open source deployment solutions (71, 81).

Non-technical challenges relate to patient data safety and privacy issues; ethical, legal and financial barriers to developing and distributing tools that may impact a patient's treatment course; medical device regulation; usability evaluation; clinical acceptance and medical education around the implementation of CDS software (14, 82). Medical education includes articulating the CDS software limitations to ensure there is judicious patient and imaging selection reflecting the cohort used for validation of the model (11).

5 CONCLUSION

A range of ML-based solutions primed as glioblastoma treatment response monitoring biomarkers may soon be ready for clinical adoption. To ensure clinical adoption, it would be beneficial during the development and validation of ML models that studies include large, well-annotated datasets where there has been meticulous consideration of the potential for confounding.

DATA AVAILABILITY STATEMENT

The original contributions presented in the study are included in the article/**Supplementary Material**. Further inquiries can be directed to the corresponding author.

AUTHOR CONTRIBUTIONS

TB: experimental design and implementation, analysis and interpretation of the data, performance accuracy statistical analysis, writing of draft manuscript, approval of the final version. AC, AR, AAB, CD, HS, AL, AM, BA, NM, JL, FV, KA, SO, MM: the implementation, analysis, and interpretation of the data and approval of the final version. MG: implementation, analysis and interpretation of the data, meta-analysis statistical analysis, writing of draft manuscript, approval of the final version. All authors contributed to the article and approved the submitted version.

FUNDING

This research was supported by the Wellcome/EPSRC Centre for Medical Engineering (WT 203148/Z/16/Z) (TB, MG, AC, MM, SO) which includes open access fees, The Royal College of Radiologists (TB) and King's College Hospital Research and Innovation (TB).

SUPPLEMENTARY MATERIAL

The Supplementary Material for this article can be found online at: https://www.frontiersin.org/articles/10.3389/fonc.2022.799662/full#supplementary-material

REFERENCES

1. Stupp R, Mason WP, van den Bent MJ, Weller M, Fisher B, Taphoorn MJB, et al. Radiotherapy Plus Concomitant and Adjuvant Temozolomide for Glioblastoma. *N Engl J Med* (2005) 352:987–96. doi: 10.1056/NEJMoa043330
2. FDA-NIH Biomarker Working Group. *BEST (Biomarkers, EndpointS, and Other Tools) Resource. 1st edn*. Silver Spring, MD: Food and Drug Administration (US), co-published by Bethesda, MD: National Institutes of Health US (2016). Available at: https://www.ncbi.nlm.nih.gov/books/NBK326791.
3. MacDonald D, Cascino TL, Schold SC, Cairncross JG. Response Criteria for Phase II Studies of Supratentorial Malignant Glioma. *J Clin Oncol* (2010) 8:1277–80. doi: 10.1200/JCO.1990.8.7.1277
4. Wen PY, Macdonald DR, Reardon DA, Cloughesy TF, Sorensen AG, Galanis E, et al. Updated Response Assessment Criteria for High-Grade Gliomas: Response Assessment in Neuro- Oncology Working Group. *J Clin Oncol* (2010) 28:1963–72. doi: 10.1200/JCO.2009.26.3541

5. Booth TC, Tang Y, Waldman AD, Quigley A-M, Lewis D, Soloviev D, et al. Neuro-Oncology Single-Photon Emission CT: A Current Overview. *Neurographics* (2011) 01:108–20. doi: 10.3174/ng.3110014
6. Chamberlain MC, Glantz MJ, Chalmers L, Van Horn A, Sloan AE. Early Necrosis Following Concurrent Temodar and Radiotherapy in Patients With Glioblastoma. *J Neurooncol* (2007) 82:81–3. doi: 10.1007/s11060-006-9241-y
7. Brandsma D, Stalpers L, Taal W, Sminia P, van den Bent MJ. Clinical Features, Mechanisms, and Management of Pseudoprogression in Malignant Gliomas. *Lancet Oncol* (2008) 9(5):453–61. doi: 10.1016/S1470-2045(08)70125-6
8. Radbruch A, Fladt J, Kickingereder P, Wiestler B, Nowosielska M, Baumer P, et al. Pseudoprogression in Patients With Glioblastoma: Clinical Relevance Despite Low Incidence. *Neuro Oncol* (2015) 17(1):151–9. doi: 10.1093/neuonc/nou129
9. Dhermain FG, Hau P, Lanfermann H, Jacobs AH, van den Bent MJ. Advanced MRI and PET Imaging for Assessment of Treatment Response in Patients With Gliomas. *Lancet Neurol* (2010) 9(9):906–20. doi: 10.1016/S1474-4422(10)70181-2
10. Verma N, Cowperthwaite MC, Burnett MG, Markey MK. Differentiating Tumor Recurrence From Treatment Necrosis: A Review of Neuro-Oncologic Imaging Strategies. *Neuro Oncol* (2013) 15(5):515–34. doi: 10.1093/neuonc/nos307
11. Booth TC, Williams M, Luis A, Cardoso J, Ashkan K, Shuaib H. Machine Learning and Glioma Imaging Biomarkers. *Clin Radiol* (2020) 75:20–32. doi: 10.1016/j.crad.2019.07.001
12. Howick J, Chalmer I, Glasziou P, Greenhalgh T, Heneghan C, Liberati A, et al. *Oxford Centre for Evidence-Based Medicine The Oxford 2011 Levels of Evidence* (2016). Oxford. Available at: http://www.cebm.net/index.aspx?o1/45653 (Accessed 1 August, 2018).
13. Lui YW, Chang PD, Zaharchuk G, Barboriak DP, Flanders AE, Wintermark M, et al. Artificial Intelligence in Neuroradiology: Current Status and Future Directions. *AJNR Am J Neuroradiol* (2020) 41(8):E52–9. doi: 10.3174/ajnr.A6681
14. Jin W, Fatehi M, Abhishek K, Mallya M, Toyota B, Hamarneh G. Artificial Intelligence in Glioma Imaging: Challenges and Advances. *J Neural Eng* (2020) 17(2):021002. doi: 10.1088/1741-2552/ab8131
15. Dean J, Patterson D, Young C. A New Golden Age in Computer Architecture: Empowering the Machine-Learning Revolution. *IEEE Micro* (2018) 38:(2):21–9. doi: 10.1109/MM.2018.112130030
16. Booth TC, Akpinar B, Roman A, Shuaib H, Luis A, Chelliah A, et al. Machine Learning and Glioblastoma: Treatment Response Monitoring Biomarkers in 2021. In: SM Kia, H Mohy-ud-Din, A Abdulkadir, C Bass, M Habes, JM Rondina, et al, editors. *Machine Learning in Clinical Neuroimaging and Radiogenomics in Neuro-Oncology. MLCN 2020, RNO-AI 2020. Lecture Notes in Computer Science*, vol. 12449 . Heidelberg: Springer (2020). p. 212–8.
17. McInnes MDF, Moher D, Thombs BD, McGrath TA, Bossuyt PM. the PRISMA-DTA Group. Preferred Reporting Items for a Systematic Review and Meta-Analysis of Diagnostic Test Accuracy Studies: The PRISMA-DTA Statement. *JAMA* (2018) 319:388–96. doi: 10.1001/jama.2017.19163
18. Bossuyt PM, Leeflang MM. Developing Criteria for Including Studies. In: PM Bossuyt, editor. *Cochrane Handbook for Systematic Reviews of Diagnostic Test Accuracy Version 0.4*. London: The Cochrane Collaboration (2008). p. 1–7.
19. de Vet HCW, Eisinga A, Riphagen II, Aertgeerts B, Pewsner D. Searching for Studies. In: PM Bossuyt, editor. *Cochrane Handbook for Systematic Reviews of Diagnostic Test Accuracy Version 0.4*. London: The Cochrane Collaboration (2008). p. 1–60.
20. Reitsma JB, Rutjes AWS, Whiting P, Vlassov VV, Leeflang MMG, Deeks JJ. Assessing Methodological Quality. In: JJ Deeks, PM Bossuyt, C Gatsonis, editors. *Cochrane Handbook for Systematic Reviews of Diagnostic Test Accuracy Version 1.0.0*. London: The Cochrane Collaboration (2009). p. 1–28.
21. Whiting PF, Rutjes AW, Westwood ME, Mallett S, Deeks JJ, Reitsma JB, et al. QUADAS-2: A Revised Tool for the Quality Assessment of Diagnostic Accuracy Studies. *Ann Intern Med* (2011) 155(8):529–36. doi: 10.7326/0003-4819-155-8-201110180-00009
22. Mongan J, Moy L, Kahn CE. Checklist for Artificial Intelligence in Medical Imaging (CLAIM): A Guide for Authors and Reviewers. *Radiol Artific Intell* (2020) 2(2):e200029. doi: 10.1148/ryai.2020200029
23. Booth TC, Ashkan K, Brazil L, Jäger R, Waldman AD. Re: "Tumour Progression or Pseudoprogression? A Review of Post-Treatment Radiological Appearances of Glioblastoma". *Clin Radiol* (2016) 71(5):495–6. doi: 10.1016/j.crad.2016.01.014
24. Booth TC, Waldman AD, Jefferies S, Jäger R. Comment on "The Role of Imaging in the Management of Progressive Glioblastoma. A Systematic Review and Evidence-Based Clinical Practice Guideline". *J Neurooncol* (2015) 121(2):423–4. doi: 10.1007/s11060-014-1649-1
25. Ellingson BM, Wen PY, Cloughesy TF. Modified Criteria for Radiographic Response Assessment in Glioblastoma Clinical Trials. *Neurotherapeutics* (2017) 14:307–20. doi: 10.1007/s13311-016-0507-6
26. Booth TC, Larkin TJ, Yuan Y, Dawson SN, Scoffings D, Canuto HC, et al. Analysis of Heterogeneity in T2-Weighted MR Images can Differentiate Pseudoprogression From Progression in Glioblastoma. *PLoS One* (2017) 12(5):e0176528. doi: 10.1371/journal.pone.0176528
27. Gahramanov S, Muldoon LL, Varallyay CG, Li X, Kraemer DF, Fu R, et al. Pseudoprogression of Glioblastoma After Chemo- and Radiation Therapy: Diagnosis by Using Dynamic Susceptibility-Weighted Contrast-Enhanced Perfusion MR Imaging With Ferumoxytol Versus Gadoteridol and Correlation With Survival. *Radiology* (2013) 266(3):842–52. doi: 10.1148/radiol.12111472
28. Reitsma JB, Glas AS, Rutjes AWS, Scholten RJPM, Bossuyt PM, Zwinderman AH. Bivariate Analysis of Sensitivity and Specificity Produces Informative Summary Measures in Diagnostic Reviews. *J Clin Epidemiol* (2005) 58:982–90. doi: 10.1016/j.jclinepi.2005.02.022
29. Zhou X-H, Obuchowski NA, McClish DK. *Statistical Methods in Diagnostic Medicine. 2nd ed*. Chicester: John Wiley & Sons (2011) p. 55.
30. Harbord RM, Whiting P. Metandi: Meta-Analysis of Diagnostic Accuracy Using Hierarchical Logistic Regression. *Stata J* (2009) 9(2):211–29. doi: 10.1177/1536867X0900900203
31. Schwarzer G, Carpenter JR, Rücker G. *Meta-Analysis With R*. Heidelberg: Springer (2015). 252 p.
32. Zwinderman A, Bossuyt P. We Should Not Pool Diagnostic Likelihood Ratios in Systematic Reviews. *Stat Med* (2008) 27:687–97. doi: 10.1002/sim.2992
33. Doebler P. *Mada: Meta-Analysis of Diagnostic Accuracy. R Package Version 0.5.10* (2020). Available at: http://www.cran.R-project.org/packages/mada (Accessed Apr 21, 2021).
34. Kim JY, Park JE, Jo Y, Shim WH, Nam SJ, Kim JH, et al. Incorporating Diffusion- and Perfusion-Weighted MRI Into a Radiomics Model Improves Diagnostic Performance for Pseudoprogression in Glioblastoma Patients. *Neuro Oncol* (2019) 21:404–14. doi: 10.1093/neuonc/noy133
35. Kim JY, Yoon MJ, Park JE, Choi EJ, Lee J, Kim HS. Radiomics in Peritumoral non-Enhancing Regions: Fractional Anisotropy and Cerebral Blood Volume Improve Prediction of Local Progression and Overall Survival in Patients With Glioblastoma. *Neuroradiology* (2019) 61:1261–72. doi: 10.1007/s00234-019-02255-4
36. Bacchi S, Zerner T, Dongas J, Asahina AT, Abou-Hamden A, Otto S, et al. Deep Learning in the Detection of High-Grade Glioma Recurrence Using Multiple MRI Sequences: A Pilot Study. *J Clin Neurosci* (2019) 70:11–3. doi: 10.1016/j.jocn.2019.10.003
37. Elshafeey N, Kotrotsou A, Hassan A, Elshafei N, Hassan I, Ahmed S, et al. Multicenter Study Demonstrates Radiomic Features Derived From Magnetic Resonance Perfusion Images Identify Pseudoprogression in Glioblastoma. *Nat Commun* (2019) 10:3170. doi: 10.1038/s41467-019-11007-0
38. Verma G, Chawla S, Mohan S, Wang S, Nasrallah M, Sheriff S, et al. Three-Dimensional Echo Planar Spectroscopic Imaging for Differentiation of True Progression From Pseudoprogression in Patients With Glioblastoma. *NMR BioMed* (2019) 32:4042. doi: 10.1002/nbm.4042
39. Ismail M, Hill V, Statsevych V, Huang R, Prasanna P, Correa R, et al. Shape Features of the Lesion Habitat to Differentiate Brain Tumor Progression From Pseudoprogression on Routine Multiparametric MRI: A Multisite Study. *AJNR Am J Neuroradiol* (2018) 39:2187–93. doi: 10.3174/ajnr.A5858
40. Bani-Sadr A, Eker OF, Berner LP, Ameli R, Hermier M, Barritault M, et al. Conventional MRI Radiomics in Patients With Suspected Early- or Pseudo-Progression. *Neurooncol Adv* (2019) 1:1–9. doi: 10.1093/noajnl/vdz019
41. Gao XY, Wang YD, Wu SM, Rui WT, Ma DN, Duan Y, et al. Differentiation of Treatment-Related Effects From Glioma Recurrence Using Machine Learning Classifiers Based Upon Pre-And Post-Contrast T1WI and T2 FLAIR

Subtraction Features: A Two-Center Study. *Cancer Manag Res* (2020) 12:3191–201. doi: 10.2147/CMAR.S244262
42. Jang BS, Jeon SH, Kim IH, Kim IA. Prediction of Pseudoprogression Versus Progression Using Machine Learning Algorithm in Glioblastoma. *Sci Rep* (2019) 8:12516. doi: 10.1038/s41598-018-31007-2
43. Li M, Tang H, Chan MD, Zhou X, Qian X. DC-AL GAN: Pseudoprogression and True Tumor Progression of Glioblastoma Multiform Image Classification Based on DCGAN and AlexNet. *Med Phys* (2020) 47:1139–50. doi: 10.1002/mp.14003
44. Akbari H, Rathore S, Bakas S, Nasrallah MP, Shukla G, Mamourian E, et al. Histopathology - Validated Machine Learning Radiographic Biomarker for Noninvasive Discrimination Between True Progression and Pseudo-Progression in Glioblastoma. *Cancer* (2020) 126(11):2625–36. doi: 10.1002/cncr.32790
45. Li X, Xu G, Cao Q, Zou W, Xu Y, Cong P. Identification of Glioma Pseudoprogression Based on Gabor Dictionary and Sparse Representation Model. *NeuroQuantology* (2018) 16:43–51. doi: 10.14704/nq.2018.16.1.1178
46. Manning P, Daghighi S, Rajaratnam MK, Parthiban S, Bahrami N, Dale AM, et al. Differentiation of Progressive Disease From Pseudoprogression Using 3d PCASL and DSC Perfusion MRI in Patients With Glioblastoma. *J Neurooncol* (2020) 147(3):681–90. doi: 10.1007/s11060-020-03475-y
47. Park JE, Ham S, Kim HS, Park SY, Yun J, Lee H, et al. Diffusion and Perfusion MRI Radiomics Obtained From Deep Learning Segmentation Provides Reproducible and Comparable Diagnostic Model to Human in Post-Treatment Glioblastoma. *Eur Radiol* (2021) 31(5):3127–37. doi: 10.1007/s00330-020-07414-3
48. Lee J, Wang N, Turk S, Mohammed S, Lobo R, Kim J, et al. Discriminating Pseudoprogression and True Progression in Diffuse Infiltrating Glioma Using Multi-Parametric MRI Data Through Deep Learning. *Sci Rep* (2020) 10 (1):20331. doi: 10.1038/s41598-020-77389-0
49. Kebir S, Schmidt T, Weber M, Lazaridis L, Galldiks N, Langen KJ, et al. A Preliminary Study on Machine Learning-Based Evaluation of Static and Dynamic FET-PET for the Detection of Pseudoprogression in Patients With IDH-Wildtype Glioblastoma. *Cancers* (2020) 12(11):3080. doi: 10.3390/cancers12113080
50. Cluceru J, Nelson SJ, Wen Q, Phillips JJ, Shai A, Molinaro AM, et al. Recurrent Tumor and Treatment-Induced Effects Have Different MR Signatures in Contrast Enhancing and non-Enhancing Lesions of High-Grade Gliomas. *Neuro Oncol* (2020) 22(10):1516–26. doi: 10.1093/neuonc/noaa094
51. Jang BS, Park AJ, Jeon SH, Kim IH, Lim DH, Park SH, et al. Machine Learning Model to Predict Pseudoprogression Versus Progression in Glioblastoma Using MRI: A Multi-Institutional Study (KROG 18-07). *Cancers* (2020) 12 (9):2706. doi: 10.3390/cancers12092706
52. Wang S, O'Rourke DM, Chawla S, Verma G, Nasrallah MP, Morrissette JJD, et al. Multiparametric Magnetic Resonance Imaging in the Assessment of Anti-EGFRvIII Chimeric Antigen Receptor T Cell Therapy in Patients With Recurrent Glioblastoma. *Br J Cancer* (2019) 120:54–6. doi: 10.1038/s41416-018-0342-0
53. Yang K, Jung SW, Shin H, Lin DH, Lee JI, Kong DS, et al. Cancer Genetic Markers According to Radiotherapeutic Response in Patients With Primary Glioblastoma - Radiogenomic Approach for Precision Medicine. *Radiother Oncol* (2019) 131:66–74. doi: 10.1016/j.radonc.2018.11.025
54. Lundemann M, Munck af Rosenschöld P, Muhic A, Larsen VB, Poulsen HS, Engelholm SA, et al. Feasibility of Multi-Parametric PET and MRI for Prediction of Tumour Recurrence in Patients With Glioblastoma. *Eur J Nucl Med Mol Imaging* (2019) 46:603–13. doi: 10.1007/s00259-018-4180-3
55. Louis DN, Perry A, Wesseling P, Brat DJ, Cree IA, Figarella-Branger D, et al. The 2021 WHO Classification of Tumors of the Central Nervous System: A Summary. *Neuro Oncol* (2021) 23(8):1231–51. doi: 10.1093/neuonc/noab106
56. Buwanabala J, Mirchandani A, Booth TC. (2019). The (Mis)Use of Imaging Criteria in the Assessment of Glioblastoma Treatment Response. In: *Proceedings of the 57th American Society of Neuroradiology*, Boston, USA, 2019 May 18-23. p. 1. Oak Brook.
57. Holdhoff M, Ye X, Piotrowski AF, Strowd RE, Seopaul S, Lu Y, et al. The Consistency of Neuropathological Diagnoses in Patients Undergoing Surgery for Suspected Recurrence of Glioblastoma. *J Neurooncol* (2019) 141:347–54. doi: 10.1007/s11060-018-03037-3
58. Müller DMJ, Robe PAJT, Eijgelaar RS, Witte MG, Visser M, de Munck JC, et al. Comparing Glioblastoma Surgery Decisions Between Teams Using Brain Maps of Tumor Locations, Biopsies, and Resections. *JCO Clin Cancer Inform* (2019) 3:1–12. doi: 10.1200/CCI.18.00089
59. Haider AS, van den Bent M, Wen PY, Vogelbaum MA, Chang S, Canoll PD, et al. Toward a Standard Pathological and Molecular Characterization of Recurrent Glioma in Adults: A Response Assessment in Neuro-Oncology Effort. *Neuro Oncol* (2020) 22(4):450–6. doi: 10.1093/neuonc/noz233
60. Cao Y, Sundgren PC, Tsien CI, Chenevert TT, Junck L. Physiologic and Metabolic Magnetic Resonance Imaging in Gliomas. *J Clin Oncol* (2006) 24 (8):1228–35. doi: 10.1200/JCO.2005.04.7233
61. Booth TC, Thompson G, Bulbeck H, Boele F, Buckley C, Cardodo J, et al. A Position Statement on the Utility of Interval Imaging in Standard of Care Brain Tumour Management: Defining the Evidence Gap and Opportunities for Future Research. *Front Oncol* (2021) 11:620070. doi: 10.3389/fonc.2021.620070
62. Ellingson BM, Harris RJ, Woodworth DC, Leu K, Zaw O, Mason WP, et al. Baseline Pretreatment Contrast Enhancing Tumor Volume Including Central Necrosis Is a Prognostic Factor in Recurrent Glioblastoma: Evidence From Single- and Multicenter Trials. *Neuro Oncol* (2017) 19:89–98. doi: 10.1093/neuonc/now187
63. Lacroix M, Abi-Said D, Fourney DR, Gokaslan ZL, Shi W, DeMonte F, et al. A Multivariate Analysis of 416 Patients With Glioblastoma Multiforme: Prognosis, Extent of Resection, and Survival. *J Neurosurg* (2001) 95:190–8. doi: 10.3171/jns.2001.95.2.0190
64. Sanai N, Polley M-Y, McDermott MW, Parsa AT, Berger MS. An Extent of Resection Threshold for Newly Diagnosed Glioblastomas. *J Neurosurg* (2011) 115:3–8. doi: 10.3171/2011.2.JNS10998
65. Booth TC, Luis A, Brazil L, Thompson G, Daniel RA, Shuaib H, et al. Glioblastoma Post-Operative Imaging in Neuro-Oncology: Current UK Practice (GIN CUP Study). *Eur Radiol* (2021) 31(5):2933–43. doi: 10.1007/s00330-020-07387-3
66. Müller Bark J, Kulasinghe A, Chua B, BW D, Punyadeera C. Circulating Biomarkers in Patients With Glioblastoma. *Br J Cancer* (2020) 122(3):295–305. doi: 10.1038/s41416-019-0603-6
67. Clement P, Booth T, Borovechi F, Emblem KE, Figueiredo P, Hirschler L, et al. GliMR: Cross-Border Collaborations to Promote Advanced MRI Biomarkers for Glioma. *J Med Biol Eng* (2021) 41(2):115–25. doi: 10.1007/s40846-020-00582-z
68. Patel P, Baradaran H, Delgado D, Askin G, Christos P, Tsiouris J, et al. MR Perfusion-Weighted Imaging in the Evaluation of High-Grade Gliomas After Treatment: A Systematic Review and Meta-Analysis. *Neuro-Oncology* (2017) 19:118–27. doi: 10.1093/neuonc/now148
69. White H. Learning in Artificial Neural Networks: A Statistical Perspective. *Neural Comput* (1989) 1(4):425–64. doi: 10.1162/neco.1989.1.4.425
70. Ratib O, Rosset A, Heuberger J. Open Source Software and Social Networks: Disruptive Alternatives for Medical Imaging. *Eur J Radiol* (2011) 78(2):259–65. doi: 10.1016/j.ejrad.2010.05.004
71. Medical Open Network for AI (MONAI). Available at: https://docs.monai.io/projects/monai-deploy-app-sdk/en/latest/release_notes/v0.2.0.html (Accessed 30 Dec 2021).
72. Cabitza F, Rasoini R, Genisi GF. Unintended Consequences of Machine Learning in Medicine. *JAMA* (2017) 318(6):517–8. doi: 10.1001/jama.2017.7797
73. Tu JV. Advantages and Disadvantages of Using Artificial Neural Networks Versus Logistic Regression for Predicting Medical Outcomes. *J Clin Epidemiol* (1996) 49(11):1225–31. doi: 10.1016/s0895-4356(96)00002-9
74. Hoff T. Deskilling and Adaptation Among Primary Care Physicians Using Two Work Innovations. *Health Care Manage Rev* (2011) 36(4):338–48. doi: 10.1097/HMR.0b013e31821826a1
75. Reyes M, Meier R, Pereira S, Silva CA, Dahlweid F-M, von Tengg-Kobligk H, et al. On the Interpretability of Artificial Intelligence in Radiology: Challenges and Opportunities. *Radiol Artif Intell* (2020) 2(3):e190043. doi: 10.1148/ryai.2020190043
76. Davatzikos C, Barnholtz-Sloan JS, Bakas S, Colen R, Mahajan A, Quintero CB, et al. AI-Based Prognostic Imaging Biomarkers for Precision Neurooncology: The ReSPOND Consortium. *Neuro-Oncology* (2020) Pii:noaa045. doi: 10.1093/neuonc/noaa045
77. Rajendran J, Irpan A, Jang E. *Meta-Learning Requires Meta-Augmentation. Advances in Neural Information Processing Systems 33* (2020). Available at: https://papers.nips.cc/paper/2020/hash/3e5190eeb51ebe6c5bbc54ee8950c548-Abstract.html.

78. Paul A, Tang YX, Summers RM. Fast Few-Shot Transfer Learning for Disease Identification From Chest X-Ray Images Using Autoencoder Ensemble. *Med Imaging* (2020). doi: 10.1117/12.2549060
79. Jing L, Tian Y. Self-Supervised Visual Feature Learning With Deep Neural Networks: A Survey. *IEEE Transactions on Pattern Analysis and Machine Intelligence*. (2021) 43:4037–58. doi: 10.1109/TPAMI.2020.2992393
80. Shin HC, Tenenholtz NA, Rogers JK, Schwarz CG, Senjem ML, Gunter JL. Medical Image Synthesis for Data Augmentation and Anonymization Using Generative Adversarial Networks. In: A Gooya, O Goksel, I Oguz, N Burgos, editors. *Simulation and Synthesis in Medical Imaging. SASHIMI 2018. Lecture Notes in Computer Science*, vol. 11037. Heidelberg: Springer (2018). p. 1–11.
81. Davatzikos C, Rathore S, Bakas S, Pati S, Bergman M, Kalarot R, et al. Cancer Imaging Phenomics Toolkit: Quantitative Imaging Analytics for Precision Diagnostics and Predictive Modeling of Clinical Outcome. *J Med Imaging (Bellingham)* (2018) 5:011018. doi: 10.1117/1.JMI.5.1.011018
82. Senders JT, Harary M, Stopa BM, Staples P, Broekman MLD, Smith TR, et al. Information-Based Medicine in Glioma Patients: A Clinical Perspective. *Comput Math Methods Med* (2018), 8572058. doi: 10.1155/2018/8572058

Conflict of Interest: The authors declare that the research was conducted in the absence of any commercial or financial relationships that could be construed as a potential conflict of interest.

frontiers | Frontiers in Oncology

ORIGINAL RESEARCH
published: 26 April 2022
doi: 10.3389/fonc.2022.874924

The Role of 3D-pCASL MRI in the Differential Diagnosis of Glioblastoma and Brain Metastases

Kristina Solozhentseva, Artem Batalov, Natalia Zakharova, Sergey Goryaynov, Eduard Pogosbekyan and Igor Pronin*

N.N. Burdenko National Medical Research Center of Neurosurgery, Ministry of Health of the Russian Federation, Moscow, Russia

Purpose: The first aim of this study was to compare the intratumoral and peritumoral blood flow parameters in glioblastomas and brain metastases measured by pseudocontinuous arterial spin labeling MRI (3D pCASL). The second aim of this study was to determine whether pCASL could aid in identifying the source of brain metastases.

Materials and Methods: This study included 173 patients aged 12 to 83 years (median age—61 years), who were observed at the National Medical Research Center for Neurosurgery. All patients underwent preoperative MRI with pCASL perfusion. Thereafter patients were operated on and received histological diagnosis. No patients received preoperative chemo or radiotherapy.

Results: The values of maximum and normalized intratumoral blood flow were significantly higher in the group with gliblastoma than in the group with brain metastases: 168.98 + –91.96 versus 152.1 + –173.32 and 7.6 + –8.4 versus 9.3 + –5.33 respectively ($p < 0.01$). However, ROC analysis showed low AUC specificity and sensitivity (0.64, 70%, 60% for mTBF and 0.66, 77%, 62% for nTBF). Peritumoral blood flow parameters were also higher in the glioblastoma group (29.61 + –22.89 versus 16.58 + –6.46 for mTBF and 1.63 + –1.14 versus 0.88 + –0.38 for nTBF, respectively; $p < 0.01$). ROC analysis showed the following measurements of AUC, specificity, and sensitivity (0.75, 68%, 73% for mTBF and 0.77, 58%, 91% for nTBF). Regarding pCASL and various histological subsets of brain metastases, the study found statistically significant differences between the lung and melanoma metastases and the lung and kidney metastases. ROC analysis gave the following values for lung and melanoma metastases: AUC—0.76, specificity—75%, and sensitivity—73% for mTBF; 0.83, 67%, and 93% respectively, for nTBF. For lung and kidney metastases: AUC—0.74, specificity—70%, and sensitivity—93% for mTBF; 0.75, 70%, and 93% respectively, for nTBF.

Conclusions: pCASL could aid in differential diagnosis between glioblastoma and brain metastases. Measurement of peritumoral blood flow demonstrates higher specificity and sensitivity than with intratumoral blood flow. Moreover, pCASL provides the ability to distinguish lung metastases from kidney and melanoma metastases.

Keywords: glioblastoma, brain metastases, blood flow, peritumoral zone, intratumoral blood flow

OPEN ACCESS

Edited by:
Fu Wang,
Xi'an Jiaotong University, China

Reviewed by:
Xudong Shen,
Guizhou Medical University, China
Kun Zheng,
Peking Union Medical College Hospital Chinese Academy of Medical Sciences (CAMS), China

****Correspondence:***
Kristina Solozhentseva
solozhentseva4256043@gmail.com

Specialty section:
This article was submitted to Cancer Imaging and Image-directed Interventions, a section of the journal Frontiers in Oncology

Received: *13 February 2022*
Accepted: *21 March 2022*
Published: *26 April 2022*

Citation:
Solozhentseva K, Batalov A, Zakharova N, Goryaynov S, Pogosbekyan E and Pronin I (2022) The Role of 3D-pCASL MRI in the Differential Diagnosis of Glioblastoma and Brain Metastases. Front. Oncol. 12:874924. doi: 10.3389/fonc.2022.874924

INTRODUCTION

The differential diagnosis of metastatic brain lesions and malignant gliomas is an extremely important task, since further approaches to the diagnosis and treatment of these patients differ significantly. Current methods for differentiating glioblastoma from brain metastases are primarily based on the multiplicity of brain metastases, however 50% of metastases are single lesions (1) (**Figure 1**). Even worse, there are multicentric glioblastomas (2). Secondly, location is important. Metastases rarely involve the corpus callosum and tend to be located gray and white matter junctions, whereas glioblastomas tend to be centered in the white matter (3). Morphologically, the presence of infiltration characterizes glioblastoma—small growths of tumor tissue along the white matter (3). In addition to that, there is an essential feature—glioblastoma can have non-enhancing tumor tissue, which is not typical for metastatic brain damage (4).

To conclude, making a differential diagnosis between glioblastoma and brain metastases using only standard MRI sequences alone could be a challenging task (5).

In terms of advanced MRI technology, MRI-perfusion and MRI-spectroscopy play a significant role in differentiating these two entities. This study explores the role of ASL-perfusion.

Previously, studies of intratumoral and peritumoral blood flow using contrast MR perfusion (DSC) were conducted, which showed that the values of blood flow in the peritumoral zone were significantly higher for glioblastomas (6). However these studies did not reveal statistically significant differences in intratumoral blood flow (7–9). pCASL MRI-perfusion is a quantitative method for non-contrast assessment of blood flow (10). This method is widely used in the examination of patients with brain tumors, but its role in the differential diagnosis of metastatic lesions and glioblastomas has not been studied enough (11, 12).

Another diagnostic task to determine the histological subtype of brain metastases. Distinguishing different types of brain metastases by blood flow may be clinically important, especially in cases when PET-CT is not available. The assumption of the source of metastases by MRI can affect the order in which diagnostic tests are applied to a patient.

Attempts have been made to differentiate metastases using MR spectroscopy, MR diffusion and CT perfusion (13, 14). The sensitivity and specificity of these methods were found to be low. The use of MR spectroscopy made it possible to distinguish melanoma metastases from all other histological subgroups (15). In the SWI study, it was shown that with quantitative analysis it is possible to differentiate metastases of melanoma from metastases of breast and lung cancer. In the study of diffusion-weighted MRI, no statistically significant differences in diffusion coefficients were found for different histological subtypes of metastases (16).

The study evaluated the role of pCASL in the differential diagnosis of metastases and glioblastomas and studied the blood flow in various histological subtypes of metastases.

MATERIALS AND METHODS

This study included 173 patients aged 12 to 83 years (median age—61 years) who were observed at the National Medical Research Center for Neurosurgery from 2012 to 2020. Fifty-two percent were women, and 48% were men. The study was retrospective. The inclusion criteria for the study were: 1. All patients must have a diagnosis of either glioblastoma or brain metatastatic disease; 2. All patients must have an MRI with T2-FLAR, T1 after contrast enhancement, and pCASL-perfusion performed at our hospital before surgery. 3. All patients must have had histological verification, which was done by our pathology department.

Of the 173 patients, 55 were diagnosed with brain metastases and 118 with glioblastomas. All patients underwent further tumor resection or stereotactic biopsy with subsequent histological verification of the process. In the group with Brain metastases the

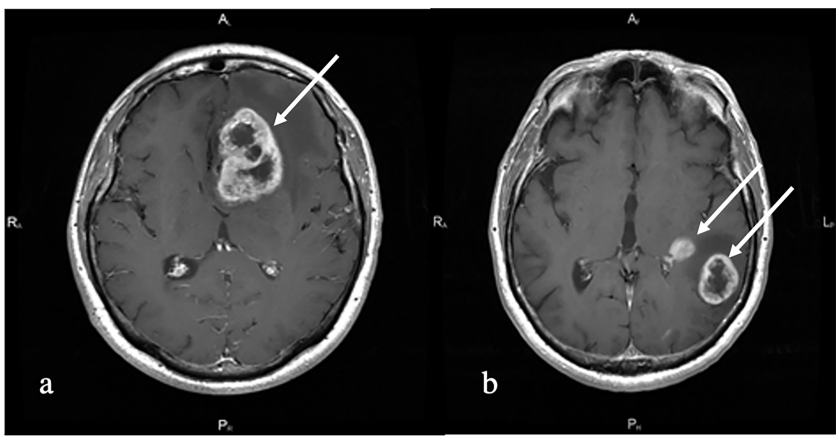

FIGURE 1 | T1 with contrast enhancement. **(A)** Melanoma metastases (white arrow). Left frontal lobe solitary irregularly contrast-enhancing tumor with central non-enhancing areas and perifocal edema is shown. **(B)** Multiple primary glioblastoma (white arrows). Left temporal multiple irregularly contrast-enhancing lesions with perifocal edema and non-enhancing central part are shown.

following subgroups/subtypes depending on the primary tumor source were established: melanoma (n = 12), kidney cancer (n = 10), breast cancer (n = 12), lung cancer (n = 15), intestinal cancer (n = 4), other tumors (n = 2). The subgroup "other tumors" included patients with diagnoses of metastases of myeloid sarcoma and metastases of cancer of unknown primary origin.

MRI was performed on a 3.0 T General Electric Signa HD MR tomography (GE Healthcare) with an 8-channel head coil. The MRI protocol for all patients consisted of T2, T2-FLAIR, DWI, 3D pCASL, and T1 before and after contrast enhancement.

ASL-scanning was carried out with the following parameters: 3D FSE, 8-lead spiral scanning with the capture of the entire volume of the brain and subsequent reforming with a section thickness of 4 mm; FOV = 240 × 240 mm; matrix 128 × 128, ZIP 512; TR—4717 ms; TE—9.8 ms; NEX = 3; PLD—1525 ms; pixel bandwidth—976.6 Hz/pixel. The duration of scanning was 4 min 30 s.

The ReadyView software package (GE Healthcare) was used to post-process the obtained data

The absolute maximum blood flow in the tumors was measured in all patients, and normalized values were calculated. To do this, an experienced neuroradiologist (>5 years of experience) placed the 4–5 ROIs (Region of Interest) of a small area (20 ± 10 mm^2) on a color TBF map in every slice within the tumoral stroma. Then the ROI with the highest blood flow was chosen.

Normalization of blood flow values was carried out by dividing the TBF value in the tumor and peritumoral zone by the TBF value in the unchanged white matter of the contralateral side.

In all patients, the values of blood flow in the peritumoral zone were calculated. The ROI area was 20 ± 10 mm^2. All patients received three ROIs in the peritumoral zone at the same level where the intratumoral ROI was placed: ROI1 was drawn in the area of increased MR signal in T2-FLAIR, where there was no accumulation of contrast agent, close to the contrasted part of the tumor (no further than 5 mm). ROI3 was drawn in the area of increased MR signal in T2-FLAIR, at the greatest distance from the contrasted part of the tumor, close to the unchanged white matter, and ROI2 was indicated at an equal distance between ROI1 and ROI3.

In the group of metastases and glioblastomas, a comparison was made of tumor blood flow parameters, ROI1 values, and ROI1–ROI3 gradient values, followed by ROC analysis. The gradient was calculated by subtracting the TBF values at ROI3 from the TBF values at ROI1.

Also, we performed a comparison between the maximum blood flow and normalized values in the histological subtypes of metastases.

The Neuro registration program was used to align blood flow maps with anatomical images (T2-FLAIR, T1 with contrast enhancement).

Statistical processing was carried out in the R-project program; the pROC library was used for ROC analysis. The Spirimen method was used to calculate the correlation coefficients. The Mann–Whitney U test was used to evaluate group comparisons.

RESULTS

First, we obtained the average absolute and normalized values of tumor blood flow in the groups of metastases and glioblastomas. TBF measurements in metastatic brain disease (**Figure 2**) were statistically lower than in glioblastomas (**Figure 3**) (p-value <0.05). The data are presented in **Table 1** and **Figure 4**.

ROC analysis was performed to determine the sensitivity and specificity of ASL perfusion in the differential diagnosis of glioblastomas and secondary brain damage. The ROC analysis data are presented in **Figure 5**.

In our work, the mean absolute and normalized values of blood flow in the peritumoral zone of groups of glioblastomas and metastases were calculated (**Table 2**). When comparing absolute and normalized parameters (ROI1), peritumoral blood flow in the glioblastoma group was significantly higher (p-value <0.0001). Simultaneously, there were no significant differences in the values of ROI2 and ROI3. However, it was noticed that the blood flow in the peritumoral zone of glioblastomas toward the unchanged white matter decreases and does not change with metastatic brain damage. These results are illustrated in **Figure 6**.

For ROI1 values, ROC analysis was carried out, which showed rather high sensitivity and specificity values. The area under the

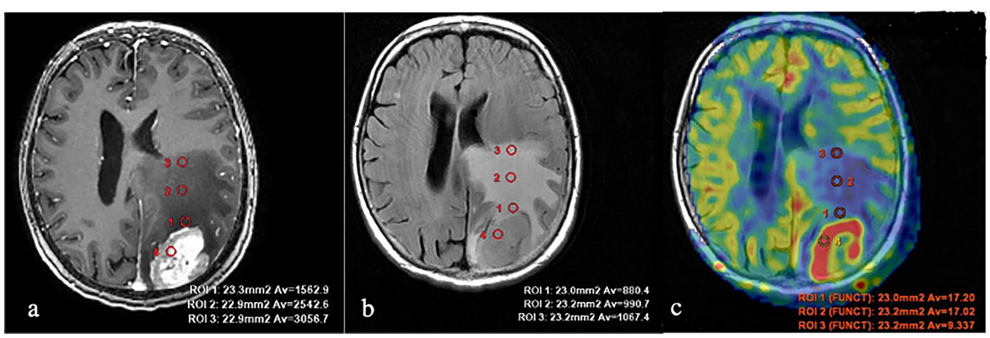

FIGURE 2 | Breast cancer metastases. **(A)** T1 with contrast enhancement; **(B)** T2-FLAIR; and **(C)** TBF blood flow maps aligned with T2-FLAIR. Measurements of hemodynamic parameters in the tumor and peritumoral zone are shown.

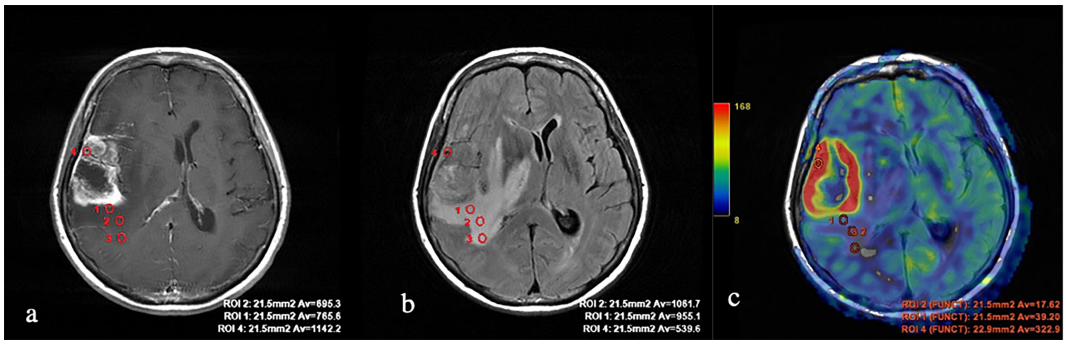

FIGURE 3 | Glioblastoma. **(A)** T1 with contrast enhancement; **(B)** T2-FLAIR; and **(C)** TBF blood flow maps aligned with T2-FLAIR. Measurements of hemodynamic parameters of tumor blood flow in the peritumoral zone are shown.

TABLE 1 | Average values of blood flow in metastatic and glioblastoma subgroups.

Group	Maximum absolute TBF t	Standard deviation TBF t	Maximum normalized TBF t (norm)	Standard deviation TBF t (norm)
Metastases	152.1	173.32	7.6	8.4
Glioblastoma	168.98	91.96	9.3	5.33

TBF, cerebral blood flow.

curve was 0.75 and 0.77 for absolute and normalized values, respectively, which indicates good diagnostic capabilities of TBF measurement in the peritumoral zone (**Figure 7**).

Gradient values (ROI1–ROI3) were also calculated for the group of metastases and glioblastomas (**Table 3**). The mean ROI–ROI3 gradient for the group of metastases turned out to be negative, which indicates lower values of blood flow in the white matter near the contrasted part of the tumor. It was proven that there was a statistically significant difference between glioblastoma and metastases (p-value was 0.0008). A comparative analysis of ROI1–RO3 gradients was carried out. The area under the curve was 0.67 (**Figure 8**).

In the second part of our work, a comparative analysis of intratumoral blood flow in histological subgroups of metastatic brain lesions was carried out. Average values of TBF for metastases of the kidney, melanoma, breast, lung, and intestine are presented in **Table 4** and **Figure 9**.

Intratumoral TBF was shown to be statistically lower in the subgroup of lung cancer metastases compared to the metastatic kidney and melanoma groups ($p < 0.05$). In the subgroups of the

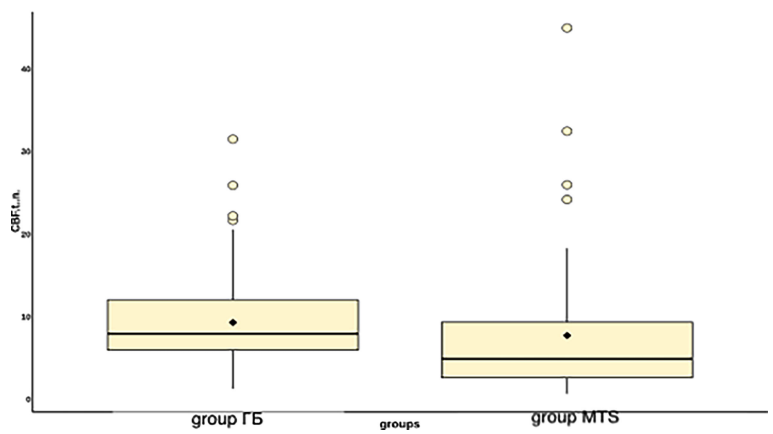

FIGURE 4 | Boxplot displaying blood flow values in groups of metastases and glioblastomas.

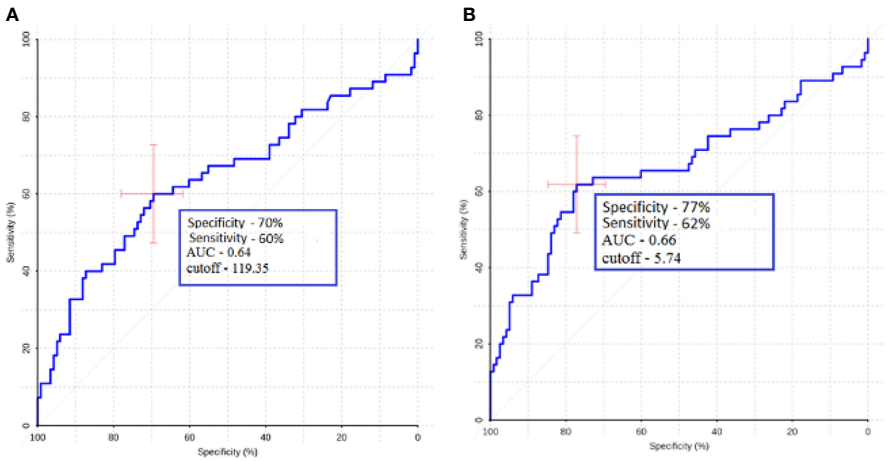

FIGURE 5 | ROC analysis data obtained by comparing the maximum **(A)** and normalized values **(B)** of intratumoral blood flow in the groups of metastases and glioblastomas. The values of the optimal threshold are presented, in brackets—specificity and sensitivity.

TABLE 2 | Average values of absolute and normalized indices of peritumoral blood flow in the groups of metastases and glioblastomas.

Group	Maximum absolute TBF ROI1	Maximum normalized TBF ROI1	Maximum absolute TBF ROI2	Maximum normalized TBF ROI2	Maximum normalized TBF ROI3	Maximum normalized TBF ROI3
Metastases	16.58 ± 6.46	0.88 ± 0.38	15.53 ± 6.67	0.8 ± 0.39	17.15 ± 4.13	0.88 ± 0.4
Glioblastoma	29.61 ± 22.89	1.63 ± 1.14	23.45 ± 21.24	1.25 ± 0.96	21.98 ± 11.67	1.17 ± 0.65

TBF, tumor blood flow; ROI, region of interest.

lung and breast, statistically significant differences were also obtained. However, when analyzing the normalized values, the p-value was 0.09.

The lowest mean blood flow values were obtained in the subgroup of intestinal cancer metastases. However, when performing a comparative analysis with all other histological types, no significant differences were obtained (p-value >0.05), which is probably due to a small sample of patients with metastases of intestinal cancer (n = 4).

ROC analysis was performed for groups that showed statistically significant differences.

ROC-analysis showed high sensitivity and sensibility in melanoma and lung cancer metastases (**Figure 10**).

ROC analysis was performed for metastatic subgroups of lung cancer and kidney cancer. High values of sensitivity and specificity were obtained (**Figure 11**). Thus, ASL perfusion can be recommended for inclusion in the diagnostic algorithm for patients with metastatic brain lesions of unknown origin.

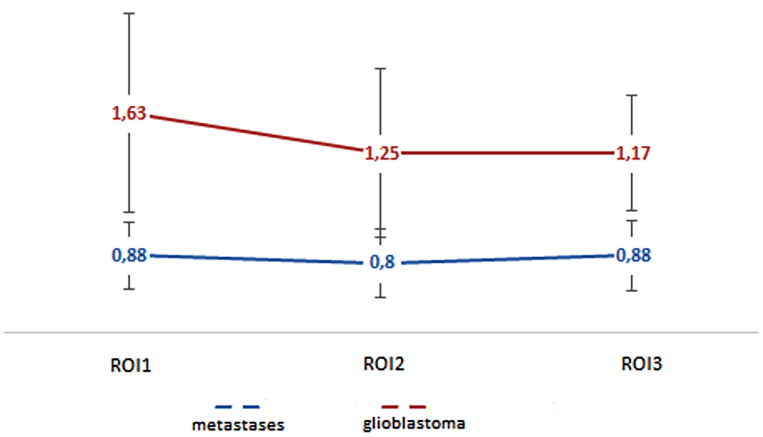

FIGURE 6 | Changes in blood flow indicators in areas of interest: edema (metastases) and edema with infiltrative component (glioblastoma).

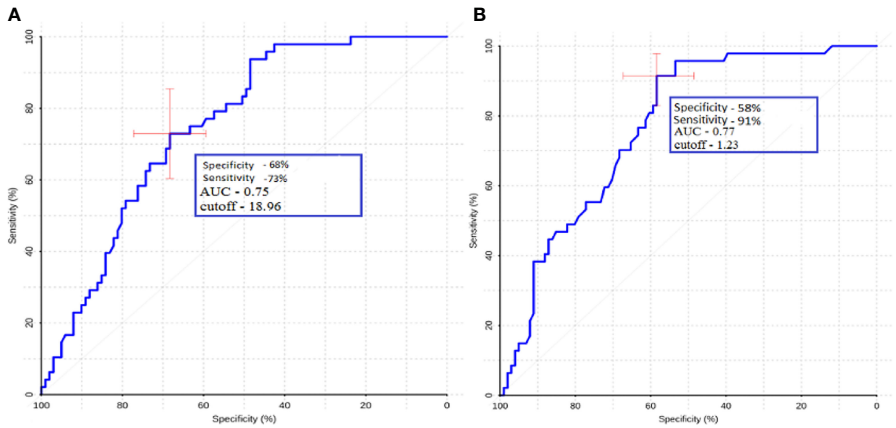

FIGURE 7 | ROC-analysis data obtained by comparing the maximum absolute **(A)** and normalized **(B)** TBF values at the ROI1 point in the groups of metastases and glioblastomas. The values of the optimal threshold are presented, in brackets—specificity and sensitivity.

TABLE 3 | Mean values of peritumoral blood flow gradient (ROI1–ROI3) for metastases and glioblastomas.

Group	Maximum absolute TBF ROI1–ROI3	ROI1–ROI3 standard deviation
Metastases	–0.82	6.03
Glioblastoma	7.63	11.22

DISCUSSION

This study has demonstrated the role of ASL-perfusion in distinguishing brain metastasis from glioblastoma. In addition to this, we studied the blood flow in different subgroups of brain metastasis.

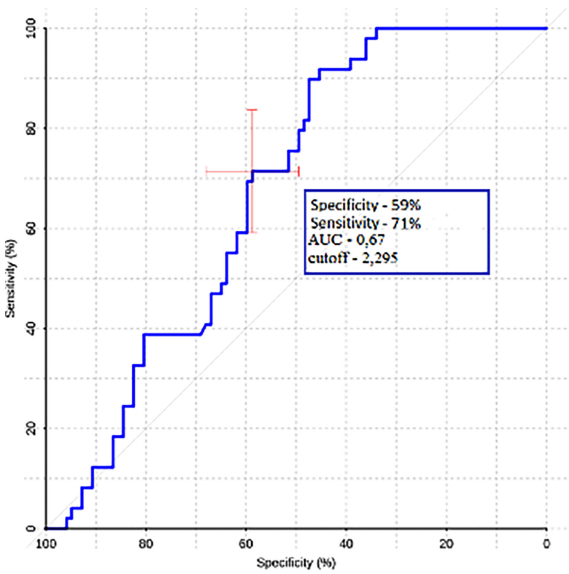

FIGURE 8 | ROC-analysis data obtained by comparing the maximum absolute values of the ROI1–ROI3 gradient in the groups of metastases and glioblastomas.

We observed statistically significant differences in intratumoral and peritumoral blood flow between glioblastoma and metastasis. Moreover, we calculated AUC, specificity, and sensitivity and found that for peritumoral blood flow, these values were 0.75, 68, and 73%, respectively, for the maximum TBF and 0.77, 58, and 91% for normalized TBF. For intratumoral blood flow AUC, specificity and sensitivity were 0.64, 70, and 60%, respectively, for maximal TBF and 0.66, 77, and 62% for normalized TBF.

Our results are explained by the biological characteristics of glioblastoma (4). Engelhorn et al. (17) and other studies (6) showed that the boundaries of glioblastoma do not coincide with the contrasted part of the mass on MRI. Tumor cells and alterations of the glial enviroment can be detected in the perifocal zone of increased MR signal in the T2 and T2-FLAIR. The researchers (17) have shown this through *in vivo* experiments in mice. All laboratory animals underwent an MRI study with contrast enhancement, then the brain was removed, and histological examination and immunohistochemistry were conducted, in which tumor cells and were found in the area of perifocal edema. Due to these features of glioblastoma growth, the term "perifocal edema" does not apply to the designation of the perifocal zone of an altered MR signal without signs of accumulation of a contrast agent; it is more correct to use the term "edema-infiltration" or "infiltrative edema" (18, 19).

We compared our results to other studies in the literature. Sunwoo et al. studied intratumoral and peritumoral TBF in 128 patients with GB and metastases (20).

TABLE 4 | Mean values of tumor blood flow in different subtypes of metastatic lesions.

Group	TBF (melanoma)	TBF (lung)	TBF (kidney)	TBF (intestines)	TBF (breast)
maxTBF	148.43	82.19	331.46	66.62	138.42
Standard deviation	88.32	65.05	326.03	7.35	81.91

MaxTBF, maximal TBF.

For the peritumoral blood flow, we acquired results, which are in the same range—Sunwoo et al. obtained 64 and 89.7%, while in our work, values of 58 and 91% were obtained.

A comparison of intratumoral blood flow yielded sensitivity and specificity values of 92.1 and 43.6%, respectively. For intratumoral nTBF, our results were 77 and 62%.

The difference between the results can be due to the different composition of the group of metastases. In addition to that, methods of normalization and ROI selection are different—Sunwoo et al. performed normalization to gray matter values, while in our institute normalization is traditionally performed to white matter TBF. In the study by Sunwoo, at least two ROIs for each region were drawn and the average of the mean of each ROI was recorded (20) while in our study we manually put 4–6 ROIs in every slice with the tumor tissue and then chose the ROI with the highest TBF.

Lin et al. studied 52 patients with glioblastomas and metastases (21). These authors concentrated on ROI gradients in their work and on intratumoral and peritumoral blood flow.

For intratumoral blood flow, the authors did not obtain statistically significant differences. This factor is distinct from our work, probably due to the different composition of the metastasis group In the Lin's study the majority of the brain metastases were of the lung cancer origin.

For peritumoral blood flow adjacent to tumor, the authors obtained values of sensitivity and specificity of 64.29 and 83.33%, respectively. Normalized peritumoral blood flow numbers were 57.14 and 100%. In comparison, we calculated 68 and 73% for mTBF and 58 and 91% for nTBF. While these results are roughly in the same range (especially for the nTBF), the difference in the specificity for maxTBF could be due to the fact that ¼ of patients in the Lin work received steroids, which could affect the study results.

Also, these authors studied the gradient between ROI1 and ROI3 and calculated 92.86 and 100% sensitivity and specificity. Despite the fact that we were able to obtain statistically significant differences between ROI gradients in metastases and glioblastoma our ROC analysis yielded much lower results—59 and 71%.

In the work of Abdel et al. (22), the role of ASL perfusion in the differential diagnosis of glioblastomas and metastases in a group of 36 patients [n (GB) = 21, n (MTS) = 15] was studied. When comparing intratumoral blood flow, the authors obtained high sensitivity and specificity values of 86.7 and 95.2. A comparative analysis of peritumoral blood flow was carried out (ROI with a diameter of 0.5–2 cm was established within 1 cm of the contrasted part of the tumor) and sensitivity and specificity values of 86.7 and 90.5 were obtained. These indicators significantly exceed the values obtained by us and by other authors, which may be associated with a small sample of patients in this work and a different process of ROI selection.

To conclude, measuring peritumoral blood flow may be of greater diagnostic value due to better AUC, specificity, and sensitivity as well as better interstudy agreement.

Secondly, we studied blood flow in different subgroups of brain metastases and compared them with each other. A statistically significant difference was obtained between TBF in the lung cancer and melanoma subgroups and the lung cancer and kidney cancer subgroups. ROC analysis was also carried out.

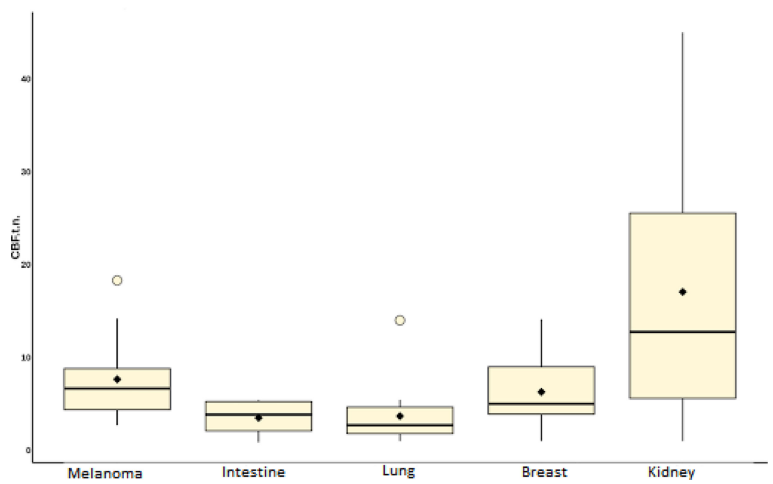

FIGURE 9 | Box plot showing the value of intratumoral blood flow in the group of metastatic brain lesions.

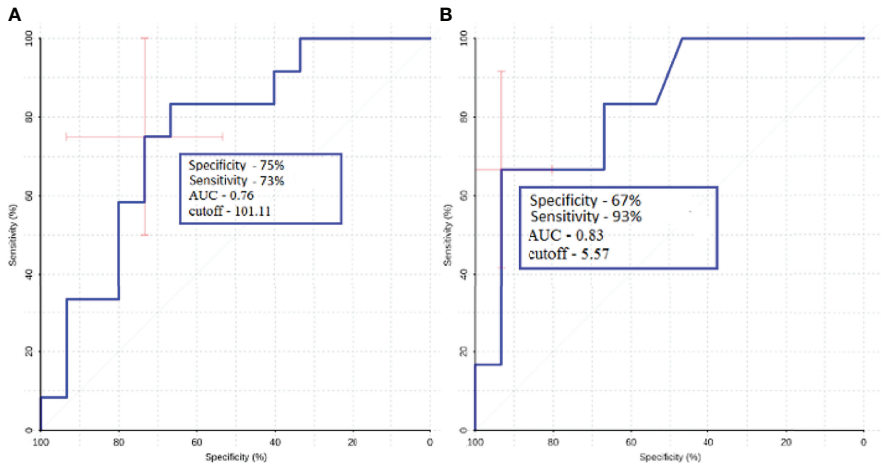

FIGURE 10 | ROC-analysis data obtained when comparing the maximum absolute **(A)** and normalized **(B)** values of intratumoral blood flow in the groups of metastatic lesions in lung cancer and melanoma.

The lowest mean blood flow was obtained in the metastatic colon cancer group. However, when comparing this group with others, no statistically significant differences in tumor blood flow were found, which may be due to the small number of patients in this group.

The highest blood flow values were obtained in the metastatic kidney cancer group, where all patients had clear cell carcinoma. When analyzing blood flow in these patients, two subgroups emerged: one with a very significant increase in blood flow compared to the white matter of the contralateral side (more than 10 times), and the other with low blood flow values, which practically did not differ from those in unchanged white matter, which is probably due to a pronounced necrotic component in the second subgroup.

In our study, the role of pCASL-perfusion in the differential diagnosis of various histological subtypes of metastases was investigated. We calculated the maximum TBF in lung, melanoma, kidney, and intestinal cancers and compared them to each other.

In the article by Dolgushin (23), the average values of blood flow using CT-perfusion in different histological types of metastases were calculated. The highest TBF in this work was obtained for melanoma metastases (113.99 ± 29.19). For the lung, breast, kidney, and intestine subgroups, values of 85.12; 92.05; 73.94; and 97.05 ml/100 g/min were calculated, respectively. Differences from this work may be due to different physical methods for measuring hemodynamic parameters (24). In the study by Qui et al. (25) where ASL perfusion was studied compared with CT with xenon, it was shown that the pCASL values are closest to the physiological values of blood flow, whereas with CT perfusion, these parameters may vary. The most significant differences with this work are presented

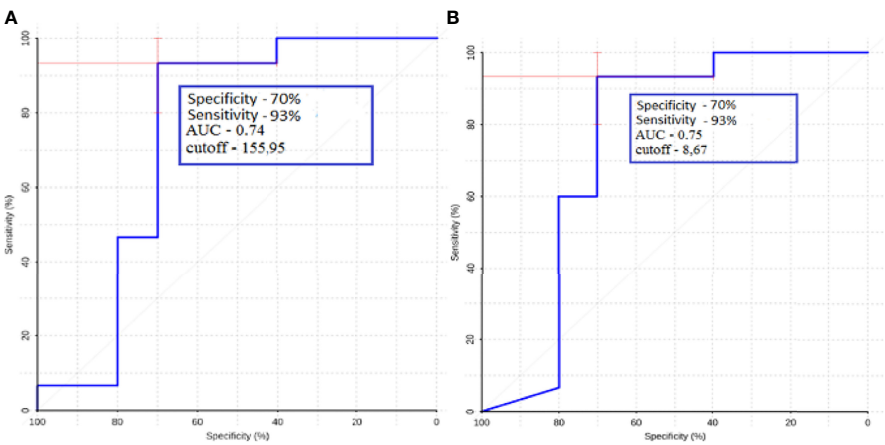

FIGURE 11 | ROC-analysis data obtained when comparing the maximum absolute **(A)** and normalized **(B)** values of intratumoral blood flow in the groups of metastatic lesions in lung cancer and kidney cancer.

in the values of blood flow in metastases of renal cell carcinoma. However, in our study, it was revealed that these metastases can be characterized by both very high blood flow and TBF values that practically do not differ from the white matter, which probably determines these differences.

Our study has several limitations. First, it was a retrospective study. Secondly, the study groups are not equal and, for example, patients with metastasis of colon cancer are not represented enough.

CONCLUSIONS

In our study, we could obtain statistically significant differences between the intra and peritumoral TBF in glioblastoma and metastases. An interesting feature that could be used in making a diagnosis is the presence of zones with high blood flow in the peritumoral area of glioblastoma. This fact could be explained by the infiltrative nature of glioblastoma growth.

When studying blood flow in various histological subtypes of metastases, significant differences in TBF were found. High sensitivity and specificity values were obtained between the groups of melanoma and lung, lung and kidney, which suggests that pCASL-perfusion could contribute to identify the source of metastatic tumor.

DATA AVAILABILITY STATEMENT

The raw data supporting the conclusions of this article will be made available by the authors, without undue reservation.

ETHICS STATEMENT

The studies involving human participants were reviewed and approved by the local committee of the N.N. Burdenko National Neurosurgery Institute. Written informed consent to participate in this study was provided by the participants' legal guardian/ next of kin. Written informed consent was obtained from the individual(s) for the publication of any potentially identifiable images or data included in this article.

AUTHOR CONTRIBUTIONS

Conceptualization, AB and KS. Methodology, AB. Software, EP. Validation, IP, NZ and AB. Formal analysis, AB, and SG. Investigation, KS. Resources, KS and SG. Data curation, AB and SG. Writing—original draft preparation, KS. Writing—review and editing, IP, NZ, and SG. Visualization, EP. Supervision, IP. Project administration, AB. All authors listed have made a substantial, direct, and intellectual contribution to the work and approved it for publication.

FUNDING

This study was supported by the Ministry of Higher Education Agreement 075-15-2021-1343.

REFERENCES

1. Li X, Wang D, Liao S, Guo L, Xiao X, Liu X, et al. Discrimination Between Glioblastoma and Solitary Brain Metastasis: Comparison of Inflow-Based Vascular-Space-Occupancy and Dynamic Susceptibility Contrast MR Imaging. *Am J Neuroradiol* (2020) 41(4):583–90. doi: 10.3174/ajnr.A6466
2. Osborn AG, Hedlund G, Salzman KL. *Osborn's Brain 2nd Edition*. The Netherlands: Elsevier (2017).
3. Fordham AJ, Hacherl CC, Patel N, Jones K, Myers B, Abraham M, et al. Differentiating Glioblastomas from Solitary Brain Metastases: An Update on the Current Literature of Advanced Imaging Modalities. *Cancers (Basel)* (2021) 13(12):2960. doi: 10.3390/cancers13122960
4. Chen XZ, Yin XM, Ai L, Chen Q, Li SW, Dai JP. Dai Differentiation between Brain Glioblastoma Multiforme and Solitary Metastasis: Qualitative and Quantitative Analysis Based on Routine MR Imaging. *AJNR Am J* (2012) 33(10):1907–12. doi: 110.3174/ajnr.A3106
5. Bauer AH, Erly W, Moser FG, Maya M, Nael K. Differentiation of Solitary Brain Metastasis from Glioblastoma Multiforme: A Predictive Multiparametric Approach Using Combined MR Diffusion and Perfusion. *Neuroradiology* (2015) 57(7):697–703. doi: 10.1007/s00234-015-1524-6
6. Server A, Orheim TE, Graff BA, Josefsen R, Kumar T, Nakstad PH. Diagnostic Examination Performance by Using Microvascular Leakage, Cerebral Blood Volume, and Blood Flow Derived from 3-T Dynamic Susceptibility-Weighted Contrast-Enhanced Perfusion MR Imaging in the Differentiation of Glioblastoma Multiforme and Brain Metastasis. *Neuroradiology* (2011) 53 (5):319–30. doi: 10.1007/s00234-010-0740-3
7. Cha S, Lupo JM, Chen MH, Lamborn KR, McDermott MW, Berger MS, et al. Differentiation of Glioblastoma Multiforme and Single Brain Metastasis by Peak Height and Percentage of Signal Intensity Recovery Derived From Dynamic Susceptibility-Weighted Contrast-Enhanced Perfusion MR Imaging. *AJNR Am J Neuroradiol* (2007) 28(6):1078–84. doi: 10.3174/ajnr.A0484
8. Law M, Cha S, Knopp EA, Johnson G, Arnett J, Litt AW. High-Grade Gliomas and Solitary Metastases: Differentiation by Using Perfusion and Proton Spectroscopic MR Imaging. *Radiology* (2002) 222(3):715–21. doi: 10.1148/radiol.2223010558
9. Neska-Matuszewska M, Bladowska J, Sąsiadek M, Zimny A. Differentiation of Glioblastoma Multiforme, Metastases and Primary Central Nervous System Lymphomas Using Multiparametric Perfusion and Diffusion MR Imaging of a Tumor Core and a Peritumoral Zone-Searching for a Practical Approach. *PloS One* (2018) 13(1):e0191341. doi: 10.1371/journal.pone.0191341
10. Jarnum H, Steffensen EG, Knutsson L, Frund ET, Simonsen CW, Lundbye-Christensen S, et al. Perfusion MRI of Brain Tumors: A Comparative Study of Pseudo-Continuous Arterial Spin Labeling and Dynamic Susceptibility Contrast Imaging. *Neuroradiology* (2010) 52:307–17. doi: 10.1007/s00234-009-0616-6
11. Warmuth C, Gunther M, Zimmer C. Quantification of Blood Flow in Brain Tumors: Comparison of Arterial Spin Labeling and Dynamic Susceptibility-Weighted Contrast-Enhanced MR Imaging. *Radiology* (2003) 228:523–32. doi: 10.1148/radiol.2282020409
12. Dolgushin MB, Kornienko VN, Pronin IN. *Diagnostic Neuroradiology*. Moscow, Russia: Brain Metastases (2017).
13. Wang Q, Zhang J, Xu W, Chen X, Zhang J, Xu B. Role of Magnetic Resonance Spectroscopy to Differentiate High-Grade Gliomas from Metastases. *Tumour Biol* (2017) 39(6):1010428317710030. doi: 10.1177/1010428317710030
14. Pope WB. Brain Metastases: Neuroimaging. *Handb Clin Neurol* (2018) 149:89–112. doi: 10.1016/B978-0-12-811161-1.00007-4
15. Huang BY, Kwock L, Castillo M, Smith JK. Association of Choline Levels and Tumor Perfusion in Brain Metastases Assessed With Proton MR Spectroscopy and Dynamic Susceptibility Contrast-Enhanced Perfusion Weighted MRI. *Technol Cancer Res Treat* (2010) 9:327–337.

16. Duygulu G, Ovali GY, Calli C, Kitis O, Yünten N, Akalin T, et al. Intracerebral Metastasis Showing Restricted Diffusion: Correlation with Histopathologic Findings. *Eur J Radiol* (2010) 74(1):117–20. doi: 10.1016/j.ejrad.2009.03.004
17. Engelhorn T, Savaskan NE, Schwarz MA, Kreutzer J, Meyer EP, Hahnen E, et al. Cellular Characterization of the Peritumoral Edema Zone in Malignant Brain Tumors. *Cancer Sci* (2009) 100:1856–62. doi: 10.1111/j.1349-7006.2009.01259.x
18. Kornienko. Pronin Diagnostic Neuroradiology in 5 Volumes.
19. Batalov AI, Zakharova NE, Pogosbekyan EL, Fadeeva LM, Goryaynov SA, Baev AA, et al. Beskontrastnaia ASL-Perfuziia V Predoperatsionnoĭ Diagnostike Supratentorial'nykh Gliom [Non-Contrast ASL Perfusion in Preoperative Diagnosis of Supratentorial Gliomas]. *Zh Vopr Neirokhir Im N N Burdenko* (2018) 82(6):15–22. doi: 10.17116/neiro20188206115
20. Sunwoo L, Yun TJ, You SH, Yoo RE, Kang KM, Choi SH, et al. Differentiation of Glioblastoma From Brain Metastasis: Qualitative and Quantitative Analysis Using Arterial Spin Labeling MR Imaging. *PLoS One* (2016) 11(11):e0166662. doi: 10.1371/journal.pone.0166662
21. Lin L, Xue Y, Duan Q, Sun B, Lin H, Huang X, et al. The Role of Cerebral Blood Flow Gradient in Peritumoral Edema for Differentiation of Glioblastomas from Solitary Netastatic Lesions. *Oncotarget* (2016) 7 (42):69051–59. doi: 10.18632/oncotarget.12053
22. Abdel Razek AAK, Talaat M, El-Serougy L, Abdelsalam M, Gaballa G. Differentiating Glioblastomas from Solitary Brain Metastases Using Arterial Spin Labeling Perfusion- and Diffusion Tensor Imaging-Derived Metrics. *World Neurosurg* (2019) 127:e593–8. doi: 10.1016/j.wneu.2019.03.213
23. Dolgushin MB, Pronin IN, Holodny EA, Fadeeva LM, Holodny AI, Kornienko VN. Use of CT Perfusion to Discriminate Between Brain Metastases From Different Primaries. *Clin Imaging* (2015) 39(1):9–14. doi: 10.1016/j.clinimag.2014.10.006
24. Shultz EI, Pronin IN, Batalov AI, Solozhentseva KD, Pavlova GV, Drozd SF, et al. CT-Perfusion in Assessment of the Malignant Gliomas Hemodynamics. *Medical Visualization* (2020) 24(2):105–118. (In Russ.)
25. Qiu D, Straka M, Zun Z, Bammer R, Moseley ME, Zaharchuk G. CBF Measurements Using Multidelay Pseudocontinuous and Velocity-Selective Arterial Spin Labeling in Patients With Long Arterial Transit Delays: Comparison With Xenon CT CBF. *J Magn Reson Imaging* (2012) 36 (1):110–9. doi: 10.1002/jmri.23613

Conflict of Interest: The authors declare that the research was conducted in the absence of any commercial or financial relationships that could be construed as a potential conflict of interest.

Publisher's Note: All claims expressed in this article are solely those of the authors and do not necessarily represent those of their affiliated organizations, or those of the publisher, the editors and the reviewers. Any product that may be evaluated in this article, or claim that may be made by its manufacturer, is not guaranteed or endorsed by the publisher.

frontiers | Frontiers in Oncology

ORIGINAL RESEARCH
published: 27 May 2022
doi: 10.3389/fonc.2022.873839

Preoperative and Noninvasive Prediction of Gliomas Histopathological Grades and IDH Molecular Types Using Multiple MRI Characteristics

Ningfang Du[1†], Xiaotao Zhou[2†], Renling Mao[3], Weiquan Shu[3], Li Xiao[4], Yao Ye[4], Xinxin Xu[5], Yilang Shen[6], Guangwu Lin[1], Xuhao Fang[3] and Shihong Li[1*]*

[1] Department of Radiology, Huadong Hospital, Fudan University, Shanghai, China, [2] Department of Emergency, Changhai Hospital, Naval Medical University, Second Military Medical University, Shanghai, China, [3] Department of Neurosurgery, Huadong Hospital, Fudan University, Shanghai, China, [4] Department of Pathology, Huadong Hospital, Fudan University, Shanghai, China, [5] Clinical Research Center for Gerontology, Huadong Hospital, Fudan University, Shanghai, China, [6] Institute of Business Analytics, Adelphi University, Garden City, NY, United States

OPEN ACCESS

Edited by:
Tone Frost Bathen,
Norwegian University of Science and Technology, Norway

Reviewed by:
Oliver Geier,
Oslo University Hospital, Norway
Morteza Esmaeili,
Akershus University Hospital, Norway
Jonn Geitung,
University of Oslo, Norway

***Correspondence:**
Shihong Li
lishihong@fudan.edn.cn
Xuhao Fang
215192661@qq.com

[†]These authors have contributed equally to this work

Specialty section:
This article was submitted to Cancer Imaging and Image-directed Interventions, a section of the journal Frontiers in Oncology

Received: 11 February 2022
Accepted: 05 May 2022
Published: 27 May 2022

Citation:
Du N, Zhou X, Mao R, Shu W, Xiao L, Ye Y, Xu X, Shen Y, Lin G, Fang X and Li S (2022) Preoperative and Noninvasive Prediction of Gliomas Histopathological Grades and IDH Molecular Types Using Multiple MRI Characteristics. Front. Oncol. 12:873839. doi: 10.3389/fonc.2022.873839

Background and Purpose: Gliomas are one of the most common tumors in the central nervous system. This study aimed to explore the correlation between MRI morphological characteristics, apparent diffusion coefficient (ADC) parameters and pathological grades, as well as IDH gene phenotypes of gliomas.

Methods: Preoperative MRI data from 166 glioma patients with pathological confirmation were retrospectively analyzed to compare the differences of MRI characteristics and ADC parameters between the low-grade and high-grade gliomas (LGGs vs. HGGs), IDH mutant and wild-type gliomas (IDH^{mut} vs. IDH^{wt}). Multivariate models were constructed to predict the pathological grades and IDH gene phenotypes of gliomas and the performance was assessed by the receiver operating characteristic (ROC) analysis.

Results: Two multivariable logistic regression models were developed by incorporating age, ADC parameters, and MRI morphological characteristics to predict pathological grades, and IDH gene phenotypes of gliomas, respectively. The Noninvasive Grading Model classified tumor grades with areas under the ROC curve (AUROC) of 0.934 (95% CI=0.895-0.973), sensitivity of 91.2%, and specificity of 78.6%. The Noninvasive IDH Genotyping Model differentiated IDH types with an AUROC of 0.857 (95% CI=0.787-0.926), sensitivity of 88.2%, and specificity of 63.8%.

Conclusion: MRI features were correlated with glioma grades and IDH mutation status. Multivariable logistic regression models combined with MRI morphological characteristics and ADC parameters may provide a noninvasive and preoperative approach to predict glioma grades and IDH mutation status.

Keywords: glioma, magnetic resonance imaging, isocitrate dehydrogenase, diffusion-weighted magnetic resonance imaging, apparent diffusion coefficient

INTRODUCTION

Glioma is the most common primary tumor in the central nervous system. Clinically, glioma is usually divided into low-grade gliomas (LGGs) and high-grade gliomas (HGGs) based on the histopathological assessment. LGGs are well-differentiated, while HGGs are poorly differentiated and have a relatively poor prognosis (1–3). In recent years, more and more studies have shown that traditional histopathological grading of glioma has certain limitations due to the remarkable heterogeneity of tumors. For example, some LGGs overlap genetically with primary glioblastoma and show similar rapid disease progression (4, 5). It is difficult to distinguish them just by evaluating proliferation markers and cell morphology (6).

The 2016 World Health Organization (WHO) Classification of Tumors of the Central Nervous System officially listed molecular detection results as one of the important diagnostic bases for glioma classification for the first time (7), and the newly released 2021 guidance (WHO CNS5) emphasized the diagnostic value of molecular diagnosis for glioma subgroup (8). This substantial change has been achieved by further advancing the role of molecular diagnosis in the classification of CNS tumors, but still relying on other established methods for diagnosis of tumor characteristics including histology and immunohistochemistry. Isocitrate dehydrogenase (IDH) is a common molecular marker in glioma and is frequently used for predicting prognosis. Prior studies have shown that the prognosis of IDH-mutant gliomas is better than IDH-wild type gliomas (9, 10). This genetic grouping serves an important clinical indicator of stratifying tumors with differential susceptibility to adjuvant treatment. The biological similarities between some LGGs and glioblastomas make it critical to identify glioblastomas and separate them from more favorable IDH-mutant entities (11).

Unfortunately, preoperative distinction between different glioma grades and subtypes remains challenging with insufficient sensitivity and specificity. In addition, in the cases that gliomas at certain specific sites cannot be resected or punctured, or in patients who cannot undergo surgery due to age or other problems, the method based on image analysis can be used as a supplementary diagnostic tool for molecular classification of gliomas, and thus may have great potential value in treatment decisions (12). Magnetic resonance imaging (MRI) has been demonstrated a promising approach to non-invasively distinguish various tumor entities (13, 14).

MRI is also the preferred imaging method for glioma. Morphological characteristics and enhancement pattern of gliomas can be obtained by conventional MRI. Prior studies have shown that gliomas with different grades and IDH mutation status have differences in lesion properties such as location, internal signal and enhancement patterns (15, 16). Several imaging biomarkers contribute to the diagnosis of molecular subtypes of gliomas. Such as, T2-FLAIR mismatch (T2FM), which is a sign demonstrated a specificity of almost 100% for IDH mutant astrocytoma in recent studies (17, 18). However, morphological indicators are difficult to be quantified, so it cannot predict glioma grades and molecular subtypes accurately. Diffusion-weighted imaging (DWI) is an important sequence of MRI and serve for the identification and differential diagnosis in a broad spectrum of cancers (19). The assessment of cancers using DWI is based on the assumption that free water motion in tissues diminishes with growing tumor cellularity (20). The calculation of apparent diffusion coefficient (ADC) maps from DWI (at least with two b values) is a fast and straightforward procedure that can support grading and have shown the capability for IDH typing in gliomas (21–23). However, it is often difficult to identify the grades or even molecular subtypes of gliomas with single indicators obtained only by conventional MRI sequences. Few studies have combined MRI morphological features and ADC values to predict glioma grades and IDH mutation status. Additionally, consideration of patient age may help diagnosis because it has been shown that IDH-wild type gliomas are more common in older patients (11).

The purpose of our study was to explore the correlation between MRI morphological characteristics, ADC parameters and glioma grades, IDH mutation status. The developed multivariate predictive models may provide a new strategy for the formulation of glioma treatment, follow-up plan and prognosis evaluation.

MATERIALS AND METHODS

Patient Selection

A total of 166 glioma patients admitted to our hospital from 2016 to 2020 were selected, including 92 males and 74 females, aged from 14 to 85 years old, with a median age of 53 years old. There were 43 cases in LGGs (12 cases in grade I, 31 cases in grade II), 123 cases in HGGs (18 cases in grade III, 105 cases in grade IV). There were 48 IDH-mutant cases and 112 IDH-wild type cases. Inclusion criteria: (1) Meet the diagnostic criteria of glioma; (2) All patients underwent surgical treatment and obtained postoperative pathological results and molecular diagnosis results. (3) The patients underwent preoperative MRI examination with complete data. Exclusion criteria: (1) Receiving conservative treatment; (2) MRI imaging quality was poor and cannot be studied and analyzed; (3) Complicated with other neurological diseases, such as cerebral infarction, cerebral hemorrhage. All patients signed informed consent before the enhanced MRI examination according to the hospital regulations. This retrospective study was exempted from ethical review.

MRI Parameters

MR images were acquired with a 3.0-T MRI scanner (MAGNETOM Prisma; Siemens Healthineers, Erlangen, Germany). The MRI protocols for brain tumor at our hospital included T2-weighted, T2-weighted fluid-attenuated inversion recovery (FLAIR), T1-weighted sequences before and after administration of a gadolinium-based contrast agent and DWI. The parameters of MRI scanning are attached in **Supplementary Material**. Gadolinium-diethylenetriamine pentaacetic acid (Gd-DTPA) as injected *via* the cubital vein mass with a high-pressure syringe at a dose of 0.1 mmol per kilogram of body weight and a flow rate of 5 mL/s. Enhanced T1W scanning was performed at axial, coronal, and sagittal positions.

The ADC map is created by dividing the signal from the trace-DWI image by the signal from each corresponding point in the b0 image and taking logarithms:

$$ADC = -\frac{1}{b_1} \times In(S_{b1}/S_{b0})$$

Where ADC stands for apparent diffusion coefficient, b0 = 0 s/mm^2 and b1 = 1000 s/mm^2, S_{b0} and S_{b1} are the signal intensities of each image at b0 and b1. ADC maps are mathematically calculated using the inline technique, as the pure display of consolidated ADC values.

To ensure high-quality ADC maps, the DWI sequence was optimized to maximize signal noise ratio (SNR) and reduce artifacts that may be caused by motion, B0 inhomogeneity, chemical shifts, Nyquist ghosting, susceptibility effects, and noise amplification. Eddy current of the diffusion-encoding gradient was minimized by using a twice-refocused bipolar diffusion preparation. In order to get the ideal ADC map, the noise level was set to 40, as recommended by the equipment manufacturer. Correspondingly, we can get the ADC values from the ADC map by drawing regions of interest (ROIs).

Image Analysis

Two radiologists with more than 10 years of experience in radiology independently reviewed the MR images. The disagreements were resolved through consultation. The morphological signs of MRI were observed, including (1) hemorrhage; (2) cystic lesion; (3) tumor boundary, including clear or blur; (4) peritumoral edema, including no edema, mild edema (the longest diameter of edema < the longest diameter of the tumor), severe edema (the longest diameter of edema ≥ the longest diameter of the tumor); (5) enhancement pattern, including no enhancement, patchy enhancement and rim enhancement; and (6) distribution of lesions, which were divided into the single lobe, trans-lobe growth with corpus callosum involvement, trans-lobe growth with insula involvement, trans-lobe growth (neither corpus callosum involvement nor insula involvement), thalamus or brain stem.

In this study, ADC values and derived parameters were measured at Syngo. *Via* workstation (Siemens healthineers, Erlangen, Germany), including (1) Minimum apparent diffusion coefficient (ADC_{min}): Three different 20-30 mm^2 ROIs) of visually lowest ADC values were outlined in each tumor, and the average value was ADC_{min}. (2) Mean apparent diffusion coefficient (ADC_{mean}): The ROI is plotted as large as possible on the largest layer of tumor transverse axis entity components, avoiding necrosis, cystic degeneration, calcification, vessels, etc., and the ADC value is measured as ADC_{mean}. (3) Map ROI in the contralateral hemispherical center of the normal white matter and measure ADC (ADC_{nawm}). ADC_{min}/ADC_{nawm} was denoted as $rADC_{min}$ (relative ADC_{min}). (4) ADC_{mean}/ADC_{nawm} was denoted as $rADC_{mean}$ (relative ADC_{mean}). The average values of the above parameters measured by 2 physicians were obtained. ADC ROI is outlined in **Figure 1**.

Histopathologic Analysis

All tissue specimens were fixed into paraffin blocks and analyzed in the Pathology Department of our hospital. The tumors were classified into grade I, II, III and IV, according to 2016 WHO Classification of Tumors of the Central Nervous System (glioma-related classification and grading). The IDH mutation status of tumor specimens were detected by immunohistochemical examination and determined according to the combination of the specimen with the monoclonal antibody that can detect IDH1 gene R132H point mutation in glioma. Positive IDH1 expression was defined as IDH-mutant group, and negative IDH1 expression was defined as IDH-wild type group.

Statistical Analysis

The statistical analysis was conducted using SPSS 22.0. The Shapiro-Wilk test was carried out to test the normality of continuous variables. Since all continuous variables in this study were normally distributed, they were described as mean ± standard deviations (SDs) and compared by Student's t-test. The categorical variables were described by number and percentage (%) and compared by Chi-square tests. For the dependent variables of dichotomies or disordered multiclassification, Pearsonχ^2 test or exact probability method was used to compare the differences between the two groups, including the Holm-Bonferroni correction of multiple tests. Wilcoxon rank-sum test was used to compare the difference between the two groups for the ordered multi-classification dependent variable (degree of peritumoral

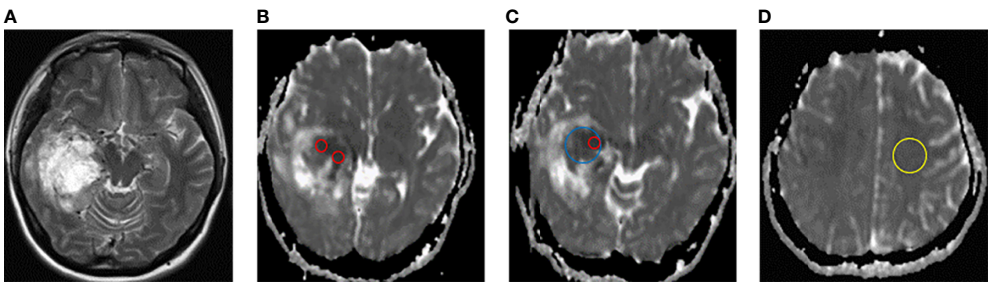

FIGURE 1 | Schematic diagram of ADC measurement. **(A)** T2W axial map of IDH-wild type glioblastoma of the right temporal lobe. **(B–D)** ADC diagram ROI delineates sketch. ADC_{min} (ROI of 3 lowest visual ADC values for each patient, red circle), ADC_{mean} (maximum cross-section of axial solid tumor, blue circle), and ADC_{nawm} (contralateral hemisphere centrum semiovale normal appearing white matter, yellow circle).

edema). The receiver-operating characteristic curve (ROC) analysis was performed to evaluate the diagnostic performance of the developed models. Variables with $P < 0.05$ in the univariate analysis were included in multivariate logistic regression analysis and model construction. $P < 0.05$ indicated that the difference was statistically significant.

RESULTS

Patient Demographics

A total of 166 patients were included in the analysis. There was no gender difference between low-grade and high-grade glioma patients ($P = 0.172$). The age of high-grade glioma patients (55.5 ± 14.5) was higher than that of low-grade glioma group (38.6 ± 12.8) ($P < 0.05$). IDH mutation was more common in LGGs than that in the HGGs (48.8% vs. 23.5%) ($P < 0.05$) (**Table 1**).

Comparison of MRI Morphological Characteristics Between LGGs Group and HGGs Group

Compared with LGGs, HGGs were more prone to have hemorrhage ($P < 0.01$) and cystic lesion ($P < 0.05$) (**Table 2**). In addition, the peritumoral edema was more severe ($P < 0.001$), and tumor boundaries were less clear ($P < 0.01$) in HGGs than those in LGGs. In terms of enhancement pattern, HGGs were more likely to show rim enhancement, while LGGs were more likely to show no obvious enhancement ($P < 0.001$). Regarding the distribution of lesions, a single lobe (41.9%) was more frequently to be observed in LGGs, while HGGs were more likely to show cross-lobe growth (66.6%) with corpus callosum and insula. There were significant differences in the distribution and location of lesions between two different grades of gliomas ($P < 0.001$) (**Table 2**).

Comparison of Morphological Characteristics Between IDH-Mutant Group and IDH-Wild Type Group

There were no significant differences between IDH-mutant gliomas and IDH-wild type gliomas in hemorrhage, cystic lesion, peritumoral edema and tumor boundary (All $P > 0.05$) (**Table 3**). In terms of enhancement pattern, IDH-wild type gliomas were more likely to be characterized by rim enhancement, while IDH mutant gliomas were more likely to be characterized by no obvious enhancement ($P < 0.001$). There were significant differences in the distribution of lesions between gliomas patients with and without IDH mutation ($P < 0.01$). Compared with IDH-wild type gliomas, IDH-mutant gliomas were more likely to be associated with insula involvement ($P < 0.001$). IDH-mutant cases tended to have one lobe, and the lesions were mostly located in the frontal lobe (11/15, 73.3%) (**Table 3**). The representative MRI features and pathological characteristics of gliomas of different IDH molecular subtypes at different grades are shown in **Figures 2**–**5**.

Comparison of ADC Values and Derived Parameters Between LGGs Group and HGGs Group

ADC_{min}, ADC_{mean}, $rADC_{min}$ and $rADC_{mean}$ of HGGs were significantly lower than those of LGGs (All $P < 0.001$) (**Table 4**). ROC curve analysis was then performed to differentiate LGGs from HGGs using ADC indicators (**Figure 6**). It was found that the diagnostic efficiency of rADCmin was higher than that of ADCmin, and rADCmean was higher than that of ADCmean. Among four different ADC parameters measured, $rADC_{min}$ had the highest diagnostic efficiency in differentiating LGGs from HGGs, with an AUROC of 0.775 (95% CI=0.695-0.856), the diagnostic optimal cut-off value of 1.26×10^{-3} mm^2/s, the sensitivity of 62.79%, specificity of 80.49%, and Yuden index of 0.443 (**Table 4**).

Comparison of ADC Values and Derivative Parameters Between IDH-Mutant Group and IDH-Wild Type Group

The ADC_{min}, ADC_{mean}, $rADC_{min}$ and $rADC_{mean}$ of IDH-wild type gliomas were significantly lower than those of IDH-mutant gliomas, and the differences were statistically significant ($P < 0.05$) (**Table 5**). The diagnostic performance of ADC parameters for distinguishing gliomas patients with and without IDH mutation was then evaluated by the ROC analysis (**Figure 7**). Analysis showed that the diagnostic efficiency of rADCmin was higher than that of ADCmin, and rADCmean was higher than that of ADCmean. Similar to the differentiation of glioma grades, $rADC_{min}$ had the highest diagnostic efficiency in differentiating IDH-mutant gliomas from IDH-wild type gliomas, with the diagnostic optimal cut-off value of 1.14×10^{-3} mm^2/s, an AUROCC of 0.656 (95% CI=0.566-0.746), the sensitivity of 62.5%, specificity of 66.96%, and Yoden index of 0.295 (**Table 5**).

Multivariate Logistic Regression Analysis

We next tested the multivariate models by combining all the above significant factors. Age was divided into two groups: < 60

TABLE 1 | Demographics of the study population.

Variables		Total	LGGs (n = 43)	HGGs (n = 123)	t/χ^2 value	*P* value
Gender	Male	92	20 (46.5%)	72 (58.5%)	1.865	0.172
	Female	74	23 (53.5%)	51 (41.5%)		
Age (years)		51.1 ± 15.9	38.6 ± 12.8	55.5 ± 14.5	-6.783	< 0.001***
IDH mutant status[#]	IDH^{mut}	48	20 (48.8%)	28 (23.5%)	9.259	0.002**
	IDH^{wt}	112	21 (51.2%)	91 (76.5%)		

[#]*Six patients had no IDH status available for assessment. LGGs, low-grade gliomas; HGGs, high-grade gliomas.*
*Significance level markers P < 0.01**, P < 0.001***.*

TABLE 2 | Comparison of MRI morphological characteristics of LGGs and HGGs.

Parameters		LGGs (*n* = 43)	HGGs (*n* = 123)	χ^2/*Z* value	*P* value
Hemorrhage[#]	Present	1 (2.3%)	29 (24.4%)	9.900	0.002**
	None	41 (97.7%)	90 (75.6%)		
Cystic lesion[†]	Present	15 (34.9%)	64 (54.2%)	4.723	0.030*
	None	28 (65.1%)	54 (45.8%)		
Peritumoral edema	None	25 (58.1%)	18 (14.6%)	-5.010	< 0.001***
	Mild	8 (18.6%)	35 (28.5%)		
	Severe	10 (23.3%)	70 (56.9%)		
Tumor boundary	Clear	28 (65.1%)	49 (39.8%)	8.187	0.004**
	Blur	15 (34.9%)	74 (60.2%)		
Enhancement pattern[‡]	No enhancement	27 (62.8%)	13 (10.7%)	52.773	< 0.001***
	Patchy enhancement	13 (30.2%)	41 (33.9%)		
	Rim enhancement	3 (7.0%)	67 (55.4%)		
Distribution of lesions	Single lobe	18 (41.9%)	28 (22.8%)	20.940	< 0.001***
	Trans-lobe growth with corpus callosum involvement	5 (11.6%)	26 (21.1%)		
	Trans-lobe growth with insula involvement	5 (11.6%)	34 (27.6%)		
	Trans-lobe growth	2 (4.7%)	22 (17.9%)		
	Thalamus or brain stem	13 (30.2%)	13 (10.6%)		

[#]Hemorrhage status was evaluated as uncertain in a total of 5 patients.
[†]Cystic lesion status was evaluated as uncertain in a total of 5 patients.
[‡]Two patients did not undergo MRI enhancement examination.
Significance level markers P < 0.05, P < 0.01**, P < 0.001***.*

TABLE 3 | Comparison of MRI morphological characteristics between IDH-mutant and IDH-wild type gliomas.

Parameters		IDH^{mut} (*n* = 48)	IDH^{wt} (*n* = 112)	χ^2/*Z* value	*P* value
Hemorrhage	Present	8 (16.7%)	22 (20.6%)	0.322	0.570
	None	40 (83.3%)	85 (79.4%)		
Cystic lesion	Present	19 (39.6%)	56 (52.3%)	2.158	0.142
	None	29 (60.4%)	51 (47.7%)		
Peritumoral edema	None	12 (25.0%)	29 (25.9%)	-7.767	0.443
	Mild	16 (33.3%)	25 (22.3%)		
	Severe	20 (41.7%)	58 (51.8%)		
Tumor boundary	Clear	21 (43.8%)	50 (56.3%)	0.011	0.917
	Blur	27 (44.6%)	62 (55.4%)		
Enhancement pattern	No enhancement	23 (48.9%)	16 (14.4%)	26.943	< 0.001***
	Patchy enhancement	16 (34.0%)	34 (30.6%)		
	Rim enhancement	8 (17.0%)	61 (55.0%)		
Distribution of lesions	Single lobe	15 (31.3%)	30 (26.8%)	14.915	0.005**
	Trans-lobe growth with corpus callosum involvement	9 (18.8%)	21 (18.8%)		
	Trans-lobe growth with insula involvement	19 (39.6%)	22 (17.9%)		
	Trans-lobe growth	3 (6.3%)	19 (17.0%)		
	Thalamus or brain stem	2 (4.2%)	22 (19.6)		

*Significance level markers P < 0.01**, P < 0.001***.*

years old and ≥ 60 years old. Relative ADC parameters ($rADC_{mean}$ and $rADC_{min}$) were divided into two groups according to the optimal cut-off value in single factor analysis. The Noninvasive Grading Model for predicting glioma grades included age, $rADC_{mean}$, $rADC_{min}$, cystic lesion, hemorrhage, tumor boundary, peritumoral edema, lesion distribution and enhancement pattern. And the predictor factor 1 (pre1) were generated. The Noninvasive IDH Genotyping Model for predicting glioma IDH mutation status generated pre2, containing age, $rADC_{mean}$, and $rADC_{min}$, lesion distribution and enhancement pattern.

We found that age (≥ 60 years), $rADC_{min}$ (< 1.26×10^{-3} mm^2/s), rim enhancement, and lesion distribution (thalamus or brainstem) were independent risk factors for predicting HGGs (**Table 6**). Age (≥ 60 years), rim enhancement, and lesion distribution (trans-lobe growth with corpus callosum involvement) were independent risk factors for IDH-wild type gliomas (**Table 7**). The accuracy of the multivariate logistic regression model combining age, morphological characteristics and ADC parameters in predicting glioma grades and IDH mutation status was improved compared with that of a single indicator (**Figures 6**, **7**). The Noninvasive Grading Model showed an AUROC of 0.934 (95% CI=0.895-0.973), a sensitivity of 91.2%, and a specificity of 78.6% in differentiating HGGs from LGGs. The AUROC of the Noninvasive IDH Genotyping Model was 0.857 (95% CI=0.787-0.926), with a sensitivity of 88.2% and specificity of 63.8% (**Table 8**).

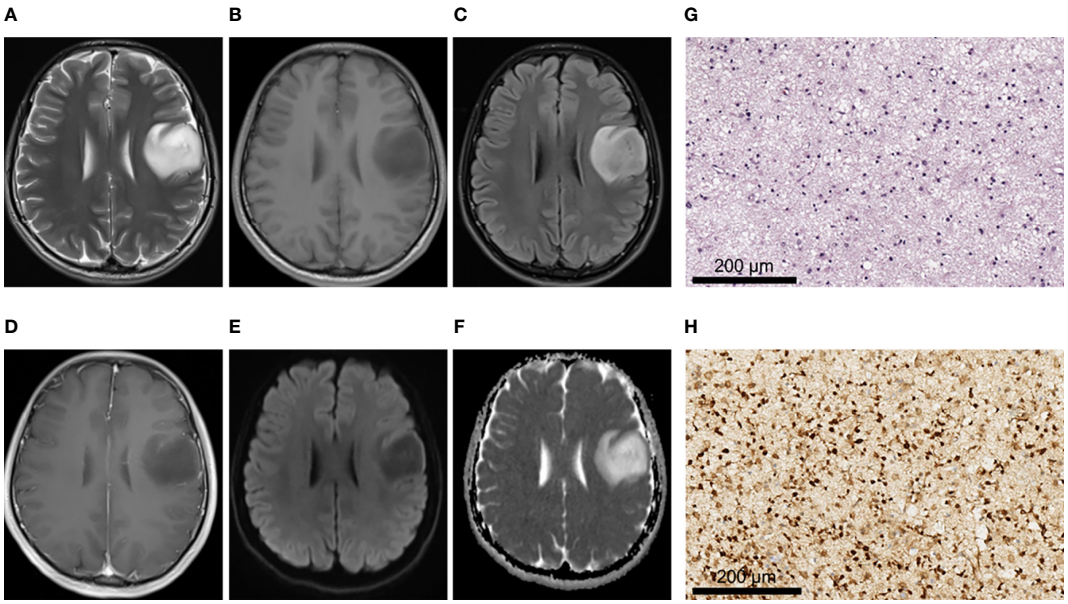

FIGURE 2 | A 28-year-old male patient with left frontal oligodendroglioma, WHO grade II, IDH-mutant type. **(A–C)** MRI axial T2W, T1W, and T2-FLAIR sequences showed clear tumor boundary, no cystic lesion, no hemorrhage, and no obvious edema around the tumor. **(D)** T1 postcontrast showed no obvious enhancement. **(E, F)** When b value was 1000, tumor was unrestricted diffusion in DWI and ADC images. **(G)** HE staining showed moderate increase in cell density, a small amount of nuclear atypia and loose background (×200). **(H)** IDH1 positive expression (×200).

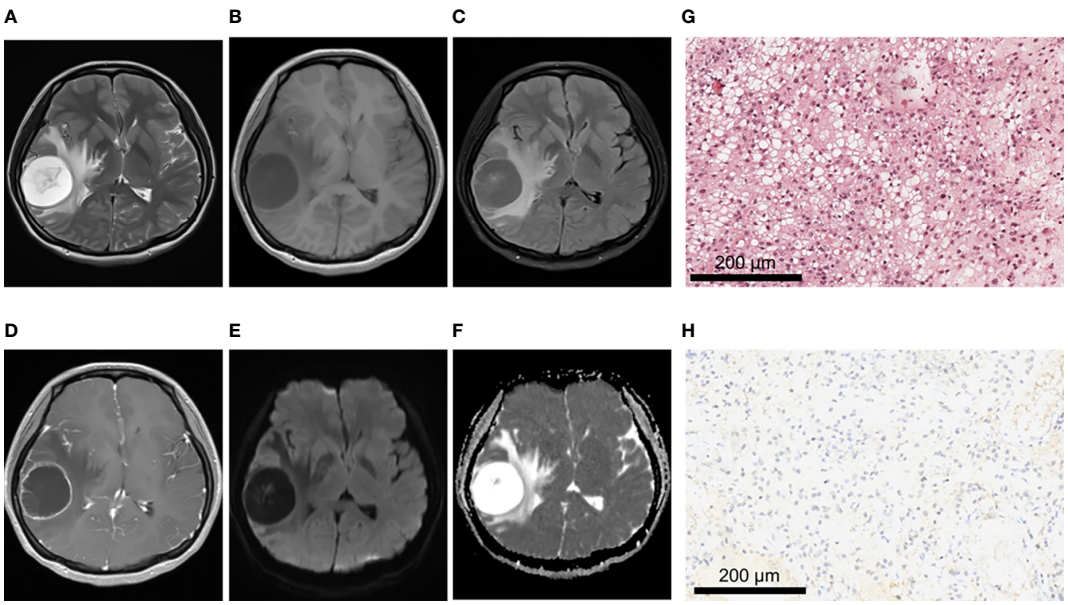

FIGURE 3 | A 21-year-old female patient with right frontoparietal temporal lobe pilocytic astrocytoma, WHO grade I, IDH-wild type. **(A–C)** MRI axial T2W, T1W, T2-FLAIR sequences showed clear tumor boundary, no hemorrhage, and severe edema around the tumor. **(D)** T1 postcontrast showed thin wall ring enhancement. **(E, F)** When b value was 1000, tumor was unrestricted diffusion in DWI and ADC images. **(G)** HE staining showed moderate cell density with oligodendrocyte like changes and a focal myxoid background (×200). **(H)** IDH1 negative expression (×200).

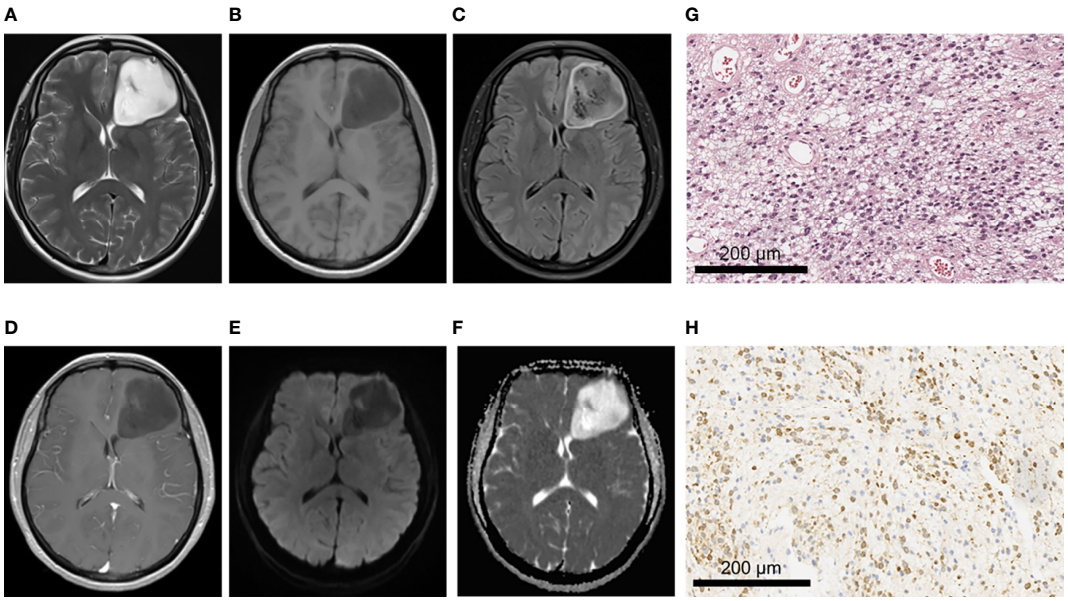

FIGURE 4 | A 43-year-old female patient with left frontal anaplastic astrocytoma, WHO grade III, IDH-mutant type. **(A–C)**MRI axial T2W, T1W, T2-FLAIR sequences showed clear tumor boundary, slightly uneven internal signal and no peritumor edema. **(D)** T1 postcontrast showed no obvious enhancement. **(E, F)** When b value is 1000, tumor was locally and slightly restricted diffusion in DWI and ADC images. **(G)** HE staining showed moderate to severe increase in cell density, accompanied by nuclear atypia and mitotic images (×200). **(H)** IDH1 positive expression (×200).

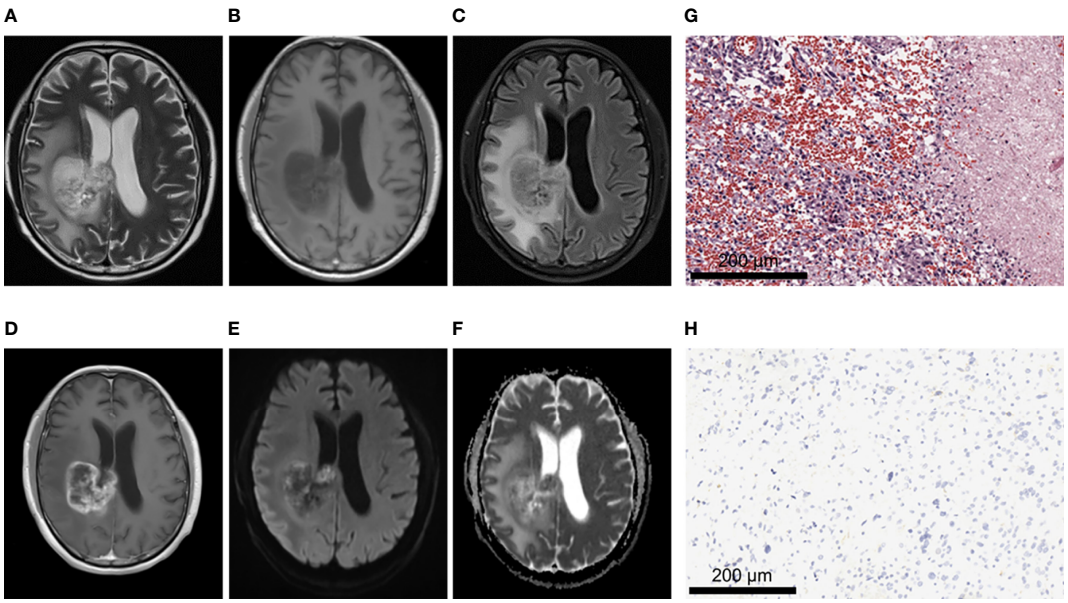

FIGURE 5 | A 62-year-old male patient with glioblastoma of the right fronto-parietal lobe with corpus callosum involvement, WHO grade IV, IDH-wild type. **(A–C)** MRI axial T2W, T1W, T2-FLAIR sequences showed multiple cystic lesions within the tumor, with uneven signals and severe peritumor edema. **(D)** T1 postcontrast showed obvious irregular and thick rim enhancement. **(E, F)** When b value is 1000, tumor was locally obvious restricted diffusion in DWI and ADC images. **(G)** HE staining showed increased cell density and marked atypia, accompanied by extensive necrosis (×200). **(H)** IDH1 negative expression (×200).

TABLE 4 | Comparison and ROC curve analysis of ADC parameters between LGGs and HGGs.

ADC parameters ($\times10^{-3}$ mm^2/s)	LGGs (n = 43)	HGGs (n = 123)	t value	P value	AUC (95% CI)	Cut-off value	Sensitivity (%)	Specificity (%)	Yuden index
ADC_{min}	1.03 ± 0.30	0.80 ± 0.21	4.626	< 0.001***	0.767 (0.686-0.849)	0.79	90.70	56.91	0.476
ADC_{mean}	1.23 ± 0.31	1.04 ± 0.25	4.130	< 0.001***	0.697 (0.608-0.786)	0.96	90.70	57.72	0.330
$rADC_{min}$	1.39 ± 0.40	1.05 ± 0.30	5.816	< 0.001***	0.775 (0.695-0.856)	1.26	62.79	80.49	0.443
$rADC_{mean}$	1.66 ± 0.44	1.35 ± 0.36	4.571	< 0.001***	0.710 (0.622-0.797)	1.41	72.09	60.98	0.331

AUC, Area under the curve; CI, Confidence Interval.
*Significance level markers P < 0.001***.*

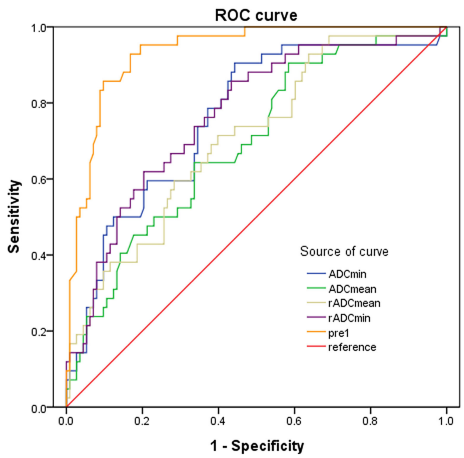

FIGURE 6 | ROC curves of ADC indicators and combined predictors for differentiating LGGs from HGGs.

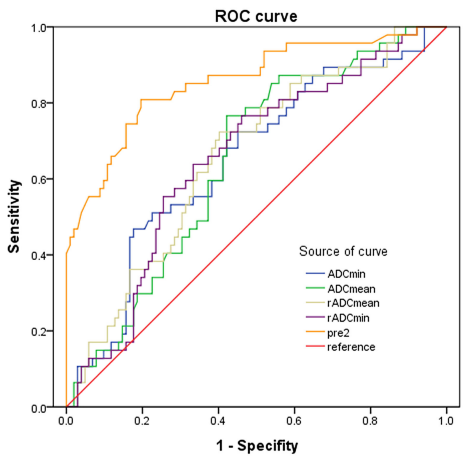

FIGURE 7 | ROC curves of ADC indicators and combined predictors for distinguishing IDH mutants from IDH-wild type gliomas.

DISCUSSION

The malignancy of glioma determines the choice of the surgical treatment plan and the prognosis of patients. The higher the tumor grade is, the worse the prognosis is. However, a single histopathological grade often has limitations. As in WHO grade IV glioblastoma, the degree of malignancy and prognosis may be different with different IDH gene types. WHO CNS5 in 2021 introduces a series of molecular diagnostic indicators on the basis of histological diagnosis, forming an integrated diagnosis and hierarchical reporting system, and defining multiple tumor types and subtypes (8). IDH gene family is still an important molecular marker of adult diffuse glioma. But something has changed. Previously, glioblastoma was diagnosed based on histological findings of microvascular proliferation and/or necrosis, including IDH mutations (10%) and IDH wild-type tumors (90%). In WHO CNS5, glioblastoma will contain only IDH wild-type tumors. IDH is a key rate-limiting enzyme of the tricarboxylic acid cycle (TCA), and IDH gene mutation in most gliomas occurs at the R132H site of IDH1 (24). Studies have shown that IDH mutation is an early event of glioma formation and has an important impact on glioma progression and tumor behavior (25). The clinical outcome of the IDH-mutant group is often better than that of the IDH-wild type group (26), and the IDH-wild type group is more aggressive, similar to the biological behavior of glioblastoma (17). Histopathological and immunohistochemical analysis is the final criteria for grade diagnosis and molecular subtype diagnosis of glioma, but there are the following limitations: (1) Internal heterogeneity and sampling bias of glioma may lead to errors in pathological results (27, 28). (2) The delayed diagnosis is not conducive to the formulation of surgical plan and the selection of preoperative treatment plan. (3) Some patients obtain pathological results by biopsy before surgery, but this is an invasive procedure, which may induce cerebral hemorrhage, epilepsy and other complications and increase the risk of iatrogenic injury (29, 30). MRI examination is an important auxiliary diagnostic method for glioma. MRI manifestations of glioma with different grades and IDH mutation status also have their characteristics. MRI can provide rich information for the diagnosis and prognosis evaluation of glioma. In this study, we successfully developed two noninvasive models by combing multiple new MRI features to distinguish low- and high-grade gliomas as well as with and without IDH mutation.

TABLE 5 | Comparison and ROC curve analysis of ADC parameters between IDH^{mut} and IDH^{wt} gliomas.

ADC parameters ($\times10^{-3}$ mm^2/s)	IDH^{mut} (n = 48)	IDH^{wt} (n = 112)	t value	P value	AUC (95%*CI*)	Cut-off value	Sensitivity (%)	Specificity (%)	Yuden index
ADC_{min}	0.94 ± 0.24	0.83 ± 0.26	2.429	0.016*	0.653 (0.561-0.745)	0.98	45.83	83.04	0.289
ADC_{mean}	1.18 ± 0.25	1.05 ± 0.29	2.611	0.010*	0.643 (0.555-0.731)	1.05	75.00	58.04	0.330
$rADC_{min}$	1.59 ± 0.37	1.37 ± 0.42	2.941	0.004**	0.656 (0.566-0.746)	1.14	62.50	66.96	0.295
$rADC_{mean}$	1.25 ± 0.33	1.09 ± 0.37	2.634	0.009**	0.652 (0.562-0.742)	1.40	70.83	59.82	0.307

Significance level markers P < 0.05, P < 0.01**.*

TABLE 6 | Multivariate logistic regression analysis of glioma grades.

Variables	Noninvasive Grading Model		
	OR	**95%*CI***	***P* value**
Age (≥ 60 years)	7.877	1.359~45.638	0.021*
rADCmean (< 1.41)	1.256	0.290~5.446	0.761
rADCmin (< 1.26)	4.548	1.162~17.799	0.030*
Lesion distribution			
Single lobe		Reference	
Trans-lobe growth with corpus callosum involvement	0.831	0.118~5.860	0.853
Trans-lobe growth with insula involvement	3.352	0.652~17.222	0.147
Trans-lobe growth	2.795	0.284~27.535	0.379
Thalamus or brain stem	0.144	0.024~0.868	0.034*
Enhancement pattern			
No enhancement		Reference	
Patchy enhancement	5.523	1.410~21.629	0.140
Rim enhancement	41.594	5.810~297.794	< 0.001***
Cystic lesion	2.867	0.758~10.838	0.121
Hemorrhage	6.426	0.465~88.896	0.165
Tumor boundary	1.390	0.408~4.744	0.599
Peritumoral edema			
None		Reference	
Mild	2.376	0.529~10.544	0.259
Severe	0.501	0.085~2.957	0.446

OR, odds ratio.
Significance level markers P < 0.05, P < 0.001***.*

TABLE 7 | Multivariate logistic regression analysis of IDH status of glioma.

Variables	Noninvasive IDH Genotyping Model		
	OR	**95%*CI***	***P* value**
Age (≥ 60years)	3.690	1.235~11.029	0.019*
rADCmean (< 1.40)	1.868	0.594~5.875	0.285
rADCmin (< 1.14)	1.593	0.488~5.197	0.441
Lesion distribution			
Single lobe		Reference	
Trans-lobe growth with corpus callosum involvement	0.266	0.085~0.835	0.023*
Trans-lobe growth with insula involvement	0.389	0.106~1.432	0.156
Trans-lobe growth	1.131	0.226~5.669	0.881
Thalamus or brain stem	4.673	0.856~25.497	0.075
Enhancement pattern			
No enhancement		Reference	
Patchy enhancement	2.348	0.844~6.535	0.102
Rim enhancement	6.371	1.931~21.016	0.002**

Significance level markers P < 0.05, P < 0.01**.*

These multivariate models led to a better predictive performance for glioma severity and IDH mutation than the single predictor.

In addition to IDH, many other molecular markers of glioma have been studied more and more in recent years, such as 1p/19q co-deletion, MGMT promoter methylation, TP53 mutation, EGFR amplification, etc. (31). These molecular markers have been confirmed to be related to the prognosis and treatment response in glioma patients. And in the fifth edition of the

TABLE 8 | Diagnostic efficiency of multivariate Logistic regression model.

Model	AUC (95%*CI*)	Sensitivity (%)	Specificity (%)	PPV (%)	NPV (%)	Yuden index
Noninvasive Grading Model	0.934 (0.895-0.973)	91.2	78.6	92.0	76.7	0.698
Noninvasive IDH Genotyping Model	0.857 (0.787-0.926)	88.2	63.8	84.1	71.4	0.520

PPV, Positive Predictive Value; NPV, negative predictive value.

guidelines (WHO CNS5), glioblastoma, IDH-wildtype should be diagnosed in the setting of an IDH-wildtype diffuse and astrocytic glioma in adults if there is microvascular proliferation or necrosis or TERT promoter mutation or EGFR gene amplification or +7/-10 chromosome copy (8). Therefore, the importance of molecular markers for the diagnosis of glioma has once again attracted strong attention. However, it is difficult to predict the molecular subtypes of glioma with high accuracy by conventional MRI technology and general image post-processing simply. In recent years, classical machine learning approaches and deep learning approaches have shown the ability to identify the predictive features and to perform the actual prediction (32). Deep learning technology achieving performance that exceeds humans in the identification of content in images. So it can see the unseeable to predict molecular markers from MRI of brain gliomas. It is believed that a more reliable model can be used to better identify molecular markers of glioma through the combination of MRI and machine learning in the future.

Aging is usually associated with a poor prognosis of glioma. Consistent with the recent study, in our study, we found that high-grade glioma patients were older than patients with low-grade glioma (33). We further showed that age ≥ 60 years was an independent risk factor for predicting HGGs and IDH-wild type gliomas. A previous study reported that IDH-wild type gliomas are more common in elderly patients (34). We also found that the age of IDH-wild type gliomas was higher than that of IDH-mutant gliomas.

MRI morphological characteristics of gliomas with different grades and IDH mutation status may differ greatly. In this study, HGGs are more prone to cystic lesions and hemorrhage, which may be related to the high microvascular density and strong invasiveness of HGGs. We did not observe significant difference between IDH-mutant gliomas and IDH-wild type gliomas in terms of the cystic lesion, hemorrhage and peritumoral edema. However, Lasocki et al. showed that the proportion of edema was statistically significant between IDH-mutant gliomas and IDH-wild type gliomas. All five IDH-mutant patients had an edema rate of 5-33%, whereas most IDH-wild type patients had an edema rate of > 33% (44% of IDH-wild type patients had an edema rate of 34-67% and 14% had an edema rate of 68-95%) (35). The differences may be related to the subjective classification of the degree of edema and the selection bias of the enrolled cases.

The enhancement of glioma mainly depends on the degree of damage to the blood-brain barrier. The contrast agent retention in abnormal angiogenesis thus produces characteristic enhanced images (36). Therefore, MRI enhancement features are of high value for the judgment of the malignant degree of gliomas. In this study, most HGGs and IDH-wild type gliomas showed rim enhancement, while most LGGs and IDH-mutant gliomas showed hypovascular, which is basically consistent with previous literature reports (3, 11). Lasocki et al. suggested that unenhanced tumor volume > 33% was associated with IDH-mutant glioblastoma (35). Tumor location and distribution of lesions are one of the important factors affecting the prognosis of glioma patients. In this study, it was found that LGGs are more common to involve a single lobe, while HGGs are more common to involve multiple lobes, and more likely to involve corpus callosum and insula. The differences in the distribution of lesions in gliomas with different IDH mutation status have also been reported in previous literature. Nakae et al. showed that tumor location in the unilateral frontal lobe was highly correlated with IDH-mutant gliomas ($P < 0.001$) (37). Goze et al. found that 100% of LGGs with insula centers were IDH mutants (38). In our study, we also showed that compared with IDH-wild type gliomas, IDH-mutant gliomas were more likely to be associated with insula involvement, and frontal lobe involvement was more common in cases involving the single lobe.

A meta-analysis showed that ADC was significantly negatively correlated with the number of tumor cells in gliomas (39). The results of our study are consistent with previous studies, and the four ADC parameters of HGGs are lower than those of LGGs. The white matter cell substructure of HGGs was greatly damaged, and the diffusion of water molecules was limited. Therefore, In DWI imaging, HGGs showed higher signals, and LGGs showed lower signals. And accordingly, HGGs had lower ADC values (40, 41). In addition, The ADC value of IDH-wild type gliomas was significantly lower than that of IDH-mutant gliomas (13, 22, 23), which was consistent with the results obtained in this study. Patel et al. noted that histologically observed microcysts tended to increase in IDH mutant LGG cases, which could explain the higher ADC values in these cases, but the pathophysiological mechanism needed to be further elucidated (17).

In this study, we demonstrated the effectiveness of the combination of ADC parameters and MRI morphological features in predicting glioma grades and IDH molecular subtypes. The two multivariate logistic regression models combined with age, ADC parameters and MRI morphological qualitative parameters performed better in distinguishing the LGGs group from the HGGs group and the IDH-mutant group from the IDH-wild type group than using any single ADC value parameter alone.

However, this study also had some limitations, such as (1): This study was a single-center retrospective analysis, and the number of enrolled cases was relatively small. (2) Conventional MRI sequences and enhanced sequence were used instead of multimodality MRI imaging to obtain multi-parameter characteristics of tumors. Compared with other diffusion imaging, ADC has some limitations. (3) Subjective judgment errors may occur in the judgment of certain imaging features. For example, in some cases, it is difficult to distinguish simple vasogenic edema from non-enhanced tumors.

In conclusion, gliomas with different grades and IDH mutation status had significant differences in MRI morphology

and ADC parameters. By combining age, MRI morphological characteristics and ADC value parameters, the accuracy of predicting histopathological grades and IDH molecular subtypes of glioma was greatly improved.

DATA AVAILABILITY STATEMENT

The raw data supporting the conclusions of this article will be made available by the authors, without undue reservation.

ETHICS STATEMENT

All patients signed written informed consent before the enhanced MRI examination according to the regulations of Huadong Hospital, Fudan University. This retrospective study was exempted from ethical review and were conducted in accordance with the World Medical Association Declaration of Helsinki-Ethical Principles for Medical Research Involving Human Subjects.

AUTHOR CONTRIBUTIONS

SL and XF conceived and presented idea. ND, XZ and YY collected the data. RM, WS, LX, YS and GL analyzed the data. XX provided statistical guidance. ND drafted the manuscript. All authors reviewed the manuscript, and SL made corrections to the manuscript. All authors contributed to the article and approved the submitted version.

SUPPLEMENTARY MATERIAL

The Supplementary Material for this article can be found online at: https://www.frontiersin.org/articles/10.3389/fonc.2022.873839/full#supplementary-material

REFERENCES

1. Wang TJC, Mehta MP. Low-Grade Glioma Radiotherapy Treatment and Trials. *Neurosurg Clin N Am* (2019) 30(1):111–8. doi: 10.1016/j.nec.2018.08.008
2. Gusyatiner O, Hegi ME. Glioma Epigenetics: From Subclassification to Novel Treatment Options. *Semin Cancer Biol* (2018) 51:50–8. doi: 10.1016/j.semcancer.2017.11.010
3. Lasocki A, Anjari M, Örs Kokurcan S, Thust SC. Conventional MRI Features of Adult Diffuse Glioma Molecular Subtypes: A Systematic Review. *Neuroradiology* (2021) 63(3):353–62. doi: 10.1007/s00234-020-02532-7
4. Eckel-Passow JE, Lachance DH, Molinaro AM, Walsh KM, Decker PA, Sicotte H, et al. Glioma Groups Based on 1p/19q, IDH, and TERT Promoter Mutations in Tumors. *N Engl J Med* (2015) 372(26):2499–508. doi: 10.1056/NEJMoa1407279
5. Stichel D, Ebrahimi A, Reuss D, Schrimpf D, Ono T, Shirahata M, et al. Distribution of EGFR Amplification, Combined Chromosome 7 Gain and Chromosome 10 Loss, and TERT Promoter Mutation in Brain Tumors and Their Potential for the Reclassification of IDHwt Astrocytoma to Glioblastoma. *Acta Neuropathol* (2018) 136(5):793–803. doi: 10.1007/s00401-018-1905-0
6. Louis DN, Perry A, Burger P, Ellison DW, Reifenberger G, von Deimling A, et al. International Society Of Neuropathology–Haarlem Consensus Guidelines for Nervous System Tumor Classification and Grading. *Brain Pathol* (2014) 24(5):429–35. doi: 10.1111/bpa.12171
7. Louis DN, Perry A, Reifenberger G, von Deimling A, Figarella-Branger D, Cavenee WK, et al. The 2016 World Health Organization Classification of Tumors of the Central Nervous System: A Summary. *Acta Neuropathol* (2016) 131(6):803–20. doi: 10.1007/s00401-016-1545-1
8. Louis DN, Perry A, Wesseling P, Brat DJ, Cree IA, Figarella-Branger D, et al. The 2021 WHO Classification of Tumors of the Central Nervous System: A Summary. *Neuro Oncol* (2021) 23(8):1231–51. doi: 10.1093/neuonc/noab106
9. Nobusawa S, Watanabe T, Kleihues P, Ohgaki H. IDH1 Mutations as Molecular Signature and Predictive Factor of Secondary Glioblastomas. *Clin Cancer Res* (2009) 15(19):6002–7. doi: 10.1158/1078-0432.Ccr-09-0715
10. Delgado-López PD, Corrales-García EM, Martino J, Lastra-Aras E, Dueñas-Polo MT. Diffuse Low-Grade Glioma: A Review on the New Molecular Classification, Natural History and Current Management Strategies. *Clin Transl Oncol* (2017) 19(8):931–44. doi: 10.1007/s12094-017-1631-4
11. Maynard J, Okuchi S, Wastling S, Busaidi AA, Almossawi O, Mbatha W, et al. World Health Organization Grade II/III Glioma Molecular Status: Prediction by MRI Morphologic Features and Apparent Diffusion Coefficient. *Radiology* (2020) 296(1):111–21. doi: 10.1148/radiol.2020191832
12. Lee MK, Park JE, Jo Y, Park SY, Kim SJ, Kim HS. Advanced Imaging Parameters Improve the Prediction of Diffuse Lower-Grade Gliomas Subtype, IDH Mutant With No 1p19q Codeletion: Added Value to the T2/FLAIR Mismatch Sign. *Eur Radiol* (2020) 30(2):844–54. doi: 10.1007/s00330-019-06395-2
13. Zhang L, Min Z, Tang M, Chen S, Lei X, Zhang X. The Utility of Diffusion MRI With Quantitative ADC Measurements for Differentiating High-Grade From Low-Grade Cerebral Gliomas: Evidence From a Meta-Analysis. *J Neurol Sci* (2017) 373:9–15. doi: 10.1016/j.jns.2016.12.008
14. Juratli TA, Tummala SS, Riedl A, Daubner D, Hennig S, Penson T, et al. Radiographic Assessment of Contrast Enhancement and T2/FLAIR Mismatch Sign in Lower Grade Gliomas: Correlation With Molecular Groups. *J Neurooncol* (2019) 141(2):327–35. doi: 10.1007/s11060-018-03034-6
15. Villanueva-Meyer JE, Wood MD, Choi BS, Mabray MC, Butowski NA, Tihan T, et al. MRI Features and IDH Mutational Status of Grade II Diffuse Gliomas: Impact on Diagnosis and Prognosis. *AJR Am J Roentgenol* (2018) 210(3):621–8. doi: 10.2214/ajr.17.18457
16. Song SS, Yu F, Yan XT, Pu YS, Xu JX, Lu J. Value of MRI in Prediction of Glioma Isocitrate Dehydrogenase1mutation Status. *Chin J Med Imaging Technol* (2019) 35(11):1632–7. doi: 10.13929/J.1003-3289.201901063
17. Patel SH, Poisson LM, Brat DJ, Zhou Y, Cooper L, Snuderl M, et al. T2-FLAIR Mismatch, an Imaging Biomarker for IDH and 1p/19q Status in Lower-Grade Gliomas: A TCGA/TCIA Project. *Clin Cancer Res* (2017) 23(20):6078–85. doi: 10.1158/1078-0432.Ccr-17-0560
18. Broen MPG, Smits M, Wijnenga MMJ, Dubbink HJ, Anten M, Schijns O, et al. The T2-FLAIR Mismatch Sign as an Imaging Marker for non-Enhancing IDH-Mutant, 1p/19q-Intact Lower-Grade Glioma: A Validation Study. *Neuro Oncol* (2018) 20(10):1393–9. doi: 10.1093/neuonc/noy048
19. White NS, McDonald C, Farid N, Kuperman J, Karow D, Schenker-Ahmed NM, et al. Diffusion-Weighted Imaging in Cancer: Physical Foundations and Applications of Restriction Spectrum Imaging. *Cancer Res* (2014) 74(22):6733. doi: 10.1158/0008-5472.Can-14-2893
20. Patterson DM, Padhani AR, Collins DJ. Technology Insight: Water Diffusion MRI–a Potential New Biomarker of Response to Cancer Therapy. *Nat Clin Pract Oncol* (2008) 5(4):220–33. doi: 10.1038/ncponc1073
21. Leu K, Ott GA, Lai A, Nghiemphu PL, Pope WB, Yong WH, et al. Perfusion and Diffusion MRI Signatures in Histologic and Genetic Subtypes of WHO Grade II-III Diffuse Gliomas. *J Neurooncol* (2017) 134(1):177–88. doi: 10.1007/s11060-017-2506-9
22. Xing Z, Yang X, She D, Lin Y, Zhang Y, Cao D. Noninvasive Assessment of IDH Mutational Status in World Health Organization Grade II and III Astrocytomas Using DWI and DSC-PWI Combined With Conventional MR Imaging. *AJNR Am J Neuroradiol* (2017) 38(6):1138–44. doi: 10.3174/ajnr.A5171

23. Hempel JM, Schittenhelm J, Brendle C, Bender B, Bier G, Skardelly M, et al. Histogram Analysis of Diffusion Kurtosis Imaging Estimates for *In Vivo* Assessment of 2016 WHO Glioma Grades: A Cross-Sectional Observational Study. *Eur J Radiol* (2017) 95:202–11. doi: 10.1016/j.ejrad.2017.08.008
24. Agarwal S, Sharma MC, Jha P, Pathak P, Suri V, Sarkar C, et al. Comparative Study of IDH1 Mutations in Gliomas by Immunohistochemistry and DNA Sequencing. *Neuro Oncol* (2013) 15(6):718–26. doi: 10.1093/neuonc/not015
25. Poetsch L, Bronnimann C, Loiseau H, Frénel JS, Siegfried A, Seizeur R, et al. Characteristics of IDH-Mutant Gliomas With Non-Canonical IDH Mutation. *J Neurooncol* (2021) 151(2):279–86. doi: 10.1007/s11060-020-03662-x
26. Nakae S, Sasaki H, Hayashi S, Hattori N, Kumon M, Nishiyama Y, et al. PCR-Based Simple Subgrouping Is Validated for Classification of Gliomas and Defines Negative Prognostic Copy Number Aberrations in IDH Mutant Gliomas. *PloS One* (2015) 10(11):e0142750. doi: 10.1371/journal.pone.0142750
27. van den Bent MJ. Interobserver Variation of the Histopathological Diagnosis in Clinical Trials on Glioma: A Clinician's Perspective. *Acta Neuropathol* (2010) 120(3):297–304. doi: 10.1007/s00401-010-0725-7
28. Cahill DP, Sloan AE, Nahed BV, Aldape KD, Louis DN, Ryken TC, et al. The Role of Neuropathology in the Management of Patients With Diffuse Low Grade Glioma: A Systematic Review and Evidence-Based Clinical Practice Guideline. *J Neurooncol* (2015) 125(3):531–49. doi: 10.1007/s11060-015-1909-8
29. Jiang B, Chaichana K, Veeravagu A, Chang SD, Black KL, Patil CG. Biopsy Versus Resection for the Management of Low-Grade Gliomas. *Cochrane Database Syst Rev* (2017) 4(4):Cd009319. doi: 10.1002/14651858.CD009319.pub3
30. Patel KS, Carter BS, Chen CC. Role of Biopsies in the Management of Intracranial Gliomas. *Prog Neurol Surg* (2018) 30:232–43. doi: 10.1159/000464439
31. Oltra-Sastre M, Fuster-Garcia E, Juan-Albarracin J, Sáez C, Perez-Girbes A, Sanz-Requena R, et al. Multi-Parametric MR Imaging Biomarkers Associated to Clinical Outcomes in Gliomas: A Systematic Review. *Curr Med Imaging Rev* (2019) 15(10):933–47. doi: 10.2174/1573405615666190109100503
32. Korfiatis P, Erickson B. Deep Learning can See the Unseeable: Predicting Molecular Markers From MRI of Brain Gliomas. *Clin Radio* (2019) 74(5):367–73. doi: 10.1016/j.crad.2019.01.028
33. Zhang G, Chen WS, Chen F, Zhao YM. Relationship Between Multimodal MRI and Pathology on Diagnosis of Grade II~IV Supratentorial Glioma. *Radiol Pract* (2021) 36(07):837–42. doi: 10.13609/j.cnki.1000-0313.2021.07.003
34. Zhou H, Vallières M, Bai HX, Su C, Tang H, Oldridge D, et al. MRI Features Predict Survival and Molecular Markers in Diffuse Lower-Grade Gliomas. *Neuro Oncol* (2017) 19(6):862–70. doi: 10.1093/neuonc/now256
35. Lasocki A, Tsui A, Gaillard F, Tacey M, Drummond K, Stuckey S. Reliability of Noncontrast-Enhancing Tumor as a Biomarker of IDH1 Mutation Status in Glioblastoma. *J Clin Neurosci* (2017) 39:170–5. doi: 10.1016/j.jocn.2017.01.007
36. Alkanhal H, Das K, Poptani H. Diffusion- and Perfusion-Weighted Magnetic Resonance Imaging Methods in Nonenhancing Gliomas. *World Neurosurg* (2020) 141:123–30. doi: 10.1016/j.wneu.2020.05.278
37. Nakae S, Murayama K, Sasaki H, Kumon M, Nishiyama Y, Ohba S, et al. Prediction of Genetic Subgroups in Adult Supra Tentorial Gliomas by Pre- and Intraoperative Parameters. *J Neurooncol* (2017) 131(2):403–12. doi: 10.1007/s11060-016-2313-8
38. Gozé C, Mansour L, Rigau V, Duffau H. Distinct IDH1/IDH2 Mutation Profiles in Purely Insular Versus Paralimbic WHO Grade II Gliomas. *J Neurosurg* (2013) 118(4):866–72. doi: 10.3171/2012.11.Jns121100
39. Chen L, Liu M, Bao J, Xia Y, Zhang J, Zhang L, et al. The Correlation Between Apparent Diffusion Coefficient and Tumor Cellularity in Patients: A Meta-Analysis. *PloS One* (2013) 8(11):e79008. doi: 10.1371/journal.pone.0079008
40. Suh CH, Kim HS, Jung SC, Kim SJ. Diffusion-Weighted Imaging and Diffusion Tensor Imaging for Differentiating High-Grade Glioma From Solitary Brain Metastasis: A Systematic Review and Meta-Analysis. *AJNR Am J Neuroradiol* (2018) 39(7):1208–14. doi: 10.3174/ajnr.A5650
41. Cao M, Suo S, Han X, Jin K, Sun Y, Wang Y, et al. Application of a Simplified Method for Estimating Perfusion Derived From Diffusion-Weighted MR Imaging in Glioma Grading. *Front Aging Neurosci* (2017) 9:432. doi: 10.3389/fnagi.2017.00432

Conflict of Interest: The authors declare that the research was conducted in the absence of any commercial or financial relationships that could be construed as a potential conflict of interest.

frontiers | Frontiers in Oncology

TYPE Original Research
PUBLISHED 20 October 2022
DOI 10.3389/fonc.2022.968759

OPEN ACCESS

EDITED BY
Fu Wang,
Xi'an Jiaotong University, China

REVIEWED BY
Ri Ji,
Shanghai Jiao Tong University, China
Li Zhang,
Huazhong University of Science and Technology, China
Bin Chen,
First Affiliated Hospital of Wenzhou Medical University, China

*CORRESPONDENCE
Yunyu Chen
1254296913@qq.com
Qiyun Fan
13560399979@163.com
Hongying Wang
why0118@163.com

†These authors have contributed equally to this work and share first authorship

SPECIALTY SECTION
This article was submitted to Cancer Imaging and Image-directed Interventions, a section of the journal Frontiers in Oncology

RECEIVED 14 June 2022
ACCEPTED 23 September 2022
PUBLISHED 20 October 2022

CITATION
Shentu W, Zhang Y, Gu J, Wang F, Zhao W, Liu C, Lin Z, Wang Y, Liu C, Chen Y, Fan Q and Wang H (2022) Contrast-enhanced ultrasonography for differential diagnosis of adnexal masses.
Front. Oncol. 12:968759.
doi: 10.3389/fonc.2022.968759

Contrast-enhanced ultrasonography for differential diagnosis of adnexal masses

Weihui Shentu[1†], Yin Zhang[1†], Jiaojiao Gu[1†], Fa Wang[1], Wei Zhao[1], Chunmei Liu[2], Zimei Lin[2], Yao Wang[2], Chen Liu[1], Yunyu Chen[1*], Qiyun Fan[1*] and Hongying Wang[1*]

[1]Department of Medical Ultrasonics, Guangzhou Women and Children's Medical Center, Guangzhou Medical University, Guangzhou, China, [2]Department of Medical Ultrasonics, The Second Affiliated Hospital of Zhejiang University School of Medicine, Hangzhou, China

Background: Quantitative contrast-enhanced ultrasonography parameters are affected by various factors. We evaluated corrected quantitative contrast enhanced ultrasonography in differentiating benign adnexal tumors from malignant tumors.

Methods: Patients with adnexal masses who underwent conventional and contrast-enhanced ultrasonography were included. Contrast-enhanced ultrasonography parameters such as base intensity, arrival time, peak intensity, time to peak intensity, ascending slope, and descending slope were measured. Corrected (time to peak intensity – arrival time) $_{mass}$/(time to peak intensity – arrival time) $_{uterus}$ and (peak intensity – base intensity) $_{mass}$/(peak intensity – base intensity) $_{uterus}$ were calculated. Lesions were confirmed by pathologic examination of surgical specimens.

Results: This study included 31 patients with 35 adnexal lesions including 20 (57.10%) benign and 15 (42.90%) malignant lesions. The corrected contrast-enhanced ultrasonography quantitative parameters in lesions were statistically different between malignant and benign groups (P<0.05). The optimal cut-off value for (time to peak intensity – arrival time) $_{mass}$/(time to peak intensity – arrival time) $_{uterus}$, ascending slope, and (peak intensity – base intensity) $_{mass}$/(peak intensity – base intensity) $_{uterus}$, and descending slope for differentiating malignant adnexal masses from benign tumors were 1.05 (area under curve: 0.93, P<0.05), 1.11 (area under curve: 0.83, P<0.05), 0.82 (area under curve: 0.73, P<0.05), and –0.27 (area under curve: 0.66, P=0.16), with sensitivity and specificity of 93.33% and 85.00%, 86.67% and 75.00%, 86.67% and 60.00%, and 54.55% and 66.67%, respectively.

Conclusions: Corrected contrast-enhanced ultrasonography parameters provide practical differential diagnosis value of adnexal lesions with high reliability for sonologists.

KEYWORDS

contrast-enhanced ultrasound, adnexal mass, ovarian cancer, benign, malignant

Introduction

Adnexal masses are commonly encountered in daily radiology practice and occur in women of all ages. Adnexal malignancy accounts for 2.5% of all malignancies among females and 5% of all cancer-related deaths (1). Adnexal malignancy has been termed a "silent killer" because most patients present with few symptoms or are diagnosed at advanced stages (III and IV) (1, 2). While patients with late-stage disease have a high fatality rate, women with early-stage disease have an overall 5-year survival of approximately 93% (1, 3). Thus, developing strategies to improve early diagnosis of adnexal malignancy is critical to improve the efficacy of treatment.

Gray-scale and Doppler ultrasonography is a convenient imaging modality for visualizing adnexal masses, with advantages such as cost-effectiveness and radiation-free safety (4, 5). However, there are many overlapping ultrasonic features between benign and malignant adnexal masses (6, 7). Furthermore, although color Doppler flow imaging can provide helpful information about blood flow in adnexal masses, it has limitations such as low sensitivity to display slow or deeply located blood flow vessels.

Tumor angiogenesis is necessary for tumor growth and is an independent prognostic indicator for survival in cancer patients, such as in ovarian carcinoma (8, 9). Advances in contrast enhanced ultrasonography (CEU) have enabled the characterization of tumor vascularity, such as in hepatic (10, 11), breast (12, 13), gastric (14), prostate (15), and cardiac masses (16). Several studies have reported that qualitative (17) and quantitative (18–20) CEU can improve the performance of sonography in distinguishing benign adnexal masses from malignancy. However, several factors impact CEU parameter values such as respiration, depth of mass, heart rate, and patient characteristics. Contrast intensity is also affected by contrast agent dosage, administration speed and instrument setting. Therefore, the primary objective of this study was to evaluate the usefulness of corrected CEU parameters in the differential diagnosis of adnexal masses.

Methods

Study population

Between January 2021 and December 2021, we prospectively studied 51 consecutive patients (40 ± 14 years old, range: 19–78 years old) with adnexal masses. All patients underwent a conventional ultrasonography examination and CEU. The inclusion criteria were as follows: (1) patients with ultrasound diagnosis of unilocular-solid (a single cyst without septa and without solid parts or papillary excrescences), multilocular-solid (a cyst with at least one septum but no solid parts or papillary excrescences) or a unilocular solid cyst (a single cyst containing solid parts or papillary excrescences but no septa), a multi-locular solid cyst (a cyst with at least one septum and solid parts or papillary excrescences), or a solid tumor (a tumor with solid components in 80% or more of the tumor), solid adnexal mass, or multi-locular adnexal cyst (21); and (2) patients with pathology results obtained from a surgical specimen within three months of surgery. Exclusion criteria were as follows: refusal to sign informed consent forms, severe renal insufficiency, right-to-left shunt heart disease syndrome, pregnancy or lactation, and age less than 18 years. Borderline tumors were classified as malignant.

This study was approved by the ethics committees of Guangzhou Women and Children Medical Center (approval number # 194A01) and the Second Affiliated Hospital of Zhejiang University School of Medicine (approval number # 0741). Written informed consent was obtained from all patients before CEU.

Conventional ultrasonography and CEU imaging

Conventional ultrasonography and transabdominal CEU examinations were performed with a commercially available ultrasound machine (Mindray, China) and an M3S transducer SC5-1U with a transmission frequency of 1.2–6.0 MHz. All gray scale and color Doppler images were acquired by a radiologist with more than 5 years of experience through transabdominal and transvaginal ultrasonography examination. The location, size, shape, internal echogenicity of the mass, peritoneal effusion, and vascularity were recorded, and the patients then underwent CEU. The vascularity in the adnexal mass was assessed according to International Ovarian Tumor Analysis color Doppler scoring system as follows: 1=no vascularization, 2=minimal vascularization, 3=moderate vascularization, and 4=high vascularization (21). Uterus and adnexal masses were simultaneously imaged in the same plane using real-time CEU preset with coded pulse inversion technique after bolus intravenous infusion of 1.5 ml SonoVue (Brocco, Geneva, Switzerland) through the antecubital vein. To reduce microbubble destruction, we preset the mechanical index (MI) to a low MI setting of 0.082. Image depth was adjusted to 8–12 cm according to the location of the adnexal mass. Time gain compensation was adjusted to achieve a homogeneous signal intensity of the mass. All settings were kept constant throughout each examination.

The target lesion was observed continuously for 2–3 min after bolus injection of 1.5 ml contrast agents. The real-time contrast perfusion cine loop was digitally stored for subsequent analysis. Patients were observed for complications for 30 min before being permitted to leave.

Imaging analysis

Contrast enhancement of adnexal masses after the injection of contrast agent was quantitatively analyzed by two independent

radiologists who were blinded to the clinical information and the final diagnosis of the patients. A region of interest (ROI) was drawn both within the adnexal mass and adjacent to the myometrium. The time-intensity curve (TIC) and contrast parameters of ROI, including base intensity (BI), arrival time (AT), peak intensity (PI), time to peak intensity (TTP), ascending slope (AS), and descending slope (DS), were obtained automatically with quantitative imaging analysis software. To reduce the impact of contrast agent dosage and injection speed on CEU parameters, corrected $(TTP-AT)_{mass}/(TTP-AT)_{uterus}$ and $(PI-BI)_{mass}/(PI-BI)_{uterus}$ were calculated. All lesions were confirmed by pathologic examination of surgical specimens.

Statistical analysis

Data analysis was performed with SPSS version 26 (SPSS Inc.) and Graph Pad Prism version 8.0 (Graph Pad, La Jolla, CA, USA). Continuous variables were expressed as mean ± standard deviation. Two groups were compared using a two-sample t-test (continuous variables with normal distribution) or a Wilcoxon-Mann-Whitney test (continuous variables with non-normal distribution or ordinal parameters). Categorical data comparisons were analyzed with Pearson chi-squared tests or Fisher's exact test. Receiver operating characteristic (ROC) curves were generated for each CEU parameter. The optimal cut-off value was determined as the point at which the Youden index (sensitivity + specificity-1) was maximal. The intra- and interobserver reproducibility of the measurements were evaluated by the intraclass correlation coefficients (ICCs) using a two-way mixed-effects model and a two-way random-effects model. ICC>0.80 and ICC = 0.60–0.80 were considered excellent and good, respectively. $P<0.05$ was considered to indicate statistical significance.

Results

Patient characteristics

From January 2021 to November 2021, 51 patients with adnexal masses and conventional transabdominal or transvaginal ultrasonography examination in Guangzhou Women and Children Medical Center and the Second Affiliated Hospital Zhejiang University School of Medicine were initially enrolled. Among the 51 patients, 20 cases were excluded. The flowchart for patient selection for this study is illustrated in Figure 1. The final study group included 31 patients with 35 adnexal lesions including 20 (57.10%) benign lesions and

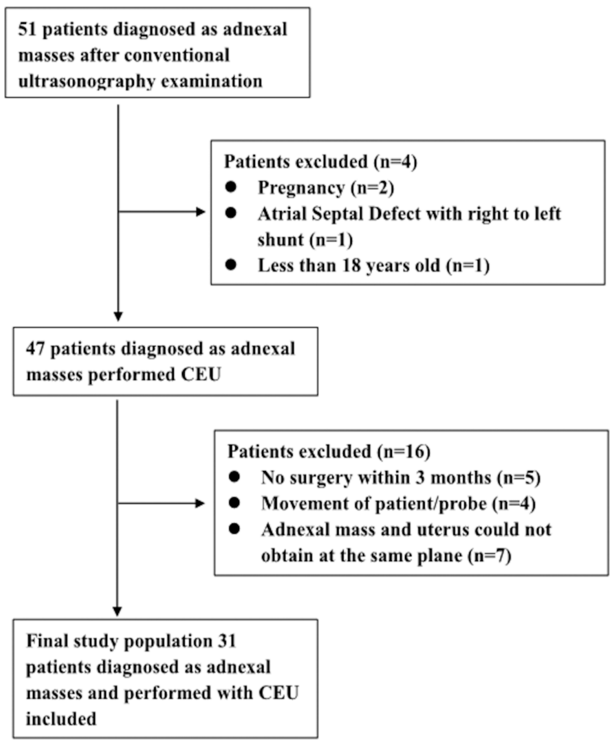

FIGURE 1
Flowchart for selection of patients with adnexal mass. In total, 31 out of 51 patients were included according to the selection criteria.

TABLE 1 Pathological types of adnexal masses (n = 35).

Pathological type	n (%)
Benign	20 (57.14%)
Simple cyst	1 (2.86%)
Mesosalpinx cyst	1 (2.86%)
Mature teratoma	4 (11.43%)
Hydrosalpinx	1 (2.86%)
Serous cystadenoma	4 (11.43%)
Mucinous cystadenoma	2 (5.71%)
Fibrothecoma	1 (2.86%)
Endometrioma	5 (14.29%)
Brenner tumor	1 (2.86%)
Malignant	15 (42.86%)
Serous cystadenocarcinoma	3 (8.57%)
Mucinous cystadenocarcinoma	2 (5.71%)
Endometroid adenocarcinoma	2 (5.71%)
Granulosa cell tumor	1 (2.86%)
Spertoli-Leydig cell tumor	1 (2.86%)
Clear cell carcinoma	1 (2.86%)
Borderline cystadenoma	3 (8.57%)
Immature teratoma	2 (5.71%)

15 (42.90%) malignant lesions. All adnexal masses underwent histological verification, and characteristics are listed in Table 1. Eight patients with malignancy presented as asymptomatic; their adnexal masses were discovered incidentally during a routine medical examination.

The clinical characteristics and laboratory results of the patients are summarized in Table 2. Peritoneal effusion and increased carbohydrate antigen 125 were more common in malignant masses compared with benign lesions, but the difference was not statistically significant (P=0.06 and 0.01, respectively).

Conventional sonography findings

The conventional ultrasound features of the 35 adnexal masses including maximum diameter of lesions, color score, and resistance index (RI) value of vascularization in masses are listed in Table 2. There was no statistically significant difference in the maximum diameter of lesions between malignant and benign groups. The color score and RI of the vascularization of adnexal tumors were significantly different between the malignant and benign groups (both P = 0.01).

Differential diagnostic ability of CEU with quantitative analysis

As shown in Table 3, the corrected CEU quantitative parameters in lesions of $(TTP - AT)_{mass}/(TTP - AT)_{uterus}$ and $(PI - BI)_{mass}/(PI - BI)_{uterus}$ were statistically different between malignant and benign adnexal mass groups (both P<0.05). The AS in the malignant tumor group was also significantly greater than that in benign tumors (Figures 2, 3). The DS in the malignant group tended to be higher than that in benign masses but did not reach a statistically significant difference. Using ROC curve analysis, the optimal cut-off value for $(TTP - AT)_{mass}/(TTP - AT)_{uterus}$, AS, and $(PI - BI)_{mass}/(PI - BI)_{uterus}$, DS, TTP_{mass}, and PI_{mass} for differentiating malignant adnexal masses from benign tumors were 1.05 (area under the curve (AUC): 0.93, P<0.05), 1.11 (AUC: 0.83, P<0.05), 0.82 (AUC: 0.73, P<0.05), −0.27(AUC: 0.66, P=0.16), 29.50(AUC:0.69, P=0.06), and 50.69(AUC:0.68, P=0.07) with a sensitivity and specificity of 93.33% and 85.00%, 86.67% and 75.00%, 86.67% and 60.00%, and 54.55% and 66.67%, 60% and 80%, 73.33% and 60.00% respectively (Table 4).

TABLE 2 Clinical and conventional sonography characteristics of patients with adnexal masses (n = 35).

Characteristic	Benign (n = 20)	Malignant (n = 15)	*P* value
Age (year)	41.00 (32.50-51.50)	39.00 (30.50-63.00)	0.80
Postmenopausal (n)	5 (25.00%)	5 (33.30%)	0.71[a]
Maximum diameter of lesions (cm)	81.50 (68.00-101.50)	84.00 (37.00-114.50)	0.91
Bilateral (n)	3 (15.00%)	1 (6.70%)	0.62[a]
Peritoneal effusion (n)	3 (15.00%)	7 (46.70%)	0.06[a]
Color score			0.01
1	12 (60.00%)	3 (20.00%)	
2	6 (30.00%)	7 (46.67%)	
3	2 (10.00%)	3 (20.00%)	
4	0 (0%)	2 (13.33%)	
RI	0.56 (0.51-0.68)	0.45 (0.38-0.48)	0.01
CA-125 (u/ml)	26.45 (16.60-71.15)	74.70 (53.20-283.10)	0.01
HE-4 (pmol/L)	38.40 (29.35-52.75)	35.90 (35.35-81.35)	0.24

RI, resistance index; CA-125, carbohydrate antigen 125; HE-4, human epididymis protein-4.
[a]Calculated with Fisher's exact test.

TABLE 3 Comparison of CEU parameters between benign and malignant masses.

Parameter	Benign tumor	Malignant tumor	*P* value
$(TTP - AT)_{mass}/(TTP - AT)_{uterus}$	1.48 (1.29–1.63)	0.72 (0.67–0.98)	<0.05
$(PI - BI)_{mass}/(PI - BI)_{uterus}$	0.74 (0.56–1.02)	1.04 (0.87–1.06)	<0.05
AS	0.96 (0.59–1.11)	1.29 (1.16–1.54)	<0.05
DS	-0.23 (-0.28– -0.16)	-0.28 (-0.36– -0.21)	0.16

Data are shown as mean (range), CEU, contrast enhanced ultrasonography; TTP, time to peak intensity; AT, arrival time; PI, peak intensity; BI, base intensity; AS, ascending slope; DS, descending slope.

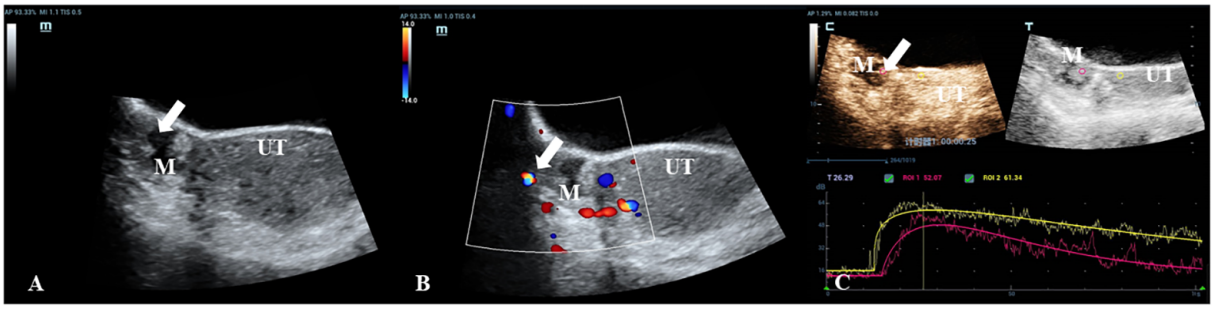

FIGURE 2
A 30-year-old woman with a pathologically proven borderline cystadenoma. **(A)** Transabdominal gray-scale ultrasound shows an 18-mm cystic mass (M) with a small 13 x 8mm papillary component at the right of uterus (UT). **(B)** Color Doppler reveals no blood flow signal in the papillary portion (color score=1). **(C)** CEU curve demonstrates that the tumor showed hypoenhancement in initial perfusion and faster washout compared with myometrium (mass: red, myometrium: yellow).

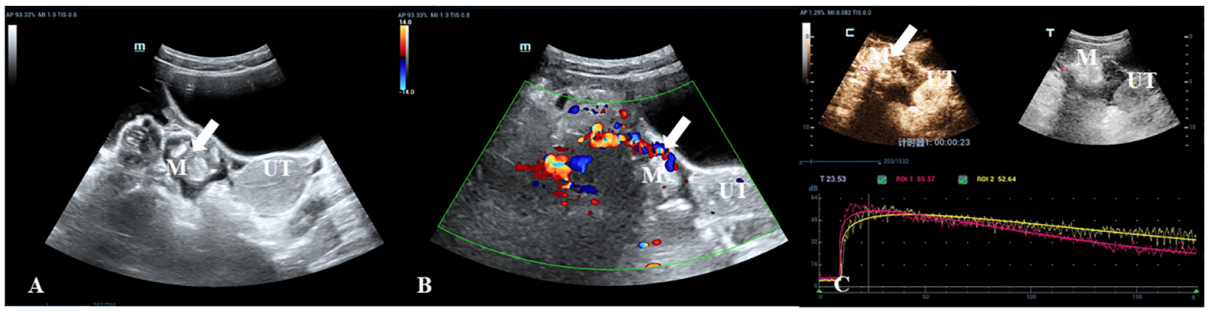

FIGURE 3
A 35-year-old woman with a pathologically proven immature teratoma. **(A)** Transabdominal gray-scale ultrasound shows a 30-mm complex cystic-solid mass (M) in the right adnexa. **(B)** Color Doppler reveals the color flow within the mass (color score=4). **(C)** CEU curve demonstrates that the tumor showed hyperenhancement in initial perfusion and faster washout compared with myometrium (mass: red, myometrium: yellow).

TABLE 4 ROC curve analysis of the predicted probability of CEU parameters for evaluation of benign and malignant adnexal mass.

Parameter	Sensitivity	Specificity	Cut-off value	AUC	Std. error	*P* value	95% confidence interval	
							Lower limit	Upper limit
(TTP − AT)mass/(TTP − AT)uterus	93.33%	85.00%	1.05	0.93	0.04	<0.05	0.84	1
AS	86.67%	75.00%	1.11	0.83	0.07	<0.05	0.7	0.97
(PI − BI)mass/(PI − BI)uterus	86.67%	60.00%	0.82	0.73	0.09	<0.05	0.56	0.9
DS	54.55%	66.67%	-0.27	0.66	0.11	0.16	0.45	0.86
TTP mass	60.00%	80.00%	29.50	0.69	0.09	0.06	0.50	0.87
PI mass	73.33%	60.00%	50.69	0.68	0.09	0.07	0.49	0.86

ROC, receive operating characteristic; CEU, contrast enhanced ultrasonography; TTP, time to peak intensity; AT, arrival time; PI, peak intensity; BI, base intensity; AS, ascending slope; DS, descending slop.

Inter-observer and intra-observer reproducibility

As shown in Table 5, the ICC for the same observer ranged from 0.93 (95% CI, 0.65–0.97) to 0.99 (95% CI, 0.98–0.99). The ICC between the two observers ranged from 0.88(95% CI, 0.60–0.95) to 0.99 (95% CI, 0.97–0.99).

Discussion

Our study results showed that the corrected quantitative visual temporal CEU parameters were statistically different between malignant adnexal masses and benign tumors. The values of $(TTP - AT)_{mass}/(TTP - AT)_{uterus}$, AS, and $(PI - BI)_{mass}/(PI - BI)_{uterus}$ had high diagnostic accuracy in distinguishing benign adnexal lesions from malignant tumors. The usefulness of CEU parameters demonstrated in this study provides practical differential diagnosis value of adnexal lesions with high reliability for radiologists.

Numerous efforts and international studies, such as International Ovarian Tumor Analysis simple rules (22), Gynecologic Imaging Reporting and Data System (23), and Ovarian-Adnexal Reporting and Data System (24), have been conducted to improve the ability of ultrasonography imaging for the diagnosis of adnexal masses. The diagnostic accuracy of malignant tumors has been enhanced by the combination of gray-scale ultrasound morphology and color Doppler flow imaging information (25). However, evaluation of gray-scale and Doppler ultrasound examination of adnexal masses is dependent on experience. Furthermore, malignant and benign lesions show overlapping features on gray-scale morphology and blood flow features (26).

Angiogenesis is a prerequisite for the growth of malignant tumors and an early event during tumor development (27). Microvessel density (MVD) influences the nutritional status of tumors and facilitates tumor growth, proliferation and invasion. MVD is associated with a poorer prognosis in breast and kidney cancer patients (27, 28) and correlates with the depth of tumor invasion (29). Intravenous CEU has been used widely to assess tumor angiogenesis *in vivo* (10–20) and provides detailed information about the vascularity and blood flow kinetics in normal and pathologic tissues. Previous studies have shown that malignant ovarian masses generally have a greater PI compared with benign masses (17–20). However, Li et al. calculated PI – BI for quantitative analysis of the microvasculature. The authors revealed that PI – BI in carcinoma tissues was significantly higher than that in normal or benign tissues ($P<0.001$) and demonstrated that PI – BI corresponds with MVD, which was calculated by counting CD34-positive vascular endothelial cells (r=0.921, $P<0.001$) (29). Tang et al. showed that visual assessment of the degree of

TABLE 5 Intraobserver and interobserver reliability of CEU parameters.

Parameters	Intraobserver		Interobserver	
	ICC	95% CI	ICC	95% CI
BI	0.97	0.88–0.99	0.95	0.83–0.99
AT	0.93	0.75–0.98	0.88	0.60–0.97
TTP	0.99	0.97–0.99	0.99	0.95–0.99
PI	0.95	0.78–0.99	0.94	0.79–0.99
AS	0.91	0.65–0.98	0.89	0.61–0.97
DS	0.95	0.81–0.99	0.97	0.61–0.99

CEU, contrast enhanced ultrasonography; ICC, intraclass correlation; CI, confidence interval; BI, base intensity; AT, arrival time; TTP, time to peak intensity; PI, peak intensity; AS, ascending slope; DS, descending slope.

enhancement of cardiac masses to the adjacent myocardium during contrast perfusion echocardiography had high diagnostic accuracy for the differentiation of benign tumors from malignant tumors, with a sensitivity and specificity of 100% and 97%, respectively (16). In our study, we found that $(PI - BI)_{mass}/(PI - BI)_{uterus}$ was significantly higher in the adnexal carcinoma group than that in the benign group ($P<0.05$). ROC curve analysis revealed that the sensitivity and specificity of $(PI - BI)_{mass}/(PI - BI)_{uterus}$ in differentiating benign lesions from malignancy were 86.67% and 60.00%, respectively (cut-off: 0.82, AUC: 0.73, $P<0.05$). The specificity was only 60.00%, indicating substantial overlap between the benign and malignant tumors, especially between benign and borderline tumors.

Furthermore, the temporal features AT and TTP are affected by patient heart rate and cardiac function as well as by the velocity of bolus injection. To reduce these individual factors impacting CEU parameters, we measured $(TTP - AT)_{mass}/(TTP - AT)_{uterus}$. We found that $(TTP - AT)_{mass}/(TTP - AT)_{uterus}$ was significantly smaller in the malignant tumor group than in the benign tumor group. The result was consistent with the report by Sconfienza (30), in which the authors used the absolute value of TTP. We also found that $(TTP - AT)_{mass}/(TTP - AT)_{uterus}$ performed better with higher accuracy than the other parameters in distinguishing between benign adnexal masses and malignant cases. When the optimal cut-off was 1.05, the sensitivity, specificity, and AUC were 93.33%, 85.00%, and 0.93, respectively ($P<0.05$).

The other kinetics CEU parameter AS for malignant tumors was significantly greater than that for benign lesion. To our knowledge, no CEU study has used AS to distinguish malignant adnexal tumors from benign one. Our result was consistent with the findings reported by Kazerooni, who applied dynamic contrast-enhanced MRI to classify adnexal masses (31). Parameters like wash-out time could help differentiate benign and malignant tumors and even be more accurate than Doppler sonography for the discrimination of adnexal cancer from benign tumors. However, the kinetics CEU parameter DS that reflects wash-out of vascularity did not show a significant difference between malignant tumors and benign tumors in this study, indicating that the results obtained with this approach show a wide variability (18, 32). The tumor vasculature exhibits atypical morphological features and is characterized by dilated, tortuous disorganized blood vessels, arteriovenous fistula, and incomplete muscularization of vessel walls. This results in lower resistance to flow, few systolic-diastolic variations in blood flow velocity, and shorter wash-out time compared with that in normal vessels (27, 28, 33).

This study has several limitations. First, the number of cases included in this study is small, and we could not analyze the differences in the subtypes of adnexal mass, since there are some overlaps in different lesions. Second, we did not compare the difference between absolute and corrected CEU parameters in this study. However, other authors have previously studied the absolute CEU parameters.

Conclusions

Malignant and benign adnexal tumors have different degrees of the kinetics of CEU parameters. We showed that both visual assessment and temporal assessment of the degree of enhancement of adnexal masses to adjacent myometrium after administration of contrast agents had high diagnostic accuracy in the discrimination of benign tumors from malignant tumors.

Data availability statement

The datasets presented in this study can be found in online repositories. The names of the repository/repositories and accession number(s) can be found in the article/Supplementary Material.

Ethics statement

The studies involving human participants were reviewed and approved by the ethics committees of Guangzhou Women and Children Medical Center and the Second Affiliated Hospital of Zhejiang University School of Medicine. Written informed consent was obtained from all patients before CEU. The patients/participants provided their written informed consent to participate in this study.Written informed consent was obtained from the individual(s) for the publication of any potentially identifiable images or data included in this article.

Author contributions

Conception and design: WS, HW, and JG. Administrative support: HW. Provision of materials or patients: WS, QF, and CL. Collection and assembly of data: YZ, YW and WZ. Data analysis and interpretation: ZL, YW, FW and CML. Manuscript Writing: WS and YC. Final approval of manuscript: All the authors contributed

Funding

We thank Funding of Guangzhou Institute of Pediatrics/Guangzhou Women and Chindren's Medical Center (grant number: 4001022) for supporting the manuscript preparation and publication.

Acknowledgments

We are grateful to Youbin Deng, MD (Department of Medical Ultrasonics, Tongji Hospital, Tongji Medical College, Huazhong University of Science & Technology, Wuhan, China), for writing assistance and review of the English in the manuscript.

Conflict of interest

The authors declare that the research was conducted in the absence of any commercial or financial relationship that could be construed as a potential conflict of interest.

Publisher's note

All claims expressed in this article are solely those of the authors and do not necessarily represent those of their affiliated organizations, or those of the publisher, the editors and the reviewers. Any product that may be evaluated in this article, or claim that may be made by its manufacturer, is not guaranteed or endorsed by the publisher.

Supplementary material

The Supplementary Material for this article can be found online at: https://www.frontiersin.org/articles/10.3389/fonc.2022.968759/full#supplementary-material

References

1. Torre LA, Trabert B, DeSantis CE, Miller KD, Samimi G, Runowicz CD, et al. Ovarian cancer statistics, 2018. *CA Cancer J Clin* (2018) 68:284–96. doi: 10.3322/caac.21456

2. Matulonis UA, Sood AK, Fallowfield L, Howitt BE, Sehouli J, Karlan BY. Ovarian cancer. *Nat Rev Dis Primers* (2016) 2:16061. doi: 10.1038/nrdp.2016.61

3. Siegel RL, Miller KD, Jemal A. Caner statistics, 2018. *CA Cancer J Clin* (2018) 68:7–30. doi: 10.3322/caac.21442

4. American college of Obstetricians and Gynecologists' Committee on Practice Bulletins-Gynecology. Practice bulletin no. 174: Evaluation and management of adnexal masses. *Obstet Gynecol* (2016) 128:e210–26. doi: 10.1097/AOG.0000000000001768

5. Andreotti RF, Timmerman D, Strachowski LM, Froyman W, Benacerraf BR, Bennett G, et al. O-RADS US risk stratification and management system: A consensus guideline from the ACR ovarian-adnexal reporting and data system committee. *Radiology* (2020) 294:168–85. doi: 10.1148/radiol.2019191150

6. Valentin L, Ameye L, Jurkovic D, Metzger U, Lécuru F, Huffel SV, et al. Which extrauterine pelvic masses are difficult to correctly classify as benign or malignant on the basis of ultrasound findings and is there a way of making a correct diagnosis? *Ultrasound Obstet Gynecol* (2006) 27:438–44. doi: 10.1002/uog.2707

7. Yazbek J, Raju KS, Ben-Nagi J, Holland T, Hillaby K, Jurkovic D. Accuracy of ultrasound subjective 'pattern recognition' for the diagnosis of borderline ovarian tumors. *Ultrasound Obstet Gynecol* (2007) 29:489–95. doi: 10.1002/uog.4002

8. Palmer JE, Cassia LJS, Irwin CJ, Morris AG, Rollason TP. Prognostic value of measurements of angiogenesis in serous carcinoma of the ovary. *Int J Gynecol Pathol* (2007) 26:395–403. doi: 10.1097/pgp.0b013e318063bed7

9. Wang J, Lv F, Fei X, Cui Q, Wang L, Gao X, et al. Study on the characteristics of contrast-enhanced ultrasound and its utility in assessing the microvessel density in ovarian tumors or tumor-like lesions. *Int J Biol Sci* (2011) 7:600–6. doi: 10.7150/ijbs.7.600

10. Zhou H, Sun J, Jiang T, Wu J, Li Q, Zhang C, et al. A nomogram based on combining clinical features and contrast enhanced ultrasound LI-RADS improves prediction of microvascular invasion in hepatocellular carcinoma. *Front Oncol* (2021) 11:699290. doi: 10.3389/fonc.2021.699290

11. Kim TK, Choi BI, Han JK, Hong HS, Park SH, Moon SG. Hepatic tumors: contrast agent-enhancement patterns with pulse-inversion harmonic US. *Radiology* (2000) 216:411–7. doi: 10.1148/radiology.216.2.r00jl21411

12. Xiao X, Jiang Q, Wu H, Guan X, Qin W, Luo B. Diagnosis of sub-centimetre breast lesions: combining BI-RADS-US with strain elastography and entrast-enhanced ultrasound- a preliminary study in China. *Eur Radiol* (2017) 27:2443–50. doi: 10.1007/s00330-016-4628-4

13. Lu J, Zhou P, Jin C, Xu L, Zhu X, Lian Q, et al. Diagnostic value of contrast-enhanced ultrasounography with SonoVue in the differentiation of benign and malignant breast lesions: a meta-analysis. *Technol Cancer Res Treat* (2020) 19:1533033820971583. doi: 10.1177/1533033820971583

14. Pan M, Huang P, Li S, Chen J, Wei S, Zhang Y. Double contrast-enhanced ultrasonography in preoperative borrmann classification of advanced gastric carcinoma: comparison with histopathology. *Sci Rep* (2013) 3:3338. doi: 10.1038/srep03338

15. Halpern EJ, Rosenberg M, Gomella LG. Prostate cancer: contrast-enhanced us for detection. *Radiology* (2001) 219:21925. doi: 10.1148/radiology.219.1.r01ap21219

16. Tang QY, Guo LD, Wang WX, Zhou W, Liu YN, Liu HY, et al. Usefulness of contrast perfusion echocardiography for differential diagnosis of cardiac masses. *Ultrasound Med Biol* (2015) 41:2382–90. doi: 10.1016/j.ultrasmedbio.2015.05.010

17. Zhang X, Mao Y, Zheng R, Zheng Z, Huang Z, Huang D, et al. The contribution of qualitative CEUS to the determination of malignancy in adnexal masses, indeterminate on conventional US – a multicenter study. *PloS One* (2014) 9:e93843. doi: 10.1371/journal.pone.0093843

18. Ordén MR, Jurvelin JS, Kirkinen PP. Kinetics of a US contrast agent in benign and malignant adnexal tumors. *Radiology* (2003) 226:405–10. doi: 10.1148/radiol.2262011450

19. Szymanski M, Socha MW, Kowalkowska ME, Zielińska LB, Eijaszewicz A, Szymanski W. Differentiating between benign and malignant adnexal lesions with contrast-enhanced transvaginal ultrasonography. *Int J Gynaecol Obstet* (2015) 131:147–51. doi: 10.1016/j.ijgo.2015.04.047

20. Delaney LJ, Machado P, Torkzaban M, Lyshchik A, Wessner CE, Kim C, et al. Characterization of adnexal masses using contrast-enhanced subharmonic imaging: a pilot study. *J Ultrasound Med* (2020) 39:977–85. doi: 10.1002/jum.15183

21. Timmerman D, Valentin L, Bourne TH, Collins WP, Verrelst H, Vergote I, et al. Terms, definitions and measurements to describe the sonographic features of adnexal tumors: a consensus opinion from the international ovarian tumor analysis group. *Ultrasound Obstet Gynecol* (2000) 16:500–5. doi: 10.1046/j.1469-0705.2000.00287.x

22. Timmerman D, Testa AC, Bourne T, Ameye L, Jurkovic D, Holsbeke CV, et al. Simple ultrasound-based rules for the diagnosis of ovarian cancer. *Ultrasound Obstet Gynecol* (2008) 31:681–90. doi: 10.1002/uog.5365

23. Amor F, Vaccaro H, Alcázar JL, León M, Craig JM, Martinez J. Gynecologic imaging reporting and data system: a new proposal for classifying adnexal masses on the basis of sonographic findings. *J Ultrasound Med* (2009) 28:285–91. doi: 10.7863/jum.2009.28.3.285

24. Andreotti RF, Timmerman D, Benacerraf BR, Bennett G, Bourne T, Brown DL, et al. Ovarian-adnexal reporting lexicon for ultrasound: A white paper of the ACR ovarian-adnexal reporting and data system committee. *J Am Coll Radiol* (2018) 15:1415–29. doi: 10.1016/j.jacr.2018.07.004

25. Cao L, Wei M, Liu Y, Fu J, Zhang H, Huang J, et al. Validation of American college of radiology ovarian-adnexal reporting and data system ultrasound (O-RADS US): analysis on 1054 adnexal masses. *Gynecol Oncol* (2021) 162:107–12. doi: 10.1016/j.ygyno.2021.04.031

26. Testa AC, Timmerman D, Belle VV, Fruscella E, Holsbeke CV, Savelli L, et al. Intravenous contrast ultrasound examination using contrast-tuned imaging (CnTI) and the contrast medium SonoVue for discrimination between benign and

malignant adnexal masses with solid. *Ultrasound Obstet Gynecol* (2009) 34:699–710. doi: 10.1002/uog.7464

27. Harris AL. Antiangiogenesis for cancer therapy. *Lancet* (1997) 349: suppl 2: SII13–5. doi: 10.1016/s0140-6736(97)90014-3

28. Shubik P. Vascularization of tumors: a review. *J Cancer Res Clin Oncol* (1982) 103:211–26. doi: 10.1007/BF00409698

29. Li S, Huang P, Wang Z, Huang F, Zheng Z, Yang Y, et al. The relationship between enhanced intensity and microvessel density of gastric carcinoma using double contrast-enhanced ultrasonography. *Ultrasound Med Biol* (2009) 35:1086–91. doi: 10.1016/j.ultrasmedbio.2009.03.010

30. Sconfienza LM, Perrone N, Delnevo A, Lacelli F, Murolo C, Gandolfo N, et al. Diagnositic value of contrast-enhanced ultrasonogrphy in the characterization of ovarian tumors. *J Ultrasound.* (2010) 13:9–15. doi: 10.1016/j.jus.2009.09.007

31. Kazerooni AF, Malek M, Haghighatkhah H, Parviz S, Nabil M, Torbati L, et al. Semiquantitative dynamic contrast-enhanced MRI for accurate classification of complex adnexal masses. *J Magn Reson Imaging* (2017) 45:418–27. doi: 10.1002/jmri.25359

32. Ordén MR, Gudmundsson S, Kirkinen P. Contrast-enhanced sonography in the examination of benign and malignant adnexal masses. *J Ultrasound Med* (2000) 19:783–8. doi: 10.7863/jum.2000.19.11.783

33. Deng S, Jiang Q, Wang Y, Lu X, Zahang Y. Relationship between quantitative contrast-enchanced ultrasonography parameters and angiogenesis in primary small hepatocellular carcinoma: A retrospective study. *Medicine (Baltimore)* (2021) 100:e26489. doi: 10.1097/MD.0000000000026489

frontiers | Frontiers in Oncology

TYPE Original Research
PUBLISHED 22 March 2023
DOI 10.3389/fonc.2023.1083216

OPEN ACCESS

EDITED BY
Abhishek Mahajan,
The Clatterbridge Cancer Centre,
United Kingdom

REVIEWED BY
Ujjwal Raghunandan Baid,
Shri Guru Gobind Singhji Institute of Engineering and Technology, India
Carole Sudre,
University College London,
United Kingdom

*CORRESPONDENCE
Weihua Liao
ouwenliao@163.com

†These authors have contributed equally to this work

SPECIALTY SECTION
This article was submitted to Cancer Imaging and Image-directed Interventions, a section of the journal Frontiers in Oncology

RECEIVED 28 October 2022
ACCEPTED 07 March 2023
PUBLISHED 22 March 2023

CITATION
You W, Mao Y, Jiao X, Wang D, Liu J, Lei P and Liao W (2023) The combination of radiomics features and VASARI standard to predict glioma grade. *Front. Oncol.* 13:1083216. doi: 10.3389/fonc.2023.1083216

The combination of radiomics features and VASARI standard to predict glioma grade

Wei You[1†], Yitao Mao[1†], Xiao Jiao[1], Dongcui Wang[1], Jianling Liu[1], Peng Lei[1] and Weihua Liao[1,2,3,4*]

[1]Department of Radiology, Xiangya Hospital, Central South University, Changsha, China, [2]National Engineering Research Center of Personalized Diagnostic and Therapeutic Technology, Xiangya Hospital, Central South University, Changsha, China, [3]National Clinical Research Center for Geriatric Disorders, Xiangya Hospital, Central South University, Changsha, China, [4]Molecular Imaging Research Center, Central South University, Changsha, China

Background and Purpose: Radiomics features and The Visually AcceSAble Rembrandt Images (VASARI) standard appear to be quantitative and qualitative evaluations utilized to determine glioma grade. This study developed a preoperative model to predict glioma grade and improve the efficacy of clinical strategies by combining these two assessment methods.

Materials and Methods: Patients diagnosed with glioma between March 2017 and September 2018 who underwent surgery and histopathology were enrolled in this study. A total of 3840 radiomic features were calculated; however, using the least absolute shrinkage and selection operator (LASSO) method, only 16 features were chosen to generate a radiomic signature. Three predictive models were developed using radiomic features and VASARI standard. The performance and validity of models were evaluated using decision curve analysis and 10-fold nested cross-validation.

Results: Our study included 102 patients: 35 with low-grade glioma (LGG) and 67 with high-grade glioma (HGG). Model 1 utilized both radiomics and the VASARI standard, which included radiomic signatures, proportion of edema, and deep white matter invasion. Models 2 and 3 were constructed with radiomics or VASARI, respectively, with an area under the receiver operating characteristic curve (AUC) of 0.937 and 0.831, respectively, which was less than that of Model 1, with an AUC of 0.966.

Conclusion: The combination of radiomics features and the VASARI standard is a robust model for predicting glioma grades.

KEYWORDS

nomogram, glioma grade, radiomics, VASARI, high-grade glioma, pre-operation diagnosis

Introduction

Glioma, one of the most common central nervous system tumors (CNS), has a five-year survival rate of less than 5% and is widely recognized as a highly malignant tumor (1, 2). According to the WHO classification of brain tumors, pathology and clinical practices typically divide gliomas into low and high grades (3, 4). The prognosis of glioma patients would be improved by timely and accurate preoperative diagnosis (2). The primary treatment for gliomas is surgical resection followed by radiotherapy or chemotherapy (5). As a non-invasive technique, MRI will likely be utilized in the clinical setting to detect glioma and its clinical grade early and reduce misdiagnosis (6). When developing clinical strategies for patients suspected of having glioma, conventional MRI sequences, such as T1-weighted, contrast-enhanced T1-weighted MR images, T2-weighted, and fluid-attenuated inversion recovery (7) are frequently employed.

Recent neoplasia research (8–10) has extensively used radiomics as a promising method for evaluating tumor characteristics. This semiautomatic method can quantify the high-dimensional imaging features of glioma by extracting the radiomic features from conventional medical images and combining these features with other clinical information to design a machine-learning model, which will improve the accuracy and efficiency of clinical decisions (11–14). In contrast to the tumor phenotype and microenvironment provided by clinical reports and histopathology, this information is based on intensity, shape, size, volume, and texture (15). Park et al. (16) extracted radiomic features from multiparametric MRI to predict LGGs and a subgroup of LGGs without enhancement. In the internal validation set, the area under the receiver operating characteristic curve (AUC) was 0.85 and 0.82, indicating the best performance. Mao et al. (17) predicted glioma grade using an artificial neural network model based on image data. The model had a means accuracy of 90.32%, sensitivity of 87.86%, and specificity of 92.49%. With the exponential growth of medical image analysis, radiomics is increasingly used to detect cancer, evaluate prognosis and treatment, and monitor tumor status. Glioma grade has been the subject of much research; however, it is still of utmost importance because of its relevance to clinical treatment and pre-surgical strategies.

Visually AcceSAble Rembrandt Images (VASARI) features of glioma have 25 qualitative features for human gliomas in particular (18). On standard pre- and post-contrast-enhanced MRI, these features represent common characteristics of primary cerebral neoplasia and are described using standardized terminology. Chen et al. (19) combined radiomics with qualitative features (VASARI annotations and T2-FLAIR mismatch signs) to predict molecular subtypes in patients with lower-grade glioma. The AUC of the model containing radiomics and qualitative features was higher than the AUC of the model containing radiomics alone, with 0.8623 versus 0.6557. Cao et al. (20) demonstrated that the AUC of the IDH1 mutation predictive model with VASARI features alone was approximately 0.827 in the training group; however, in the fusion model with optimal VASARI and radiomics features, the AUC improved to 0.879, with an accuracy of 0.771, exceeding that of the model with VASARI alone (approximately 0.726). Therefore, a fusion model combining radiomics and VASARI features would better predict glioma grade than either model alone.

Our study aimed to determine the impact of VASARI features on the basics of radiomics and whether the introduction of VASARI features adds predictive value to glioma grade. The research was conducted exclusively at Xiangya Hospital.

Materials and methods

Patients

The Medical Ethics Committee of our institution provided Ethical approval, followed by the informed consent principle. From March 2017 to September 2018, 102 patients who met the following criteria were enrolled in this study: pathologic diagnosis of glioma without prior treatment and MR data free of severe artifacts. Medical records were extracted from an institutional database. Our institutional Ethics Committee and Review Board approved this retrospective study. Written informed consent was waived owing to the retrospective nature of this investigation. Additional information regarding the patient recruitment procedure and exclusion criteria is presented in Figure 1.

Pathological re-assessment

The paraffin-embedded surgical specimens were re-assessed by two experienced pathologists at our institution (with over 10 and 15 years of experience, respectively) in tumor imaging diagnosis of the central nervous system (CNS), using the 2021 WHO classification of CNS tumors (4).

Image acquisition

Untreated glioma patients underwent MRI using a 3.0-T imaging unit (Siemens, Erlangen, Germany) and a 64-channel receiver head coil. In the transverse plane, spoiled gradient-recalled images were used to acquire T1-weighted anatomic images (T1WI), T2-weighted anatomic images (T2WI), and fluid-attenuated inversion recovery (FLAIR). Dynamic gadodiamide (SFDA approval number J20100063, produced by GE Healthcare Ireland) high-resolution, three-dimensional magnetization-prepared rapid acquisition with gradient-echo sequences (3D-T1-MPRAGE) were used to perform 10 ml contrast material-enhanced MRI on patients.

Image segmentation

Segmentation of regions of interest (ROI) was performed on the T1WI, T2WI, FLAIR, and contrast-enhanced 3D-T1-MPRAGE images. Using ITK-SNAP (21) (http://www.itksnap.org), two

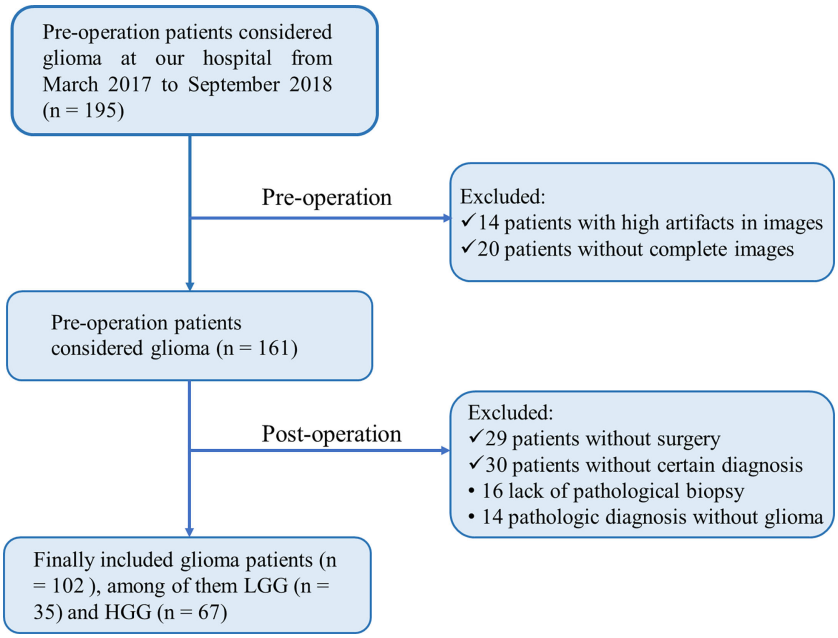

FIGURE 1
Flowchart of inclusion and exclusion process for patients to be enrolled.

experienced radiologists (reader 1 and 2, with more than ten years of experience in neuroimaging) manually delineated the tumor boundaries slice-by-slice. The two radiologists were blinded to the patient information, including radiological and clinicopathological data. Fifty patients were randomly selected to evaluate the inter-observer (reader 1 versus reader 2) and intra-observer (reader 1 twice at intervals of four weeks) correlation coefficient (ICC). Generally, consistency was indicated by an ICC greater than 0.75. For the randomly selected 50 patients, the first segmentation of reader 1 was used. The ROI contouring work of the remaining patients was completed only by reader 1. The tumor ROIs were manually delineated on T1WI, T2WI, FLAIR, and contrast-enhanced 3D-T1-MPRAGE images, and only the axial direction was involved in ROI contouring.

Radiomic feature selection

The radiomic features were extracted using PyRadiomics in Python (version. 3.7, https://www.python.org/). Extracted features included Shape, first-order intensity statistics, Gray Level Co-occurrence Matrix, Gray Level Size Zone Matrix, Gray Level Run Length Matrix, Gray Level Dependence Matrix, logarithm, and Wavelet. Features with ICC values less than or equal to 0.75 were supposed to be excluded from further analyses. Using the least absolute shrinkage and selection operator (LASSO) method (22), the most relevant radiomics features associated with glioma grading were determined. *Z*-score normalization was used as a preprocessing step for LASSO. Then, the weighted average method with the respective LASSO coefficients was used to linearly combine the most relevant features into a single index called radiomic signature (Rad-score). This Rad-score was deemed an independent variable, along with other image-related VASARI variables.

Clinical feature selection

Univariate and multivariate logistic regression were used to select the most relevant predictors (including Rad-score and the VASARI features) for high-grade glioma, with a p-value of 0.10 (for univariate logistic regression) and 0.05 (for multivariate logistic regression) as the significance level, respectively. In this study, logistic regression was utilized because its outputs were probabilities, which allowed subsequent calibration analysis, nomogram plotting, and decision curve analysis, which are required to comprehensively assess the performance of a predictive model. Two neuroradiologists assessed all VASARI imaging features on standard pre- and post-contrast-enhanced MRI with 8 and 12 years of experience on the open-source picture archiving and communication system (PACS) workstation. Disagreements were addressed through discussions.

Model assessment and validation

In this study, we assessed four aspects of a predictive model, *i.e.*, robustness, discrimination, accuracy, and clinical applicability. The robustness of the model was evaluated by 10-fold nested cross-validation (with an outer loop of ten folds for test cohorts and an

inner loop of nine folds for training and validation cohorts). The folds in this cross-validation were stratified, that is, similarly distributed for the positive and negative samples.

The area under the curve (AUC) of the receiver operating characteristic (ROC) curves was used as the performance index. The standard deviation of the ten AUCs was then calculated to assess the robustness (stability) of the model. The discrimination performance of the model was evaluated solely based on the AUC itself. The calibration curve assessed the accuracy of the model, which indicated the degree of agreement between the observed probabilities and model-predicted probabilities using a bootstrap method (1000 resampling iterations). The Hosmer-Lemeshow test was conducted to determine if the level of agreement was statistically significant (23). Clinical applicability was evaluated using a decision curve analysis, which quantitatively suggested whether the model would result in a net benefit for those patients who use it in clinical practice compared to arbitrary decisions (*i.e.*, treat all patients or treat none) (24).

Statistical analysis

All statistical analyses were conducted with R software version 4.0.2 (http://www.Rproject.org) using the following packages: "glmnet," "rms," "pROC," "rmda," and "broom." The "glmnet" was used to execute the LASSO method. A nomogram was created using the "rms" function. The AUCs of different ROC curves were compared using the deLong test (25) in "pROC" package. Calibration was assessed using R software, with the "calibrate" function in R package "rms". The Hosmer-Lemeshow test (23) was used to determine the significance of the calibration curve. All statistical tests were two-sided, and the *p*-value of statistical significance was set to 0.05, except for the univariate logistic regression used to screen out potential variables, for which the *p*-value was set to 0.10. The workflow of this study is illustrated in Figure 2.

Results

Patient characteristics

Our study included 102 patients, with 37 in LGG group (I/II 2/35) and 65 in HGG group (III/IV, 26/39). Table 1 summarizes the VASARI features, Rad-score, and age and gender ratio for LGG and HGG groups.

Radiomic feature extraction

A total of 3840 features from T1WI, T2WI, FLAIR, and contrast-enhanced 3D-T1-MPRAGE images were extracted using Pyradiomics, including shape (14 features), first-order intensity statistics (18 features), Gray Level Co-occurrence Matrix (22 features), Gray Level Size Zone Matrix (16 features), Gray Level Run Length Matrix (16 features), Gray Level Dependence Matrix (14 features), logarithm (172 features), and wavelet (688 features). All features had high ICCs (0.8491 0.9807). Using LASSO logistic regression on the entire cohort, only 16 features survived based on the minimum criterion; the remaining features were omitted because their coefficients were compressed to zero per the LASSO minimum criterion (Figure 2, Feature Selection). The remaining 16

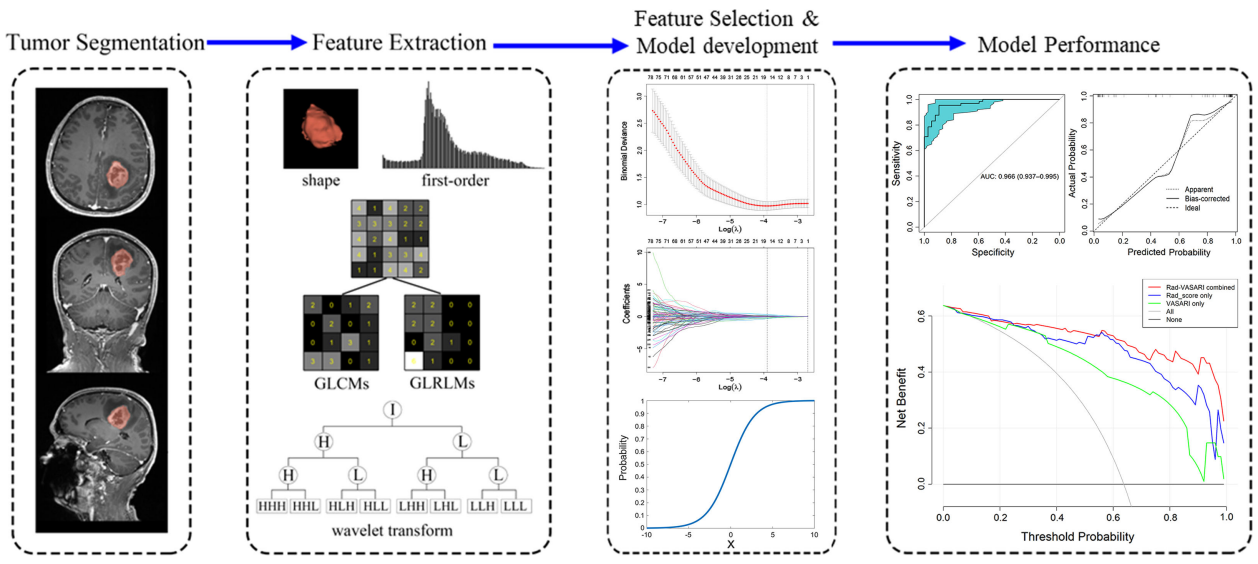

FIGURE 2
Workflow for the method section. Firstly, tumor segmentation was depicted on the MRI images. Secondly, five categories of radiomic features were extracted from the tumor, including shape, first-order, gray level co-occurrence matrix (GLCM), gray level run-length matrix (GLRLM), and wavelet transform. Thirdly, the least absolute shrinkage and selection operator (LASSO) method was used on feature selection, with model development shown. Finally, the ROC, calibration curve and decision curve analysis was used to assess the model performance.

TABLE 1 The results of binary logistic regression analysis for predictive models.

Factors	Univariate analysis			Multivariate analysis		
	OR	95% CI	*p* value	OR	95% CI	*p* value
Gender	0.957	0.688-1.331	0.882			
Age	1.080	0.659-1.770	0.908			
VASARI						
F1	1.036	0.857-1.252	0.922			
F2	1.541	0.926-2.565	0.465			
F3	0.916	0.645-1.301	0.787			
F4	1.255	0.831-1.895	0.652			
F5	0.946	0.722-1.240	0.897			
F6	1.178	0.885-1.568	0.736			
F7	0.933	0.691-1.260	0.807			
F8	2.036	1.029-4.029	0.046	1.136	0.986-1.309	0.088
F9	1.252	0.836-1.875	0.688			
F10	0.853	0.492-1.479	0.162			
F11	1.461	0.896-2.382	0.507			
F12	0.952	0.757-1.197	0.776			
F13	1.281	0.853-1.924	0.439			
F14	3.638	1.088-12.165	0.029	2.152	1.029-4.501	0.036
F15	1.109	0.905-1.371	0.786			
F16	1.266	0.932-1.720	0.409			
F17	0.899	0.673-1.201	0.533			
F18	1.426	0.811-2.507	0.427			
F19	1.058	0.957-1.170	0.456			
F20	1.436	0.913-2.259	0.221			
F21	3.895	1.120-13.546	0.011	2.487	1.094-5.654	0.026
F22	0.895	0.616-1.300	0.436			
F23	1.127	0.882-1.440	0.649			
F24	2.587	1.031-6.491	0.035	1.195	0.992-1.440	0.062
F25	1.225	0.894-1.679	0.587			
Rad-score	13.661	3.688-50.603	<0.001	18.604	4.257-81.303	<0.001

CI, confidence interval; OR, odds ratio. VASARI, The Visually AcceSAble Rembrandt Images. F1: Tumor Location. F2: Side of Tumor Epicenter, F3: Eloquent Brain. F4: Enhancement Quality. F5: Proportion Enhancing. F6: Proportion nCET. F7: Proportion Necrosis. F8: Cyst(s). F9: Multifocal or Multicentric. F10: T1/FLAIR RATIO. F11: Thickness of enhancing margin. F12: Definition of the enhancing margin. F13: Definition of the non -enhancing margin. F14: Proportion of Edema. F15: Edema Crosses Midline. F16: Hemorrhage. F17: Diffusion. F18: Pial invasion. F19: Ependymal invasion. F20: Cortical involvement. F21: Deep White Matter Invasion. F22: nCET tumor Crosses Midline. F23: Enhancing tumor Crosses Midline. F24: Satellites. F25: Calvarial remodeling.

features are listed in Table 2. The Rad-score is then calculated as the linear sum of these 16 non-zero coefficient weighted features (26).

Construction of predictive models

The results of univariate and multivariate logistic regression analyses are presented in Table 1. As final predictors, three variables remained: edema proportion, deep white matter invasion, and Rad-score. Note that the percentages of edema and deep white matter invasion are VASARI features. Based on the outcomes of logistic regression, three predictive models were developed. Model 1 was constructed with all three final predictors; Model 2 was constructed with Rad-score alone, and Model 3 was constructed with the remaining two VASARI variables after Rad-score was omitted.

TABLE 2 Selected radiomic features and its coefficients.

	Selected features	Coefficient
Contrast-enhanced 3D-T1-MPRAGE	original_firstorder_MeanAbsoluteDeviation	0.008376
	original_firstorder_Mean	-0.21765
	logsigma_3_0_mm_3D_glcm_Correlation	0.014965
	log_sigma_5_0_mm_3D_glszm_GrayLevelNonUniformityNormalized	0.163822
	log_sigma_5_0_mm_3D_glszm_SmallAreaLowGrayLevelEmphasis	0.354926
	wavelet_LHL_gldm_DependenceVariance	-0.02259
	wavelet_LHH_gldm_LargeDependenceHighGrayLevelEmphasis	0.061954
	wavelet_HLL_glcm_JointEntropy	-0.1377
	wavelet-LLL_gldm_SmallDependenceLowGrayLevelEmphasis	0.069576
T1WI	log-sigma-5-0-mm-3D_glcm_SumEntropy	0.176542
	wavelet-HHL_glcm_JointAverage	0.000975
T2WI	log-sigma-5-0-mm-3D_gldm_LowGrayLevelEmphasis	0.027959
	wavelet-LHH_glrlm_LongRunEmphasis	-0.26765
FLAIR	log-sigma-5-0-mm-3D_gldm_GrayLevelVariance	-0.036765
	wavelet-LHL_gldm_SmallDependenceLowGrayLevelEmphasis	-0.316588
	wavelet-HLL_firstorder_Kurtosis	0.117975

Model performance

Robustness

The 10-fold nested cross-validation was performed to assess the performance stability of the model. Figure 3 depicts the performance of the three models in 10-fold nested cross-validation. The ten iterations for the test cohort had standard deviations of 0.0362, 0.0458, and 0.0355 for models 1, 2, and 3, respectively. Thus, all three models were relatively stable throughout the ten repetitions in terms of AUC.

Discrimination

ROC curve indicates the discriminatory ability of a diagnostic/predictive model. Figure 4 displays the ROC curve analyses of the three models. Model 1, Model 2, and Model 3 had AUCs of these ROC curves for predicting glioma grade of 0.966 (95% CI: 0.937–0.995), 0.937 (95% CI: 0.889–0.985), and 0.831 (95% CI: 0.745–0.917), respectively. Table 3 displays the remaining indices of ROC curves, including the sensitivity, specificity, positive predictive value, negative predictive value, and accuracy.

Accuracy

The accuracy refers to the consistency between the predicted and observed values, which is reflected in the calibration curve. The calibration curves of the three models demonstrated a good agreement between the predicted and observed probabilities of HGG (Figure 5). All these curves failed to reach statistical significance according to the Hosmer-Lemeshow test (all $p > 0.05$), indicating that there is good agreement with the ideal diagonal line (i.e., good fitting between the predicted and the observed HGG

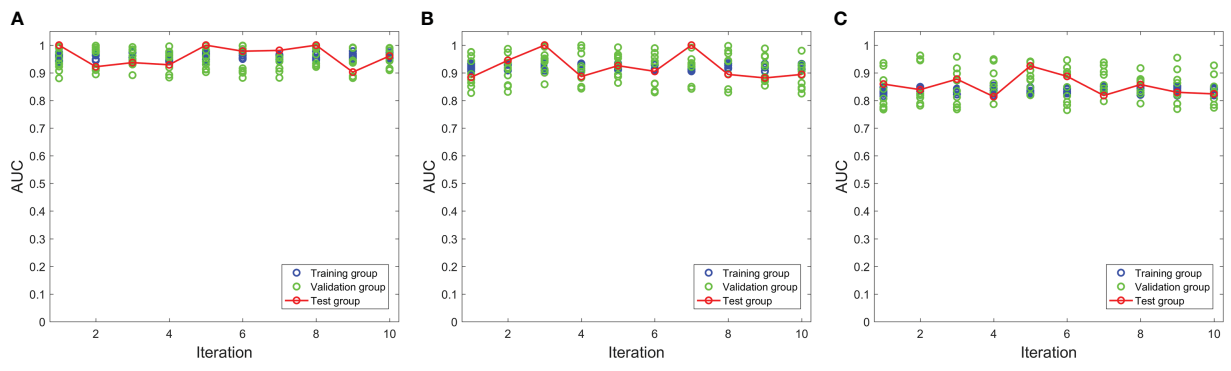

FIGURE 3
The performances of three models in the nested cross-validation. **(A–C)** represent model 1, model 2 and model 3 respectively.

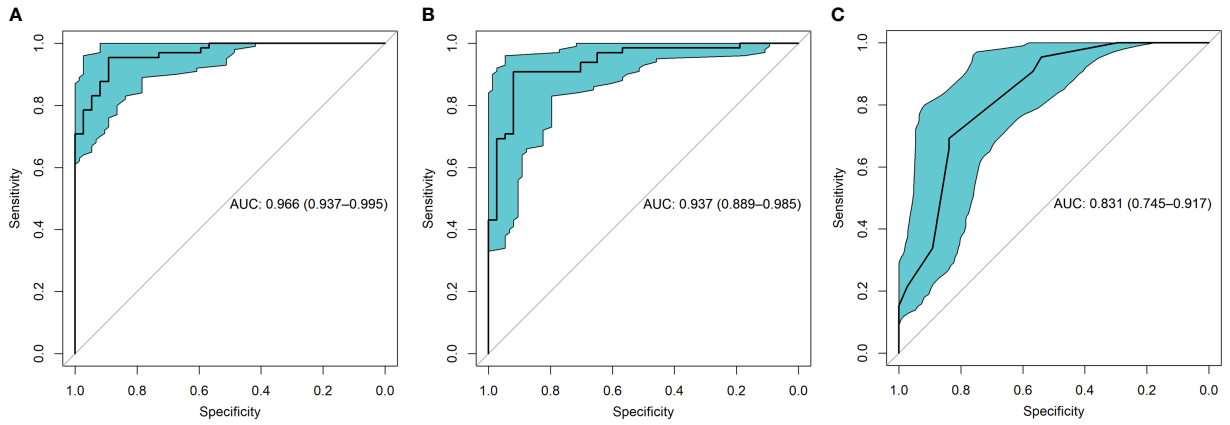

FIGURE 4
The receiver operating characteristic (ROC) curves for the three models were shown. **(A)** presented the ROC of model 1 which combined radiomic and VASARI features, with the area under the curve (AUC) of 0.966. **(B)** displayed the ROC of model 2 including radiomic alone, with the AUC of 0.937. **(C)** presented the ROC of model 3 including VASARI features alone, with the AUC of 0.831.

probability). Because all three calibration curves were statistically well-fitted and exhibited no discernible deviation from the ideal line, we could not select the best-fitted curve.

Clinical applicability

Figure 6 depicts the decision curves of the models. These models are separated from the "treat all" or "treat none" lines, indicating that they may have clinical utility. However, Model 1 appears to have the highest position, indicating that using Model 1 to grade glioma would provide patients with the greatest net benefit compared with Models 2 and 3. Regarding glioma grading, our results indicate that Model 1 (combining radiomics and VASARI variables) is the optimal model among the three models and could be the preferable model for regular clinical practice. Figure 7 depicts the nomogram of model 1 to facilitate its clinical application.

Discussion

In this study, we developed a predictive model for glioma grade before surgery and histopathology. This model, constructed using radiomics and two VASARI features, performed well in distinguishing LGG from HGG patients. The performance of the model was comprehensively evaluated based on its discrimination, calibration, and clinical utility. The 10-fold nested cross-validation also confirmed the stability and robustness of the model. In addition, our study suggests that radiomics and VASARI could be used to independently predict glioma grade.

With only 102 patients enrolled, the conventional method of dividing the samples into training and testing cohorts was insufficient to evaluate the robustness of our model. Our study evaluated the robustness of the predictive models using 10-fold cross-validation. There have been published radiomics studies with validation cohorts as small as 20–30 patients, making the performance of such models questionable owing to the risks of overfitting and high instability (27). Meanwhile, the external validation cohort sample size should ideally be between 25%–40% of the training cohort (27), although it is common for published studies to violate this requirement. Wang et al. (28) recruited 85 patients and divided them into a training cohort (n = 56) and a validation cohort (n = 29) to develop a radiomics nomogram for glioma grade prediction. The authors discovered that the radiomics nomogram had an excellent C-index of 0.971 in the training cohort and 0.961 in the validation cohort. Given the limited number of

TABLE 3 Performance of the three predictive models.

Metrics	Model 1 (Rad–VASARI combined)	Model 2 (Rad_score only)	Model 3 (VASARI only)
AUC	0.966	0.937	0.831
Accuracy	0.931	0.912	0.761
Sensitivity	0.954	0.908	0.776
Specificity	0.892	0.919	0.723
PPV	0.939	0.952	0.681
NPV	0.917	0.850	0.596

AUC: area under the receiver operating characteristic curve; PPV: positive predictive value; NPV: negative predictive value.
The AUC cut-off was determined based on Youden index maximization criterion. Specifically, Youden index = true positive rate (sensitivity) – false positive rate (1-specificity). In the ROC curve, a series of Youden indices was calculated, then the maximum Youden index of this series was picked out and the corresponding value of the test variable which matched this maximum Youden index was the cut-off value.

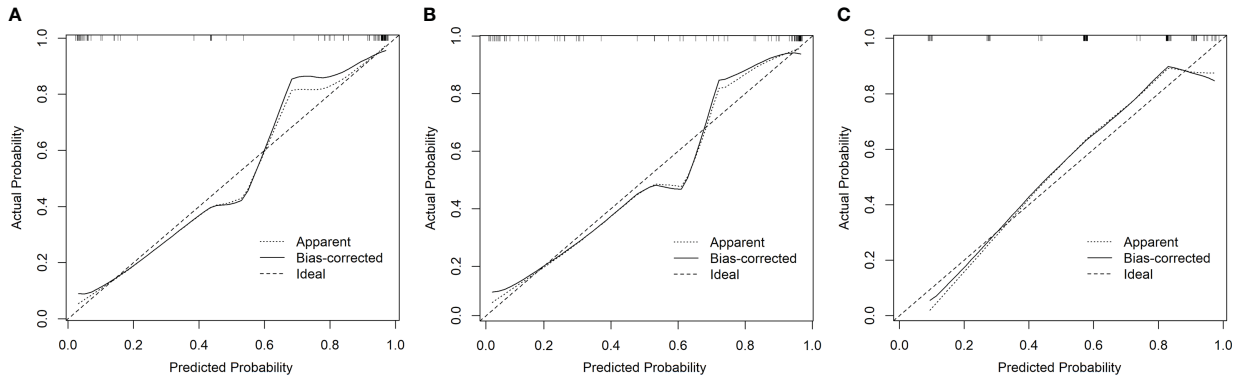

FIGURE 5
The calibration curves of the three models showed good consistency between the predicted probability of HGG and the observed probability of HGG (**A** model 1, **B** model 2, and **C** model 3).

samples and the disparity between HGG and LGG, separating the data into training and validation datasets would further reduce the sample size, resulting in highly unstable performance. For a limited cohort, nested cross-validation could be a preferable method to assess whether the selected features are stable across the different folds and to avoid circularity bias while measuring prediction performance (29–31). Our study provided additional information on nested cross-validation from the dividing cohort to AUC scores, enhancing the credibility and confirming the robustness of our models by presenting a transparently detailed procedure.

Regarding the clinical features we selected, the proportion of edema and deep white matter invasion were two key indicators of the malignant behavior of glioma. First, the incidence of peritumoral edema (PTE) is significantly associated with glioma morbidity and mortality. According to previous studies, the average or overall survival of patients with significant edema (> 10 mm) was reduced by more than half compared to those with minor edema (32, 33). In a previous study, Wu et al. (33) hypothesized that edema shape resulting from the extent of edema also influences patient survival. Patients with an irregular edema shape (such as a radial or finger-like shape) tended to have a worse prognosis than those with round edema. In addition, Jeong et al. (34) found that amplification of the epidermal growth factor receptor (EGFR) plays a significant role in the formation of PTE and causes the volume of edema to increase, thereby negatively affecting overall survival. Some studies have indicated that HMGB1 suppression and LINC00665 expression are closely associated with PTE (35, 36).

The deep white matter invasion that we selected to represent malignant glioma was also significant in a previous study. Tumor location, a crucial parameter for patient care, correlates strongly with molecular subtypes, histopathological characteristics, clinical presentation and surgery, surgical management, glioma malignancy level, and prognosis (37–42). Roux et al. (38) presented probabilistic maps based on clinical presentations and survival analysis. Their results demonstrated that tumors in the deep location and eloquent brain regions were more likely to be associated with poor prognosis and shorter overall survival than those in the superficial location distant from the eloquent area.

Invasion along the white matter tracts is an important clinicopathological characteristic of gliomas, indicative of poor therapeutic prognosis (37, 43). Our study utilized the VASARI standard and combined it with contrast-enhanced 3D-T1-MPRAGE radiomics for analysis, which should be superior to using VASARI alone because radiomics analysis should be more objective, accurate, and

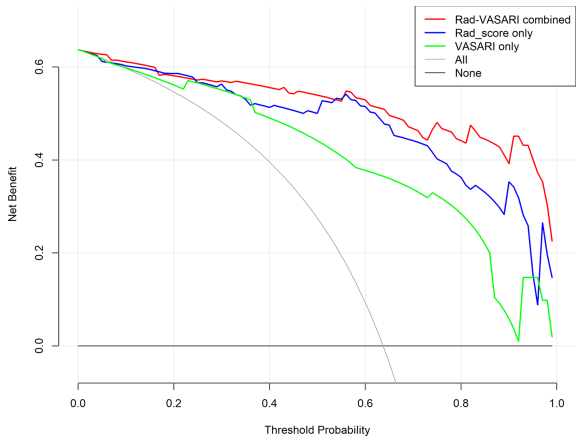

FIGURE 6
Decision curves for the three models. Red, combined radiomic and VASARI features model; blue, radiomic model; green, VASARI features model.

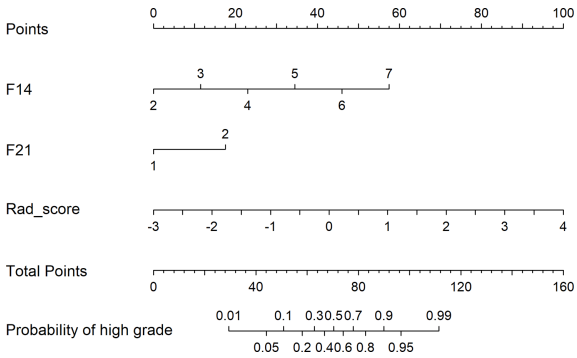

FIGURE 7
The nomogram of Model 1 combined radiomic and VASARI features.

reliable as a quantitative method. As a non-invasive diagnostic method, radiomic features extracted from images reflect cellular behaviors in the intratumoral microenvironment, which correlates with the prognosis of the tumor (44–46). Heterogeneity, an important parameter of the clinicopathological characteristics of gliomas, is associated with the degree of malignant behavior (47). For instance, tumors with more aggressive behavior may indicate higher heterogeneity, whereas tumors with more favorable behavior tend to exhibit less heterogeneity. Our study filtered kurtosis and entropy-related radiomic features using the LASSO method, indicating greater heterogeneity. According to a previous study (48), kurtosis and entropy are significant indicators of glioma heterogeneity. Spatial and temporal vascular anomalies, which result from hypoxia and acidosis within the tumor caused by angiogenesis, are primary contributors to tumor heterogeneity (47). The models in our study were consistent with those in previous research, suggesting that kurtosis and entropy reflect greater heterogeneity and a worse prognosis. Among the most relevant 16 radiomic features (Table 2), nine features were derived from contrast-enhanced 3D-T1-MPRAGE, two were derived from T1WI, two were derived from T2WI, and three were derived from FLAIR, indicating that 3D-T1-MPRAGE could be the essential sequence and exerted the largest contribution for identifying the glioma grade.

Our study had several limitations. First, the small sample size was insufficient to maintain the stability of the results. Therefore, we utilized nested cross-validation to confirm the validity of the predictive model. Second, our study lacked the molecular subtype for the samples, while the molecular phenotype is crucial for the prognosis of glioma (49, 50). Future medical imaging research should focus on the molecular characteristics of glioma, which could aid in more accurate subtype prediction and the development of individual treatment strategies.

Conclusion

This study demonstrates the significance of a predictive model combining radiomics features with VASARI standard for glioma grade analysis before surgical intervention. This non-invasive imaging-centered strategy would aid in advancing clinical research and guiding individualized treatment for patients with high-grade glioma.

Data availability statement

The raw data supporting the conclusions of this article will be made available by the authors, without undue reservation.

Ethics statement

Written informed consent was obtained from the individual(s) for the publication of any potentially identifiable images or data included in this article.

Author contributions

WY, YM, XJ, PL, and WL contributed to conception and design of the study. WY and XJ organized the database, finished image segmentation and evaluated clinical features. DW extracted radiomic features. JL was responsible to the data collection in prior. WY and YM processed the pictures and tables, and performed the statistical analysis. PL also joined the pictures processing. WY wrote the first draft of the manuscript. YM wrote sections of the manuscript. All authors contributed to manuscript revision, read, and approved the submitted version.

Conflict of interest

The authors declare that the research was conducted in the absence of any commercial or financial relationships that could be construed as a potential conflict of interest.

Publisher's note

References

1. Rafique Z, Awan MW, Iqbal S, Usmani NN, Kamal MM, Arshad W, et al. Diagnostic accuracy of magnetic resonance spectroscopy in predicting the grade of glioma keeping histopathology as the gold standard. *Cureus* (2022) 14(2):1–10. doi: 10.7759/cureus.22056

2. Munir S, Khan SA, Hanif H, Khan M. Diagnostic accuracy of magnetic resonance imaging in detection of intra-axial gliomas. *Pak J Med Sci* (2021) 37(1):125–30. doi: 10.12669/pjms.37.1.2489

3. Louis DN, Perry A, Reifenberger G, von Deimling A, Figarella-Branger D, Cavenee WK, et al. The 2016 world health organization classification of tumors of the central nervous system: A summary. *Acta Neuropathol* (2016) 131(6):803–20. doi: 10.1007/s00401-016-1545-1

4. Louis DN, Perry A, Wesseling P, Brat DJ, Cree IA, Figarella-Branger D, et al. The 2021 who classification of tumors of the central nervous system: A summary. *Neuro Oncol* (2021) 23(8):1231–51. doi: 10.1093/neuonc/noab106

5. Yang K, Wu Z, Zhang H, Zhang N, Wu W, Wang Z, et al. Glioma targeted therapy: Insight into future of molecular approaches. *Mol Cancer* (2022) 21(1):1–32. doi: 10.1186/s12943-022-01513-z

6. Ujjwal Baid SG, Mohan S, Bilello M, Calabrese E, Colak E, Kalpathy-Cramer J, et al. The rsna-Asnr-Miccal brats 2021 benchmark on brain tumor segmentation and radiogenomic classification. *Comput Vision Pattern Recognition* (2021) 1–19. doi: 10.48550/arXiv.2107.02314

7. Nakamoto T, Takahashi W, Haga A, Takahashi S, Kiryu S, Nawa K, et al. Prediction of malignant glioma grades using contrast-enhanced T1-weighted and T2-weighted magnetic resonance images based on a radiomic analysis. *Sci Rep* (2019) 9 (1):1–12. doi: 10.1038/s41598-019-55922-0

8. Kumar V, Gu Y, Basu S, Berglund A, Eschrich SA, Schabath MB, et al. Radiomics: The process and the challenges. *Magn Reson Imaging* (2012) 30(9):1234–48. doi: 10.1016/j.mri.2012.06.010

9. Lambin P, Leijenaar RTH, Deist TM, Peerlings J, de Jong EEC, van Timmeren J, et al. Radiomics: The bridge between medical imaging and personalized medicine. *Nat Rev Clin Oncol* (2017) 14(12):749–62. doi: 10.1038/nrclinonc.2017.141

10. Baid U, Rane SU, Talbar S, Gupta S, Thakur MH, Moiyadi A, et al. Overall survival prediction in glioblastoma with radiomic features using machine learning. *Front Comput Neurosci* (2020) 14:61. doi: 10.3389/fncom.2020.00061

11. Wang J, Yi X, Fu Y, Pang P, Deng H, Tang H, et al. Preoperative magnetic resonance imaging radiomics for predicting early recurrence of glioblastoma. *Front Oncol* (2021) 11:769188. doi: 10.3389/fonc.2021.769188

12. Yang F, Xie Y, Tang J, Liu B, Luo Y, He Q, et al. Uncovering a distinct gene signature in endothelial cells associated with contrast enhancement in glioblastoma. *Front Oncol* (2021) 11:683367. doi: 10.3389/fonc.2021.683367

13. Choi YS, Ahn SS, Kim DW, Chang JH, Kang S-G, Kim EH, et al. Incremental prognostic value of adc histogram analysis over mgmt promoter methylation status in patients with glioblastoma. *Radiology* (2016) 281(1):175–84. doi: 10.1148/radiol.2016151913

14. Li Y, Ammari S, Lawrance L, Quillent A, Assi T, Lassau N, et al. Radiomics-based method for predicting the glioma subtype as defined by tumor grade, idh mutation, and 1p/19q codeletion. *Cancers (Basel)* (2022) 14(7):1–26. doi: 10.3390/cancers14071778

15. Robert J, Gillies PEK, Hricak H. Radiomics: Images are more than pictures, they are data. *Radiology* (2016) 278(2):563–77. doi: 10.1148/radiol.2015151169

16. Park YW, Choi YS, Ahn SS, Chang JH, Kim SH, Lee SK. Radiomics mri phenotyping with machine learning to predict the grade of lower-grade gliomas: A study focused on nonenhancing tumors. *Korean J Radiol* (2019) 20(9):1381–9. doi: 10.3348/kjr.2018.0814

17. Mao Y, Liao W, Cao D, Zhao L, Wu X, Kong L, et al. An artificial neural network model for glioma grading using image information. *Zhong Nan Da Xue Xue Bao Yi Xue Ban* (2018) 43(12):1315–22. doi: 10.11817/j.issn.1672-7347.2018.12.006

18. Verduin M, Primakov S, Compter I, Woodruff HC, van Kuijk SMJ, Ramaekers BLT, et al. Prognostic and predictive value of integrated qualitative and quantitative magnetic resonance imaging analysis in glioblastoma. *Cancers (Basel)* (2021) 13(4):1–19. doi: 10.3390/cancers13040722

19. Sun C, Fan L, Wang W, Wang W, Liu L, Duan W, et al. Radiomics and qualitative features from multiparametric mri predict molecular subtypes in patients with lower-grade glioma. *Front Oncol* (2021) 11:756828. doi: 10.3389/fonc.2021.756828

20. Park YW, Han K, Ahn SS, Bae S, Choi YS, Chang JH, et al. Prediction of Idh1-mutation and 1p/19q-codeletion status using preoperative Mr imaging phenotypes in lower grade gliomas. *AJNR Am J Neuroradiol* (2018) 39(1):37–42. doi: 10.3174/ajnr.A5421

21. Baid U, Talbar S, Rane S, Gupta S, Thakur MH, Moivadi A, et al. Deep learning radiomics algorithm for gliomas (drag) model: A novel approach using 3d Unet based deep convolutional neural network for predicting survival in gliomas. Brainlesion: Glioma, multiple sclerosis, stroke and traumatic brain injuries. Lecture Notes in Computer Science (2019) 369–79.

22. Sauerbrei W, Royston P, Binder H. Selection of important variables and determination of functional form for continuous predictors in multivariable model building. *Stat Med* (2007) 26(30):5512–28. doi: 10.1002/sim.3148

23. Kramer AA, Zimmerman JE. Assessing the calibration of mortality benchmarks in critical care: The hosmer-lemeshow test revisited. *Crit Care Med* (2007) 35(9):2052–6. doi: 10.1097/01.CCM.0000275267.64078.B0

24. Vickers AJ, Cronin AM, Elkin EB, Gonen M. Extensions to decision curve analysis, a novel method for evaluating diagnostic tests, prediction models and molecular markers. *BMC Med Inform Decis Mak* (2008) 8:1–17. doi: 10.1186/1472-6947-8-53

25. DeLong ER, DeLong DM, Clarke-Pearson DL. Comparing the areas under two or more correlated receiver operating characteristic curves: A nonparametric approach. *Biometrics* (1988) 44(3):837–45. doi: 10.2307/2531595

26. Huang YQ, Liang CH, He L, Tian J, Liang CS, Chen X, et al. Development and validation of a radiomics nomogram for preoperative prediction of lymph node metastasis in colorectal cancer. *J Clin Oncol* (2016) 34(18):2157–64. doi: 10.1200/JCO.2015.65.9128

27. Papanikolaou N, Matos C, Koh DM. How to develop a meaningful radiomic signature for clinical use in oncologic patients. *Cancer Imaging* (2020) 20(1):1–10. doi: 10.1186/s40644-020-00311-4

28. Wang Q, Li Q, Mi R, Ye H, Zhang H, Chen B, et al. Radiomics nomogram building from multiparametric mri to predict grade in patients with glioma: A cohort study. *J Magn Reson Imaging* (2019) 49(3):825–33. doi: 10.1002/jmri.26265

29. Kohavi R ed. A study of cross-validation and bootstrap for accuracy estimation and model selection, in: *International Joint Conference on Artificial Intelligence*. San Francisco, CA, United States: Morgan Kaufmann (1995).

30. Varoquaux G, Raamana PR, Engemann DA, Hoyos-Idrobo A, Schwartz Y, Thirion B. Assessing and tuning brain decoders: Cross-validation, caveats, and guidelines. *Neuroimage* (2017) 145:166–79. doi: 10.1016/j.neuroimage.2016.10.038

31. Fleuren LM, Dam TA, Tonutti M, de Bruin DP, Lalisang RCA, Gommers D, et al. Predictors for extubation failure in COVID-19 patients using a machine learning approach. *Crit Care* (2021) 25(1):448. doi: 10.1186/s13054-021-03864-3

32. Schoenegger K, Oberndorfer S, Wuschitz B, Struhal W, Hainfellner J, Prayer D, et al. Peritumoral edema on mri at initial diagnosis: An independent prognostic factor for glioblastoma? *Eur J Neurol* (2009) 16(7):874–8. doi: 10.1111/j.1468-1331.2009.02613.x

33. Wu CX, Lin GS, Lin ZX, Zhang JD, Chen L, Liu SY, et al. Peritumoral edema on magnetic resonance imaging predicts a poor clinical outcome in malignant glioma. *Oncol Lett* (2015) 10(5):2769–76. doi: 10.3892/ol.2015.3639

34. Jeong KH, Song YJ, Han JY, Kim KU. Relationship between cytogenetic complexity and peritumoral edema in high-grade astrocytoma. *Ann Lab Med* (2016) 36(6):583–9. doi: 10.3343/alm.2016.36.6.583

35. Hong B, Muili K, Bolyard C, Russell L, Lee TJ, Banasavadi-Siddegowda Y, et al. Suppression of Hmgb1 released in the glioblastoma tumor microenvironment reduces tumoral edema. *Mol Ther Oncolytics* (2019) 12:93–102. doi: 10.1016/j.omto.2018.11.005

36. Chen W, Hong L, Hou C, Zong G, Zhang J. Up-regulation of Linc00665 contributes to the progression of glioma and correlates with its mri characteristics. *Am J Transl Res* (2022) 14(5):2988–3002.

37. Zhang S, Su X, Kemp GJ, Yang X, Wan X, Tan Q, et al. Two patterns of white matter connection in multiple gliomas: Evidence from probabilistic fiber tracking. *J Clin Med* (2022) 11(13):1–12. doi: 10.3390/jcm11133693

38. Roux A, Roca P, Edjlali M, Sato K, Zanello M, Dezamis E, et al. Mri atlas of idh wild-type supratentorial glioblastoma: Probabilistic maps of phenotype, management, and outcomes. *Radiology* (2019) 293(3):633–43. doi: 10.1148/radiol.2019190491

39. Woo P, Ho J, Lam S, Ma E, Chan D, Wong WK, et al. A comparative analysis of the usefulness of survival prediction models for patients with glioblastoma in the temozolomide era: The importance of methylguanine methyltransferase promoter methylation, extent of resection, and subventricular zone location. *World Neurosurg* (2018) 115:375–85. doi: 10.1016/j.wneu.2018.04.059

40. Awad AW, Karsy M, Sanai N, Spetzler R, Zhang Y, Xu Y, et al. Impact of removed tumor volume and location on patient outcome in glioblastoma. *J Neurooncol* (2017) 135(1):161–71. doi: 10.1007/s11060-017-2562-1

41. Pallud J, Roux A, Zanello M. Relationship between tumour location and preoperative seizure incidence depends on glioma grade of malignancy. *Epileptic Disord* (2016) 18(1):107–8. doi: 10.1684/epd.2016.0799

42. Paldor I, Pearce FC, Drummond KJ, Kaye AH. Frontal glioblastoma multiforme may be biologically distinct from non-frontal and multilobar tumors. *J Clin Neurosci* (2016) 34:128–32. doi: 10.1016/j.jocn.2016.05.017

43. Aabedi AA, Young JS, Chang EF, Berger MS, Hervey-Jumper SL. Involvement of white matter language tracts in glioma: Clinical implications, operative management, and functional recovery after injury. *Front Neurosci* (2022) 16:932478. doi: 10.3389/fnins.2022.932478

44. Mao Y, Pei Q, Fu Y, Liu H, Chen C, Li H, et al. Pre-treatment computed tomography radiomics for predicting the response to neoadjuvant chemoradiation in locally advanced rectal cancer: A retrospective study. *Front Oncol* (2022) 12:850774. doi: 10.3389/fonc.2022.850774

45. He Z, Mao Y, Lu S, Tan L, Xiao J, Tan P, et al. Machine learning-based radiomics for histological classification of parotid tumors using morphological MRI: A comparative study. *Eur Radiol* (2022) 32(12):8099–110. doi: 10.1007/s00330-022-08943-9

46. Wesdorp NJ, Hellingman T, Jansma EP, van Waesberghe JTM, Boellaard R, Punt CJA, et al. Advanced analytics and artificial intelligence in gastrointestinal cancer: A systematic review of radiomics predicting response to treatment. *Eur J Nucl Med Mol Imaging* (2021) 48(6):1785–94. doi: 10.1007/s00259-020-05142-w

47. Yip C, Landau D, Kozarski R, Ganeshan B, Thomas R, Michaelidou A, et al. Primary esophageal cancer: Heterogeneity as potential prognostic biomarker in patients treated with definitive chemotherapy and radiation therapy. *Radiology* (2014) 270(1):141–8. doi: 10.1148/radiol.13122869

48. Ditmer A, Zhang B, Shujaat T, Pavlina A, Luibrand N, Gaskill-Shipley M, et al. Diagnostic accuracy of mri texture analysis for grading gliomas. *J Neurooncol* (2018) 140(3):583–9. doi: 10.1007/s11060-018-2984-4

49. Hrapșa I, Florian IA, Șușman S, Farcaș M, Beni L, Florian IS. External validation of a convolutional neural network for idh mutation prediction. *Medicina (Kaunas)* (2022) 58(4):526. doi: 10.3390/medicina58040526

50. Guo H, Liu J, Hu J, Zhang H, Zhao W, Gao M, et al. Diagnostic performance of gliomas grading and idh status decoding a comparison between 3d amide proton transfer apt and four diffusion-weighted mri models. *J Magn Reson Imaging* (2022). 56 (6):1834–44. doi: 10.1002/jmri.28211

Frontiers in Oncology

Advances knowledge of carcinogenesis and tumor progression for better treatment and management

The third most-cited oncology journal, which highlights research in carcinogenesis and tumor progression, bridging the gap between basic research and applications to imrpove diagnosis, therapeutics and management strategies.

Discover the latest Research Topics

See more →

Frontiers

Avenue du Tribunal-Fédéral 34
1005 Lausanne, Switzerland
frontiersin.org

Contact us

+41 (0)21 510 17 00
frontiersin.org/about/contact